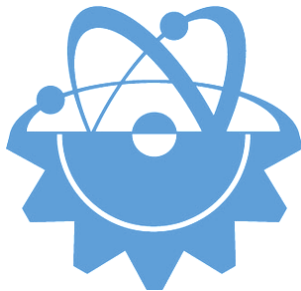


ISSN-Printed: 2536-5010
ISSN-Online: 2536-5134

Volume 13, No 2, 2023

EJT

EUROPEAN JOURNAL OF TECHNIC



Copyright © 2017

International Engineering, Science & Education Group

Email (for orders and customer services enquiries): info@ineseg.org, ejt@ineseg.org

Visit our home page on www.ineseg.org

All Rights Reserved. No part of this publication may be reproduced, stored in a retrieval system or transmitted in any form or by any means, electronic, mechanical, photocopying, recording, scanning or otherwise, except under the terms of the Copyright, under the terms of a license issued by the Copyright International Engineering, Science & Education Group (INESEG), without the permission in writing of the Publisher. Requests to the Publisher should be addressed to the Permissions Department, International Engineering, Science & Education Group (INESEG), or emailed to info@ineseg.org

Designations used by companies to distinguish their products are often claimed as trademarks. All brand names and product names used in this journal are trade names, service marks, trademarks or registered trademarks of their respective owners. The Publisher is not associated with any product or vendor mentioned in this journal.

This publication is designed to provide accurate and authoritative information in regard to the subject matter covered. It is sold on the understanding that the Publisher is not engaged in rendering professional services. If professional advice or other expert assistance is required, the services of a competent professional should be sought.



EUROPEAN JOURNAL OF TECHNIQUE (EJT)

ISSN-Printed: 2536-5010

ISSN-Online: 2536-5134

Scope: European Journal of Technique (EJT) established in 2010. It is a peer –reviewed international journal to be of interest and use to all those concerned with research in various fields of, or closely related to, Engineering disciplines. European Journal of Technique (EJT) aims to provide a highly readable and valuable addition to the literature which will serve as an indispensable reference tool for years to come. The coverage of the journal includes all new theoretical and experimental findings in the fields of Engineering or any closely related fields. The journal also encourages the submission of critical review articles covering advances in recent research of such fields as well as technical notes.

The scopes include:

- Mechanical Engineering
- Textile Engineering
- Electrical-Electronics Engineering
- Computer and Informatics Engineering
- Civil and Architecture Engineering
- Mining Engineering
- Chemical Engineering
- Metallurgical and Materials Engineering
- Environmental Engineering
- Food Engineering
- Geological Engineering
- Industrial Engineering
- Renewable Energy

EDITORIAL BOARD MEMBERS

Editor-in-Chief

- Musa YILMAZ

Publisher Of Journal

- Heybet KILIÇ

ETHICS and POLICIES

European Journal of Technique (EJT) is committed to following the Code of Conduct and Best Practice Guidelines of COPE (Committee on Publication Ethics). It is a duty of our editors to follow Cope Guidance for Editors and our peer-reviewers must follow COPE Ethical Guidelines for Peer Reviewers. We expect all prospective authors to read and understand our Ethics Policy before submitting any manuscripts to our journals.

Please note that submitted manuscripts may be subject to checks using the iThenticate service, in conjunction with CrossCheck, in order to detect instances of overlapping and similar text.

The [iThenticate](#) software checks submissions against millions of published research papers, documents on the web, and other relevant sources. If plagiarism or misconduct is found, consequences are detailed in the policy.

The chief goal of our policy is threefold: to provide advice for our authors, to maintain the scholarly integrity of our journals and their content, and to detail the ethical responsibilities of EJT, our editors and authors.

We expect all authors to read and understand our ethics policy before submitting to any of our journals. This is in accordance with our commitment to the prevention of ethical misconduct, which we recognise to be a growing problem in academic and professional publications. It is important to note that most incidents of plagiarism, redundant publication, copyright infringement or similar occur because of a lack of understanding, and not through fraudulent intent. Our policy is one of prevention and not persecution.

If you have any questions, please contact the relevant editorial office, or European Journal of Technique (EJT)' ethics representative: ejtineseg@gmail.com

Download a PDF version of the Ethics and Policies [PDF,392KB].

Authors' Responsibilities

Authors should:

- Ensure that all researched work submitted is original, fully referenced and that all authors are represented accurately. The submission must be exclusive and not under consideration elsewhere.
- Provide accurate contact details for a designated corresponding author, who shall be deemed by the publisher and editor as fully responsible for the authorship of the paper and all communications concerning the ethical status and originality of the paper. This includes any queries or investigations that may arise, pre- or post publication.
- Openly disclose the source of all data and third party material, including previously unpublished work by the authors themselves. Anything that could compromise the originality of the submission should be expressly avoided and/or discussed with the editorial office in the first instance.
- Identify any third party material that they intend to include in their article, and obtain written permission for re-use in each instance from the relevant copyright holders. Such permissions should be submitted once the manuscript is accepted, or requires small changes to be accepted. For further guidance on seeking permission to use 3rd party material please see the Rights and Permissions section.
- Openly disclose any conflict of interest - for example, if publication were to benefit a company or services in which the author(s) has a vested interest.

- Expect to formally agree publication terms which defines the author and the publishers rights for the work. Visit our website for further information.
- Expect the editor to scan submissions using plagiarism detection software at [iThenticate](#) to check a paper's originality before sending out for review.
- Fully correspond and comply with the editor and publisher in any requests for source data, proof of authorship or originality in a timely manner, providing reasonable explanation for discrepancies or failures to disclose vital information.
- Fully co-operate with any consequent investigations if the editor and/or publisher are dissatisfied with the evidence available or the explanations provided.
- Expect transparency, efficiency and respect from the publisher and the editor during the submissions process.
- Remain in good communication with both the publisher and the editor.
- When necessary, submit corrigenda in a timely and responsible fashion.
- Co-operate fully with the publication of errata and with the retraction of articles found to be unethical, misleading or damaging.
- Remain in good communication with the editor(s), the publisher and any co-authors.

Editors' Responsibilities

Editors should:

- Read and understand COPE guidelines as well as EJT's ethics policy, and follow them during all editorial processes.
- Protect the reputation of their journal(s) and published work by only publishing content of the highest quality and relevance in a timely and responsible manner.
- Carry out thorough, objective and confidential peer review for original article submissions that pass the initial quality check and editorial assessment, in adherence with COPE guidelines and EJT' ethics policy.
- Detail and justify any article types which will not be peer reviewed (e.g. editorials, opinion pieces etc.).
- Provide a transparent review and publication process as far as is possible, with full respect and care paid to the author(s).
- Provide advice and give reasonable explanation and updates to authors during the submissions process and once a decision has been made.
- Allow authors the right to appeal any editorial decision.
- Only accept papers based on the original merit, quality and relevance of their content.
- Support authors in queries concerning the originality of their submissions and request the support of EJT if necessary.
- Advise the publisher of any third party material which has been included for which they do not believe sufficient permission has been cleared.

- Be ready and prepared to publish corrections, corrigenda, errata when necessary, as well as retract articles that (the editor and EJT) deem unethical, misleading or damaging.
- Remain in good communication with both the publisher and the author(s).

Reviewers' Responsibilities

Reviewers should:

- Adhere to EJT's policy of confidential peer review of their journals. This includes, but is not restricted to, keeping their identity hidden from authors and not externally distributing any work that is passed to them for their eyes only.
- Only accept invitations to review work that is relevant to their own expertise and speciality.
- Review submitted work in a responsible, impartial and timely manner.
- Report any suspected ethical misconduct as part of a thorough and honest review of the work.
- Avoid the use of unnecessarily inflammatory or offensive language in their appraisal of the work.
- Accept the commitment to review future versions of the work and provide 'follow up' advice to the editor(s), if requested.
- Seek advice from the editor if anything is unclear at the time of invitation.
- Remain in good communication with both the publisher and the editor.

EJT's Responsibilities

EJT will:

- Protect the reputation of our journals and published work by only publishing content of the highest quality and relevance in a timely and responsible manner.
- Provide detailed information concerning both our understanding of publication ethics and our implementation of the same. Emphasise a desire for prevention, not eventual detection, of ethical misconduct.
- Uphold our COPE membership (or of such similar organisations) and keep our editorial offices, publishing staff and society partners up-to-date with their guidelines and policies, adapting our own where appropriate (and publicising any update).
- When necessary, request proof of originality/accuracy from the corresponding author of any work submitted to any of our journals.
- Use plagiarism detection software when necessary for any submission to any journal at any stage of the submissions and publication process.
- Provide a transparent submissions and publication process, with full respect and care paid to the author. This includes detailed and dedicated instructions to authors for each journal, outlining referencing style, accepted article types and submission processes.
- Investigate thoroughly any suggestion of ethical misconduct detected during any stage of the submissions process. This can include, but is not restricted to, the following: plagiarism, redundant publication, fabrication or misuse of data and authorial disputes.

- When necessary, retract articles that we deem to be unethical, misleading or damaging.
- When necessary, publish errata, corrigenda and retractions in a timely and responsible fashion, detailing the decision online in an open access format and publishing in print as soon as possible.
- Remain in good communication with editors, authors, reviewers and society partners (where applicable).

Further reading

- Authorship of the paper: Authorship should be limited to those who have made a significant contribution to the conception, design, execution, or interpretation of the reported study.
- Originality and plagiarism: The authors should ensure that they have written entirely original works, and if the authors have used the work and/or words of others that this has been appropriately cited or quoted.
- Data access and retention: Authors may be asked to provide the raw data in connection with a paper for editorial review, and should be prepared to provide public access to such data.
- Multiple, redundant or concurrent publication: An author should not in general publish manuscripts describing essentially the same research in more than one journal or primary publication. EJT do not view the following uses of a work as prior publication: publication in the form of an abstract; publication as an academic thesis; publication as an electronic preprint. Information on prior publication is included within each EJT and its journal Guideline for Authors.
- Acknowledgement of sources: Proper acknowledgment.
- Disclosure and conflicts of interest: All submissions must include disclosure of all relationships that could be viewed as presenting a potential conflict of interest.
- Fundamental errors in published works: When an author discovers a significant error or inaccuracy in his/her own published work, it is the author's obligation to promptly notify the journal editor or publisher and cooperate with the editor to retract or correct the paper.
- Reporting standards: Authors of reports of original research should present an accurate account of the work performed as well as an objective discussion of its significance.
- Hazards and human or animal subjects: Statements of compliance are required if the work involves chemicals, procedures or equipment that have any unusual hazards inherent in their use, or if it involves the use of animal or human subjects.
- Use of patient images or case details: Studies on patients or volunteers require ethics committee approval and informed consent, which should be documented in the paper.

EJT has also accessed and learned from the existing policies of other publishers and leading experts as well as open access articles that detail and define ethical misconduct.

- 'Plagiarism and the law', Joss Saunders, Learned Publishing, 23:279-202: <http://www.ingentaconnect.com/content/alpsp/lp/2010/00000023/00000004/art00002>
- iThenticate Plagiarism Resources: <http://www.ithenticate.com/resources/6-consequences-of-plagiarism>

EDITORIAL BOARD MEMBERS

Editor-in-Chief : Musa Yilmaz, University of California Riverside, US

International Editorial Board

Aayush Shrivastava University of Petroleum and Energy Studies, Dehradun, India
Abdulkerim Oztekin Batman University, Batman, Turkey
Adelino Pereira Engineering Institute of Coimbra, Portugal
Ahmad Fakharian Islamic Azad University, Qazvin, Iran
Ahmed Saber Cairo University, Egypt
Arvind Kumar Jain Rustam Ji Institute of Technology, India
Aydogan Ozdemir Istanbul Technical University, Turkey
Baseem Khan Hawassa University, Hawassa, Ethiopia
Behnam Khakhi University of California Los Angeles, US
Behnam Mohammadi-ivatloo University of Tabriz, Tabriz, Iran
Bharti Dwivedi Institute of Engineering & Technology, Lucknow, UP, India
Carlos A. Castro University of Campinas – UNICAMP, Brasil
Cafer Budak Dicle University, Turkey
Deepak Kumar University of Petroleum & Energy Studies (UPES), India
Ernesto Vazquez University of Nuevo Leon, Mexico
Faisal Khan COMSATS Institute of Information Technology, Pakistan
Farhad Shahnia Murdoch University, Perth, Australia
Farrokh Aminifar University of Tehran, Iran
Fatih Kocyigit Dicle University, Turkey
Fiaz Ahmad National University of Computer and Emerging Sciences, Pakistan
Gouthamkumar Nadakuditi V R Siddhartha Engineering College, India
Hafiz Ahmed School of Mechanical, Coventry University, UK
Hamed Pourgharibshahi Lamar University, US
Hassan Bevrani University of Kurdistan, Iran
Hayri Yildirim Dicle University, Turkey
Hemant Kumar Gianey Thapar University, Patiala, Punjab, India
Hessam Golmohamadi Semnan University, Semnan, Iran
Heybet Kilic Dicle University, Turkey
Hilmy Awad Helwan University, Cairo, Egypt
Hüseyin Acar Dicle University, Turkey
Idris Candan Kocaeli University, Turkey
Jamshed Ahmed Ansari Sukkur IBA University, Pakistan
José A. Domínguez-Navarro University of Zaragoza, Spain
Kalpana Chauhan Galgotias College of Engineering and Technology, India
Khaled Ellithy Qatar University, Doha, Qatar
Kim-Doang Nguyen South Dakota State University, US
Kundan Kumar KIIT University, India
Lalit Kumar GBPIET Pauri, India
Leila Mokhnache University of Batna 2, Algeria
Linqun Bai ABB Inc., US
Mehmet Emin Asker Dicle University, Turkey
Md Shafiqullah King Fahd University of Petroleum & Minerals, Saudi Arabia
Mohamed Shaaban Universiti Malaysia Sarawak, Malaysia
Mohammed Albadi Sultan Qaboos University, Oman
Mohd Tariq Aligarh Muslim University, India
Mousa Marzband Northumbria University, Newcastle upon Tyne, United Kingdom
Necmettin Sezgin Batman University, Batman, Turkey
Neeraj Kanwar Manipal University Jaipur, India
Nishant Kumar Indian Institute of Technology Delhi, India
Nitin Kumar Saxena Wolaita Sodo University, Ethiopia
Nouar Tabet University of Sharjah, UAE
Omar Hafez Umm Al-Qura University, Makkah, Saudi Arabia
Omveer Singh Gautam Buddha University, India
Payam Teimourzadeh Baboli University of Mazandaran (UMZ), Iran
Payman Dehghanian George Washington University, US
Ragab A. El Sehiemy Faculty of Engineering, Kafrelsheikh University, Egypt
Rajeev Kumar Chauhan Galgotias College of Engineering and Technology, India
Rajiv Singh G.B. Pant University of Agriculture & Technology, India
Reza Sharifi Amir Kabir University Tehran, Iran
Rudranarayan Senapati Kalinga Institute of Industrial Technology, India
Saleh Y. Abujarad Universiti Teknologi Malaysia, Malaysia
Sanjay Dambhare College of Engineering, Pune, India
Saptarshi Roy NIT Warangal, India
Shailendra Kumar Indian Institute of Technology Delhi, India
Shariq Riaz The University of Sydney, Australia
Shengen Chen University of Maine, US
Syafaruddin Universitas Hasanuddin, Indonesia
T. Sudhakar Babu VIT University, Vellore, India
Thamer Alquthami King Abdulaziz University, Saudi Arabia
Theofilos Papadopoulos Democritus University of Thrace, Greece
Uday P. Mhaskar CSA Group, US
Vedat Veli Cay Dicle University, Turkey
Yogesh Rohilla K Lakshmi Pat University, Jaipur, India
Yunfeng Wen School of Electrical Engineering, Chongqing University, China
Zbigniew M. Leonowicz Wroclaw University of Science and Technology, Poland

Publisher of Journal

Heybey Kilic Dicle University, Turkey / Aalborg University, Denmark



CONTENTS

1 Determination of Condensation and Its Effect On Insulation and Wall Envelop Layers	Research Article	68-73
2 STATCOM Application to Increase Voltage Stability of Wind Farms	Research Article	74-80
3 Capacitated Network Traffic Assignment using Lagrange Neural Networks	Research Article	81-87
4 Production of CuNiSi Composites by Powder Metallurgy Method: Effects of Ti on the Microstructural and Corrosion Properties	Research Article	88-93
5 ICT-Based Vehicle-to-Grid Operation Based on the Fast Discharge Power for Economic Value	Research Article	94-100
6 Twin Rotor Control via Second Order Sliding Modes	Research Article	101-107
7 Detection of Shadow IT Incidents for Centralized IT Management in Enterprises using Statistical and Machine Learning Algorithms	Research Article	108-115
8 Multilayer LSTM Model for Wind Power Estimation in the Scada System	Research Article	116-122
9 Design and Testing of a Wireless Communication Enabled FPGA Development Board: A Comprehensive Education and Application Platform from IoT to Circuit Design	Research Article	123-129
10 Data Management and Ontology Development for Provenance-Aware Organizations in Linked Data Space	Research Article	130-141
11 Performance Evaluation of Capuchin Search Algorithm Through Non-linear Problems, and Optimization of Gear Train Design Problem	Research Article	142-149
12 Comparison of Road Luminance Data Estimated by Fuzzy Logic and ANN, A Case study of Kocaeli Sakıp Sabancı Street	Research Article	150-158
13 The Investigation Of Performance And Emission Characteristics Of Waste Transmission Oil On A Diesel Engine	Research Article	159-163
14 Changes in the Electrical Output Power and Efficiency of a Photovoltaic Panel Cooled by a Hybrid Method	Research Article	164-173
15 Determining the Advantages of a Linear Driven 3-Axis Industrial Robot by Structural and Force Analysis	Research Article	174-183
16 MATLAB/Simulink Modeling of Regenerative Recovery Circuit with Bidirectional DC-DC Converter for Scooter	Research Article	184-190
17 Investigating the Impact of Hydrogen Gas Moisture Content on Electricity Generation in PEM Fuel Cells	Research Article	191-196
18 Leakage-Free Wood-Derived Activated Carbon/Methyl Palmitate Composite Phase Change Material for Thermal Management Applications	Research Article	197-201
19 Experimental Investigation of the Effect of Curing Pressure on Strength of Single Lap Adhesive Joints	Research Article	202-206
20 Consistency Axioms of Choice for Ismail's Entropy Formalism(IEF) Combined with Information-Theoretic(IT) Applications to advance 6G Networks	Research Article	207-213
21 The SMaRt: Design, implementation, and experiment	Research Article	214-223
22 A Deep Learning Approach for Motor Fault Detection using Mobile Accelerometer Data	Research Article	224-228
23 Artificial Intelligence-Based Tools in Software Development Processes: Application of ChatGPT	Research Article	229-240
24 Leader-Follower Based Formation Control of Heterogeneous UAV-AGV Multi-Agent System	Research Article	241-248
25 Investigating the Relationship between Chuck and Tailstock Pressure in Turning by Using Full Factorial Design	Research Article	249-255
26 Determination of Winding Deformations in Power Transformers by Sweep Frequency Response Analysis and a Sample Field Study	Research Article	256-264

Research Article

Determination of Condensation and Its Effect On Insulation and Wall Envelop Layers

Selman Çağman¹, Ümit Ünver²

¹Kocaeli University, Energy Systems Engineering Department, Umuttepe, 41380, Kocaeli, Turkey. (e-mail: selman.cagman@gmail.com).

²Yalova University, Engineering Faculty, Yalova Turkey, Czech Technical University in Prague, Prague Czech Republic. (e-mail: umitunver@gmail.com)

ARTICLE INFO

Received: May., 11. 2023
Revised: Jul., 25. 2023
Accepted: October, 06. 2023

Keywords:

Interstitial condensation
Freeze-thaw
Moisture condensation
Building envelope
Glaser diagram

Corresponding author: Selman Çağman

ISSN: 2536-5010 / e-ISSN: 2536-5134

DOI: <https://doi.org/10.36222/ejt.1295570>

ABSTRACT

The condensation, occurs between the building envelope layers, is important for both human health and the functioning of the layers. Freezing of the condensed water in cold weather regions like 3rd degree-day locations means another solid layer that creates freeze-thaw effect. In this study, the amount of condensation between layers for 3 wall types is investigated in Kütahya. The condensation phenomena are determined by Glaser Diagram Method and the condensation amount is calculated by considering climatic data. Wall 3 gives the best result and that one has 0.001696833 kg/h.m² at 0 °C, it is 0.002142743 kg/h.m² at -21 °C condensed water amount due to low outside temperature.

1. INTRODUCTION

Energy efficiency studies especially in buildings became popular after the European Green Deal is signed in developed countries [1]. The energy consumption in the building sector constitutes nearly 30% of the total global energy consumption [2]. Therefore, there is a huge potential to reduce energy consumption in buildings with energy efficiency studies [3]. One of the main application in a building is insulation to minimize the heat losses. It is calculated that 80% of the energy is consumed for heating, and cooling in buildings [4] so insulation is a common way to reduce the energy bill for a building envelope. Additionally, proper insulation might be used against condensation. The air in a room hits a surface with a temperature below its dew point; the water vapor in the air condenses and causes surface condensation. Condensation causes problems, such as mold, corrosion, material wetting, icing, and warping, and indoor condensation must be minimized [5]. Average temperatures are considered while insulating but the temperatures might drop below the seasonal average. This leads to condensation between the building envelopes layers especially at cold weather [6]. Condensation between the layers causes mold formation between the external wall layers and resulted in a poor performance of the insulation material [7]. When the insulation loses its characteristic, heat

loss and more condensation take place. The number of layers in the building envelope also brings the risk of condensation [8]. Insufficient or damaged insulation will let water vapor diffusion between wall layers. Organic thermal insulation materials such as expanded polystyrene (EPS) and extruded polystyrene (XPS) are used in buildings as they have low thermal conductivity and low cost. The given materials are likely to be affected by severe cold weather conditions [9, 10] such as freeze-thaw due to water vapor. As temperature goes below zero, the water turns into ice and expands by 9% in volume [11, 12] and the frost-heaving force will cause the destruction of insulation material and/or other layers. In a study, the variation of the insulation thickness was analyzed in Bitlis and it was found out that as the relative humidity differs, the risk of condensation on the wall also increases. Another outcome was the ice applies a push force on the insulation and plaster. This repulsion could cause space between these envelop layers in time. This gap also resulted in the external plaster or insulation to shed [13]. It was proved in another study that freeze-thaw and temperature-drop occurred mainly in the thermal insulation layer. In addition, the annual energy consumption of the insulation system with freeze-thaw was calculated as on average 1 kWh/m² of surface area higher than that without freeze-thaw [14]. In cold regions, the surface of concrete structures is prone to ice and snow, leading to serious

freeze-thaw damage [15] and the damage caused by freeze-thaw cycles can lead to a reduction in the compressive and tensile strength of the concrete [16]. In some studies, various materials are tried as insulation material like hydrophilic mineral wool. Performance of a concrete building envelope was analyzed for freezing cycles during the five-year period. Hydrophilic mineral wool material presented the most prospective solution for the thermal insulating layer in a building envelope [17]. They made a conclusion to a specific insulation material depending on their analysis, but they did not compare various thickness layers of insulation material. Some other studies concentrated on the freeze-thawing damage and effects on building thermal physical parameters and energy consumption. The expanded polystyrene (EPS) was numerically analyzed as an exterior surface of the envelope. One of the results showed that the freezing of the moisture in the building envelope would affect the insulation performance seriously. EPS was analyzed but the behavior of the insulation at various temperatures should have been included to this study [18]. Additionally, an interesting study was made on concrete to modify the concrete's water resistance. It was stated that the strength of this new concrete was only reduced by 12% after 20 freeze-thaw cycles, showing a far better result than traditional cement concrete. Thus, laboratory modified concrete can be used as a good insulation material for frost resistant buildings. This composite looks preferable on a laboratory scale trial, but the economic feasibility of this new composite concrete is needed to be assessed in details. Both investment and operational cost comparison with traditional insulation materials should be done to be able to make a decision [19]. Some recent studies also proposed that freeze-thaw could cause degradation of thermal and mechanical properties of insulation and even malfunction during severe weather conditions. Some modern insulation materials have been developed such as closed cell foam, vacuum insulation panel (VIP), gas filled panel, aerogel, and phase change materials with higher and better performance comparing with traditional ones [20, 21, 22]. Silica aerogel products are often mentioned as promising materials to increase the thermal resistance of the building envelope [23]. Existing studies are concentrated on the investigation of the effects of newly developed materials at the external wall layers [24]. However, considering the climate data, the amount of condensed and frozen water, different layers, and various temperature effects is missing in this study. This paper highlights all these points with the free-thaw problem. To achieve this aim, three different wall envelopes are analyzed with Glaser Diagram Method. The calculations are compared for three options and the best performance is identified. A formula is created from various outside temperatures for this best wall envelope to calculate the amount of condensed water amount in Kütahya for a specific outside temperature. Annual temperature data of Kütahya in 2020 is analyzed and used in this study. This study presents a new formula to calculate condensed water amount due to temperature differences between building enveloped layers. This study can be applicable for another location if the temperature data is known, which makes this paper valuable in terms of sharing knowledge.

2. MATERIAL AND METHOD

In this study, three types of wall envelopes are used and these envelopes can easily be seen in Kütahya. All three walls

have the same insulation material (5 cm thick XPS panel) with a conduction coefficient of 0.03W/mK. Initially, walls are assessed to determine the condensation level to find out the best one.

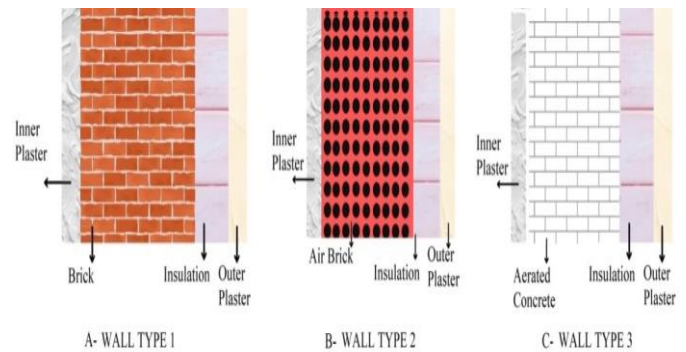


Figure 1. Wall envelope layers

Wall 1: In this wall type, the masonry brick is used before energy efficiency studies started. The wall is given in Figure 1A and the brick thickness is 0.135 m. Wall 2: After the increase in the use of perforated bricks in the 70s, thermal insulation of buildings using such walls are tried to prevent thermal leaks. The wall component using this brick type is shown in Figure 1B and the air brick thickness is 0.19 m. Wall 3: In recent years, aerated concrete has been preferred due to its thermal advantages. Aerated concrete material is very good in thermal insulation thanks to its porous structure. However, the porous structure also increases the mass transfer. The aerated concrete wall is shown in Figure 1C and the aerated concrete thickness is 0.2 m.

2.1 Detection of the Critic Temperatures for Condensation Analysis in Each Wall Type with Glaser Diagram Method

In this method, first the wall surface temperatures in the intermediate layers and then the condensation amount between the wall layers are calculated. The calculation method is explained in [25, 26]. Additionally, the equations of energy and mass conservation for heat and mass transfer through the walls can be found in [27, 28]. Each wall layer's surface temperatures are calculated and then the water vapor partial humidity at the surface of each layer is determined by equation 1 and 2 [29].

$$\text{If } T < 0 \quad P_s = 610.5 \cdot e^{\left(\frac{21.875 \cdot T}{265.5 + T}\right)} \quad (1)$$

$$\text{If } T \geq 0 \quad P_s = 610.5 \cdot e^{\left(\frac{17.269 \cdot T}{237.3 + T}\right)} \quad (2)$$

As addressed in several literature, water vapor flows is through a material from a high pressure to a low pressure, or the warm side to a cold side of a wall. There will be condensation between the wall layers especially at the insulation layer. This liquid layer may freeze and increase in volume when the air temperature drops below 0 °C, especially in cold climates like 3rd and 4th degree-day zones in Turkey [30, 31]. This volume increase occurs as expansion in the direction in which the layer can do. Figure 2 shows an example for solidification expansion of unit area.

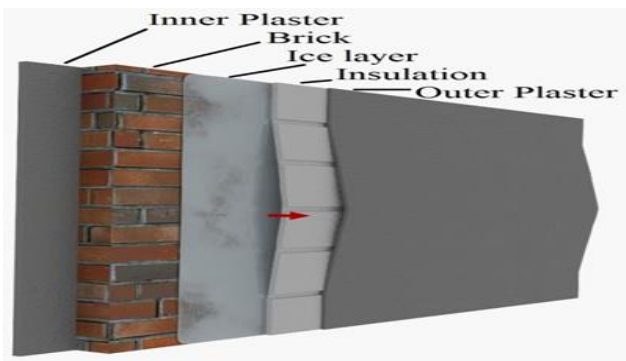


Figure 2. The ice layer that formed between layers of wall

The expansion caused by the freezing of the condensed water layer creates a thrust on the insulation and plaster layers. The thrust can be described by the deflection (displacement) that occurs in the insulation layer. This displacement can escalate as the condensed water amount increases, which can be calculated by equation (3).

$$dV = A \cdot dx. \quad (3)$$

The change in the x-direction per unit area is calculated with Eq. 4 as the volume is a function of mass;

$$dx = \frac{\dot{m} \cdot \Delta\rho}{A}. \quad (4)$$

Here, \dot{m} is the condensation amount in (kg/h). $\Delta\rho$ is the density difference of the condensing fluid. A is the unit area is 1 (m^2) and dx is the thrust applied to the insulation layer in one hour by the freezing fluid in (mm/h). Finally, the hourly condensed water amount can be calculated by Eq. (5) [32, 33].

$$\dot{m} = \delta_0 \left(\frac{p_i - p_{sw}}{S_{d,T} - S_{d,sw}} - \frac{p_{sw} - p_d}{S_{d,sw}} \right). \quad (4)$$

Here, P_i is partial pressure of water vapor at inner surface of the wall (Pa), P_d is partial pressure of water vapor at inner surface of the wall (Pa), P_{sw} is the partial pressure of water vapor where condensation begins (Pa). δ_0 is the water vapor permeability, which is assumed to be constant 2.10-10 (kg/msPa) [34]. $S_{d,sw}$ is the permeance of the wall layers where condensation begins and $S_{d,T}$ is the total permeance of the wall. $S_{d,T}$ can be calculated by using Eq. (6);

$$Sd = \mu \cdot d. \quad (6)$$

μ is the vapor diffusion resistance factor and d is the thickness of the layer (m).

3. RESULT AND DISCUSSION

The condensed water amount is needed to be determined so the thickness and thrust of the ice can be assessed. This calculation is done for three wall types separately with Glaser Diagram Method and Figure 3, Figure 4 and Figure 5 illustrate the results of sthis methodology. In this method, the blue lines

in the figures are theoretical saturation pressure of vapor passing through the wall. The dots on the broken red line illustrate the partial pressure of water vapor at layer surfaces. If the red dot touches the blue line, that means the pressure drops below saturation pressure and condensation begins. In Wall 1, standard masonry brick type is selected. The critical outside temperature is 0°C and the relative humidity both indoor and outdoor is taken 80%. Masonry brick is commonly used in construction in Turkey. It is seen that condensation begins outside the insulation from 0°C. It can also be stated that the amount of condensation increases as the atmospheric temperature decreases (Fig. 3).

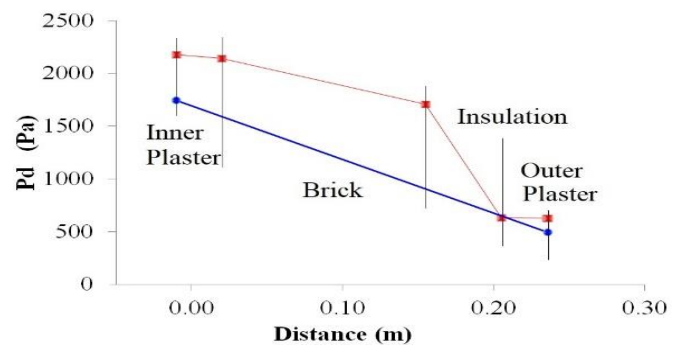


Figure 3. Internal condensation analysis for Wall 1 at 0°C, $\phi_{in} = \phi_{out} = 0.8$

Wall 2 (air brick) is also widely used in construction. The analysis showed that Wall 2 has also condensation (Fig. 2).

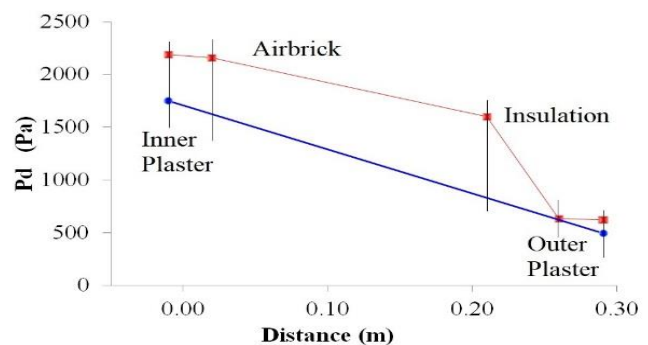


Figure 4. Internal condensation analysis for Wall 2 at 0°C, $\phi_{in} = \phi_{out} = 0.8$

In some buildings, aerated concrete component (Wall 3) with a lower heat transfer coefficient is also preferable. Wall 3 has condensation at the outer side of the insulation where the conditions are the same with Wall 1 and Wall 2. In all 3 cases, condensation below 0°C means that the condensed water vapor freezes and affects the insulation layer performance. Water vapor begins to occupy space between the layers once the condensation starts freezing.

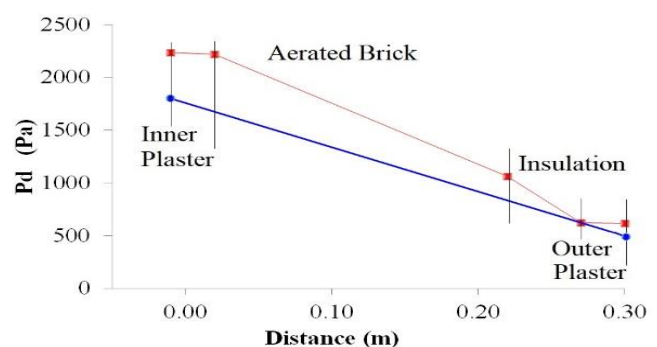


Figure 5. Internal condensation analysis for Wall 3 at 0°C, $\phi_{in} = \phi_{out} = 0.8$

All analysis proved that there will be a solid layer of ice which is not considered while choosing the insulation material or the thickness of the insulation material. The ice layer deforms the insulation material and pushes the insulation layer, resulting in displacement. It can also be said that as the indoor humidity increases, the condensation intensity also increases. Controversially, an increase in the relative humidity of the outdoor environment causes a decrease in the condensation amount. Another factor that increases the condensation between the building envelope layers is the outdoor temperature drop. A decrease in atmospheric temperature increases condensation [35]. Among all envelopes, Wall 3 gives the best results, as it has the least water condensation amount. This analysis is done for 0 °C ambient temperature, the temperature goes further below zero in Kütahya. In order to check the condensed water amount, the above calculations for various outside temperature level from 0 °C to -21 °C is done for Wall 3. Results are presented in Table 1.

TABLE 1.

Condensed water amount related to ambient temperature	
Ambient Temperature	Condensed Water Amount
0	0,001696833
-1	0.001742621
-2	0.001784777
-3	0.00182354
-4	0.001859133
-5	0.00189177
-6	0.001921647
-7	0.001948954
-8	0.001973866
-9	0.001996549
-10	0.002017157
-11	0.002035837
-12	0.002052725
-13	0.002067949
-14	0.00208163
-15	0.00209388
-16	0.002104803
-17	0.002114498
-18	0.002123056
-19	0.002130564
-20	0.002137102
-21	0.002142743

These values (Table 1) put into a curve fitting given at Figure 6 and a formula created to use for a Wall 3 type building in Kütahya.

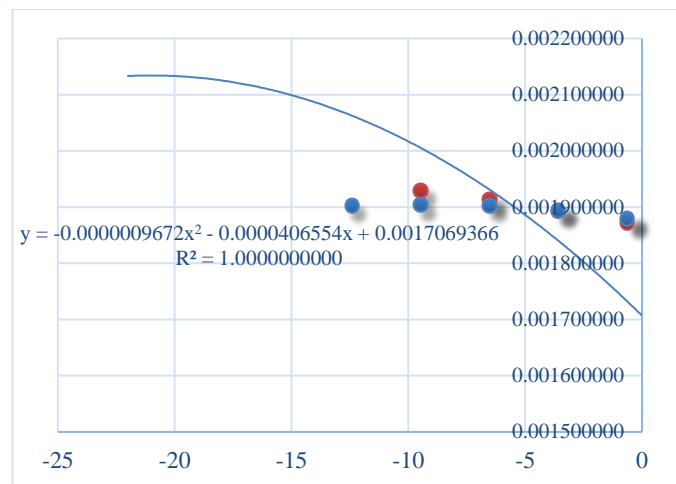


Figure 6. Curve fittings for various temperature values

This formula can be used to find the amount of condensed water at a specific outside temperature for a Wall 3 type enveloped building in Kütahya.

$$y = -0.0000009672x^2 - 0.0000406554x + 0.0017069366 \quad (7)$$

In this equation y stands for condensed water amount, and x stands for the outside temperature. The condensed water freezes under severe weather conditions and create a solid layer. This layer stays on the cold site of the insulation and negatively affect the insulation. In a specific time, the condensed water amount between the enveloped layers at the Wall 3 buildings can be calculated with this equation (Eq. 7). As it is given in Table 1 and Figure 6, the condensed water amount increases as the outside temperature drops.

In existing literature, there are some studies mentioning the negative affect of cold weather conditions on insulation material but this paper created a formula to calculate the condensed water amount. Recent studies mentioned that condensed water turns into ice and ice pushes the insulation and plaster. This study results show same results with these researches. In this paper, three different wall types are analyzed and one of them represent a better result in condensed water amount. Having compared three wall options make the study findings valuable. In other studies, different insulations materials or various thickness of insulation materials are studied but there is no formula given in these papers. In this study, a formula is created to calculate the condensed water amount for a very common building envelope in Kütahya.

4. CONCLUSION

Insulation of a building for the purpose of lesser the energy consumption content is a widely accepted application in nowadays. However, analyzing the condensed water due to drastic temperature drops between buildings envelop layers is the next era for building energy efficiency studies. The effect of insulation thickness on water condensation amount is not the main perspective of this research. It is known that there will some condensation and this condensed water might freeze but there is no direct formula to find the condensed water amount between envelop layers. In this paper, condensation analysis is made with Glaser Diagram Method. Results are compared and Wall 3 gives the best insulation performance in terms of condensed water amount. Wall 3 is taken as an example to

generate condensation water amount at below zero temperatures. The amount of water is calculated as $0.001696833 \text{ kg/h.m}^2$ at 0°C , and it is $0.002142743 \text{ kg/h.m}^2$ at -21°C . The created formula will help engineers to find the condensed water amount for a Wall 3 type building in Kütahya. The condensation has been observed even when the external ambient relative humidity is 50% in the buildings using masonry bricks. Here it can also be stated that as the indoor and outdoor relative humidity increases, the amount of condensation increases. In addition to the traditional insulation materials, a variety of new high performance thermal insulation materials have been developed in recent years like gas filled panel, aerogel, and phase change materials. In this study, traditional insulation material is used. Some other insulation material performance should also be assessed especially the new generation insulation materials like aerogel and/or phase changing material. This study can also be repeated for some other regions for colder conditions with some other building materials. The thickness of the materials that are constructing the building enveloped can be also changed to see the effect of the insulation performance and condensing water amount. Especially, the thickness of the new types of insulation materials effect on condensed water amount is one of the topics that the authors are intending to carry on a further research on.

NOMENCLATURE

EPS	Expanded Polystyrene
Eq.	Equation
kWh	Kilowatt-hour
m^2	Square meter
Pa	Pascal
VIP	Vacuum Insulation Panel
W/mK	Watt/Meter Kelvin
XPS	Extruded Polystyrene

REFERENCES

- [1] N. Buckley, G. Mills, C. Reinhart, and Z. M. Berzolla, "Using urban building energy modelling (UBEM) to support the new European Union's Green Deal: Case study of Dublin Ireland", *Energy and Buildings*, c. 247, p. 111-115, 2021, doi: 10.1016/j.enbuild.2021.111115, 2021.
- [2] H. Erbiyik, T. Catal, S. Durukan, D. G. Topaloglu, and Ü. Ünver, "Assessment of Yalova University Campus According to LEED V.4 Certification System", *Environmental Research and Technology*, c. 4, January, p. 18–28, 2021, doi: 10.35208/ert.812339.
- [3] A. Bahadıroğlu, A. Y. Koç, E. Parlak, N. Larsson, W. Kujawski, and U. Ünver, "Sustainable building evaluation: a case study", *Energy Sources, Part A: Recovery, Utilization and Environmental Effects*, c. 44, sayı 2, ss. 3149–3163, 2022, doi: 10.1080/15567036.2022.2061646.
- [4] U. Ünver, E. Adiguzel, E. Adiguzel, S. Civi, and K. Roshanei, "Application of Thermal Insulation in Buildings by Climate Zones in Turkey", *Journal of Advanced Engineering Studies and Technologies*, c. 1, sayı 2, ss. 171–187, 2020.
- [5] Y. Choi, E. S. Jeong, J. H., Mun, K. H. Yang, S. J. Lee, and H. Lim, "Thermal performance and condensation analysis of insulated concrete panels using a thermal-meta structure", *Applied Thermal Engineering*, 230, 120761. <https://doi.org/10.1016/j.applthermaleng.2023.120761>
- [6] A. Galvin, "Solving mould and condensation problems: A dehumidifier trial in a suburban house in Britain", *Energy and Buildings*, c. 42, sayı 11, ss. 2118–2123, doi: 10.1016/j.enbuild.2010.07.00, 2010.
- [7] A. Torres-Rivas, M. Palumbo, A. Haddad, L. F. Cabeza, L. Jiménez, and D. Boer, "Multi-objective optimisation of bio-based thermal insulation materials in building envelopes considering condensation risk", *Applied Energy*, c. 224, p. 602–614, 2018, doi: 10.1016/j.apenergy.2018.04.079, September, 2017.
- [8] P. L. Simona, P. Spiru, and I. V. Ion, "Increasing the energy efficiency of buildings by thermal insulation", *Energy Procedia*, c. 128, p. 393–399, doi: 10.1016/j.egypro.2017.09.044, 2017.
- [9] N. Belayachi, D. Hoxha, and M. Slaimia, "Impact of accelerated climatic aging on the behavior of gypsum plaster-straw material for building thermal insulation", *Construction and Building Materials*, vol. 125, pp. 912–918, 2016.
- [10] C. Hatipoglu, E. Tosun, Ş. Türkmen, H. Atalay, and Ü. Ünver, "Examination of Internal Condensation in Composite Walls for Different Wall Types", 2022 7th International Conference on Smart and Sustainable Technologies (SpliTech), Split / Bol, Croatia, 2022, pp. 1–6, doi: 10.23919/SpliTech55088.2022.9854319.
- [11] L. Li, D. Li, X. Zhu, K. Zhang, and Y. Mu, "Freeze-thaw resistance of thermal insulating materials used in cold regions engineering: A state-of-the-art review", *Geofluids*, –11. <https://doi.org/10.1155/2022/9015055>, 2022.
- [12] F. Niu, H. Jiang, W. Su, W. Jiang, and J. He, "Performance degradation of polymer material under freeze-thaw cycles: a case study of extruded polystyrene board", *Polymer Testing*, vol. 96, pp. 107067–107068, 2021.
- [13] A. H. Bademlioglu, A. S. Canbolat, ve Ö. Kaynaklı, "Bina Dış Duvarlarında Yoğuşma Dikkate Alınarak Gerekli Yalıtım Kalınlığının Belirlenmesi: Bitlis İli için örnek çalışma", *Uludağ University Journal of The Faculty of Engineering*, 23(3), 333–340. <https://doi.org/10.17482/uumfd.487773>, 2018.
- [14] X. Shen, L. Li, W. Cui, and Y. Feng, "Thermal and moisture performance of external thermal insulation system with periodic freezing-thawing", *Applied Thermal Engineering*, 181, 115920. <https://doi.org/10.1016/j.applthermaleng.2020.115920>, 2020.
- [15] Z. Liu, J. Jiang, X. Jin, Y. Wang, and Y. Zhang, "Experimental and numerical investigations on the inhibition of freeze-thaw damage of cement-based materials by a methyl laurate/diatomite microcapsule phase change material", *Journal of Energy Storage*, 68, 107665. <https://doi.org/10.1016/j.est.2023.107665>, 2023.
- [16] J. Nilimaa, and Z. Vasiola, "An Overview of Smart Materials and Technologies for Concrete Construction in Cold Weather", *Eng 4*, no. 2: 1550–1580. <https://doi.org/10.3390/eng4020089>, 2023.
- [17] V. Kočí, J. Maděra, and R. Černý, "Exterior thermal insulation systems for AAC building envelopes: Computational Analysis aimed at increasing service life", *Energy and Buildings*, 47, 84–90. <https://doi.org/10.1016/j.enbuild.2011.11.030>, 2012.
- [18] F. Kong, and Q. Zhang, "Effect of heat and mass coupled transfer combined with freezing process on building exterior envelope", *Energy and Buildings*, 62, 486–495. <https://doi.org/10.1016/j.enbuild.2013.03.012>, 2013.
- [19] D. Zhong, S. Wang, Y. Gao, L. Wang, and K. Feng, "Experimental study on freeze-thaw resistance of modified magnesium oxychloride cement foam concrete", *Journal of Physics: Conference Series*, 1885(3), 032009. <https://doi.org/10.1088/1742-6596/1885/3/032009>, 2021.
- [20] M. Kayfeci, A. Keçebaş, and E. Gedik, "Determination of optimum insulation thickness of external walls with two different methods in cooling applications" *Applied Thermal Engineering*, 50 (1), 217–224. <https://doi.org/10.1016/j.applthermaleng.2012.06.031>, 2013.
- [21] Y. Sun, Z. Zhao, and X. Li, "A novel aerogels/porous Si₃N₄ ceramics composite with high strength and improved thermal insulation property," *Ceramics International*, v. 44, no. 5, pp. 5233–5237, 2018.
- [22] S. Deng, and H. Zhao, "A Potential Novel Building Insulation Material under Carbon Peaking and Carbon Neutrality Goals: Fully Biomass-Based Aerogel with Enhanced Flame Retardancy", *Science China Press*, 2022.
- [23] A. Lakatos, "Thermal insulation capability of nanostructured insulations and their combination as hybrid insulation systems", *Case Studies in Thermal Engineering*, v. 41, 102630, ISSN 2214-157X, <https://doi.org/10.1016/j.csite.2022.102630>, 2023.
- [24] A. E. Kılıcaslan, and H. Kus, "Evaluation of the hygrothermal performance of external thermal insulation applications on the outer walls of existing buildings", *Journal of the Faculty of Engineering and Architecture of Gazi University*, c. 36, sayı 1, ss. 89–103, doi: 10.17341/gazimmfd.634585, 2021.
- [25] A. H. Bademlioglu, "Duvarlarda Yoğuşma Dikkate Alınarak Yalıtım Kalınlığının Belirlenmesi", *Bursa Uludağ*, 2014.
- [26] A. H. Bademlioglu, A. S. Canbolat, ve Ö. Kaynaklı, "Bina Dış Duvarlarında Yoğuşma Dikkate Alınarak Gerekli Yalıtım Kalınlığının Belirlenmesi Bitlis İli İçin Örnek Çalışma", *Uludağ University Journal of The Faculty of Engineering*, c. 23, sayı 3, ss. 333–340, doi: 10.17482/uumfd.487773, 2018.
- [27] F. Kong, and H. Wang, "Heat and mass coupled transfer combined with freezing process in building materials: Modeling and experimental verification", *Energy and Buildings*, c. 43, sayı 10, ss. 2850–2859, 2011, doi: 10.1016/j.enbuild.2011.07.004, 2011.

- [28] F. Kong, and Q. Zhang, "Effect of heat and mass coupled transfer combined with freezing process on building exterior envelope", *Energy and Buildings*, c. 62, ss. 486–495, doi: 10.1016/j.enbuild.2013.03.012, 2013.
- [29] U.S. Environmental Protection Agency, "Moisture Control Guidance for Building Design, Construction and Maintenance", December, p. 144., 2013.
- [30] V. J. Kočí, J. Maděra, and R. Černý, "Exterior thermal insulation systems for AAC building envelopes: Computational analysis aimed at increasing service life", *Energy and Buildings*, c. 47, ss. 84–90, doi: 10.1016/j.enbuild.2011.11.030, 2012.
- [31] V. Kočí, "Service life assessment of historical building envelopes constructed using different types of sandstone: A computational analysis based on experimental input data", *Scientific World Journal*, doi: 10.1155/2014/802509, 2014.
- [32] İzocam-Türk Standardı, Açıklamalı ve Örneklerle 'TS 825 - Binalarda Isı Yalıtım Kuralları' Standardı, <https://www.izocam.com.tr/>, 2013, [Çevrimiçi]. Available at: https://birimler.dpu.edu.tr/app/views/panel/ckfinder/userfiles/74/files/erbas/ts_825.pdf.
- [33] M. Özel, and N. İ. Beyazıt, "Yalıtımın duvar içerisindeki farklı konumlarına göre yoğuşma analizi", *DÜMF Mühendislik Dergisi*, c. 9, sayı 2, ss. 785–794, [Çevrimiçi]. Available at: <http://dergipark.gov.tr/dumf/issue/38874/458270>, 2018.
- [34] L. Bellia, and F. Minichiello, "A simple evaluator of building envelope moisture condensation according to an European Standard", *Building and Environment*, c. 38, issue 3, p. 457–468, doi: 10.1016/S0360-1323(02)00060-4, 2003.

- [35] I. Nesrin, "Investigation of The Effect of Insulation on Condensation (In Turkish)", M.Sc. Thesis, Firat University, Applied Science Institute. Elazığ, 2019.

BIOGRAPHIES

Selman Çağman holds a BSc degree in mechanical engineering from Uludağ University (2002). He received his MSc. degree in Management from the Manchester Metropolitan University, UK in 2004. He has completed his PhD degree in Graduate School of Science, Mechanical Engineering at Kocaeli University in 2014. He worked for TUBITAK Marmara Research Center as an Senior Researcher between 2007 and 2012. He joined the Faculty of Technology at Energy Systems Engineering Department at Karabük University in 2012. After he has completed his PhD, he moved to Kocaeli University and currently he has been teaching there as Asst. Prof. His expertise are energy efficiency in industry & building & transportation, renewable energy sources, energy conversion from waste, energy production biogas.

Ümit Ünver received M.Sc and Ph.D. degrees from Uludağ University Mechanical Engineering Department, Energy and Thermodynamics division in 2000 and 2004. He has experienced private sector as executive between 2006-2011. He was assigned as Vice Director to Yalova University Applied Research Center. Beginning from 2015 to 2020 he coordinated Yalova city University – Industry collaborations. In 2018 he assigned as Assoc. Prof. to Yalova University Mechanical Engineering department. His study areas are industrial energy efficiency and energy efficiency in buildings, zero energy buildings.



Research Article

STATCOM Application to Increase Voltage Stability of Wind Farms

Abdulfetah Abdela Shobole^{1*}

¹Department of Electrical and Electronics Engineering, Istanbul Sabahattin Zaim University, 34303, Istanbul, Türkiye
(abdulfetah.shobole@izu.edu.tr)

ARTICLE INFO

Received: October 22, 2023

Revised: October 26, 2023

Accepted: October 27, 2023

Keywords:

DFIG Wind Turbine.

DigSILENT;

STATCOM

Corresponding author: *Abdulfetah Abdela SHOBOLE*

ISSN: 2536-5010 / e-ISSN: 2536-5134

DOI: <https://doi.org/10.36222/ejt.1379560>

ABSTRACT

The integration ratio of wind farms to the grid is increased tremendously derived by the need for cleaner and renewable energy. However, the stability of the grid is a major concern due to large wind and other renewable resource-based power plants. Thus, wind turbine generators must adhere to the regulations of other conventional forms of generation. To boost stability, especially voltage-based, Flexible AC Transmission Systems such as Static Var Compensators (SVC) or Static Synchronous Compensator (STATCOM) are put in the vicinity of the wind farm's connection point to the grid. This study is intended to model and simulate dynamically a wind farm using the Doubly Fed Induction Generator (DFIG) turbine type and STATCOM under faulty conditions. The dynamic equation of turbine aerodynamics, drive train, pitch angle controller, frequency controller, and doubly-fed induction machine is provided in this study. Furthermore, STATCOM is also modeled. The aggregated modeling approach is used to model the wind farm. The models are implemented inside the DigSILENT Power Factory simulation tool. The results show that STATCOM can improve the voltage stability of wind farms at the point of connection to the grid.

1. INTRODUCTION

The wind is among the renewable energy sources that has matured technology. Wind turbines are used to convert the kinetic energy of the wind to electrical energy. Wind turbines are available in a variety of technologies and sizes. Both Fixed-speed and Variable-speed wind turbines have been used in large-scale wind farms. The variable speed type wind turbines are more efficient and common. Under variable speed category Doubly Fed Induction Generator (DFIG) and Permanent Magnet Synchronous Generator (PMSG) technologies of wind turbines are very common and usable in large-scale MW wind farms.

As wind is available almost everywhere and again derived by the renewable energy demand, the wind power plant ratio in the power system is steadily increasing. Due to variations in wind speed from time to time, its output is not like conventional power generation systems. In addition, it consumes reactive power when connected to the grid. The fault may cause wind turbine generators to trip due to grid voltage drop below the set limit, furthermore, large-scale wind farm tripping can result then severe system oscillation aggravating the transient instability. This will affect the power quality and stability of the grid if it is not compensated for and handled accordingly. In addition to mitigation of problems caused by wind farms, compensation of reactive power can improve the utilization of the equipment, efficiency of

transmission line, and the power quality. After clearance of the fault, wind generators require large amounts of reactive power. If this is not available, the machine speeds out of control and the protection system disconnects it from the power system [1-2]. If the wind power plant is small, the capacity loss may be acceptable, but large wind farms are subject to Grid Code which requires them not to disconnect easily. The grid code requires them not to be disconnected for specified voltage and power conditions based on the strength or weakness of the system. It is now possible to meet the grid code and increase system stability by utilizing FACTS controllers like SVCs, STATCOMs, and Unified Power Flow Controllers (UPFCs) [3-4].

The majority of STATCOMS are voltage source converters with appropriate energy storage systems, such as batteries, fuel cells, flywheel storage, supercapacitors, etc., that have substantial capacity for power modulation.

This work discusses the compensation of the wind farm by using STATCOM. The STATCOM has the following advantageous:

- It can ensure minimal losses while transmitting the electrical energy generated to the main grid by maintaining the voltage profile of the wind farm at the proper level.
- It can assist the wind farm in meeting the reactive power-related grid connection needs.

In this work one of the most effective power system software programs with an integrated graphical one-line interface is DigSILENT, which stands for "Digital Simulation and Electrical Network Calculation Program." and it has fast simulation. Three phase short circuit is applied at the connection point of the wind farm to the grid.

2. DFIG WIND TURBINE MODELING

Modeling all systems involved in energy conversion system, rotor, pitch controller, frequency converter, generator etc. have been done in many studies [5] and in this work only brief discussion will be made and more focus will be made on STATCOM. Furthermore, the components that affect the system's dynamics are the primary objective of this study.

2.1 Wind Model

The simulation study is about the dynamics of the system under faults which will last for a very small time (Milli seconds). The wind speed can be assumed constant [5] in this period. Thus, wind speed modeling is not a concern of this work.

2.2 Aerodynamic Model

The rotor of the turbine converts the available aerodynamic power in the flowing wind stream into mechanical power. The associated wind energy that the rotor blades change into mechanical energy can be calculated using [6-7]:

$$P_{rot} = 0.5\rho\pi R^2 u^3 C_p(\theta, \lambda). \quad (1)$$

The following static relations are used to simulate the aerodynamic torque τ_{rot} (in N.m) developed on the main shaft of a wind turbine with radius R (in m) and air density ρ (in kg/m³) at a wind speed u (in m/s).

$$\tau_{rot} = 0.5\rho\pi R^3 u^2 C_q(\theta, \lambda). \quad (2)$$

Where λ is the tip speed ratio ($\frac{R\omega_{rot}}{u}$), C_p is the aerodynamic power coefficient, C_q is the torque power coefficient and θ is the pitch angle.

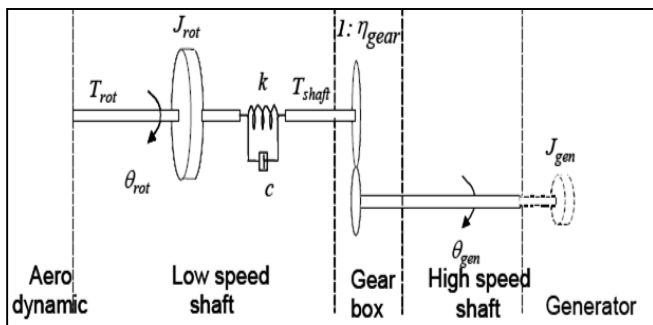


Figure 1. Two Mass Drive Train Model

2.3 Drive Train Model

Mostly for the simulation of dynamic response of wind turbines, a two-mass drive train model is used as shown in Figure 1. It improves the simulation efficiency and can give accurate results [8]. The following are the fundamental equations for the representation of the dynamics of a two-mass drive train: [8-9]:

$$\omega_k = \omega_{rot} - \frac{\omega_{gen}}{n_{gear}}. \quad (3)$$

$$\dot{\omega}_{rot} = \frac{\tau_{rot} - \tau_{shaft}}{J_{rot}}. \quad (4)$$

$$\tau_{shaft} = c\omega_k + k\theta_k. \quad (5)$$

Where: θ_k and ω_k are the angle and angular speed differences between the two ends of the flexible shaft, respectively; ω_{gen} and ω_{rot} are generator and rotor angular speeds respectively; J_{rot} is rotor inertia; τ_{rot} and τ_{shaft} are aerodynamic torques at low and high speed shafts respectively. The n_{gear} is the gear ratio; k and c are the low-speed shaft stiffness and a is damping coefficient respectively.

2.4 Pitch Angle Controller Model

When the wind speed exceeds the rated value, pitch angle control is used to limit power to the rated value. When the wind speed is lower than the rated wind speed, it is also employed to maximize the power extracted from the wind. Additionally, it aids in emergency stops and startup.

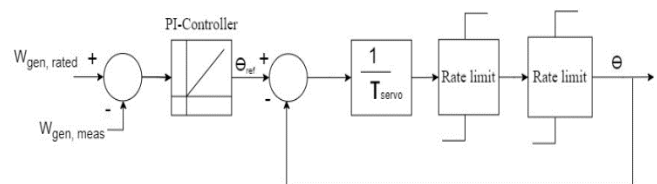


Figure 2. Pitch angle controller

Pitch angle controller model is described in references [7-8]. As in shown Figure 2 it contains the PI controller and servo controller.

2.5 Frequency Converter Model

In this work the fundamental frequency model of converter is used; thus, the AC and DC voltage relation is described as in equation 6 [9-12].

$$|U_{ac}| = K_o m U_{dc}. \quad (6)$$

Where m stands for the pulse-width-modulation index and is constrained to a value of 0-1 to prevent saturation effects. The modulation method, such as sinusoidal or rectangular modulation, is indicated by the factor K_o . For frequency converter control as in the literature [9–12] primarily vector control method is used. The frequency converter model is available as an inbuilt module in the DigSILENT Power Factory simulation tool.

2.6 The Doubly Fed Induction Machine Model

The equation of the doubly fed machine is derived from single-fed induction machine equations (Figure 3).

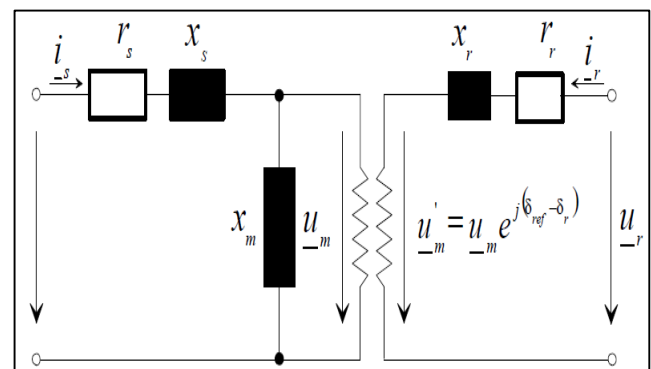


Figure 3: DFIG model [1]

The rotating reference frame with ω_{ref} is chosen and the dynamic equations described as follows [14]:

$$\underline{u}_s = r_s \underline{i}_s + \frac{d\underline{\Psi}_s}{\omega_n dt} + j \frac{\omega_{ref}}{\omega_n} \underline{\Psi}_s. \quad (7)$$

$$\underline{u}_r = r_r \underline{i}_r + \frac{d\underline{\Psi}_r}{\omega_n dt} + j \frac{\omega_{ref} - \omega_g}{\omega_n} \underline{\Psi}_r. \quad (8)$$

$$J \frac{d\omega_g}{dt} = t_m + t_{el}. \quad (9)$$

$$t_{el} = \text{Im}(\underline{\Psi}_s i_s^*). \quad (10)$$

Where: r_s and \underline{i}_s are stator resistance and current respectively; \underline{u}_s is stator voltage; $\underline{\Psi}_s$ is stator flux; ω_n and ω_{ref} nominal and reference speeds respectively; \underline{u}_r is rotor voltage; r_r and \underline{i}_r are rotor resistance and current respectively; J is moment of inertia; $\underline{\Psi}_r$ is the rotor flux; ω_g is generator speed; t_m and t_{el} are mechanical and electrical torques respectively.

The model of DFIG machine model is available in DigSILENT PowerFactory as an inbuilt model.

2.7 STATCOM Modeling

A voltage source converter (VSC) with rapidly controllable amplitude and phase angle serves as the building block of a STATCOM. On the grid side, a coupling transformer filter and the DC bus capacitor are also present. The VSC is used along with an appropriate energy storage system. (Figure 4). The difference between grid voltage and power converter voltage determines STATCOM reactive current. The reactive power supply in STATCOM is not impacted by the connection point's actual voltage [15–16].

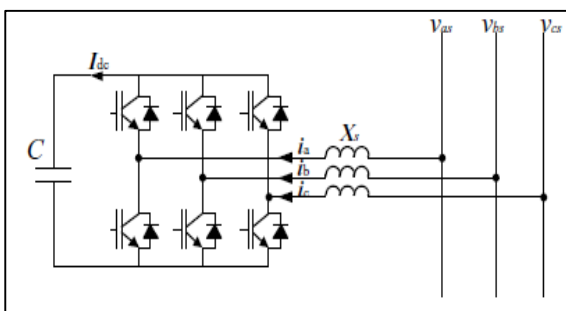


Figure 4. STATCOM model

It can be demonstrated that the output of the VSC can be expressed as follows if the bus voltage is denoted by V_1 and the VSC voltage is V_2 [17]:

$$P = \frac{V_1 V_2}{X} \sin \delta. \quad (11)$$

$$Q = \frac{V_1 (V_2 \cos \delta - V_1)}{X}. \quad (12)$$

If the phase shift between the bus voltage and the VSC voltage is zero, the VSC will act as a purely reactive element. The phase shift angle can determine the direction of active power while the magnitude of the voltage determines the direction of reactive power flow. The VSC will have a capacitive character if $V_2 > V_1$ and act as a generator of

reactive power. If $V_1 > V_2$, the VSC will have an inductive character and act as a reactive power absorber.

The vector control technique can be used as a control strategy in STATCOM. The i_d and i_q currents on the d- and q-axes can be quickly controlled using the vector control technique. The real and reactive power output of the STATCOM is primarily determined by these currents, as shown in the equations 13-14.

$$P_s = \frac{3}{2} V_q i_q \quad (13)$$

$$Q_s = \frac{3}{2} V_q i_d \quad (14)$$

By controlling the DC voltage, we can indirectly control the real power ($P_s = V_{AC} i_{AC} = V_{DC} i_{DC}$). The DC voltage measured from the DC bus of the STATCOM is subtracted from the DC reference voltage. The error signal passes through PI controller and module limiter giving i_{d_ref} (Figure 5). In a similar way the AC voltage is measured from the point the STATCOM is connected to the network.

Then the error between reference and measured AC voltage passes through the PI controller to give i_{q_ref} (Figure 5). The interconnected DigSILENT frame model is shown in Figure 6. These signals are used in the internal current control loop of the converter inside the VSC model to generate the PWM signals P_{md} and P_{mq} as shown in Figure 7. It contains voltage measurement devices for AC and DC, the controller block whose detail is shown in Figure 5 and the VSC. In addition, it contains a phase locked loop for synchronization.

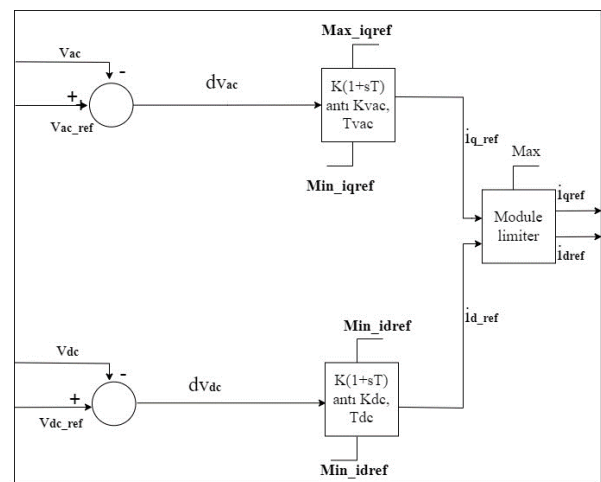


Figure 5. STATCOM Outer Controller loop DigSILENT model

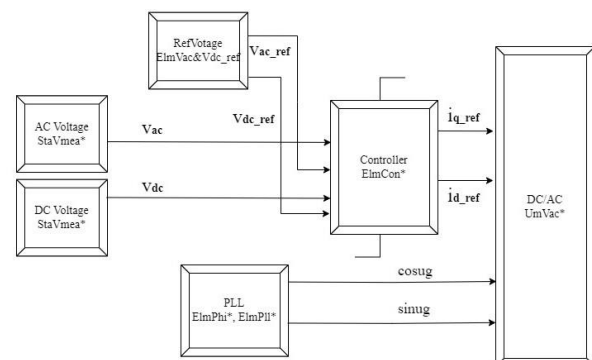


Figure 6. STATCOM frame DigSILENT model

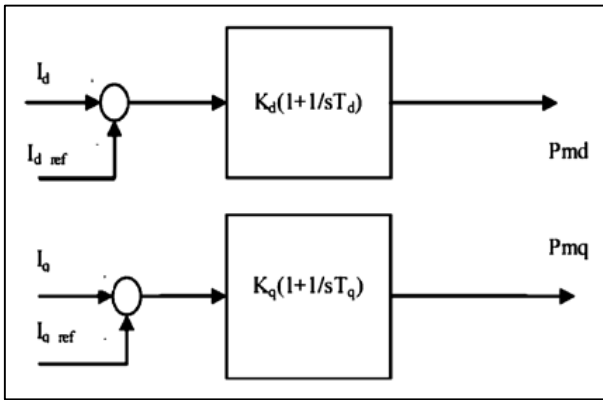


Figure 7. Internal current control loop

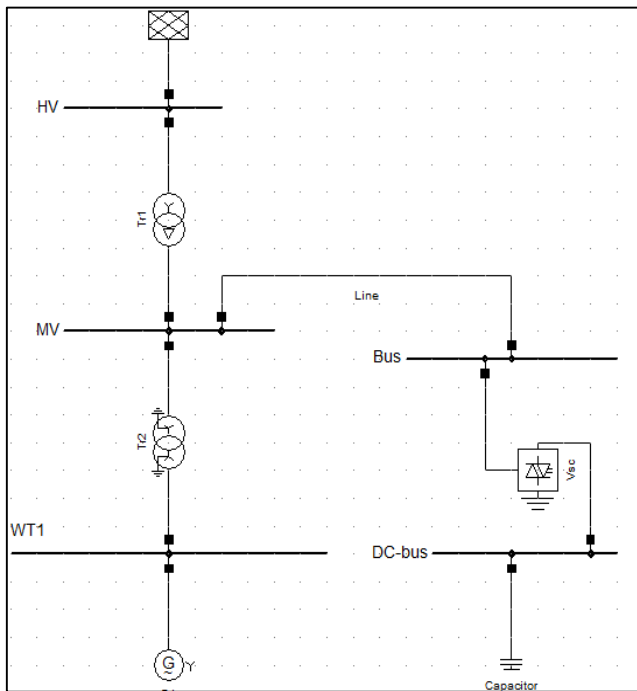


Figure 8. Wind farm, STATCOM and Network DigSILENT PowerFactory interconnection.

3. SIMULATION AND ANALYSIS

The modeling of DFIG wind turbines was discussed in the previous sections. To model wind farms for dynamic study, a mostly aggregated modeling approach is used. In the aggregated modulating approach, each component is rated to the capacity of the wind farm [17]. For example, in this study 30 DFIG with 2 MW capacity wind turbines are used with total wind farm installed capacity of 60 MW. Rather than

putting 30 models of every equipment, the equivalent wind turbine, transformer, and other components rated to 60 MW is used. DigSILENT has an inbuilt aggregating facility and only specifying the number “n” of equipment to be aggregated is enough to model the equipment.

The wind farm is connected to a weak system with short circuit capacity of 952.6279 MVA. The STATCOM used in the simulation is 30 Mvar and connected to 33.6 kV voltage level (Figure 8). The voltage output of the wind turbine is 0.69 kV and then stepped up to 33.6 kV by unit transformers. In the main substation, the voltage is stepped up to 132 kV.

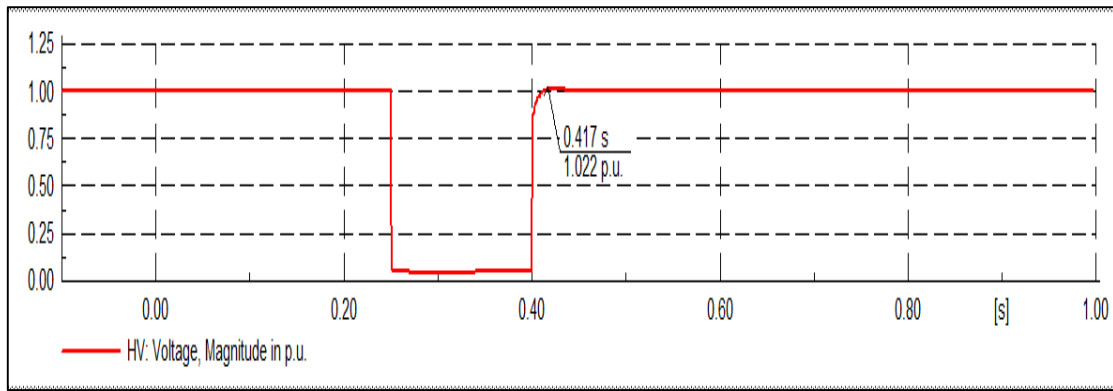
Three phase short circuit fault is applied on the high voltage (HV) side of the network when simulation time is 0.25 seconds. The fault is cleared when the time is 0.4 seconds (the fault duration is 1.5 s). The AC voltage and reactive power variations are observed when the STATCOM is connected to the medium voltage (MV) side of the network and by also disconnecting the STATCOM.

Figure 9(a) shows that the voltage on high voltage side is reduced to about 4.8% because of three phase short circuit fault. In this case STATCOM is out of service. The voltage returned to almost pre fault of value about 1.022 pu with 17 ms. This shows that the DFIG wind turbines have fault ride through capability. When STATCOM is connected to the system even though the same short circuit is applied, the voltage is reduced to about 20.4%. (Figure 9(b)). In 17 ms after the clearance of the fault, the voltage returned to about 0.987 pu (Figure 9(b)) showing good performance as summarized in Table 1. Figure 9 (a) shows the voltage under a similar condition of fault, but on the MV side. In this case voltage returns to pre fault value after reduced to very low voltage when the STATCOM is not connected. The STATCOM is connected on MV bus and voltage profile is shown in Figure 10(b). In this case voltage reduction is not an issue; rather the voltage increased and returned to almost pre fault values of 0.971 pu within 17 ms.

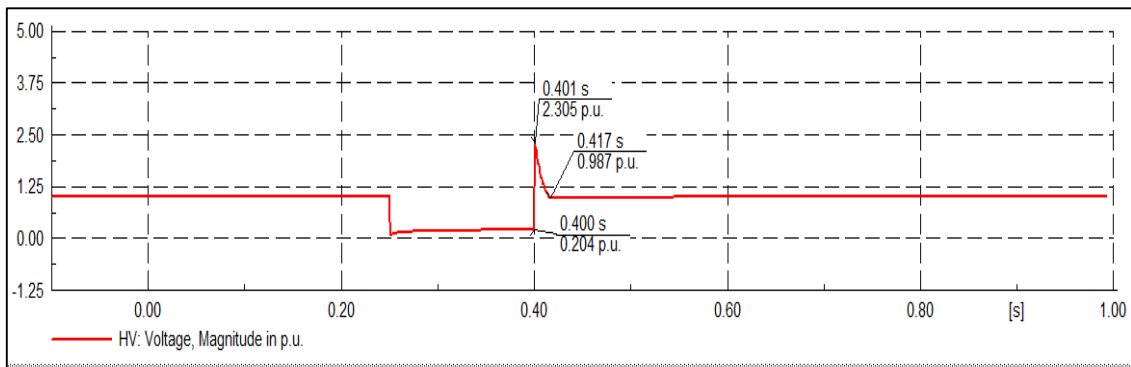
Figures 11 - 12 show the reactive power on the HV and MV sides of the network. On the MV without STATCOM, Figure 12(a) the reactive power only varied at the beginning and end of the short-circuit fault. But in Figure 12(b) it is varied by MV side to support the voltage.

TABLE 1
COMPARISON OF VOLTAGE REDUCTION

STATCOM	VOLTAGE REDUCTION (PU)	POST FAULT VOLTAGE (PU)	Difference from nominal value (%)
Out of service	4.8	1.022	2.2
In service	20.4	0.987	1.3

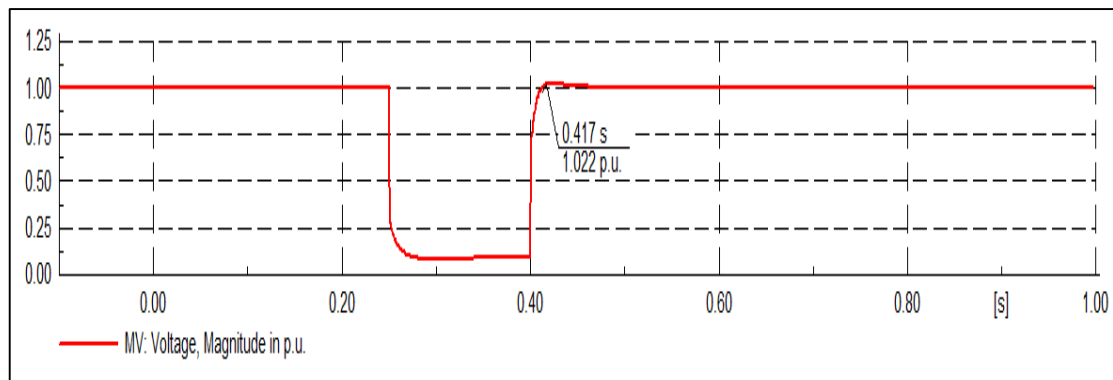


(a)

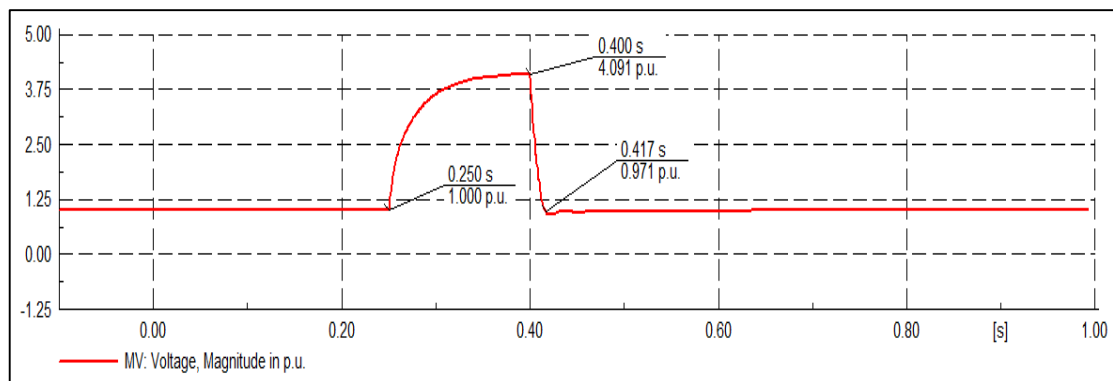


(b)

Figure 9. HV AC voltage (a) without STATCOM (b) with STATCOM

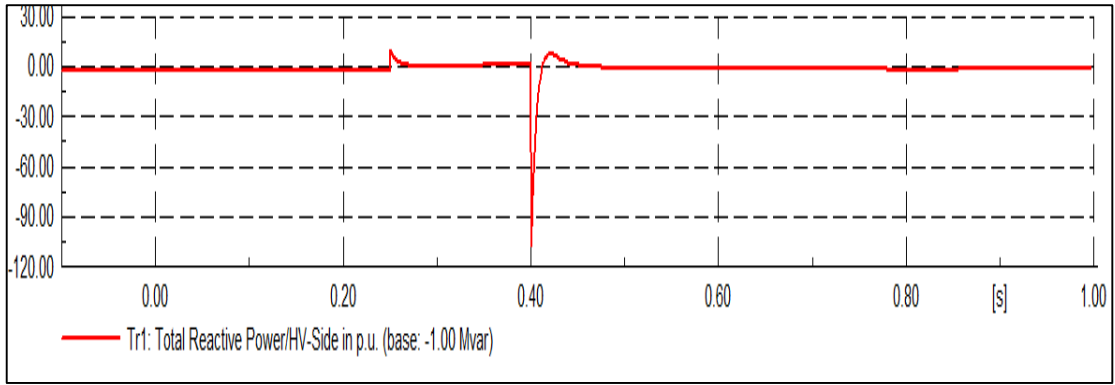


(a)

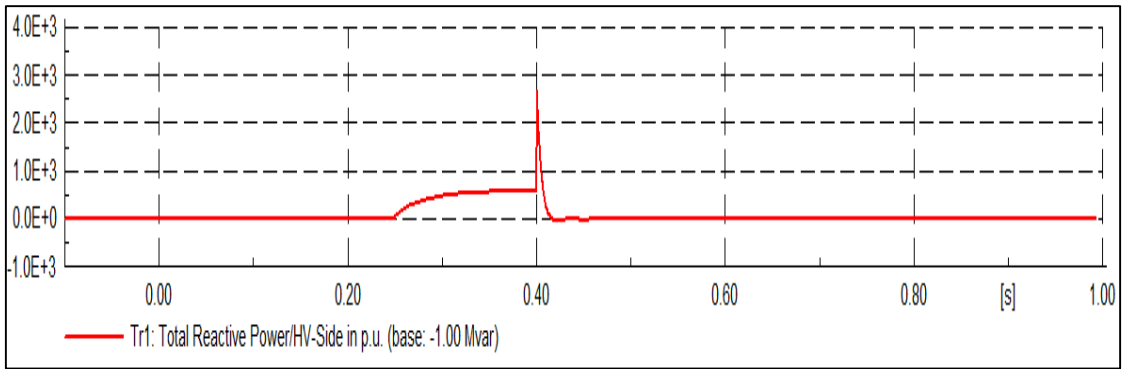


(b)

Figure 10: MV AC voltage (a) without STATCOM (b) with STATCOM

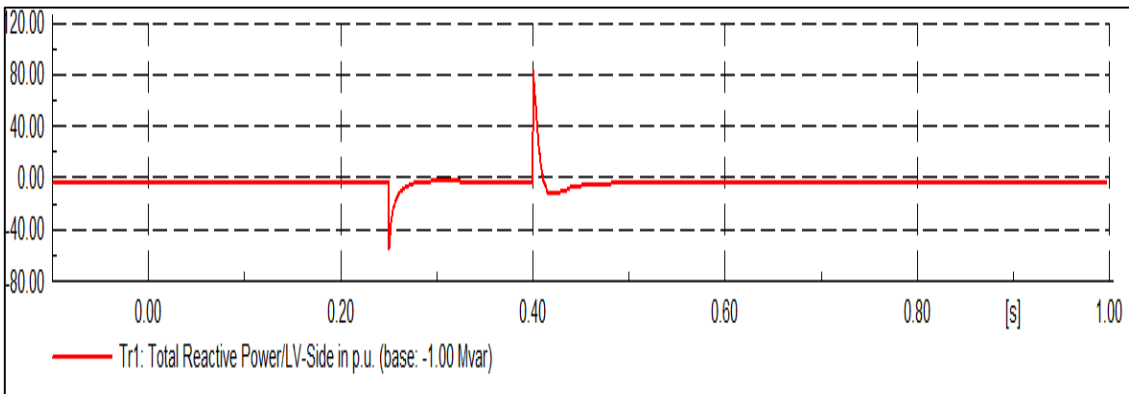


(a)

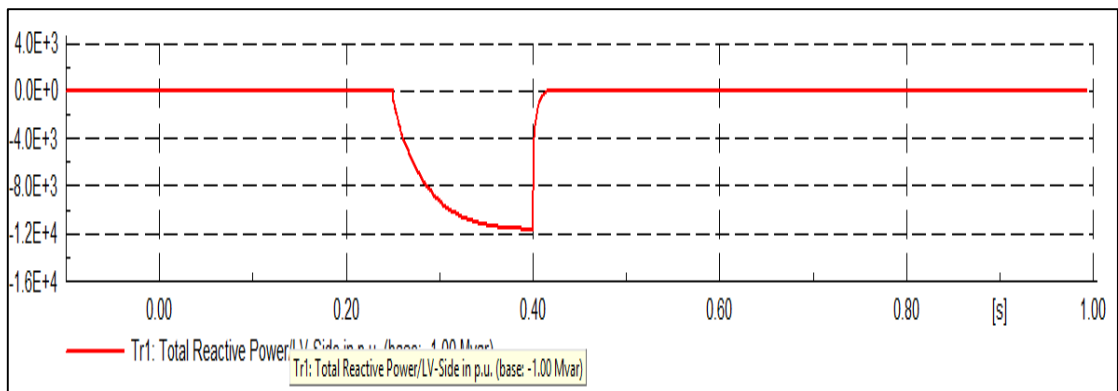


(b)

Figure 11. HV reactive power (a) without STATCOM (b) with STATCOM



(a)



(b)

Figure 12. MV reactive power (a) without STATCOM (b) with STATCOM

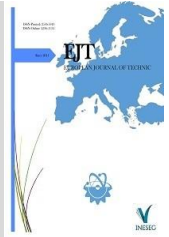
4. CONCLUSION

In this work wind farm with 30 DFIG wind turbines are dynamically modeled. In addition, STATCOM is also modeled and connected to the wind farm at medium voltage level. The case when this wind farm is connected to a weak system is considered in simulation by applying three phase short circuit at high voltage point of common coupling to the grid. Since wind turbines have inherent fault ride through capability, it was observed that the wind farm voltage on high voltage performed well even though the STATCOM is not connected. When the STATCOM is connected to the system, the voltage on HV did not drop to zero which could be considered as an advantage. In the medium voltage level where the STATCOM is connected, the voltage is observed to increase during fault on high voltage level which can be considered as another advantage. But when the STATCOM is not connected the voltage is decreased. In addition, when the STATCOM is connected, the reactive power is observed to increase in negative direction increasing the voltage on medium voltage side. Generally, the STATCOM can increase the system stability when connected to the wind farm terminal. But the influence is more significant in the area near to the connection point.

5. REFERENCES

- [1] Abdulfetah SHOBOLE: Tur, M. R. (2020). Reliability assessment of distribution power system when considering energy storage configuration technique. *IEEE Access*, 8, 77962-77971.
- [2] Abdulfetah SHOBOLE: Shobole, A., Baysal, M., Wadi, M., & Tur, M. R. (2020). An adaptive protection technique for smart distribution network. *Elektronika ir Elektrotechnika*.
- [3] A-A. Edris, Adapa, M. H. Baker, L. Bohmann K. Clark, K. Habashi, L. Gyugyi, J. Lemay, A.S. Mehraban, A.K. Myres, J. Reeve, F. Sener, D.R. Torgerson, R.R. Wood, "Proposed Terms and Definitions for Flexible AC Transmission System (FACTS)", *IEEE Transactions on Power Delivery*, Vol. 12, No. 4, October 1997.
- [4] Pavlos S. Georgilakis, a and Peter G. Vernados, "Flexible AC Transmission System Controllers: An Evaluation", *Materials Science Forum* Vol. 670 (2011) pp 399-406.
- [5] IEEE Special Stability Controls Working Group, "Static Var Compensator Models for Power Flow and Dynamic Performance simulation" *IEEE Transactions on Power Systems*, Vol. 9, No. 1, February 1994.
- [6] Hansen AD, Michalke G, "Multi-pole permanent magnet synchronous generator wind turbines' grid support capability in uninterrupted operation during grid faults, *IET Renewable Power Generation*", November 2008.
- [7] Ackermann, T., "Wind Power in Power Systems", New York: John Wiley & Sons, 2005.
- [8] Dynamic Wind Turbine Models in Power System Simulation Tool DIGSILENT, Risoe Report R-1400 (Ed. 2) (EN), Risø National Laboratory, Denmark, August 2007.
- [9] Abram Perdana, "Dynamic Models of Wind Turbines A Contribution towards the Establishment of Standardized Models of Wind Turbines for Power System Stability Studies", ISBN 978-91-7385-226-5, Chalmers University of Technology, Göteborg, Sweden 2008.
- [10] DIGSILENT Technical Documentation PWM Converter Published by DIGSILENT GmbH, Germany, 2007
- [11] Hansen AD, Michalke G, "Modelling and Control of Variable speed Multi-pole Permanent Magnet Synchronous Generator Wind Turbine", *Wind Energy* 2008; 11:537-554.
- [12] Hansen AD, Michalke G, "Multi-pole permanent magnet synchronous generator wind turbines' grid support capability in uninterrupted operation during grid faults", *IET Renewable Power Generation*, November 2008.
- [13] DIGSILENT Technical Documentation, Doubly-Fed Induction Machine Published by DIGSILENT GmbH, Germany, 2007.
- [14] G.D. Galanos, C.I. Hatziaioniu X-j. Cheng, D. Maratukularn, "Advanced Static Compensator For Flexible Ac Transmission", *IEEE Transactions on Power Systems*, Vol. 8, No. 1, February 1993.
- [15] Tran Thi Ngoat and Le Ngoc Giang, "Transient Stability Study of a Reality 500kV Power System Using Statcom", *International Journal of Hybrid Information Technology* Vol.7, No.5 (2014), pp.137-146.
- [16] Bindeshwar Singh, "Introduction to FACTS Controllers in Wind Power Farms: A Technological Review", *INTERNATIONAL JOURNAL OF RENEWABLE ENERGY RESEARCH* Bindeshwar Singh, Vol.2, No.2, 2012.
- [17] Vladislav Akhmatove, "Analysis of Dynamic Behaviour of Electrical Power Systems with Large amount of wind farms", Ph. D. Thesis, Electrical Power Engineering, ORSTD-DTU, Technical University of Denmark, April 2003.

Abdulfetah Abdela Shobole is an Assistant Professor in the Electrical Engineering Department at Istanbul Sabahattin Zaim University. He has been working in the industry in substations, wind farms, solar power plants, and transmission and distribution networks since 2011. His research area includes smart grid protection, Cyber security, smart grid automation, and renewable energy integration with the smart grid.



Research Article

Capacitated Network Traffic Assignment using Lagrange Neural Networks

Hasan Dalman^{1*} ^{1*}Batman University, Mathematics Department, Batman, Turkey. (e-mail: hasan.dalman@batmnan.edu.tr).

ARTICLE INFO

Received: Jun., 28. 2023
 Revised: Jul., 12. 2023
 Accepted: Nov., 11. 2023

Keywords:

Nonlinear Optimization,
 Neural Dynamics,
 Traffic assignment,
 Neural Networks

Corresponding author: *Hasan Dalman*

ISSN: 2536-5010 | e-ISSN: 2536-5134

DOI: <https://doi.org/10.36222/ejt.1320824>

ABSTRACT

The purpose of this paper is to examine the travel time within a network by analyzing the changes in link volume of network traffic assignment issues that are impacted by capacity constraints using a Lagrange neural network methodology. To achieve this objective, the optimization problem associated with network traffic assignment, which includes capacity constraints, is transformed into a Lagrange problem. Following this, the Lagrange function is reduced to a system of differential equations consisting of neural equations using the gradient method. The dynamic system, which includes initial values, is solved through the well-established Runge-Kutta method. Finally, a numerical example is provided to illustrate the solution process and demonstrate the effectiveness of the presented neural network approach.

1. INTRODUCTION

The Traffic Assignment Problem (TAP) is a fundamental topic in transportation analysis and applications. Its objective is to determine the equilibrium flow patterns in a given transportation network while considering the origin-destination demands. In recent years, this problem has received significant attention, leading to the development of various modeling and solution techniques based on Wardrop's two optimization principles: User Equilibrium (UE) and System Optimal (SO). These principles have been extensively researched and analyzed, resulting in a comprehensive body of literature and practical applications [9].

The pioneering research undertaken by Beckmann and colleagues (2) demonstrated the potential for determining traffic flow on a road network through the application of the UE principle. However, the estimation of cost and/ or time functions, selection of appropriate forms, and calibration of parameters present significant challenges in this context. UE solutions may often involve congested links exceeding their designated capacities, thus necessitating the imposition of capacity restrictions on link flows to enhance traffic distribution. While the Frank-Wolfe algorithm has proven effective in addressing the Traffic Assignment Problem (TAP), incorporating capacity constraints complicates the model and

poses additional challenges. As such, solving the Capacity-constrained Traffic Assignment Problem (CTAP) becomes a computationally demanding and time-consuming endeavor. To address this intricate problem, researchers have explored various methodologies, such as asymptotic link performance functions or penalty-based approaches, as extensively discussed in the literature by scholars [3-9].

Recent research has been exploring the application of neural networks for solving nonlinear optimization problems. Hopfield network, introduced by Tank and Hopfield [10], was proposed for linear optimization problems and since then, neural networks have been increasingly used in areas such as linear optimization and nonlinear optimization, with their results analyzed on various problems [11-19]. These neural networks are dynamic systems that utilize energy functions, which are a combination of the objective function and constraints of the original problem, similar to the Lagrange function. This particular method has not yet been applied to UE traffic assignment problems with capacity constraints. Therefore, this study aims to analyze a nonlinear network traffic assignment problem with capacity constraints, using the Lagrange neural network method. This will examine the effects of capacity limits on connection flows and the effects of traffic volume changes over time on the travel times of the network. The study begins by introducing the static CTAP model, which

is then transformed into a neural dynamic system using the Lagrange function of the static CTAP model to examine the effect of capacity on connection flows and the development of traffic over time. The points obtained from this system satisfy the Karush-Kuhn-Tucker conditions, which is the user optimality condition, and therefore an UE solution is obtained in the static CTAP model.

This research involves utilizing the fourth-order Runge-Kutta method to conduct numerical simulations to solve the neural network model with specific initial conditions. Through observing the changes over time in the system and Lagrange neurons shown on graphs, the impact of traffic formation in connection flows is observed, particularly the volume formed in the network, on user travel time. The findings are then compared to those in previous literature [20] to demonstrate the precision and validity of the proposed solution process in this study. The findings of this paper contribute to the understanding of network traffic behavior and provide a valuable framework for addressing CTAPs. The utilization of neural networks and dynamic modeling techniques offers new perspectives for analyzing and optimizing traffic flow in real-world transportation systems.

The paper's structure is organized as follows: Section 2 details the optimization problem for CTAP. Section 3 outlines the Lagrange neural network utilized to optimize CTAP. Section 4 provides a numerical example, while Section 5 features a discussion. Lastly, Section 6 concludes with remarks concerning the results.

2. PROBLEM FORMULATION

In transportation network analysis, the traffic network can be represented as $G(N, A)$, where N represents the set of nodes and A denotes the set of connections. The sources and destinations of the network are denoted as R and S , respectively. To incorporate user equilibrium traffic assignment with link capacity constraints, a nonlinear programming problem can be formulated:

$$\begin{aligned} \min z(h) &= \sum_a \int_0^{f_a} c_a(x) dx \\ \text{s.t.} & \\ \left\{ \begin{array}{l} \sum_k h_k^{rs} = q_{rs} \quad \forall r \in R, s \in S \\ h_k^{rs} \geq 0 \quad \forall k \in K_{rs}, r \in R, s \in S \\ f_a = \sum_r \sum_s \sum_k h_k^{rs} \delta_{a,k}^{rs} \quad \forall a \in A, k \in K_{rs}, r \in R, s \in S \\ f_a \leq C_a \quad \forall a \in A \end{array} \right. \end{aligned} \quad (1)$$

where z represents the objective function; f_a represents the total flow on link a ; c_a represents a separable, piecewise linear link cost function; q_{rs} represents the total traffic demand between r and s ; h_k^{rs} represents the flow on chain(route) k between r and s ; K_{rs} represents the set of chains between r and s ; $\delta_{a,k}^{rs}$ represents the link-chain incidence matrix; and C_a represents the link capacity on link a .

The problem at hand is non-linear and comprises of both equality and inequality constraints. However, it must be transformed into a problem that solely consists of equality constraints.

$$\begin{aligned} \min z(h) &= \sum_a \int_0^{f_a} c_a(x) dx \\ \text{s.t.} & \\ \left\{ \begin{array}{l} q_{rs} - \sum_k h_k^{rs} = 0 \quad \forall r \in R, s \in S \\ C_a - (f_a \oplus (\rho_a)^2) = 0 \quad \forall a \in A \\ h_k^{rs} \geq 0 \quad \forall k \in K_{rs}, r \in R, s \in S \\ \rho_a \geq 0 \quad \forall k \in K_{rs}, r \in R, s \in S \end{array} \right. \end{aligned} \quad (2)$$

where ρ_a represents the slack variables for capacitated constraints. In order to maintain simplicity, ρ_a^2 is chosen as the representation, although other differentiable positive functions of ρ could be employed, provided they possess the necessary dynamic range.

$f_a = \sum_r \sum_s \sum_k h_k^{rs} \delta_{a,k}^{rs} \quad \forall a \in A, k \in K_{rs}, r \in R, s \in S$ is the predefined link flows.

The Lagrange function for this problem can be expressed as follows:

$$\begin{aligned} L(h, \rho, \lambda, \nu) &= \sum_a \int_0^{f_a} c_a(x) dx \\ &+ \sum_{r \in R} \sum_{s \in S} \lambda_{rs} \left(q_{rs} - \sum_{k \in K_{rs}} h_k^{rs} \right) \\ &+ \sum_a \nu_a \left(C_a - \left(\sum_{r \in R} \sum_{s \in S} \sum_{k \in K_{rs}} h_k^{rs} \delta_{a,k}^{rs} + (\rho_a)^2 \right) \right) \end{aligned} \quad (3)$$

where L represents the Lagrange function. Additionally, h refers to the chain flow variables, while ρ represents the slack variables for capacitated constraints. The Lagrange multiplier associated with the capacity and flow conservation constraints are denoted by λ and ν , respectively. The Lagrange function includes the objective function, flow conservation constraints, flow-variable definition constraints, and capacity constraints, which allows us to determine the best solution by minimizing this function.

Definition 1: A Kuhn-Tucker point is defined as a point $(h^*, \rho^*, \lambda^*, \nu^*)$ that meets specific conditions.

$$\begin{aligned} \frac{\partial L(h^*, \rho^*, \lambda^*, \nu^*)}{\partial h_k^{rs}} &= \frac{\partial z(h^*)}{\partial h_k^{rs}} + \frac{\partial \left(\sum_{r \in R} \sum_{s \in S} \lambda_{rs}^* \left(q_{rs} - \sum_{k \in K_{rs}} h_k^{rs} \right) \right)}{\partial h_k^{rs}} \\ &- \frac{\partial \left(\sum_a \nu_a^* \left(C_a - \left(\sum_{r \in R} \sum_{s \in S} \sum_{k \in K_{rs}} h_k^{rs} \delta_{a,k}^{rs} + (\rho_a^*)^2 \right) \right) \right)}{\partial h_k^{rs}} = 0 \end{aligned} \quad (5)$$

Primal Feasibility:

$$\sum_k h_k^{rs*} = q_{rs} \quad \forall r \in R, s \in S,$$

$$\left(C_a - \left(\sum_r \sum_s \sum_k h_k^{rs*} \delta_{a,k}^{rs} + \rho_a^* \right) \right) \leq 0, \quad \forall a \in A, k \in K_{rs} \quad (6)$$

$$h_k^{rs*} \geq 0 \quad \forall k \in K_{rs}, r \in R, s \in S, \rho_a \geq 0, \forall a \in A$$

Dual Feasibility:

$$\lambda_{rs}^* \geq 0 \quad \forall r \in R, s \in S \text{ and } \nu_a^* \geq 0 \quad \forall a \in A. \quad (7)$$

Complementary Slackness:

$$\lambda_{rs}^* \left(q_{rs} - \sum_{k \in K_{rs}} h_k^{rs*} \right) = 0, \quad \forall r \in R, s \in S;$$

$$\nu_a^* \left(C_a - \left(\sum_r \sum_s \sum_k h_k^{rs*} \delta_{a,k}^{rs} + \rho_a^* \right) \right) = 0, \quad \forall a \in A \quad (8)$$

The presence of certain conditions signifies the activation of the corresponding constraint, which is denoted by positive values of λ_{rs} and ν_a . The gradient of the Lagrange function with respect to variables h_k^{rs} , ρ_a , λ_{rs} , and ν_a can be expressed as follows:

$$\frac{\partial L(h, \rho, \lambda, \nu)}{\partial h_k^{rs}} = \left(c_a(f_a) \delta_{a,k}^{rs} - \sum_{r \in R} \sum_{s \in S} \lambda_{rs} + \sum_a \nu_a \delta_{a,k}^{rs} \right) = 0 \quad (9)$$

$$\frac{\partial L(h, \rho, \lambda, \nu)}{\partial \rho_a} = 2\nu_a \rho_a = 0 \quad (10)$$

$$\frac{\partial L(h, \rho, \lambda, \nu)}{\partial \lambda_{rs}} = q_{rs} - \sum_{k \in K_{rs}} h_k^{rs} = 0 \quad (11)$$

$$\frac{\partial L(h, \rho, \lambda, \nu)}{\partial \nu_a} = C_a - \left(\sum_{r \in R} \sum_{s \in S} \sum_{k \in K_{rs}} h_k^{rs} \delta_{a,k}^{rs} + (\rho_a)^2 \right) = 0 \quad (12)$$

From equation (9), a generalized route travel cost is obtained as:

$$\lambda_{rs} = \left(c_a(f_a) + \sum_a \nu_a \right) \delta_{a,k}^{rs} \quad (13)$$

where $c_a(f_a) \delta_{a,k}^{rs}$ denotes the cost on link a .

A capacitated user equilibrium flow can be determined the following conditions:

$$h_k^{rs} > 0 \rightarrow \left(c_a(f_a) + \sum_a \nu_a \right) \delta_{a,k}^{rs} = \lambda_{rs} \quad (14)$$

$$h_k^{rs} = 0 \rightarrow \left(c_a(f_a) + \sum_a \nu_a \right) \delta_{a,k}^{rs} \geq \lambda_{rs} \quad (15)$$

$f_a = \sum_r \sum_s \sum_k h_k^{rs} \delta_{a,k}^{rs} \quad \forall a \in A, k \in K_{rs}, r \in R, s \in S$ is the predefined link flows.

We can also observe from the complementary slackness conditions (8) that

$$\text{if } \nu > 0 \rightarrow C_a = f_a \quad (16)$$

or

$$\text{if } \nu = 0 \rightarrow f_a < C_a. \quad (17)$$

The positive values of Lagrange multipliers, denoted by ν_a , are reasonably associated with delays caused by capacity limitations when link flows become saturated. Empirical observations indicate that the total travel time on a road segment typically comprises two distinct components: the travel time itself and the waiting time at the exit point when it reaches capacity. Lagrange multipliers can be interpreted as the waiting times experienced by a vehicle on the link during equilibrium conditions, reflecting the delay experienced by a vehicle during the equilibrium state.

3. LAGRANGE NEURAL NETWORKS FOR CTAPS

The primary aim of this research is to develop and educate a neural network with the ability to attain a state of equilibrium. This state of equilibrium is indicative of a fixed point of the Lagrange function (4), which implies that the dynamic behavior of the neural network is governed by the gradient of this function. By computing the gradient of the Lagrange function, we can construct the following neural network model to resolve problem (1):

$$\begin{cases} \frac{\partial h}{\partial t} = -\nabla_h L(h, \rho, \lambda, \nu) \\ \frac{\partial \rho}{\partial t} = -\nabla_\rho L(h, \rho, \lambda, \nu) \\ \frac{\partial \lambda}{\partial t} = \nabla_\lambda L(h, \rho, \lambda, \nu) \\ \frac{\partial \nu}{\partial t} = \nabla_\nu L(h, \rho, \lambda, \nu) \end{cases} \quad (18)$$

If the network is physically stable, the equilibrium point $(h^*, \rho^*, \lambda^*, v^*)$ described by $\frac{\partial h}{\partial t} = 0$, $\frac{\partial \rho}{\partial t} = 0$, $\frac{\partial \lambda}{\partial t} = 0$, and $\frac{\partial v}{\partial t} = 0$ at $(h^*, \rho^*, \lambda^*, v^*)$ obviously meets (9) and (12) and thus provides a Lagrange solution to traffic assignment problem (1). In component form, we can express as follows:

$$\begin{cases} \frac{\partial h_k^{rs}}{\partial t} = - \left(c_a(f_a) \delta_{a,k}^{rs} - \sum_{r \in R} \sum_{s \in S} \lambda_{rs} + \sum_a v_a \delta_{a,k}^{rs} \right) \\ \frac{\partial \rho}{\partial t} = -(-2v_a \rho_a) \\ \frac{\partial \lambda}{\partial t} = q_{rs} - \sum_{k \in K_{rs}} h_k^{rs} \\ \frac{\partial v}{\partial t} = C_a - \left(\sum_{r \in R} \sum_{s \in S} \sum_{k \in K_{rs}} h_k^{rs} \delta_{a,k}^{rs} + (\rho_a)^2 \right) \end{cases} \quad (19)$$

where h and p acquire a physical interpretation as representations of neuronal activity.

The aim is to identify the lowest value of problem (1), thereby giving rise to the creation of the Lagrange dual of problem (4). The objective is to optimize the Lagrange multipliers while concurrently minimizing the decision variables h and p . This indicates a decrease in the system variables as time progresses alongside a corresponding increase in the Lagrange multipliers.

Theorem 1: Consider the stationary point $(h^*, \rho^*, \lambda^*, v^*)$ of problem (4). Assuming that $\nabla_h^2 L(h, \rho, \lambda, v) > 0$ and (h^*, ρ^*) is a regular point of problem (2), it follows that $(h^*, \rho^*, \lambda^*, v^*)$ serves as an asymptotically stable point within the neural network.

Proof: Applying the principles of nonlinear dynamic system theory, we proceed by linearizing equation (18) around the equilibrium point $(h^*, \rho^*, \lambda^*, v^*)$.

The local properties of the equilibrium are determined by analyzing the behavior of the linearized system.

To establish the local asymptotic stability of the system, we linearize equation (18) by performing a Taylor series expansion around the equilibrium point $(h^*, \rho^*, \lambda^*, v^*)$. The linearized system represents the behavior of the equilibrium point in the vicinity of $(h^*, \rho^*, \lambda^*, v^*)$.

The linearized system takes the following form:

$$\begin{cases} \frac{\partial h}{\partial t} = -\nabla_h L \Big|_{(h^*, \rho^*, \lambda^*, v^*)} (h - h^*) \\ \frac{\partial \rho}{\partial t} = -\nabla_\rho L \Big|_{(h^*, \rho^*, \lambda^*, v^*)} (\rho - \rho^*) \\ \frac{\partial \lambda}{\partial t} = \nabla_\lambda L \Big|_{(h^*, \rho^*, \lambda^*, v^*)} (\lambda - \lambda^*) \\ \frac{\partial v}{\partial t} = \nabla_v L \Big|_{(h^*, \rho^*, \lambda^*, v^*)} (v - v^*) \end{cases} \quad (20)$$

The local asymptotic stability of the equilibrium point is determined by analyzing eigenvalues of the linearized system in the vicinity of point $(h^*, \rho^*, \lambda^*, v^*)$. Specifically, if all eigenvalues of the linearized system have negative real parts, it indicates that the equilibrium point exhibits local asymptotic stability.

When using neural networks for optimization, our main focus is on achieving global stability. It is essential that the network remains globally stable, meaning it avoids oscillations or chaos regardless of the starting point. This ensures that an optimal solution can always be obtained by initializing the network with any value. Lyapunov's method is a highly effective approach for stability analysis, as it involves finding a suitable Lyapunov function.

Definition 2: Let's define the Lyapunov function using the Euclidean norm of absolute values as follows:

$$\begin{aligned} E(h, \rho, \lambda, v) = & \frac{1}{2} |\nabla_h L(h, \rho, \lambda, v)|^2 + \frac{1}{2} |\nabla_\rho L(h, \rho, \lambda, v)|^2 \\ & + \frac{1}{2} |\nabla_\lambda L(h, \rho, \lambda, v)|^2 + \frac{1}{2} |\nabla_v L(h, \rho, \lambda, v)|^2 \end{aligned} \quad (21)$$

where $L(h, \rho, \lambda, v)$ represents the Lagrange function of the system.

Proof: To prove the stability of the system, we need to show that Lyapunov function $E(h, \rho, \lambda, v)$ satisfies the stability conditions.

1. Positive definiteness:

First, let's prove that $E(h, \rho, \lambda, v)$ is positive definite. This means that the function is always greater than zero for any non-zero input. Since $E(h, \rho, \lambda, v)$ is defined as the sum of the squares of the absolute values of each term, it is clear that each term is positive or zero. Therefore, $E(h, \rho, \lambda, v)$ is a positive definite function.

2. Negativity of the derivative:

To demonstrate the negativity of the derivative, the Lyapunov function $E(h, \rho, \lambda, v)$ is the time derivative along the trajectories of the system (within the system of differential equations). We need to show that this time derivative is always negative or zero, and can only be zero at equilibrium points. Let's take the time derivative of $E(h, \rho, \lambda, v)$:

$$\frac{dE}{dt} = \frac{\partial E}{\partial h} \frac{dh}{dt} + \frac{\partial E}{\partial \rho} \frac{d\rho}{dt} + \frac{\partial E}{\partial \lambda} \frac{d\lambda}{dt} + \frac{\partial E}{\partial v} \frac{dv}{dt}$$

By substituting expressions for $\frac{dh}{dt}$, $\frac{d\rho}{dt}$, $\frac{d\lambda}{dt}$, and $\frac{dv}{dt}$ from system of equations (18), we obtain:

$$\begin{aligned} \frac{dE}{dt} = & -|\nabla_h L(h, \rho, \lambda, v)|^2 - |\nabla_\rho L(h, \rho, \lambda, v)|^2 \\ & - |\nabla_\lambda L(h, \rho, \lambda, v)|^2 - |\nabla_v L(h, \rho, \lambda, v)|^2 \leq 0 \end{aligned}$$

The negative sign in front of each term ensures that the time derivative of $E(h, \rho, \lambda, v)$ is always negative or zero, indicating stability. The derivative can only be zero at equilibrium points.

Therefore, since the Lyapunov function $E(h, \rho, \lambda, v)$ satisfies the necessary conditions for stability, the system is stable.

4. A NUMERICAL EXAMPLE

Let's examine a traffic system that comprises of three central nodes and ten connections, as described in [20]. Figure 1 represents the travel demands between Origin-Destination (O-D) points. The link costs in the problem are given by piecewise polynomials, as follows:

- For $0 \leq f_a < 5$, the cost of link a is $\frac{1}{5 - f_a}$, where a ranges from 1 to 5.
- For $6 \leq f_a \leq 10$, the cost of link a is 0, where a ranges from 6 to 10.

It's important to note that only the first five links in the network have flow, while the remaining five links have no flow.

Since link costs are rational expressions, each link capacity must be less than five, and a natural capacity has been added to the problem. The O-D pairs are numbered as follows: $O^{(12)} - D^{(12)}$ represents trips from node 1 to node 2, $O^{(2)} - D^{(2)}$ represents trips from node 1 to node 3, $O^{(3)} - D^{(3)}$ represents trips from node 3 to node 1, and $O^{(4)} - D^{(4)}$ represents trips from node 3 to node 2. Therefore, our notation for $O - D$ travel demand is $q_{12} = 3$; $q_{13} = 6$; $q_{31} = 2$; $q_{32} = 5$.

There are four commodities with seven chains, and the chain flows are displayed as matrix form in Figure 2. Each row represents a chain flow from left to right, where the first column indicates the starting point of the chain and the last column indicates the destination point.

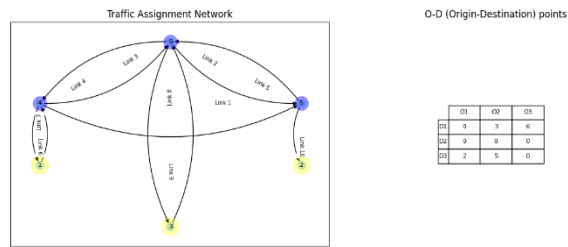


Figure 1. A traffic assignment network with the travel demands between different O-D points.

The conservation equations impose a requirement on the flows within chains, ensuring their adherence.

$$\begin{aligned} h_1^{(12)} + h_2^{(12)} &= 3, & h_1^{(13)} + h_2^{(13)} &= 6, \\ h_1^{(31)} &= 2, & h_1^{(32)} + h_2^{(32)} &= 5, \\ h_k^{(rs)} &\dots 0 \end{aligned} \tag{22}$$

Additionally, as seen in Figure 2, the link-to-chain flow equations for links 1 to 5 can be expressed by utilizing the link-to-chain flow matrix provided therein.

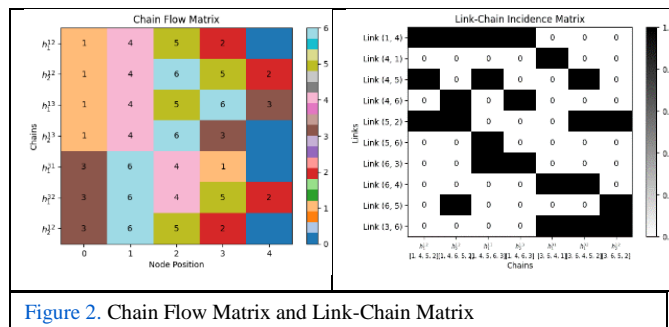


Figure 2. Chain Flow Matrix and Link-Chain Matrix

These equations can be obtained by summing flows of chains that connect relevant nodes, with each column representing the flow of a chain and each row representing the flow of a link between two nodes.

$$\begin{aligned} h_1^{(12)} + h_1^{(13)} + h_1^{(32)} &= f_1, \\ h_1^{(13)} &= f_2, \\ h_2^{(12)} + h_2^{(13)} &= f_3, \\ h_1^{(31)} + h_1^{(32)} &= f_4, \\ h_2^{(12)} + h_2^{(32)} &= f_5. \end{aligned} \tag{23}$$

Thus, the equivalent problem to problem (1) can be written as follows:

$$\min z(h) = \sum_a \int_0^{f_a} \frac{1}{5-x} dx, \quad a = 1, 2, \dots, 5 \tag{24}$$

s.t.

Chain Flows Constraints: (25)

$$\begin{cases} h_1^{(12)} + h_2^{(12)} = 3, & h_1^{(13)} + h_2^{(13)} = 6, \\ h_1^{(31)} = 2, & h_1^{(32)} + h_2^{(32)} = 5, \\ h_1^{(12)}, h_2^{(12)}, h_1^{(13)}, h_2^{(13)}, h_1^{(31)}, h_1^{(32)}, h_2^{(32)} \geq 0 \end{cases}$$

Capacity Constraints:

$$\begin{cases} h_1^{(12)} + h_1^{(13)} + h_1^{(32)} \leq 4.999, \\ h_1^{(13)} \leq 4.999, \\ h_2^{(12)} + h_2^{(13)} \leq 4.999, \\ h_1^{(31)} + h_1^{(32)} \leq 4.999, \\ h_2^{(12)} + h_2^{(32)} \leq 4.999. \end{cases} \quad (26)$$

By introducing additional variables $\rho_a, a = 1, 2, \dots, 5$ for the capacity constraints, an equivalent formulation for problems (2) and (3) can be obtained as:

$$\min z(h) = \sum_a \int_0^{f_a} \frac{1}{5-x} dx, \quad a = 1, 2, \dots, 5$$

s.t.

Chain Flows Constraints:

$$\begin{cases} h_1^{(12)} + h_2^{(12)} = 3, & h_1^{(13)} + h_2^{(13)} = 6, \\ h_1^{(31)} = 2, & h_1^{(32)} + h_2^{(32)} = 5, \\ h_1^{(12)}, h_2^{(12)}, h_1^{(13)}, h_2^{(13)}, h_1^{(31)}, h_1^{(32)}, h_2^{(32)} \geq 0 \end{cases}$$

Capacity Constraints:

$$\begin{cases} h_1^{(12)} + h_1^{(13)} + h_1^{(32)} + (\rho_1)^2 = 4.999, \\ h_1^{(13)} + (\rho_2)^2 = 4.999, \\ h_2^{(12)} + h_2^{(13)} + (\rho_3)^2 = 4.999, \\ h_1^{(31)} + h_1^{(32)} + (\rho_4)^2 = 4.999, \\ h_2^{(12)} + h_2^{(32)} + (\rho_5)^2 = 4.999. \\ \rho_1, \rho_2, \rho_3, \rho_4, \rho_5 \geq 0 \end{cases}$$

As capacity constraints cannot be exact in optimization problems and the capacity constraints in this case are less than 5, they are taken as 4.999. After constructing an equivalent Lagrange function for this problem, the problem reduces to a set of ordinary differential equations, similar to (18), which describe the transient behavior of the neural network. These equations can be solved using the classical fourth-order Runge-Kutta method. All computation and modeling steps were performed using Python 3.11.1 on Jupyter Notebook, executed on a personal computer with the following specifications: CPU: AMD PRO A10-8700B R6, 10 Compute Cores 4C+6G, 1.80 GHz, RAM: 8 GB.

The research findings illustrated in Figures 3 and 4 were obtained through the use of specified initial conditions:

$$(1, 1, 1, 1, 1, 1, 0.1, 0.1, 0.1, 0.1, 0.1, 0.1, 0.1, 0.1, 0.1, 0.1, 0.1, 0.1, 0.1)$$

$$h_1^{12}, h_2^{12}, h_1^{13}, h_2^{13}, h_1^{31}, h_1^{32}, h_2^{12}, \lambda_1, \lambda_2, \lambda_3, \lambda_4, \nu_1, \nu_2, \nu_3, \nu_4, \nu_5, \rho_1, \rho_2, \rho_3, \rho_4, \rho_5.$$

Figure 3 portrays the temporal variations of neurons in the neural network and the corresponding link flows when calculated values are applied to the optimization problem. Additionally, Table I presents the outcomes garnered from solving the neural network. Meanwhile, Figure 4 displays the relationship between link flows and traffic congestion. It is evident that, as traffic congestion increases, there is a noticeable decline in link flows. These outcomes represent the user equilibrium results for the network traffic assignment problem utilizing the Lagrange neural network.

TABLE 1:

USER EQUILIBRIUM RESULTS FOR NETWORK TRAFFIC ASSIGNMENT PROBLEM USING LAGRANGE NEURAL NETWORK.

System Neurons	Lagrange Neurons	Link Flows	Objective Function
$h_1^{12} = 3.009537,$	$\lambda_1 = 0.371703,$	$f_1 = 4.638500,$	9.086326
$h_2^{12} = 1.319719,$	$\lambda_2 = 2.766433,$	$f_2 = 1.319719,$	
$h_1^{13} = 0.0,$	$\lambda_3 = 3.038079,$	$f_3 = 4.680359,$	
$h_2^{13} = 4.680359,$	$\lambda_4 = 3.137963,$	$f_4 = 2.309238,$	
$h_1^{31} = 1.999994,$	$\nu_1 = 0.0,$	$f_5 = 4.690839$	
$h_1^{32} = 0.309243,$	$\nu_2 = 0.0,$		
$h_2^{12} = 4.690839,$	$\nu_3 = 0.0,$		
$\rho_1 = 0.6330851,$	$\nu_4 = 0.0,$		
$\rho_2 = 1.9181470,$	$\nu_5 = 0.0,$		
$\rho_3 = 0.6127112,$			
$\rho_4 = 1.6400531,$			
$\rho_5 = 0.6061630$			

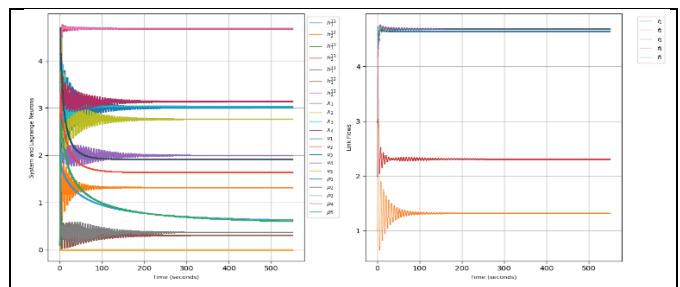


Figure 3. The change in system and Lagrange neurons over time, as well as the variation of link flows over time

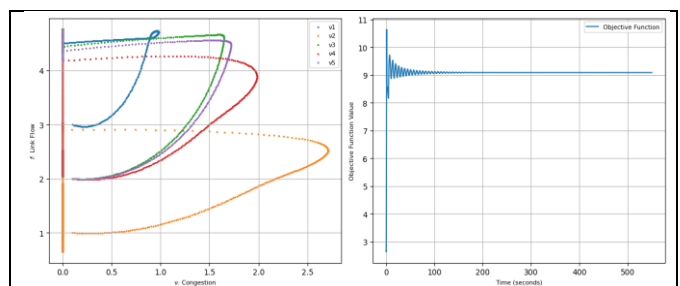


Figure 4. The relationship between link flow and traffic congestion, and tracks the changes in the objective function over time.

5. DISCUSSION

The presence of asymptotic stability in a given system indicates that any existing oscillations or disturbances will gradually diminish and converge towards the equilibrium point. This behavior holds true regardless of the initial conditions or perturbations introduced into the system, as they will eventually fade away over an infinite duration, leading to a permanent settlement at the equilibrium point. The convergence of all neurons towards the equilibrium point over time, as demonstrated in Figures 3 and 4, ensures the fulfillment of capacity constraints in the link flows while minimizing the objective function. Furthermore, the accuracy of the obtained results, as presented in Table I, can be validated by comparing them with the outcomes of a previous study employing classical methods, as denoted in literature [20].

6. CONCLUSION

The present study concerns the optimization model of static CTAP and its transformation into a dynamic system to analyze the effects of capacity constraints on connection flows and temporal variations of traffic in the network. Specifically, the gradient of the Lagrange function of the static CTAP optimization problem was transformed into a Lagrangian neural network, which allowed for the derivation of a set of differential equations that capture the dynamic behavior of the network. The numerical solution of the neural network was obtained using the fourth-order Runge-Kutta method, taking into account the initial conditions. By examining the temporal evolution of the system and the Lagrange neurons within the dynamic system, we were able to visualize the changes in traffic volume occurring in the connection flows over time and the traffic occurring on the connections with these changes. We also compared our results with an existing numerical example from the literature and confirmed the accuracy of our proposed Lagrange neural network method.

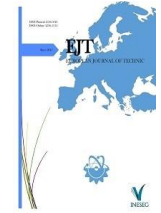
REFERENCES

- [1] J. G. Wardrop, "Some theoretical aspects of road traffic research," in *Proc. Inst. Civ. Eng., Part II*, vol. 1, no. 3, pp. 325-378, 1952.
- [2] M. Beckmann, C.B. McGuire, and C.B. Winsten, "Studies in the Economics of Transportation," New Haven, CT: Yale University Press, 1956.
- [3] J.A. Tomlin, "Minimum-cost multicommodity network flows," *Oper. Res.*, vol. 14, no. 1, pp. 45-51, 1966.
- [4] C.F. Daganzo, "On the traffic assignment problem with flow dependent costs—I," *Transp. Res.*, vol. 11, no. 6, pp. 433-437, 1977.
- [5] C.F. Daganzo, "On the traffic assignment problem with flow dependent costs—II," *Transportation Res.*, vol. 11, no. 6, pp. 439-441, 1977.
- [6] H. Inouye, "Traffic equilibria and its solution in congested road networks," in R. Genser (Ed.), *Proc. IFAC Conf. Control in Transportation Systems*, Vienna, pp. 267-272, 1987.
- [7] H. Yang and S. Yagar, "Traffic assignment and traffic control in general freeway-arterial corridor systems," *Transp. Res.*, vol. 28, no. 6, pp. 463-486, 1994.
- [8] T. Larsson and M. Patriksson, "An augmented Lagrangean dual algorithm for link capacity side constrained traffic assignment problems," *Transp. Res. Part B: Methodol.*, vol. 29, no. 6, pp. 433-455, 1995.
- [9] Y. Nie, H. M. Zhang, and D. H. Lee, "Models and algorithms for the traffic assignment problem with link capacity constraints," *Transp. Res. Part B: Methodol.*, vol. 38, no. 4, pp. 285-312, 2004.
- [10] D. W. Tank and J. J. Hopfield, "Simple 'neural' optimization networks: An A/D converter, signal decision circuit, and a linear programming circuit," *IEEE Trans. Circuits Syst.*, vol. CAS-33, pp. 533-541, May 1986.

- [11] S. Zhang and A. G. Constantinides, "Lagrange programming neural networks," *IEEE Trans. Circuits Syst. II*, vol. 39, no. 7, pp. 441-452, 1992.
- [12] R. Feng, C. S. Leung, A. G. Constantinides, and W. J. Zeng, "Lagrange programming neural network for nondifferentiable optimization problems in sparse approximation," *IEEE Trans. Neural Netw. Learn. Syst.*, vol. 28, no. 10, pp. 2395-2407, Oct. 2016.
- [13] Y. Lv, T. Hu, G. Wang, and Z. Wan, "A neural network approach for solving nonlinear bilevel programming problem," *Comput. Math. Appl.*, vol. 55, no. 12, pp. 2823-2829, 2008.
- [14] H. S. Shih, U. P. Wen, E. S. Lee, et al., "A neural network approach to multi-objective and multilevel programming problems," *Comput. Math. Appl.*, vol. 48, no. 1-2, pp. 95-108, 2004.
- [15] K. M. Lan, U. P. Wen, et al., "A hybrid neural network approach to bilevel programming problems," *Appl. Math. Lett.*, vol. 20, no. 8, pp. 880-884, Aug. 2007.
- [16] M. P. Kennedy and L. O. Chua, "Neural Network for nonlinear programming," *IEEE Trans. Circuits Syst.*, vol. 35, no. 5, pp. 554-562, 1998.
- [17] Y. Leung, K.Z. Chen, Y.C. Jiao, X.B. Gao, and K.S. Leung, "A new gradient-based neural network for solving linear and quadratic programming problems," *IEEE Trans. Neural Netw.*, vol. 12, no. 5, pp. 1074-1083, 2001.
- [18] A. R. Nazemi, "A dynamic system model for solving convex nonlinear optimization problems," *Commun. Nonlinear Sci. Numer. Simulat.*, vol. 17, no. 4, pp. 1696-1705, 2012.
- [19] L. Jin, S. Li, B. Hu, and M. Liu, "A survey on projection neural networks and their applications," *Appl. Soft Comput.*, vol. 76, pp. 533-544, 2019.
- [20] R. B. Potts and R. M. Oliver, "Flows in transportation networks," New York and London: Academic Press, 1972.

BIOGRAPHIES

Hasan Dalman obtained his Ph.D. in Mathematical Engineering from Yildiz Technical University in Istanbul, Turkey in 2015. He currently holds the position of Associate Professor in the Mathematics Department at Batman University, located in Batman, Turkey. He focuses his research on fuzzy sets and systems, game theory and nonlinear optimization.



Research Article

Production of CuNiSi Composites by Powder Metallurgy Method: Effects of Ti on the Microstructural and Corrosion Properties

Cihan ÖZORAK¹ , Tarek Mousa K. TABONAH² , Mehmet AKKAŞ³ 

¹Kastamonu University, Civil Aviation School / Aircraft Maintenance and Repair Department, Kastamonu, Turkey. (e-mail: ozorak@kastamonu.edu.tr).

²Kastamonu University, Department of Materials Science and Engineering, Kastamonu, Turkey. (e-mail: tarekmousaktabonah@gmail.com).

³Kastamonu University, Department of Mechanical Engineering, Kastamonu, Turkey. (e-mail: mehmetakkas@kastamonu.edu.tr).

ARTICLE INFO

Received: Oct., 07. 2023
Revised: Oct., 23. 2023
Accepted: Nov., 16. 2023

Keywords:
CuNiSi composite
Powder metallurgy
Ti reinforced
Microstructure
Corrosion

Corresponding author: *Mehmet AKKAŞ*

ISSN: 2536-5010 / e-ISSN: 2536-5134

DOI: <https://doi.org/10.36222/ejt.1372650>

ABSTRACT

In this study, composite samples were produced by supplementing the CuNiSi powder mixture with Ti particles at different weight ratios using the powder metallurgy (PM) method. The prepared CuNiSi and Ti powder mixtures were turned into pellets by cold pressing under 500 MPa pressure. The pelletized samples were subjected to sintering in an atmosphere-controlled oven at 900 °C for 2 hours. Scanning electron microscopy (SEM-EDS), SEM-Mapping and corrosion experiments were performed to determine the microstructures of the produced samples. From the microstructure results, it was determined that Ti particles were distributed homogeneously within the structure. As the amount of Ti increased, the resistance of the composite to corrosion increased.

1. INTRODUCTION

In this comprehensive investigation, we will scrutinize the microstructure and mechanical properties of CuNiSi alloy samples, meticulously pressed under a consistent pressing pressure and sintered at a precisely controlled temperature. To provide a reference point, we will also employ CuNiSi alloy samples, pressed and sintered under identical conditions, as a control group [1]. CuNiSi and similar high-engineering alloys have established themselves as indispensable materials in a wide array of industries, spanning aerospace, automotive, biomedical, electronics, and various industrial applications [2]. However, even these exceptional alloys may encounter challenges related to mechanical properties and wear resistance. Thus, our research aims to address these limitations head-on by introducing Ti reinforcements into the CuNiSi alloy matrix [3,4].

In recent times, the utilization of advanced manufacturing methods has significantly impacted the production of CuNiSi alloys, particularly through the innovative technique of powder metallurgy (PM) [5]. This method has garnered substantial attention due to its unique ability to precisely tailor

the chemical composition of these alloys, setting the stage for a new era of material engineering and design [6]. Unlike traditional production methods such as casting, machining, or hot and cold pressing, powder metallurgy offers a versatile alternative that opens up a myriad of possibilities in materials engineering [7,8]. The powder metallurgy method, with its inherent flexibility and precision, has the potential to revolutionize the way we enhance material properties. Through the creation of composite materials, PM enables us to achieve remarkable improvements in key attributes such as wear resistance, corrosion resistance, surface friction, and surface tension [9,10]. This is a game-changer in engineering applications, as composite materials empower the development of lighter, thinner, and yet stronger products, effectively boosting the coveted strength-to-weight ratio. The outcome? Reduced production and operating costs, a goal pursued relentlessly in various industries [11,12].

CuNiSi alloys, distinguished by their remarkable combination of lightness and durability, have emerged as standout candidates for the production of composite materials. These alloys offer an exceptional platform for innovation. Therefore, the central objective of our study is to delve into

the intriguing realm of CuNiSi alloys, exploring the transformative effects of incorporating Titanium (Ti) particles into the CuNiSi matrix, all achieved through the powder metallurgy method [13]. The potential outcomes of this groundbreaking endeavor are transformative. By enhancing the mechanical properties and wear resistance of CuNiSi alloys, we anticipate meeting significant industrial demands while expanding the horizons of CuNiSi alloy applications [14-17]. This research endeavor is not just a study in materials science; it represents a leap forward in the engineering world, with the promise of unlocking novel solutions and capabilities across multiple sectors. As we explore the intricate interplay between Ti and CuNiSi, we are poised to pioneer a new era of high-performance materials that push the boundaries of what is possible in engineering and design [18].

2. EXPERIMENTAL STUDIES

Within the scope of this study, Copper (Cu), Nickel (Ni), Silicon (Si) and Titanium (Ti) powders were supplied from Nanografi company. These powders are supplied in a form where Cu, Si and Ti are 99.9% pure and have an average grain size of 44 microns. Ni powder is 99.95% pure and has an average grain size of 44 microns. Using these powders, production was carried out using the powder metallurgy method to add Ti particles in different proportions (0.5, 1 and 2% by weight) to the CuNiSi alloy.

During the production process, the prepared powders were mixed for 2 hours with a three-dimensional turbula located in the Metallurgical and Materials Engineering Laboratory of Kastamonu University Faculty of Engineering and Architecture. After the mixing process, the powders were pressed with a press in the same laboratory. In this cold pressing process, 500 MPa pressure was applied and Specac brand GS15011 model hydraulic raw sample press was used. A cylindrical mold with a diameter of 13 mm was preferred as a mold.

The sintering process of the produced raw samples was carried out with the atmosphere-controlled heat treatment furnace (Protherm) located in the Metallurgical and Materials Engineering Laboratories of Kastamonu University Faculty of Engineering and Architecture. The sintering process took 240 minutes in total. In this process, the temperature was increased to 900 °C in 90 minutes during the heat treatment in order to remove the oil and other wastes contained in the samples, and then the temperature was kept constant at 900 °C for 60 minutes. The cooling of the samples was carried out in the oven under atmospheric control until room temperature in 90 minutes.

After the sintering process, the samples were prepared for metallographic analysis. These analyzes included sanding, polishing and etching stages, respectively. The surfaces of the samples were sanded with 120, 200, 400, 600, 800, 1000 and 1200 mesh sandpapers, respectively, and then polished with 3 and 1 μ diamond suspensions. Finally, the etching process was applied by immersion in the etching reagent. After the etching process of the samples, scanning electron microscope (SEM) images were taken from the "FEI QUANTA 250 FEG" brand device located at Kastamonu University Central Research Laboratories.

Corrosion tests were measured on the Reference 3000 Potentiostat / Galvanostat / ZRA device located in the Mechanical Engineering Research Laboratory of our University. Before starting the corrosion experiments, the

prepared samples were ultrasonically cleaned with acetone for 15 minutes, distilled water for 15 minutes and ethanol for 15 minutes at 35 °C, and then dried in an oven at 60 °C for 45 minutes.

1M HCL solution was prepared for corrosion experiments. Open circuit potentials of cleaned samples were measured in 1M HCL solution for approximately 30 minutes. Potentiodynamic polarization experiments and Electrochemical impedance spectroscopy (EIS) measurements were performed on all samples. Three experiments were performed for each sample, in each experiment the samples were cleaned, a new solution was used and the arithmetic average of the results was taken. Corrosion current density, corrosion potential, corrosion rate and polarization resistance were calculated from the curves read directly from the device according to the ASTM-G102 standard.

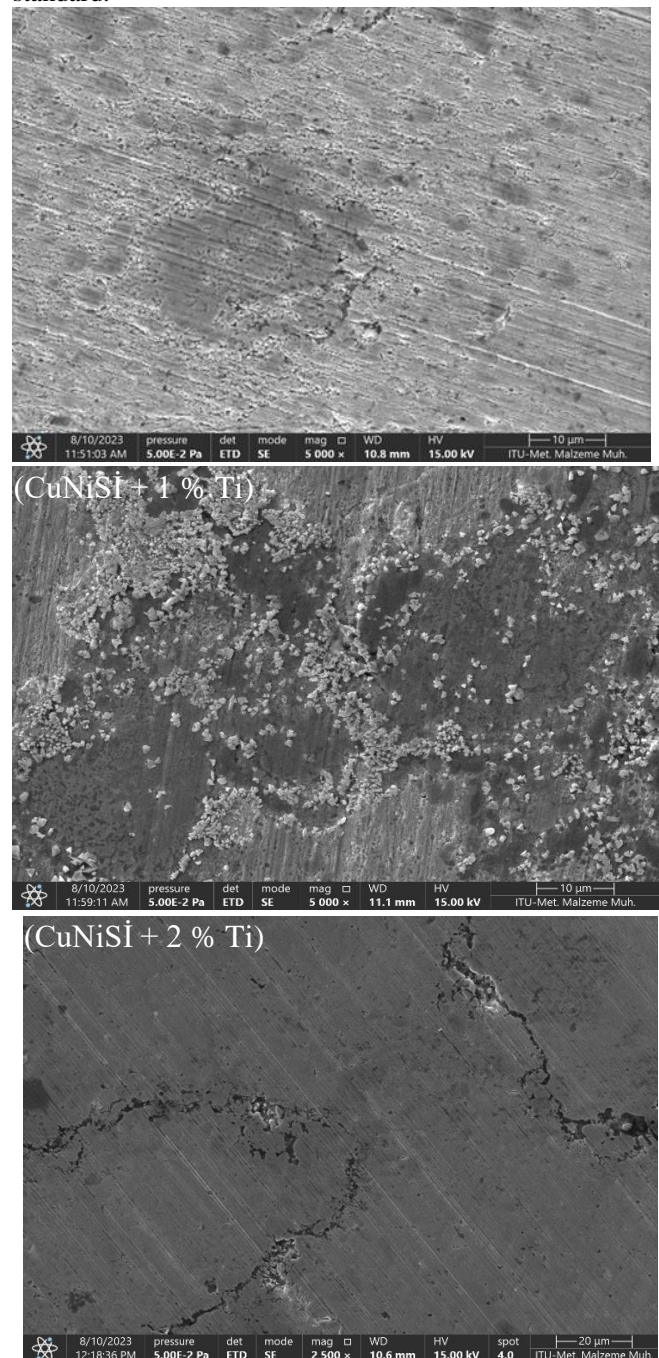


Figure 1. SEM micrographs of CuNiSiTi composites

3. EXPERIMENTAL RESULTS AND DISCUSSION

CuNiSiTi composites were successfully produced by pressing under 500 MPa pressure and sintering at 900 °C for 2 hour. SEM images taken from the produced samples are given in Figure 1.

The scanning electron microscope (SEM) images presented in Figure 1 provide a rich visual analysis that sheds light on important information. These images reveal in detail the microstructure of the CuNiSi alloy and the distribution of Titanium (Ti) reinforcement particles. First of all, the regions that appear in light gray in these images represent the matrix of the CuNiSi alloy. This matrix is the basic building block of the alloy and consists of the main components [19].

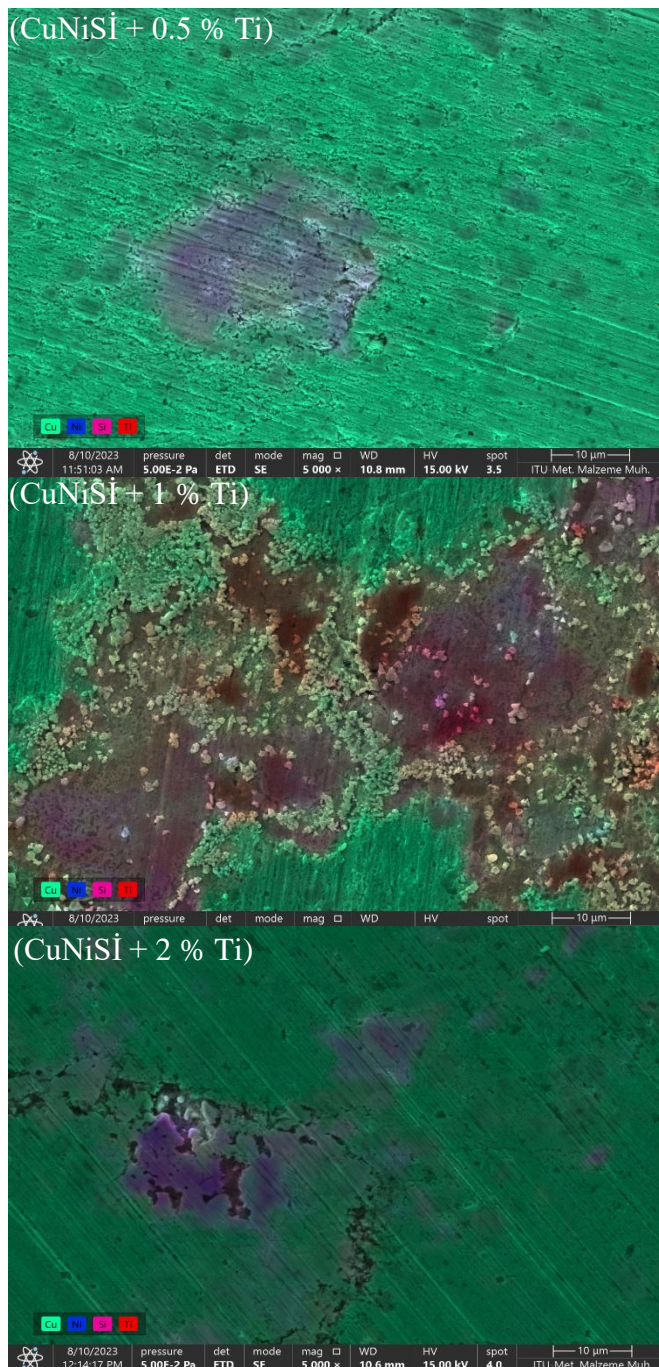


Figure 2. Mapping marked in the SEM micrographs for CuNiSiTi composites

Another notable feature is the grains, which are dark gray and have distinct boundaries. These grains indicate Titanium (Ti) particles. Titanium was added to the alloy as a reinforcement and appears as a dark gray in these images. What is particularly noteworthy is that the Titanium grains are homogeneously distributed. This shows that Titanium particles are well dispersed during the powder metallurgy process, providing a homogeneous distribution within the matrix [20].

Additionally, it is possible to make an important observation that the proportions of Titanium particles increase in the SEM images. That is, it is clearly seen that as the amount of Titanium reinforcement particles increases, the amount of Titanium in the microstructure also increases. This helps us understand how different Ti addition rates affect the properties of the alloy. As a result, SEM images have been used as a powerful tool to determine the distribution and quantity of Titanium reinforcement particles, as well as to examine the microstructure of the CuNiSi alloy. These analyzes provide important information from a materials engineering perspective and provide a valuable starting point for optimizing the performance of the alloy [21].

SEM-EDS images obtained from your CuNiSiTi composites provide critical information that enables an even deeper understanding of your material. These images in Figure 2 help us examine the microstructure and chemical composition of CuNiSiTi composites in more detail.

EDS (Energy Dispersive Spectroscopy) analysis results for the CuNiSiTi composites, as illustrated in Figure 2, provide crucial insights into the composition and structure of the material. The EDS analysis clearly indicates that the composite is composed entirely of CuNiSiTi, with no other detectable elements [22].

The "100% CuNiSiTi" composition revealed by the EDS analysis underscores the precision and accuracy of the manufacturing process. This outcome confirms that the desired composite material, consisting of Copper (Cu), Nickel (Ni), Silicon (Si), and Titanium (Ti), was successfully produced with the intended chemical composition. The absence of other elements in the EDS analysis demonstrates the high purity and quality of the CuNiSiTi composites, meeting the specifications and requirements of the engineering application. Furthermore, the EDS analysis results validate the homogeneity of the material, indicating that the Ti reinforcement particles are uniformly distributed throughout the CuNiSi matrix. This even distribution of Ti particles is crucial for achieving the desired mechanical and chemical properties, as it enhances the composite's strength, wear resistance, and corrosion resistance. In summary, Figure 2 presents EDS analysis results that unequivocally confirm the composition of the CuNiSiTi composites as 100% CuNiSiTi. This finding not only attests to the accuracy of the manufacturing process but also provides valuable assurance

regarding the material's suitability for its intended engineering applications. The homogeneity and precise composition are essential factors in ensuring the overall performance and reliability of the composite material [23].

0.5%, 1%, 2% Titanium was added into the samples CuNiSi. Potentiodynamic polarization experiments were carried out to determine the effects on the corrosion of a total of 3 different samples in 1 M HCl solution. The E-log curves obtained for 3 different samples in 1M HCl environment are given in the Figure 3. I_{corr} values were determined from the E-log curves obtained by the Tafel extrapolation method.

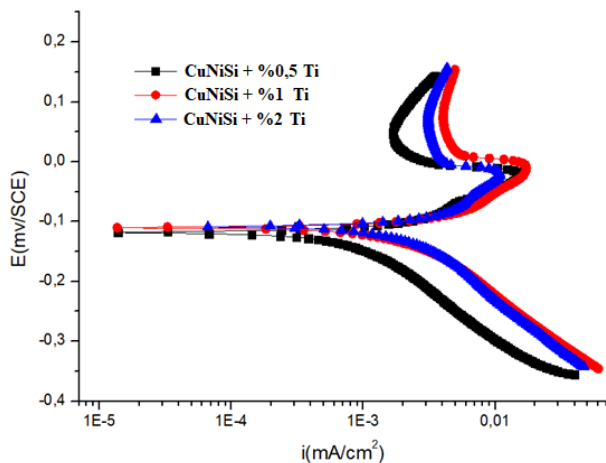


Figure 3. Potentiodynamic polarization curves of CuNiSiTi composites.

The results of potentiodynamic polarization experiments are given in the Table I. As the amount of titanium additive increases in the prepared samples, the porosity value also increases. Considering the data in the table and the polarization curves in the figure, it is seen that the corrosion rate of the sample with lower porosity is quite low and the corrosion rate increases with the increase in additive amounts [24].

TABLE I

THE RESULTS OF POTENTIODYNAMIC POLARIZATION EXPERIMENTS.

	CuNiSi+ %0.5 Ti	CuNiSi+ %1 Ti	CuNiSi+ %2 Ti
E _{corr} (mV)	-228	-289	-293
I _{corr} (μA)	18,6	20,1	61,8
Corr. Rate (mpy)	3,374	4,122	12,68

As seen in the current potential curves of the samples obtained in 1 M HCl solution, increases were observed in both anodic and cathodic regions and current values. Although there appears to be a positive shift in the corrosion potential (E_{corr}) of the samples, this shift is not very pronounced for all samples. The electrochemical behaviors at the interface of the samples' surface and the acid solution, and the corrosion of three different samples in 1 M HCl solution (Electrochemical impedance spectroscopy) were examined by the EIS method.

Nyquist diagrams of Ti doped samples are given in Figure 4. Nyquist diagrams obtained from reactions in solution show a capacitive loop in the form of depressed semicircles. This capacitive loop is related to the charge transfer process that

controls the protective film layer formed between the surface of the sample and the 1 M HCl solution [25].

Figure 4. Nyquist diagrams of Ti reinforced samples.

As the amount of additives increased, the diameter of the impedance spectrum decreased, and as the amount of additive decreased, the diameter of the impedance spectrum increased. Experimental data show that roughness and porosity on the metal surface have negative effects on the metal surface. Nyquist diagrams were analyzed using Framework Data Acquisition Software and the equivalent circuit was defined for the samples as given below (Figure 5).

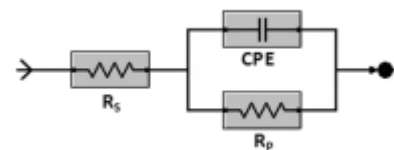
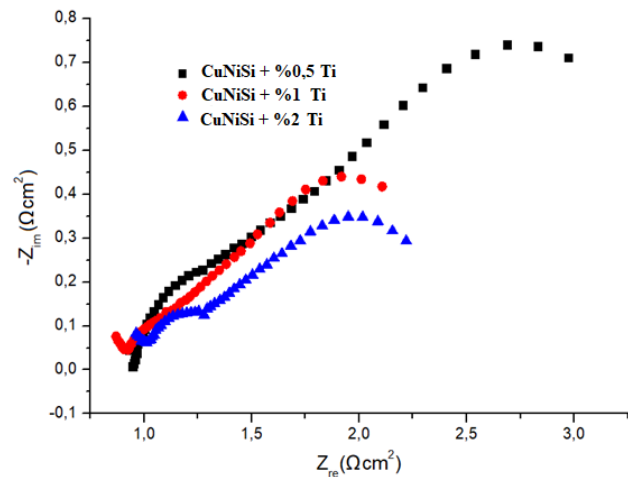


Figure 5. Electrochemical equivalent circuit used for the metal/solution interface of impedance spectra

The equivalent circuit consists of solution resistance (R_s), polarization resistance (R_p) and fixed phase element (CPE) connected in parallel. Here, R_p values show the load transfer resistance values measured in the environment. Additionally, R_p is given in Table II. As seen in the table, polarization resistance showed a decreasing trend with increasing additives to the samples. The samples with the highest R_p values are those containing less titanium additives, and the r_p value is 1.105 Ω cm². Decreases in R_p values were observed with increasing doping ratios in the samples, and the lowest R_p values were seen in samples containing 2 percent titanium with high doping ratios, with value of 0.8001 Ω cm².

As the contribution rate in the samples decreases, the R_p value increases. This increase causes the charge transfer on the surface of the samples to be slower, meaning they are more difficult to corrode [25-27].

TABLE II

THE RESULTS OF POTENTIODYNAMIC POLARIZATION.

	CuNiSi+ %0.5 Ti	CuNiSi+ %1 Ti	CuNiSi+ %2 Ti
R _p (Ωxcm ²)	1,105	0,868	0,8001

4. CONCLUSION

In this comprehensive study, we embarked on the production of Titanium (Ti) reinforced CuNiSi composites through the highly effective powder metallurgy method. This innovative approach allowed us to harness the synergistic benefits of these elements to engineer advanced materials with exceptional properties. Through a meticulous investigation employing various analytical techniques such as Scanning Electron Microscopy (SEM), SEM-EDS (Energy Dispersive Spectroscopy), and corrosion analysis, we have delved deep into the characteristics and performance of the CuNiSiTi composites. The production process itself was executed with precision, utilizing specific parameters to ensure the desired material properties. A pressure of 500 MPa was applied during the compaction phase, followed by sintering at a temperature of 900 °C for a duration of 2 hours, all carried out within an argon atmosphere. These carefully chosen production parameters played a pivotal role in achieving the desired composite structure.

The results of our exhaustive investigations are indeed promising. The Ti-reinforced CuNiSi composites were not only successfully pressed but also effectively sintered. This accomplishment underscores the capability of the powder metallurgy method in producing complex and high-performance materials with the desired microstructure. The SEM-EDS images obtained from the CuNiSiTi composites have been invaluable in our quest to understand the material at a microstructural level. These images provide critical insights into the distribution and homogeneity of the Ti reinforcement particles within the CuNiSi matrix. Such uniform distribution is paramount in enhancing the composite's mechanical strength, wear resistance, and corrosion resistance, factors of utmost importance in various engineering applications. Furthermore, the EDS analysis results have shed light on the precise chemical composition of the material. It is with great confidence that we report that the EDS analysis unequivocally confirms that the composite is composed entirely of CuNiSiTi, with no other detectable elements. This high degree of purity is a testament to the efficacy of the manufacturing process and ensures the material's suitability for a wide range of engineering applications.

Finally, our corrosion analysis has revealed an interesting correlation between the contribution rate in the samples and the Rp (polarization resistance) value. As the contribution rate decreases, the Rp value increases. This phenomenon indicates that the charge transfer on the surface of the samples becomes slower, rendering them more resistant to corrosion. This information is of paramount importance, as it provides crucial insights into the material's corrosion behavior, which is a critical consideration in applications exposed to harsh environments. In conclusion, this comprehensive study of Ti-reinforced CuNiSi composites, produced through the powder metallurgy method, represents a significant advancement in materials science and engineering. The combination of analytical techniques, precise manufacturing parameters, and insightful findings has laid the foundation for the development of high-performance materials with a wide range of applications, from aerospace to automotive industries, and beyond. These materials promise to revolutionize the way we approach engineering challenges, offering enhanced durability and performance in demanding environments.

REFERENCES

- [1] Wang, W., Chen, Z., Guo, E., Zhang, S., Kang, H., & Wang, T. (2023). Effects of Cr Addition on the Precipitation and Properties of Cryo-Rolled CuNiSi Alloys. *Metals*, 13(4), 758.
- [2] Ercetin, A., Aslantaş, K., Özgün, Ö., Perçin, M., & Chandrashekarappa, M. P. G. (2023). Optimization of Machining Parameters to Minimize Cutting Forces and Surface Roughness in Micro-Milling of Mg13Sn Alloy. *Micromachines*, 14(8), 1590.
- [3] Ahn, J. H., Han, S. Z., Choi, E. A., Lee, H., Lim, S. H., Lee, J., ... & Han, H. N. (2020). The effect of bimodal structure with nanofibers and normal precipitates on the mechanical and electrical properties of CuNiSi alloy. *Materials Characterization*, 170, 110642.
- [4] Kılıç, M. (2020). Effect Of Welding Parameters On Wear Performance Of Boron Coating Made With PTA. *European Journal of Technique (EJT)*, 10(1), 106-118.
- [5] Fincato, R., & Tsutsumi, S. (2022). Ductile fracture modeling of metallic materials: a short review. *Frattura ed Integrità Strutturale*, 16(59), 1-17.
- [6] Ercetin, A., Özgün, Ö., Aslantaş, K., Der, O., Yalçın, B., Şimşir, E., & Aamir, M. (2023). Microstructural and Mechanical Behavior Investigations of Nb-Reinforced Mg–Sn–Al–Zn–Mn Matrix Magnesium Composites. *Metals*, 13(6), 1097.
- [7] Akkaş, M. (2022). Synthesis and Characterization of MoSi2 Particle Reinforced AlCuMg Composites by Molten Salt Shielded Method. *Türk Doğa ve Fen Dergisi*, 11(4), 11-17.
- [8] Kaya, N., Çavdar, Ş., Öztürk, Ö., Ada, H., & Koralay, H. (2021). Investigation of microhardness properties of the multi-walled carbon nanotube additive MgB2 structure by using the vickers method. *Cryogenics*, 116, 103295.
- [9] Wang, W., Xiao, Z., Lei, Q., Meng, H., Guo, Q., Yang, Y., & Li, Z. (2021). A multiphase strengthened Cu-Nb-Si alloy with high strength and high conductivity. *Materials Characterization*, 182, 111565.
- [10] Ada, H., Türkmen, E., Kaplan, Y., Özçatalbaş, E., Şatir, E. Y., & Aksöz, S. (2023). An examination of microstructure, microhardness and tribological properties of ceramic reinforced bronze matrix composite materials. *Science of Sintering*, (00), 42-42.
- [11] Buytoz, S., Kilic, M., & Carboga, C. (2022). Microstructure and wear behaviour of Ni-based/TiC composite coating. *International Journal of Surface Science and Engineering*, 16(1), 71-90.
- [12] Kim, H., Ahn, J. H., Han, S. Z., Jo, J., Baik, H., Kim, M., & Han, H. N. (2020). Microstructural characterization of cold-drawn Cu–Ni–Si alloy having high strength and high conductivity. *Journal of Alloys and Compounds*, 832, 155059.
- [13] Kılıç, M. (2021). Toz metalurjisi ile Üretilen NiTi Alaşımına Al'un Etkisi. *Bitlis Eren Üniversitesi Fen Bilimleri Dergisi*, 10(1), 256-267.
- [14] Konieczny, J., & Labisz, K. (2021). Thermal Analysis and Selected Properties of CuNi2Si Alloy Used for Railway Traction. *Materials*, 14(16), 4613.
- [15] Li, L., Kang, H., Zhang, S., Li, R., Yang, X., Chen, Z., ... & Wang, T. (2023). Microstructure and properties of Cu-Cr-Zr (Mg) alloys subjected to cryorolling and aging treatment. *Journal of Alloys and Compounds*, 938, 168656.
- [16] Tang, S., Zhou, M., Zhang, Y., Xu, D., Zhang, Z., Zheng, X., ... & Marchenko, E. S. (2023). Improved microstructure, mechanical properties and electrical conductivity of the Cu–Ni–Sn–Ti–Cr alloy due to Ce micro-addition. *Materials Science and Engineering: A*, 871, 144910.
- [17] Kılıç, M., Imak, A., & Kirik, I. (2021). Surface modification of AISI 304 stainless steel with NiBSi-SiC composite by TIG method. *Journal of Materials Engineering and Performance*, 30, 1411-1419.
- [18] Wang, W., Zhu, J., Qin, N., Zhang, Y., Li, S., Xiao, Z., ... & Li, Z. (2020). Effects of minor rare earths on the microstructure and properties of Cu-Cr-Zr alloy. *Journal of Alloys and Compounds*, 847, 155762.
- [19] Çetin, T., & Akkaş, M. (2020). Effect of WC reinforced on microstructure and mechanical properties of CuAlMn alloys produced by hot pressing method. *European Journal of Technique (EJT)*, 10(1), 173-183.
- [20] Wei, H., Chen, Y., Li, Z., Shan, Q., Yu, W., & Tang, D. (2021). Microstructure evolution and dislocation strengthening mechanism of Cu–Ni–Co–Si alloy. *Materials Science and Engineering: A*, 826, 142023.
- [21] Xie, H., Tang, X., Chen, X., Sun, F., Dong, L., Tan, Y., ... & Fu, S. (2023). The effect of build orientations on mechanical and thermal properties on CuCrZr alloys fabricated by laser powder bed fusion. *Journal of Materials Research and Technology*, 23, 3322-3336.

- [22] Akkaş, M., & Boushiha, K. F. I. (2021). Investigation of wc reinforced cunisi composites produced by mechanical alloying method. *El-Cezeri*, 8(2), 592-603.
- [23] Wei, H., Chen, Y., Zhao, Y., Yu, W., Su, L., & Tang, D. (2021). Correlation mechanism of grain orientation/microstructure and mechanical properties of Cu–Ni–Si–Co alloy. *Materials Science and Engineering: A*, 814, 141239.
- [24] Zhang, J., Zhang, S., Cao, X., Li, L., Yang, X., Chen, Z., ... & Wang, T. (2023). Effect of temperature on mechanical behavior of Cu–Cr–Co–Ti alloys. *Materials Characterization*, 200, 112904.
- [25] Samant, A. V., & GrenSinG, F. C. (2015). Corrosion of Copper Alloys in Consumer Electronics Environments. *Mater. Perform.*, 54, 64-67.
- [26] Yang, H., Ma, Z., Lei, C., Meng, L., Fang, Y., Liu, J., & Wang, H. (2020). High strength and high conductivity Cu alloys: A review. *Science China Technological Sciences*, 63(12), 2505-2517.
- [27] Ada, H., El Rubaye, A. Q. J., Tokeser, E. A., Mavi, A., & Aksoz, S. (2023). Coating of Ti6Al4V Alloys by Physical Vapor Deposition Method and Micro-scratch and Corrosion Test Investigations of Coated Samples. *Journal of Advanced Applied Sciences*, 2(1), 36-45.

BIOGRAPHIES

Cihan Özorak is working as Assistant Professor Kastamonu University, Civil Aviation School / Aircraft Maintenance and Repair Department. His main research fields are composites and adhesion and adhesives.

Tarek Mousa K. Tabonah contained him doktora degree in material science and engineering from Kastamonu University. His research interests are adhesive materials, additive manufacturing and composite materials.

Mehmet Akkaş obtained his BSc degree in Metal Teaching Program from Fırat University in 2010. He received the MSc. Diploma in Metallurgy Education from Fırat University in 2013. He received the Ph.D. diploma in Manufacturing Engineering Department from the Karabük University in 2017. His research interests are powder metallurgy, powder production, gas atomization and composite materials. In 2018 he joined the Department of Mechanical Engineering, Faculty of Engineering and Architecture, Kastamonu University as an Associate Professor, where he is presently an Associate Professor.



Research Article

ICT-Based Vehicle-to-Grid Operation Based on the Fast Discharge Power for Economic Value

Sid-Ali Amamra^{1*} , Hakan Kızmaz² 

¹University of Huddersfield, Engineering and Technology Department, Huddersfield, U.K., (e-mail: SidAli.Amamra@hud.ac.uk).

²University of Batman, Electrical and Electronics Engineering Department, Batman, Turkey. (e-mail: hakan.kizmaz@batman.edu.tr).

ARTICLE INFO

Received: Sep., 19. 2023
Revised: Oct., 02. 2023
Accepted: Nov., 27. 2023

Keywords:

Economic value
Energy arbitrage
High discharge rate operation
Lithium-Ion Battery

Corresponding author: *Hakan Kızmaz*

ISSN: 2536-5010 / e-ISSN: 2536-5134

DOI: <https://doi.org/10.36222/ejt.1362587>

ABSTRACT

Renewable energy sources require effective energy management systems to be efficient in smart grids. Although electric vehicles are all potential consumers, using electric vehicle batteries is an effective utilisation strategy for smart grids. Vehicle-to-grid (V2G) is a crucial future technology for the smart grid. V2G technology proposes employing electric vehicles to contribute the stored energy to the other intelligent grid users. Expansion of the V2G technology is possible by funding, installing, and optimal managing the charging stations. In this work, an economic value of V2G operation is proposed. An advanced scheme of a V2G operations communication protocol that enables flexible control of the charging and discharging operations of the E.V. in an optimisation way has been developed, based on an energy arbitrage service, using two different discharge rates study. An economic study based on energy arbitrage using problem optimisation has been depicted. A use case based on the Nissan Leaf 40 kWh was simulated. The results show the economic benefit of using high discharge rate power (i.e., 3C) to the Li-ion battery over the regular discharge rate (1C).

1. INTRODUCTION

The fitful energy resources cause a decrease in the reliability of the generation and distribution network of national electric grids. The energy demand-supply inequities occur due to the unpredictability of renewable energy generation and demand from grids. This case causes load volatility and inefficiency of the resource. In the initial stages of vehicle electrification adoption, ‘demand-responsive’ vehicle charging could assist in redistributing peak loads on the electric grid [1-5]. As the population of plug-in electric vehicles grows, their potential to contribute to the grid by supplying electricity becomes more significant and sophisticated. This concept, known as vehicle-to-grid or V2G, was initially introduced by Kempton [6]. Vehicle batteries can connect to grids, so electric grids can be involved in energy markets. In this way, the volatility and inefficiency of the power supply installation can be compensated.

Energy arbitrage performs the most significant earnings opportunity for battery storage. In the open energy market, it is well known that low energy prices correspond to periods of low energy demand, indicating an abundance of energy in the grid. In contrast, high energy prices align with periods of high energy demand, indicating energy scarcity in the grid. With this mindset, the energy price can be leveraged to create a market where electric vehicle (E.V.) batteries are charged when energy prices are low. Energy stored in E.V. batteries is fed back into

the grid when energy prices are high, supporting the grid. This study proposes that the Vehicle-to-Grid (V2G) process is a function of the energy market and aims to maximise gains from energy exchange transactions. The profit from arbitrage consists of buying the cheapest energy when low energy demand occurs and selling it at the highest price when the highest energy demand occurs. The maximisation of profit depends on optimising the buying and selling periods. The comprehensive research has majored in optimising energy storage arbitrage problems to maximise profit. In [7-8], the authors calculated the anticipated revenue generated by V2G services across different power markets, i.e. frequency regulation, spinning reserve, or energy arbitrage. In the context of V2G energy arbitrage (charging during low-cost periods and discharging during high-cost periods), Rahman et al. [9] approximated the V2G advantage to be in the range of \$392 to \$561 annually for a single E.V. operating under typical conditions, with limited discharging power. This estimation could incentivise users to engage in V2G services voluntarily. In [10-11], a mixed integer linear approach was proposed to optimise the profits in real-time markets. A scenario-based stochastic formulation was developed against the electricity price’s uncertainty [12]. In [13], a bidding mechanism utilising a two-stage stochastic programming approach is proposed for a consortium of energy storage systems participating in the day-ahead reserve market. Some robust optimisation-based bidding strategy is demonstrated in [14-15].

However, the Lithium-Ion Battery (LIB) is considered a high-energy and low-power density storage system [16]. Hence, increasing the discharge power during V2G operation could provide more benefits for the E.V. owner.

The accomplishment of the V2G solution depends on the consumers' collaboration and perspective. The location number of charging stations determines how to use E.V.s, such as some people prefer charging at home or work.

Several techniques are engaged for charging and discharging E.V.s [17]. V2G operations require a controllable charge/discharge station that allows the operator to decide when to charge and discharge, providing more freedom and control to the grid. When the energy demand is high, the operator can stop charging to the market less. Uncontrollable charge/discharge does not need to know about energy demand or generation. That method does not seem to be popular in the future for E.V. charging. Intelligent techniques decide when to charge/discharge E.V. according to grid requirements such as energy prices. The methods allow users to set their car for a lower price or discharge, probably for a small profit. That requires demand-side efficient management strategies.

Numerous communication technologies facilitate monitoring data exchange and control commands between smart meters and external systems. A V2G communication system differs from other existing communication systems in many conditions, such as charging/discharging operations, locations, fast authentication, etc. Besides, classified information such as vehicle and station I.D., vehicle type, and charging/discharging time are required to be secured over the communication network. The Information and Communication Technologies (ICT) sector is crucial in smart grids [18-22]. The concept specifies the power grid modernised with ICT technology or a digital network that merges the electrical providers and consumers. ICT is used in power grid systems, allowing energy and information to flow two-way [23-26]. It facilitates renewable energy integration into the power grid and entrusts energy-optimising tools for optimal consumption and prices. In other words, that concept imposes advanced communication techniques into the conventional power distribution base. That case enables the communication systems' two-way data transmission.

Smart grid establishment takes time due to requirements such as large-scale changes in existing classical power grids. ICT ensures the security, performance, reliability, and control of all smart grid elements, such as power generation, storage, transmission, and consumption. It also roles grid usage authorisation, detection of faults and errors, and control of charge period timing.

This paper's main contributions are as follows: Energy management-arbitrage strategy is proposed to maximise the profit of the parking lot. The energy flow control and charging/discharging periods are provided and decided by ICT-based novel communication protocol. Another innovation of the proposed V2G strategy is using rapid discharge operations to bolster the power grid frequency. Unlike the conventional approach of achieving a 1C discharge rate, the proposed strategy enhances control power by a factor of three by discharging the vehicle's battery at a rate of 3C, with the primary aim of supporting the power grid.

The objective is to highlight the economic value of the proposed operating environment of V2G operation based on energy arbitrage service. The rest of this paper is outlined in

Section II - a U.K. scheduling approach for energy arbitrage based on V2G operation, Section III - UK ICT-Based communication, and Section IV - Economic study results. Conclusions are drawn in Section V.

2. UK SCHEDULING APPROACH FOR ENERGY ARBITRAGE BASED ON V2G OPERATION

The goal of energy arbitrage utilising battery storage is to maximise revenue. The literature includes three comparably simple assumptions in energy storage arbitrage that obstruct their adoptions: Sufficient foresight about energy prices, battery charging/discharging stabilisation, and battery lifetime modelling. Based on a proposed energy arbitrage service within the U.K. energy market, this study aims to understand the economic benefits of using high-rate discharge during V2G operation throughout the day. An E.V. participating in V2G operation using an energy arbitrage approach can charge at off-peak hours when there is a low electricity price and then discharge at on-peak hours when the price is high - thus making 'arbitrage' profit from the price difference. This study proposes a scheduling approach based on an optimisation problem to achieve maximum daily arbitrage profits. The process would maximise the E.V. owner's return revenue. The proposed optimisation scheduling method is based on the typical daily electricity price pattern - the E.V.'s plug-in and plug-out times and the desired final E.V. battery SOC. The historical U.K. grid pricing was used to examine the general impact pattern of the daily electricity price on the economic benefits of using V2G. The historical data chosen was over all four seasons during 2019 - Wednesday, 6th February, Wednesday, 6th May - Wednesday, 6th August - Wednesday, 6th November (from winter to autumn, respectively). The data was extracted as sample electricity price profiles (Figure 1) [27]. It is clear from the samples of the selected days demonstrated in Figure 1 that seasonal U.K. system prices show the highest volatility during off-peak and on-peak hours. It has been noted that the system price exhibits a notably higher level in February, May, and November. The high energy demand on the grid peaks during these colder months and is reflected in the higher price per M/Wh when more costly peak-load power stations are typically employed. The system price sharply decreases in the summer season, especially in August, due to better weather conditions where base load generation provides most of the electricity.

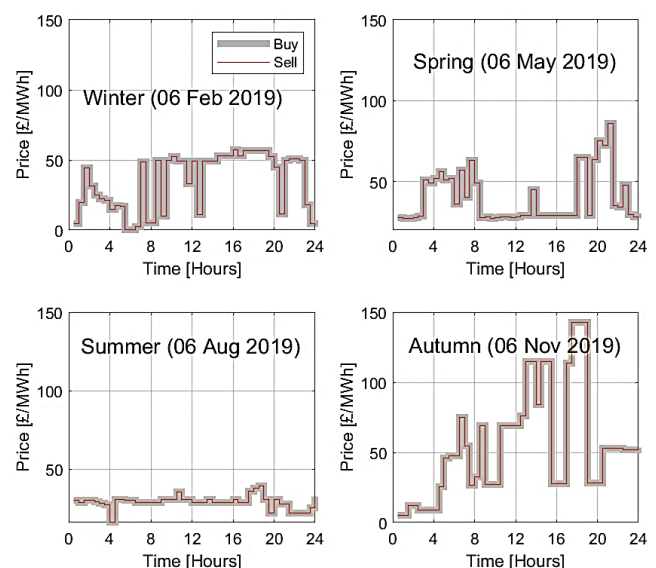


Figure 1. UK electricity system price of 6th February, 6th May, 6th August and 6th November of 2019

This study implemented an energy arbitrage optimisation method in the proposed scheduling approach to generate profits from energy arbitrage for E.V. owners. The scheduling optimisation problem using the objective function $J(\bullet)$ can be stated to maximise E.V.'s revenue by participating in V2G operations for energy arbitrage service during vehicle parking periods. To buy electricity during low-price periods and sell it during high-price periods, effective management of electric vehicle (E.V.) charging and discharging is essential. The objective function consists of the difference between the total cost of energy sold and the total cost of energy purchased. As the \pounds_{sell} and \pounds_{buy} are sales and purchase prices, the above objective function is as follows.

$$J = E^{\uparrow}(t) \times \pounds_{\text{sell}}(t) - E^{\downarrow}(t) \times \pounds_{\text{buy}}(t). \quad (1)$$

where $E^{\uparrow}(t)$ and $E^{\downarrow}(t)$ are the amount of energy exchanged within the power grid of the E.V. under consideration during discharging and charging operations, respectively, for each half hour, such as;

$$E^{\uparrow}(t) = P^{\uparrow}(t) * T_{\text{step}}. \quad (2)$$

$$E^{\downarrow}(t) = P^{\downarrow}(t) * T_{\text{step}}. \quad (3)$$

where $P^{\uparrow}(t)$ and $P^{\downarrow}(t)$ are the E.V.'s discharge and charge power rates are under consideration to control the energy exchanged within the power grid during participation in V2G operations. E^{\uparrow} and E^{\downarrow} are discharged and charged energy. T_{step} is the step time corresponding to periods of charging/discharging decisions. The optimisation algorithm generates the different charge/discharge operation scenarios. They also depend on different pricing and investment strategies. The optimisation mentioned above problem is subject to the four sub-mentioned constraints: constraints (4) specify the lower and upper bounds of the charging power;

$$-P^{\max} \leq P^{\downarrow}(t) \leq 0. \quad (4)$$

Constraints (5) specify the lower and the upper bounds of the discharging power;

$$0 \leq P^{\uparrow}(t) \leq P^{\max}. \quad (5)$$

The linear battery model can be used to predict the SOC behaviour for any E.V. Constraints defined in (6) are the instant energy constraints, which require the energy of E.V. at the end of step time $t+T_{\text{step}}$ to be between 5% and 95% SOC, so 90% DOD;

$$0.05 \leq \text{SOC}(t) + \left(\frac{P^{\downarrow}(t) \times \eta^{\downarrow} - \frac{P^{\uparrow}(t)}{\eta^{\uparrow}}}{E^{\max}} \right) \times T_{\text{step}} \leq 0.95. \quad (6)$$

where η is efficiency, and E^{\max} is E.V.'s maximum energy. Constraints (7) are the final energy constraints; the E.V. should meet the absolute energy requirement (i.e., SOC^{fin} of battery, E.V.) at the end of V2G operation to allow the outgoing E.V. enough energy for the following travel plan. The following equation can be used to build a final value for the SOC.

$$\text{SOC}^{\text{ini}} + \sum_{t=\text{rini}}^{\text{rfin}} \left(\frac{P^{\downarrow}(t) \times \eta^{\downarrow} - P^{\uparrow}(t) / \eta^{\uparrow}}{E^{\max}} \right) \times T_{\text{step}} = \text{SOC}^{\text{fin}}. \quad (7)$$

The abovementioned problem represents a constrained nonlinear multivariable problem with P^{\uparrow} and P^{\downarrow} as the decision variables. The object of the optimisation problem with (4)-(7) constraints is to maximise the revenue by charging when the energy price is minimum and discharging when the energy price is maximum. An optimisation algorithm makes the charging or discharging decisions with a communication protocol.

3. ICT-BASED COMMUNICATION

This section focuses on a charging station used to charge an E.V. The charging station is considered equipped with smart meters and an electrical storage system. It is deemed that the daily energy cost profile and double-way flow are available.

Upon plugging the charging plug into the charging point and establishing powerline communication, communication via the higher-level smart charge protocol can commence. The protocol rigorously pursues communication between the client and the grid server so the vehicle sends requests and gets responses. The charging point can trigger a request by setting specified flags. This chapter proposes a communication protocol between electric vehicles and the grid. Figure 2 depicts the ICT-Based communication scheme for smart grid-based V2G operation.

The problem is defined in a discrete-time setting, where the sampling time is T_{step} . Each plugged-in vehicle is charged at a constant power P_{ref} . The E.V. arrival T_{in} and departure T_{fin} times are uncertain. Assume that the reference charging/discharging time interval between T_{in} and T_{fin} is divided into $(T_{\text{fin}} - T_{\text{in}}) / T_{\text{step}}$ time slots where the initial time slots start at $t=0$, while the last at $t=T_{\text{fin}} - T_{\text{in}}$.

At first, the charger plug in the charge station grid receives the plug, and the grid requests bidirectional V2G/G2V operations. The grid then demands the availability of electric vehicles. Suppose the V2G operation is disabled for the car. In that case, the charging is finalised, and the vehicle requests to complete the charging process (FCP) from the grid. When the car is available for V2G operations, the vehicle logs in and initialises the communication session. Initialisation includes submitting the session identification number (session I.D.) and vehicle identification number (vehicle I.D.) to the grid.

The vehicle triggers service discovery requests to obtain the offered services, such as ways of payment. The grid then responds to service discovery. The vehicle then sets up the charging process (SCP). The setup charging process includes the defining initial and final time of charging/discharging (T_{in} and T_{fin}); the charge/discharge time interval (T_{step}); initial and final state of charge (SOC_{in} and SOC_{fin}); maximum energy capacity (E_{max}); full power (P_{max}) and efficiency of the vehicle. The vehicle sends the SCP request to the grid, which processes these SCP parameters. The grid also interacts with energy markets and obtains energy price vectors at different intervals. T_{step} is the sample rate as belonging to a digital control system.

There is an optimisation problem about when to charge/discharge process. According to an optimisation rule, the electric vehicle decides when to launch or buy the energy. The solution to the optimisation problem gives a dynamic charging profile power array, including charge/discharge power reference values for each step. The grid sends the power reference array P_{ref} to the electric vehicle charger. The symbol t is the current time as minutes. The current power reference value is taken from the array according to element number k .

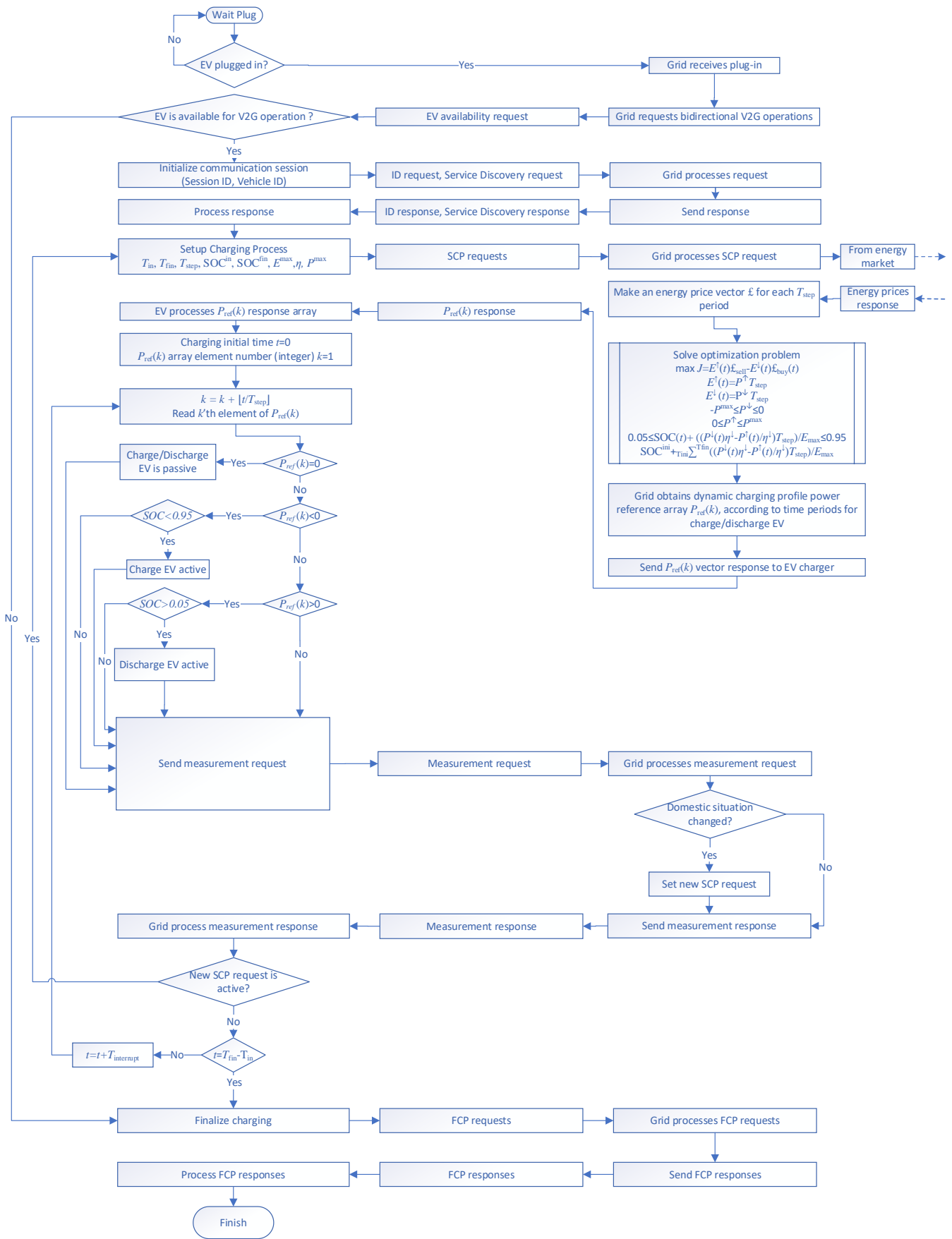


Figure 2. ICT-Based communication scheme

If the reference power value equals zero, the charging/discharging will be passive. If the reference power value is negative and the state of charge is smaller than 0.95, the charging process will be active; otherwise, the discharging

will be busy. The grid must check the charging and discharging cycles. That requires momentary measurement values from the charge station to the grid. The measurement values are processed and investigated whether there is a domestic

situation change, such as plug disconnection or fuse failure. That kind of problem requires changing the charge profile. If the domestic situation changes, the grid sends a new charge processing setup request to the electric vehicle. When the new setup request is active, the program changes the setup charging process. Suppose a new setup charging request is inactive, and the final time is not yet. In that case, the algorithm adds the processing interruption time $T_{interrupt}$ to the time index t . The program then jumps to read the new reference power value. The algorithm begins a charge process finalisation when the final time finishes. The electric vehicle sends the final charge process (FCP) request to the grid and receives a response. The response finishes the charge/discharge processing, and the state of charge value of the battery becomes the SOC_{fin} value at the end of the V2G operation.

4. ECONOMIC STUDY RESULTS

The optimisation problem is simulated in MATLAB/Simulink using a real-energy price data set obtained from the [27].

This paper examines the battery used in the Nissan LEAF 40 kWh, composed of Lithium Nickel Manganese Cobalt Oxide (NMC) prismatic/pouch cells. These cells are arranged into 24 modules, each containing 8 cells, and these modules are then grouped to form the battery pack [28] Table I.

TABLE I
NISSAN LEAF 40 kWh BATTERY CHARACTERISTICS [28]

	Cell level	Module level (8 cells)	Pack level (24 Modules)
Rated capacity [Ah]	56.30	56.3	112.6
Nominal voltage [V]	03.65	29.2	350.4
Rated energy [kWh]	0.205	1.64	39.50
	Battery pack price [k£]		06.00

This electric vehicle (E.V.) and its battery size were selected because they represent the typical storage capacity of E.V.s since the battery can meet users' needs in various countries [28]. It is based on the same chemistry studied and presented in section II of this work.

Table II shows the load current, load power and discharge duration of the Leaf battery back under two different discharge rates, i.e. 1C and 3C; as it can be seen, the maximum current and power that can be extracted from the battery are 112.6A and 39.5 kW at 1C discharge rate, and 337.8A and 118.5 kW at 3C discharge rate.

TABLE II
NISSAN LEAF 40 kWh BATTERY CURRENT AND POWER OUTPUT FOR DIFFERENT DISCHARGE RATES (I.E., 1C AND 3C)

Discharge rates	1C	3C
Load current [A]	112.6	337.8
Load power [kW]	39.5	118.5
Discharge duration [min]	60	20

TABLE III
V2G BENEFIT IN £/DAY FOR WINTER, SPRING, SUMMER AND AUTUMN PERIODS, AT DIFFERENT DISCHARGE RATES (I.E., 1C AND 3C) AND DIFFERENT PARKING LOCATIONS (I.E., HOME AND OFFICE)

		Winter	Spring	Summer	Autumn	
V2G benefit (£/day)	1C	Home	+5.33	+2.98	+0.78	+3.69
		Office	+2.75	+0.05	+0.33	+5.43
	3C	Home	+7.39	+4.33	+1.38	+3.75
		Office	+4.98	+0.71	+0.06	+8.73

Table III shows the daily V2G benefit in £/day for one Nissan Leaf participating in V2G operation two times per day, during office parking time, during home parking time, for four seasons and based on both regular discharge rates (1C) and fast discharge rate (3C). To highlight the actual reward/cost of the E.V. owner participating in V2G operation, Figure 3 depicts the total benefit/cost of the E.V. participating in V2G during four seasons.

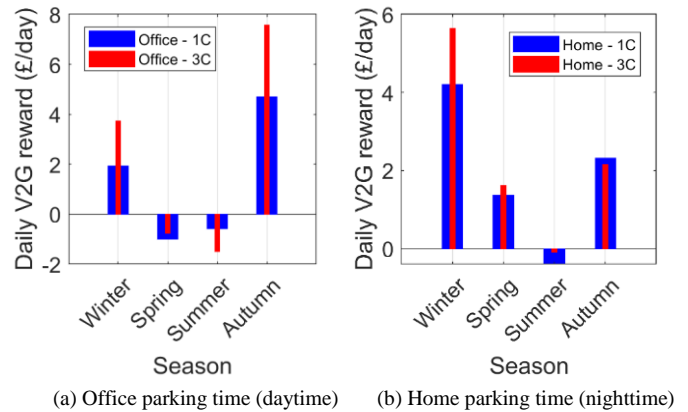


Figure 3. Daily E.V. owner benefits for Winter, Spring, Summer and Autumn periods, participating in V2G operation, (a) during office parking time, and (b) home parking time

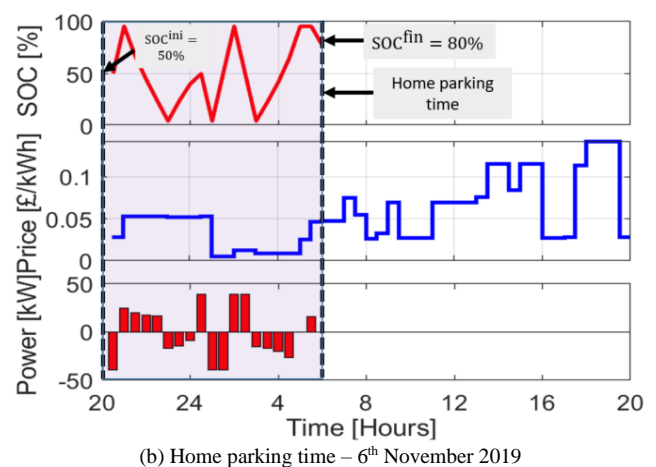
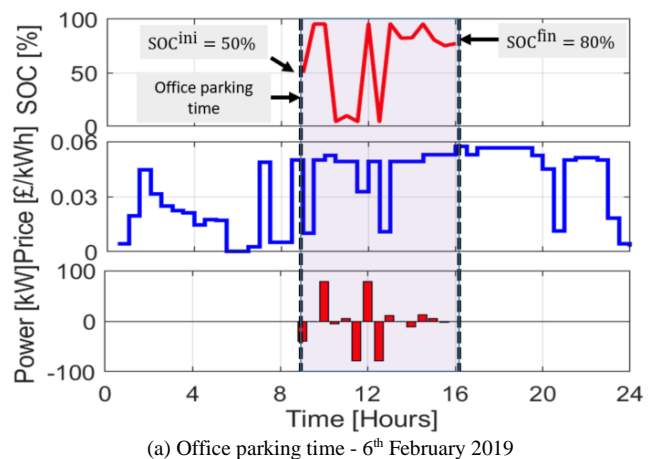


Figure 4. Daily EV SOC and Power profile participating in V2G operations, (a) during office parking time of winter season, and (b) home parking time during the autumn season.

As can be seen from Figure 3, two seasons of economic benefit for the owner in V2G were highlighted during office parking time (daytime), i.e. winter and autumn, while three seasons were of benefit during home parking time (nighttime), i.e., winter, spring, and autumn. In all cases, the summer season showed an additional cost while participating in V2G. For all benefit cases, the E.V. owner could benefit by an average of 1.6 times by using a high discharge rate over the regular discharge rate, except in the autumn season during home parking time; in this case, the normal discharge rate provided more benefit - of 1.1 times more than fast discharge rate.

Figure 4 shows an example of a daily V2G operation during day and night for the winter and autumn, respectively. As seen, the V2G scheduling for the E.V. considers the final desired SOC, allowing the E.V. owner to plan the next trip after performing a V2G operation.

5. CONCLUSIONS

Supplying energy without adverse ecology is the decisive factor for sustainable development worldwide. This paper's economic study is based on an energy arbitrage service for an E.V. participating in a V2G operation. To develop an effective revenue strategy under certain E.V. demand, an optimisation algorithm problem is defined. An economic survey of the energy arbitrage for an E.V. participating in V2G operation has been presented. Simulation results based on a Nissan Leaf 39.5 kWh battery model highlight the extra financial benefit to the E.V. owner participating in V2G and using a high discharge rate in preference to the standard discharge rate, yielding an average of 1.6 times the benefit per day during the winter and autumn season.

Smart grid requires integrating information technology with renewable energy to advance how to generate and consume electricity. Using ICT is an inevitable way of supporting two-way data and power, which facilitates the integration of renewable energy sources into the grids. An ICT-based smart communication protocol is proposed. Economic solution on the energy arbitrage required to solve an optimisation algorithm. The algorithm is settled in the protocol scheme. The communication protocol provides instructions for power stabilisation of the grid.

REFERENCES

- [1]. Dik, A.; Omer, S.; Boukhanouf, R. Electric Vehicles: V2G for Rapid, Safe, and Green EV Penetration. *Energies* 2022, 15, 803.
- [2]. Qi, J.; Li, L. Economic Operation Strategy of an E.V. Parking Lot with Vehicle-to-Grid and Renewable Energy Integration. *Energies* 2023, 16, 1793.
- [3]. Salvatti, G.A.; Carati, E.G.; Cardoso, R.; da Costa, J.P.; Stein, C.M.d.O. Electric Vehicles Energy Management with V2G/G2V Multifactor Optimization of Smart Grids. *Energies* 2020, 13, 1191.
- [4]. He, T.; Lu, D.D.-C.; Wu, M.; Yang, Q.; Li, T.; Liu, Q. Four-Quadrant Operations of Bidirectional Chargers for Electric Vehicles in Smart Car Parks: G2V, V2G, and V4G. *Energies* 2021, 14, 181.
- [5]. Iqbal, S.; Xin, A.; Jan, M.U.; Salman, S.; Zaki, A.u.M.; Rehman, H.U.; Shinwari, M.F.; Abdelbaky, M.A. V2G Strategy for Primary Frequency Control of an Industrial Microgrid Considering the Charging Station Operator. *Electronics* 2020, 9, 549.
- [6]. Taghizad-Tavana, K.; Alizadeh, A.; Ghanbari-Ghalehjoughi, M.; Nojavan, S. A Comprehensive Review of Electric Vehicles in Energy Systems: Integration with Renewable Energy Sources, Charging Levels, Different Types, and Standards. *Energies* 2023, 16, 630.
- [7]. Kempton, W.; Tomic, J. Vehicle-to-grid power fundamentals: Calculating capacity and net revenue. *J. Power Sources* 2005, 144, 268–279.

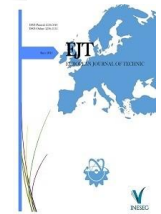
- [8]. Kempton, W.; Kubo, T. Electric-drive vehicles for peak power in Japan. *Energy Policy* 2000, 28, 9–18.
- [9]. Han, S.; Han, S. Economic Feasibility of V2G Frequency Regulation in Consideration of Battery Wear. *Energies* 2013, 6, 748–765.
- [10]. Peterson, S.; Whitacre, J.; Apt, J. The economics of using plug-in hybrid electric vehicle battery packs for grid storage. *J. Power Sources* 2010, 195, 2377–2384.
- [11]. H. Khani and M. R. D. Zadeh, "Real-Time Optimal Dispatch and Economic Viability of Cryogenic Energy Storage Exploiting Arbitrage Opportunities in an Electricity Market," *IEEE Tran. on Smart Grid*, vol. 6, no. 1, pp. 391–401, JAN 2015
- [12]. D. Metz and J. T. Saraiva, "Use of battery storage systems for price arbitrage operations in the 15-and 60-min German intraday markets," *Electric Power Systems Research*, vol. 160, pp. 27–36, JUL 2018.
- [13]. D. Krishnamurthy, C. Uckun, Z. Zhou, P. R. Thimmapuram, and A. Botterud, "Energy Storage Arbitrage Under Day-Ahead and Real-Time Price Uncertainty," *IEEE Tran. On Power Systems*, vol. 33, no. 1, pp. 84–93, JAN 2018.
- [14]. H. Akhavan-Hejazi and H. Mohsenian-Rad, "Optimal operation of independent storage systems in energy and reserve markets with high wind penetration," *IEEE Tran. on Smart Grid*, vol. 5, no. 2, pp. 1088–1097, March 2014.
- [15]. A.A. Thatte, L. Xie, D. E. Viassolo, and S. Singh, "Risk Measure Based Robust Bidding Strategy for Arbitrage Using a Wind Farm and Energy Storage," *IEEE Tran. on Smart Grid*, vol. 4, no. 4, pp. 2191–2199, DEC 2013.
- [16]. A. Attarha, N. Amjadi, and S. Dehghan, "Affinely Adjustable Robust Bidding Strategy for a Solar Plant Paired With a Battery Storage," *IEEE Tran. on Smart Grid*, vol. 10, no. 3, pp. 2629–2640, MAY 2019.
- [17]. Derek Wong, Biju Shrestha, David A. Wetz, John M. Heinzl, "Impact of high rate discharge on the aging of lithium nickel cobalt aluminum oxide batteries", *Journal of Power Sources*, Volume 280, 2015, Pages 363-372.
- [18]. Solañke, T.U.; Ramachandaramurthy, V.K.; Yong, J.Y.; Pasupuleti, J.; Kasinathan, P.; Rajagopalan, A. A review of strategic charging-discharging control of grid-connected electric vehicles. *J. Energy Storage* 2020, 28, 101193.
- [19]. Mazhar, T.; Asif, R.N.; Malik, M.A.; Nadeem, M.A.; Haq, I.; Iqbal, M.; Kamran, M.; Ashraf, S. Electric Vehicle Charging System in the Smart Grid Using Different Machine Learning Methods. *Sustainability* 2023, 15, 2603.
- [20]. Ortega-Fernandez, I.; Liberati, F. A Review of Denial of Service Attack and Mitigation in the Smart Grid Using Reinforcement Learning. *Energies* 2023, 16, 635.
- [21]. Malla, T.B.; Bhattarai, A.; Parajuli, A.; Shrestha, A.; Chhetri, B.B.; Chapagain, K. Status, Challenges and Future Directions of Blockchain Technology in Power System: A State of Art Review. *Energies* 2022, 15, 8571.
- [22]. Seven, S.; Yoldas, Y.; Soran, A.; Yalcin Alkan, G.; Jung, J.; Ustun, T.S.; Onen, A. Energy Trading on a Peer-to-Peer Basis between Virtual Power Plants Using Decentralised Finance Instruments. *Sustainability* 2022, 14, 13286.
- [23]. H. Farzin, M. Fotuhi-Firuzabad and M. Moeini-Aghtaie, "A Practical Scheme to Involve Degradation Cost of Lithium-Ion Batteries in Vehicle-to-Grid Applications," in *IEEE Transactions on Sustainable Energy*, vol. 7, no. 4, pp. 1730-1738, Oct. 2016.
- [24]. Mehmood, U.; Agyekum, E.B.; Kotb, H.; Milyani, A.H.; Azhari, A.A.; Tariq, S.; Haq, Z.u.; Ullah, A.; Raza, K.; Velkin, V.I. Exploring the Role of Communication Technologies, Governance, and Renewable Energy for Ecological Footprints in G11 Countries: Implications for Sustainable Development. *Sustainability* 2022, 14, 12555.
- [25]. Žarković, M.; Lakić, S.; Četković, J.; Pejović, B.; Redzepagic, S.; Vodenska, I.; Vujadinović, R. Effects of Renewable and Non-Renewable Energy Consumption, GHG, ICT on Sustainable Economic Growth: Evidence from Old and New EU Countries. *Sustainability* 2022, 14, 9662
- [26]. Soares, F.; Madureira, A.; Pagès, A.; Barbosa, A.; Coelho, A.; Cassola, F.; Ribeiro, F.; Viana, J.; Andrade, J.; Dorokhova, M.; Morais, N.; Wyrsh, N.; Sørensen, T. FEEdBACK: An ICT-Based Platform to Increase Energy Efficiency through Buildings' Consumer Engagement. *Energies* 2021, 14, 1524.
- [27]. Strielkowski, W.; Firsova, I.; Lukashenko, I.; Raudeliūnienė, J.; Tvaronavičienė, M. Effective Management of Energy Consumption during the COVID-19 Pandemic: The Role of ICT Solutions. *Energies* 2021, 14, 893.

- [28]. L. Calearo, A. Thingvad and M. Marinelli, "Modeling of Battery Electric Vehicles for Degradation Studies," 2019 54th International Universities Power Engineering Conference (UPEC), Bucharest, Romania, 2019, pp. 1-6.
- [29]. Elexon: 'System sell and buy prices'. Available at <https://www.bmreports.com/bmrs/?q=balancing/systemsellbuyprices>, accessed 20 July 2018

BIOGRAPHIES

Sid-Ali Amamra is a Senior Lecturer in Electrical Engineering at the School of Computing and Engineering, University of Huddersfield. He received his PhD in Electrical Engineering / Power Electronics from The University of Versailles Saint-Quentin-En-Yvelines (UVSQ) in 2013. Dr. Amamra has significant teaching and research experience at international academic institutions. Before joining the University of Huddersfield, he worked as Research Fellow in Vehicle-to-grid technology at the University of Warwick, Warwick Manufacturing Group, where he contributed to project management and research in Innovate U.K. research projects.

Hakan Kızmaz earned his Electrical and Electronics Engineering bachelor's degree from Sakarya University's Faculty of Engineering in 2006. Subsequently, he pursued his academic journey at the same institution, obtaining his master's degree from the Faculty of Science in 2009 and completing a second master's degree in 2015. With a commitment to academia and industry, Kızmaz gained valuable experience as an automation engineer at Kromel Makine Sanayi A.Ş. from 2007 to 2009. His passion for research and teaching led him to join Sakarya University as a research assistant in the Faculty of Engineering, where he contributed from 2009 to 2016. In 2016, Kızmaz embarked on a new academic endeavour by joining Siirt University, where he served until 2018. He holds the position of Assistant Professor at Batman University, a role he has held since 2018. His primary research interests lie in Control Systems and Control Theory, where he has made significant contributions to the academic community through his research and teaching efforts.



Research Article

Twin Rotor Control via Second Order Sliding Modes

Hasan Ömür Özer^{1*}, Yüksel Hacıoğlu², Nurkan Yağız³

^{1*}, Istanbul University-Cerrahpaşa, Vocational School of Technical Science, Department of Electricity and Energy, Istanbul, Türkiye.

(e-mail: hasanmur.ozer@iuc.edu.tr).

² Istanbul University-Cerrahpaşa, Faculty of Engineering, Department of Mechanical Engineering, Istanbul, Türkiye. (e-mail:

yukselh@iuc.edu.tr).

³ Istanbul University-Cerrahpaşa, Faculty of Engineering, Department of Mechanical Engineering, Istanbul, Türkiye. (e-mail:

nurkany@iuc.edu.tr).

ARTICLE INFO

Received: Oct., 26. 2023

Revised: Nov., 19. 2023

Accepted: Nov, 20. 2023

Keywords:

Second Order Sliding Mode Control

Twin rotor model

Numerical Results

Equivalent Control Estimation

Corresponding author: *Hasan Ömür ÖZER*

ISSN: 2536-5010 / e-ISSN: 2536-5134

DOI: <https://doi.org/10.36222/ejt.1381813>

ABSTRACT

The control problem of a twin rotor system is considered in this study. Since the twin rotor system has highly nonlinear and coupled dynamics, a second order sliding mode controller is proposed which reduces chattering. An estimation for the equivalent part of the controller is also proposed. The classical sliding controller is also calculated and adapted to the twin-rotor system to compare.

The numerical results presented that the designed controller achieved superior performance than the classical sliding mode controller in terms of reference tracking and chatter attenuation.

1. INTRODUCTION

The twin rotor system exhibits similarities to a helicopter in various aspects when it comes to its dynamics. [1]. Thus during the last decade, studies concerning twin rotor, have increased. Juang et. al. [2] implemented a hybrid proportional integral derivative (PID) controller to a twin rotor system. Taskin [3] investigated the performance of twin rotor system under hovering conditions with fuzzy logic controller (FLC). Aras and Kaynak [4] developed a neural fuzzy controller for the twin rotor system. The designed controller was compared with a traditional neuro-fuzzy structure and an interval type-2 fuzzy neural system. Hacıoğlu [5] proposed a new Multi Input Multi Output PIPD type fuzzy logic controller for experimental setup. Juang et al. [6] designed a fuzzy PID control algorithm with a real-valued optimization for twin rotor. Mondal and Mahanta proposed a second order sliding mode (SOSM) controller to experimental twin-rotor system. [7]. The simulation results of that controller showed sufficient tracking performance and robustness to external disturbances. To improve controller performance, a new sliding surface has been developed by Ahmed et al. to handle transverse effects in those system. [8]. Ilyas et al. [9] designed a hybrid controller with backstepping-sliding mode and validated their performances on a twin-rotor

system via simulations. Raghavan and Thomas [10] proposed an implementable control design for a twin rotor system. Sliding mode control (SMC) is known for its robust behavior. For nonlinear and uncertain systems, it may be modified. [11-14]. According to this control method, the control system is not sensitive to outside sources and parameter changes when the system is on the sliding surface. [12]. Alternatively, the control signal and system states may experience rapid oscillations at high frequencies, known as chattering. The components of the dynamic systems, such as the servomotors, may be damaged. Various approaches have been suggested to prevent this problem [15-16]. Huseyinoglu and Abut [17] proposed a SMC using a saturation function to prevent chattering for a two-degree-of-freedom (2-DOF) robotic arm. Aydin et al. [18] used a sigmoid function in sliding mode observer based control method to reduce chattering effect on a permanent magnet synchronous motor.

Nevertheless, the motion that occurs is not an ideal sliding motion. Thus, higher order sliding mode controller techniques have been proposed in the research area to suppress or almost eliminate chattering [19, 20]. In particular, the Super Twisting Algorithm (STA), a famous Second Order Sliding Mode method, is described by Levant [20] and has been applied for this area [20-24].

In this paper, a second-order SMC with estimation (SOSMCE) via the super twisting algorithm is designed for a twin-rotor model. The designed controller adopts an estimation law for the equivalent part of the control input, which separates it from previous high order sliding mode controllers in the current research. The coefficients are selected by multi objective genetic algorithm (MOGA) optimization. To verify the capability and chattering suppression of the designed controller, a classical sliding mode controller is also proposed, then implemented on the twin rotor model for validation. The capabilities of the proposed controllers are validated by numerical results.

2. CONTROLLER DESIGN

2.1. Twin Rotor Model

An attempt is made to control the position, speed [25], torque production [26] and energy consumption [27] values of dynamic electromechanical systems and their interactions. Due to its simple structure and good representation of the behaviour of cross-coupled axial motions, the twin rotor system is widely preferred by researchers.

Figure 1 shows the twinrotor model where m_{hel} stands for the mass of the helicopter, l is the distance from the center of mass to the pitch axis along the helicopter body, B_{pitch} , B_{yaw} are the equivalent viscous damping, I_{pitch} , I_{yaw} are the total moment of inertia, respectively. Here, θ and ψ are angular displacements and $\bar{\tau}_\theta$, $\bar{\tau}_\psi$ represent moments. The mathematical model is obtained using Lagrange's method, as shown below:

$$m_{hel}l^2\ddot{\theta} + I_{pitch}\ddot{\theta} + m_{hel}l^2(\dot{\psi})^2 \cos(\theta) \sin(\theta) + B_{pitch}\dot{\theta} + m_{hel}gl\cos(\theta) = \bar{\tau}_\theta + \bar{d}_\theta \quad (1)$$

$$m_{hel}l^2\ddot{\psi}\cos^2(\theta) - 2m_{hel}l^2\dot{\theta}(\dot{\psi}) \cos(\theta) \sin(\theta) + I_{yaw}\ddot{\psi} + B_{yaw}\dot{\psi} = \bar{\tau}_\psi + \bar{d}_\psi \quad (2)$$

\bar{d}_θ , \bar{d}_ψ are the outside effects that are applied to the model.

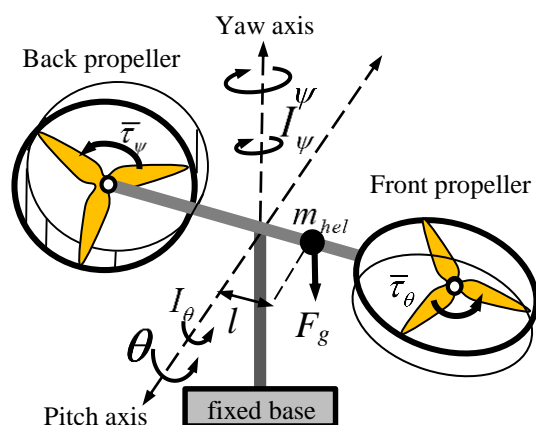


Figure 1. The physical of the twin rotor

Using the state variables

$$[x_1 \ x_2 \ x_3 \ x_4]^T = [\theta \ \dot{\theta} \ \psi \ (\dot{\psi})]^T \quad (3)$$

$$\dot{x}_1 = x_2 \quad (4)$$

$$\dot{x}_2 = \frac{-m_{hel}l^2(x_4)^2 \cos(x_1) \sin(x_1)}{(m_{hel}l^2 + I_{pitch})} + \frac{-B_{pitch}x_2 - m_{hel}gl\cos(x_1)}{(m_{hel}l^2 + I_{pitch})} + \frac{\bar{\tau}_\theta}{(m_{hel}l^2 + I_{pitch})} + \bar{d}_\theta \quad (5)$$

$$\dot{x}_3 = x_4 \quad (6)$$

$$\dot{x}_4 = \frac{2m_{hel}l^2(x_2)(x_4)\cos(x_1)\sin(x_1)}{m_{hel}l^2\cos^2(x_1) + I_{yaw}} + \frac{-B_{yaw}(x_4)}{m_{hel}l^2\cos^2(x_1) + I_{yaw}} + \frac{\bar{\tau}_\psi}{m_{hel}l^2\cos^2(x_1) + I_{yaw}} + \bar{d}_\psi \quad (7)$$

2.2. The designed Second Order Sliding Mode Controller with Estimation (SOSMCE)

In this section, a SOSMC based on the super twisting algorithm is presented. This controller design is different from other studies in that it includes the estimation of equivalent control. That estimation will be emphasized along with the controller design.

SOSMC can be described as the motion on nonempty set $\sigma = \dot{\sigma} = 0$ consisting of Filippov trajectories. $\sigma = \dot{\sigma}$ denote continuous functions of the closed-system state parameters [20, 22].

$$\eta_1 = \eta_2 \quad (8)$$

$$\dot{\eta}_2 = f(\eta_1, \eta_2) + g(\eta_1, \eta_2)\bar{u} + \bar{d} \quad (9)$$

where η_1 and η_2 are states, \bar{u} : control input and \bar{d} : limited disturbance. $g(\eta_1, \eta_2)$ is a known control input function, $f(\eta_1, \eta_2)$ may contain undefined or uncertain conditions, which are later taken into account in the estimation of the equivalent control. The sliding surface is described as

$$\sigma = \alpha(\eta_{1r} - \eta_1) + (\dot{\eta}_{1r} - \dot{\eta}_1) \quad (10)$$

where the sliding surface parameter is $\alpha > 0$. Through the determination of the time derivative of the sliding surface and the use of the Eqs. (8) - (9)

$$\dot{\sigma} = \alpha(\eta_{2r} - \eta_2) + \dot{\eta}_{2r} - f(\eta_1, \eta_2) - g(\eta_1, \eta_2)\bar{u} - \bar{d} \quad (11)$$

$$\phi(\eta_1, \eta_2) = \alpha(\eta_{2r} - \eta_2) + \dot{\eta}_{2r} - f(\eta_1, \eta_2) \quad (12)$$

$$u = -g(\eta_1, \eta_2)\bar{u} \quad (13)$$

$$d = -\bar{d} \quad (14)$$

$$\dot{\sigma} = \phi(\eta_1, \eta_2) + u + d \quad (15)$$

The disturbance is estimated to be limited as $|d| \leq \Delta\sqrt{|\sigma|}$, $\Delta > 0$. Bound condition $\dot{\sigma} = 0$ and nominal system that is $d = 0$, the equivalent control u_{eq} :

$$u_{eq} = -\phi(\eta_1, \eta_2) \quad (16)$$

We propose the super twisting method introduced in Levant [20] for the discontinuous part of the control rule.

$$u_{dc} = -k_1|\sigma|^{1/2}\text{sign}(\sigma) + v \quad (17)$$

$$\dot{v} = -k_2\text{sign}(\sigma) \quad (18)$$

Hence the cumulative control rule is,

$$u = u_{dc} + u_{eq} \quad (19)$$

The stability of the control algorithm will be ensured by this Lyapunov function [28],

$$V = 2k_2|\sigma| + \frac{1}{2}v^2 + \frac{1}{2}(k_1|\sigma|^{1/2}\text{sign}(\sigma) - v)^2 \quad (20)$$

$$V = \xi^T \mathbf{P} \xi \quad (21)$$

where

$$\xi^T = [|\sigma|^{1/2}\text{sign}(\sigma) \quad v] \quad (22)$$

$$\mathbf{P} = \begin{bmatrix} 2k_2 + \frac{k_1^2}{2} & \frac{-k_1}{2} \\ \frac{-k_1}{2} & 1 \end{bmatrix} \quad (23)$$

$$\begin{aligned} \dot{V} &= \xi^T \mathbf{P} \dot{\xi} + \dot{\xi}^T \mathbf{P} \xi = \dot{\sigma} \text{sign}(\sigma) \left(2k_2 + \frac{1}{2}k_1^2 \right) - \\ & k_1 \dot{v} |\sigma|^{1/2} \text{sign}(\sigma) - \frac{k_1 v \dot{\sigma}}{2|\sigma|^{1/2}} + 2\dot{v}v \end{aligned} \quad (24)$$

By using Eqs. (15) - (19)

$$\begin{aligned} \dot{V} &= [-k_1|\sigma|^{1/2}\text{sign}(\sigma) + v + d]\text{sign}(\sigma) \left(2k_2 + \frac{1}{2}k_1^2 \right) \\ & - k_1[-k_2\text{sign}(\sigma)]|\sigma|^{1/2} \text{sign}(\sigma) \\ & - \frac{k_1 v [-k_1|\sigma|^{1/2}\text{sign}(\sigma) + v + d]}{2|\sigma|^{1/2}} \\ & + 2[-k_2\text{sign}(\sigma)]v \\ & = - \left(k_1 k_2 + \frac{k_1^3}{2} \right) |\sigma|^{1/2} + k_1^2 v \text{sign}(\sigma) - \frac{k_1 v^2}{2|\sigma|^{1/2}} \\ & - d(t, \sigma) \frac{k_1 v}{2|\sigma|^{1/2}} \\ & + d(t, \sigma) \left[\left(2k_2 + \frac{1}{2}k_1^2 \right) \text{sign}(\sigma) \right] \\ & \leq - \left(k_1 k_2 + \frac{k_1^3}{2} \right) |\sigma|^{1/2} + k_1^2 v \text{sign}(\sigma) - \frac{k_1 v^2}{2|\sigma|^{1/2}} \\ & + \Delta \left(2k_2 + \frac{1}{2}k_1^2 \right) |\sigma|^{1/2} - \frac{k_1 v}{2} \Delta \text{sign}(\sigma) \end{aligned} \quad (25)$$

$$\dot{V} \leq \frac{-k_1}{2|\sigma|^{1/2}} \xi^T \mathbf{Q} \xi \quad (26)$$

$$\mathbf{Q} = \begin{bmatrix} 2k_2 + k_1^2 - \left(\frac{4k_2}{k_1} + k_1 \right) \Delta & -k_1 + \frac{\Delta}{2} \\ -k_1 + \frac{\Delta}{2} & 1 \end{bmatrix} \quad (27)$$

If k_1 and k_2 provide,

$$k_1 > 2\Delta \quad (28)$$

$$k_2 > \frac{k_1 \Delta^2}{8(k_1 - 2\Delta)} \quad (29)$$

$\dot{V} < 0$ will be negative definite, and attaining to the sliding surface is ensured. $\phi(\eta_1, \eta_2)$ can be undetermined or unidentified. Hence, the developed equivalent control signals can be different from the actual equivalent control signals. In this way, an estimated equivalent control \hat{u}_{eq} is used in this research, which is obtained by filtering the cumulative control input signal through a low pass filter. The main concept of applying a low pass filter is that the low frequencies define the characteristics of the input and the high frequencies arise from unknown sources. The estimated equivalent control law:

$$\hat{u}_{eq} = \frac{\varepsilon}{s + \varepsilon} u \quad (30)$$

The output of the low-pass filter tends towards equivalent control if the cut-off frequency ε is large enough to preserve the slow component undistorted, but small enough to eliminate the high-frequency component [11]. The system stability is

therefore guaranteed. The cumulative control signal rule for the designed SOSMC is described:

$$\bar{u} = -g^{-1}(\eta_1, \eta_2)u \quad (31)$$

$$u = \hat{u}_{eq} - k_1|\sigma|^{1/2}sign(\sigma) + v \quad (32)$$

$$\dot{v} = -k_2sign(\sigma) \quad (33)$$

$$\dot{\hat{u}}_{eq} = \varepsilon(u - \hat{u}_{eq}) \quad (34)$$

By using the governing Eqs. (4) - (7) for the axial motions, the control inputs of the designed SOSMCE for the model are obtained:

$$\bar{\tau}_\theta = -(m_{hel}l^2 + I_{pitch})\tau_\theta \quad (35)$$

$$\tau_\theta = \hat{\tau}_{\theta eq} - k_{1\theta} |\alpha_\theta(x_{1r} - x_1) + \dot{x}_{1r} - \dot{x}_2|^{1/2} \times sign(\alpha_\theta(x_{1r} - x_1) + \dot{x}_{1r} - \dot{x}_2) + v_\theta \quad (36)$$

$$\dot{v}_\theta = -k_{2\theta} \{sign(\alpha_\theta(x_{1r} - x_1) + \dot{x}_{1r} - \dot{x}_2)\} \quad (37)$$

$$\dot{\hat{\tau}}_{eq\theta} = \varepsilon(\tau_\theta - \hat{\tau}_{eq\theta}) \quad (38)$$

$$\bar{\tau}_\psi = -(m_{hel}l^2 \cos^2(x_1) + I_{yaw})\tau_\psi \quad (39)$$

$$\tau_\psi = \hat{\tau}_{\psi eq} - k_{1\psi} |\alpha_\psi(x_{3r} - x_3) + \dot{x}_{3r} - \dot{x}_4|^{1/2} \times sign(\alpha_\psi(x_{3r} - x_3) + \dot{x}_{3r} - \dot{x}_4) + v_\psi \quad (40)$$

$$\dot{v}_\psi = -k_{2\psi} \{sign(\alpha_\psi(x_{3r} - x_3) + \dot{x}_{3r} - \dot{x}_4)\} \quad (41)$$

$$\dot{\hat{\tau}}_{eq\psi} = \varepsilon(\tau_\psi - \hat{\tau}_{eq\psi}) \quad (42)$$

2.3. Search for optimal controller coefficients using multi-objective genetic algorithm

Genetic algorithms (GAs) utilize mechanisms derived by genetical principles found in biology to solve real-world tasks. Genetic algorithms commonly include Reproduction, Crossover and Mutation operators. For each problem to be performed, a fitness function must be designed [29]. The purpose of Multi Objective Optimization with Genetic Algorithm (MOGA) is to minimize several fitness functions at the same time. Used to solve multi objective optimization problems by defining the Pareto front, the set of uniformly distributed, non-dominated optimal solutions [30, 31].

In this study, optimal controller parameters are searched using ten proposed fitness functions. It is aimed to reduce tracking errors and attenuate possible chattering. β_1, β_2 represent

reference tracking performance. β_3, β_4 represent fluctuations in control signal. β_5, β_6 represent number of passes from zero for acceleration input. $\beta_7, \beta_8, \beta_9, \beta_{10}$, represent the mean values for variables. The optimum parameters achieved by MOGA are listed in Table 2 in Appendix.

$$\beta_1 = \sum_{i=1}^n |\theta_{refi} - \theta_i| \quad (43)$$

$$\beta_2 = \sum_{i=1}^n |\psi_{refi} - \psi_i| \quad (44)$$

$$\beta_3 = \frac{1}{\sqrt{n}} [\sum_{i=1}^n (\dot{u}_{\theta i})^2]^{1/2} \quad (45)$$

$$\beta_4 = \frac{1}{\sqrt{n}} [\sum_{i=1}^n (\dot{u}_{\psi i})^2]^{1/2} \quad (46)$$

$$\beta_5 = dimension \left[\ddot{\theta}_i \rightarrow \left\{ \begin{array}{ll} \ddot{\theta}_i < 0 & \text{and } \ddot{\theta}_{i-1} > 0 \\ \ddot{\theta}_i > 0 & \text{and } \ddot{\theta}_{i-1} < 0 \end{array} \right\} \right] \quad (47)$$

$$\beta_6 = dimension \left[\ddot{\psi}_i \rightarrow \left\{ \begin{array}{ll} \ddot{\psi}_i < 0 & \text{and } \ddot{\psi}_{i-1} > 0 \\ \ddot{\psi}_i > 0 & \text{and } \ddot{\psi}_{i-1} < 0 \end{array} \right\} \right] \quad (48)$$

$$\beta_7 = \frac{1}{n} \sum_{i=1}^n |u_{\theta i} - \frac{1}{n} \sum_{i=1}^n u_{\theta i}| \quad (49)$$

$$\beta_8 = \frac{1}{n} \sum_{i=1}^n |u_{\psi i} - \frac{1}{n} \sum_{i=1}^n u_{\psi i}| \quad (50)$$

$$\beta_9 = \frac{1}{n} \sum_{i=1}^n |\ddot{\theta}_i - \frac{1}{n} \sum_{i=1}^n \ddot{\theta}_i| \quad (51)$$

$$\beta_{10} = \frac{1}{n} \sum_{i=1}^n |\ddot{\psi}_i - \frac{1}{n} \sum_{i=1}^n \ddot{\psi}_i| \quad (52)$$

2.4. Performance indicators

In evaluating the results of this study, the following performance indicators will be used.

Integral Time Absolute Error (ITAE) [13, 32]:

$$ITAE = \int_0^t t|e|dt \quad (53)$$

Control effort indicator (CEI) [33]:

$$CEI = \sqrt{\frac{\sum_{i=1}^n (u_i)^2}{n}} \quad (54)$$

Chattering indicator (CI) [33]:

$$CI = \sqrt{\frac{\sum_{i=1}^n (\dot{u}_i)^2}{n}} \quad (55)$$

Here ITAE presents the error value of the angular displacement on time vector and penalizes the errors late in time heavily. The CEI is a measure of the control performance. The CI measures the amount of chattering in the control input.

3. NUMERICAL RESULTS

The simulation results of the twin rotor model are shown in this part for the designed second order sliding mode controller with estimation. To investigate the achievement of the designed controller in the presence of outside effects, the disturbance with 2 Hz and 0.26 Nm (\tilde{d}_θ), 2 Hz and 0.14 Nm (\tilde{d}_ψ), as presented in Figure 2, is applied to the control signal. For comparison purpose, the classical sliding mode controller was also developed and adapted to model.

Figure 3 presented the time versus motions. From this figure it is observed that both proposed SOSMCE and first order SMC tracked the reference angles for motions precisely. It is also seen that both controllers well coped with the disturbances since they continued to track the desired motion angles. Figure 4 presents the control signals. For the first order SMC it can be seen that there is chattering. Conversely, the proposed controller produced much smoother control signals.

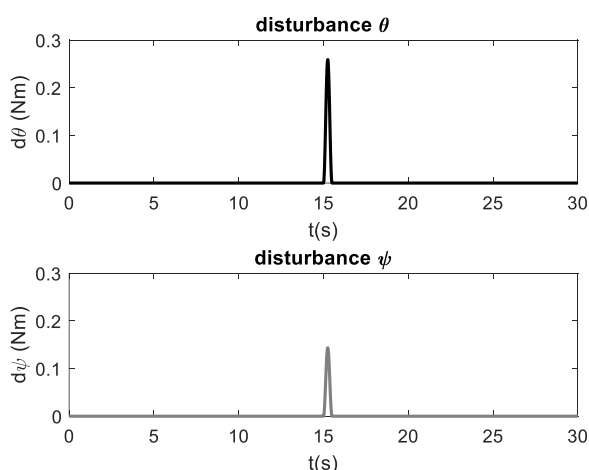


Figure 2. Disturbing torques

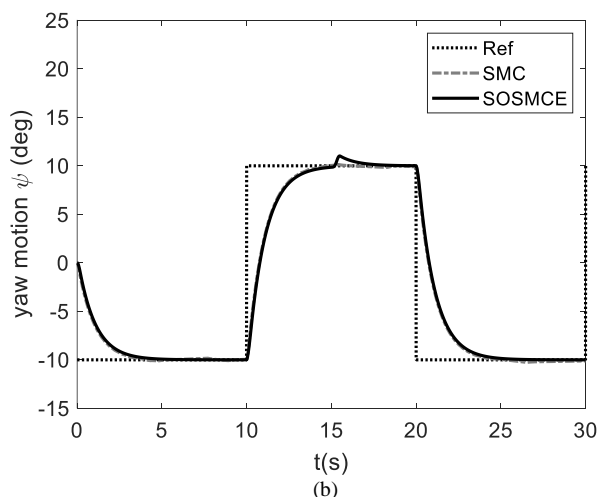
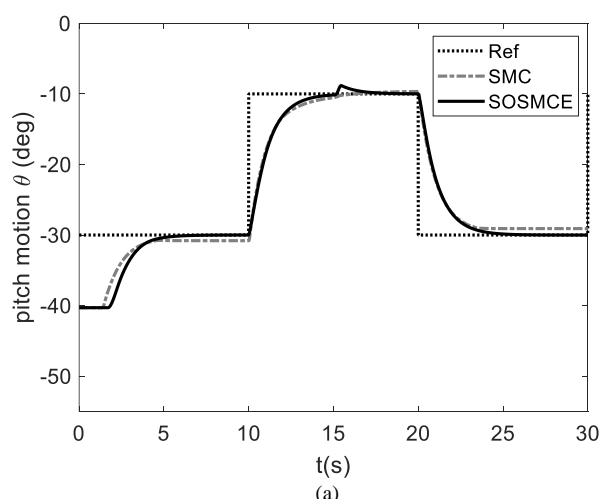


Figure 3. Tracking reference a) pitch motion, b) yaw motion

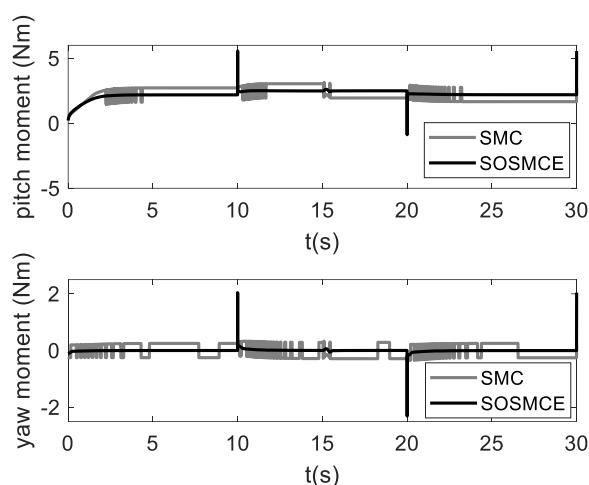


Figure 4. Pitch and yaw control signals

The performance indicators were also calculated and presented in Figure 5. It is seen that the proposed SOSMCE provided lower ITAE for the pitch motion whereas for the yaw motion performances are approximately same. The same figure also shows that although CEI both controllers are almost the same values, the proposed SOSMCE significantly suppresses chattering in the control signal.

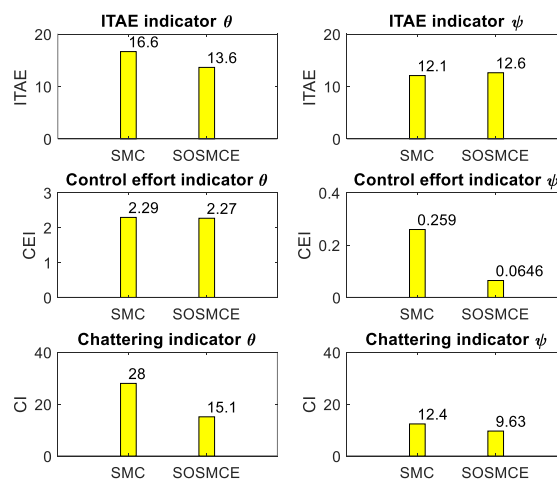


Figure 5. Performance indicators

4. CONCLUSION

In this study, a second order sliding mode controller with estimation (SOSMCE) was presented for the twin rotor model. The controller coefficients were provided by performing multi objective genetic algorithm searches. The classical sliding mode controller (SMC) was also provided and implemented to the twin rotor system for validate.

It was observed from Figure 5 that when there is external disturbance the ITAE indicator for SOSMCE (13.6) is smaller than the one for classical SMC (16.6) for pitch motions. In addition, the ITAE indicator for SOSMCE (12.6) is almost same the one for classical SMC (12.1) for yaw motions. Furthermore, it is seen that the designed SOSMCE used less control effort than the classical SMC, and the chattering indicator value is bigger for the classical SMC.

It was observed from numerical results that tracking performance was increased while chattering in the control signal was reduced with proposed controller.

For this reason, the proposed SOSMCE may be highly recommended for the control of aerial vehicles.

APPENDIX

Classical Sliding Mode Controller (SMC) Design

$$\dot{\xi}_1 = \xi_2 \quad (56)$$

$$\dot{\xi}_2 = f(\xi_1, \xi_2) + g(\xi_1, \xi_2)\bar{u} + \bar{d} \quad (57)$$

$$\sigma = \alpha(\xi_{1r} - \xi_1) + (\dot{\xi}_{1r} - \dot{\xi}_1) \quad (58)$$

$$V = \frac{1}{2}\sigma^2 \quad (59)$$

$$\dot{V} = \sigma\dot{\sigma} \quad (60)$$

with bounded condition the Eq. (60)

$$\dot{\sigma} = \alpha(\dot{\xi}_{1r} - \dot{\xi}_1) + (\ddot{\xi}_{1r} - \ddot{\xi}_1) = 0 \quad (61)$$

Eqs. (56) - (57) and (61), equivalent control \bar{u}_{eq} is defined as:

$$\bar{u}_{eq} = g^{-1}(\xi_1, \xi_2)\{\alpha(\xi_{2r} - \xi_2) + \dot{\xi}_{2r} - f(\xi_1, \xi_2)\} \quad (62)$$

$$\bar{u} = \bar{u}_{eq} + kg^{-1}(\xi_1, \xi_2)sign(\sigma) \quad (63)$$

Lyapunov function's derivative:

$$\begin{aligned} \dot{V} &= \sigma\dot{\sigma} = \sigma\{\alpha(\xi_{2r} - \xi_2) \\ &\quad + (\dot{\xi}_{2r} - f(\xi_1, \xi_2) - g(\xi_1, \xi_2)\bar{u} - \bar{d})\} \\ &= -k\sigma sign(\sigma) - \sigma\bar{d} \\ &\leq -|\sigma|(k - \Delta) \end{aligned} \quad (64)$$

$k > \Delta$, $\dot{V} < 0$, In this way, it is obliged to approach the sliding surface. Control law of is defined as

$$\bar{\tau}_\theta = \widehat{\bar{\tau}_{eq\theta}} + k_\theta (m_{hel}l^2 + I_{pitch}) \times sign\{(\alpha_\theta(\xi_{1r} - \xi_1) + \dot{\xi}_{1r} - \xi_2)\} \quad (65)$$

$$(\widehat{\bar{\tau}_{eq\theta}}) = \varepsilon(\bar{\tau}_\theta - \widehat{\bar{\tau}_{eq\theta}}) \quad (66)$$

$$\bar{\tau}_\psi = \widehat{\bar{\tau}_{eq\psi}} + k_\psi (m_{hel}l^2 \cos^2(\xi_1) + I_{yaw}) \times sign\{(\alpha_\psi(\xi_{3r} - \xi_3) + \dot{\xi}_{3r} - \xi_4)\} \quad (67)$$

$$(\widehat{\bar{\tau}_{eq\psi}}) = \varepsilon(\bar{\tau}_\psi - \widehat{\bar{\tau}_{eq\psi}}) \quad (68)$$

TABLE I
THE PARAMETERS OF TWIN ROTOR MODEL

Model Parameters	Symbol	Value	Unit
helicopter mass	m_{hel}	1.3872	kg
helicopter body length of pitch axis	l	0.186	m
pitch damping	B_{pitch}	0.8	N/V
yaw damping	B_{yaw}	0.318	N/V
pitch inertia moment	I_p	0.0384	kgm ²
yaw inertia moment	I_y	0.0432	kgm ²
θ initial value	$\theta(0)$	-40.3	°
ψ initial value	$\psi(0)$	0	°

TABLE II
CONTROLLER WITH MOGA

Controller	Parameter	Value
SMC	k_θ	6.37
	k_ψ	3.20
	$k_{1\theta}$	5.80
SOSMCE	$k_{2\theta}$	0.67
	$k_{1\psi}$	3.83
	$k_{2\psi}$	0.15

ACKNOWLEDGEMENT

This research received no specific grant from any funding agency in the public, commercial, or not-for-profit sectors.

REFERENCES

- [1] P. Wen and T.W. Lu, "Decoupling control of a twin rotor MIMO system using robust deadbeat control technique," IET Control Theory and Applications, vol. 2, no. 11, pp. 999-1007, 2008. <https://doi.org/10.1049/iet-cta:20070335>
- [2] J. Jih-Gau, L. Wen-Kai, and T. Cheng-Yu, "Intelligent control scheme for twin rotor MIMO system," presented in IEEE International Conference on Mechatronics, ICM '05, 2005. <https://doi.org/10.1109/ICMECH.2005.1529235>
- [3] Y. Taskin, "Improving pitch and yaw motion control of twin rotor MIMO system." Journal of Vibroengineering, vol. 16, no. 4, pp. 1650-1660, 2014.
- [4] A.C. Aras and O. Kaynak, "Interval Type-2 Fuzzy Neural System Based Control with Recursive Fuzzy C-Means Clustering," International Journal of Fuzzy Systems, vol. 16, no. 3, pp. 317-326, 2014.
- [5] Y. Hacioglu, "Multiple-input multiple-output proportional-integral-proportional-derivative type fuzzy logic controller design for a twin rotor system," Journal of Vibroengineering, vol. 17, no. 6, pp. 3104-3110, 2015.
- [6] J.G. Juang, W.K. Liu, and R.W. Lin, "A hybrid intelligent controller for a twin rotor MIMO system and its hardware implementation," ISA Transactions, vol. 50, no. 4, pp. 609-619, 2011. <https://doi.org/10.1016/j.isatra.2011.06.006>
- [7] S. Mondal and C. Mahanta, "Adaptive second-order sliding mode controller for a twin rotor multi-input-multi-output system," IET Control Theory and Applications, vol. 6, no. 14, pp. 2157-2167, 2012. <https://doi.org/10.1049/iet-cta.2011.0478>
- [8] Q. Ahmed, A.I. Bhatti, and S. Iqbal, "Nonlinear robust decoupling control design for twin rotor system," presented in Asian Control Conference, ASCC 2009. 7th., 2009.
- [9] M. Ilyas, N. Abbas, M. Ubaidullah, W.A. Imtiaz, M.a.Q. Shah, and K. Mahmood, "Control Law Design for Twin Rotor MIMO System with Nonlinear Control Strategy," Discrete Dynamics in Nature and Society, vol. 10, 2016. <https://doi.org/10.1155/2016/2952738>
- [10] R. Raghavan and S. Thomas, "Practically Implementable Model Predictive Controller for a Twin Rotor Multi-Input Multi-Output System," Journal of Control, Automation and Electrical Systems, vol. 28, no. 3, pp. 358-370, 2017. <https://doi.org/10.1007/s40313-017-0311-5>
- [11] V.I. Utkin, J. Guldner, and J. Shi, "Sliding mode in control in electromechanical systems," London, Taylor & Francis, 1999.
- [12] S. Laghrouche, F. Plestan, and A. Glumineau, "Higher order sliding mode control based on integral sliding mode," Automatica, vol. 43, no. 3, pp. 531-537, 2007. <https://doi.org/10.1016/j.automatica.2006.09.017>
- [13] N. Yagiz and Y. Hacioglu, "Robust control of a spatial robot using fuzzy sliding modes," Mathematical and Computer Modelling, vol. 49, no. 1-2, pp. 114-127, 2009. <https://doi.org/10.1016/j.mcm.2008.05.050>
- [14] Y. Hacioglu, Y.Z. Arslan, and N. Yagiz, "MIMO fuzzy sliding mode controlled dual arm robot in load transportation," Journal of the Franklin Institute-Engineering and Applied Mathematics, vol. 348, no. 8, pp. 1886-1902, 2011. <https://doi.org/10.1016/j.jfranklin.2011.05.009>
- [15] K. D. Young, V.I. Utkin, and U. Ozguner, "A control engineer's guide to sliding mode control," IEEE Transactions on Control Systems Technology, vol. 7, no. 3, pp. 328-342, 1999. <https://doi.org/10.1109/87.761053>
- [16] C. Edwards and S. Spurgeon, "Sliding Mode Control: Theory And Applications," Taylor & Francis, 1998.
- [17] M. Huseyinoglu and T. Abut, "Dynamic model and control of 2-DOF robotic arm," European Journal of Technique (EJT), vol 8, no. 2, pp 141-150, 2018. <https://doi.org/10.36222/ejt.497852>
- [18] C. Aydin, S. Unal, and M. Ozdemir, "Comparison between MRAS and SMO based sensorless control methods of permanent magnet synchronous motor," European Journal of Technique (EJT), vol. 11, no. 1, pp. 53-59, 2021. <https://doi.org/10.36222/ejt.811569>
- [19] G. Bartolini, A. Ferrara, and E. Usai, "Chattering avoidance by second-order sliding mode control," IEEE Transactions on Automatic Control, vol. 43, no. 2, pp. 241-246, 1998. <https://doi.org/10.1109/9.661074>
- [20] A. Levant, "Sliding Order and Sliding Accuracy in Sliding Mode Control," International Journal of Control, vol. 58, no. 6, pp. 1247-1263, 1993. <https://doi.org/10.1080/00207179308923053>
- [21] A. Levant, "Homogeneity approach to high-order sliding mode design," Automatica, vol. 41, no. 5, pp. 823-830, 2005. <https://doi.org/10.1016/j.automatica.2004.11.029>
- [22] A. Levant, "Principles of 2-sliding mode design," Automatica, vol. 43, no. 4, pp. 576-586, 2007. <https://doi.org/10.1016/j.automatica.2006.10.008>
- [23] G. Bartolini, A. Ferrara, E. Usai, and V.I. Utkin, "On multi-input chattering-free second-order sliding mode control," IEEE Transactions on Automatic Control, vol. 45, no. 9, pp. 1711-1717, 2000. <https://doi.org/10.1109/9.880629>
- [24] L. Fridman and A. Levant, "Higher order sliding modes, in Sliding Mode Control in Engineering," Marcel Dekker Inc.: New-York, USA, pp. 53-102, 2002.
- [25] O. Akar, U. K. Terzi, and O. Ozgonenel, "A new speed control technique for a separately excited direct current motor by PID controller," Balkan Journal of Electrical and Computer Engineering, vol. 6, pp. 12-17, 2018. <https://doi.org/10.17694/bajece.410209>
- [26] H. Calik, Y. Ozoglu, S. H. Undil, and U. K. Terzi, "A study on torque ripple improvement compared to a modified rotor and stator poles SRMs with classical SRMs using dynamic and FFT analysis," Electric Power Components and Systems, vol. 51, no. 13, pp. 1328-1337, 2023. <https://doi.org/10.1080/15325008.2023.2196675>
- [27] H. Uzun, O. Akar, A. Demirci, M. C. Akuner, and U. K. Terzi, "Analyzing high efficiency asynchronous motors using scalar control technique," Balkan Journal of Electrical and Computer Engineering, vol. 6, pp. 23-26, 2018. <https://doi.org/10.17694/bajece.410219>
- [28] J. A. Moreno and M. A. Osorio, "Lyapunov approach to second-order sliding mode controllers and observers," presented at the 47th IEEE Conference on Decision and Control, (Cdc 2008), pp. 2856-2861, 2008. <https://doi.org/10.1109/CDC.2008.4739356>
- [29] S. Pourzeynali, H.H. Lavasani, and A.H. Modarayi, "Active control of high rise building structures using fuzzy logic and genetic algorithms," Engineering Structures, vol. 29, no. 3, pp. 346-357, 2007. <https://doi.org/10.1016/j.engstruct.2006.04.015>
- [30] D. Kalyanmoy, "Multi-Objective Optimization using Evolutionary Algorithms," Wiley & Sons, 2001.
- [31] A.P. Wang and C.D. Lee, "Fuzzy sliding mode control for a building structure based on genetic algorithms," Earthquake Engineering & Structural Dynamics, vol. 31, no. 4, pp. 881-895, 2002. <https://doi.org/10.1002/eqe.127>
- [32] K. Ogata, "Modern Control Engineering," Prentice Hall, 2010.
- [33] H.O. Ozer, "High-Order Sliding Mode Control of Mechanical Systems," PhD. thesis in Institute of Graduate Studies in Science and Engineering, Department of Mechanical Engineering, Istanbul University: Istanbul pp. 105. (In Turkish), 2016.

BIOGRAPHIES

Hasan Ömür ÖZER received the B.S. and M.S. and Ph.D. degrees from the Department of Mechanical Engineering, Faculty of Engineering, Istanbul University, Istanbul, Turkey, in 2005, 2008 and 2016, respectively. He is currently an Assistant Professor with the Department of Electricity and Energy Vocational School of Technical Science, Istanbul University-Cerrahpaşa. His research areas include nonlinear control theory, dynamic systems modeling, dynamic absorbers modeling and control of vehicle systems, and optimization techniques.

Yüksel Hacioglu received the B.S. and M.S. and Ph.D. degrees from the Department of Mechanical Engineering, Faculty of Engineering, Istanbul University, Istanbul, Turkey, in 2002, 2004 and 2009, respectively. He is currently an Associate Professor with the Department of Mechanical Engineering, Faculty of Engineering, Istanbul University-Cerrahpaşa. His research areas include modeling and control of robotic manipulators, modeling and control of vehicle systems, nonlinear control theory, and fuzzy logic.

Nurkan Yağız received the B.S. and M.S. degrees from the Department of Mechanical Engineering, Middle East Technical University, Ankara, Turkey, in 1984 and 1986, respectively, and the Ph.D. degree from the Department of Mechanical Engineering, Faculty of Engineering, Istanbul University, Istanbul, Turkey, in 1993. He is currently a Professor with the Department of Mechanical Engineering, Faculty of Engineering, Istanbul University-Cerrahpaşa. His research areas include modeling and control of vehicle systems, control of structural vibrations, and nonlinear control theory.



Research Article

Detection of Shadow IT Incidents for Centralized IT Management in Enterprises using Statistical and Machine Learning Algorithms

Mücahit Kutsal^{1*}, Bihter Daş², Ziya Aşkar³, Ali Necdet Güvercin⁴, Resul Daş⁵

^{1*} University of Gdańsk, Institute of Theoretical Physics and Astrophysics, 80-308, Gdańsk, Poland. (m.kutsal.423@studms.ug.edu.pl).

² Firat University, Software Engineering Department, 23119, Elazığ, Turkey. (bihterdas@firat.edu.tr).

³ Arçelik A.Ş. Karaagac Caddesi 2-6, Sutluce Beyoğlu 34445 İstanbul, Türkiye. (ziya.askar@arcelik.com).

⁴ Arçelik A.Ş. Karaagac Caddesi 2-6, Sutluce Beyoğlu 34445 İstanbul, Türkiye. (alinedet.guvercin@arcelik.com).

⁵ Firat University, Software Engineering Department, 23119, Elazığ, Turkey. (rdas@firat.edu.tr).

ARTICLE INFO

Received: Oct., 30, 2023

Revised: Nov., 26 2023

Accepted: Nov, 27, 2023

Keywords:

Shadow IT
Centralized IT Management
Enterprise IT
IT Monitoring and Control

Corresponding author: Mücahit Kutsal

ISSN: 2536-5010 / e-ISSN: 2536-5134

DOI: <https://doi.org/10.36222/ejt.1382461>

ABSTRACT

Software as a Service (SaaS) is a software service where software solutions are offered to users via the internet, usually subscription-based or sometimes opened to access by selling a license key, distributed over the cloud, and updates are automatically delivered to users because they are distributed over the cloud. The number of SaaS provider companies is increasing day by day, and with this increase, unauthorized purchase of SaaS applications has become a problem for corporate-sized companies. Without the company's approval, SaaS software and hardware used by employees increase Shadow IT which means there is a potential risk of security breaches, data loss, and compliance issues as the IT department is unaware of the usage and unable to monitor and control the systems effectively. In this study, in order to avoid the problems that may be caused by Shadow IT, unauthorized SaaS applications in Arçelik Global have been detected by utilizing statistical and machine learning approaches. In the experiment, Interquartile Range, K-Means and Stabilization algorithms were used for the detection of unauthorized SaaS applications. Using all three algorithms, low, medium and high-risk shadow IT detection was made for Arçelik company. We see that the proposed stabilization approach explores unauthorized SaaS applications much more distinctively than the other two algorithms. The proposed approach can be used in the future to detect unauthorized software from other companies.

1. INTRODUCTION

Today, free, flexible, cloud-based information technology (IT) applications and services that are easily accessible over the internet are increasing rapidly [1]. In order to work more efficiently, people can use these IT applications or services from home, at work, or while traveling on personal laptops, tablets, and smartphones. While the use of these IT technologies provides an advantage in accelerating the digital transformation, on the other hand, it causes the employees to turn to IT offers without the approval of the organization they work for, in short, to increase the shadow IT [2,3]. Shadow IT is the usage of information technology systems, devices, software, applications, and services without the open approval of the IT department. The fact that software as a service (SaaS) applications are easily accessible over the internet and can offer different solutions for different problems is very attractive to users [4-6]. This situation causes different departments to purchase SaaS applications without the knowledge of the IT department, in other words the emergence of Shadow IT. Shadow IT plays a critical role in both security and financial investment in companies. Employees' use of some features such as file sharing, storage, and collaboration may result in the leakage of sensitive data [7]. The increase in the use of mobile devices in business environments, the use of wearable devices, that is, bring your own (BYO) devices, causes new forms of devices to enter businesses

and all these devices to offer different operating system types. BYO devices create an increasingly heterogeneous and difficult space for IT to manage. This trend often referred to as "shadow IT", creates a significant security risk for companies [8,9]. In addition, IT has little visibility into the implications of corporate data in cloud environments. As a result, it becomes very difficult to manage BYO devices that contain both company-provided applications and personally owned applications [10,11]. With the increasing use of shadow IT, it becomes more difficult for organizations to adjust to legal or contractual IT regulations. The reliability and accuracy of big data analytics are weakening because shadow IT increases in unknown corporate data sources. All these difficulties add great importance to the studies on shadow IT detection. Another concept, IT consumerization, refers to the transportation of software and hardware products designed for personal use to the organization and their use for business purposes. Companies can provide consumption IT or enterprise IT to their employees [12,13]. Enterprise IT is a concept that includes enterprise services and support, as well as their strategy, management, budgets, and policy. Figure 1 outlines the distinction between shadow IT and current concepts [14,15].

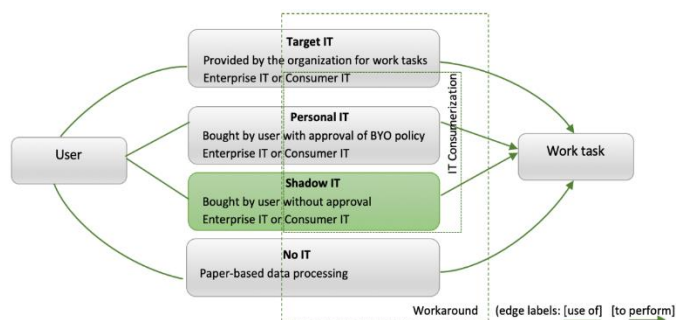


Figure 1. Shadow IT and closely related concepts [1]

1.1. Current Problems with Shadow IT and Motivation.

In order to keep security at the highest level in a company, the IT department must be aware of every software used in the company. In this way, it can be decided whether the software used in the company is safe or not. If there is a lack of control over the software used in an organization, this will cause the organization to experience different security vulnerabilities. One of the main problems that Shadow IT can cause is the loss of important internal data. An unauthorized SaaS application used can take data that should not go out of the organization by backing up/storing it without permission, and if this confidential data is in the hands of malicious people, a cyber security breach may occur within the organization. Therefore, an unauthorized SaaS application will cause a legal violation. An unauthorized SaaS application may also be in conflict with an agreement that the organization has to comply with. In order not to be exposed to all these problems, the IT department should have full authority over the SaaS applications used in the organization. Another problem that we may encounter within the organization as a result of Shadow IT is the updates for SaaS applications because SaaS applications are centrally distributed on the cloud, users do not have a choice whether to accept updates to their SaaS applications. Therefore, the IT department of the organization should be prepared to avoid errors, legal incompatibilities, and security vulnerabilities that may be caused by a new update to a SaaS application, and for this, the IT department should be aware of all the SaaS applications that the organization uses. In addition, there may be updates on the pricing of the SaaS applications used over time, and as the institution becomes dependent on this SaaS application, it has to comply with the new pricing, which means a financial risk for the institution. Finally, another problem created by Shadow IT is efficiency. A SaaS application may lose its efficiency over time, and put its customers in trouble, or a SaaS application in use may lose its ability to meet the demands of the organization. In order for the organization to cope with all these problems, shadow IT detection must be done correctly. In this study, unauthorized SaaS software currently used in Arçelik Global company in Turkey has been identified, with a suggested approach to avoid the problems that may be caused by Shadow IT in a company. In addition, in the future, a detection system has been developed in the company for SaaS applications that may be used without permission.

1.2. Main Contributions

The main contributions of this paper are outlined below:

- Shadow IT detection was performed using statistical and machine learning algorithms on firewall log data in a corporate-sized company.
- A novel shadow IT detection system was developed that works on the data flowing over the firewall.
- The number of research articles on shadow IT detection in the literature is quite low. This study will shed light on future academic studies for shadow IT detection.

1.3. Novelty.

Although the importance of Shadow IT in the business world has increased recently, it still does not receive the necessary attention in the academic world. Even if there are articles in which the concept of shadow IT is mentioned, there are very little experiments on shadow IT detection. As far as we know, there is no research paper in the literature that distinguishes shadow IT detection as low risk, medium risk and high risk. In this study, a new approach for detection of shadow IT was proposed and the performance of this approach was compared with existing methods and divided according to risk groups. Therefore, we believe that this study will contribute to the scientific world in detecting shadow IT.

The remainder of this paper is organized as follows. Section 2 presents related works and general information about K-Means and Interquartile algorithms used for shadow IT detection. Section 3 includes details of the materials and implementation. Section 4 presents the experimental results and discussion. Section 5 presents the conclusion.

2. RELATED WORK

This section examines the state of the art on the topic of shadow IT such as detection of shadow IT, and review papers. Although the importance of Shadow IT has increased a lot in the business world, there are not many scientific studies on this subject. There are hardly any articles on scanning Shadow IT. As far as we know, our study will be the first study to detect Shadow IT. Therefore, in the literature review section, the most considerable studies in which the term Shadow IT is used are mentioned. In the studies that have been cited as [16,17], it is mentioned that Shadow IT increases the security vulnerability in companies and damages the organizational data flow. In [18], 129 best shadow applications were classified as excel macro, cloud solutions, software, ERP, business intelligence systems, hardware, websites. In [19], the authors also explained other system concepts such as rogue IT and shadow, workaround and feral, which are closely related to this concept, apart from shadow IT, and stated the differences between these concepts and shadow IT. In [20,21] studies, the authors interpret shadow IT as an insider threat because a non-malicious employee is installing unapproved software. They also stated that it was caused by the company's employees not complying with the information security policies. In the studies referenced as [22,23], the authors argued that Shadow IT systems are more efficient and effective in practice than the existing official and standard systems used in companies. In [24,25], the authors discussed the concept of shadow IT in determining the relationship between business and IT. They also explored the role of social media software and self-made macros in Excel or Access software for shadow IT. In [26-28], the difficulties experienced in detecting shadow IT with increasing new technologies were mentioned. These studies stated that there are very few academic publications on shadow IT detection, which is largely due to the difficulty of accessing the data and the fact that they are unregistered. In [29], the authors did a study on the relationship of shadow IT with security. An evaluation model for shadow ITs in a company is presented in [30]. A sample shadow assessment document is presented based on several weighted and evaluated criteria. In [31], the authors conducted a review article on shadow IT.

The acquisition and preprocessing of log files from servers are of paramount importance in the realm of cybersecurity, system performance monitoring, error analysis, and overall information security management. Log files are text documents that meticulously record events in a system, and they are employed for monitoring activities, detecting errors, identifying cybersecurity

threats, and defending against security breaches. Initially, the preprocessing stage of log files obtained from servers involves transforming this data into meaningful and usable information [32, 33]. This stage encompasses steps such as cleaning up unnecessary information, organizing log records, and standardizing them into a consistent format. This process enables log data to be more effectively analyzed and interpreted. The cleaning and analysis of log files form the cornerstone of an organization's information security strategies. For instance, analyses performed on log files to detect abnormal activities can identify potential security breaches in advance, allowing for preventive measures to be taken. Moreover, the utilization of log files for monitoring system performance and error analysis facilitates the swift identification and resolution of issues. Therefore, the routine collection of log files from servers plays a critical role in maintaining a secure network and ensuring the healthy operation of information systems [34, 35].

2.1. k-Means Algorithm.

The K-Means algorithm is a clustering algorithm that tries to divide the dataset into groups it belongs to and is an unsupervised learning [36]. It makes elements within the same group as similar as possible, but tries to keep the clusters apart. The k value in K-Means determines the number of clusters. The algorithm has a simple working logic. Assigns data points to a cluster so that the sum of the squared distance between the data points and the cluster's centroid is minimal. This is how it calculates that the data belongs to that cluster. While calculating the centroid of the clusters, it takes the arithmetic average of all data points belonging to that cluster. The fact that the data in the clusters is similar to each other is determined by the fact that the data has little variation [37,38]. Since the K-Means algorithm uses distance-based measurement to determine the similarity between data points, normalization is recommended to determine which cluster the data belongs to. Because of K-Means is an iterative algorithm and centers are randomly started, using different centroids could provide a solution when K-Means stays at a local optimum and not converge to the global optimum.

2.2. Interquartile Range Algorithm.

Quartile range, which is widely used in statistics, is the rule of dividing an ordered data set into four equal parts, each consisting of quarter data. In this rule, the middle half (50%) of the data is represented as medians, while the third quartile (25%) and first quartile (25%) are represented as quartiles. The interquartile range (IQR) is calculated by subtracting the first quartile from the third quartile. The interquartile range indicates the range where most of the data values are found. The interquartile range is also expressed by Equation 1.

$$IQR = Q3 - Q1 \quad (1)$$

In this equation; Q1 is a number between the smallest number and the median of the data set. Q2 is the median of the data. Q3 is a number between the median and the highest value of the data set. The quartiles gap is preferred as a statistical measure of spread since it is not affected by extremely small or extremely large extremes in the sorted data. If there is a very extreme outlier in the dataset, the quartile range may be preferred. While IQR is used to identify outliers in a data set, it indicates where most of the data is. It also shows the central trend of the data [39, 40]. Figure 2 shows the graphical representation of the interquartile range.

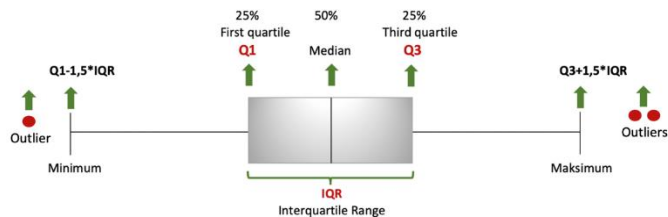


Figure 2. The graphical representation of IQR

3. MATERIALS AND METHODS

In this section, the steps of the application carried out for shadow IT detection to detect unauthorized SaaS software within Arçelik Global company are explained in detail. The Shadow IT detection system consists of 3 main parts: (i) data set collection (ii) data preprocessing (iii) data analysis. Figure 3 shows the flowchart of the proposed shadow IT detection approach.

Algorithm 1. The algorithm of the shadow IT detection model

Procedure: The shadow IT detection model

Input: Log data stored by IBM Qradar software

Output: Low, medium, high risk SaaS applications

Step 1: Collecting log data

Step 2: Extracting unnecessary columns from data stored in Qradar (Data refining)

Step 3: Extracting the matching records by filtering the data

Step 4: Converting the data to json format in Qradar and sending it to an API written in python.

Step 5: Saving the data coming to Rest API directly to a collection in Cosmos DB before analysis as a daily-report collection

Step 6: Processing of incoming data to Rest API at pre-process stage

- data transformation for analysis

- min-max normalization for K-Means algorithm

- calculating date from timestamp value

Step 7: Detection of low, medium, high risk anomalies by K-Means, IQR and Stabilization algorithms

Step 8: Saving the detected anomalies to a collection in Azure Cosmos DB as anomalies collection

3.1. Data Collection.

The log data used as a data source in this study were stored with the IBM Qradar software, which was created with the Fortinet Firewall solution. These data are taboos and raw log data that are formed as a result of requests made out of Arçelik company. In terms of volume, terabytes of data are generated monthly. Table1 shows a small and anonymized example of the used tabular log data.

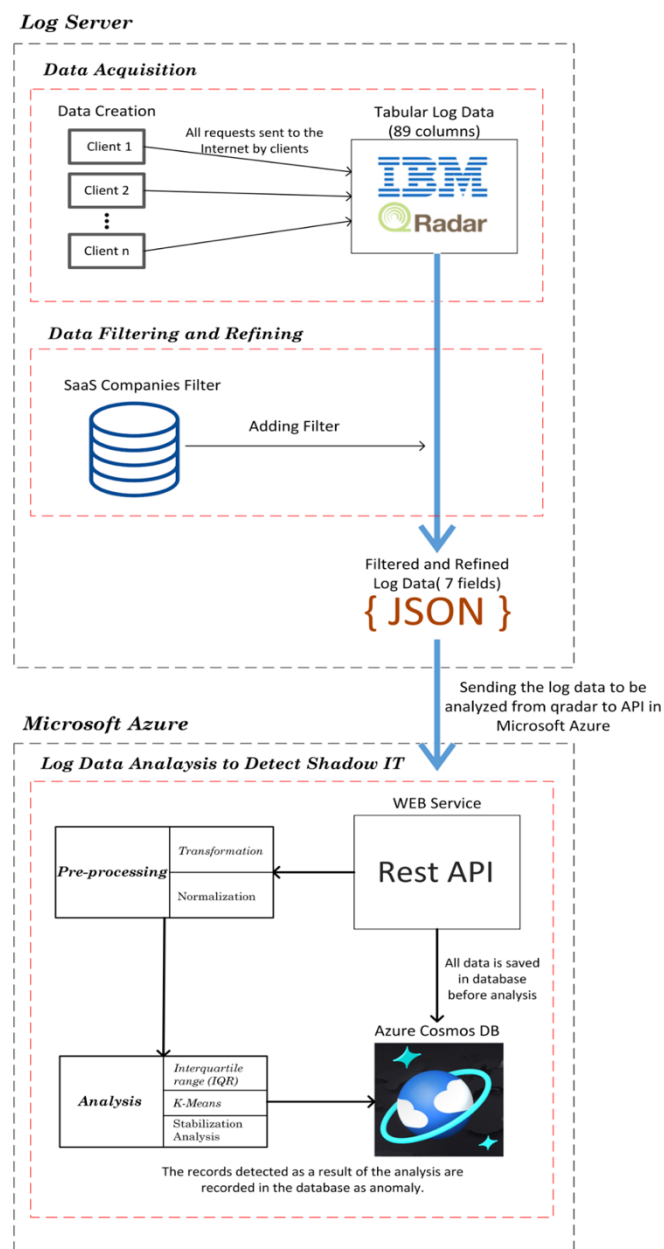


Figure 3. The shadow IT detection model

Table I
An example of tabular log data.

	Hostname	Request URL	Request Time	Source IP
1	e.g.1.com	/login	16410	10.92.*
2	e.g.2.com	/homepage	164114	10.134.*
3	e.g.3.com	/list/1	165064	10.86.*
4	e.g.4.com	/services/add	165134	10.134.*
5	e.g.5.com	/register	164624	10.92.*
6	e.g.6.com	/login	1647106	10.86.*
7	e.g.7.com	/livecall/s2	164736	10.17.*

Our log data kept in IBM Qradar software is in tabular format and is stored in a table called events. There are 89 columns in this table. The most important columns that can be used in the application are extracted in the Data refining section and are also used in the analysis section.

3.1. 1. Data Filtering and Refining

In this subsection, filtering and refining are performed on the monthly terabytes of data stored in the log server. In this study, we did not deal with all the data generated by Arçelik employees. We only used the requests sent by the employees of Arçelik company to the SaaS applications. Therefore, a filter was applied to extract the needed data, and after the filtering was completed, only the log data of the requests sent to the SaaS applications by Arçelik employees remained, and then the columns needed for this log data were extracted. Table 2 shows the event matrix after filtering and refining. The event matrix is the number of requests made by Arçelik employees to websites belonging to SaaS applications via their browsers. On the event matrix, each column corresponds to a SaaS company, and each row corresponds to a day. For example, a request made by any employee of Arçelik company to xyzsaas.com company on 01.01.2022 via browser increases the number in the relevant cell on the event matrix by one.

Table II
An example of event matrix.

Date	e.g.1.com	e.g.2.com	e.g.3.com	e.g.4.com
01.01.2022	5	14	23	16
02.01.2022	16	25	34	47
03.01.2022	68	77	86	75
04.01.2022	91	99	83	3
05.01.2022	98	89	98	0
06.01.2022	53	62	30	41
07.01.2022	56	65	74	83
08.01.2022	87	96	11	7
09.01.2022	30	49	42	51

Then, we converted the data into json format and sent it to the web service running in the cloud environment. Figure 4 shows the json object that belongs to the requests sent by three Arçelik employees to the examplesaas.com application on a daily basis.

```
{
  "Start Time (Minimum)": 1655889723818,
  "hostname": "examplesaas.com",
  "hitcount": 96,
  "request_url": "examplesaas.com/examplepath",
  "source": [
    {
      "ip": "10.███.███.60",
      "log_source": "ARCELIK_SM_FW_███",
      "hitcount": 23
    },
    {
      "ip": "10.███.███.116",
      "log_source": "ARCELIK_SM_FW_███",
      "hitcount": 17
    },
    {
      "ip": "10.███.███.173",
      "log_source": "ARCELIK_LogY_FW_███",
      "hitcount": 56
    }
  ]
}
```

Figure 4. Json Object Example for Requests of the Three Arçelik Employees.

3.2. Preprocessing

The data preprocessing is a crucial step in the data analysis pipeline, involving the cleaning and transformation of raw data into a format that is suitable for analysis. It is an essential phase that directly impacts the quality and effectiveness of subsequent data modeling or analytical processes. Preprocessing sub-stage performs the transformation and normalization of the data. Therefore, these processes make the data analyzable. The key steps involved in data preprocessing include:

3.2.1 Data Transformation

In this preprocessing subsection, a data transformation takes place. The Start time (Minimum) field in the data we obtained in json format represents a data in timestamp format. Date is calculated from this timestamp data. Date data is needed because we analyze according to days in the analysis phase. No other type of data transformation is needed in this part.

3.2.2 Normalization

Normalization is to treat the data in a single order in cases where the difference between the data is too great. By applying the normalization process, the number group is multiplied by a fixed number without disturbing the ratio between them, and by adding a fixed number, the numbers are taken into a certain range. Although there are different normalization methods, min-max normalization is a well-known and used method. In this method, the largest and smallest values in a group of data are considered. All other data is normalized to be 0 for the smallest value and 1 for the maximum value, and all data is spread over this 0-1 range. We applied min-max normalization to the data in the K-Means algorithm. Normalization is not performed in other algorithms.

3.3 Data Analysis

In this subsection, the use of 3 different algorithms for shadow IT detection is explained. k-Means and IQR algorithms are previously known algorithms used in data clustering in the literature. Here, these algorithms are not used for clustering, but for the detection of SaaS applications that can be purchased without the knowledge of the IT department. The other algorithm is an algorithm that we proposed and we call stabilization. The Stabilization algorithm is an algorithm that is used to detect the SaaS applications currently used in Arçelik Global, the constraints and steps are developed by us, and we derive from the Interquartile Range algorithm.

3.3.1 Analysis with k-means

We have previously mentioned that the K-Means algorithm is a distance-based unsupervised machine learning algorithm that tries to find k number of clusters in a data set, and that these clusters are as separate from each other, but the elements are tried to be kept as close as possible. In this study, we used the K-Means algorithm as an anomaly detection algorithm, not as a clustering algorithm. In our Shadow IT detection system, our cluster number is one and the anomalies we are trying to detect are events that are far from this cluster on the event matrix. Before an event occurred on the event matrix, we brought all the events back 30 days in the relevant column where that event would occur, and ran the K-Means algorithm on them. Since we made anomaly analysis separately for each column on the event matrix, this algorithm was applied separately for each column. Our aim is to determine a major cluster in each column on the event matrix and to determine the outlier values that are far from this cluster. In order to evaluate an event as an anomaly, the exact midpoint of the cluster is determined by the K-Means algorithm. Then, the Euclidean

distance of all events is checked for this middle value. The Euclidean distance between the points p and q is given in Equation.

$$d(p, q) = \sqrt{p^2 + q^2} \quad (2)$$

The following conditions were checked to rank the detected anomalies as low, medium and high.

- i. The Euclidean distance is between 0.75-0.85, then low.
- ii. The Euclidean distance is between 0.85-0.90, medium.
- iii. The Euclidean distance is between 0.90-1, then high.

3.3.2 Analysis with IQR

The interquartile rule is a statistical algorithm that measures the distribution and variability of the data by dividing the dataset into quarters. In the IQR algorithm, first the median of the data set is taken and the data is divided into three parts as first quartile (Q1), second quartile (Q2) and third quartile (Q3). The value of Q2 is directly equal to the median itself. Then, the Q1 value was subtracted from the Q3 value to obtain the IQR value. We added the IQR value to the Q3 value to obtain the upper threshold value. The formula we used to obtain the upper threshold value is shown in Equation 3.

$$\text{Upper threshold} = Q3 + \text{IQR} * 1.5 \quad (3)$$

In order to evaluate an event as an anomaly, we evaluated the values above the upper threshold as anomaly in the analyzed data set. In addition, the following conditions were checked in order to rank the anomalies detected here as low, medium and high.

- i. The values > upper threshold then low risk.
- ii. The values > (upper threshold) *2 then medium risk.
- iii. The values > (upper threshold) *4 then high risk.

For this algorithm, we performed a 15-day backward analysis on the event matrix. We ran the IQR algorithm for each column on the event matrix.

3.3.2 Analysis with Our Approach

This proposed approach, unlike the other two algorithms, tries to detect continuity, not exactly an outlier anomaly on the data set. The basis of this proposed approach, which we named "Stabilization", is based on the IQR algorithm. For this algorithm, not the upper limit, but the lower limit and an additional tolerance value are used. In the proposed approach, unlike the algorithm above, for determining the lower limit, the IQR value is not added to the Q3 value, instead it is subtracted from the Q1 value. The formula used for the lower bound is shown in Equation 4.

$$\text{Lower threshold} = Q3 + \text{IQR} * 1 \quad (4)$$

Here, in order to decide whether a new event will be marked as an anomaly, it is checked whether the lower limit has been exceeded. If a stable request has been sent to the said SaaS application from within the Arçelik company in the last 30 days, we have marked it as an anomaly. We used the tolerance value so that the Arçelik company is closed on holidays, holidays and similar special days and no requests are made to prevent this anomaly. As a result of such an analysis, we decided that if the number of data below the lower limit determined on the 30-day dataset is more than the

tolerance value, there is an anomaly in the dataset. In order to rank the anomalies detected here as low, medium and high, first the tolerance value was set as 10 and the following conditions were checked in turn.

- i. High risk if the number of data below the lower limit is less than $((tolerance)/2^2)$
- ii. If the number of data below the lower limit is less than $((tolerance)/2^1)$, medium risk.
- iii. If the number of data below the lower limit is less than $((tolerance)/2^0)$, that is, less than the direct tolerance, low risk.

4. EXPERIMENTAL RESULTS AND DISCUSSION

The proposed approach for detecting Shadow IT is an algorithm based on the interquartile rule statistical algorithm, the rules, and constraints of which were developed by us. With our approach, which we call stabilization, the software used by Arçelik employees without the permission of the IT department has been identified. As in other algorithms, low, middle, and high-risk shadow IT detections were made. Table 3 shows the detection results of low, medium, and high-risk shadow ITs with three algorithms for Arçelik company.

Table III
Some of the detected shadow IT incidents

Domain	Algorithms	Count	Date	Importance
E.g.1	Stabilization	915	22-05-13	High
E.g.2	Stabilization	114	2022-05-13	High
E.g.3	Stabilization	112	2022-05-13	High
E.g.4	k-means	1340	2022-05-12	Low
E.g.5	k-means	5565	2022-05-13	High
E.g.6	k-means	2126	2022-05-13	Middle
E.g.7	IQR, Stabilization	119	2022-05-11	High
E.g.8	Stabilization	935	2022-05-09	High
E.g.9	Stabilization	132	2022-05-07	Middle
E.g.10.com	k-means	128	2022-05-13	High
E.g.11.com	IQR	81	2022-05-07	High

When K-Means and IQR algorithms were first to run to detect unauthorized SaaS software in Arçelik, it was seen that with these two algorithms, SaaS applications that did not only exist before but came into use suddenly could be detected. However, we needed to detect not only newly purchased applications but also previously purchased applications that have been in use for a long time. Based on this need, we developed the stabilization algorithm. After adding this algorithm to the system, the shadow IT detection approach we developed gained the ability to detect not only unauthorized software to be purchased after the day it was actively used, but also purchased and regularly used the software before the day it was used. According to the experimental results obtained, we could say that the stabilization approach detects shadow ITs much more than the other two algorithms and is a much more useful algorithm for the company.

After detecting the shadow IT detections at Arçelik as low, medium, and high risk, one of the biggest problems we encountered was Cross-Origin Resource Sharing (CORS). CORS is simply a web page making a request to another web page, that

is, to a domain belonging to that application. For example, when an employee requests the example1.com SaaS application, it may be requesting example2.com as well, regardless of the application that is actually making the request in the background. This request is stored as a firewall log. This scenario means the following for shadow IT: Company employee actually buys and uses the "example1" application, but because the "example1" application uses the services of the "example2" application in the background, it is stored in firewall logs as if the employee also purchased and used the "example2" application. Therefore, it is possible that the "example2" application will be detected as shadow IT in Arçelik company by the shadow IT detection system we have developed. To avoid this, when the system detects an anomaly, we created a dictionary of the most common keywords in SaaS applications that we know to determine whether it is a background service used by an application or a purchased SaaS application. We looked at how many times the values in this dictionary were passed in the path of the requests. Figure 5 shows the most frequent keywords and their numbers for the "vimeo.com" web request.

- config : 3038
- events : 12
- features : 2
- contact : 0
- pricing : 0
- about : 0
- privacy-policy : 0
- privacy : 0
- careers : 0
- contact-us : 0
- integrations : 0
- terms : 0
- customers : 0
- resources : 0
- about-us : 0
- demo : 0
- login : 0
- signup : 0
- product : 0
- products : 0
- solutions : 0
- services : 0
- support : 0
- sign-up : 0
- enterprise : 0
- industries : 0

Figure 5. Dictionary matches in request path.

In addition, by calculating how many times the subdomain values of the requested application are passed, we have created a different insight in order to determine whether the data we have is really a shadow IT. Figure 6 shows the number of subdomains in the requested web address.

- Subdomain "gameberrylabs" : 23
- Subdomain "playrix" : 20
- Subdomain "tencentgames" : 17
- Subdomain "melsoft-games" : 14
- Subdomain "flipboard" : 8
- Subdomain "bitmangogames" : 7
- Subdomain "funplusgames" : 3
- Subdomain "tfgihelp" : 2
- Subdomain "gamehouse" : 2
- Subdomain "gaana" : 2
- Subdomain "api" : 2
- Subdomain "peoplefun" : 1

Figure 6. Subdomain counts.

In order to comprehensively enrich our study and develop a more robust analysis, we conducted a review of similar research efforts. Our investigation revealed a limited body of literature addressing the identification of shadow IT incidents, with most studies primarily focused on defining the concept of shadow IT. Notably, the works of Silic et al. [7] and Rentrop et al. [30] provided valuable insights into guiding our approach for this study.

5. CONCLUSION

In our study, we discussed the detection of Shadow IT that may exist within an institution with statistical and machine learning methods. Throughout the study, we applied one statistical, one machine learning algorithm and a new approach based on statistic to the event matrix obtained from the firewall logs of the company enabling the detection of SaaS applications currently used in the organization. In addition, we developed a detection system to identify SaaS applications that may be purchased without the knowledge of the IT department in the future. Our study is ready to use in the future to determine the Shadow IT situations within different institutions and organizations. Based on this paper, in the future, when it is desired to detect Shadow IT within an institution,

it will be sufficient to apply the detection algorithms to this event matrix by establishing the data pipeline in which the relevant institution creates the event matrix.

Thanks to this end-to-end shadow-IT detection system we have developed, we have presented an effective solution in terms of manageable IT. Although the work we have presented is a general solution that can be applied by different institutions in the future, researchers who will apply to this study can contact the authors in the future as well. Based on this study, different shadow IT detection systems can be developed in the future using different algorithms (e.g. deep learning time series analysis). Within the scope of our study, we did not conduct a study on the actions that can be taken within the organization after a shadow IT incident is detected, but after a shadow IT incident is detected, actions such as legalizing this SaaS software within the organization or completely removing it from the processes within the organization should be taken, so studies can be carried out on the actions that can be taken against shadow IT incidents detected in the future.

ACKNOWLEDGEMENT

This work was supported by the Arçelik A.S. Digital Transformation, AI and Big Data Research and Development Center. The authors want to thank Emre Bahadır Sever (e-mail: bahadir.sever@arcelik.com) for his contribution and support.

REFERENCES

- [1] Haag, S.; Eckhardt, A. Shadow IT. *Bus Inf Syst Eng*. 2017, vol. 59, no. 6, pp. 469–473, doi: 10.1007/s12599-017-0497-x.
- [2] Györy A.; Cleven A.; Uebernickel F.; Brenner W. Exploring the shadows: IT governance approaches to user-driven innovation. In: *Proceedings of the 20th European Conference on Information Systems*. 2012, Barcelona.
- [3] Segal M. Dealing with the realities of shadow IT. In: *Datacenter J*. <http://www.datacenterjournal.com/dealing-realities-shadow/>. Accessed 22 Nov. 2016.
- [4] Brancheau J.C; Brown, C. The management of end-user computing: Status and Directions. *ACM Computing Surveys*, 1993, vol. 25, no. 4, pp. 437–482.
- [5] Klotz, S.; Kopper, A.; Westner, M.; Strahringer, S. Causing factors, outcomes, and governance of Shadow IT and business-managed IT: a systematic literature review. *International Journal of Information Systems and Project Management*. vol.7, no.1, 2019.
- [6] Rentrop, C., Zimmermann, S. Shadow IT - Management and Control of Unofficial IT,” *ICDS 2012: The Sixth International Conference on Digital Society*, Proceedings pp. 98-102.
- [7] Silic M.; Back, A. Shadow IT – A view from behind the curtain. *Computers & Security*, vol. 45, pp. 274–283, Sep. 2014, doi: 10.1016/j.cose.2014.06.007.
- [8] Allen, D.; Burton, F.G.; Smith, S.D.; Wood, D.A. Shadow IT Use, Outcome Effects, and Subjective Performance Evaluation. *Rochester, NY*, Jun. 27, 2017. doi: 10.2139/ssrn.2993443
- [9] Alojairi, A. The Dynamics of IT Workaround Practices- A Theoretical Concept and an Empirical Assessment. *International Journal of Advanced Computer Science and Applications*, 2017, 8(7), 527-534. <https://doi.org/10.14569/IJACSA.2017.080773>.
- [10] Behrens, S. Shadow Systems: The Good, the Bad and the Ugly. *Communications of the ACM*, 2009, 52(2), 124-129. <https://doi.org/10.1145/1461928.1461960>.
- [11] Behrens, S.; Sedera, W. Why Do Shadow Systems Exist after an ERP Implementation? Lessons from a Case Study. *Proceedings of the 8th Pacific Asia Conference on Information Systems*, 2004, 1713-1726.
- [12] Burnett, M. M.; Scaffidi, C. End-User Development. In Soegaard, M. and Friis, R. (Eds.), *The Encyclopedia of Human-Computer Interaction*. Aarhus: *The Interaction Design Foundation*, 2013.
- [13] Chua, C. E. H.; Storey, V. C.; Chen, L. Central IT or Shadow IT? Factors Shaping Users’ Decision to Go Rogue with IT. *Proceedings of the 35th International Conference on Information Systems*, 2014, 1-14. Atlanta: The Association for Information Systems.
- [14] Haag, S.; Eckhardt, A. Normalizing the Shadows- The Role of Symbolic Models for Individuals ‘Shadow IT Usage. *ICIS 2014*, 2014, 1-13.
- [15] D. A. Aziz, "Webserver based smart monitoring system using ESP8266 node MCU module," *International Journal of Scientific & Engineering Research*, vol. 9, pp. 801-808, 2018.
- [16] Strong, D.M.; Volkoff O. A roadmap for enterprise system implementation. *Computer*, 37 (6) (2004), pp. 22-29.
- [17] Oliver, D.; Romm, C.T. ERP systems in universities: rationale advanced for their adoption Idea Group Publishing, *Hershey, PA* (2002).
- [18] Chefjec, T. Resultats De L'Enquete Sur Le Phenomene du Shadow IT <http://chefjec.com/2012/12/18/resultats-complets-de-lenquete-shadow-it/> (2012) Retrieved on March 2014.
- [19] Rentrop, C.; van Laak, O.; Mevius M. Schatten-IT: ein Thema für die interne Revision Revisionspraxis–Journal für Revisoren, Wirtschaftsprüfer, *IT-Sicherheits und Datenschutz beauftragte* (2) (2011), pp. 68-76.
- [20] Warkentin, M. Willison, R. Behavioral and policy issues in information systems security: the insider threat. *Eur Journal Inform System*, 18 (2) (2009), p. 101.
- [21] Puhakainen, P. Siponen, M. Improving employees' compliance through information systems security training: an action research study *MIS Q*, 34 (4) (2010).
- [22] Behrens, S.; Sedera W. Why do shadow systems exist after an ERP implementation? Lessons from a case study. *8th Pacific Asia conference on information systems*. Shanghai, China; 2004.
- [23] Harley, B. Wright, C.; Hall, R.; Dery K. Management reactions to technological change the example of enterprise resource planning. *J Appl Behav Sci*, 42 (1) (2006), pp. 58-75.
- [24] Jones, D.; Behrens, S.; Jamieson, K.; Tansley, E. The rise and fall of a shadow system: lessons for enterprise system implementation *ACIS*, Hobart, Tasmania (2004).
- [25] Sherman, R. Shedding light on data shadow systems *Inform Manage Online* (29 April, 2004), p. 1002617-1.
- [26] Haag, S.; Eckhardt, A. Justifying Shadow IT Usage, *PACIS 2015 Proceedings*. 241. <https://aisel.aisnet.org/pacis2015/241>.
- [27] Behrens S. Shadow systems: the good, the bad and the ugly *Commun ACM*, 52 (2) (2009), pp. 124-129.
- [28] Mahmood, M.A.; Siponen, M.; Straub, D.; Rao, H.R.; Raghu, T. Moving toward black hat research in information systems security: an editorial introduction to the special issue *MIS Q*, 34 (3) (2010), pp. 431-433.
- [29] Silic, M.; Back, A. Information security and open source dual use security software: trust paradox open source software: quality verification. *Springer (2013)*, pp. 194-206.
- [30] Rentrop, C.; Zimmermann, S. Shadow IT evaluation model. In *2012 Federated Conference on Computer Science and Information Systems (FedCSIS)*, Sep. 2012, pp. 1023–1027.
- [31] Raković, L.; Sakal, M.; Matković, P.; Marić, M. Shadow IT – Systematic Literature Review. *Information Technology and Control*, vol. 49, no. 1, Art. no. 1, Mar. 2020, doi: 10.5755/j01.itc.49.1.23801.
- [32] Das, R., Turkoglu, I. "Creating meaningful data from web logs for improving the impressiveness of a website by using path analysis method", Elsevier, *Expert Systems with Applications*, c. 36, sy 3, Part 2, ss. 6635-6644, Nis. 2009, doi: 10.1016/j.eswa.2008.08.067.
- [33] Daş R., Turkoglu, I. "Extraction of Interesting patterns through association rule mining for improvement of website usability", *IU-JEEE*, c. 9, sy 2, ss. 1037-1046, Oca. 2009.
- [34] Das, R., M. Z. Gündüz, "Analysis of cyber-attacks in IoT-based critical infrastructures", *International Journal of Information Security Science*, c. 8, sy 4, ss. 122-133, Ara. 2019.
- [35] Das, R., Turkoglu, I, Poyraz, M., "Analyzing of system errors for increasing a web server performance by using web usage mining", *Istanbul University - Journal of Electrical & Electronics Engineering*, c. 7, sy 2, ss. 379-386, Ocak 2012.
- [36] Minh, H.L. Sang-To, T.; Abdel Wahab, M.; Cuong-Le, T. A new metaheuristic optimization based on K-means clustering algorithm and its application to structural damage identification. *Knowledge-Based Systems*, vol. 251, p. 109189, Sep. 2022, doi: 10.1016/j.knosys.2022.109189.
- [37] Abernathy, A.; Celebi, M.E. The incremental online k-means clustering algorithm and its application to color quantization. *Expert Systems with Applications*, vol. 207, p. 117927, Nov. 2022, doi: 10.1016/j.eswa.2022.117927.
- [38] Li, Y.; Chu, X.; Tian, D.; Feng, F.; Mu, W. Customer segmentation using K-means clustering and the adaptive particle swarm optimization algorithm. *Applied Soft Computing*, vol. 113, p. 107924, Dec. 2021, doi: 10.1016/j.asoc.2021.107924.

- [39] Cho, I.; Park, S.; Kim, J. A fire risk assessment method for high-capacity battery packs using interquartile range filter. *Journal of Energy Storage*, vol. 50, p. 104663, Jun. 2022, doi: 10.1016/j.est.2022.104663.
- [40] Selvaraj, E. Collier, J.D.; Culver, E.; Brady, J.M.; Bailey, A.; Pavlides, M. THU460 - Temporal increase in interquartile range iron-corrected T1 in high-risk patients with large-duct primary sclerosing cholangitis. *Journal of Hepatology*, vol. 77, p. S322, Jul. 2022, doi: 10.1016/S0168-8278(22)01009-1.

BIOGRAPHIES

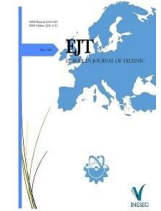
Mucahit Kutsal received his B.Sc. in Software Engineering from Firat University in 2023 and he is currently studying his M.Sc in Quantum Information Technologies at University of Gdansk. He studied at Czestochowa University of Technology for 1 academic year as part of an exchange program during his Bachelor's degree. During his Bachelor's degree, he was involved in various scientific studies and took part in various projects in the information technology industry. His current research areas include geometric deep learning, drug discovery, cryo-EM image processing, bioinformatics, cloud computing and quantum computation.

Bihter Das graduated B.S. and M.S. degrees from the Department of Computer Science at the Firat University in 2004 and 2007 respectively. Then she received Ph.D. degree at the Department of Software Engineering at the same university in 2018. She also worked between September 2017 and June 2018 as a visiting scholar at the Department of Computing Science at the University of Alberta, Edmonton, Canada. Her current research areas include data science, big data, data analytics, bioinformatic, digital signal processing, genome data analysis.

Ziya Askar received the B.Sc. degree from the Department of Computer Engineering at Istanbul Technical University in 1998. He has more than 25 years of experience in information technology and currently works as a Director of Enterprise Architecture at Arçelik Global and Emerging technologies. His current research areas include enterprise architecture, process digitalization, machine learning, functional programming, domain driven design in enterprise organizations.

Ali Necdet Guvercin received the B.Sc. degree from the Department of Computer Engineering at Çankaya University in 2009 and the M.Sc. degree from the Department of Computer Engineering at Karabük University in 2019. He is currently a Ph.D. student in the Department of Computer Engineering at Kocaeli University. He has more than 10 years of experience in information technology and currently works as a Senior Enterprise Architect at Arçelik Global. His current research areas include intelligent automation, robotic automation, artificial intelligence, machine learning, and autonomous systems.

Resul Das is a full professor in the Department of Software Engineering, Technology Faculty, Firat University, where he has been a faculty member since 2011. He graduated with B.Sc. and M.Sc. degrees from the Department of Computer Science at Firat University in 1999 and 2002 respectively. Then he completed his Ph.D. degree at the Department of Electrical-Electronics Engineering at the same university in 2008. He served as both a lecturer and network administrator at the Department of Informatics at Firat University from 2000 to 2011. In addition, he has been the CCNA and CCNP instructor and the coordinator of the Cisco Networking Academy Program since 2002 at this university. He worked between September 2017 and June 2018 as a visiting professor at the Department of Computing Science at the University of Alberta, Edmonton, Canada supported by the TÜBİTAK-BİDEB 2219 Post-Doctoral Fellowship. He has many journal papers and international conference proceedings. he served as Associate Editor for the Journal of IEEE Access and the Turkish Journal of Electrical Engineering and Computer Science from 2018 to 2021. He entered the 2% of the "World's Most Influential Scientists" list published by Stanford University researchers in 2020, 2021, 2022. His current research areas include computer networks and security, cyber-security, software design methods, software testing, IoT/M2M applications, graph visualization, knowledge discovery, and data fusion.



Research Article

Multilayer LSTM Model for Wind Power Estimation in the Scada System

Selahattin Barış Çelebi^{1*}, Ömer Ali Karaman²

^{1*}Batman University, Department of Computer Technology, Batman, Turkey. (e-mail: sbariscelebi@gmail.com).

²Batman University, Department of Electronics and Automation, Batman, Turkey. (e-mail: omerali.karaman@batman.edu.tr).

ARTICLE INFO

Received: Oct., 30, 2023

Revised: Nov., 26 2023

Accepted: Nov, 27, 2023

Keywords:

Power forecasting

Wind turbine energy

Long short-term memory

Machine learning

Regression

Corresponding author: *Selahattin Barış Çelebi*

ISSN : 2536-5010 | e-ISSN: 2536-5134

DOI: <https://doi.org/10.36222/ejt.1382837>

ABSTRACT

Wind energy is clean energy that does not pollute the environment. However, the complex and variable operating environment of a wind turbine often makes it difficult to predict the instantaneous active power generated. In this study, a wind turbine active power estimation system based on a long short-term memory network (LSTM) using time series analysis is proposed. The data obtained from the wind turbine SCADA system is used as input variables. In the proposed method, a multilayer LSTM architecture is designed to train the model. The first LSTM network consists of 64 units, and the second one consists of 32 units. This is followed by a dense layer consisting of 16 neurons. In the last layer, the architecture is finalized by using a linear activation function for the prediction process. The proposed deep learning (DL)-based LSTM model takes into account environmental factors such as wind speed and wind direction for active power forecasting. The results show that the LSTM-based time series analysis method is capable of effectively capturing time series features among the data. Thus, the proposed architecture can realize high-accuracy active power forecasting.

1. INTRODUCTION

Accurate forecasting of the active power from a wind turbine is critical for analyzing the energy demand [1], efficiency [2], and economic sustainability [3] of wind power plants. These forecasts are used to meet energy demand and reduce energy costs by influencing the structure of the energy grid [4]. Furthermore, the design and maintenance of wind turbines also rely on the predictions. If the power predictions are miscalculated, the energy production of the turbines may be lower or higher than expected. This can complicate the efficient use of resources and affect the stability of the energy grid [5]. Therefore, accurate active power forecasts are one of the key factors in the success of the wind energy industry [6].

Traditional statistical and machine learning-based prediction are the most widely used methods for turbine active power prediction [7]. Some common statistical techniques are time series analysis [8], Kalman filtering [9], and linear regression [10]. The fact that these methods are simple models is a great advantage. However, it is difficult to obtain satisfactory performance from statistical methods using big data from today's real-time applications [11]. When traditional machine learning-based methods are considered, there are some widely used algorithms such as support vector machines (SVM) [12], bagged trees (BT) [13], and extreme learning machines (ELM)

[14]. In traditional machine-learning based methods, feature selection from the dataset is a difficult task [15, 16].

Machine learning technologies such as light gradient boosting machines (LightGBM), extreme gradient boosting (XGBoost), and recurrent neural networks (RNN) have been used for time series data analysis and prediction [17, 18]. XGBoost is a method that works well on datasets with large sizes. However, overfitting problems are encountered due to incorrect hyperparameters for this technique. Also, the method needs feature engineering, which requires technical skills and experience [17]. Another method, LightGBM is a method that stands out with its speed. However, it may require more memory compared to other traditional methods [18]. While RNN networks can be successful in short-time series, they face the problem of losing the information obtained in long-time interval dependencies. Due to this problem, called the vanishing gradient, the networks may experience various problems when analyzing time series consisting of large data [19]. For these reasons, LSTM networks are distinguished from other methods as an alternative machine learning method. They are especially used for long term time series analysis and have emerged as a solution method for these problems [20].

Recently, DL-based machine learning algorithms have achieved high accuracy in time series predictions [21]. Among these algorithms, the LSTM is frequently used in the literature as one of the most successful methods [22]. LSTM(s) can

analyze complex connections between time-series data features. Nevertheless, it is crucial for the data to be continuous in order to accurately discern the relationship between features and attain a high level of prediction accuracy [23].

Time series analysis has been successfully applied in many fields, such as construction [24], transportation systems [25], and energy forecasting [26]. Output power forecasting is valuable information for the continuous support of power grids [27]. A highly accurate forecasting model with a suitable performance curve provided by the manufacturer can help renewable-based power grids operate efficiently and safely [28]. In this paper, an LSTM-based DL architecture is proposed to predict wind turbine active power using wind turbine data as input. R^2 , MAE, MSE, and RMSE metrics are used to measure the prediction performance and accuracy of the proposed method. There are limited studies in the literature on energy forecasting using LSTM-based architecture, which is a relatively new technique. Therefore, encouraged by the above findings, we aim to design an LSTM-based architecture to estimate the active output power with high accuracy. Here is a synopsis outlining the main contributions of this study.

- In the proposed architecture, high-accuracy power estimation is achieved by performing time series analysis.
- The effectiveness of the LSTM-based method in power estimation is demonstrated with statistical performance indicators.
- The actual power of a wind turbine data set obtained from real-world applications is estimated by time series analysis.

As for the rest of the paper, Section II summarizes the study in the literature for turbine energy prediction. Section III presents the data acquisition process; the preprocessing steps used for the study and the method used in this study are described in detail. Section IV presents the results and discussion. This section provides information about the experimental settings. Then the results of the proposed method are described. Section V, the concluding section, discusses the results of the study and concludes the paper with future work.

2. RELATED WORKS

Forecasting methods using machine learning-based models can be broadly divided into two categories: shallow learning and DL-based models [29]. In some shallow studies, wind energy prediction has been performed with fuzzy logic [30], wavelet analysis [31], and least squares support vector machine (LSSVM) [32]. Another shallow learning model, artificial neural networks (ANN), has the ability to capture the high correlation between data [33–35]. Sun et al. developed an ANN-based model to predict wind turbine active power. They considered environmental factors in network training. In their study, they concluded that differently positioned wind turbines should use different yaw angle strategies [36]. DL is a machine learning approach using ANNs [37].

DL, a subset of machine learning, is a relatively new technique developed to overcome the shortcomings of shallow learning models [38, 39]. DL-based methods have been successfully applied to classification [40] and prediction problems [41]. LSTM, a variant of RNN, can learn time-series information more accurately. It is capable of efficiently utilizing temporal information to predict new data points [42].

It has been successfully used in stock market forecasting [43], natural language processing [44], and medicine [45].

Studies using LSTM-based methods for energy estimation are available in the literature [46]. An LSTM method with physical constraints was proposed by Luo et al. When compared to conventional statistical and machine learning techniques, the physically constrained LSTM model greatly increased prediction accuracy [47]. Chen et al. selected strongly associated features using the Pearson correlation coefficient. Features related to temperature, humidity, and solar radiation intensity were chosen for the LSTM model's input. They contrasted the time series method, radial basis function (RBF) neural networks, and back-propagation (BP) neural networks with the one-layer LSTM model. When compared to previous methods, their suggested model made predictions with a higher accuracy [48]. Zherui et al. used the LSTM model as a deep network model to predict wind power output with appropriate reliability. To enhance the prediction outcomes, they suggested a double decomposition-based remedial method [49]. In addition, related works based on chaotic time series, hybrid back-propagation, decomposition, and wavelet transforms have been investigated in the literature [50].

Most of the methods proposed in the literature for predicting turbine output power are traditional machine learning-based techniques. These methods have problems, such as requiring feature selection engineering and overcoming the problems of dealing with big data. In addition, the studies lack visualization of time series that can help in understanding and analyzing the problems while evaluating the data set. Our research focuses on the visualization and forecasting of wind power generation. The proposed architecture helps to make sense of the problems that can be encountered in the energy forecasting process with the help of data preprocessing and visualization methods.

3. MATERIALS AND METHOD

3.1. Data Pre-processing

To forecast wind power, the features that machine learning algorithms will use must be properly chosen. The environmental factors surrounding the wind turbine should be taken into account in this situation. Additionally, a thorough assessment of its effect on the wind turbine's active power generation is necessary. In this study, the dataset is provided by Kaggle [51]. Environmental factors such as wind speed and wind direction are used as inputs in the model. The dataset is obtained from a N117/3600 model wind turbine manufactured by Nordex. The SCADA system contains time series data of the wind turbine for one year (01.01.2018–31.12.2018) recorded in 10-minute periods. The dataset consists of 50530 units and five attributes: Wind speed (m/s), wind direction ($^{\circ}$), theoretical power (kW), active power (kW), and Date/Time (Table 1).

TABLE I
DATASET DESCRIPTION

Feature	Description
Date/Time	10 minutes period.
LV Active Power (kW)	Power produced at that precise instant by the turbine.
Wind Speed (m/s)	Wind speed used by the turbine to generate electricity.
Theoretical Power Curve (kW)	The power expected to be generated by the turbine manufacturer at this wind speed.
Wind Direction ($^{\circ}$)	Wind direction measured from the turbine hub.

3.2. Impact Factors Analysis

It is of great importance to assess and quantify the effects of the characteristics in the dataset on active wind energy production. Considering the impact of several variables on energy production, understanding the relationships between these factors is a critical requirement. A correlation matrix could be used to investigate the correlations between different variables for this purpose. Pearson correlation coefficient analysis can select the appropriate influence factors of the input data for the model. Thus, it can investigate the degree to which different impacts are correlated factors of the data and active power. The Pearson correlation coefficient can be calculated using Equation 1 [52].

$$r_{jk} = \frac{\sum_{i=1}^n (x_{ij} - \bar{x}_j)(x_{ik} - \bar{x}_k)}{\sqrt{\sum_{i=1}^n (x_{ij} - \bar{x}_j)^2} \sqrt{\sum_{i=1}^n (x_{ik} - \bar{x}_k)^2}} \quad (1)$$

Where, the variables x_{ij} and x_{ik} represent the i value of data for class j and class k , respectively. Similarly, \bar{x}_j and \bar{x}_k denote the arithmetic mean of the data for class j and class k , respectively. The heat map in Figure 1 illustrates the results of Pearson correlation coefficient analysis applied to the dataset. The matrix, which numerically expresses the relationship between input variables and active power, presents the effect of one variable on the other between -1 and +1. Figure 1 shows that the correlation between actual power and wind speed is the highest, approximately 0.9. It can be seen that power and wind direction are negatively correlated. The correlation coefficient value of the wind direction is -0.063, which is less than 0.1. Therefore, the degree of correlation is weak.

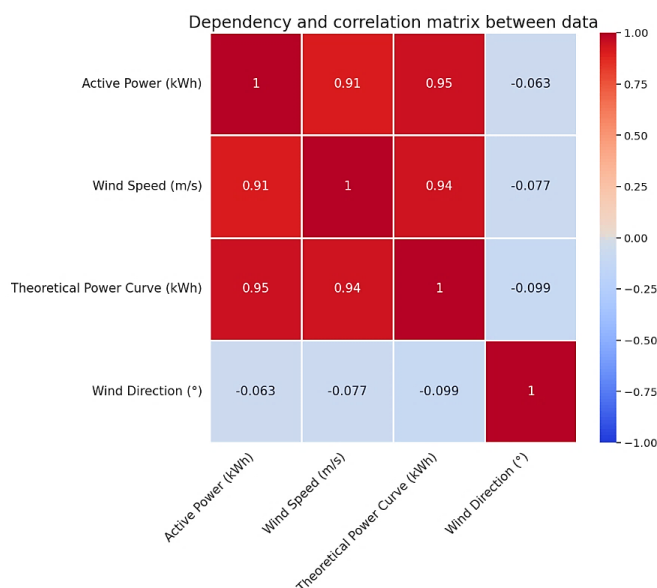


Figure 1. Pearson correlation matrix between active power and impact factors

3.3. Outlier Data Cleaning

One of the most important factors that negatively affects the performance of a model is outliers. Outliers can occur for various reasons. Outliers may occur in unexpected situations, such as wind outages and malfunctions. Due to these situations, it is difficult to obtain reliable wind power curves from raw wind data. For these reasons, it is necessary to extract these data

[53]. A turbine only begins to produce electricity when the wind speed reaches the start-up value. The wind speed at which the machine generates its rated power is known as the "rated speed". In order to avoid failure and damage, electricity generation is halted when wind speeds reach high levels. Manufacturers can generate theoretical power curves under the assumption of perfect topographical and meteorological circumstances [54].

The study begins with the cleaning of outlier data. Then, the "LV ActivePower (kW)" feature is divided into sub-datasets in the range of 50 kW. This process is performed in increments of 50 between 20 and 3400 using a loop. At the end of this process, frames of 50 data points each are obtained. Since power generation starts when the wind speed reaches 3 m/s, this lower wind speed limit is taken as the starting value of power generation. 20 m/s is the upper wind limit of the turbine. After this speed, there will be no active power generation as the turbine will protect itself. After these filtering operations, outliers are removed from each sub-frame obtained. For this process, values other than 1.5 times the lower and upper quartiles of the data (q_{low} and q_{hi}) are considered outliers. Figure 2 shows the raw data set and wind speed graph. Figure 3 shows the plot of the cleaned data set obtained after the outliers are removed as a result of the data preprocessing described above.

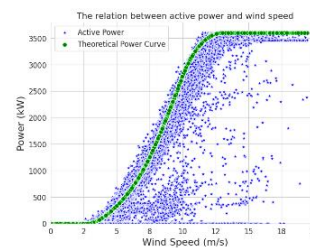


Figure 2. Relationship between actual power and wind speed in the raw data set

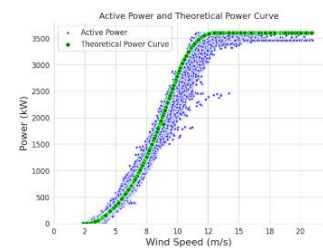


Figure 3. Relationship between actual power and wind speed in the preprocessed data set

At the end of the process, the sub-frames are merged to obtain a new data frame consisting of 37820 extracted data samples. Min-max normalization is applied to the input features to reduce the computational cost. At the end of normalization, the data range is compressed to [0, 1]. The normalization process is calculated using Equation 2 [55].

$$X_{scaled} = \frac{x_o - \min(x)}{\max(x) - \min(x)} \quad (2)$$

Here, X_{scaled} is the normalized number, x_o is the original number, and $\max(x)$ and $\min(x)$ are the maximum and minimum numbers in the series, respectively.

3.4. LSTM Structure

The LSTM proposed by Hochreiter and Schmidhuber offers a solution to the problem of vanishing gradients in RNNs [56]. LSTM has a more complex structure than traditional RNNs, which includes cells and gates. An LSTM cell has the ability to preserve the temporal data from the earlier forecast and transmit this information to the network when needed [57]. The memory cell helps to preserve the temporal information of the previous prediction in the training of the LSTM and propagates it to the network when needed. Figure 4 shows the structure of a basic LSTM model.

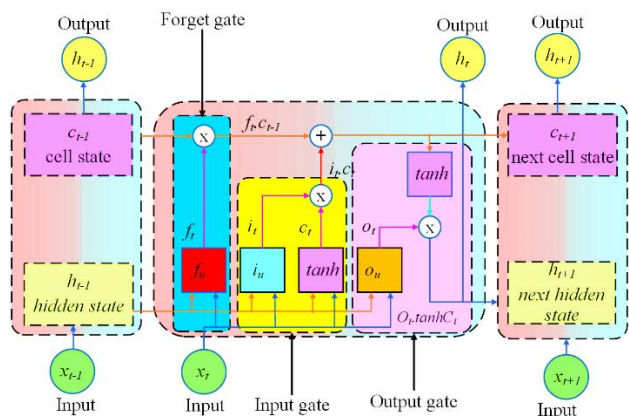


Figure 4. Basic structure of the LSTM model [57]

Compared with traditional RNN(s), the hidden layer of LSTM has more controllable units for information transfer to memory cells [58]. Three gates are added to the basic neural unit of the LSTM. These gates are input i_t , forget f_t , and output o_t . The gates take values in the interval $[0, 1]$. The primary role of the input gate is to update some attributes and determine the new attribute's content. The forget gate is designed to forget information that was previously useless. The output gate is used to determine what the output will be. All gates are connected at any time with the previous unit h_{t-1} and the current input x_t . Together, they decide the output. Below are the computational formulas for Equation (3) f_t , Equation (4) i_t , Equation (5) o_t , and the current neuron value, Equation (6) \tilde{C}_t [59].

$$f_t = \sigma(W_{fx}x_t + W_{fh}h_{t-1} + b_f) \quad (3)$$

$$i_t = \sigma(W_{ix}x_t + W_{ih}h_{t-1} + b_i) \quad (4)$$

$$o_t = \sigma(W_{ox}x_t + W_{oh}h_{t-1} + b_o) \quad (5)$$

$$\tilde{C}_t = \tanh(W_{cx}x_t + W_{ch}h_{t-1} + b_c) \quad (6)$$

Where W_{fx} , W_{fh} , W_{ix} , W_{ih} , W_{cx} , W_{ch} , W_{ox} , and W_{oh} are the matrix weights obtained by multiplying the current input value x_t by the previous unit output h_{t-1} of the relevant gate, respectively. b_f , b_i , b_o , and b_c represent the bias value and σ the sigmoid function. The input gate i_t , the forget gate f_t , the previous state value \tilde{C}_{t-1} , and the current neuron candidate value \tilde{C}_t are used to calculate the new state value \tilde{C}_{t+1} . Equation (7, 8) can be used to determine the output value h_t after the new state value has been determined [59].

$$C_{t+1} = f_t * xC_{t-1} + i_t * \tilde{C}_t \quad (7)$$

$$h_t = o_t * \tanh(S_t) \quad (8)$$

In this study, a multilayer LSTM network is designed to estimate active power. Table 2 shows the details of the designed architecture. The first layer contains 64 cell units and uses the ReLU activation function. The second layer contains 32 cell units and uses the ReLU activation function. The third and fourth layers contain a dense layer and an output dense

layer, respectively. The dense layers are fully connected and contain 16 and 1, neuron. The output of the model produces a single numerical value estimate.

TABLE II
LSTM STRUCTURE PARAMETERS

Layer	Output shape	Parameter
LSTM	(0,0,64)	19200
LSTM	(0,0,32)	12416
Dense	(0,16)	528
Dense	(0,1)	17
Total Parameter		32,161

3.5. Error Metrics

A range of statistical techniques were employed to assess the DL-based architecture's prediction. In this context, Equation (9) adjusted R-squared (R^2), Equation (10) mean squared error (MSE), Equation (11) root mean squared error (RMSE), and Equation (12) mean absolute error (MAE) metrics were used to evaluate the discrepancy between predicted and actual values [60].

$$R^2 = \frac{(\sum_{i=1}^N (x_i^* - \bar{x}_i^*)(x_i - \bar{x}_i))^2}{\sum_{i=1}^N (x_i^* - \bar{x}_i^*)^2 \sum_{i=1}^N (x_i - \bar{x}_i)^2} \quad (9)$$

In Equation 9, the R^2 value ranges from 0 to 1, with a higher value indicating a better predictive performance of the model. N is the number of data points, x is the dependent variable, x_i^* is the independent variable, \bar{x}_i^* is the mean value of the independent variable, and \bar{x}_i is the mean value of the dependent variable. In Equation 10, MSE is a statistical measure of how much error a regression model's predictions make relative to the actual data. In Equation 11, the standard deviation in prediction errors is represented by RMSE, and a lower value denotes a better model. In Equation 12, the absolute difference between the variables' expected and actual values is measured by the MAE [60, 61].

$$MSE = \frac{1}{N} \sum_{i=1}^N (x_i - x_i^*)^2 \quad (10)$$

$$RMSE = \sqrt{\frac{1}{N} \sum_{i=1}^N (x_i^* - x_i)^2} \quad (11)$$

$$MAE = \frac{1}{N} \sum_{i=1}^N |x_i - x_i^*| \quad (12)$$

Lower MSE, RMSE, and MAE values indicate that the model makes better predictions. For all three equations, N represents the number of data points, x_i represents the actual values, and x_i^* represents the expected output.

4. RESULTS AND DISCUSSION

This section analyzes the performance results obtained from the proposed LSTM-based DL model.

4.1. Experimental Settings

In this study, the data was tested using Python 3.10.12, TensorFlow 2.12, and a 64-bit system with a 2199 MHz 4-core processor and 32 GB of memory.

4.2. Hyperparameter and Optimization Techniques

The dataset was divided into training (60%), validation (20%), and testing (20%) subsets. According to this ratio, 22692, 7564, and 7564 were divided into three sets and used for training, validation, and testing, respectively. Hyperparameters are the settings that affect the performance results of the model. In order to determine these settings, the model was tested with different parameters, and the best-performing settings were selected. The learning coefficient of our model was initialized at a rate of 1e-3, and the coefficient was tried to be improved with the Adam optimizer. The training was set to 100 epochs. Table 3 shows the hyperparameters used for DL-based time series analysis.

TABLE III

TRAINING HYPERPARAMETERS	
Hyperparameter	Parameter
Learning rate	1e-3
Optimizer	Adam
Batch size	32
Loss function	MSE
Number of epochs	100
Re-scaling	MinMaxScale [0,1]

Test data is used to evaluate the accuracy of the proposed prediction model. The regression graph obtained from the test data set using the LSTM architecture is shown in Figure 5. It is seen that the actual values and the values predicted by the architecture are gathered on the regression line. It is clear that the proposed architecture has high prediction accuracy.

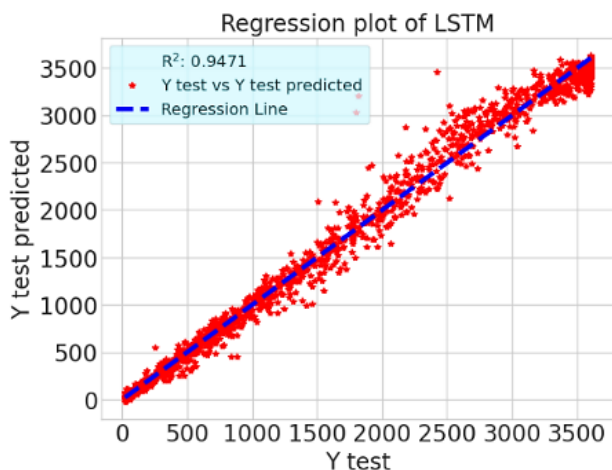


Figure 5. Regression plot of test dataset

The theoretical power curve is the graph of the power indicator expected from the turbine under ideal conditions. The prediction graph of the proposed model is consistent with the theoretical power curve graph. This shows that the model has good prediction performance. There is a direct proportionality between wind speed and actual power up to the turbine decommissioning speed point. Figure 6 shows the turbine's active power, the theoretical power, and the predicted power values obtained using the proposed method. When the graph is

analyzed, the estimated power curve, the actual active power curve, and the theoretical power curve have a similar distribution.

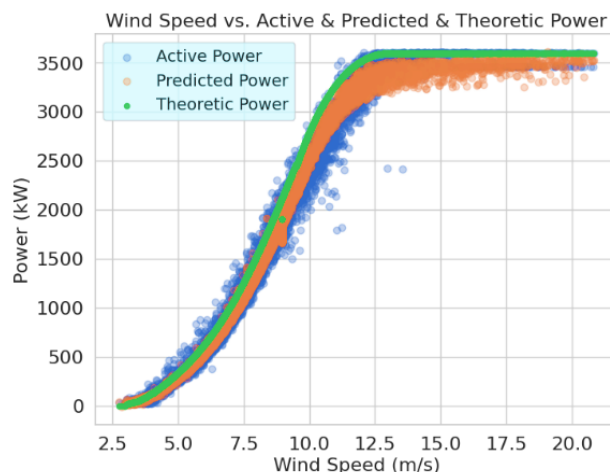


Figure 6. Graph of theoretical, active, predicted power and wind speed

Figure 7 shows the actual active power and the predicted power values by the proposed architecture for the date range 01.12.2018–05.12.2018 on the time axis graph. The actual data and the predicted data are given in the same figure. The proposed model performed well by overlapping with the actual value.

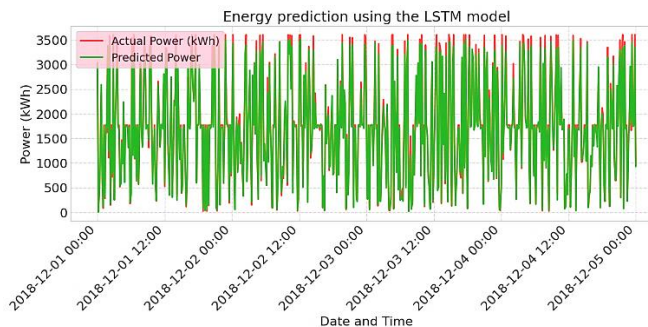


Figure 7. Time slice of predicted and active power

In this study, the performance of the model was evaluated according to the indicators described in Section 3.5. According to the results presented in Table 4, the proposed method has achieved high performance with an R² value of 96.10% on the training dataset. In addition, MAE, MSE, and RMSE values are 0.0190, 0.0034, and 0.0584, respectively. In addition, the proposed architecture achieved an R² score of 94.71% on the test dataset. This shows that the model is not overfitting and can capture the connection between the data in the newly encountered test dataset well. The MAE, MSE, and RMSE values in the test dataset are 0.0047, 0.0685, and 0.9471, respectively, and a good prediction result is obtained with low error metrics.

TABLE IV

PERFORMANCE RESULTS OF THE MODEL FROM THE TRAINING AND TEST DATASET		
	Training Dataset	Testing Dataset
MAE	0.0190	0.0226
MSE	0.0034	0.0047
RMSE	0.0584	0.0685
R ²	0.9610	0.9471

When the results are examined, the model is able to analyze the data well and shows a successful prediction capability. This is due to the ability of the LSTM-based machine learning method to capture long-term dependencies. Compared to classical machine learning-based methods, LSTM uses a special mechanism called memory cells. The cells have the ability to store previous knowledge and use it later. This allows the model to make predictions based on previous data.

5. CONCLUSION

Wind energy forecasting is an important component of energy management systems. In this study, an LSTM-based architecture for active power energy forecasting is proposed using time series data from a wind turbine. The anomalous data in the dataset is extracted by dividing it into frames. Then the cleaned data is used to feed the LSTM-based architecture. The results and performance metrics show the high success rate of the model. LSTM is a method with high prediction performance, especially in large datasets, due to its ability to capture long-term dependencies. By utilizing this, the proposed DL-based LSTM method has achieved high prediction accuracy.

For energy forecasting, LSTM-based methods can be used to achieve high accuracy in forecasting. However, the result can be improved by using different architectures. In addition, the LSTM model is a computationally expensive method due to its complexity. In our study, we used a multilayer LSTM model. These architectures are capable of successfully capturing complex relationships between data. However, increasing the number of layers may increase the computational cost. In future work, we plan to design fewer-layer architectures without degrading performance. In this way, we aim to reduce the computational cost.

REFERENCES

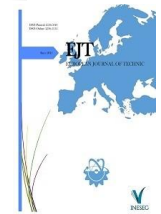
- [1] M. Sağlam, C. Spataru, and O. A. Karaman, "Electricity demand forecasting with use of artificial intelligence: The case of Gokceada Island," *Energies*, vol. 15, no. 16, p. 5950, 2022. <https://doi.org/10.3390/en15165950>
- [2] Ş. Fidan and H. Çimen, "Rüzgâr Türbinlerinde Tork ve Kanat Eğim Açısı Kontrolü," *Batman Üniversitesi Yaşam Bilimleri Dergisi*, vol. 11, pp. 12–26, 2021. Retrieved from <https://dergipark.org.tr/en/pub/buyasambid/issue/63446/880791>
- [3] Yilmaz, M. (2018). Real measure of a transmission line data with load fore-cast model for the future. *Balkan Journal of Electrical and Computer Engineering*, 6(2), 141-145. <https://doi.org/10.17694/bajece.419646>
- [4] Yilmaz, M. (2017, March). The Prediction of Electrical Vehicles' Growth Rate and Management of Electrical Energy Demand in Turkey. In 2017 Ninth annual IEEE green technologies conference (GreenTech) (pp. 118-123). IEEE. <https://doi.org/10.1109/GreenTech.2017.23>
- [5] M. Sağlam, C. Spataru, and O. A. Karaman, "Forecasting electricity demand in Turkey using optimization and machine learning algorithms," *Energies*, vol. 16, no. 11, p. 4499, 2023. <https://doi.org/10.3390/en16114499>
- [6] Z. Niu, Z. Yu, W. Tang, Q. Wu, and M. Reformat, "Wind power forecasting using attention-based gated recurrent unit network," *Energy (Oxf.)*, vol. 196, no. 117081, p. 117081, 2020. <https://doi.org/10.1016/j.energy.2020.117081>
- [7] L. Donadio, J. Fang, and F. Porté-Agel, "Numerical weather prediction and artificial neural network coupling for wind energy forecast," *Energies*, vol. 14, no. 2, p. 338, 2021. <https://doi.org/10.3390/en14020338>
- [8] S. Hanifi, X. Liu, Z. Lin, and S. Lotfian, "A critical review of wind power forecasting methods—past, present and future," *Energies*, vol. 13, no. 15, p. 3764, 2020. <https://doi.org/10.3390/en13153764>
- [9] L. Liu and Y. Liang, "Wind power forecast optimization by integration of CFD and Kalman filtering," *Energy Sources Recovery Util. Environ. Eff.*, vol. 43, no. 15, pp. 1880–1896, 2021. <https://doi.org/10.1080/15567036.2019.1668080>
- [10] J. M. González-Sopeña, V. Pakrashi, and B. Ghosh, "An overview of performance evaluation metrics for short-term statistical wind power forecasting," *Renew. Sustain. Energy Rev.*, vol. 138, no. 110515, p. 110515, 2021. <https://doi.org/10.1016/j.rser.2020.110515>
- [11] V. Cerqueira, L. Torgo, and C. Soares, "Machine learning vs statistical methods for time series forecasting: Size matters," 2019. <https://doi.org/10.48550/arXiv.1909.13316>
- [12] I. Aydin, S. B. Celebi, S. Barmada, and M. Tucci, "Fuzzy integral-based multi-sensor fusion for arc detection in the pantograph-catenary system," *Proc. Inst. Mech. Eng. Pt. F: J. Rail Rapid Transit*, vol. 232, no. 1, pp. 159–170, 2018. <https://doi.org/10.1177/0954409716662090>
- [13] Ö. A. Karaman, "Performance evaluation of seasonal solar irradiation models—case study: Karapınar town, Turkey," *Case Stud. Therm. Eng.*, vol. 49, no. 103228, p. 103228, 2023. <https://doi.org/10.1016/j.csite.2023.103228>
- [14] A. Çalışkan, S. Demirhan, and R. Tekin, "Comparison of different machine learning methods for estimating compressive strength of mortars," *Constr. Build. Mater.*, vol. 335, no. 127490, p. 127490, 2022. <https://doi.org/10.1016/j.conbuildmat.2022.127490>
- [15] Öztekin, A., & Erçelebi, E. (2019). An efficient soft demapper for APSK signals using extreme learning machine. *Neural Computing and Applications*, 31, 5715-5727. <https://doi.org/10.1007/s00521-018-3392-6>
- [16] S. B. Çelebi and B. G. Emiroğlu, "Leveraging deep learning for enhanced detection of Alzheimer's disease through morphometric analysis of brain images," *Trait. Du Signal*, vol. 40, no. 4, pp. 1355–1365, 2023. <https://doi.org/10.18280/ts.400405>
- [17] T. Chen and C. Guestrin, "XGBoost: A Scalable Tree Boosting System," in *Proceedings of the 22nd ACM SIGKDD International Conference on Knowledge Discovery and Data Mining*, 2016. <https://doi.org/10.1145/2939672.2939785>
- [18] Demir, S., & Sahin, E. K. (2023). Predicting occurrence of liquefaction-induced lateral spreading using gradient boosting algorithms integrated with particle swarm optimization: PSO-XGBoost, PSO-LightGBM, and PSO-CatBoost. *Acta Geotechnica*, 18(6), 3403-3419. <https://doi.org/10.1007/s11440-022-01777-1>
- [19] S. Hochreiter, "The vanishing gradient problem during learning recurrent neural nets and problem solutions," *Internat. J. Uncertain. Fuzziness Knowledge-Based Systems*, vol. 06, no. 02, pp. 107–116, 1998. <https://doi.org/10.1142/S0218488598000094>
- [20] Yilmaz, A., & Poli, R. (2022). Successfully and efficiently training deep multi-layer perceptrons with logistic activation function simply requires initializing the weights with an appropriate negative mean. *Neural Networks*, 153, 87-103. <https://doi.org/10.1016/j.neunet.2022.05.030>
- [21] J. F. Torres, A. Galicia, A. Troncoso, and F. Martínez-Álvarez, "A scalable approach based on deep learning for big data time series forecasting," *Integr. Comput. Aided Eng.*, vol. 25, no. 4, pp. 335–348, 2018. <https://doi.org/10.3233/ICA-180580>
- [22] J. Zhang, J. Yan, D. Infield, Y. Liu, and F.-S. Lien, "Short-term forecasting and uncertainty analysis of wind turbine power based on long short-term memory network and Gaussian mixture model," *Appl. Energy*, vol. 241, pp. 229–244, 2019. <https://doi.org/10.1016/j.apenergy.2019.03.044>
- [23] S. Zhang, Y. Wang, M. Liu, and Z. Bao, "Data-based line trip fault prediction in power systems using LSTM networks and SVM," *IEEE Access*, vol. 6, pp. 7675–7686, 2018. <https://doi.org/10.1109/ACCESS.2017.2785763>
- [24] S. Fidan, H. Oktay, S. Polat, and S. Ozturk, "An artificial neural network model to predict the thermal properties of concrete using different neurons and activation functions," *Adv. Mater. Sci. Eng.*, vol. 2019, pp. 1–13, 2019. <https://doi.org/10.1155/2019/3831813>
- [25] I. Aydin, O. Yaman, M. Karakose, and S. B. Celebi, "Particle swarm based arc detection on time series in pantograph-catenary system," in *2014 IEEE International Symposium on Innovations in Intelligent Systems and Applications (INISTA) Proceedings*, 2014. <https://doi.org/10.1109/INISTA.2014.6873642>
- [26] S. F. Stefenon, L. O. Seman, V. C. Mariani, and L. dos S. Coelho, "Aggregating prophet and seasonal trend decomposition for time series forecasting of Italian electricity spot prices," *Energies*, vol. 16, no. 3, p. 1371, 2023. <https://doi.org/10.3390/en16031371>

- [27] M. Ş. Üney and Ö. A. Karaman, "Load Frequency Control (LFC) of a Microgrid using PSCAD/EMTDC Simulation Program," *Adıyaman Üniversitesi Mühendislik Bilimleri Dergisi*, vol. 8, no. 15, pp. 328–342, 2021. <https://doi.org/10.54365/adyumbd.939716>
- [28] Ş. Fidan, M. Cebeci, and A. Gündoğdu, "Extreme Learning Machine Based Control of Grid Side Inverter for Wind Turbines," *Tehnički vjesnik*, vol. 26, pp. 1492–1498, 2019. <https://doi.org/10.17559/TV-20180730143757>
- [29] B. Zazoum, "Solar photovoltaic power prediction using different machine learning methods," *Energy Rep.*, vol. 8, pp. 19–25, 2022. <https://doi.org/10.1016/j.egy.2021.11.183>
- [30] W. Zou, C. Li, and P. Chen, "An inter type-2 FCR algorithm based T-S fuzzy model for short-term wind power interval prediction," *IEEE Trans. Industr. Inform.*, vol. 15, no. 9, pp. 4934–4943, 2019. doi: 10.1109/TII.2019.2910606.
- [31] P. Du, J. Wang, W. Yang, and T. Niu, "A novel hybrid model for short-term wind power forecasting," *Appl. Soft Comput.*, vol. 80, pp. 93–106, 2019. <https://doi.org/10.1016/j.asoc.2019.03.035>
- [32] X. Yuan, Q. Tan, X. Lei, Y. Yuan, and X. Wu, "Wind power prediction using hybrid autoregressive fractionally integrated moving average and least square support vector machine," *Energy (Oxf.)*, vol. 129, pp. 122–137, 2017. <https://doi.org/10.1016/j.energy.2017.04.094>
- [33] S. Agatonovic-Kustrin and R. Beresford, "Basic concepts of artificial neural network (ANN) modeling and its application in pharmaceutical research," *J. Pharm. Biomed. Anal.*, vol. 22, no. 5, pp. 717–727, 2000. [https://doi.org/10.1016/S0731-7085\(99\)00272-1](https://doi.org/10.1016/S0731-7085(99)00272-1)
- [34] B. Birecikli, Ö. A. Karaman, S. B. Çelebi, and A. Turgut, "Failure load prediction of adhesively bonded GFRP composite joints using artificial neural networks," *J. Mech. Sci. Technol.*, vol. 34, no. 11, pp. 4631–4640, 2020. <https://doi.org/10.1007/s12206-020-1021-7>
- [35] H. A. N. Kubilay, G. Öztürk, and A. Aslan, "Yapay Sinir Ağları Kullanarak Yüzeysel Pürüzlülüğü Tespiti," *International Conference on Pioneer and Innovative Studies*, vol. 1, pp. 487–492, 2023.
- [36] H. Sun, C. Qiu, L. Lu, X. Gao, J. Chen, and H. Yang, "Wind turbine power modelling and optimization using artificial neural network with wind field experimental data," *Appl. Energy*, vol. 280, no. 115880, p. 115880, 2020. <https://doi.org/10.1016/j.apenergy.2020.115880>
- [37] Yılmaz, A., Simsek, C., Tozlu, B. H., Aydemir, O., & Karavelioglu, Y. (2022). Selection of suitable sensors of the electronic nose used for classification of myocardial infarction, stable coronary artery disease and healthy individuals. *Selcuk University Journal of Engineering Sciences*, 21(1), 39-43. <https://sujes.selcuk.edu.tr/sujes/article/view/597>
- [38] S. B. Çelebi and B. G. Emiroğlu, "A novel deep dense block-based model for detecting Alzheimer's disease," *Appl. Sci. (Basel)*, vol. 13, no. 15, p. 8686, 2023. <https://doi.org/10.3390/app13158686>
- [39] Şimşek, C., Yılmaz, A., Tozlu, B. H., Aydemir, Ö., & Karavelioglu, Y. (2022). Classification of Cardiovascular Diseases Using Electronic Nose Dataset with Artificial Neural Network Classifier. *Avrupa Bilim ve Teknoloji Dergisi*, (38), 479-483. <https://doi.org/10.31590/ejosat.1165991>
- [40] S. B. Çelebi and B. G. Emiroğlu, "Alzheimer Teşhisi için Derin Öğrenme Tabanlı Morfometrik Analiz," *İğdır Üniversitesi Fen Bilimleri Enstitüsü Dergisi*, vol. 13, no. 3, pp. 1454–1467, 2023. <https://doi.org/10.21597/jist.1275669>
- [41] F. Emmert-Streib, Z. Yang, H. Feng, S. Tripathi, and M. Dehmer, "An introductory review of deep learning for prediction models with big data," *Front. Artif. Intell.*, vol. 3, 2020. <https://doi.org/10.3389/frai.2020.00004>
- [42] R. DiPietro and G. D. Hager, "Deep learning: RNNs and LSTM," in *Handbook of Medical Image Computing and Computer Assisted Intervention*, Elsevier, 2020, pp. 503–519. <https://doi.org/10.1016/B978-0-12-816176-0.00026-0>
- [43] S. Zaheer et al., "A multi parameter forecasting for stock time series data using LSTM and deep learning model," *Mathematics*, vol. 11, no. 3, p. 590, 2023. <https://doi.org/10.3390/math11030590>
- [44] M. Fazil, S. Khan, B. M. Albahlal, R. M. Alotaibi, T. Siddiqui, and M. A. Shah, "Attentional multi-channel convolution with bidirectional LSTM cell toward hate speech prediction," *IEEE Access*, vol. 11, pp. 16801–16811, 2023. <https://doi.org/10.1109/ACCESS.2023.3246388>
- [45] V. Rai, G. Gupta, S. Joshi, R. Kumar, and A. Dwivedi, "LSTM-based adaptive whale optimization model for classification of fused multimodality medical image," *Signal Image Video Process.*, vol. 17, no. 5, pp. 2241–2250, 2023. <https://doi.org/10.1007/s11760-022-02439-1>
- [46] Ö. A. Karaman, "Prediction of wind power with machine learning models," *Appl. Sci. (Basel)*, vol. 13, no. 20, p. 11455, 2023. <https://doi.org/10.3390/app132011455>
- [47] X. Luo, D. Zhang, and X. Zhu, "Deep learning based forecasting of photovoltaic power generation by incorporating domain knowledge," *Energy (Oxf.)*, vol. 225, no. 120240, p. 120240, 2021. <https://doi.org/10.1016/j.energy.2021.120240>
- [48] H. Chen and X. Chang, "Photovoltaic power prediction of LSTM model based on Pearson feature selection," *Energy Rep.*, vol. 7, pp. 1047–1054, 2021. <https://doi.org/10.1016/j.egy.2021.09.167>
- [49] Z. Ma et al., "Application of hybrid model based on double decomposition, error correction and deep learning in short-term wind speed prediction," *Energy Convers. Manag.*, vol. 205, no. 112345, p. 112345, 2020. <https://doi.org/10.1016/j.enconman.2019.112345>
- [50] T. Ouyang, H. Huang, Y. He, and Z. Tang, "Chaotic wind power time series prediction via switching data-driven modes," *Renew. Energy*, vol. 145, pp. 270–281, 2020. <https://doi.org/10.1016/j.renene.2019.06.047>
- [51] Kaggle.com. [Online]. Available: <https://www.kaggle.com/datasets/berkerisen/wind-turbine-scada-dataset>. [Accessed: 28-Oct-2023]
- [52] P. Schober, C. Boer, and L. A. Schwarte, "Correlation coefficients: Appropriate use and interpretation," *Anesth. Analg.*, vol. 126, no. 5, pp. 1763–1768, 2018. <https://doi.org/10.1213/ANE.0000000000002864>
- [53] V. Hodge and J. Austin, "A survey of outlier detection methodologies," *Artif. Intell. Rev.*, vol. 22, no. 2, pp. 85–126, 2004. <https://doi.org/10.1023/B:AIRE.0000045502.10941.a9>
- [54] S. Shokrzadeh, M. Jafari Jozani, and E. Bibeau, "Wind turbine power curve modeling using advanced parametric and nonparametric methods," *IEEE Trans. Sustain. Energy*, vol. 5, no. 4, pp. 1262–1269, 2014. <https://doi.org/10.1109/TSTE.2014.2345059>
- [55] S. G. K. Patro and K. K. Sahu, "Normalization: A Preprocessing Stage," 2015. <https://doi.org/10.48550/arXiv.1503.06462>
- [56] Bilal, M. A., Wang, Y., Ji, Y., Akhter, M. P., & Liu, H. (2023). Earthquake Detection Using Stacked Normalized Recurrent Neural Network (SNRNN). *Applied Sciences*, 13(14), 8121. <https://doi.org/10.3390/app13148121>
- [57] S. Hochreiter and J. Schmidhuber, "Long short-term memory," *Neural Comput.*, vol. 9, no. 8, pp. 1735–1780, 1997. <https://doi.org/10.1162/neco.1997.9.8.1735>
- [58] F. Shahid, A. Zameer, and M. Muneeb, "A novel genetic LSTM model for wind power forecast," *Energy (Oxf.)*, vol. 223, no. 120069, p. 120069, 2021. <https://doi.org/10.1016/j.energy.2021.120069>
- [59] A. T. Mohan and D. V. Gaitonde, "A deep learning based approach to reduced Order Modeling for turbulent flow control using LSTM neural networks," 2018. <https://doi.org/10.48550/arXiv.1804.09269>
- [60] T. Chai and R. R. Draxler, "Root mean square error (RMSE) or mean absolute error (MAE)-Arguments against avoiding RMSE in the literature," *Geoscientific model development*, vol. 7, no. 3, pp. 1247–1250, 2014. <https://doi.org/10.5194/gmd-7-1247-2014>
- [61] Öztekin, A., & Erçelebi, E. (2016). An early split and skip algorithm for fast intra CU selection in HEVC. *Journal of Real-Time Image Processing*, 12, 273-283. <https://doi.org/10.1007/s11554-015-0534-2>

BIOGRAPHIES

Selahattin Barış Çelebi, received his bachelor's degree in computer engineering from Selçuk University, Konya. He received his master's degree in computer engineering from the department of computer engineering at Firat University, Elazığ. Subsequently, he obtained his doctoral degree in computer engineering from Kırıkkale University, Kırıkkale. His research interests are in the fields of artificial intelligence, data science, machine learning, image processing.

Ömer Ali Karaman received the M.Sc. in DTC control of asynchronous motor in 2010 and the Ph.D. degree in harmonics active power filter in Firat University in 2018. He is a Full Asst. Professor in Electronics and automation department in Batman University. His research focuses on renewable energy systems, energy and solar radiation forecasting.



Research Article

Design and Testing of a Wireless Communication Enabled FPGA Development Board: A Comprehensive Education and Application Platform from IoT to Circuit Design

Nebi Karagedik¹ , Sezen Bal²  and Ayşe Yayla^{3*} 

¹TELFIX, Istanbul, Turkey. (e-mail: n.karagedik@hotmail.com).

²Marmara University, Vocational School of Technical Sciences, Department of Computer Technologies Kartal, İstanbul, Turkey. (e-mail: sezen.bal@marmara.edu.tr).

^{3*}Marmara University, Vocational School of Technical Sciences, Department of Electronics and Automation, Kartal, İstanbul, Turkey. (e-mail: acetinkaya@marmara.edu.tr).

ARTICLE INFO

Received: Dec., 03. 2023

Revised: Dec., 27. 2023

Accepted: Dec, 27. 2023

Keywords:

FPGA

Circuit Design

Digital Design Lecture

VHDL

IoT

Corresponding author: *Ayşe YAYLA*

ISSN: 2536-5010 / e-ISSN: 2536-5134

DOI: <https://doi.org/10.36222/ejt.1399107>

ABSTRACT

Field Programmable Gate Array (FPGA) is an integrated circuit (IC) that can be reprogrammed or configured by the customer or designer after production for rapid prototyping and post-process development. In this study, a cost-effective FPGA development board is designed to create basic engineering education applications and implement them in real-time. The Printed Circuit Board (PCB) design of the FPGA development board layout was precisely crafted using EasyEDA software to ensure robust and reliable connectivity between the FPGA and its peripherals. The FPGA development board utilizes an Altera Cyclone IV E-series chip and includes Bluetooth and Wi-Fi modules to provide a wider range of applications. This integration simplifies the use of wireless communication in various projects and applications for researchers and engineers. To verify the accuracy of the proposed board, simulations of selected digital designs and Bluetooth applications were first performed in VHDL (Very High Speed Integrated Circuit Hardware Description Language) using Intel® Quartus® Prime Lite Edition software. Then, experiments were performed on the board following the pin assignment configurations. It was observed that the developed applications worked successfully on the FPGA development board. As a result, this board, equipped with Bluetooth and Wi-Fi modules, offers a fast and cost-effective solution for users in various fields such as mobile, robotics, smart home systems, and remote monitoring and control devices.

1. INTRODUCTION

Digital Logic Design course has an important position in the curriculum for both computer engineering and the electrical engineering departments [1]. The objective of this course is to provide students to get their exposure to the hardware design by learning the basic concepts of digital design and performing their corresponding experiments. It is very important that the content of the digital design course reflects the current design styles used in the industry. For this reason, FPGA (Field Programmable Gate Array) technology has been incorporated into the experimental education of digital logic design course in order to train expert engineers to adapt to the development trend of digital electronic technology that the industry requires.

FPGAs are programmable, reconfigurable semiconductor devices developed for the purpose of implementing and testing the digital circuits required by the designer [2-4].

FPGAs are generally used to create prototypes of newly designed ASIC circuits or to test the physical implementation of an algorithm. Today, FPGAs are used in a wide range of areas, especially in the military and defense industry [5], communications [6], audio [7] and image processing [8], automotive [9,10] and consumer electronics [11,12].

When developing FPGA-based applications, usually existing development boards are preferred. Procuring these development boards from abroad and their high costs create difficulties in accessing development boards for researchers who want to improve and progress in this field. For this reason, in this study, a low-cost FPGA development board has been designed that can be easily accessed by students studying in universities, especially engineering faculties and vocational schools, academicians who want to develop applications, and anyone interested in hardware design as a hobby. Thus, with this developed board, students studying in relevant departments of universities will be able to access this development board in

a cost-effective manner and thus, students who are more equipped on FPGA can be trained. By adding Bluetooth and Wi-Fi modules that are not included in the Altera DE2 board, which is closest to it in the market, a wider range of application development areas have been created in this designed board.

The study is organized as follows: Related works about applications developed using the FPGA board are described in the second section, and the development of the FPGA development board is described in the third section. The VHDL software of the applications implemented using the FPGA development board and the processes regarding the results obtained as a result of assignment to the board are explained in the fourth section. In the fifth and last chapter, the cost study of the developed board was conducted and the results were interpreted.

2. RELATED WORKS

This chapter deals with FPGA technology under two separate subheadings. The first part presents the applications performed with the existing FPGA boards available in the market and produced by various companies. The second part presents new FPGA boards specially designed and developed by researchers for specific needs and the applications performed with these boards.

2.1. Studies Performed Using FPGA Development Board

Saif and et all. designed and implemented an educational processor based on RISC-V architecture on FPGA. Additionally, an assembler was designed and developed that can translate assembly code into RISC-V standard machine codes that can help the users to operate the CPU easily [13].

Surekha and et all described the VLSI (Very Large Scale Integration) design of an Arithmetic Logic Unit (ALU). The design has been simulated and tested by using Xilinx ISE design suite 14.7 that is a prominent tool in FPGA development. The proposed ALU design is generated a delay of 125.711 ns [14].

Panigrahi and et all. designed a 4-bit ALU using Xilinx VIVADO 2016.2 and analyze the design parameters on FPGA by using VERILOG. They simulated and synthesized the various parameters such as speed improvement, less power consumption and better utilization of ALU to measure the efficiency of an algorithm [15].

Sağlam and Kaçar designed a 64-bit ALU by using the VHDL and Altera FPGA families, synthesized and simulated with the help of Altera Quartus II and Modelsim-Altera v10.1d software. The proposed design allows the processing of the signed numbers and also Conditional Sum Adder (COSA) is used in addition operation instead of Carry Ripple Adder (CRA) or Carry Look-ahead Adder (CLA). The output of the addition operation was obtained in a shorter time that the adder with COSA is approximately 6 times faster than adder with CRA [16].

Karakaya and et all. introduced a systematic methodology for implementing digital piecewise linear (PWL) functions within nonlinear dynamical systems, enabling the representation of complete behaviors within a single model. The proposed design takes the number of scrolls as input and efficiently generates chaotic PWL signals using a reduced number of FPGA resources. The implementation stage of the

study realized by using Xilinx Kintex-7 KC705 Evaluation Board [17].

2.2. Studies Designing and Developing FPGA Development Board

Keskin and Koyuncu designed an FPGA-based development board in their study. The development board was developed by selecting the FPGA chip of the XC2C64A-7-VQ44 family from Xilinx, and half adder and up counter applications were implemented as sample applications [18].

Zhao and et all designed a pocket development board that consists of two parts: the core circuit and the peripheral circuit. The core circuits include Altera company Cyclone IV series EP4 CE10 f-17 type FPGA chip, as the core of the hardware circuit of the control unit. Also the hardware circuit of the development board consists of the peripheral circuits that are LED lights, 6 seven-segment digital tubes, buttons and buzzers. These peripheral circuits can carry out independent experiments, and they can be combined with each other [19].

Gao developed Altera EPM7164S chip based FPGA Experiment and Development Board that has high on-board resource utilization, expandable, easy self-design and reasonable cost to overcome the shortcomings of fixed connections, large and fully functional of FPGA experimental box. FPGA Experiment and Development Board can use Quartus II integrated development environment to complete the design. It is suitable for VHDL hardware language and Verilog hardware language [20].

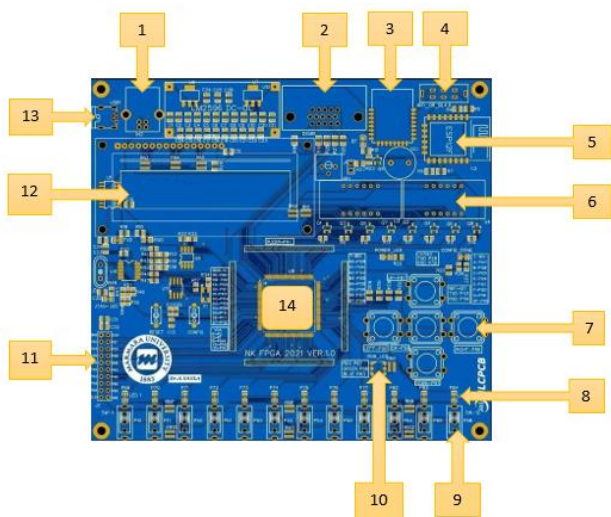
3. DESIGN PROCESS OF FPGA DEVELOPMENT BOARD

In this study, an FPGA development board was designed to execute fundamental digital logic design applications as well as Bluetooth and Wi-Fi applications. EP4CE6E22C8N chip from the Altera Cyclone IV family was used as the FPGA chip in the design of the development board.

In the development of the FPGA board, first the connections of the FPGA chip with the peripherals were determined and the necessary PCB drawings were made using the EasyEDA program.

The features of the developed FPGA board can be listed as follows: EP4CE10E22C8N was used as the FPGA chip. There is an integrated JTAG interface for programming and debugging FPGA chip, 50MHZ crystal, 5 button inputs and AT24C04 Serial EEPROM for I2C serial communication protocol on the board. With the USB-TTL serial port on the board, it will be possible to communicate with external hardware units such as PCs and embedded systems in accordance with RS232 standards.

The board also includes 1 X 12 slide switches to obtain input at logic 0 and logic 1 levels in the experiments, 12-bit LEDs, 8 pieces of 7 segment displays with common anode coded 3461BS (4x2 indicator block) and a buzzer. There is also a 1602 character-type LCD (Liquid Crystal Display) interface, VGA display port for visual applications, Input/ Output Pins, a Bluetooth and Wi-Fi modules communicating with UART protocol on the board. The FPGA development board PCB layout and feature callout is shown in Fig. 1.



Callout	Component Description	Callout	Component Description
1	USB Type B	8	12 X LEDs
2	VGA Connector	9	12 X slide switches
3	Wi-Fi Module	10	RGB Led
4	Select jumper (Wi-Fi/Bluetooth)	11	GPIO Pins
5	Bluetooth Module	12	LCD Display
6	8 digit 7 Segment display	13	UART/JTAG USB Port
7	5 X push buttons	14	Altera Cyclone IV FPGA

Figure 1. FPGA board PCB layout design and feature callout

4. SAMPLE APPLICATIONS REALIZED ON DEVELOPMENT BOARD

Altera Intel® Quartus® Prime Lite Edition design software was used for testing this FPGA-based development board and coded using the VHDL language. 4-bit Arithmetic Logic Unit (ALU) design, 3- bit Down Counter design and Bluetooth application were realized on this board.

4.1. ALU Design

ALU is the main component of the central processing unit in the computer system, which means arithmetic logic unit and performs arithmetic and logic operations [14]. ALU mainly handles arithmetic operations such as addition, subtraction, division, multiplication, and logical operations such as “AND”, “OR”, “EXCLUSIVE OR (XOR)”, etc., and performs scroll-rotation operations [15].

In this study, a 4-bit ALU design, the diagram of which is shown in Fig. 2, was realized by using the switches and LEDs on the designed FPGA development board.

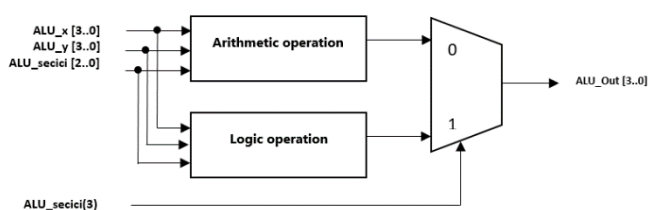


Figure 2. ALU Design Diagram

In this application, which is carried out using the VHDL hardware description language, the x and y inputs given as N bits, are set to 4 bits. The first 3 bits of the selective inputs,

which is determined as 4 bits, are used to select arithmetic and logical operations, and the 4th bit determines which operation result will be transferred to the output in the MUX circuit. The table of arithmetic and logic operations that can be performed with this ALU design is given in Table I.

In this application, which was carried out using VHDL structural style, the necessary VHDL code files were first created to perform arithmetic and logical operations. Then, a main file called ALU was created to interconnect the components (arithmetic and logic) within an architecture. The VHDL code of the ALU main file is shown in Fig. 3.

TABLE I

ALU OPERATIONS AND SELECT LINES

Operation	Selective inputs	Function	
Arithmetic operation	0 0 0 0	transfer the x value to the output	
	0 0 0 1	x value increased by 1	
	0 0 1 0	x value decreased by 1	
	0 0 1 1	transfer the y value to the output	
	0 1 0 0	y value increased by 1	
	0 1 0 1	y value decreased by 1	
	0 1 1 0	add the value of x to the value of y	
	0 1 1 1	subtract the value of y from the value of x	
	Logical operation	1 0 0 0	NOT x
		1 0 0 1	NOT y
1 0 1 0		AND (x and y)	
1 0 1 1		OR (x or y)	
1 1 0 0		NAND (Not AND)	
1 1 0 1		NOR (Not OR)	
1 1 1 0		XOR (Exclusive OR)	
1 1 1 1		XNOR (Exclusive NOR)	

Before testing the created ALU application on the FPGA development board, it is necessary to test whether the codes work correctly or not as a simulation. MODELSIM program was used for this. For this process, first a test file was created. The testbench file of the ALU design is shown in Fig. 4.

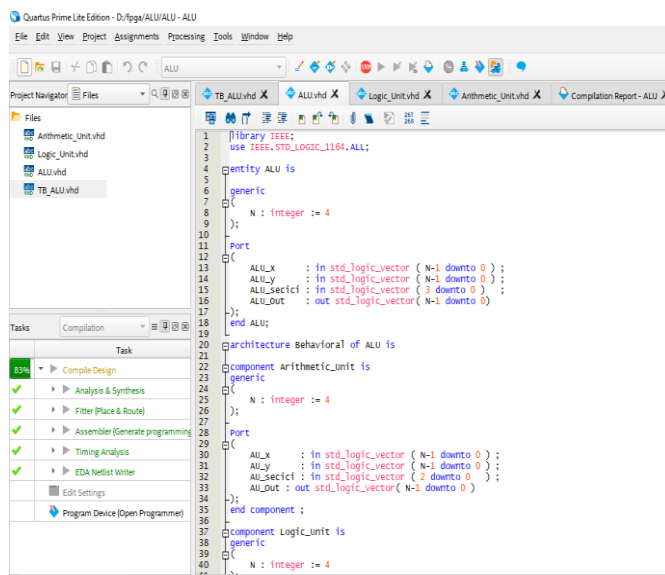


Figure 3. ALU Design VHDL File

RTL (Register Transfer Level) diagram visually illustrates how a design written in a hardware description language will be converted into gate-level logic during the logic synthesis process. This visualization allows the designer to evaluate the behavior and performance of the design and make improvements where necessary. The RTL diagram of the ALU design is shown in Fig 5.

```

1  library IEEE;
2  use IEEE.Std_logic_1164.all;
3  use IEEE.Numeric_Std.all;
4
5  entity ALU_tb is
6  end;
7
8  architecture bench of ALU_tb is
9
10 constant N : integer := 4;
11
12 component ALU
13 generic
14 (
15     N : integer := 4
16 );
17 port
18 (
19     ALU_x : in std_logic_vector ( N-1 downto 0 ) ;
20     ALU_y : in std_logic_vector ( N-1 downto 0 ) ;
21     ALU_secici : in std_logic_vector ( 3 downto 0 ) ;
22     ALU_Out : out std_logic_vector ( N-1 downto 0 ) ;
23 );
24 end component;
25
26 signal ALU_x : std_logic_vector ( N-1 downto 0 );
27 signal ALU_y : std_logic_vector ( N-1 downto 0 );
28 signal ALU_secici : std_logic_vector ( 3 downto 0 );
29 signal ALU_Out : std_logic_vector ( N-1 downto 0 );
30
31 begin
32
33 -- Insert values for generic parameters !!
34 uut: ALU generic map (
35     N => N )
36 port map (
37     ALU_x => ALU_x,
38     ALU_y => ALU_y,
39     ALU_secici => ALU_secici,
40     ALU_Out => ALU_Out );
41
42 stimulus: process
43 begin
44     ALU_x <= "0101";
45     ALU_y <= "1010"; wait for 50 ns ;
46     ALU_secici <= "0000"; wait for 20ns; ALU_secici <= "0001"; wait for 20ns;
47     ALU_secici <= "0010"; wait for 20ns; ALU_secici <= "0011"; wait for 20ns;
48     ALU_secici <= "0100"; wait for 20ns; ALU_secici <= "0101"; wait for 20ns;
49     ALU_secici <= "0110"; wait for 20ns; ALU_secici <= "0111"; wait for 50ns ;

```

Figure 4. Testbench File for ALU Design

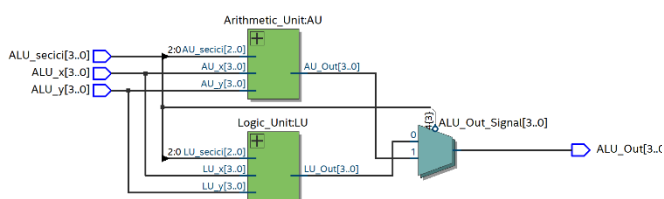


Figure 5. RTL Schematic for ALU Design

In the test file, x input value was selected as “0101 (Decimal 5)” and y input value was selected as “1010 (Decimal 10-Hexadecimal A)”. The first 8 states of the 4-bit selective bit are used to select arithmetic operations and the last 8 states are used to select logic operations. The result screen obtained by running this simulation, in which all arithmetic and logic operations are tested, is shown in Fig. 6.

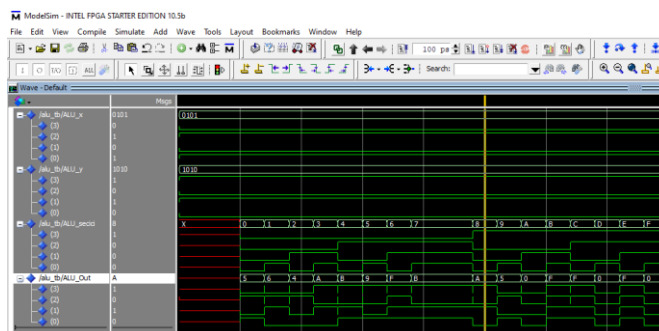


Figure 6. MODELSIM Simulation Result for ALU Design

In the next stage, the pin assignments of the FPGA chip are carried out so that the code tested to work correctly as a result of the simulation can be tested by placing it on the FPGA

development board. The first 4 keys of the 12 keys of the FPGA board are designated for the selector bits, the next 4 keys are determined for the x value, and the last 4 keys are determined for the y value. In order to observe the results, 4 LEDs were selected as seen in Fig. 7.

Node Name	Direction	Location	I/O Bank	VREF Group	Filter Location	I/O Standard	Reserved	Current Strength	Slow Rate	Differential Pair	Strict Placement
ALU_Out[0]	Output	PH_70	4	84_N0	PH_70	2.5 V		8mA (default)	2 (default)		
ALU_Out[1]	Output	PH_71	4	84_N0	PH_71	2.5 V		8mA (default)	2 (default)		
ALU_Out[2]	Output	PH_72	4	84_N0	PH_72	2.5 V		8mA (default)	2 (default)		
ALU_secici[3]	Input	PH_51	3	83_N0	PH_51	2.5 V		8mA (default)			
ALU_secici[2]	Input	PH_50	3	83_N0	PH_50	2.5 V		8mA (default)			
ALU_secici[1]	Input	PH_11	1	81_N0	PH_11	2.5 V		8mA (default)			
ALU_secici[0]	Input	PH_10	1	81_N0	PH_10	2.5 V		8mA (default)			
ALU_In[0]	Input	PH_20	3	83_N0	PH_20	2.5 V		8mA (default)			
ALU_In[1]	Input	PH_53	3	83_N0	PH_54	2.5 V		8mA (default)			
ALU_In[2]	Input	PH_54	4	84_N0	PH_55	2.5 V		8mA (default)			
ALU_In[3]	Input	PH_55	4	84_N0	PH_56	2.5 V		8mA (default)			
ALU_In[4]	Input	PH_60	4	84_N0	PH_60	2.5 V		8mA (default)			
ALU_In[5]	Input	PH_64	4	84_N0	PH_64	2.5 V		8mA (default)			
ALU_In[6]	Input	PH_65	6	86_N0	PH_65	2.5 V		8mA (default)			
ALU_In[7]	Input	PH_66	6	86_N0	PH_66	2.5 V		8mA (default)			

Figure 7. Pin Assignment for ALU Design

After the pin assignment is completed, the FPGA development board is programmed. Images of the ALU application performed on the designed FPGA development board are presented in Fig. 8 and Fig. 9, respectively.

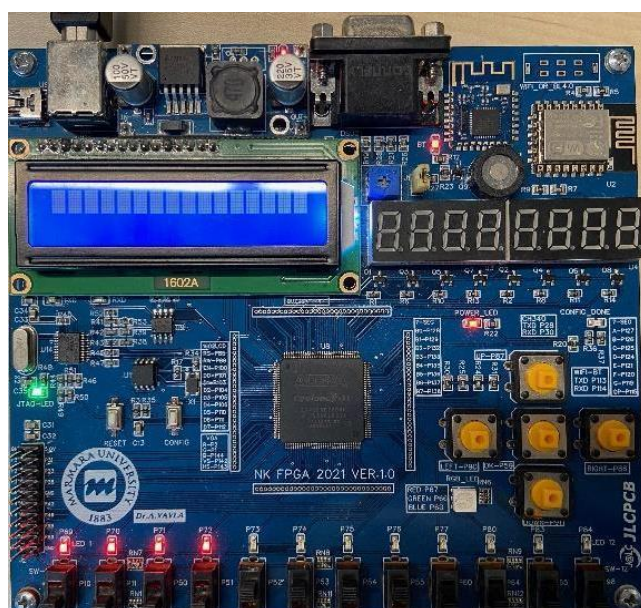


Figure 8. Selection Bits 0000 and s <= x (x = 1111)

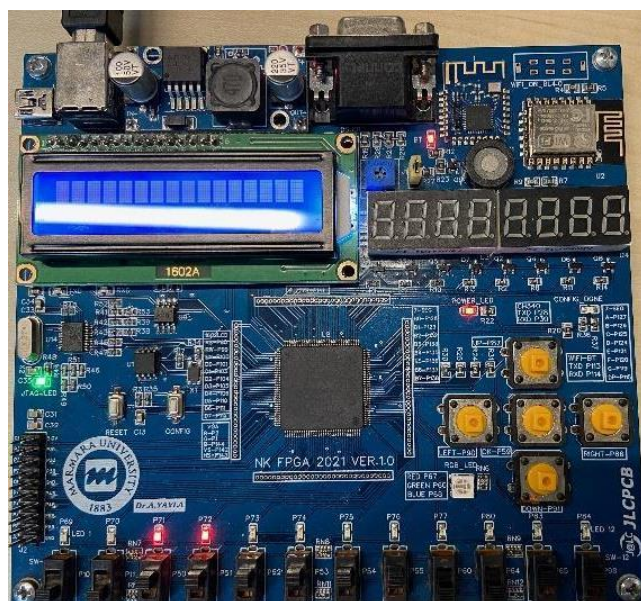


Figure 9. Selection Bits 0011 and s <= y (y = 0011)

4.2. 3-bit Down Counter (Schematic Application)

3-bit down counter circuit has been designed as a schematic application in the Quartus® Prime Lite Edition design software, where both schematic and code design is possible. Since the designed FPGA development board has a 50 MHz crystal oscillator, changes that will occur in a counter application using this internal clock pulse may not be discernible by the human eye. For this reason, in the design of this application, a schematic design for a five-bit frequency divider using J-K Flip Flop which is the one-bit memory element was initially designed to reduce the internal clock pulse as seen in Fig. 10.

This frequency divider schematic file saved as symbol to be used in the 3-bit down counter circuit. The down counter designed by using J-K FF and 7447 BCD to Seven Segment Decoder was used to transfer the counter values to the seven segment display as seen in Fig. 11.

In this application designed with positive-edge triggering, after creating BDF files, the developed study was tested in a simulation environment to verify its correct functionality. In this study simulated using the University Program VWF, the necessary signals for driving the seven-segment display are illustrated in Fig. 12.

After the successful completion of the testing process in the simulation environment, the necessary pin assignments for the seven-segment display have been implemented, and the counting process has occurred as depicted in Fig. 13.

4.3. Bluetooth Application

In the board design, a Bluetooth module is placed on the development board to enable easy communication between mobile applications and the FPGA. This module communicates with the FPGA chip via Universal Asynchronous Receiver Transmitter (UART) communication protocol. The oscillator on the development board operates at 50 MHz Bluetooth supports UART protocol communication utilizing a range of baud rates, from 1200 to 115200 baud and in this application, the baud rate was chosen 115200 baud. In the VHDL code, a generic is used to determine how many clock cycles there are in each bit by using the code: (Main Frequency) / (UART Baud Rate). The VHDL implementation of UART receiver is shown in Fig. 14.

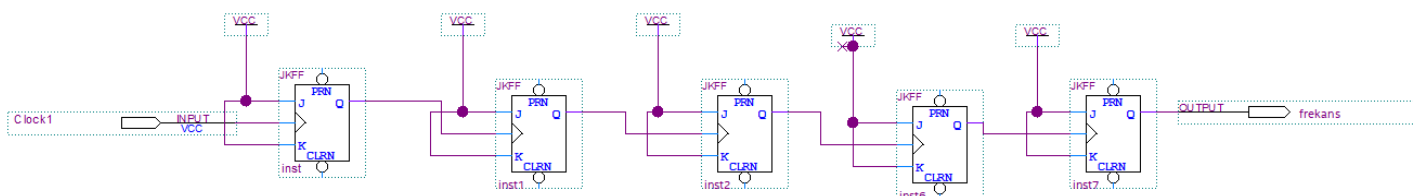


Figure 10. Frequency Divider (f clock /5) bdf file

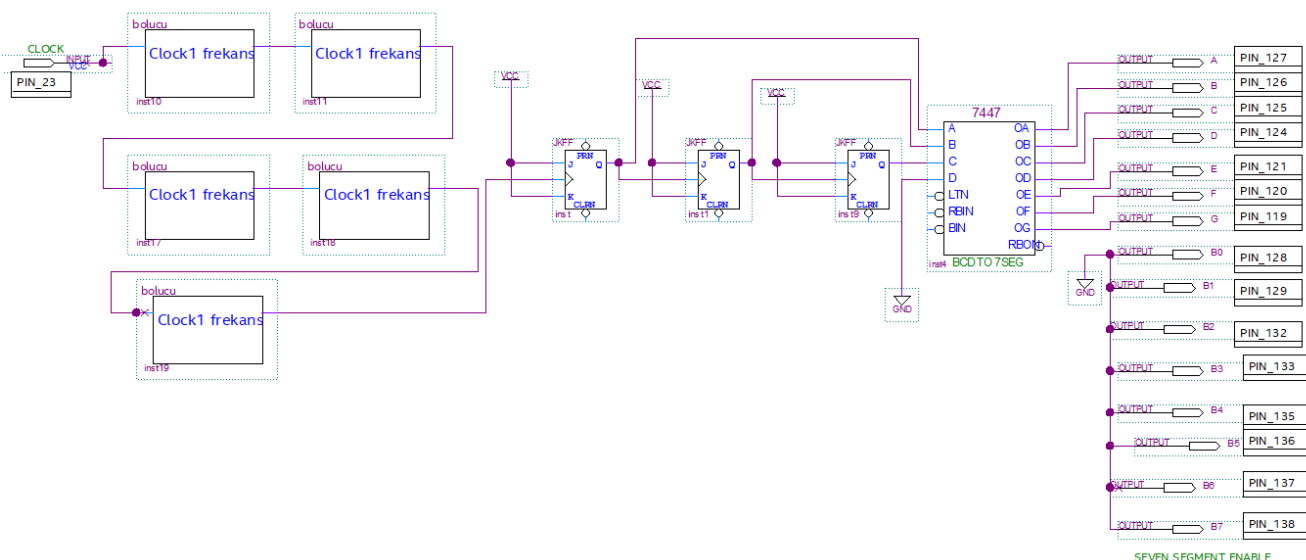


Figure 11. 3-bit down counter bdf file

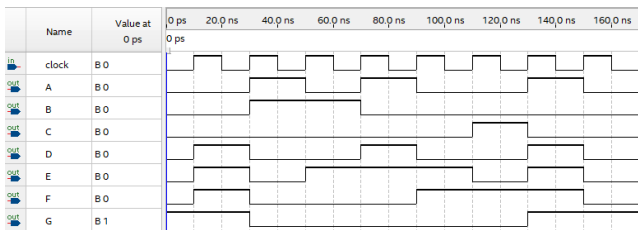


Figure 12. 3-bit down counter wave chart

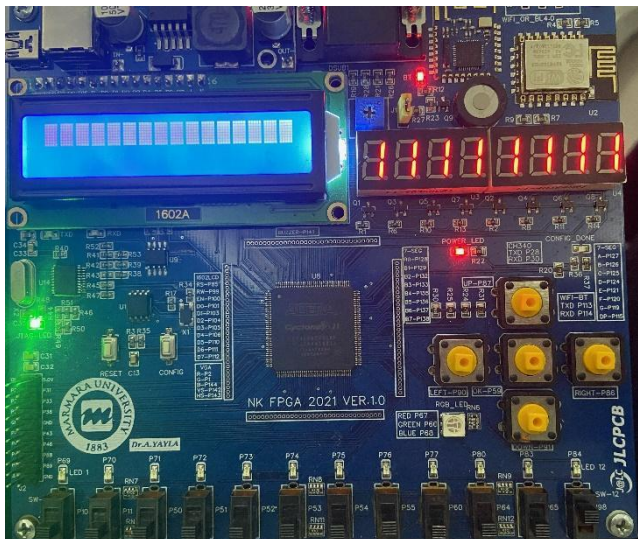


Figure 13. 3-bit down counter 7 Segment Display Result

In this study, an application was developed to display the binary equivalent of the data in the ASCII table on LEDs that we send from devices (tablet or phone) running on the Android operating system. Additionally, in this application, the RGB LED on the development board is set to light up in different colors for a few values. For example, when the value 1 is sent, it turns red, when the value 2 is sent, it turns blue, and when the value 3 is sent, it turns green. When a value outside of these specified values is encountered, the LED displays white, which is a combination of the three primary colors at equal intensities. In Fig. 15, the screenshot of the application is shown for the value G.

```

library ieee;
use ieee.std_logic_1164.ALL;
use ieee.numeric_std.all;
entity UART_RX is
generic (
CLKS_PER_BIT : integer := 434 -- 50.000.000/115200=434 Baudrate için
);
port (
rst : in std_logic;--reset pin 25
i_Clk : in std_logic;--clock giriř 50 MHz pin 23
i_RX_Serial : in std_logic;--uart rx data pin 114
o_RX_DV : out std_logic;--uart data geçerli pin 28 led
o_RX_Byte : out std_logic_vector(7 downto 0);
r_LED_Pin1 : out std_logic;--pin 66 green
r_LED_Pin2 : out std_logic;--pin 67 red
anode : out STD_LOGIC_VECTOR (7 downto 0);
cathodes : out STD_LOGIC_VECTOR (7 downto 0)
);
end UART_RX;
architecture rtl of UART_RX is
type t_SM_Main is (s_Idle, s_RX_Start_Bit, s_RX_Data_Bits,s_RX_Stop_Bit, s_Cleanup);
signal r_SM_Main : t_SM_Main := s_Idle;
signal r_RX_Data_R : std_logic := '0';
signal r_RX_Data : std_logic := '0';
signal r_Clk_Count : integer range 0 to CLKS_PER_BIT-1 := 0;
signal r_Bit_Index : integer range 0 to 7 := 0; -- Toplam 8 bit
signal r_RX_Byte : std_logic_vector(7 downto 0) := (others => '0');
signal r_RX_DV : std_logic := '0';
begin
p_SAMPLE : process (i_Clk)
begin
if rising_edge(i_Clk) then
r_RX_Data_R <= i_RX_Serial;
r_RX_Data <= r_RX_Data_R;
end if;
end process p_SAMPLE;

```

Figure 14. VHDL file for UART application

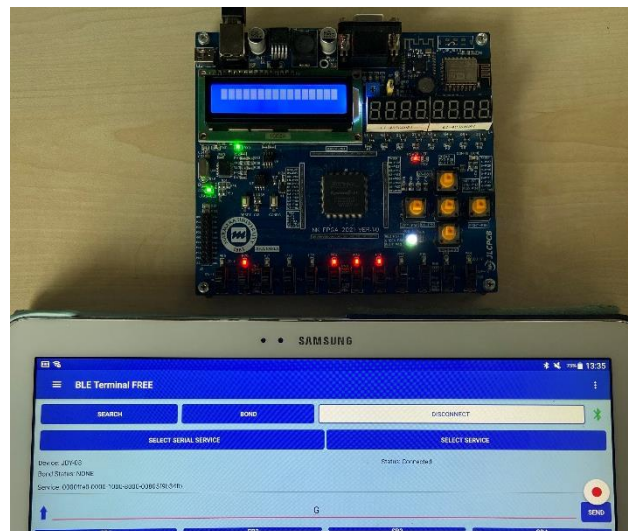


Figure 15. Bluetooth Application Result for the value “G”

5. DISCUSSIONS AND RESULTS

Without the need for additional wireless components, users may quickly and affordably develop and test design solutions for IoT applications with the help of the suggested FPGA evaluation board. Table II contains the table that displays the cost of this board. Additionally, this FPGA development board is approximately 50% below the price of other boards available on the market [21].

The integration of an FPGA development board with internal modules for Bluetooth and Wi-Fi can prove to be especially helpful in fields like defense, aerospace, automotive, medical devices, and smart city infrastructure that demand high-performance hardware solutions and wireless communication. Since internal modules are usually pre-tested and integrated, their usage may be simple. In difficult environments, wireless communication is very beneficial.

TABLE II
COMPONENT PRICES USED IN FPGA DEVELOPMENT BOARD

Component	Quantity	Unit Price (Dollars)	Total Price (Dollars)
Altera Cyclone IV EP4CE6E22C8N	1	16	16
PIC16F45	1	0.8	0.8
LCD	1	0.8	0.8
Bluetooth Module	1	0.6	0.6
ESP 12F Wi-Fi Module	1	0.8	0.8
7 Segment Display	2	0.2	0.4
Switches	12	1	12
Power Module	1	0.5	0.5
VGA Socket	1	0.2	0.2
SPI Flash and EEPROM	1	1	1
Other Materials (Led, resistor, buzzer, transistor, etc.)	1	2	2
PCB	1	2	2
Total			37.1

6. CONCLUSION

In this study, FPGA development board with the necessary hardware components has been designed in order to implement the real-time implementation of fundamental digital applications and designs in the field of engineering. EasyEDA program has been used to design the PCB for the FPGA development board. The development board is equipped with Bluetooth and Wi-Fi modules to offer a wider range of application development areas such as mobile, robotics, smart home systems, and remote monitoring and control devices. FPGA development board has been tested using Intel® Quartus® Prime Lite Edition software for sample digital design and Bluetooth applications that have been coded in VHDL language. Testing of sample digital system design projects was initially carried out in a simulation environment.

After the successful execution of simulation tests, the necessary pin assignments for inputs and outputs have been done, and subsequently, FPGA chip has been programmed via JTAG interface. As a result, it was observed that sample digital system design projects and the Bluetooth project worked successfully on the FPGA development board.

With the FPGA development board presented in this study, a cost-effective FPGA development board that can be used in basic engineering education fundamental applications as an alternative to the FPGA development boards procured from abroad at high expenses has been successfully implemented.

REFERENCES

- [1] S. Azimi and S. Abba Ali, "FPGA programming with VHDL: A laboratory for the students in the Switching Theory and Digital Design course," Bachelor's Thesis in Computer Science and Engineering, 2023.
- [2] İ. Savran, "Donanım Tanımlama Dili VHDL ve FPGA Uygulamaları," İstanbul: PapatyaBilim, 2017.
- [3] S. Denholm, "Improving low latency applications for reconfigurable devices," PhD Thesis, Department of Computing, Imperial College, London, United Kingdom, 2023.
- [4] B. Grady and J. H. Anderson, "Synthesizable heterogeneous FPGA fabrics," in 2018 International Conference on Field-Programmable Technology (FPT), 2018: IEEE, pp. 222-229.
- [5] N. Pillutla and S. Kumar, "FPGA Implementation of Multi-RT Protocol for Avionics Simulation" IEEE International Systems Conference (SysCon) pp. 1-4, 2023.
- [6] S. Ricci, S. Caputo, and L. Mucchi, "FPGA-Based Pulse Compressor for Ultra Low Latency Visible Light Communications," Electronics, vol. 12, no. 2, p. 364, 2023.
- [7] M. A. A. Al-Dulaimi, H. A. Wahhab, and A. A. Amer, "Design and Implementation of Communication Digital FIR Filter for Audio Signals on the FPGA Platform," Journal of Communications, vol. 18, no. 2, 2023
- [8] S. S. Antora, Y. K. Chang, T. Nguyen-Quang, and B. Heung, "Development and Assessment of a Field-Programmable Gate Array (FPGA)-Based Image Processing (FIP) System for Agricultural Field Monitoring Applications," AgriEngineering, vol. 5, no. 2, pp. 886-904, 2023.
- [9] P. Chen, Y. Chen, and T. Shi, "Real-time simulation and research of motor controller based on FPGA," in Third International Conference on Mechanical Design and Simulation (MDS 2023), 2023, vol. 12639: SPIE, pp. 483-489.
- [10] K. Ghosh, K. Hatua, and A. Mitra, "Design and Development of DSP-FPGA based Control Board for Electric Vehicle (EV) Applications," in 2022 Second International Conference on Power, Control and Computing Technologies (ICPC2T), 2022: IEEE, pp. 1-6.
- [11] L. A. Ajao, J. Agajo, B. U. Umar, T. T. Agboade, and M. A. Adegboye, "Modeling and implementation of smart home and self-control window using FPGA and Petri net," in 2020 IEEE PES/IAS PowerAfrica, 2020: IEEE, pp. 1-5.
- [12] M. Kumar, A. Jayalaxmi, and W. Malemnganbi, "Design and Implementation of Secured Car Parking System using FPGA," International Journal of Applied Engineering Research, vol. 17, no. 3, pp. 180-188, 2022.
- [13] M. H. B. Saif, N. U. Sadad, and M. N. I. Mondal, "FPGA Implementation of Educational RISC-V Processor Suitable for Embedded Applications," in 2023 International Conference on Electrical, Computer and Communication Engineering (ECCE), 2023: IEEE, pp. 1-5.
- [14] G. Surekha, G. Madesh, M. P. Kumar, and H. Sriramoju, "Design and Implementation of Arithmetic and Logic Unit (ALU)," in 2023 2nd International Conference on Applied Artificial Intelligence and Computing (ICAAIC), 2023: IEEE, pp. 1530-1536.
- [15] A. K. Panigrahi, S. Patra, M. Agrawal, and S. Satapathy, "Design and Implementation of a high speed 4bit ALU using BASYS3 FPGA Board," in 2019 Innovations in Power and Advanced Computing Technologies (i-PACT), 2019, vol. 1: IEEE, pp. 1-6.
- [16] N. Sağlam and F. Kaçar, "Design and Simulation of 64 Bit FPGA Based Arithmetic Logic Unit," Electronica, vol. 19, no. 2, pp. 158-165, 2019.
- [17] B. Karakaya, F. Çulcu and M. Türk, "Digitally Programmable Multi-Scroll Chaos Generator On FPGA" European Journal of Technique (EJT), vol.10, no.2, pp.207-216,2020.
- [18] A. Keskin and İ. Koyuncu, "Yeni Bir FPGA Geliştirme Kartı Tasarımı ve Uygulaması.," Bilgisayar Bilimleri ve Teknolojileri Dergisi, vol.3, no.2, pp.46-55, 2022.
- [19] J. Zhao, Z. Wang, and J. Chen, "Design of Pocket Development Board Based on FPGA," in IOP Conference Series: Materials Science and Engineering, 2018, vol. 382, no. 4: IOP Publishing, p. 042030.
- [20] L. Gao, "Development of FPGA experiment and development board," in World Automation Congress 2012, 2012: IEEE, pp. 1-4.
- [21] <https://www.fpgadeveloper.com/list-of-fpga-dev-boards-with-wifi-bluetooth/> (accessed 30.11.2023).

BIOGRAPHIES

Nebi Karagedik graduated from Marmara University, Department of Electronic Communications Technology in 2022. He has been working as a general manager for 5 years in his own electronic R&D company headquartered in Istanbul. Smart Home Systems (KNX Bus) has been developed and offered as a product. It has developed a domestic PLC module and offered it as a product. With some of his studies in the field of reverse engineering, he developed low-cost educational FPGA boards. His current research interests include RF communication, Industrial Control Devices, FPGA and MCU based Embedded Systems.

Sezen Bal received her B.Sc. degree in Electronic and Computer Department from Technical Education Faculty in Marmara University, Turkey, in 2004. She received M.Sc. and Ph.D. degree in Electronics and Computer Education from Marmara University Institute for Graduate Studies in Pure and Applied Sciences, in 2007 and 2014, respectively. She is currently working at the Department of Computer Technologies at Marmara University, Turkey. Her research interests include Remote Laboratories, Electronic Circuit Design with Embedded Systems, Computer Programming Languages.

Ayşe Yayla received her B.Sc. degree in Electronic and Computer Department from Technical Education Faculty in Marmara University, Turkey. She received M.Sc. and Ph.D. degree in Electronics and Computer Education from Marmara University Institute for Graduate Studies in Pure and Applied Sciences, in 2007 and 2018, respectively. She is an Assistant Professor in the Department of Electronics and Automation in Marmara University, Istanbul, Turkey since 2018. Her research interests include Speech Recognition, Communication Systems, Remote and Mobile Laboratories, LabVIEW, and Digital Circuit Design. She has participated 3 national projects and authored or co-authored papers in major conferences and journals.



Research Article

Data Management and Ontology Development for Provenance-Aware Organizations in Linked Data Space

Fatih Soygazi^{1*}, Tuğkan Tuğlular², Oğuz Dikenelli³

^{1*}Aydın Adnan Menderes University, Computer Engineering Department, Aydın, Turkey. (e-mail: fatih.soygazi@adu.edu.tr).

²Izmir Institute of Technology, Computer Engineering Department, Izmir, Turkey. (e-mail: tugkantuglular@iyte.edu.tr).

³Ege University, Computer Engineering Department, Izmir, Turkey. (e-mail: oguz.dikenelli@ege.edu.tr).

ARTICLE INFO

Received: Dec., 08. 2023

Revised: Dec., 26. 2023

Accepted: Dec., 26. 2023

Keywords:

Linked data space

Organization

Ontology

VoID

Metadata

Corresponding author: *Fatih Soygazi*

ISSN: 2536-5010 / e-ISSN: 2536-5134

DOI: <https://doi.org/10.36222/ejt.1402149>

ABSTRACT

The importance of tracing the source of shared datasets has become evident. It is also crucial to monitor factors such as trust in the data, especially considering the widespread use of social media. The concept of Linked Data Space needs to be addressed in conjunction with organizations. From this point of view, provenance tracking in organizations, with respect to their origin, needs attention. This study elaborates on the concept of Linked Data Space, introducing the terms Interior Data and Exterior Data to the literature. Additionally, an architecture for Linked Data Space and data management for organizations is defined. Furthermore, the study explains how organizations can access Exterior Data in the Linked Data Space and how provenance metadata and ontologies will be created. These developed methods are illustrated in the News Aggregator Scenario, a main scenario for provenance, demonstrating how it can work in a use case.

1. INTRODUCTION

The Web consisted of HTML pages and the links between these pages until recently. However, the problem here is that the content of the Web pages can be understood only by people and not interpreted by machines. Semantic data models, such as Resource Description Framework (RDF), Resource Description Framework Schema (RDF Schema), and Web Ontology Language (OWL), which enable the machine interpretation of web content, have ensured that information can be processed not only by humans but also by machines. Linked Data (LD) [1, 2] is a set of best practices for publishing and connecting structured data on the Web using the expressed semantic data models. Linked Open Data (LOD) extends the principles of LD by emphasizing the use of open standards and licenses, ensuring that data is openly accessible and usable by anyone without restrictions. The Web of Data (WoD) is an evolution from the traditional Web of documents, embodying LD principles. While LOD is a specific approach to publishing and interlinking data on the Web, focusing on openness and reusability, the WoD is a broader vision of a globally interconnected data space enabled by semantic technologies and standards. The Data Space (DS) is a powerful conceptual

model residing on heterogeneous data sources, providing a virtualization layer [3]. Linked Data combines data sources within Linked Dataspaces (LDSs) [4, 5], where applications are executed using the semantic data models and LD standards.

The concept of the DS has already been defined in the field of databases to manage the distributed data utilized by an organization, and the core services in a DS have been determined [5-7]. Some of these services include querying, tracing the data sources, and managing changes to data/metadata [6]. While the concept of the DS has been explained in the literature for LD, the services and integration of these services with data have not been examined in detail.

When the DS is considered in terms of data management at the organizational scale, it is necessary to clarify the relationship between the organization and the services and data it will use. One of the most serious challenges faced by organizations today is the need for an excessive number of interrelated data sources. Relevant services should be available in the DS for organizations to effectively use the data sources they need within a specific domain. The DS should offer solutions that keep users within the organization independent when providing these services, addressing how the data is integrated.

This manuscript proposes a data architecture in terms of organizations. We propose that the data used by organizations is expressed in two different ways: Exterior Data (ED) and Interior Data (ID). ID defines the organization's own data, organizational preferences, and metadata of accessible datasets on the Web needed by the organization. Organizational preference expresses the demand for the dataset to be obtained when accessing ED. For example, an organization may prefer to receive datasets only published in Turkey related to news. ED represents data located in the WoD. It covers whole accessible raw or semantic data on the Web and the metadata of those data.

Provenance is a concept guiding the processes of establishing trustworthiness and ensuring data quality [8]. In this paper, we focus on provenance from LD perspective [9]. Applications that publish and consume LD represent definitions of trust through the use of provenance metadata. Our proposal also concentrates on provenance for ED and ID

2. PROVENANCE

A vast amount of data on the Web is created through copying, modifying, or combining. The same data or dataset can be copied or presented at different locations. Datasets can be linked together using RDF links created with different tools. Thus, conflicting copies of the same sets of entities can be linked to each other. It is necessary to consider the quality of the data thus produced. This is important because this type of data can rapidly spread on the web and lead to the WoD being comprised of low-quality data.

When attempting to find an entity, data from various sources linked to many URIs can be returned. At this point, the question that needs to be answered is which links to follow to reach the desired data. The data source to be used should be a source that provides more reliable or up-to-date data. When accessing a data source, it is not sufficient to have only data about the entity. Furthermore, metadata expressed with a

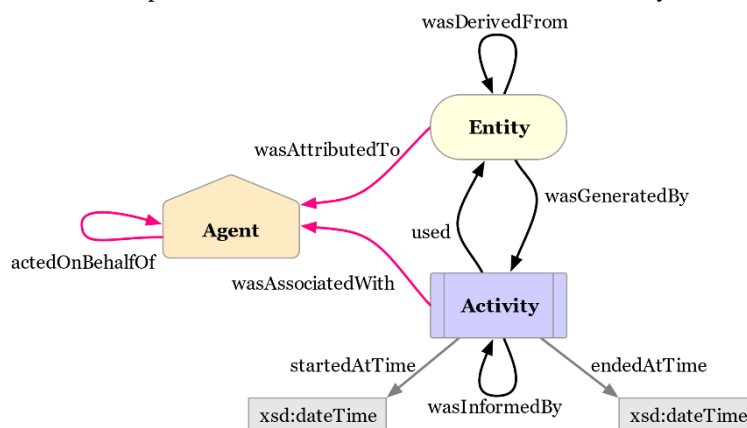


Figure 1. The PROV-O [11] Ontology

to conduct a quality assessment of the data architecture for an organization operating within an LDS. We express provenance metadata to extend dataset metadata which belongs to ED. Additionally, provenance definitions related to raw dataset, semantic dataset and dataset metadata are clarified. Furthermore, we built an ontology that considers organizational and provenance concepts to construct ID. The ontology covers terms for querying provenance independent of the domain.

Organizations may have diverse preferences, one of which pertains to provenance. Consequently, another ontology has been developed to represent the provenance preferences of the organizations. Despite the existence of various provenance dimensions and the associated provenance preferences, this ontology addresses sample preference dimensions under different conditions. As a result, the method for establishing organizational preferences is exemplified.

The contributions of this manuscript are:

- the description of the architecture for organizations gathering data from an LDS.
- proposing Interior Data (ID) and Exterior Data (ED) concepts to the LD literature by explaining these concepts in the context of LDS.
- the development of provenance ontologies with respect to ED and ID perspectives.
- the development of a provenance preference ontology.

dictionary for the discovery of the data source can not also answer questions about how or when the data source was produced. Therefore, data or metadata about data discovery is not sufficient, and additional metadata for provenance tracking is also needed. In this respect, it should be considered how the data and provenance-related metadata should be used in the WoD.

There is a need for a provenance data model that expresses how actions such as the creation of provenance data, its publication on the Web, and the access to published data. An ontology is a semantic data model that provides shared representation of knowledge. Ontologies have been developed for the modeling of provenance [10-13]. RDF-based provenance descriptions can be published on the Web and consumed by relevant actors in organizations.

2.1. Provenance ontologies

It is necessary to first clarify the core concepts of the provenance when defining a provenance model. Although core concepts are expressed similarly in all ontologies, the most popular and commonly used work is the W3C PROV Ontology (PROV-O) [12, 13]. PROV-O is composed of domain-independent and general-purpose concepts. Its most important reason for being created as a general-purpose ontology is to produce a dictionary that can cover different needs and to encourage studies addressing provenance [14-18]. It represents tracking changes that occur during the creation or updating of sources on the Web. The basic concepts are defined as Entity, Agent, and Activity in PROV-O, as shown in Figure 1. An

entity can be derived from another entity, produced by an activity, or attributed to an agent. For example, let's consider a journalist working at a news agency. When creating a news article, the news entity is attributed to the journalist as the agent. Since the news agency is also expressed as an agent, it can be indicated that the journalist works at the news agency. The news creation activity is associated with the journalist, and this activity is linked to the created news.

prov:wasAttributedTo property used for attribution in PROV-O, which has been expanded to include giving existence to the work expressed by the digital resource (*pav:authoredBy*), contribute to the work by the given agent (*pav:contributedBy*), specify an agent specialist responsible for shaping the expression in an appropriate format (*pav:curatedBy*), create the digital artifact or resource representation (*pav:createdBy*), indicate the software/tool used by the creator when making the

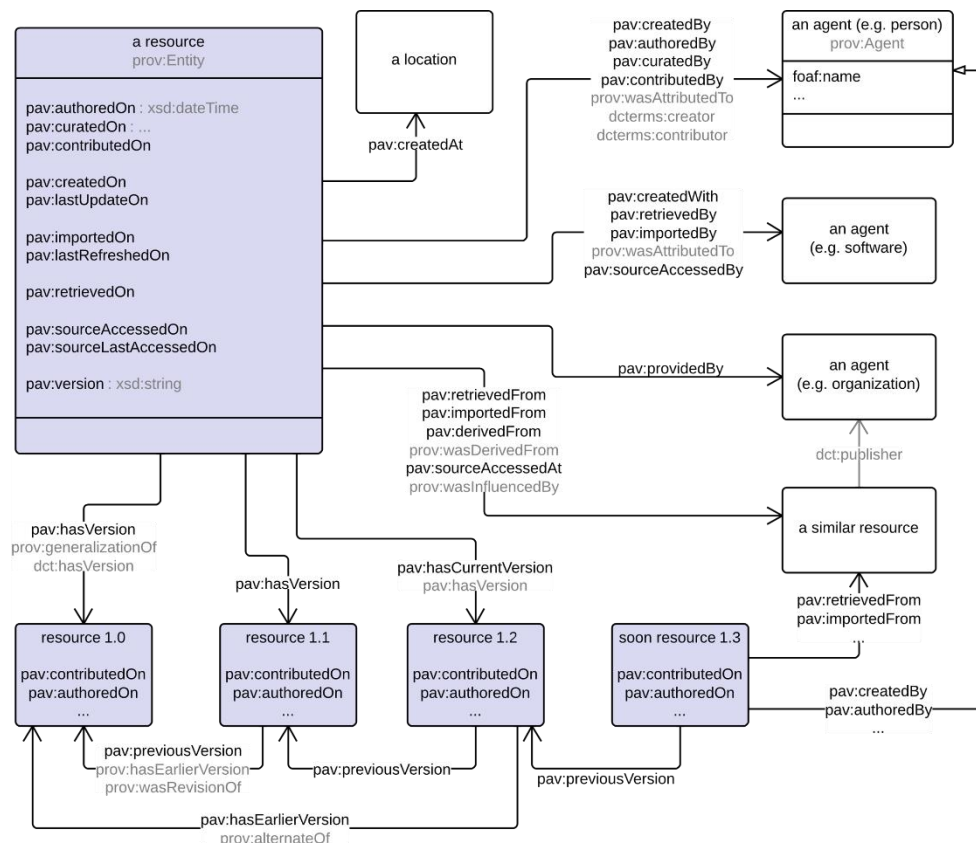


Figure 2. The PAV [19] Ontology

Provenance, Authoring and Versioning (PAV) ontology [19, 20] extends PROV-O to focus on the authoring, editing, and digital creation of data (Figure 2). The PAV ontology has introduced terms to distinguish between the different roles of agents providing content to existing Web-based systems. These roles concern the stages involved in the creation of a document in textual form and its publication on the Web, such as resource authoring, contribution, creation or curation. Hence, the provenance of digital resources can be traced during creation, retrieval or derivation processes. The PAV ontology customizes the general-purpose model of the PROV-O ontology to provide a more comprehensive and interoperable approach. There is an important distinction between authoring and creation of a resource that is described by PAV ontology. Provenance defines the creation of digital data, while Authoring describes the actual creation of data and its related features. For example, although the novel "Ince Memed" was written in 1955 (Authoring), it was first published as an e-book in 2010 (Provenance). Versioning shows the evolution of digital assets over time.

The creation of data, data derivation, data acquisition from another source, versioning, and similar concepts related to origin are found in PROV-O and PAV ontology, so the developers of the PAV ontology have expanded similar terms found in the PROV-O ontology. Especially the

digital resource (*pav:createdWith*), describe an entity responsible for importing the data (*pav:importedBy*), and define entity to retrieve the data from a specific source without transformation (*prov:retrievedBy*).

A standard vocabulary is required to define the metadata of the datasets [21] and an extension of this vocabulary with provenance is also necessary. VoID (Vocabulary of Interlinked Datasets), a dictionary enabling the discovery and utilization of linked datasets, defines the metadata of datasets found on the WoD [22, 23]. In addition to a general provenance model created to define the provenance, customized approaches should also be expressed at the dataset level in the context of VoID. The extension of provenance to VoID, VoIDp [24], can be described as an enhanced version of the VoID vocabulary with provenance information. The aim of VoIDp is to assist dataset publishers in providing metadata related to the origin of their datasets so that data-consuming tools (or organizations) can access more reliable and higher-quality data. VoIDp provides a metadata extension within VoID that allows for the storage of information specifically about the origin of the source and modified resulting datasets. However, considering only the source and modified resulting datasets for their origin is not sufficient when filtering among the many datasets available. In this paper, one of our objectives is to define a broader vocabulary that extends VoID, covering more general

and usable situations by considering the provenance metadata of each dataset.

It has been observed that it can be used together with some extensions considering VoID, PROV-O and PAV ontologies to trace provenance in an LDS. In this paper, the ontological adaptation with provenance seems that it is related to Provenance and Versioning expressed in the PAV Ontology. Therefore, the creation of the VoID document and the processes through which the associated dataset was published are developed using the higher-level metadata from PROV-O and PAV ontology. The details of these ontologies are given in Section 4.

3. THE INTEGRATED ARCHITECTURE OF ORGANIZATIONS AND LINKED DATA SPACES FROM PROVENANCE PERSPECTIVE

The proposed conceptual architecture, which considers both an organization and LDS, is illustrated in Figure 3. An LDS encompasses LD services, with organizational LD applications consuming data provided by these services. Organizational LD applications may concurrently use one or more LD services based on their objectives.

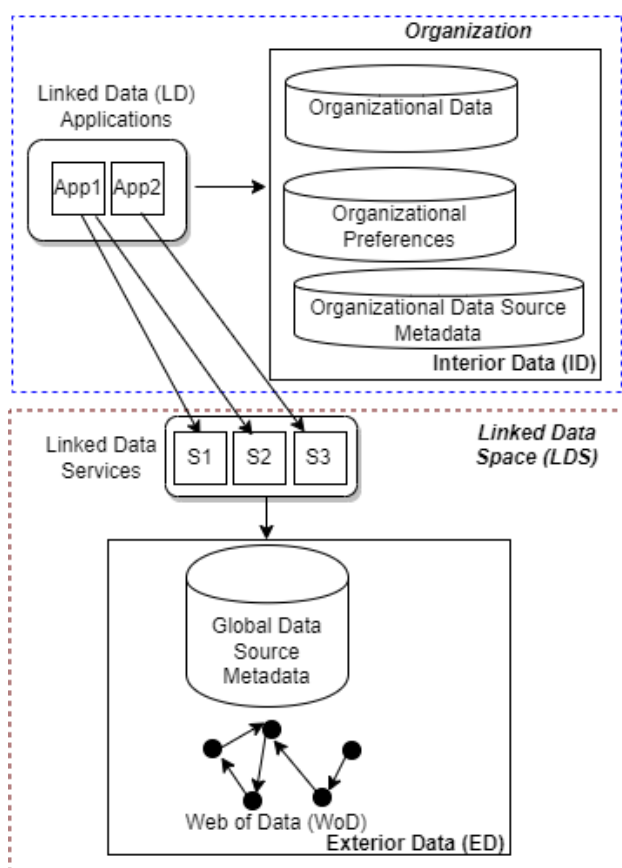


Figure 3. The architecture for integrating an organization and LDS

In order for ED to be discovered by LDS services, it is necessary to define the metadata of the data sources. Organizational Data Source Metadata stores these metadata of the datasets to be accessed by the organization. The data about datasets (metadata) in WoD should be defined by a vocabulary. VoID is used to create examples in Global Data Source Metadata and it is also commonly used by data federation systems [25] to define upper-level standards. Federated query

engines [26-28] discover relevant datasets in WoD by querying with the help of VoID. An LDS is responsible for providing the organization with a service related to the selection of these datasets (One of the Linked Data Services from S_1, \dots, S_n in Figure 3).

When the data consumer (organization in our case) attempts to obtain data on the Web, the requested data may be available from multiple sources. For example, when searching for a photograph of a person for a news article to be published in a newspaper, the most up-to-date accessible photograph is obtained and intended to be published. The data consumer (or organization) similarly demands that the news content and the media related to the news (such as photographs) be current and reliable. The application in the Organizational Domain, which is expected to take into account similar situations, organizational data, organizational preferences, and local VoID metadata, is considered within the ID scope. The metadata of datasets relevant to the organization should be stored locally within the organization, referred to as local VoID metadata. Organizational Data Source Metadata should be able to keep up-to-date by tracking changes in Global Data Source Metadata [29, 30]. This allows the organization to access the data it needs in a way that meets its expectations in a current form. ED encompasses all linked data sources that can be queried via global VoID metadata in Global Data Source Metadata and the data accessed by these global VoID metadata in the WoD.

Provenance is a research direction that can be expanded by adding metadata to ED [31]. In the literature, there are similar extension studies using VoID [32, 33], but these studies are not sufficient to express the provenance in detail. Our manuscript emphasizes semantically expressing organizational preferences in ID with the added provenance metadata in ED. Therefore, a provenance-aware approach has been suggested.

According to Heath and Bizer [5], the data consumption method in LDS involves various LD services, such as access to WoD, data quality assessment and more. Our paper specifically focuses on provenance, and the detailed representation of Figure 3 is provided in Figure 4, considering provenance from an organizational perspective.

In Figure 4, Query Service gathers instances from WoD. The Provenance-Aware Filtering Service filters datasets based on provenance using the Organizational Data, Organizational Preferences, Enriched Organizational Data Source Metadata and stores them as Filtered Organizational Data Source Metadata. The Query Service uses Filtered Organizational Data Source Metadata to query the data in the WoD with respect to organizational expectations. The Monitoring Service is responsible for tracking changes in the Provenance-Enriched Global Datasource Metadata. The objective of the Monitoring Service is to report the modified VoID documents to the Enriched Organizational Data Source Metadata to keep it up-to-date. The actors in the organization are the Organizational User and the Organizational Infrastructure Administrator. The Organizational User accesses WoD via the Query Service and consumes the required data within the organization. The Organizational Infrastructure Administrator executes administrative services with the aim of providing the data to be used in LD applications as organization-specific data. The Administrative Application uses the Administrative Service(s) within each organization, and these services generate

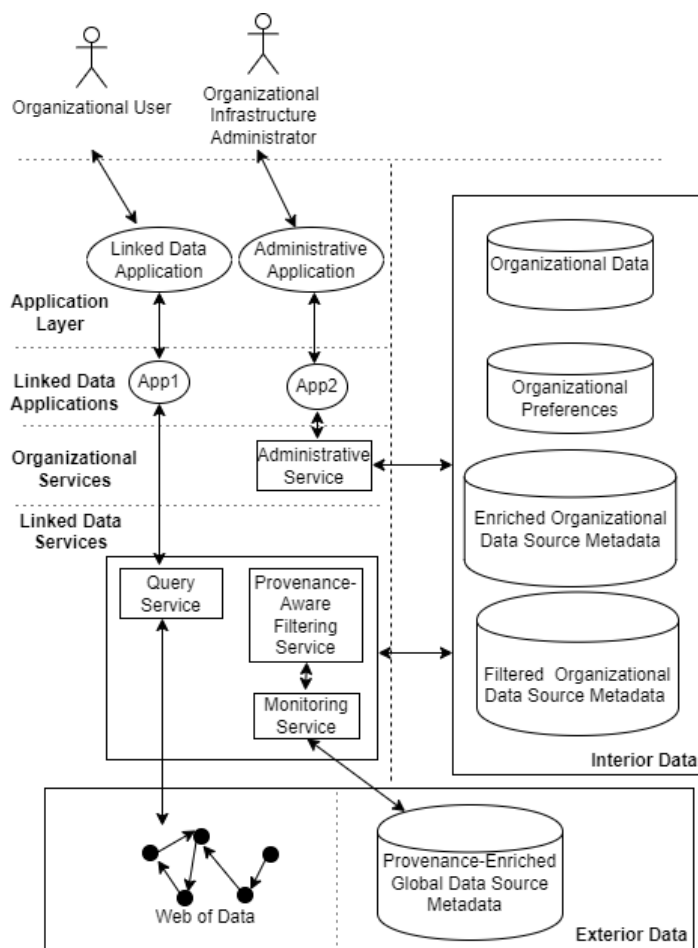


Figure 4. The architecture for integrating an organization and LDS considering provenance

Organizational Data and Organizational Preferences or provide datasets that could be published about that organization.

4. PROPOSED ONTOLOGIES FOR PROVENANCE-AWARE ORGANIZATIONS IN LINKED DATA SPACE

The data on the Web represents all data on the Web independently of semantics. Web of Data (WoD) [34] is a term that emerged to combine data sources containing a large amount of data. WoD aims to create a usable structure by leveraging non-semantic web data and semantic web technologies together.

Raw data is the data expressed in a representation format other than RDF that humans can understand (for example, Wikipedia). Semantic data is data that can also be understood by machines and is represented with RDF (for example, DBpedia). The data on the Web encompasses raw data and semantic data, but there are not many semantic connections between these different types of data. The WoD has emerged as a result of establishing links between these data and making these links explicit and discoverable. For example, documents on the Web are mostly presented with HTML pages. It is observed that raw data is represented on Wikipedia web page in Figure 5. In HTML documents, there are links within the document, and when these links are clicked, access to other documents on the internet is achieved through the HTTP protocol. When considering data on the Web, one should think at the data level, which is a more granular structure than the document level. Therefore, rather than reading an entire

document, semantic meaning should be taken into account to elements within sentences, establishing links with relevant entities. In Figure 5, there is a semantic representation of data in triple format for the DBpedia and DBLP datasets. By using the concept of Paul Erdős mentioned in the example, links can be established with relevant entities published in hundreds of datasets across different datasets. When linking all of these relevant elements, it introduces another challenge in discovering the required entity in WoD. VoID [22, 23] documents are being created to establish the metadata of datasets for the purpose of improving data discovery. The relationship between the DBpedia dataset and the DBLP dataset, which contains publication information for academics, is established at the dataset level using a VoID document in Figure 5.

It has been observed that in addition to publishing raw data as semantic data and creating VoID descriptions for semantic data, it is also necessary to express the provenance. At this point, one should consider what kind of metadata needs to be provided for each of the three data levels (raw level, semantic level, metadata level).

Dublin Core Metadata refers to a set of standardized metadata elements used to describe digital resources such as documents, images, web pages, and other types of media. The Dublin Core Metadata Initiative (DCMI) [35] developed and maintains these standards to facilitate the discovery, sharing, and management of information resources on the internet. Dublin Core (*dc*) is widely used in various digital libraries, archives, and content management systems. In Figure 5, *dc* is used to illustrate the relationship between entities in DBLP

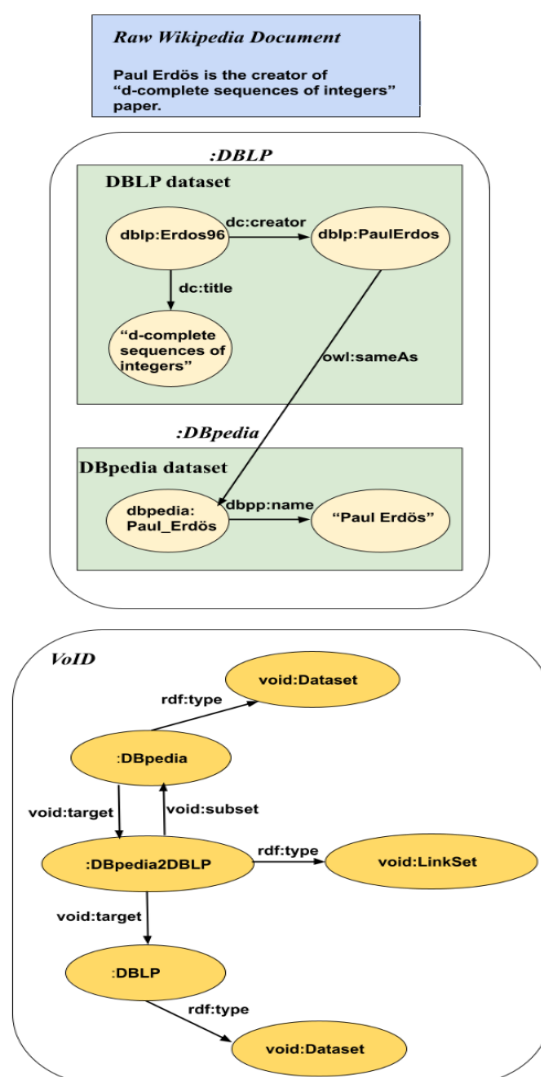


Figure 5. A sample representation of raw data, semantic data and VoID metadata

dataset where the knowledge of researchers are stored semantically. However, there is potential ambiguity when representing the author of the paper, as it is defined as the creator term in *dc*, while in Section 2.1, we defined it as "Authoring" in the PAV ontology. This discrepancy reflects different perspectives among ontology developers. In this paper, we aim to reconcile these viewpoints by considering the data elements and the dataset that includes these data elements.

4.1. Proposed ontologies considering Linked Data Space

Data from different datasets is merged to generate knowledge in the LDS. During this merging process, the links between datasets are taken into account (Figure 5). When dealing with these links, it is necessary to select the dataset that can provide higher quality data from datasets capable of offering similar data. Systems suitable for making such selections should present the user/organization with the most suitable integrated data using data about the provenance, such as where the data came from, when it was obtained, or how the links were created. On the other hand, it is necessary to provide upper-level data (metadata) regarding data creation and versioning, along with establishing links using this data during the dataset description.

The dataset metadata provided by VoID (that is supplied as metadata of datasets in ED) is not sufficient to meet all the requirements, needed on the Web [36]. Dataset publishers should think from a broad perspective to adapt the metadata of datasets along with the data to meet new requirements. Therefore, quality requirements such as provenance should be expressible with the metadata enriched by dataset publishers by using vocabularies such as VoIDp [24], as explained in Section 2.1. However, VoIDp is not sufficient for the requirements in [36] and another proposal is required, which we focus on in this paper.

There is a need for a comprehensive vocabulary that can fit into the working domain of organizations to consider organizational data alongside metadata of datasets in ED. While creating this vocabulary, it is considered that it should be aligned with the fundamental concepts of organizational preferences and organizational data in ID. The same considerations about ID should also be applicable to Enriched Organizational Data Source Metadata. Therefore, it is considered necessary to use ontologies containing established concepts related to provenance and expand them according to the requirements from ED and ID perspectives.

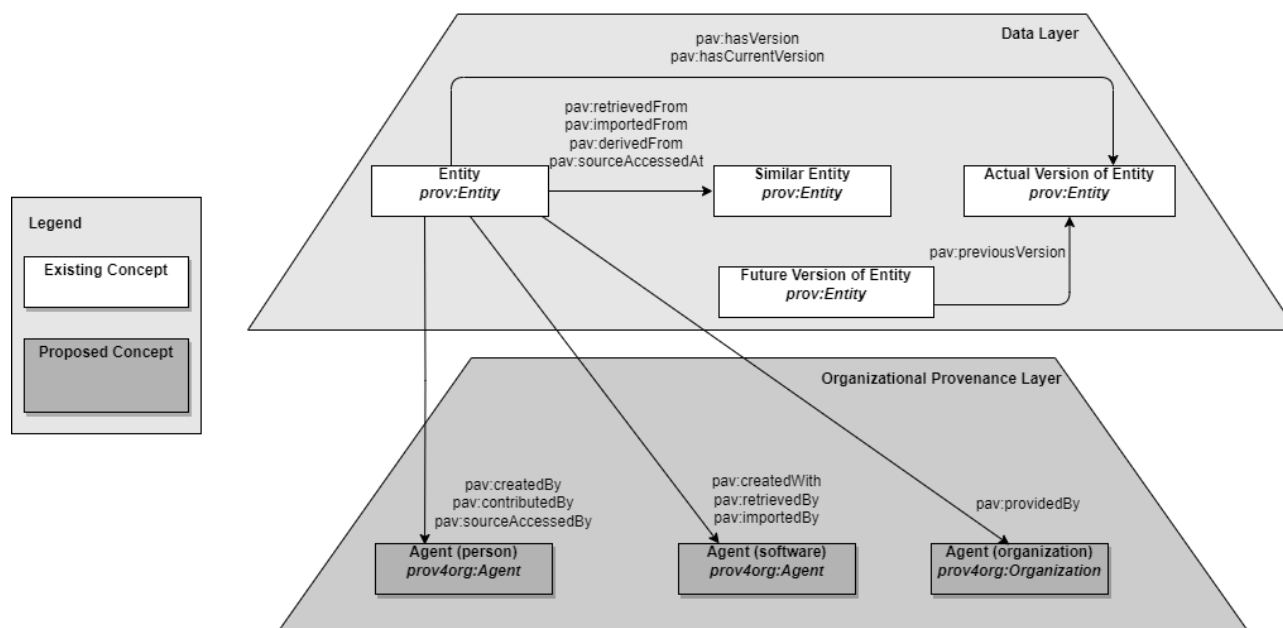


Figure 6. VoID enhancement by using PROV-O and PAV

4.2. Perspective of Exterior Data

Our proposal anticipates that VoID should be extended to define metadata for datasets and provenance expressions for organizational data. With this regard, these enhanced requirements should be considered in a layered manner as the Data Layer and the Organizational Provenance Layer, as shown in Figure 6. The Data Layer consists of the concepts and relationships required to express the provenance of the datasets. The Organizational Provenance Layer expresses the agents (person, software or organization) that are involved in the creation or update of the Entities. While the Organizational Provenance Layer is developed as a contribution, its namespace is given as *prov4org*.

As seen in the Data Layer of Figure 6, all these operations are defined by *prov:Entity*, however the operations on the entities differ. Accordingly, the concept referred to as an entity can be a VoID document, a raw dataset, or a semantically published dataset. During the creation of the provenance information, attention should be paid to three points with respect to these entities. First, attention should be paid to the provenance information of the created VoID metadata, second, if available, the provenance data before the dataset becomes semantic, and third, the expression of the provenance data for the semantically published dataset. The provenance data of the VoID metadata includes who (*pav:createdBy*) or which tool (*pav:createdWith*) created the document, made contribution during creation (*pav:contributedBy*), when it was created (*pav:createdOn*), and when it was last updated (*pav:lastUpdateOn*).

Secondly, the provenance data before the dataset becomes semantic includes the data about the dataset creation process and the agents in this process. The raw dataset mentioned can be obtained from any data source and used without modification. In order to express this situation, the software agent retrieving the data (*pav:retrievedBy*) and the source from which it is retrieved (*pav:retrievedFrom*) are important for knowing who originally created the data. In addition to obtaining and using the raw dataset without making any changes, it may also be possible to have a processed dataset that provides insights and comments about the data. Let's assume that after obtaining data from the E-Government

website and processing it, it becomes the data presented by the Turkish Statistical Institute. In this case, the primary source of the data is the E-Government website. To enable provenance tracking, the software accessing this data (*pav:sourceAccessedBy*) and the actual location of this data (*pav:sourceAccessedAt*) should be expressed within VoID. The raw dataset may be modified despite being obtained in the same data format. In this case, metadata regarding from which dataset the dataset is derived (*pav:derivedFrom*) needs to be expressed. The data about the organization providing the source (*pav:providedBy*) should also be expressed as metadata. Defining data about the versions of datasets that are derived with these changes (*pav:hasVersion*, *pav:hasCurrentVersion*, *pav:previousVersion*) helps in understanding whether there are major or minor changes during data modification.

For the third and last consideration, it is necessary to keep data about the transformation of the content of the raw dataset into a semantic format. Specifying the software (*pav:importedBy*) that performs the transformation from the source dataset (*pav:importedFrom*) to the semantic dataset is necessary for provenance tracking. It is also important to specify the creator (*pav:createdBy*) of newly generated semantic datasets, the person who contributed to the creation of the dataset (*pav:contributedBy*), and the software tool (*pav:createdWith*) used in creating the dataset. Just like in the raw dataset, for the semantic dataset, it is important to express the data about the organization providing the primary source (*pav:providedBy*).

4.3. Perspective of Interior Data

The ontology that defines the concepts required for each organization is shown in Figure 7. The details and relationships of our definitions, *prov4org:Agent* and *prov4org:Organization*, using *prov:Agent* in Figure 6 are illustrated in Figure 7. This ontology has been developed by reusing organization ontology (ORG) [37], PROV-O [12, 13], and SWP (Semantic Web Publishing Vocabulary) [38] for provenance adaptation to the organization.

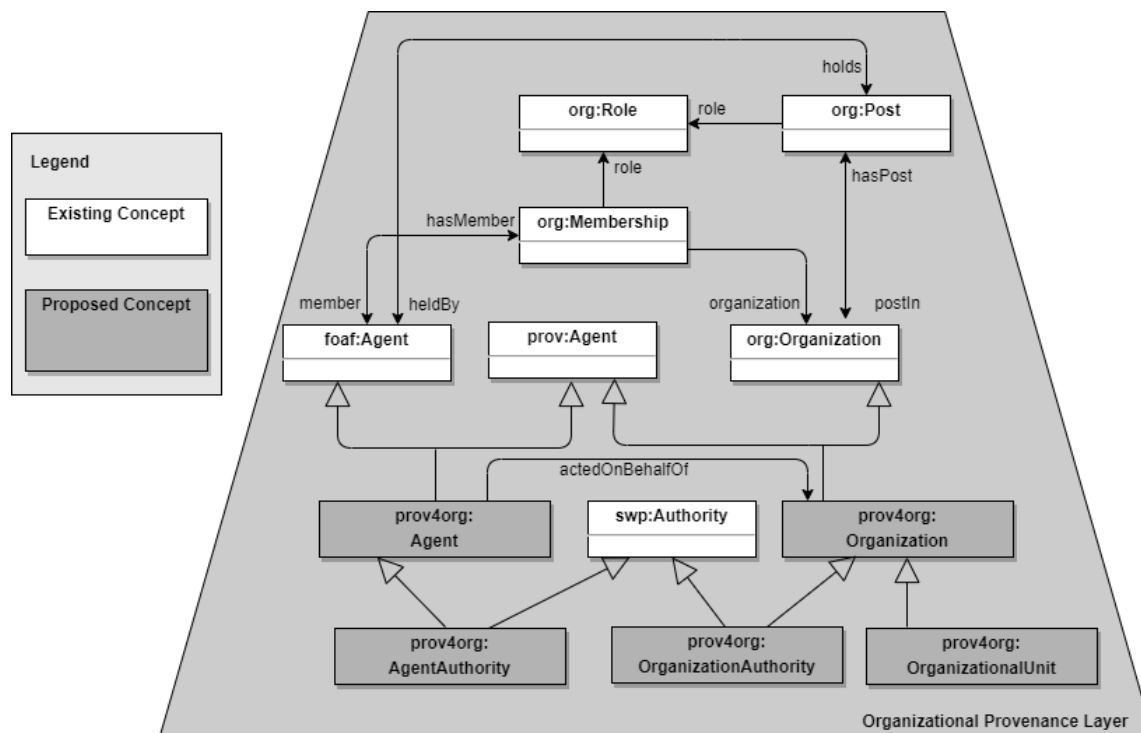


Figure 7. Organizational Provenance Ontology

prov4org:Agent can refer to a person within the organization as well as to a software. When considered as a person (Organizational User in Figure 4), it is necessary to take into account that the agent is a member of the organization (*org:Membership*). The concept of membership represents the hierarchical position within a company. Membership is expressed through a relational structure that includes the individual's role (*org:Role*), the organization he/she belongs to (*org:Organization*), and his/her personal information (*foaf:Agent*). Therefore, every employee in the organization has a membership. It has been observed that the concept of membership needs to be considered for tracking the duration of membership and changes in roles (such as employees being promoted over time). The position information (*org:Post*) represents situations in the organizational hierarchy where it is expressed, but it is not necessary for there to be a person assigned to the position. In this sense, a position can exist without being filled by a person. However, membership represents a relationship that connects the organization and the agent and does not exist without them. When creating an organizational profile, usually either a position or membership is preferred for defining it. If an independent structure of individuals working in the organization is desired, positions are defined. If the goal is to keep records of the individuals who constitute the organization and to make queries about their provenance according to their abilities, then the concept of membership needs to be created. Organizational Unit (*prov4org:OrganizationalUnit*) represents smaller units within a large organization, such as departments. Therefore, it is seen that the concept of organizational unit needs to be expressed for the provenance of rules to be created at the organizational unit level for the execution of certain operations organizationally. There are two concepts defined for the expression of trust within the organization, namely, agent authority (*prov4org:AgentAuthority*) and organization authority (*prov4org:OrganizationAuthority*).

Another important point with respect to Interior Data (ID) is taking into account the preferences of the organization itself or other agents within the organization. Therefore, a domain independent ontology is required to express these preferences. Thus, by considering organizational preferences, the most suitable dataset from the datasets in the Exterior Data (ED) can be selected to meet the needs of the organization. When considering preferences, two scenarios are observed: the preferences of the organization (ID) for the Linked Data Space (ED) or the preferences of the Linked Data Space (ED) for the organization (ID). As illustrated in Figure 8, preferences should be adaptable to organizational ontological definitions independently of the domain. The development of a general preference ontology also enables the transfer of individuals' or organizational units' preferences (such as the continuation of an employee's preferences when moving from one organizational unit to another or the use of an organizational unit's preferences in different units).

As illustrated in Figure 8 adapted from Figure 7, *prov4org:Agent* and *prov4org:Organization* demonstrate that preferences can be expressed at the agent or organizational level. Preferences actually represent the constraints of the elements in ID. Therefore, *provpref:Restriction* is used to indicate the constraints on the preference of an agent or organization within an organization, or on another agent, organization, or entity. The filtering condition within the constraint (*provpref:FilterCondition*) indicates the expectation regarding the element on which the preference is made. The filtering condition is associated with different preferences via the blank node. Blank nodes nodes in a graph data structure that does not have an explicit identifier or a value. They are used when a web resource wants to define multiple pieces of data. For example, when expressing a professor, if we assume that the professor worked in different places at different times, this structure can be used to express the institution and department where he/she worked. In our work, we have resorted to the use

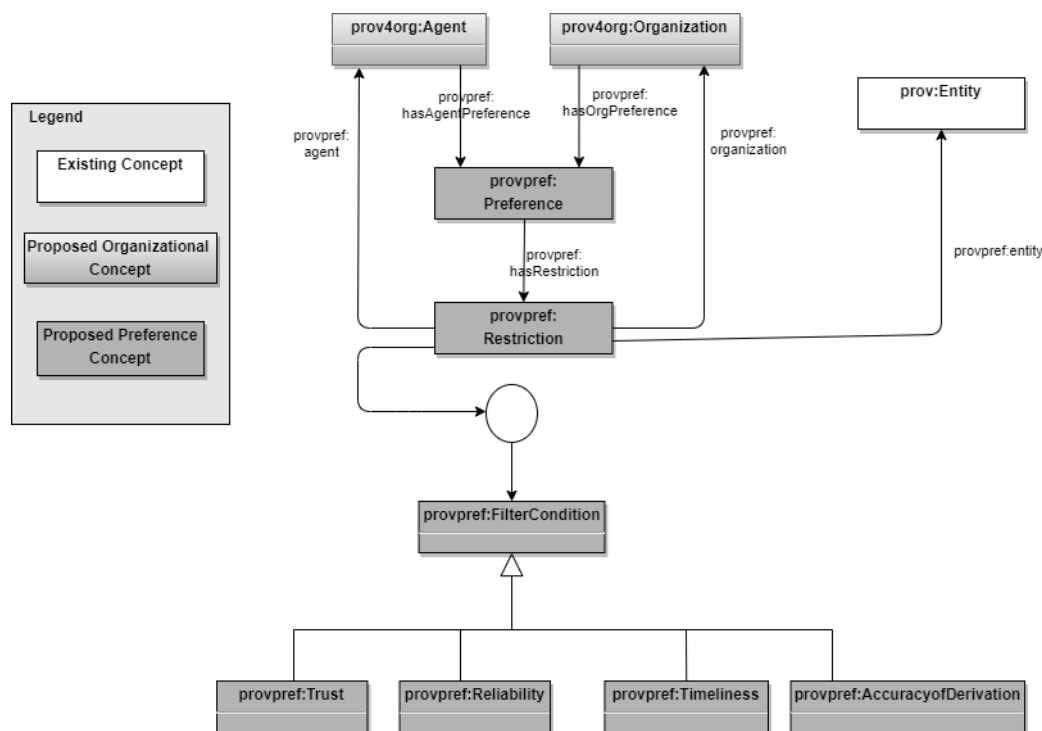


Figure 8. Organizational Preference Ontology

of blank nodes because Agents or Organizations can create preferences with different expectations in various situations. When considering the filter condition in the ontology, the preference types have been inspired by [39], where the terms *prov:pref:Trust*, *prov:pref:Reliability*, *prov:pref:Timeliness*, and *prov:pref:AccuracyofDerivation* are described. Trust represents the preference of whether the actor involved in generating the data is reliable or not during provenance tracking. Reliability is taken into account at the point of preference for activities during the derivation of the data (such as the creation of raw data, the transformation of raw data into semantic data). The data that is reliable may have been published in an unreliable manner through a different transformation by an activity. In this case, defining the reliability of the activity as a preference by the organization becomes important. Timeliness is related to tracking the times of creation and update of the data and creating preferences for the organization accordingly. Accuracy of Derivation focuses on tracking the changes made to the data since its creation. In data evaluation, the data is preferable if it has been generated with the least number of derivations.

The critical point in this study is to enable provenance tracking for the dataset at the metadata level. Thus, it is possible to create examples of how Agents, Activities, and Entities that affect the metadata of the dataset have made changes. From the perspective of preference, the important point is which features related to Agents, Activities, and Entities that affect the metadata of the dataset should be taken into account by the organization. Figure 9 illustrates how preferences are expressed for defined different filter conditions of the datasets.

Figure 9 illustrates how preferences will be expressed in terms of the datasets. Trust preference is used to express which agents are involved in creating, assisting in the creation, or providing access to the datasets that the organization will use. If the agent is a software agent, trust preferences can also be specified in the stages of data creation, acquisition, and transfer to the organization. If the data is provided by an organization,

preferences specific to that organization can also be established. In the Reliability preference, preferences regarding the activity that creates the dataset are specified. The Timeliness preference reveals the preferences regarding the times when the dataset is acquired, created, or accessed by the organization. Additionally, preferences regarding the current version of the dataset can also be defined. The preference for Accuracy of Derivation anticipates obtaining the dataset with the least amount of change by examining the operations that have occurred since the dataset was acquired by the organization.

4.3. Sample use case for provenance

The ontology related to the organizational provenance layer should be created differently for each field of study, as the scope of each organization varies. In order to express the provenance concepts, there are three main scenarios defined in [36]. These scenarios are the News Aggregator Scenario, the Disease Outbreak Scenario, and the Business Contract Scenario. In the scope of this article's case study, the News Aggregator Scenario has been selected. This scenario aims to combine news items obtained from different sources (such as news websites, social media feeds, and news-related images).

The sample data to be generated in the News Aggregator Scenario consists of media such as photographs, videos, or the content of the news produced. For the generated data to be selected based on the origin of the media or news content, it must be licensed or published by a reliable provider. The requirement for selection is for the metadata that defines the provenance to be accessible to all data consumers. Therefore, the provenance metadata needs to be published along with the data. This way, the most suitable data source can be selected from data sources with similar accessible data.

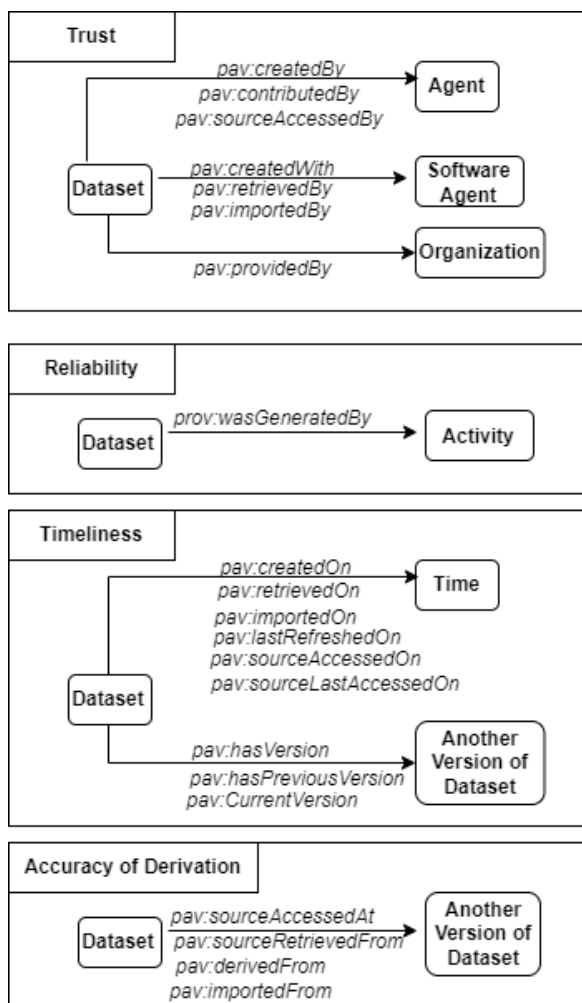


Figure 9. Representation of Various Organizational Filter Condition Preferences

Figure 10 illustrates the provenance metadata to be expressed for the New York Times (NYT) data in News Aggregator Scenario instantiating Figure 6. There can be three types of Agents for creating data and all other operations: user, organization, or software. The important point for raw NYT dataset is the creator of the dataset. However, when looking at the related NYT dataset, the focus should not be on the creation

of the data but rather on the user and organization providing the created data or the software converting the raw data into semantic data. Another point is the activity that transforms the data from raw form to semantic data. Entity, Agent and Activity classes with their relationships have all been represented in terms of this use case.

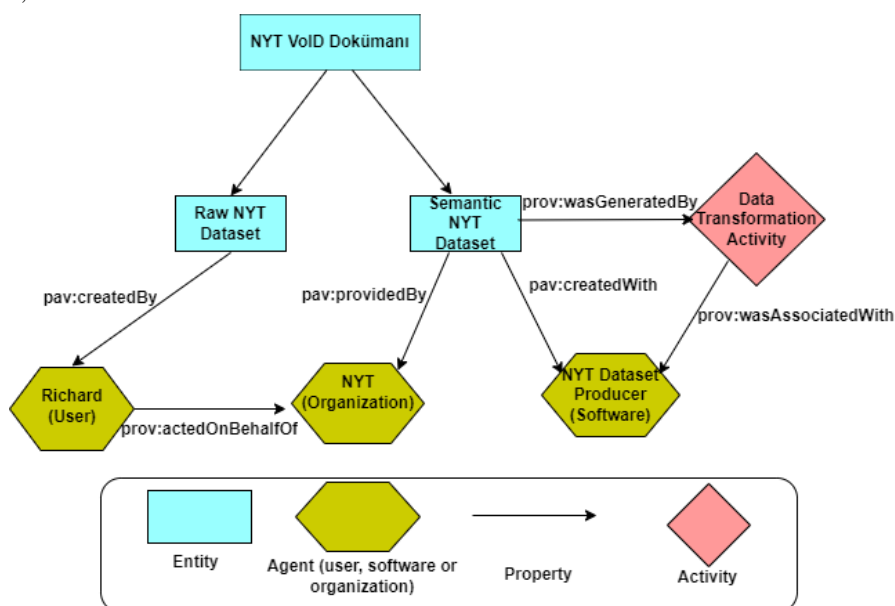


Figure 10. The Scenario Used to Express Provenance on VoID

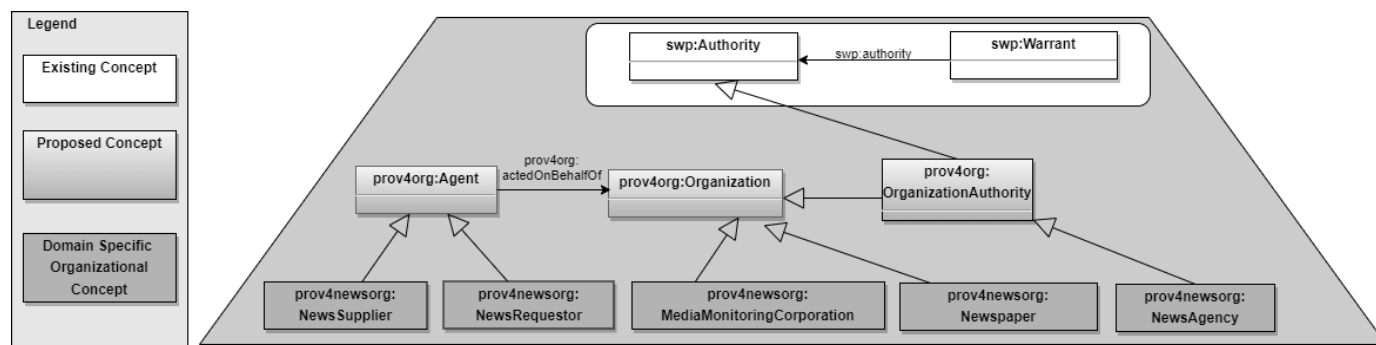


Figure 11. Organizational Provenance Ontology for News Aggregator Scenario

Figure 11 deals with the organizational provenance ontology for the News Aggregator Scenario instantiating the ontology in Figure 7. The agent (*prov4org:Agent*), organization (*prov4org:Organization*), and organizational authority (*prov4org:OrganizationAuthority*) are the fundamental elements that constitute the News Aggregator Scenario in Figure 11. In the scenario, the agent can be expanded as the news supplier (*prov4newsorg:NewsSupplier*) as the person producing the data or the news requestor (*prov4newsorg:NewsRequestor*) as the person consuming the data. The organization can be a newspaper (*prov4newsorg:Newspaper*), a media monitoring corporation (*prov4newsorg:MediaMonitoringCorporation*), or a news agency (*prov4newsorg:NewsAgency*). The organizational authority (*prov4org:OrganizationAuthority*) indicates who is responsible for publishing or modifying the news in the newspaper. In the example, it is anticipated that the news agency will assume the authority role. SWP [38] was used and associated with the organizational provenance ontology to express the concepts related to authority in order to fulfill the trust requirement for the selected scenario. Considering only trust is not sufficient as the sole dimension of provenance where the other dimensions have been mentioned in Figure 9. This ontology has been worked on to be expressed appropriately for the example, so only trust has been taken into account.

5. CONCLUSION

The widespread publication of linked datasets leads to the availability of similar data sources, creating a scenario where the selection of the most suitable and reliable dataset becomes essential. In order to make a selection from similar datasets based on higher quality or personal preferences, data sources need to be considered with certain processes. One of the objectives of this study is to establish processes for selecting datasets using and extending VoID metadata. It is envisioned that VoID should maintain metadata based on provenance-aware quality criteria using additional ontological definitions on VoID. The process of this selection demonstrates how an organization can access the Linked Data Space (LDS) and acquire suitable data or datasets through specific data and processes. In this context, the proposed method is illustrated through a scenario.

Complex rules can be generated for preferences in the organizations within its own dimension or in conjunction with different preferences. The representation of how more preferable datasets can be created will be emphasized by defining the superiority of preferences over each other [39] or by assigning separate weights to provenance preferences [40].

In future work, linked rules and provenance-based preferences will be combined for a more comprehensive provenance tracking.

In future studies, all the proposed methods for provenance will be executed within an LDS, and experiments will be conducted to explore the details of the query process, as well as the applicability and performance of the developed method. Additionally, Trustworthy AI (TAI) will be examined to see how provenance can serve as a means to enhance trustworthiness in LDSs [41]. Furthermore, constructing knowledge graphs and training them in graph neural networks (GNNs) [42], considering provenance might lead to explainability of these graphs by provenance features. Hence, Explainable AI (XAI) also could be examined in our proposed method by projecting the GNNs' decision boundary onto the interpretable feature space [43] from an organizational perspective in LDSs.

The actors in the organizations may exhibit certain attitudes that can be learnt by some organizational data. Considering these attitudes [44] may lead to learning and providing data with respect to preference-based biases. Hence, another area for future work could involve learning the attitudes of the actors and adapting the dataset selections in LDSs based on these attitudes.

ACKNOWLEDGEMENT

This study has been conducted as part of the doctoral dissertation titled "Açık Bağlı Veri Sistemlerinde Köken Bazlı Erişim Gerçekleştirimi" [45] in Ege University.

REFERENCES

- [1] C. Bizer, T. Heath, T. Berners-Lee, "Linked data: the story so far", Linking the World's Information: Essays on Tim Berners-Lee's Invention of the World Wide Web, Association for Computing Machinery (ACM), New York, NY, United States, pp. 115-143, September 2023.
- [2] F. Tekbacak, İ. Korkmaz, "Bağlı veri: veri ağının yapı taşı," Akademik Bilişim Konferansı, 2015.
- [3] E. Curry, S. Scerri, T. Tuikka (ed.), Data Spaces: Design, Deployment and Future Directions. Springer Nature, 2022.
- [4] E. Curry, Real-time Linked Dataspace: Enabling Data Ecosystems for Intelligent Systems. Springer Nature, 2020.
- [5] T. Heath, C. Bizer, Linked Data: Evolving the Web into a Global Data Space. Springer Nature, 2022.
- [6] M. Franklin, A. Halevy, D. Maier. "From databases to dataspace: a new abstraction for information management," ACM Sigmod Record, vol 34, no. 4, pp. 27-33, 2005.
- [7] A. Halevy, M. Franklin, D. Maier. "Principles of dataspace systems," Twenty-fifth ACM SIGMOD-SIGACT-SIGART Symposium on Principles of Database Systems, pp. 1-9, 2006.
- [8] M. Herschel, R. Diestelkämper, H. Ben Lahmar, "A survey on provenance: what for? what form? what from?," The VLDB Journal, vol. 26, pp. 881-906, 2017.

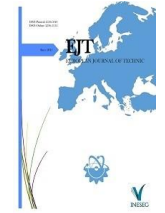
- [9] L. Moreau, P. Groth, *Provenance: An Introduction to PROV*. Springer Nature, 2022.
- [10] L. Moreau, B. Clifford, J. Freire, J. Futelle, Y. Gil, P. Groth, N. Kwasnikowska, S. Miles, P. Missier, J. Myers, B. Plale, Y. Simmhan, E. Stephan, J. V. den Bussche, "The open provenance model core specification (v1.1)," *Future Generation Computer Systems*, vol. 27, no. 6, pp. 743-756, 2011.
- [11] Internet: O. Hartig, J. Zhao, *Provenance Vocabulary Core Ontology Specification*, <https://trdf.sourceforge.net/provenance/ns.html>, 02.12.2023.
- [12] Internet: K. Belhajjame, J. Cheney, D. Corsar, D. Garijo, S. Soiland-Reyes, S. Zednik, J. Zhao, T. Lebo, S. Sahoo, D. McGuinness (eds.), *PROV-O: The PROV Ontology*, <https://www.w3.org/TR/prov-o/>, 02.12.2023.
- [13] P. Missier, K. Belhajjame, J. Cheney, "The w3c prov family of specifications for modelling provenance metadata," *Proceedings of the 16th International Conference on Extending Database Technology (EDBT'13)*, Genoa, Italy, pp. 773-776, 18-22 March 2013.
- [14] C. Baillie, P. Edwards, E. Pignotti, D. Corsar, "Short paper: assessing the quality of semantic sensor data," *Proceedings of the Sixth International Workshop on Semantic Sensor Networks (SSN'13)*, 1063, pp. 71-76, 22 October 2013.
- [15] M. Markovic, P. Edwards, D. Corsar, "Utilising provenance to enhance social computation," *12th International Semantic Web Conference (ISWC 2013)*, Sydney, NSW, Australia, Springer Berlin Heidelberg, pp. 440-447, October 21-25, 2013.
- [16] P. Missier, S. Dey, K. Belhajjame, V. Cuevas-Vicentín, B. Ludäscher, "{D-prov}: extending the {prov} provenance model with {workflow} structure," *5th USENIX Workshop on the Theory and Practice of Provenance (TaPP 13)*, pp. 1-7, 2013.
- [17] K. Belhajjame, J. Zhao, D. Garijo, M. Gamble, K. Hettne, R. Palma, E. Mina, O. Corcho, J. M. Gomez-Perez, S. Bechhofer, G. Klyne, C. Goble, "Using a suite of ontologies for preserving workflow-centric research objects," *Journal of Web Semantics*, vol. 32, pp. 16-42, May 2015.
- [18] L. McKenna, C. Debruyne, D. O'Sullivan, "Modelling the provenance of linked data interlinks for the library domain", *Companion Proceedings of the 2019 World Wide Web Conference (WWW'19)*, pp. 954-958, May 2019.
- [19] Internet: P. Ciccarese, S. Soiland-Reyes, PAV - Provenance, Authoring and Versioning, <http://pav-ontology.github.io/pav/>, 04.12.2023
- [20] P. Ciccarese, S. Soiland-Reyes, K. Belhajjame, A. J. Gray, C. Goble, T. Clark, "PAV ontology: provenance, authoring and versioning," *Journal of Biomedical Semantics*, vol. 4, pp. 1-22, 2013.
- [21] L. Rietveld, W. Beek, R. Hoekstra, S. Schlobach, "Meta-data for a lot of lod," *Semantic Web*, vol. 8, no. 6, pp. 1067-1080, 2017.
- [22] K. Alexander, R. Cyganiak, M. Hausenblas, J. Zhao, "Describing linked datasets-on the design and usage of void, the vocabulary of interlinked datasets," *Proceedings of the Linked Data Workshop at WWW09 (LDOW'09)*, Madrid, Spain, 2009.
- [23] Internet: J. Zhao, K. Alexander, M. Hausenblas, R. Cyganiak, *Digital Enterprise Research Institute, Vocabulary of Interlinked Datasets (VoID)*, <http://vocab.deri.ie/void>, 02.12.2023.
- [24] T. Omítola, L. Zuo, C. Gutteridge, I. C. Millard, H. Glaser, N. Gibbins, N. Shadbolt, "Tracing the provenance of linked data using void," *Proceedings of the International Conference on Web Intelligence, Mining and Semantics (WIMS'11)*, pp. 1-7, 2011.
- [25] Z. Gu, F. Corcoglioniti, D. Lanti, A. Mosca, G. Xiao, J. Xiong, D. Calvanese, "A systematic overview of data federation systems," *Semantic Web*, pp. 1-59, 2022.
- [26] O. Görlitz, S. Staab, "Splendid: sparql endpoint federation exploiting void descriptions," *Second International Workshop on Consuming Linked Data (COLD'11)*, 782, 2011.
- [27] Z. Akar, T. G. Halaç, E. E. Ekinici, O. Dikenelli, "Querying the web of interlinked datasets using void descriptions," *Workshop on Linked Data on the Web (LDOW'12)*, 937, 2012.
- [28] L. Heling, M. Acosta, "Federated sparql query processing over heterogeneous linked data fragments," *Proceedings of the ACM Web Conference*, pp. 1047-1057, Virtual, 25-29 April 2022.
- [29] F. Tekbacak, T. Tuğular, O. Dikenelli, "Policies for role based agents in environments with changing ontologies", *Proceedings of the 10th International Conference on Autonomous Agents and Multiagent Systems (AAMAS 2011)*, pp. 1335-1336, Taipei, Taiwan, May 2-6, 2011.
- [30] R. C. Erdur, O. Alatlı, T. G. Halaç, O. Dikenelli, "Monitoring the dynamism of the linked data space through environment abstraction," *9th International Conference on Semantic Systems (I-SEMANTICS'13)*, New York, NY, USA, ACM, pp. 81-88, September 2013.
- [31] L. F. Sikos, D. Philp, "Provenance-aware knowledge representation: a survey of data models and contextualized knowledge graphs," *Data Science and Engineering*, vol. 5, pp. 293-316, 2020.
- [32] C. Böhm, J. Lorey, F. Naumann, "Creating void descriptions for web-scale data," *Journal of Web Semantics*, vol. 9, no. 3, pp. 339-345, 2011.
- [33] M. Mountantonakis, C. Allocca, P. Fafalios, N. Minadakis, Y. Marketakis, C. Lantzaki, Y. Tzitzikas, "Extending void for expressing connectivity metrics of a semantic warehouse," *Proceedings of the PROFILES@ESWC*, Anissaras, Greece, 26 May 2014.
- [34] A. Hogan, "Web of data," *The Web of Data*, Springer International Publishing, pp. 15-57, 2020.
- [35] Internet: S. Weibel, J. Kunze, C. Lagoze, M. Wolf, *Dublin Core Metadata for Resource Discovery*, <https://www.rfc-editor.org/rfc/rfc2413>, 05.12.2023.
- [36] P. Groth, Y. Gil, J. Cheney, S. Miles, "Requirements for provenance on the web," *International Journal of Digital Curation*, vol. 7, no. 1, pp. 39-56, 2012.
- [37] Internet: D. Reynolds (ed.), *The Organization Ontology*, <https://www.w3.org/TR/vocab-org/>, 06.12.2023.
- [38] C. Bizer, "Semantic web publishing vocabulary (swp) user manual," *Freie Universität Berlin*, November 2006.
- [39] A. Toniolo, F. Cerutti, N. Oren, T. J. Norman, K. Sycara, "Making informed decisions via provenance and argumentation schemes," *Proceedings of the Eleventh International Workshop on Argumentation in Multi-Agent Systems (ArgMAS'14)*, 2014.
- [40] R. Dividino, G. Gröner, S. Scheglmann, M. Thimm, "Ranking rdf with provenance via preference aggregation," *18th International Conference on Knowledge Engineering and Knowledge Management (EKAW 2012)*, Galway City, Ireland, Springer Berlin Heidelberg, pp. 154-163, October 8-12, 2012.
- [41] A. Kale, T. Nguyen, F. C. Harris Jr, C. Li, J. Zhang, X. Ma, "Provenance documentation to enable explainable and trustworthy ai: a literature review," *Data Intelligence*, vol. 5, no. 1, pp. 139-162, 2023.
- [42] R. Das, M. Soylu, "A key review on graph data science: The power of graphs in scientific studies," *Chemometrics and Intelligent Laboratory Systems*, vol. 240, 104896, 15 September 2023.
- [43] K. Mukherjee, J. Wiedemeier, T. Wang, M. Kim, F. Chen, M. Kantarcioglu, K. Jee, "Interpreting gnn-based ids detections using provenance graph structural features," *arXiv preprint arXiv:2306.00934*, 2023.
- [44] M. Soylu, A. Soylu, R. Das, "A new approach to recognizing the use of attitude markers by authors of academic journal articles," *Expert Systems with Applications*, vol. 230, 120538, 15 November 2023.
- [45] F. Tekbacak, "Açık bağıl veri sistemlerinde köken bazlı erişim gerçekleştirimi," *Doctoral dissertation*, Computer Engineering Department, Ege University, Izmir, Turkey, 2015.

BIOGRAPHIES

Fatih Soygazi, also known as Fatih Tekbacak, earned a Bachelor of Science and Master of Science degree from the Izmir Institute of Technology, Computer Engineering Department, followed by a Ph.D. from Ege University, Computer Engineering Department. His current research interests are knowledge graphs, linked data, machine learning, deep learning, natural language processing, agent-based software engineering, distributed ledger technologies and knowledge management.

Tuğkan Tuğular received the B.S., M.S., and Ph.D. degrees in Computer Engineering from Ege University, Turkey, in 1993, 1995, and 1999. He worked as a research associate at Purdue University from 1996 to 1998. He has been with Izmir Institute of Technology since 2000. After becoming an Assistant Professor at Izmir Institute of Technology, he worked as Chief Information Officer in the university from 2003-2007. In addition to his academic duties, he acted as IT advisor to the Rector between 2010-2014. In 2018, he became an Associate Professor in the Department of Computer Engineering of the same university. He has more than 75 publications and an active record of duties with international and national conferences. His current research interests include model-based testing and software quality with machine learning support.

Oğuz Dikenelli currently works as a Professor in Ege University, Computer Engineering Department. His research interests are agent-based software engineering and linked data.



Research Article

Performance Evaluation of Capuchin Search Algorithm Through Non-linear Problems, and Optimization

Erdal EKER^{1*} ^{1*}Muş Alparslan University, Vocational School of Social Science, Muş, Turkey. (e-mail: e.eker@alparslan.edu.tr).

ARTICLE INFO

Received: Nov., 15. 2023

Revised: Dec., 11. 2023

Accepted: Dec., 21. 2023

Keywords:

Metaheuristic algorithm

Optimization

CapSA

Gear train design problem

Corresponding author: *Erdal EKER*

ISSN: 2536-5010 / e-ISSN: 2536-5134

DOI: <https://doi.org/10.36222/ejt.1391524>

ABSTRACT

The purpose of this paper is to demonstrate the superiority of the Capuchin Search Algorithm (CapSA), a metaheuristic, in competitive environments and its advantages in optimizing engineering design problems. To achieve this, the CEC 2019 function set was used. Due to the challenging characteristics of the CEC 2019 function set in reaching a global solution, it effectively showcases the algorithm's quality. For this comparison, sea-horse optimizer (SHO), grey wolf optimizer (GWO), sine-cosine algorithm (SCA), and smell agent optimization (SAO) were chosen as current and effective alternatives to the CapSA algorithm. Furthermore, the gear train design problem (GTD) was selected as an engineering design problem. In addition to the CapSA algorithm, a hybrid of SCA and GWO algorithm (SC-GWO) and genetic algorithm (GA) were chosen as alternatives for optimizing this problem. The performance superiority and optimization power of the CapSA algorithm were assessed using statistical metrics and convergence curves, then compared with alternative algorithms. Experimental results conclusively demonstrate the significant effectiveness and advantages of the CapSA algorithm.

1. INTRODUCTION

Real-world problems, in general, can be expressed as complex non-linear programming problems. Due to their combinatorial nature, these problems have been described as hard problems [1]. The structure of the objective functions at the core of these problems also determines the optimization process leading to the solution. Non-linear programming (NLP) is a mathematical programming technique in which the objective function is non-linear or one or more of the constraints have a non-linear relationship. NLP problems can be modeled in Eq. 1 given below [1]. Here, the objective function n is the number of variables, g and h are the constraints.

$$\left. \begin{aligned} f_{min}(x) &= f(x_1, x_2, x_3, \dots, x_n) \\ g_i(x) &\leq 0, i = 1, 2, \dots, n \\ h_j(x) &\leq 0, j = 1, 2, \dots, n \end{aligned} \right\} \quad (1)$$

Traditional methods exist in the literature for solving the NLP problem. These methods, defined as gradient optimization techniques, attempt to solve these problems by using special mathematical structures and formulations [1]. Examples of these methods include the sequential unconstrained minimization technique [2], the augmented lagrangian [3], Newton-Raphson [4], the successive quadratic programming algorithm [5], the steepest descent algorithm [6], dynamic integer programming [7], and the stochastic Newton optimization method [8] as optimization

techniques. The disadvantage of these techniques is that they are not suitable for solving complex optimization problems. Especially as the complexity of the problem increases with the addition of uncertainties to the system, more complex optimization techniques that overcome the limitations of classical approaches should be used. Metaheuristics have been developed with this goal in mind [9, 10]. Since metaheuristic algorithms do not use the derivative or second derivative of the objective function, they produce solutions in the neighborhood of the optimal solution. They avoid getting stuck in the local search space, reach the global solution in less time, and can hybridize with other algorithms to deal with different problems, having a flexible structure with all these features [11-13]. Due to their repetitive working methods and memory utilization, they can make new explorations without having to go back to the beginning each time [14]. Metaheuristic algorithms consist of three different mechanisms: the initialization phase, containing the candidate solution set; the exploitation phase, which divides the search space into regions to concentrate on narrow areas; and the exploration phase, which scans the entire space, selects, and improves the best solutions obtained in the exploitation phase. The success of metaheuristic algorithms is directly proportional to the strength of the balance between the exploitation and exploration phases [15]. The CapSA algorithm considered in this paper is one of the current and efficient metaheuristic algorithms produced in 2021 [16].

Many studies on CapSA can be mentioned in the literature. The main ones are explained as follows. In the first paper introducing the algorithm, Braik et al experienced the optimization power of the CapSA algorithm in classic engineering design problems such as welded beam design, pressure vessel design, tension-compression spring design, speed reducer design [16]. Braik, one of the inventors of the CapSA algorithm, proposed the MGP-CapSA algorithm by combining the CapSA algorithm with the multigene genetic algorithm, and with this algorithm, he produces a new simulator model for the wrapping problem from non-linear problems and uses CapSA to optimize the coefficients of the regression equations of MGP [17]. Kanipariya et al produced the ICSA algorithm by hybridising the CapSA algorithm with adversarial learning and chaotic local search algorithms and used it to classify lung nodule abnormalities [18]. Fathy et al used the CapSA algorithm to minimize grid active power loss by maintaining power flow, bus voltage and transmission line within their normal ranges in electricity distribution networks [19]. A similar study was conducted by Zakaria et al [20]. Ramu et al used the modified CapSA algorithm (MCS) to solve the cloud performance scheduling problem, which minimizes the completion time and improves resource utilisation [21]. Broumandnia et al hybridized the CapSA algorithm with the inverted ant colony optimization (IACO) algorithm for the optimization of some processes related to the cloud system and obtained better performance [22]. Qin et al, CapSA based PID control system for solving industrial problems [23]. Kumar et al used CapSA algorithm as an optimizer to classify normal and malicious attacks by strengthening the security scheme of IoT (Internet of Things) [24]. In a similar study, Rani and Burty hybridized CapSA with different machine learning algorithms for smart home energy management [25]. Ehteram et al used the CapSA algorithm as a basis for training ANNs to carry out evaporation prediction [26]. Alphonse et al used the ECapSA technique, a combination of CapSA and wild horse optimizer, to enable the simultaneous allocation of electric vehicle charging station (EVCS) and photovoltaic (PV) energy sources in the smart grid [27]. The gear train design problem, which is optimized in this study, has been studied by many metaheuristic algorithms before and effective results have been obtained [28-32].

The organization of the paper is as follows. Section 1 consists of the introduction and the optimization process of the study. The second section consists of the introduction and mathematical modelling of the CapSA algorithm. Experimental studies are included in the third section. The sub-sections of this section consist of the introduction of the CEC 2019 function set and the comparison of the CapSA algorithm with alternative algorithms through statistical results and observing the performance superiority of the CapSA algorithm through tables and converge curves. The other subsection includes the optimization of the Gear train design problem with the help of CapSA and alternative algorithms, The performance results are shown through tables and convergence curves, and the fourth section contains the conclusions of the study.

2. CAPUCHIN SEARCH ALGORITHM (CapSA)

The CapSA algorithm, based on swarm intelligence, was created by simulating the foraging behavior of Capuchin

monkeys living in the Americas, with a particular emphasis on their jumping abilities [16, 33]. The mathematical model of the CapSA algorithm is constructed to align the jumping movements of Capuchin monkeys with the exploration phase, while the swinging and climbing movements correspond to the exploitation phase. In the first stage, a random initial set of a specific number of candidates is created [16]. The initial set is represented by a matrix of size $d \times n$.

$$x = \begin{bmatrix} x_1^1 & \dots & x_d^1 \\ \vdots & \dots & \vdots \\ x_1^n & \dots & x_d^n \end{bmatrix}_{d \times n} \quad (2)$$

The initial location of each Capuchin monkey is expressed in Eq. 3. Here ub_j and lb_j , denotes the upper and lower boundaries of the i . monkey in the j th dimension, respectively operator r corresponds to a random number uniformly distributed in the closed interval $[0,1]$.

$$x^j = ub_j + r \times (ub_j - lb_j) \quad (3)$$

The position of the leader monkey during the tree climbing behavior is modelled in Eq. 4. Here, the i . positions of the leader and accompanying monkeys in the j . dimension x_j^i , F_j the location of the food,

v_j^i the speed of the monkey, P_{bf} , the probability of balance provided by the monkey's tail throughout the jumping movement, The gravitational force, g , corresponding to the number 9.81, ε operator expresses a random number informly distributed in the interval $[0,1]$.

$$x_j^i = F_j + \frac{P_{bf}(v_j^i)^2 \sin(2\pi)}{g} \quad \left\{ \begin{array}{l} i < \frac{n}{2}, 0.10 < \varepsilon \leq 0.20 \end{array} \right\} \quad (4)$$

Monkeys jump angle (θ) is given in Eq. 5. Here operator r expresses a random number irregularly distributed in the interval $[0,1]$.

$$\theta = \frac{3}{2}r \quad (5)$$

In Eq. 6, we show that CapSA is a system that updates the monkeys' locations to quickly detect the location of the food source by exploring and exploiting the search space. τ operator is defined.

$$\tau = \beta_0 e^{\beta_1 \left(\frac{t}{T}\right)^{\beta_2}} \quad (6)$$

where t and T , denote the current iteration and maximum iteration, respectively, β_0 , β_1 , β_2 it is stated that after many experimental studies, the author has chosen 2, 21 and 2 as the most appropriate values for the parameters, respectively. The appropriate value of the parameter τ strengthens the exploration and exploitation capabilities of the CapSA algorithm.

In Eq.7, the speed of monkey i . in the j th dimension is modelled. Here, the velocity of monkey i th in the j th

dimension v_j^i , their location x_j^i , best location $x_{best_j}^i$ refers to r_1 ve r_2 is a random number uniformly in the range [0,1]. ρ , coefficient of inertia controls the effect of the previous velocity on the motion. In this equation, there are also two fixed control parameters namely a_1 and a_2 that control the speed of the monkeys by adjusting the parameters $x_{best_j}^i$ and F_j . ρ , a_1 and a_2 are parameters arbitrary.

$$v_j^i = \rho v_j^i + \tau a_1 (x_{best_j}^i - x_j^i) r_1 + \tau a_2 (F_j - x_j^i) r_2 \quad (7)$$

The new position of the leader and the accompanying monkeys as a result of the jump is modelled in Eq.8

$$x_j^i = F_j + \frac{P_{ef} P_{bf} (v_j^i) \sin(2\theta)}{g}, i < \frac{n}{2}, 0.20 < e \leq 0.30 \quad (8)$$

given P_{ef} is the probability of the monkey yawning. The new position of the Alpha monkey is modelled in Eq. 10. Given by $P_{bf} = 0.7$ and $P_{ef} = 9$.

$$x_j^i = x_j^i + v_j^i, i < \frac{n}{2}, 0.20 < e \leq 0.30 \quad (9)$$

Local foraging is achieved by the swaying movement that alpha and its companion monkeys use to collect food. The positions of the monkeys in this situation are formulated below.

$$x_j^i = F_j + \tau P_{bf} \times \sin(2\theta), i < \frac{n}{2}, 0.50 < e \leq 0.75 \quad (10)$$

Similar to local foraging, the leader and its companion monkeys may repeat the behavior of foraging repeatedly. The positions of monkeys displaying this behavior are modelled following.

$$x_j^i = F_j + \tau P_{bf} (v_j^i - v_{j-1}^i) i < \frac{n}{2}, 0.75 < e \leq 1.00 \quad (11)$$

where the i th monkey in the j th dimension v_j^i current speed, v_{j-1}^i indicates the previous speed.

Monkeys can also move randomly to find food. This is given in the equation below. In the equation P_r is equal to 0 and expresses the random search probability of the monkeys. The randomization capability and the monkey herd behavior expressed here improves the global search capability of the algorithm and supports the escape from local optimum points. τ parameter has the role of strengthening the equilibrium position between exploration and exploitation.

$$x_j^i = \tau \times (lb_j + e \times (ub_j - lb_j)), i < \frac{n}{2}, e \leq P_r \quad (12)$$

Eq. 13 models the leader monkey updating the position of its followers based on the third law of motion.

$$x_f = x_i + v_0 t + \frac{1}{2} a t^2 \quad (13)$$

$$a = \frac{\Delta v}{\Delta t} = \frac{v_f - v_0}{t_1 - t_0} \quad (14)$$

$$v_f = \frac{\Delta x}{\Delta t} = \frac{x_f - x_0}{t_1 - t_0} \quad (15)$$

given in Eq.13 x_f and x_i with the displacements in the initial and final phases t time, v_0 initial speed, a is the slope whose formula is given in Eq. 14. v_f final speed, v_0 initial velocity, respectively t_1 ve t_0 give the final and start times. In Eq. 16 $v_0 = 0$ when taken a becomes as formulated in Eq.16.

$$a = \frac{x_f - x_0}{(t_1 - t_0)^2} \quad (16)$$

Since Capuchin monkeys live in herds, it is important to simulate the behavior of the leader as well as the behavior of the followers as they follow the leader.

$$x_j^i = \frac{1}{2} (x_j^i + x_j^{i-1}), \frac{n}{2} \leq i \leq n \quad (17)$$

From the expressions given in Eq.17, x_j^i current position of the followers in dimension j th, x_j^{i-1} previous location, x_j^i is the current position of the leader. Since the time intervals in the simulation refer to iterations $t_i - t_{i-1} = 1$. The fitness function for each monkey is evaluated by adjusting the solution vector values in a fitness function and stored in a matrix as expressed in Eq.18, which serves as a memory.

$$f = \begin{bmatrix} f_1([x_1^1, x_2^1, \dots, x_d^1]) \\ \vdots \\ f_n([x_1^n, x_2^n, \dots, x_d^n]) \end{bmatrix}_{d \times n} \quad (18)$$

3. EXPERIMENTAL RESULTS

The CEC2019 function set was employed to assess the optimization capability of the CapSA algorithm. This set consists of difficult problems. The goal of these problems is to highlight the optimization capability and competitive aspect of the algorithm by compelling it to reach the global solution [15]. For the alternative algorithms that CapSA will compete with, we selected current and efficient algorithms. These include the grey wolf optimizer (GWO) [34], sea-horse optimizer (SHO) [35], sine-cosine algorithm (SCA) [36], and smell agent optimization (SAO) [37]. When evaluating the performance of the algorithm, we conducted 30 independent runs with 500 iterations and 30 search agents in each run. In this study, CapSA parameters took arbitrary values ρ , a_1 and a_2 which were set to 0.7, 1, and 1 respectively.

TABLE I
CEC 2019 FUNCTIONS

Functions	Dimension	[Lower&Upper bound]	Fit. V
Function 1	9	[-8192, 8192]	1
Function 2	16	[-16384, 16384]	1
Function 3	18	[-4,4]	1
Function 4	10	[-100, 100]	1
Function 5	10	[-100, 100]	1

Function 6	10	[-100, 100]	1
Function 7	10	[-100, 100]	1
Function 8	10	[-100, 100]	1
Function 9	10	[-100, 100]	1
Function 10	10	[-100, 100]	1

In Table 1, the optimal values of CEC 2019 are provided. As the optimal value for all functions is 1, the algorithm observed to be the most effective experimentally is expected to be closer to 1 than the others. For this reason, optimal results are expected from both the best value and the average value. The difference between the best value and the worst value should not be too significant, indicating that the standard deviation value should be low.

TABLE 2
PERFORMANCE OF CEC2019

CEC2019 Functions	Metrics	Algorithms				
		CapSA	SHO	GWO	SCA	SAO
Function 1	Mean	4.1043E+04	4.5384E+04	1.3297E+08	8.5744E+09	3.3710E+11
	Std.dev.	2.6591E+03	2.5926E+03	2.4538E+08	9.4139E+09	4.2532E+11
	Best	3.7079E+04	4.0869E+04	9.0425E+04	4.5544E+07	1.0675E+06
	Worst	4.8634E+04	5.0757E+04	1.0915E+09	4.5484E+10	1.5831E+12
	Run time (sec.)	6.2867	9.4452	6.2162	6.1441	24.0524
	Rank	1	2	3	4	5
Function 2	Mean	1.7342E+01	1.7386E+01	1.7344E+01	1.7485E+01	2.1755E+03
	Std.dev.	6.4444E-05	1.0166E-01	3.4780E-04	6.6712E-02	2.1538E+03
	Best	1.7342E+01	1.7343E+01	1.7343E+01	1.7397E+01	1.7881E+01
	Worst	1.7343E+01	1.7677E+01	1.7345E+01	1.7710E+01	8.3069E+03
	Run time (sec.)	0.2711	0.8144	0.3256	0.3926	0.6813
	Rank	1	3	2	4	5
Function 3	Mean	1.2702E+01	1.2702E+01	1.2702E+01	1.2702E+01	1.2703E+01
	Std.dev.	9.0336E-15	4.8734E-06	3.4200E-04	9.4149E-05	8.5018E-04
	Best	1.2702E+01	1.2702E+01	1.2702E+01	1.2702E+01	1.2702E+01
	Worst	1.2702E+01	1.2702E+01	1.2704E+01	1.2703E+01	1.2706E+01
	Run time (sec.)	0.3935	0.8796	0.4922	0.4089	0.8863
	Rank	1	2	4	3	5
Function 4	Mean	4.3731E+01	1.4375E+03	6.1384E+01	1.5444E+03	1.6066E+04
	Std.dev.	1.9984E+01	1.5552E+03	2.2991E+01	5.5463E+02	5.1770E+03
	Best	1.0950E+01	9.5000E+01	2.0309E+01	6.3374E+02	7.1411E+03
	Worst	8.6579E+01	4.7645E+03	1.0763E+02	2.6895E+03	2.8970E+04
	Run time (sec.)	0.3186	0.7399	0.3504	0.2304	0.79839
	Rank	1	3	2	4	5
Function 5	Mean	1.3192E+00	1.7793E+00	1.4540E+00	2.2394E+00	5.3936E+00
	Std.dev.	1.7340E-01	2.5219E-01	2.5398E-01	1.2223E-01	1.2545E+00
	Best	1.0689E+00	1.2928E+00	1.0790E+00	2.0473E+00	2.8281E+00
	Worst	1.6598E+00	2.4198E+00	1.8360E+00	2.6946E+00	8.2563E+00
	Run time (sec.)	0.1385	0.4208	0.1983	0.1867	0.6286
	Rank	1	3	2	4	5
Function 6	Mean	7.9079E+00	8.0011E+00	1.1066E+01	1.0843E+01	1.0121E+01
	Std.dev.	1.3018E+00	9.9758E-01	7.0067E-01	6.3186E-01	6.9379E-01
	Best	4.8923E+00	5.7081E+00	9.7446E+00	9.3411E+00	8.9621E+00
	Worst	1.0783E+01	1.0004E+01	1.2501E+01	1.1967E+01	1.1699E+01
	Run time (sec.)	2.3342	3.5275	2.2171	2.2328	10.2188
	Rank	1	2	5	4	3
Function 7	Mean	4.3136E+02	2.8850E+02	4.3643E+02	7.7376E+02	1.1062E+03
	Std.dev.	3.2594E+02	1.0717E+02	3.0061E+02	1.7682E+02	3.9157E+02
	Best	-6.3737E+01	-1.4686E+01	5.8673E+01	3.9072E+02	3.7941E+02
	Worst	1.3055E+03	5.3524E+02	1.2014E+03	1.0398E+03	2.2533E+03
	Run time (sec.)	0.1595	0.4134	0.1704	0.1974	0.5529
	Rank	2	1	3	4	5
Function 8	Mean	5.4122E+00	5.4523E+00	5.2877E+00	6.1099E+00	6.4154E+00
	Std.dev.	6.899E-01	5.4020E-01	9.0214E-01	4.5161E-01	3.4621E-01
	Best	3.9460E+00	4.4703E+00	3.5009E+00	5.0269E+00	5.7638E+00
	Worst	6.6099E+00	6.3853E+00	6.9706E+00	6.8575E+00	7.2611E+00
	Run time (sec.)	0.1443	0.4205	0.2034	0.1816	0.6881
	Rank	2	3	1	4	5
Function 9	Mean	2.7197E+00	1.5525E+02	4.4281E+00	1.4306E+02	2.6530E+03
	Std.dev.	0.3344E-01	2.7471E+02	9.2393E-01	1.1088E+02	8.8512E+02
	Best	2.4323E+00	4.4605E+00	2.5669E+00	3.2968E+00	6.0353E+02
	Worst	4.1519E+00	8.0767E+02	6.3641E+00	4.7436E+02	4.6614E+03
	Run time (sec.)	0.1644	0.4103	0.1806	0.1978	0.5266
	Rank	1	4	2	3	5

Function 10	Mean	1.95338E+01	2.0112E+01	2.0503E+01	2.0467E+01	2.0455E+01
	Std.dev.	2.9277E+00	7.8076E-02	8.1513E-02	9.1492E-02	1.6069E-01
	Best	4.0361E+00	1.9993E+01	2.0299E+01	2.0280E+01	2.0223E+01
	Worst	2.0231E+01	2.0280E+01	2.0648E+01	2.0632E+01	2.1142E+01
	Run time (sec.)	0.1457	0.4087	0.3611	0.3172	0.6346
	Rank	1	2	5	4	3

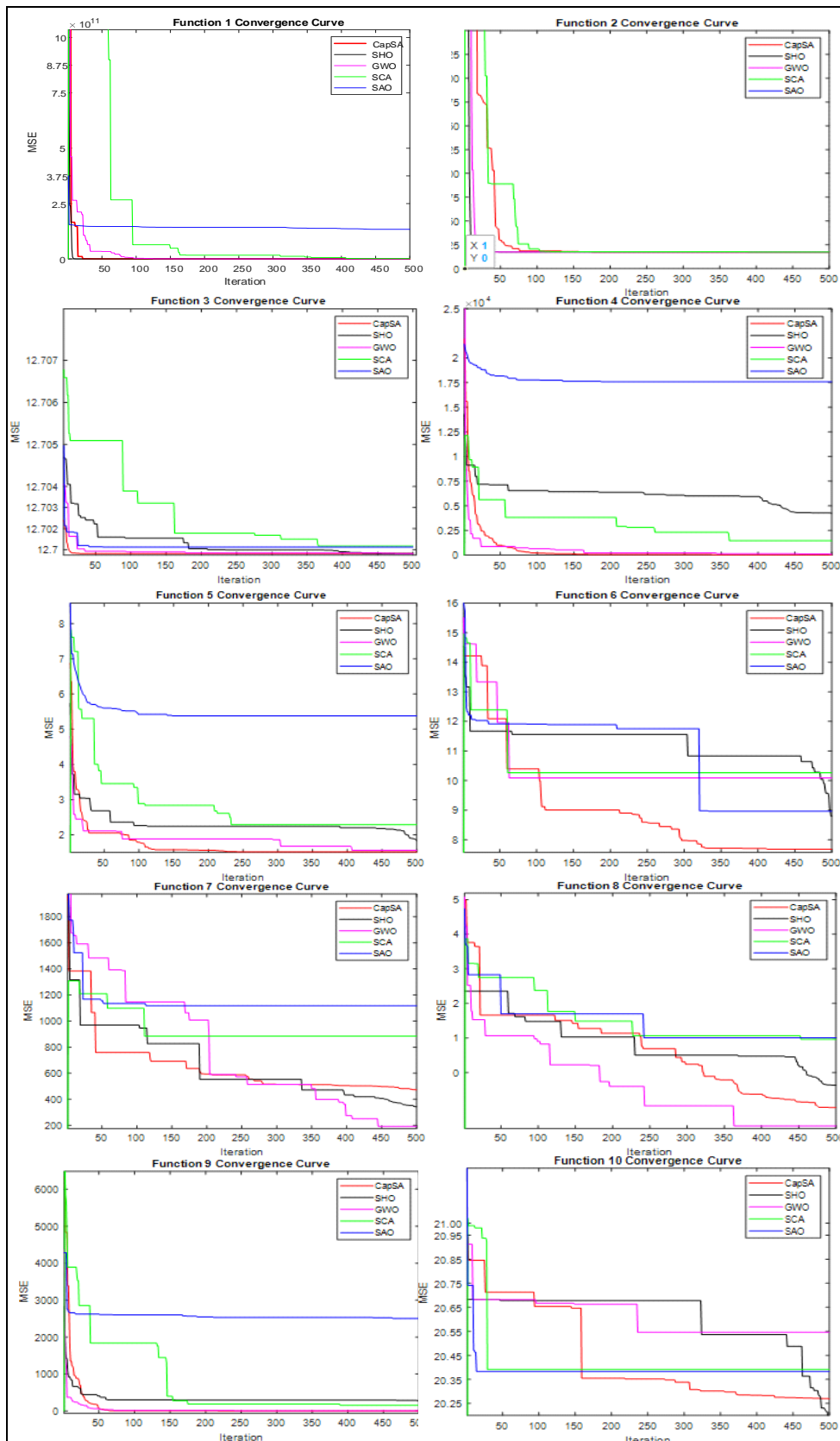


Figure 1. Convergence curve of algorithms via CEC 2019 function

In this context, upon analyzing Table 2, it is observed that the CapSA algorithm is more advantageous from function 1 to function 5. It is advantageous in terms of both average and best value in function 6, and it is superior in functions 9 and 10. While it completed the optimization process in the shortest time for almost all functions, it took slightly longer in functions 1, 4, and 6. When looking at the average values, except for functions 7 and 8, it has consistently held its status as the most superior algorithm. The CapSA algorithm was run for the first time with the CEC 2019 function set and it was clearly seen that it has a strong competitive aspect and a structure that can reach global results without getting stuck in the local area. Convergence curves are statistical measures that indicate whether algorithms are converging early or sticking to local optimum points as they iteratively progress through the process of optimizing a function. In the Figure 1, when the CAPSA algorithm is compared with alternative algorithms, the algorithm is labelled as 1. It is observed that it cannot progress to the local optimum point in the function,

but it progresses steadily towards the optimum point in the other functions for 500 iterations. In the 7th and 8th functions, GWO algorithm shows better convergence, while CapSA shows the best convergence in all other algorithms.

4. GEAR TRAIN DESIGN PROBLEM

Figure 2 shows the design of a gear train, which is set up to determine the number of teeth in each gear to produce a given speed ratio between the input and output shaft. Here A, B, C and D indicate the number of gears in each wheel. In order to minimize the ratio of angular velocity variation between input and output in accordance with the objective of the gear train design problem, a mathematical model is established by Eq. 19 [38-40].

$$\min f(x) = \left(\frac{1}{6.931} - \frac{x_2 x_3}{x_1 x_4} \right)^2 \quad (19)$$

$$\vec{x} = [A, B, C, D] = [x_1, x_2, x_3, x_4], \quad 12 \leq x_i \leq 60$$

In Eq. 18, $\frac{x_2 x_3}{x_1 x_4}$ expression gives the gear ratio.

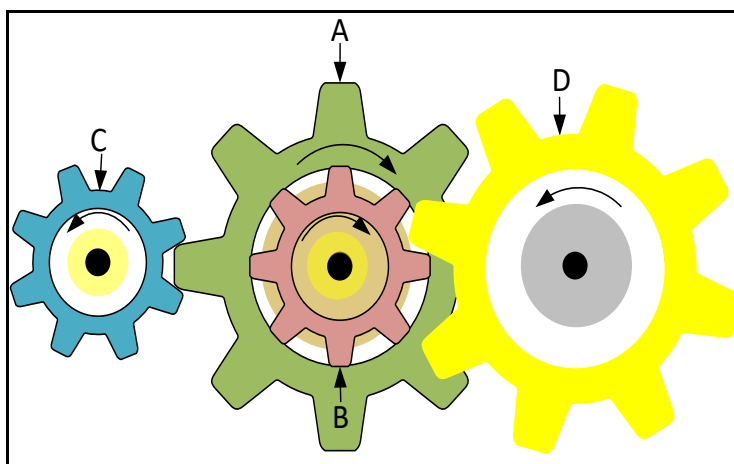


Figure 2. GTD model

TABLE 3
GTD ANALYSIS RESULTS

Algorithm	Parameters				Metrics				
	x_1	x_2	x_3	x_4	Mean	Std. Dev.	Best	Worst	Rank
CapSA	12	32	52	51	2.3987e-19	1.3080e-18	1.2326e-32	7.1655e-18	1
GWO	15	22	55	45	5.2328e-12	1.0711e-11	1.3783e-15	4.5145e-11	4
SCA	15	29	60	51	1.5854e-09	2.2843e-09	6.9337e-13	7.4779e-09	5
SHO	12	12	48	21	7.4748e-09	1.7250e-08	7.5125e-17	7.1094e-08	6
SAO	21	58	58	18	3.0622e-03	1.6206e-02	2.0291e-17	8.8858e-02	7
SC-GWO[40]	43	16	19	49	2.7009E-12	-	-	-	3
GA[41]	19	16	43	49	2.7000E-12	-	-	-	2

The results of the performance comparisons of competitive metaheuristic algorithms help to determine the most effective algorithm in the optimization of the problem and the emergence of the optimum model. In this context, the analysis results of the CapSA, GWO, SCA, SHO, SAO, SC-GWO and GA algorithms for the GTD problem are shown and evaluated in

Table 3. Here, the optimization results of SC-GWO algorithm, which is a hybrid algorithm of SCA and GWO, and Genetic algorithm (GA) for GTD problem are taken from previous studies. [40, 41].

When Table 3 is observed, the optimal result is found for the gear arrangement ratio generated by the CapSA algorithm. Here, the approximate number of gears and the synchronized encounter with each other reveal that it shows high performance compared to other algorithms. When Figure 3 is analyzed, it will be seen that the visual dimension of the table is parallel to the results in Table 3. In fact, in the convergence curve, it can be seen that the CapSA algorithm is quite stable and gets results around zero.

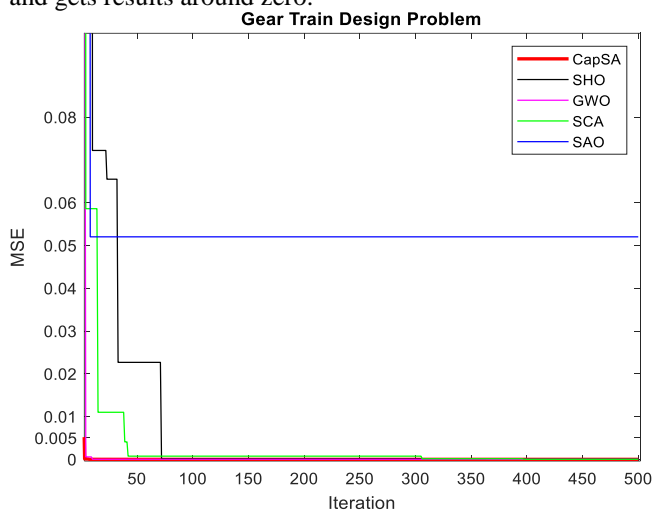


Figure 3. Convergence curve of GTD model via algorithms

5. DISCUSSION

The aim of this paper is to reveal the competitiveness and performance superiority of the CapSA algorithm by comparing it with alternative algorithms through the CEC 2019 quality function set and to optimize the gear train design problem, which is one of the classic engineering problems. CapSA has experimentally shown that it is an algorithm with more advantageous results compared to alternative algorithms with various statistical measurements. Likewise, it has been experimentally observed that CapSA algorithm has the most optimal results in the optimization of GTD problem. Based on these results, it can be stated that the CapSA algorithm has a strong competitive structure, is stable in solving real world problems and has the flexibility to overcome the problems of getting stuck in the local algorithm in some functions seen in the structure of the algorithm when it is developed. For this reason, the CapSA algorithm is a promising algorithm that can be addressed in future studies with different aspects.

REFERENCES

- [1] L. Costa ve P. Oliveira, "Evolutionary algorithms approach to the solution of mixed integer non-linear programming problems", *Computers & Chemical Engineering*, c. 25, sy 2-3, ss. 257-266, 2001.
- [2] A. V. Fiacco ve G. P. McCormick, "The Sequential Unconstrained Minimization Technique for Nonlinear Programming, a Primal-Dual Method", *Management Science*, c. 10, sy 2, ss. 360-366, Oca. 1964, doi: 10.1287/mnsc.10.2.360.
- [3] H. Adeli ve N. Cheng, "Augmented Lagrangian Genetic Algorithm for Structural Optimization", *J. Aerosp. Eng.*, c. 7, sy 1, ss. 104-118, Oca. 1994, doi: 10.1061/(ASCE)0893-1321(1994)7:1(104).
- [4] A. Ben-Israel, "A Newton-Raphson method for the solution of systems of equations", *Journal of Mathematical analysis and applications*, c. 15, sy 2, ss. 243-252, 1966.
- [5] P. T. Boggs ve J. W. Tolle, "Sequential quadratic programming", *Acta numerica*, c. 4, ss. 1-51, 1995.
- [6] B. Widrow ve J. McCool, "A comparison of adaptive algorithms based on the methods of steepest descent and random search", *IEEE transactions on antennas and propagation*, c. 24, sy 5, ss. 615-637, 1976.
- [7] J. Zou, S. Ahmed, ve X. A. Sun, "Stochastic dual dynamic integer programming", *Math. Program.*, c. 175, sy 1-2, ss. 461-502, May. 2019, doi: 10.1007/s10107-018-1249-5.
- [8] B. Bullins, K. Patel, O. Shamir, N. Srebro, ve B. E. Woodworth, "A stochastic newton algorithm for distributed convex optimization", *Advances in Neural Information Processing Systems*, c. 34, ss. 26818-26830, 2021.
- [9] K. Sørensen ve F. Glover, "Metaheuristics", *Encyclopedia of operations research and management science*, c. 62, ss. 960-970, 2013.
- [10] S. E. De León-Aldaco, H. Calleja, ve J. A. Alquicira, "Metaheuristic optimization methods applied to power converters: A review", *IEEE Transactions on Power Electronics*, c. 30, sy 12, ss. 6791-6803, 2015.
- [11] D. H. Wolpert ve W. G. Macready, "No free lunch theorems for optimization", *IEEE transactions on evolutionary computation*, c. 1, sy 1, ss. 67-82, 1997.
- [12] E. Eker, M. Kayri, S. Ekinci, ve D. İzci, "A new fusion of ASO with SA algorithm and its applications to MLP training and DC motor speed control", *Arabian Journal for Science and Engineering*, c. 46, ss. 3889-3911, 2021.
- [13] E. Eker, M. Kayri, S. Ekinci, ve D. İzci, "Comparison of Swarm-based Metaheuristic and Gradient Descent-based Algorithms in Artificial Neural Network Training", *ADCAIJ: Advances in Distributed Computing and Artificial Intelligence Journal*, c. 12, sy 1, ss. e29969-e29969, 2023.
- [14] J. O. Agushaka, A. E. Ezugwu, L. Abualigah, S. K. Alharbi, ve H. A. E.-W. Khalifa, "Efficient initialization methods for population-based metaheuristic algorithms: a comparative study", *Archives of Computational Methods in Engineering*, c. 30, sy 3, ss. 1727-1787, 2023.
- [15] E. Eker, M. Kayri, S. Ekinci, ve M. A. Kaçmaz, "Performance Evaluation of PDO Algorithm through Benchmark Functions and MLP Training", *Electrica*, c. 23, sy 3, 2023, Erişim: 04 Ekim 2023. [Çevrimiçi]. Erişim adresi: <https://electricajournal.org/Content/files/sayilar/96/597-606.pdf>
- [16] M. Braik, A. Sheta, ve H. Al-Hiary, "A novel metaheuristic search algorithm for solving optimization problems: capuchin search algorithm", *Neural Comput & Applic*, c. 33, sy 7, ss. 2515-2547, Nis. 2021, doi: 10.1007/s00521-020-05145-6.
- [17] M. Braik, "A hybrid multi-gene genetic programming with capuchin search algorithm for modeling a nonlinear challenge problem: Modeling industrial winding process, case study", *Neural Processing Letters*, c. 53, sy 4, ss. 2873-2916, 2021.
- [18] M. Kanipriya, C. Hemalatha, N. Sridevi, S. R. SriVidhya, ve S. J. Shabu, "An improved capuchin search algorithm optimized hybrid CNN-LSTM architecture for malignant lung nodule detection", *Biomedical Signal Processing and Control*, c. 78, s. 103973, 2022.
- [19] A. Fathy, D. Yousri, H. Rezk, ve H. S. Ramadan, "An efficient capuchin search algorithm for allocating the renewable based biomass distributed generators in radial distribution network", *Sustainable Energy Technologies and Assessments*, c. 53, s. 102559, 2022.

- [20] M. Zakaria, M. S. Seif, ve M. A. Mehanna, "Energy Management of MG Considering the Emission and Degradation Costs using A CAP-SA Optimization", *International Journal of Renewable Energy Research (IJRER)*, c. 12, sy 3, ss. 1452-1462, 2022.
- [21] S. Ramu, R. Ranganathan, ve R. Ramamoorthy, "Capuchin search algorithm based task scheduling in cloud computing environment", *Yanbu Journal of Engineering and Science*, c. 19, sy 1, ss. 18-29, 2022.
- [22] A. Broumandnia, S. Rostami, ve A. Khademzadeh, "An Energy-Efficient Task Scheduling Method for Heterogeneous Cloud Computing Systems Using Capuchin Search and Inverted Ant Colony Optimization Algorithms", *Available at SSRN 4270250*, Erişim: 13 Ekim 2023. [Çevrimiçi]. Erişim adresi: https://papers.ssrn.com/sol3/papers.cfm?abstract_id=4270250
- [23] C. Qin, H. Hu, H. Chen, ve B. Yan, "Research on Optimization Control of Deep Hole Machining Based on Capuchin Search Algorithm to Optimize Fuzzy PID", içinde *2022 IEEE 21st International Conference on Ubiquitous Computing and Communications (IUCC/CIT/DSCI/SmartCNS)*, IEEE, 2022, ss. 288-293. Erişim: 13 Ekim 2023. [Çevrimiçi]. Erişim adresi: <https://ieeexplore.ieee.org/abstract/document/10086312/>
- [24] C. U. Om Kumar, J. Durairaj, S. A. Ahamed Ali, Y. Justindhas, ve S. Marappan, "Effective intrusion detection system for IoT using optimized capsule auto encoder model", *Concurrency and Computation*, c. 34, sy 13, s. e6918, Haz. 2022, doi: 10.1002/cpe.6918.
- [25] V. U. Rani ve L. R. Burthi, "Power Quality Enhancement of Smart Home Energy Management System in Smart Grid Using MAORDF-CapSA Technique", *Ecological Engineering & Environmental Technology*, c. 23, 2022, Erişim: 13 Ekim 2023. [Çevrimiçi]. Erişim adresi: <https://yadda.icm.edu.pl/yadda/element/bwmeta1.element.baztech-16773c9e-e170-4b5c-a9cf-242d6fe17d16>
- [26] M. Ehteram, F. Panahi, A. N. Ahmed, A. H. Mosavi, ve A. El-Shafie, "Inclusive multiple model using hybrid artificial neural networks for predicting evaporation", *Frontiers in Environmental Science*, c. 9, s. 789995, 2022.
- [27] A. R. A. Alphonse, A. P. P. G. Raj, ve M. Arumugam, "Simultaneously allocating electric vehicle charging stations (EVCS) and photovoltaic (PV) energy resources in smart grid considering uncertainties: A hybrid technique", *Intl J of Energy Research*, c. 46, sy 11, ss. 14855-14876, Eyl. 2022, doi: 10.1002/er.8187.
- [28] L. Wang, Q. Cao, Z. Zhang, S. Mirjalili, ve W. Zhao, "Artificial rabbits optimization: A new bio-inspired meta-heuristic algorithm for solving engineering optimization problems", *Engineering Applications of Artificial Intelligence*, c. 114, s. 105082, 2022.
- [29] H. T. Sadeeq ve A. M. Abdulazeez, "Giant trevally optimizer (GTO): A novel metaheuristic algorithm for global optimization and challenging engineering problems", *IEEE Access*, c. 10, ss. 121615-121640, 2022.
- [30] N. Chopra ve M. M. Ansari, "Golden jackal optimization: A novel nature-inspired optimizer for engineering applications", *Expert Systems with Applications*, c. 198, s. 116924, 2022.
- [31] S. Mirjalili, "Moth-flame optimization algorithm: A novel nature-inspired heuristic paradigm", *Knowledge-based systems*, c. 89, ss. 228-249, 2015.
- [32] S. Mirjalili, "The ant lion optimizer", *Advances in engineering software*, c. 83, ss. 80-98, 2015.
- [33] V. F. Lenzen, "Newton's Third Law of Motion", *Isis*, c. 27, sy 2, ss. 258-260, Ağu. 1937, doi: 10.1086/347244.
- [34] S. Mirjalili, S. M. Mirjalili, ve A. Lewis, "Grey wolf optimizer", *Advances in engineering software*, c. 69, ss. 46-61, 2014.
- [35] S. Zhao, T. Zhang, S. Ma, ve M. Wang, "Sea-horse optimizer: a novel nature-inspired meta-heuristic for global optimization problems", *Applied Intelligence*, c. 53, sy 10, ss. 11833-11860, 2023.
- [36] S. M. Mirjalili, S. Z. Mirjalili, S. Saremi, ve S. Mirjalili, "Sine cosine algorithm: theory, literature review, and application in designing bend photonic crystal waveguides", *Nature-inspired optimizers: theories, literature reviews and applications*, ss. 201-217, 2020.
- [37] A. T. Salawudeen, M. B. Mu'azu, A. Yusuf, ve A. E. Adedokun, "A Novel Smell Agent Optimization (SAO): An extensive CEC study and engineering application", *Knowledge-Based Systems*, c. 232, s. 107486, 2021.
- [38] M. Mendez, D. A. Rossit, B. González, ve M. Frutos, "Proposal and comparative study of evolutionary algorithms for optimum design of a gear system", *IEEE Access*, c. 8, ss. 3482-3497, 2019.
- [39] E. Sandgren, "Nonlinear Integer and Discrete Programming in Mechanical Design Optimization", *Journal of Mechanical Design*, c. 112, sy 2, ss. 223-229, Haz. 1990, doi: 10.1115/1.2912596.
- [40] S. Gupta, K. Deep, H. Moayedi, L. K. Foong, ve A. Assad, "Sine cosine grey wolf optimizer to solve engineering design problems", *Engineering with Computers*, c. 37, sy 4, ss. 3123-3149, Eki. 2021, doi: 10.1007/s00366-020-00996-y.
- [41] S.-J. Wu ve P.-T. Chow, "Genetic Algorithms for Nonlinear Mixed Discrete-Integer Optimization Problems via Meta-Genetic Parameter Optimization", *Engineering Optimization*, c. 24, sy 2, ss. 137-159, May. 1995, doi: 10.1080/03052159508941187.

BIOGRAPHY

Erdal Eker graduated in Mathematics from Van Yuzuncu Yil University, Turkey. He received his MSc in Applied Mathematics from Ataturk University, Turkey, and his PhD from Yuzuncu Yil University in Statistics. He is currently an instructor at Mus Alparslan University, working on Artificial learning, the applications of metaheuristic optimization, and statistic. He has many studies published in national and international scientific platforms.

Research Article

Comparison of Road Luminance Data Estimated by Fuzzy Logic and ANN, A Case Study of Kocaeli Sakıp Sabancı Street

Zuleyha Ok Davarci¹ , Onur Akar²  and Umit Kemalettin Terzi^{3*} 

¹Department of Electrical and Electronics Engineering, Ok Engineering, Kırkkale, Turkey. (e-mail: okmuhendislikok@hotmail.com).

²Marmara University, Department of Electronics and Automation, Istanbul, Türkiye. (e-mail: onur.akar@marmara.edu.tr).

^{3*}Marmara University, Department of Electrical and Electronics Engineering, Marmara University, Istanbul, Turkey (e-mail: terzi@marmara.edu.tr).

ARTICLE INFO

Received: Dec., 07. 2023

Revised: Dec., 21. 2023

Accepted: Dec, 29. 2023

Keywords:

Road Lighting

Luminance

Fuzzy Logic

Artificial Neural Network

Corresponding author: Ümit K. Terzi

ISSN: 2536-5010 / e-ISSN: 2536-5134

DOI: <https://doi.org/10.36222/ejt.1401466>

ABSTRACT

Road lighting constitutes the most important part of city lighting. While correct road lighting solves the chaos in transportation, it also paves the way for smooth urban traffic flow. It also allows people to have a comfortable and safe journey. In order to reduce accidents in the evening hours, safe driving and visual comfort must be provided to drivers. Just like inadequate road lighting, excessive lighting also causes accidents and waste of electrical energy. Good visibility of objects on the road and visual comfort for drivers is possible by ensuring an equal brightness distribution on the road surface. In this article, a prediction model was created with Artificial Neural Network (ANN) and Fuzzy Logic (FL) methods to find the luminance values of the road in Sakıp Sabancı street in Kocaeli province. When the predictions obtained by ANN and FL were compared, the results were seen to be accurate and compatible. When the estimation results obtained as a result of the application were examined, it was observed that the estimation of luminance values in good and qualified road lighting could be achieved with these methods.

1. INTRODUCTION

Developments in technology are constantly increasing in the world, especially in science and industry. This situation creates increasing energy demand and the need to use energy resources efficiently. Poor design of lighting systems is the cause of many problems in society [1-5]. The presence of unnecessary lighting on the road causes light pollution, which negatively affects the illuminated place and the natural environment, and this creates various negative effects on people's mental health [6,7]. Some of these negative effects on individuals include sleep disturbance, cancer, unsafe driving, etc. [8]. For such reasons, providing the most appropriate visibility for users according to the traffic situation in road lighting is of great importance for safe night driving. According to statistics, the accident rate that occurs on a poorly lit road is three times the accident rate that occurs during the daytime. This shows that a well-lit road will reduce night accidents by 30% [9,10]. It has also been concluded that it reduces fatal accidents occurring at night by 65%, injury accidents by 30%, and property damage accidents by 15% [11,12]. The need for lighting on intercity roads, as well as urban roads, is an important fact. The

purposes of road lighting are to illuminate all objects on and around the road, including the road surface, and to provide the best visibility for drivers and pedestrians in various traffic conditions [13-15]. According to statistical studies on this subject, it has been concluded that illuminating urban roads and areas in accordance with the criteria reduces the crime rate by 20% and the crime severity rate by 40% [16]. In a different study, disruption of driving due to distraction and the resulting accidents were examined [17]. In addition, for drivers to have a comfortable driving experience while driving, it is desired that the light level of the road be within a certain range and the brightness distribution be as close to homogeneous as possible [18,19]. For this reason, it is of great importance to adjust the location and power of road lamps correctly. Road illumination is based on measuring brightness values for individual points determined on the road, and in road illumination measurements, the brightness value of an area is traditionally measured with a gloss meter. First of all, it is necessary to determine the calculation area where the measurement will be made. The calculation area is considered as the area between two determined poles in the longitudinal direction of the road where the measurement will be made [20]. On roads where seeing objects is vital, special

national and international standards have been determined to ensure that lighting meets adequate safety and comfort requirements. EN 13201 European Standard for Road Lighting is the basic lighting standard for the design and evaluation of these road parameters, and road lighting calculations are made taking into account EN 13201-3 [21-25]. In addition, road lighting standards are included in the CIE 115 standard, and in this standard there are 6 different road lighting classes discussed under the title "Lighting Recommendations for Motor and Pedestrian Traffic of Roads" [26]. On surfaces that normally cannot illuminate themselves, the brightness varies depending on the reflection product of that surface and the light level on the surface [27,28]. Safe roads are only possible by ensuring drivers' visual comfort and proper distribution of brightness. The aim of the lighting method is to create a bright road surface by preventing objects on the road from appearing as shadows. Therefore, glare control as well as the gloss level and smoothness of the road surface are important. If the brightness in the field of vision of the eye reaches too high values, it may cause accidents because the eye cannot see the surroundings as a result of glare [29,30]. Brightness values are measured according to road classes R1, R2, R3 and R4, which are the four ideal categories specified in the TS EN 13201 standard [31]. In the experimental study conducted by V. Gyurov and his colleagues, the lighting, technical and energy parameters of road lighting systems in Varna, Bulgaria were examined. It has been confirmed that the measurements made are in accordance with the standards and the results obtained provide the desired solution [32]. In a field study conducted by K. Markvica et al., the effects of conventional luminaires, state-of-the-art LED luminaires and optimized LEDs used in road lighting on people in Vienna's Blumauergasse Street were examined. It was concluded that LED luminaires have positive effects on both pedestrians and vehicle drivers in terms of street lighting integrity and comfort [33]. The study by S. Bozorg et al evaluates the potential of dimming road lighting to save energy and reduce costs, while also preventing negative effects on drivers' visibility. It has been concluded that for better visibility, road lighting should have a full 100% brightness level or an average brightness level of 0.19 cd/m², which does not rely on the influence of vehicle headlights [34]. In the study conducted by S.B. Chenani et al., the interaction between road lighting and vehicle headlights was examined at target detection distance. In this study, it was concluded that the lighting can be dimmed in order to save energy without disturbing the perception of objects [35]. S. Yoomak et al., also conducted research on LED luminaire technology and HPSV luminaire technology for road lighting applications on the highway. This research concluded that the power quality and energy savings of the LED luminaire are approximately 40% more efficient than the HPSV luminaire and perform better in terms of index reduction [36]. B. Xu et al., tried to develop a new lighting method to increase the visibility of the road and the road ahead while driving in heavy fog. As a result of the research, important reference information for autonomous driving technology was obtained. It was also concluded that if these researches are developed, they will make a great contribution to autonomous driving technology [37]. A. Ogando-Martínez et al., proposed a geometric estimation method based on three ellipsoid surfaces to reduce road brightness coefficients. The approach created to update the reflection properties of asphalt and adapt it to r-tables was

carried out within the framework of calibration and applied on a real situation. The measured luminance data via configuration by variables, optimized for modeling r-tables, were supplemented with experimental luminances [38]. Calculations have been made by A. Ekrias et al., by transferring the numerical data of the photometer to Road LumiMeter using the LumiMeter computer program. The image in the main window of the program has been converted into numerical data and associated with photometric values. A brightness map has been created from the images, the brightness has been analyzed on the captured scene, and the measurement results of the analysis have been recorded [39]. Artificial intelligence and web-based software that can make road illumination measurements using road photographs has been developed by M. Kayakuş et al., T. Kazanasmaz et al. and D. Tran et al. For this purpose, reference points have been determined on the road. The correlation between the brightness values of these points and the pixel values has been established using artificial intelligence techniques. In order to see the results obtained from the measuring device and artificial intelligence techniques more clearly, color mapping has been made according to the brightness value of the road [40-42]. Z Ok Davarci et al., performed with ANN estimation of luminance in road illumination on different roads [43, 44].

In most of the above studies, measurements and calculations used in traditional road lighting were used. In some studies, comparisons of lamps used in road lighting have been made. Some of them focus on the energy efficiency of lighting. Road lighting studies using artificial intelligence techniques are very few, and these studies are on road imaging or color mapping and brightness level estimation with artificial intelligence methods.

2. MATERIAL AND METHOD

This study was carried out on a two-lane road located on Sakıp Sabancı Street in İzmit district of Kocaeli province. By measuring at certain points on the right and left corners of the road, the luminance value of the entire road was intended to be estimated using ANN and FL. It is aimed to find the road brightness level with the ANN and FL artificial intelligence methods used and to determine whether it is time for maintenance of the road lighting system with the data obtained. The view of the road is given in Fig.1, its width is 7 m, it is bidirectional and the lighting fixtures are installed on 14 m high poles on the side of the road, on 2 m long 0 degree angled consoles, 33 meters apart.



Figure 1. Image of the measured road

There are single-sided luminaires on both sides of the road and the road is illuminated from both sides. 78 (6 transverse points x 13 longitudinal points) measurements were made by

the observer on the road surface with double-sided illumination. The measurement points of the selected road were determined as seen in Fig.2.

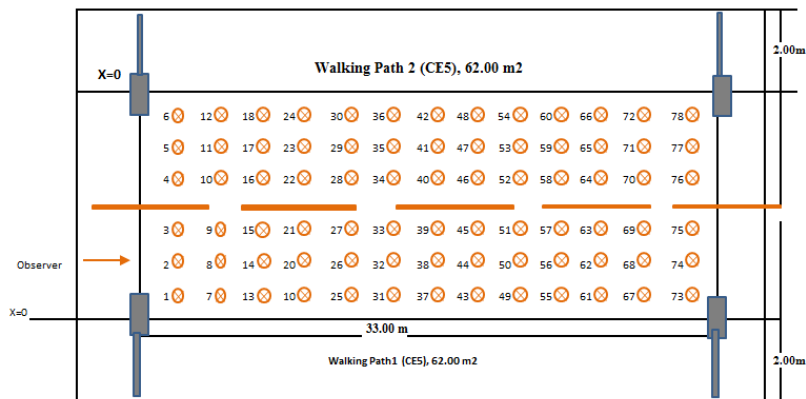


Figure 2. Observer and measurement points

The values measured from the road surface to be used in ANN training were brought together and converted into matrix format. In addition, the weight values used in ANN

are stated as measurements made in the areas marked in Table I

TABLE I
LUMINANCE VALUES MEASURED IN THE OBSERVER DIRECTION (Cd/m²)

3.5	4.4	4.5	4.2	3.9	3.7	3.6	3.1	2.6	2.4	2.5	2.7	3.1
5.7	6.2	5.7	5.3	4.8	4.5	4.5	4.1	3.7	3.6	3.9	4.3	4.8
6.1	6	5.5	5	5.2	4.8	4.9	4.8	4.5	4.6	4.7	4.9	5.1
5.2	4.9	4.6	4.4	4.6	4.5	4.7	5.2	5.1	5.1	5	5.2	4.9
4.5	4	3.7	3.7	3.9	4.2	4.7	5.7	5.4	5.2	4.9	4.7	4.6
3.5	3	2.7	2.6	2.8	3.1	3.6	4.2	4.6	4.4	4.1	3.9	3.9

2.1. Application of Prediction with ANN

80% of the values obtained in the measurements are used for training and 20% for testing purposes. The ones used for ANN training are input (weight) values and output (target) values. In order not to disrupt road traffic and to ensure that

the road is not closed, the input data values are marked with dashed lines on the right and left sides of the road determined in Fig.2. After the training process was completed, the data was predicted by the ANN. The weight and target values of the created ANN Model are shown in Fig.3.

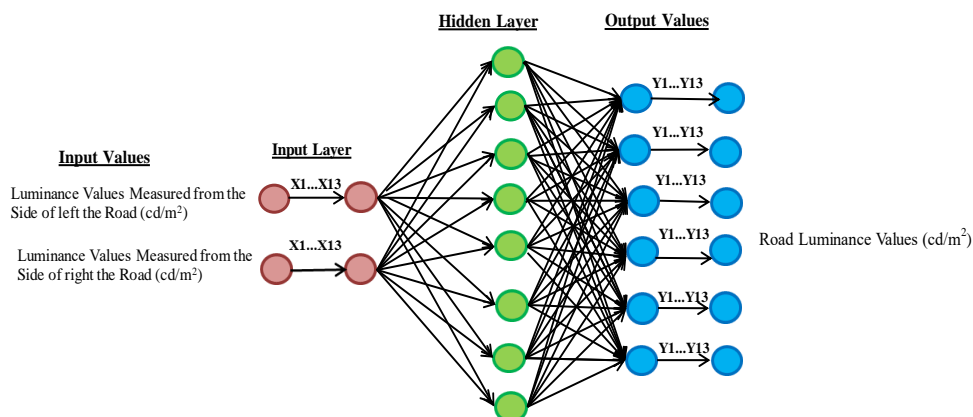


Figure 3. Input and Output values of the ANN model

With the back propagation algorithm of ANN, it is aimed to minimize the error, that is, the difference between the desired output from the network and the produced output. In the feed-forward ANN calculation, the input values coming to the input layer are arranged with weight matrices and the output values are determined. Then, according to the training algorithm, the difference between the network output and the real output is found, that is, the error is propagated backwards again and the network weights are rearranged. This process continues until the desired output is obtained from the network. In the training phase, one of various model algorithms is selected for the input and target values and the forward output values of the j_s in the "q" layer are calculated according to equation 1. Here, q refers to the unit output result and i refers to the layer.

$$y_i^q = f(\sum_i y_i^{q-1} w_{ij}^q) \tag{1}$$

Error calculation of output units is as given in Eq. (2).

$$\delta_i^q = (y_i^q - y_i^t) f'(H_i^q) \tag{2}$$

The backpropagation error calculation for units i in layers is given in Eq. (3).

$$\delta_i^{q-1} = f'(H_i^{q-1}) \left(\sum_i \delta_i^q w_{ij}^q \right) \tag{3}$$

Where;

y_i^q : i'th output values,

f' : Activation Function,

w_{ij}^q : Weight values from input to hidden layer

Q : Number of training pairs

H_i : Hessian matrix

q : unit output result value

I : number of layers

δ_i : Output unit error value

Levenberg-Marquardt (LM) algorithm was preferred in ANN training. The main reason for this is the speed and stability features it provides. Log-sigmoid was used as the transfer function in ANN. The graph showing the error rate of the ANN model created with the Matlab nntool program is as shown in Fig.4.

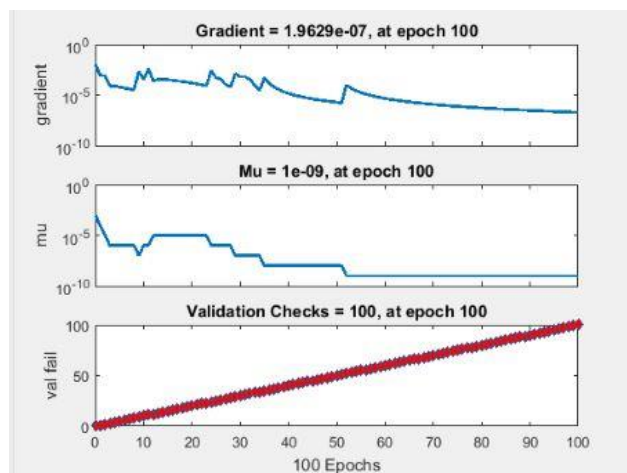


Figure 4. Graph showing the error rate of the created ANN model

As seen in Fig.4, the desired result was obtained and recorded in the 100th iteration for the minimum error rate as a result of network training. As seen in Fig.5, the ANN training value of the weight values was carried out with a regression of 0.95699. The validation value of the created ANN prediction values was 0.98525, and the test regression values of the target values were 0.96366 with a high validity. The regression value of the entire input was found to be 0.96085. From this situation, it was observed that the training values were correct at a rate of 95.699%.

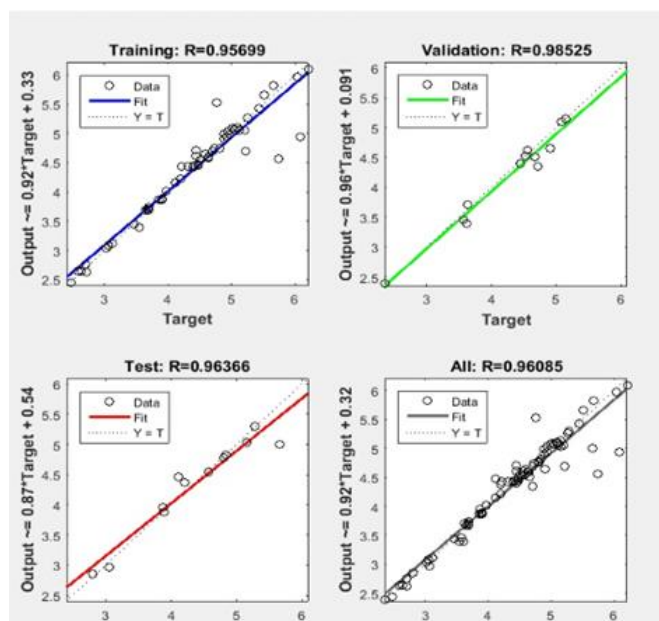


Figure 5. Training, Validation, Test, and All Values in the Estimation Made.

As seen in Fig.6, the best performance value in the developed model was determined as 0.02439. Since the correlation value is equal to 1, it can be seen that there is a perfect similarity between the network output and the target output.

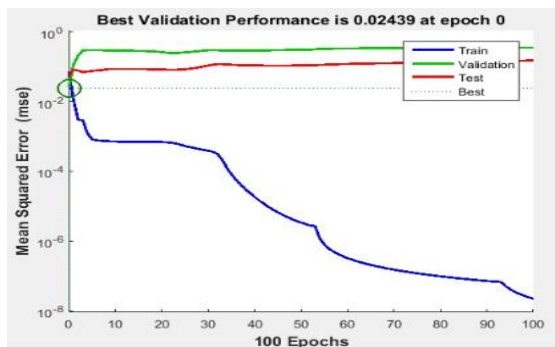


Figure 6. Best Validation performance of the created ANN.

Fig.7 shows the 3D view of the data resulting from ANN prediction. Here, the brighter and clearer yellow color scale indicates that the luminance values are increasing, and the closer it gets to the dark blue color, the more luminance values are decreasing.

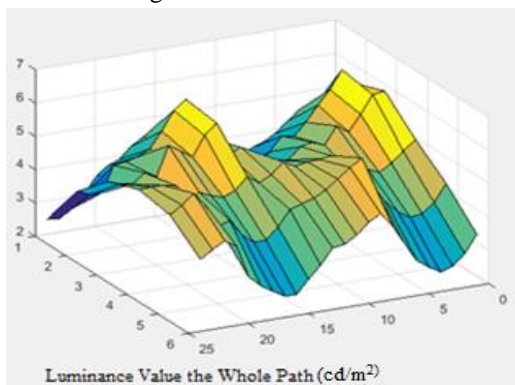


Figure 7. 3D image and glare distribution of the prediction result obtained in ANN.

2.2. Prediction with FL

In the prediction made with the FL method, 2 input and 1 output parameters were used. The parameters used were determined with reference to previous studies. The input parameters are the luminance value measured from the right side of the road (cd/m²) and the luminance value measured from the left side of the road (cd/m²). The predicted luminance value of the entire path (cd/m²) is the output parameter. The representation of the created model in the MATLAB program Fuzzy Logic Toolbox is shown in Fig.8.

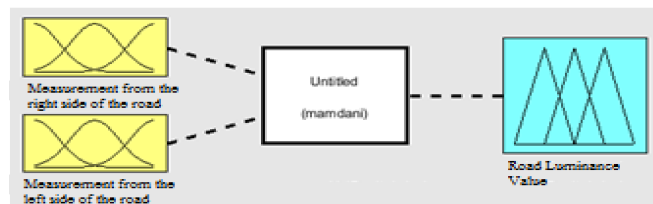


Figure 8. Display of the created model in the MATLAB program Fuzzy Logic Toolbox.

Membership functions were created for the input and output parameters determined in the FL application. While creating membership functions, membership functions that are widely used in the literature were preferred. Here, it is as shown in Table II, which shows the effect of the luminance values (cd/m²) measured from the right edges of the road with FL on the output value, which is the luminance value of the road (cd/m²).

TABLE II
EFFECT OF LUMINANCE VALUES (Cd/m²) MEASURED FROM THE RIGHT AND LEFT EDGES OF THE ROAD ON THE OUTPUT VALUE

		Road Right-Left Side				
		VS	S	N	B	VB
Road Luminance Value	VVS	VVS	VS	N	VVS	VVS
	VS	VS	VS	N	VVS	VVS
	S	VS	VS	N	VS	VVS
	N	N	N	N	N	S
	B	VS	VS	N	B	VB
	VB	VB	VB	N	B	VB

The membership functions shown in Fig.9, Fig.10 and Fig.11 define fuzzy sets identified as A_i and B_i. Triangular membership function was used in equations (4) and (5) for input and output variables. The clusters defined in Fig.9, Fig.10 and Fig.11 have been verified with membership functions. Cells within μ_A are clusters. Here a, b and c are the boundary ranges of comprehensive logical sets, and x is the searched variable value. The σ value is the learning rate [45,46].

$$\mu_A = \mu_A(x; a, b, c) = \left\{ \begin{array}{ll} \frac{(x-a)}{(a-b)} & \text{if } a \leq x < b \\ \frac{(c-x)}{(c-b)} & \text{if } b \leq x \leq c \\ 0 & \text{if } x > c \text{ or } x < a \end{array} \right\} \quad (4)$$

$$A = \sum_i^n \mu_{A_i} \left(\frac{x_i}{x_i} \right) \Rightarrow \{(x, \mu_A(x))\} \quad x \quad (5)$$

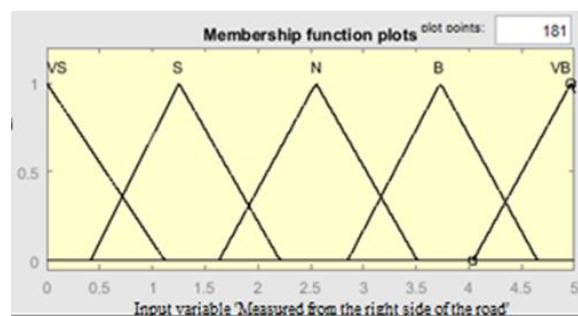


Figure 9. Membership function for the luminance parameter measured from the right edge of the road.

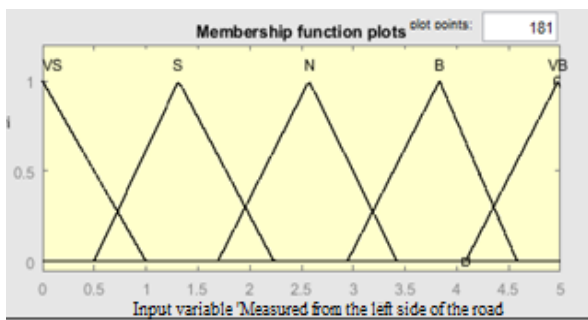


Figure 10. Membership function for the luminance parameter measured from the left edge of the road

In the designed study, it is aimed to determine the luminance value of the entire road by using the luminance values measured from the right and left edges of the road. Range values in membership functions are shown in Table III. The rules of the Fuzzy method were determined according to the cluster numbers coming from the membership functions of the input parameters. The luminance value of the entire road (cd/m^2) was created in 7 clusters, the luminance value measured from the right side of the road (cd/m^2) in 5 clusters,

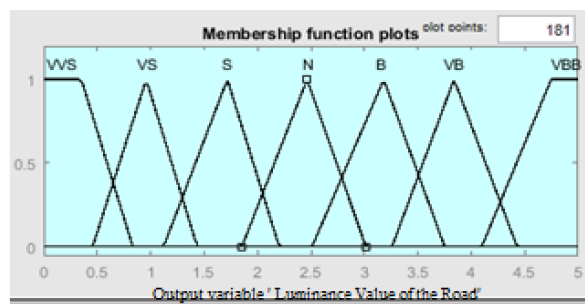


Figure 11. Membership function for the estimation parameter of road luminance (cd/m^2) values

and the luminance value measured from the left side of the road (cd/m^2) in 5 clusters.

The luminance (cd/m^2) value measured from the right side of the road was created with a triangular membership function and consists of 5 clusters: Very Small (VS) - Small (S) - Normal (N) - Large (B) - Very Large (VB). The membership function for the measured luminance value parameter is shown in Fig.9. In the function, data is in cd/m^2 .

TABLE III
RANGE VALUES IN CREATED MEMBERSHIP FUNCTIONS

		CLUSTER NAME	MINIMUM VALUE	MAXIMUM VALUE
Inputs	Measurement from the Right of the Road(Cd/m^2)	Very Small	0.00	1.18
		Small	0.41	2.21
		Normal	1.63	3.50
		Big	2.85	4.65
		Very Big	4.00	5.00
	Measurement from the Left of the Road(Cd/m^2)	Very Small	0.00	1.00
		Small	0.50	2.23
		Normal	1.69	3.42
		Big	2.94	4.58
		Very Big	4.08	5.00
Outputs	Luminance Value of the Road(Cd/m^2)	Very very small	0.00	0.83
		Very Small	0.46	1.44
		Small	1.12	2.20
		Normal	1.85	3.01
		Big	2.51	3.75
		Very Big	3.26	4.43
		Very Very Big	4.10	5.00

The triangular membership function of the luminance value (cd/m^2) parameter measured from the left edge of the road is created from 5 clusters: Very Small (VS), Small (S), Normal (N), Large (B), Very Large (VB). The membership function for the measured luminance values parameter is seen in Fig.10.

The luminance value parameter of the road is determined by triangular and trapezoidal membership functions as Very Very Small (VVS) - Very Small (VS) - Small (S) - Normal (N) - Large (B) - Very Large (VB) - Very Very Large (VVB). It contains 7 clusters: The membership function for the road luminance value (cd/m^2) parameter is seen in Fig.11. In the function, data is in cd .

After entering the rules in FL, the 3D graph resulting from road luminance (cd/m^2) value estimates is as seen in Fig.12.

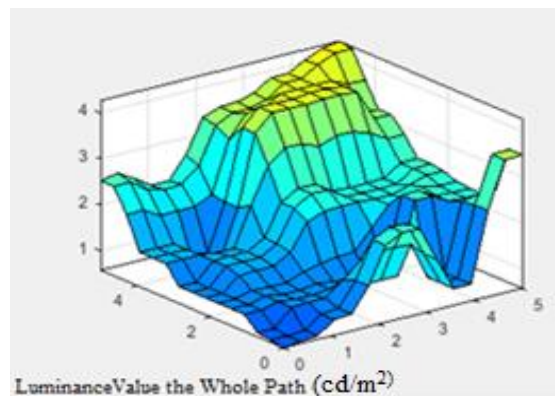


Figure 12. Result and distribution of estimation of road luminance (cd/m^2) values

As can be seen here, there is less prediction similarity compared to the values obtained in ANN. An approximately correct result was obtained, but it is less clear than ANN.

3. IMPLEMENTATION

It can be seen in Fig.13 that the desired values and the predicted values in the training carried out with the ANN here coincide exactly with the reference values. A successful prediction was achieved with a verification value of ANN prediction of 0.98525.

The accuracy rate of the prediction corresponding to the rules defined in FL was found to be 97.43%, and a part of the image of the results obtained by using different input values in addition to the defined rules is shown in Fig.14.

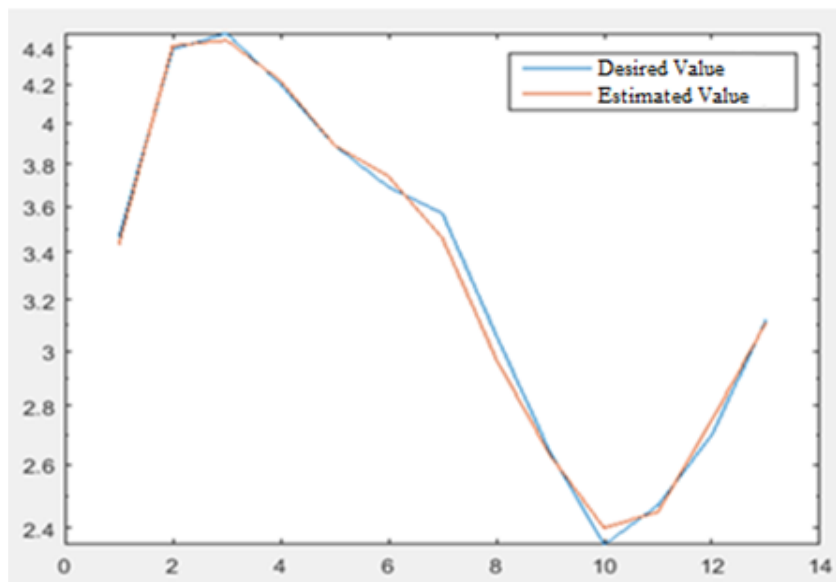


Figure 13. Graph showing the overlap between the desired luminance value (cd/m²) and the predicted luminance value (cd/m²)

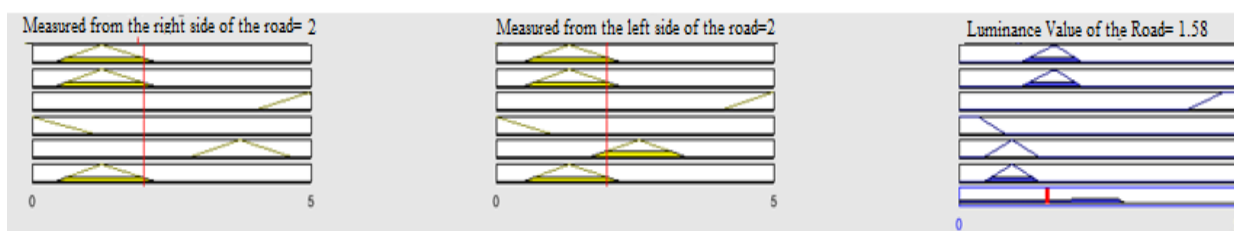


Figure 14. Membership function for the road luminance value (cd/m²) estimation parameter

The comparison of ANN and FL methods used to find the luminance value on the road surface is as follows;

- The predicted values of the prediction models created with ANN and FL for estimating the luminance value (cd/m²) on the road surface are not far from the experimental results. The graphs obtained as a result of the predictions showed that an accurate prediction can be made through ANN and FL. However, the accuracy rate of those obtained with FL was slightly lower than the prediction method with ANN.
- The accuracy rate in prediction with ANN was found to be 98.525%, and the accuracy rate in prediction with FL was found to be 97.43%. This shows that the prediction error made with ANN is lower.
- Although prediction with ANN performs slightly better than FL, prediction with FL may be preferred in estimating the luminance value.
- While FL is encoded similar to the human mind, the ANN prediction model is a black box that humans cannot see.
- With normalization in ANN, input and output values must be in the range (0.1). It is not necessary to normalize in FL. However, inference must be made by blurring the data. Specific rules must be defined and formulated.

- In ANN, input, output and test data and some functions are introduced to the program. In FL, in addition to input and output, membership functions are defined and a table is created.
- 2 input data and 6 output data were used with ANN. Additionally; 8 neurons were used as hidden layers. nntool
- Software in Matlab was used. The same input and output data were used in FL. Significantly, FL used “fuzzy” software in Matlab.
- In FL, membership functions were required as estimation conditions. However, introducing the inputs and outputs of the system was sufficient for ANN.

4. RESULTS

In this study, the values found using ANN and FL methods were compared. ANN made its prediction with a validation value of 98.525%. The test regression value of the target values was achieved with a high validity of 96.366%. The entire input regression value was found to be 98.525%. We see that the training values in Training are 95.699% correct. It is observed that the prediction was 96.085% correct in total. When the results obtained in the prediction made with FL were tested with the approximate values given, it was seen that it was realized at a rate of 96%. 4% of the errors were obtained depending on the defined rules. As a result of

the predictions made by classifying numerical data according to qualitative characteristics in FL, the accuracy rate in prediction with FL was found to be 97.43%. Approximately 2.57% incorrect results were obtained depending on the defined rules. According to the results of both prediction methods, the accuracy rate in the calculation with ANN was found to be approximately 98.525% and in the calculation with FL was approximately 97.43%.

REFERENCES

- [1] Jin H., Jin S., Chen L. et al. Research on the Lighting Performance of LED Street Lights With Different Colour Temperatures, IEEE Photonics Journal, Aralık 2015, Cilt: 7 , Sayı: 6. <https://doi.org/10.1109/JPHOT.2015.2497578>
- [2] Dursun S., Terzi U.K., Akar O. et al. Comparative Analysis of Lighting Elements Effects on Electric System, European Journal of Technique (EJT), 2021, Vol. 11, .2. <https://doi.org/10.36222/ejt.981153>
- [3] Onaygil S., Guler O., Erkin E. Cost Analyses of LED Luminaires In Road Lighting, Light & Engineering, 2012, Vol. 20, 2, pp. 39–45.
- [4] Cengiz M.S. The Relationship between Maintenance Factor and Lighting Level in Tunnel Lighting, Light & Engineering, 2019, Vol. 27, 3, pp. 75–88. <https://doi.org/10.33383/2018>
- [5] Pracki P., A proposal to classify road lighting energy efficiency”, Lighting Research & Technology, Vol. 43, 3, pp. 271–280, 2011.
- [6] Falchi F., Cinzano P., Elvidge C.D. et al. Limiting the impact of light pollution on human health, environment and stellar visibility, Journal of Environmental Management, 2011, Vol. 92, 10, pp. 2714–2722. <https://doi.org/10.1016/j.jenvman.2011.06.029>
- [7] Akgun I., Ustaoglu E., Multi-Methodological Design Framework for Roadway Illumination, Light & Engineering, 2022, Vol. 30, 1, pp. 39–50. <https://doi.org/10.33383/2021-084>
- [8] International Dark Sky Association, Visibility, Environmental and Astronomical Issues Associated with Blue Rich White Outdoor Lighting, Technical Report, Tucson-Washington, DC, 2010.
- [9] CIE (Commission Internationale de l’Eclairage), Road lighting as an accident countermeasure, Vienna (Austria): CIE No. 093–1993, pp. 1–43, 1993. ISBN: 978 3 900734 30 5
- [10] Elvik R. Meta-analysis of evaluation of public lighting as accident countermeasure, Transp. Res. Rec., 1995, 1485.1, pp.112–123. <https://onlinepubs.trb.org/Onlinepubs/trr/1995/1485/1485-015.pdf>
- [11] Wanvik A. Effects of road lighting: an analysis based on Dutch accident statistics 1987–2006, Dutch statistics report, 2006. <https://doi.org/10.1016/j.aap.2008.10.003>
- [12] Sun C., Lee X., Morenoet I. al. Design of LED Street Lighting Adapted for Free-Form Roads, IEEE Photonics Journal, 2017, Vol. 9, 1, pp. 1–13. <https://doi.org/10.1109/JPHOT.2017.2657742>
- [13] Gan F., Grabosky P. Improved Street Lighting and Crime Reduction, the Promise of Crime Prevention, 2nd ed., 2000, ISBN0 642 24172 4; ISSN1326–6004 Canberra, Australian Institute of Criminology.
- [14] Guler O., Onaygil S. The effect of luminance uniformity on visibility level in road lighting, Lighting Research & Technology, Sep.2003, Vol. 35, 3, pp. 199–215. <https://doi.org/10.1191/1365782803i074oa>
- [15] Hirakawa S., Karasawa Y., Funaki T. et al. Evaluation Index of Visibility in Tunnel Lighting, Journal of Light & Visual Environment, , 2014, Vol. 38. <https://doi.org/10.2150/jlve.IEJ130000529>
- [16] Painter K.A., Farrington D.P. Evaluating Situational Crime Prevention a Young People’s Survey, The British Journal of Criminology, London, Spring 2001, V. 41, 2, pp. 266–284. <https://doi.org/10.1093/bjc/41.2.266>
- [17] Robbins C.J., Fotios S. Road lighting and distraction whilst driving: Establishing the significant types of distraction roads, Lighting Research & Technology, APR8. 2020. <https://doi.org/10.1177/1477153520916515>
- [18] Ekriasa A., Eloholma M., Halonen L. et al. Road lighting and headlights: Luminance measurements and automobile lighting simulations, Building and Environment, Elsevier, Vol.43,4,pp.530–536,2008. <https://doi.org/10.1016/j.buildenv.2007.01.017>
- [19] H. Nikunen, Correspondence: A proposed new LED road lighting concept, Lighting Research & Technology, 2014, Vol.46, 2, pp. 238–239. <https://doi.org/10.1177/1477153514524902>
- [20] CIE Publication CIE140–2000: Road lighting calculations /ISBN:3–901–906–03–7. <https://www.scribd.com/document/351164108/CIE-Road-Light-Calculations-CIE140-2000-pdf>
- [21] Wandachowicz K., Przybyla M. The Measurements of the Parameters of Road Lighting- Theory and Practice, IEEE, 2018, VII. Lighting Conference of the Visegrad Countries (Lumen V4) Proceeding, 2018, pp. 1–5. <https://doi.org/10.1109/LUMENV.2018.8521148>
- [22] TS CEN/TR13201–1: Road Lighting, Selection of Road Lighting Classes ,Turkish Standards Institute, 2006.
- [23] TS EN13201–2: Road Lighting, Performance Characteristics ”, Turkish Standards Institute, 2006.
- [24] Gaston, K.J., Gaston, S., Bennie, J., et al. Benefits and costs of artificial nighttime lighting of the environment, Environmental Reviews, 2014. <https://doi.org/10.1139/er-2014-0041>
- [25] TS EN13201–3:Road Lighting, Calculation of Performance, Turkish Standards Institute, 2006.
- [26] Sutandi A.C., Pinem, R.D.A. The application of road lighting standard towards sustainable transportation in large cities in Indonesia, Procedia Engineering,2017, Vol. 171,pp.1463–1471. <https://doi.org/10.1016/j.proeng.2017.01.471>
- [27] TS EN13201–4:Road Lighting, Lighting Performance Measurement Methods, Turkish Standards Institute, 2006.
- [28] Lighting with Artificial Booklet 1. Förläggare: Gutes Licht, 2008.
- [29] Thomson W.D. Eye problems and visual display terminals – the facts and the fallacies, Ophthalmic Physiol. Opt., Mar.1998, Vol.18,2,pp.111–119. [https://doi.org/10.1016/S0275-5408\(97\)00067-7](https://doi.org/10.1016/S0275-5408(97)00067-7)
- [30] Buchner A., Mayr S., Brandt M. The advantage of positive text background polarity is due to high display luminance, Ergonomics,2009, Vol.52,7,pp.882–886. <https://doi.org/10.1080/00140130802641635>
- [31] Bhattacharya S., Chakraborty S., Ray S. An Approach to Comparative simulation of Road Lighting and Estimation of Associated Quality Parameters, Light& Engineering, 2021, Vol.29,1,pp. 77–87. <http://dx.doi.org/10.33383/2020-058>
- [32] Gyurov V., Panchev H. Experimental Research on Light and Energy Parameters of Intelligent Street and Road Lighting Systems, 11th Electrical Engineering Faculty Conference (BulEF),1–4, IEEE Explore Digital Library, Sep. 2019. <https://doi.org/10.1109/BulEF48056.2019.9030760>
- [33] Markvica K., Richter G., Lenz G., Impact of urban street lighting on road users’ perception of public space and mobility behavior, Elsevier, Building and Environment,2019, Vol. 154, pp. 32–43. <https://doi.org/10.1016/j.buildenv.2019.03.009>
- [34] Bozorg S., Tetri E., Kosonen I. et al. The Effect of Dimmed Road Lighting and Car Headlights on Visibility in Varying Road Surface Conditions, Leukos, 2018, Vol. 14,4,pp.259–273. <https://doi.org/10.1080/15502724.2018.1452152>
- [35] Chenani S. B., Vaaja M.T., Kurkela M. et al. Target detection Distances under different road lighting intensities, Transport Research Review: An Access Journal, June 2017, Vol. 9, 2, pp. 1–10, Springer Nature Journals. <https://doi.org/10.1007/s12544-017-0234-z>
- [36] Yoomak S., Jettanaseen C., Ngaopitakkul A. et al. Comparative study of lighting quality and power quality for LED and HPS luminaires in a

- roadway lighting system, Elsevier, Energy and Buildings, 2018, Vol. 159, pp. 542–557. <https://doi.org/10.1016/j.enbuild.2017.11.060>
- [37] Xu B., Yang S., Lai G. et al. Towards Autonomous Driving Technology: A Method to Enhance Visibility in Fog Based on Low-Position Road Lighting, Proceedings of 2018 IEEE3rd Optoelectronics Global Conference (OGC), Sep 2018, pp. 205–208. <https://doi.org/10.1109/OGC.2018.8529877>
- [38] Ogando-Martínez A., Troncoso-Pastoriza F., Granada-Álvarez E. et al. Ellipsoid-based approximation method for the estimation of the actual reduced luminance coefficients of road surfaces for accurate lighting simulations, Elsevier, Sustainable Cities and Society, 2020. <https://doi.org/10.1016/j.scs.2020.102502>
- [39] Ekrias A., Eloholma M., Halonen L. et al. Road lighting and headlights: Luminance measurements and automobile lighting simulations, Building and Environment; 2008, Vol.43,pp.530-536. <https://doi.org/10.1016/j.buildenv.2007.01.017>
- [40] Kayakus M., Uncu I. Research note: the measurement of road lighting with developed artificial intelligence software, Lighting Research & Technology, 2019, Vol. 51, 6. <https://doi.org/10.1177/1477153519825564>
- [41] Kazanasmaz T., Gunaydın M., Binol S. Artificial neural networks to predict daylight illuminance in office buildings, Building and Environment, 2009, Vol. 44, 8, pp. 1751–1757. <https://doi.org/10.1016/j.buildenv.2008.11.012>
- [42] Tran D., Tan Y. K. Sensor less illumination control of a networked LED lighting system using feedforward neural network, IEEE transactions on industrial electronics, 2013, Vol. 61, 4, pp. 2113–2121. <https://doi.org/10.1109/TIE.2013.2266084>
- [43] Ok Davarci Z. Yol Aydınlatma Sistemlerine Ait Etkinlik Faktorlerinin ve Parlak Duzgunluğunun Yapay Sinir Ağı ile Tahmini, Afyon Kocatepe Universitesi, Fen Bilimleri Enstitüsü, Yüksek lisans, Afyon, 2022. <https://info.eu-repo/semantics/openAccess>
- [44] Ok Davarci Z. et al. Yol Aydınlatma Sistemlerinde Parlaklığın YSA Tahmini, ELECO 2022, Elektrik-Elektronik ve Biyomedikal Mühendisliği Konferansı, Bursa, Turkey. http://www.eleco.org.tr/ELECO2022/eleco2022_papers/48.pdf
- [45] Es H. A., Kalender F. Y., Hamzaçebi C. Yapay Sinir Ağı ile Türkiye Net Enerji Talep Tahmini, Gazi Univ. Muh. Mim. Fak. Der., 29 (3), 495-504, 2014. <https://www.researchgate.net/profile/Coskun-Hamzaçebi-2/publication/284449011>
- [46] Kelesoglu O., Firat A. Tuğla Duvardaki ve Tesisattaki Isı Kaybının Yapay Sinir Ağı ile Belirlenmesi, Firat Üniversitesi Fen ve Muh. Dergisi, 18(2), 133-141, 2006. <https://search.trdizin.gov.tr/tr/yayin/detay/64898>

1996 to 2000 as a lecturer, from 2000 to 2013 as an Assistant Prof. Dr., from 2013 to 2020 as an Asc. Prof. Dr. for university of Marmara. Since 2020 he has been working as an Prof. Dr. for Electrical and Electronics department of Technology Faculty of Marmara University.

BIOGRAPHIES

Zuleyha OK DAVARCI, was born in Lubeck, Germany. He graduated from Kırıkkale University, Department of Electrical and Electronics Engineering in 2002. He completed his master's degree at Afyon Kocatepe University, Faculty of Technology, Department of Electrical and Electronics Engineering. He works as a manager at OK Engineering. His research areas include Lighting and systems, ANN and applications.

Onur AKAR, was born in Giresun in 1981. He received his bachelor's, master's and doctoral degrees from Marmara University in 2005, 2011 and 2020, respectively. He worked as a lecturer at Istanbul Gedik University between 2010-2020. He served as Head of Electrical Program at Istanbul Gedik University between 2012 and 2015. In 2021, he served as Assistant Professor and Head of the Electricity and Energy Department at the same university. In 2023, he is still working as an Assistant Professor at Marmara University, Department of Electronics and Automation. His research areas include; Control Systems, Renewable Energy Systems, Power Systems and Lighting Systems.

Umit K. TERZI, was born in Zonguldak in 1968. He received his B.S. degree from Electrical Education Department of Technical Education Faculty of University of Marmara, Istanbul, in 1989 and his M.Sc. and Ph.D. degree from Electrical Education Department of Institute of Pure and Applied Sciences, University of Marmara, Istanbul, in 1994 and 2000 respectively. From 1989 to 1996, he worked as a research assistant, from

Research Article

The Investigation of Performance And Emission Characteristics Of Waste Transmission Oil On A Diesel Engine

Mehmet Zerrakki IŞIK^{1*}, Serkan DEMİR²

^{1*} Department of Mechanical Engineering Batman University, 72100 Batman, Turkey. (e-mail: mehmetzerrakki.isik@batman.edu.tr).

²İC İçtaş İnşaat A.Ş., Batman, Turkey. . (e-mail: serkan.demir23@hotmail.com)

ARTICLE INFO

Received: May., 09. 2023

Revised: Dec., 23. 2023

Accepted: Dec, 29. 2023

Keywords:

Pyrolysis Method

Diesel Fuel

Transmission Waste Oil

Diesel Generator

Corresponding author: M. Zerrakki

IŞIK

ISSN: 2536-5010 / e-ISSN: 2536-5134

DOI: <https://doi.org/10.36222/ejt.1294386>

ABSTRACT

Environmental issues such as ever-increasing energy demand, declining fossil fuel deposits, global warming and higher levels of air pollution necessitate the transition to renewable fuels. It is necessary to develop a cleaner, safer, sustainable and renewable alternative for fossil fuels. For the production of such fuels using thermochemical processes, it is important to use products with a fuel potential in a waste state. In this context, it is proposed to convert waste transmission oil. Accordingly, in the study, Diesel-like fuel was obtained from waste transmission oil through the pyrolysis method. The fuel produced is a mixture of diesel with waste transmission oil, 80% diesel and 20% waste transmission oil. Engine tests were carried out with the use of the produced mixture fuel and pure diesel fuel in a diesel generator engine and the necessary comparisons were carried out. Performance and emission tests were carried out in the study. Compared to diesel fuel, an increase of 4% in thermal efficiency at low loads and an increase of 2.5-3% in specific fuel consumption was determined. The NO_x emission of blended fuel is much higher than diesel fuel at all loads. The change with increasing load is limited to 18.5-25%. A 25% reduction in HC emissions was observed. According to the test results obtained, it can be said that the waste transmission oil-doped mixture fuel produced can be used instead of diesel fuel for its intended purpose.

1. INTRODUCTION

Environmental issues such as ever-increasing energy demand, decreasing fossil fuel deposits, global warming and higher levels of air pollution; require the transition to renewable fuels. Engineering studies; aim to develop a cleaner, safer, sustainable and renewable alternative to fossil fuels. In the process, it is important to use wastes that can be converted into fuel. In this regard, it has been proposed to convert waste transmission oil to produce such fuels using thermochemical processes [1].

Production of various fuels; thermochemical conversion, torrefaction, pyrolysis and gasification etc. possible by using various methods [2]. Fast pyrolysis, it is considered an important route as it results in a high energy density diesel fuel. These diesel fuels, oil products that are not suitable for use, etc. can be produced from fuels [3]. Thus, the abundance of raw materials suitable for the fuel production process, promotes thermochemical transformations.

Carbon and hydrogen, it forms the origin of diesel fuel, like most fossil fuels. For ideal thermodynamic equilibrium, a full combustion of diesel fuel will only produce CO₂ and H₂O in the engine combustion chambers [4]. However, many reasons (air-fuel ratio, ignition timing, turbulence in the combustion

chamber, combustion form, air-fuel concentration, combustion temperature, etc.) make this impossible and a number of harmful products are produced during combustion. The most important harmful products are CO, HC, NO_x and Particulate Matter (PM).

Any mineral oil or synthetic oil becomes chemically and physically contaminated and loses its originality after a certain period of use in industrial or non-industrial areas. These types of oils cannot perform well due to long usage over time. In this direction, it is preferred to replace used oils with new oils in order for the engine to work better.

On the other hand, waste oils have eco-toxic properties, pollute the environment they are in and harm all living organisms in the environment. It is forbidden to dispose of them in places such as stoves or small ovens. The reason for this is that the heavy metal and chlorine compounds in the waste oil are released into the atmosphere together with the waste air, polluting the air and harming human health.

Arpa et al. [5] conducted an experimental study on diesel-like fuel (DLF) for engine performance and exhaust emission change. In the study, it was observed from the test results that approximately 60 cc of waste oil was converted to DLF from every 100 cc of waste oil. This result showed that the produced DLF can be used in diesel engines without any problems in

terms of engine performance. DLF increased torque, brake average effective pressure and brake thermal efficiency, and also reduced the brake-specific fuel consumption of the engine for full operating power.

In addition to the information given above, we can mention that the properties of fuels and distillation temperatures are other effects on performance parameters [6]. Obviously, these properties lead to the fact that fuels give better mixing and combustion properties and reduce heat loss. Because lower distillation temperatures ensure better performance results [7].

İlkılıç and Aydın [8] conducted an experimental study on an alternative fuel obtained by pyrolysis of waste vehicle tires. In the study, pure diesel, pure tire pyrolysis oil and their mixtures in different fractions were used. At the end of the study, it was determined that the power values of all fuel mixtures of pyrolysis fuel and diesel fuels showed increasing trends according to the increase in engine speed.

Pyrolysis is the thermochemical decomposition of organic matter caused by heat, in the absence of oxygen or any other reagent. During the pyrolysis process, large complex hydrocarbon molecules are converted into different smaller molecules of gas, liquid and coal. While temperatures of 450 °C and above are preferred for obtaining liquid products, lower temperatures are preferred for liquid production. Although the pyrolysis liquid has a dark color, it may vary depending on the sample used and its content [9]. The processed raw material enters the reactor, where it is heated up to the pyrolysis temperature (maximum temperature) at which decomposition will begin. The next stage is when the condensable and non-condensable vapors released from the feedstock leave the compartment. Although the vast majority of the solid coal produced remains in the compartment, a small part of it also remains in the gas. The next stage is to separate the gas from the coal and cool the downstream of the reactor. The final stage is the condensation of the condensable steam as pyrolysis oil, it is the process of separating the non-condensable steam from the reactor as product gas. In this process, solid coal is collected as a commercial product or used as a combustible to produce the heat necessary for pyrolysis [10].

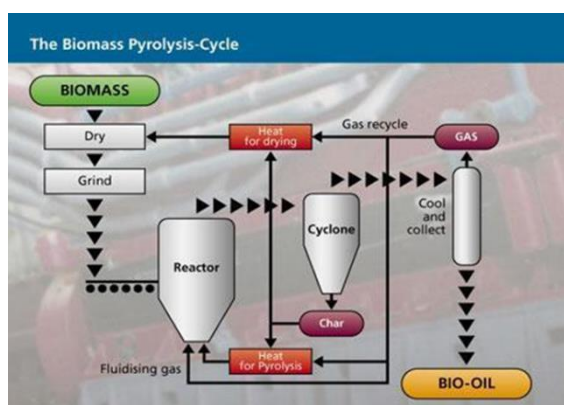


Figure 1. Pyrolysis Cycle [Abnisa and Wan Daud, 2014]

The most important products to be obtained by pyrolysis method are liquid products. Because liquid products can be an important substitute for fossil fuels, the nature of which depends on different parameters. The factors mentioned are; the type of raw material used in the process, temperature depending on the characteristics of the raw material, heating rate, reaction time and the particle size of the feed. The

parameters affecting the pyrolysis process at this point are the type of raw material used in the process, the temperature which depends on the characteristics of the raw material, heating rate, reaction time and particle size of the feed [11].

2. MATERIALS AND METHODS

In this research, fuel obtained from waste transmission oil by pyrolysis method and pure diesel fuel were used in a single cylinder generator engine as a mixture. Volumetric ratios of diesel and mixed fuel are given in Table 1.

TABLE I
VOLUMETRIC RATIOS OF DIESEL AND DIESEL-LIKE FUEL

	Volumetric Percentage of Diesel Fuel	Volumetric Percentage of Waste Transmission Oil
D80WTO20	80	20
DIESEL	100	0

Table 2 provides information about the chemical and physical properties of the fuels to be used in the experiments.

TABLE II
THE DETERMINATION OF THE PHYSICAL AND CHEMICAL PROPERTIES OF FUELS TO BE USED IN DIESEL ENGINE EXPERIMENTS

Properties	DF	Pyrolytic Fuel
Density (gr/cm ³)	0,830	0,860
Viscosity (mm ² /sn)	2,90	3,60
Flash Point (°C)	60	51,5
Lower Thermal Value (kj / kg)	43200	40400
The Amount of Sulfur (ppm)	50	>1000
Cetane Number	53	48

A schematic representation of the experimental setup created for the study is given in Figure 2.

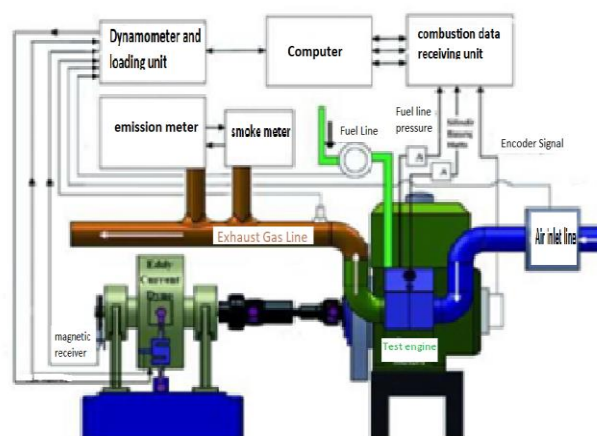


Figure 2. Schematic Representation of the Experimental Setup

3. RESULTS AND DISCUSSIONS

At the point of meeting the increase in energy demand which is an increasing value every day, we are faced with two options. The first is to find new renewable energy sources. The second

is to obtain fuel from waste. In order to serve this purpose in the study, waste transmission oils (WTO), which pollute the nature, have been converted into a form that can be used in engines. After that, combustion, performance and emission tests were performed. Two types of fuel were used in the experiments. These fuels have been subjected to engine tests under 3 different loads. These loads are respectively; no load, 5 kg and 10 kg. At the end of the study, the engine test results of two different fuels under different loads.

3.1. Statistical analysis

In order to better confide on the measurement data from the experimental engine, this section of the paper has been presented. The confidence level of 0.95 or $\alpha=0.05$, standard error, means and confidence intervals of the test values of the test engine operated with varied test fuels are included in Table III for emissions and in Table 4 for engine performance that contains statistical analysis parameters. For all experiments, the target level of test confidence was 95%. The test findings include standard error and mean those were computed. These data were used to compute the confidence intervals, which are displayed in Table III and Table IV as the level of deviation from means for each parameter of the applied tests. The experimental data points' confidence intervals are calculated by subtracting and adding the confidence from the mean values. It is simple to conclude that the confidence intervals and other statistical parameters for the chosen confidence levels are significant and well-concordant, indicating that the used tests parameters are quite stable and reliable.

TABLE III

THE STATISTICAL ANALYSIS PARAMETERS OF EXPERIMENTAL POLLUTANT EMISSION INDICATORS

		D100	D80WTO20
CO	Confidence Level	0.05	0.05
	Standard Error	0.01	0.01
	Number of Experiments	3.00	3.00
	Mean Values	0.02	0.02
	Confidence interval	0.01	0.01
CO₂	Confidence Level	0.05	0.05
	Standard Error	0.55	0.65
	Number of Experiments	3.00	3.00
	Mean Values	1.27	1.57
	Confidence interval	0.62	0.74
HC	Confidence Level	0.05	0.05
	Standard Error	0.58	1.73
	Number of Experiments	3.00	3.00
	Mean Values	11.3	7.00
	Confidence interval	0.65	1.96
NO_x	Confidence Level	0.05	0.05
	Standard Error	95.7	132.5
	Number of Experiments	3.00	3.00
	Mean Values	126	146
	Confidence interval	108	150

TABLE IV

THE STATISTICAL ANALYSIS PARAMETERS OF EXPERIMENTAL PERFORMANCE INDICATORS

		D100	D80WTO20
η_{th} (%)	Confidence Level	0.05	0.05
	Standard Error	22.18	21.70
	Number of Experiments	3.00	3.00
	Mean Values	26.94	26.43
	Confidence interval	25.10	24.56
Be (gr/kWh)	Confidence Level	0.05	0.05
	Standard Error	147.64	143.95
	Number of Experiments	3.00	3.00
	Mean Values	458.63	466.12
	Confidence interval	167.06	162.89
η_e (%)	Confidence Level	0.05	0.05
	Standard Error	0.55	0.65
	Number of Experiments	3.00	3.00
	Mean Values	1.27	1.57
	Confidence interval	0.62	0.74

3.2. Performance Parameters Tests

Equivalent heater resistance groups were used to draw energy from the engine generator group. In order to determine the engine performance parameters in the experimental setup, fuel consumption values were taken from precision scales. For this purpose, 1-minute fuel consumption values were determined in order to stabilize the engine operating conditions during fuel changes, and the average value obtained was accepted as kg/h fuel consumption value with the formula below. The performance characterizes of both fuels are analyzed and depicted in Fig. 3.

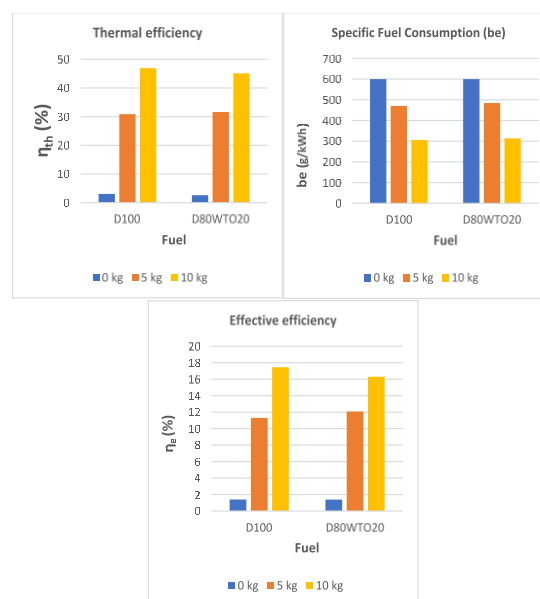


Figure 3. Performance Parameters of fuels

The η -thermic values of the blended fuel compared to the diesel fuel were found to be very close to each other for all loads. In both types of fuel, the values in the unloaded state are quite low compared to the η -thermic values in other loads. In addition, as the amount of load increased in both fuels, their η -thermic values have also increased. In other words, a direct proportion was found between them.

Specific fuel consumption is expressed as the value in grams (g/kWh) of the fuel that the engine should consume per kWh of work in stable operation. As can be seen, the highest specific fuel consumption was recorded in the no-load condition. As the load amount increased, the specific fuel consumption was decreased. In other words, an inverse proportion was observed between them. In addition, the specific fuel consumption of blended fuel is slightly higher than that of diesel. Specific fuel consumption is an important parameter for determining performance in engines and can be defined as the amount of fuel that must be spent to obtain unit power. There is higher specific fuel consumption compared to diesel since the heating value decreases in the use of the mixture.

The effective efficiency is described as the ratio of the work received from the motor shaft to the total energy delivered. The thermal values of the fuels used in the experiments are given in Table V.

TABLE V
THERMAL VALUES OF THE FUELS USED IN THE EXPERIMENTS

Fuel	Thermal Value (kJ/kg)
Diesel	42700
Waste Transmission Oil	41500

According to the data, the effective efficiency increased as the load amount increased in both types of fuel. The effective efficiency in the no-load state is quite low compared to the conditions under load. The effective efficiency of the blended fuel is close to that of diesel. However, with the increase in load, partial reductions have appeared, depending on the development of the combustion process, its duration and thermal value.

3.3 Emission Tests

The emission characterizes of both fuels are analyzed and depicted in Fig. 4. Oxygen emission has been measured as a percentage by volume of the total air expelled from the exhaust. As the speed of the test engine operated with diesel fuel is increased, the amount of oxygen emitted from the exhaust also decreases. It is thought that the reason for this is the combustion efficiency of the parameter. When there is a lack of oxygen in combustion, carbon (C) does not burn sufficiently. When the speed is increased, the amount of fuel that needs to be burned per unit time and the amount of O₂ that will be used in the combustion reaction will also increase. Therefore, due to the increase in speed, the amount of oxygen needed in the face of fuel has increased. Thus, the amount of oxygen entering into the reaction also has increased. In this respect, it is thought that the O₂ released from the exhaust decreases. The amount of oxygen emitted by diesel and D80WTO20 fuels from the exhaust has been obtained inversely proportional to the

increase in the amount of load. In other words, as the amount of load increased, the amount of O₂ released has decreased. As can be understood from here, it can be said that the combustion efficiency is well realized.

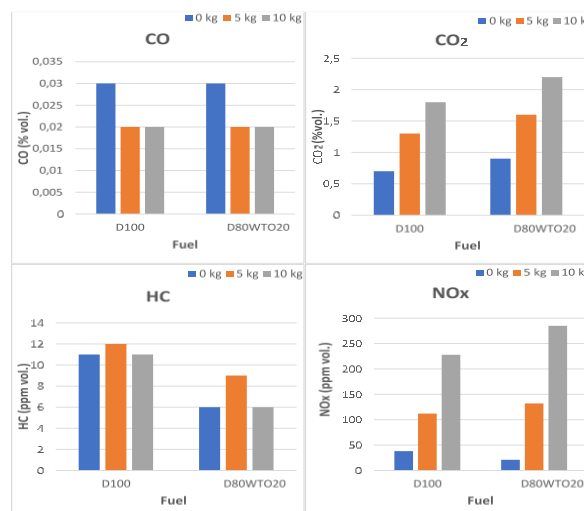


Figure 4. Emission formation of fuels

Carbon monoxide (CO), when taken too much into the human body, sticks to hemoglobin, reducing the oxygen carrying capacity of the blood. In the brain and heart, which are the basic organs of life, functional disorders occur due to oxygen deficiency. For this reason, it is not desirable that the amount of CO in vehicle exhaust waste is excessive. As can be seen in the given graph, CO emissions has decreased for both fuels depending on the increase in the load. CO emissions are greatest at no load. In other loads, the CO release is the same amount. In addition, the emission amounts of both fuels has given the same result. While the highest CO emission is 0,03 %vol, other emission amounts are 0,02 %vol. However, emissions are at an acceptable level in both these fuel samples. High temperature, incomplete air and incomplete combustion have increased the amount of CO at low speeds.

Carbon dioxide (CO₂) is odourless, colorless and tasteless. CO₂ does not appear as a toxic gas, but when it exceeds 30%, it causes damage to breathing [12]. Depending on the load increase in both fuel types, an increase in CO₂ emissions was observed. However, the amount of CO₂ emission of D80WTO20 fuel was found to be more than diesel in each load amount. As the load amount increases, the better the combustion has given off due to increased air movements. In addition, combustion at low loads gave a better result. In this case, while the amount of CO decreased, it has caused an increase in CO₂. The increase in CO₂ emissions can be explained by the improvement of combustion and therefore the conversion of more CO to CO₂.

Hydrocarbons (HC) are unburned fuel components that arise as a result of an irregular reaction in which combustion does not occur to the desired extent. These components, which can come out of the exhaust in different forms, have negative effects on human health, such as cancer [13]. While a decrease is expected in the number of carbons released from the cylinder with a good combustion, an increase in the number of carbons is expected in the exhaust with a bad combustion. While the increase in the amount of HC continued, it was determined that the amount of HC in diesel fuel was higher. The D80WTO20 is more efficient than diesel in terms of the amount of HC. It

can be said that the reason for the high level of HC emissions is insufficient combustion. It has been shown that the reason why fuels produce high HC emissions is that the thickness of the extinction zone increases due to low temperature.

Internal combustion engines powered by diesel fuel account for more NO_x than gasoline engines. Nitrogen oxides are released due to engine operation under high temperature conditions [14]. The main reason for this is that diesel fuel needs more air for combustion. During combustion, nitrogen (N₂) and oxygen (O₂) combine at high temperatures to form Nitrogen oxides (NO_x). Arpa et al. [15] in the study of, NO emissions of diesel-like fuels were higher than diesel. NO_x values are highest at the moment when the weight was highest. Figure 6 was shown data on NO_x emissions of nitrogen oxides. Accordingly, the NO_x emission of the blended fuel is much higher than that of diesel fuel at all loads. When D80WTO20 fuel was examined, it was seen that NO_x emissions increased in direct proportion with increasing the load amount. It can be said that at low speeds, poor combustion occurs due to excessive load and insufficient air. The temperature increase due to the load has increased the amount of NO_x. Evaporation of fuel depends on its properties, such as its interaction with air and viscosity. All these factors affect the spray advance, ignition delay, pre-combustion and flame spread, that is the formation of NO_x as a result.

4. CONCLUSIONS

As a result of the conducted experimental research, the following conclusions were reached:

- As a result of the pressure increase rate test; as the load amount increased, the characteristic similarity of the fuel types increased. With the increase in the load amount, the pressure increase rate also has increased.
- The cumulative heat release between fuels has differed depending on the content of the fuels. The cumulative heat release for the D80WTO20 has steadily increased as the amount of load has increased. But it consistently has a lower cumulative heat release value than diesel fuel. The heat release for D80ASY20 is close to 90% of the diesel fuel value. The reason for this situation is that the emulsified mixture contains low heat.
- As the load amount increases, the cylinder pressure increases. The cylinder pressure in diesel fuel has always given more results than in D80WTO20 fuel.
- It is observed that the specific fuel consumption of D80WTO20 fuel is higher than diesel fuel. The change is limited to 2.5-3%.
- It has been determined that the amount of oxygen released from the exhaust of the D80WTO20 fuel mixture is inverse with the increase in the load it carries. It can be said that an efficient combustion has taken place.
- With the increase in the load amount, the CO emission decreased for the blended fuel.
- It has been observed that CO₂ emissions increase in diesel and blended fuels with the increase in the load amount. However, compared to diesel fuel, the CO₂ emission of the blended fuel is lower.
- Since hydrocarbons (HC) enter the combustion reaction at desired levels, the amount of O₂ and HC discharged

from the exhaust is lower than diesel fuels. The change is limited to 25%.

- The NO_x emission of blended fuel is much higher than diesel fuel at all loads. At low speeds, it can be said that poor combustion occurs due to overload and insufficient air. The change with increasing load is limited to 18.5-25%.

Due to the excess of waste transmission oil, using it instead of fuel will be beneficial for both the environment and fuel economy.

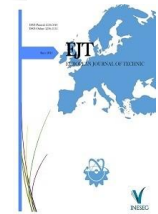
REFERENCES

- [1] Roy, P. ve Dias, G. Prospects for pyrolysis technologies in the bioenergy sector: A review, *Renew. Sustain. Energy Rev.* 77 (2017) 59–69.
- [2] Bridgwater, T. Biomass for energy, *J. Sci. Food Agric.* 86 (2006) 1755–1768.
- [3] Sipra, A.T. Gao,N. Sarwar,H. (2018). Municipal solid waste (MSW) pyrolysis for bio-fuel production: A review of effects of MSW components and catalysts, *Fuel Process. Technol.* 175 (2018) 131–147.
- [4] Prasad R, Bella VR (2010) A review on diesel soot emission, its effect and control. *Bull Chem React Eng Catal* 5(2):69–86
- [5] Arpa O, Recep Y, Zeki A Experimental investigation of the effects of diesel-like fuel obtained from waste lubrication oil on engine performance and exhaust emission. *Fuel Process. Technol.* 91:1241-1249 (2010a).
- [6] Koç M, Sekmen Y, Topgul T, Yucesu HS (2009). The effect of ethanolunleaded gasoline blends on engine performance and exhaust emissions in a sparkignition engine. *Renew. Energy* 34:2101-2106.
- [7] Al-Ghouti MA, Al-Degs YS, Amer M (2008). Determination of motor gasoline adulteration using FTIR spectroscopy and multivariate calibration. *Talanta* 76:1105e12.
- [8] İlkılıç, C., Aydın, H. Fuel production from waste vehicle tires by catalytic pyrolysis and its application in a diesel engine, *Fuel Processing Technology*, 2011 – Elsevier.
- [9] Uyar M, Aydın H; Production of low sulfur diesel-like fuel from crude oil wastes by pyrolytic distillation and its usage in a diesel engine. *Energy*, Volume 244, Part A, 1 April 2022, 122683
- [10] Basu, P. Biomass gasification, Pyrolysis and Torrefaction, Second Edi. 2013.
- [11] Abnisa F. and W. M. A. Wan Daud, “A review on co-pyrolysis of biomass: An optional technique to obtain a high-grade pyrolysis oil,” *Energy Convers. Manag.*, vol. 87, pp. 71–85, Nov. 2014.
- [12] Ayaz, M. E. (2003). Hacıralı ve Karayün (Sivas) Çevresinin Jeolojisi ve DoğalKarbon dioksit Potansiyeli. *FÜ Fen ve Mühendislik Bilimleri Dergisi*, 15(4), 523-538.
- [13] Aydoğan, H. (2006). Dizel Motorlarında Çeşitli Yakıt Enjeksiyon Sistemlerinin EgzoEmisyonlarına Etkilerinin Deneysel incelenmesi. Yüksek Lisans Tezi, Gazi Üniversitesi,Ankara.
- [14] Hanbey H, Uyar M, Aydın H; The Effects of Apricots Seed Oil Biodiesel with Some Additives on Performance and Emissions of a Diesel Engine. *International Journal of Automotive Engineering and Technologies* Vol. 5, Issue 3, pp. 102 –114, 2016
- [15] Arpa O, Yumrutas R, Alma MH Effects of turpentine and gasoline-like fuel obtained from waste lubrication oil on engine performance and exhaust emission. *Energy* 35:3603-3613, (2010b).

BIOGRAPHIES

Mehmet Zerrakki İŞİK obtained his BSc degree in mechanical engineering from Fırat University in 2004. He received the MSc diploma in Mechanical Engineering from the Fırat University and Phd degree in Graduate School of Science from Batman University. His research interests are energy, internal combustion engine systems. In 2010 he joined the Faculty of Mechanical Engineering, Batman University as a research assistant, where he is presently a assistant professor.

Serkan DEMİR obtained his BSc degree in Petroleum and Natural Gas Engineering from Batman University in 2017. He received the MSc diploma in Mechanical Engineering from the Batman University in 12021 respectively. Her works as an workover and well completion engineer.



Research Article

Changes in the Electrical Output Power and Efficiency of a Photovoltaic Panel Cooled by a Hybrid Method

Ömer Karaozan¹ , Mehmet Emin Asker^{2*} 

¹Dicle University, Electrical Engineering Department, Diyarbakır, Turkey. (e-mail: karaozan_47@hotmail.com).

^{2*}Dicle University, Department of Electricity and Energy, Vocational School of Technical Sciences, Diyarbakır, Turkey (e-mail: measker@dicle.edu.tr).

ARTICLE INFO

Received: Dec., 13. 2023

Revised: Dec., 28. 2023

Accepted: Dec., 29. 2023

Keywords:

Water cooling

Electrical power increase

Aluminum finned

Heat sink

Transformer oil

Corresponding author: Mehmet Emin ASKER

ISSN: 2536-5010 / e-ISSN: 2536-5134

DOI: <https://doi.org/10.36222/ejt.1404493>

ABSTRACT

This study examines two cooling methods for photovoltaic panels to counteract efficiency loss due to high temperatures and radiation. The first method employed active cooling with water, while the second combined active and passive cooling using an aluminum heat sink with water as the medium. Three identical 100 W monocrystalline photovoltaic panels were analyzed, with one serving as the reference. The second panel utilized active cooling with transformer oil in a liquid reservoir and copper pipes, covered by a thin metal plate. The third panel, prepared for the hybrid method, featured a similar setup but with a rectangular finned aluminum heat sink. Transformer oil was used in both methods for insulation and thermal conduction. The copper pipes, connected to a radiator and pump, formed a closed circuit for water circulation. The experiment measured temperature and liquid flow using various sensors. The data showed that the hybrid method increased electrical power and efficiency by 4.7% and 0.84%, respectively, compared to 2.94% and 0.52% in the active method. The study's energy consumption was powered by wind energy.

1. INTRODUCTION

The interest in renewable energy sources has increased due to the rapid depletion of conventional energy sources, environmental concerns, and energy security issues. Solar energy emerges as a significant energy source due to its unlimited and clean nature [1]. Photovoltaic (PV) technology offers several advantages, including various power options, low operational and installation costs, and lower maintenance costs compared to other renewable energy technologies. However, PV systems are adversely affected by factors such as shading, hail, humidity, dust accumulation, and heating.

Factors like wind speed, ambient temperature, relative humidity, dust accumulation, and solar radiation affect the surface temperature of PV panels. Due to the increase in temperature, PV cells cannot convert all solar energy into electrical energy. To adhere to the law of energy conservation, the remaining solar energy is converted into heat [2]. The heating of PV cells increases the current while decreasing the voltage, resulting in decreased output power and electrical efficiency [3]. Additionally, non-uniform heating in PV panels can lead to hotspots due to uneven temperature distribution. This condition can cause damage to the PV panel, reducing its lifespan and safety [4,5].

Solar energy systems can be categorized into three main groups: solar thermal systems, solar PV systems, and combined photovoltaic/thermal (PV/T) systems [6]. In PV systems, efforts are made to increase electrical power and efficiency, while PV/T systems also aim to harvest thermal energy in addition to electricity. Studies have shown that, despite higher cell temperatures in PV/T systems, they produce more electricity compared to traditional PV systems. Therefore, improving the physical properties of materials and integrating PV and thermal systems can enhance electrical efficiency [7].

PV panels can overheat due to factors such as high ambient temperatures, intense sunlight exposure, and partial shading, leading to hotspots and reduced energy efficiency. Continuous heating of PV cells over extended periods can also shorten their operational lifespan [5,8].

Various cooling techniques have been developed to address the overheating issues of photovoltaic panels. Active cooling methods involve using energy to cool panels with air, water, or nanofluids. This process employs fans for air cooling and pumps for water or nanofluid cooling. Passive cooling, on the other hand, is an energy-free method. Passive cooling methods can include passive air cooling, passive water cooling, and conductive cooling [5]. Additionally, liquid immersion cooling, phase change materials (PCM) cooling [9,10], Peltier-

based thermoelectric cooling, and microchannel evaporative foils have been used as different approaches [2,11,13].

Air cooling methods can be both active and passive, with some cooling techniques involving no energy consumption. Increasing the air gap behind the panel or attaching finned metal materials to the back surface of the panel can provide cooling without energy consumption [14]. In addition, in some cooling methods, a reservoir created on the back of the panel with aluminum fins is used to transfer heat from the panel to a liquid, and this liquid is circulated to provide cooling through a high-surface-area element. The use of nanofluids has been prevalent in recent PV panel cooling studies [8,15,18]. However, the cooling capacity of nanofluids depends on the appropriate mixture of nanoparticles and base fluids, and over time, the efficiency of the cooled panel decreases, negatively affecting its lifespan [5]. Studies have also explored cooling methods involving fans with various structures and air blowing [13,14,21].

Liquid cooling methods include forced water circulation, water spraying, liquid immersion cooling, and combinations of water and air spraying [2,11,22]. Additionally, simultaneous application of water spraying and air blowing has been tested in some methods [23].

Power transformers are used in power generation, transmission, and distribution systems, where voltage levels are changed. They operate at high power levels and can heat up. Transformer oils are used as cooling fluids in transformers. In addition to having high electrical insulation properties, transformer oils also possess reasonably good thermal conductivity properties. The thermal conductivity of transformer oils ranges from approximately 0.13 to 0.17 (W/m K) at temperatures around 20°C [24].

In this study, two different setups were created. In the first setup, active cooling was achieved by passing copper pipes through a reservoir filled with transformer oil, located behind the panel and sealed with a metal plate. The copper pipes were connected to an automotive radiator for heat dissipation. In the second setup, aluminum heat sinks with a rectangular geometry replaced the metal plate in the same configuration. In the first panel, the performance of active cooling was measured, while in the second study, the effect of aluminum fins was also evaluated. PV panel performance analysis was conducted based on electrical power increase and electrical efficiency increase. All measurements in the experiment were automated using sensors. Values such as solar radiation, wind speed, ambient temperature, liquid temperatures, surface temperatures, humidity, radiation, and water flow rate were automatically measured and recorded using suitable sensors.

2. MATERIALS AND METHODS

2.1. Experiment Setup

The experiment setup was installed on the terrace of the Technical Sciences Vocational School building at Dicle University, Diyarbakir province, Turkey, located at GPS coordinates 37° 55' 5" North and 40° 15' 47" East. The mounting platform used for the panels was adjusted to have a 360-degree orientation, considering local conditions in Diyarbakir, which has a high solar radiation potential.

Three identical 100 W monocrystalline photovoltaic panels were used in the study, with one serving as a reference. The reference panel remained unchanged, while the other two

panels had a 1.5 cm high liquid reservoir created on their rear surfaces for transformer oil, with copper pipes installed inside. The first panel served as the reference panel, the second panel had active cooling (AC) applied, and the third panel had a hybrid cooling (HC) method applied.

In the AC method, a liquid reservoir was created on the rear surface of the panel to fill it with transformer oil. The oil reservoir was sealed with a flat metal plate with a thickness of 2 mm. A 0.5-inch copper pipe was placed inside the oil reservoir and connected to an automotive radiator with appropriate converters. Approximately 1.5 liters of water in the radiator was circulated through the copper pipe placed on the back of the panel using a 27W electric combination pump. The circulating water continuously absorbed heat stored in the transformer oil and transferred it to the connected radiator, where it was cooled. This process was repeated in a loop, with part of the heat being dissipated from the radiator's large surface area fins through air convection. This effectively removed heat from the oil reservoir. The radiator was cooled by a fan, which also cooled the water inside it. Thus, active cooling was achieved by cooling the heated water in the reservoir on the rear side of the panel.

In the HC method, the liquid reservoir on the rear surface of the panel was covered with a rectangular aluminum heat sink with fins, unlike the AC method that used a flat metal plate. The active cooling part was the same for both panels. This allowed for separate observations of the effects of active and passive cooling. Active cooling was achieved through the radiator, while passive cooling occurred with the assistance of the aluminum heat sink. Therefore, this method was named the hybrid system.

In both methods, transformer oil was used on the back of the panel to ensure both electrical insulation and heat conduction between the panel and copper pipes. Transformer oil is widely used in transformers for cooling purposes due to its excellent electrical insulation properties.

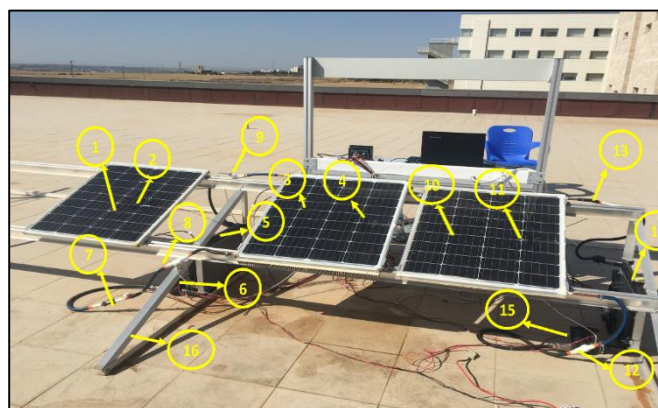


Figure 1. Front View of the Experimental Setup (1-Reference panel 2-Ref. panel surface sensor 3-HC panel 4-HC panel surface sensor 5-HC radiator and fan 6-HC pump 7-Liquid flow sensor 8-HC panel liquid inlet temperature sensor 9- HC panel liquid outlet temperature sensor 10-AC panel 11-AC panel surface sensor 12-AC panel liquid inlet temperature sensor 13- HC panel liquid outlet temperature sensor 14-AC radiator and fan 15-AC pump 16-Mounting platform)

In the AC method, the rear side of the panel was sealed with a metal plate, while in the HC method, it was covered with an aluminum heat sink with a rectangular fin geometry to create a reservoir for transformer oil. The preparation process of the solar panel covered with the metal plate and the heat sink is

illustrated in Fig. 3. The purpose of using transformer oil is to benefit from its electrical insulation and thermal heat conduction properties. Moreover, the use of transformer oil ensures a relatively homogeneous heat distribution on the backside of the PV panel.

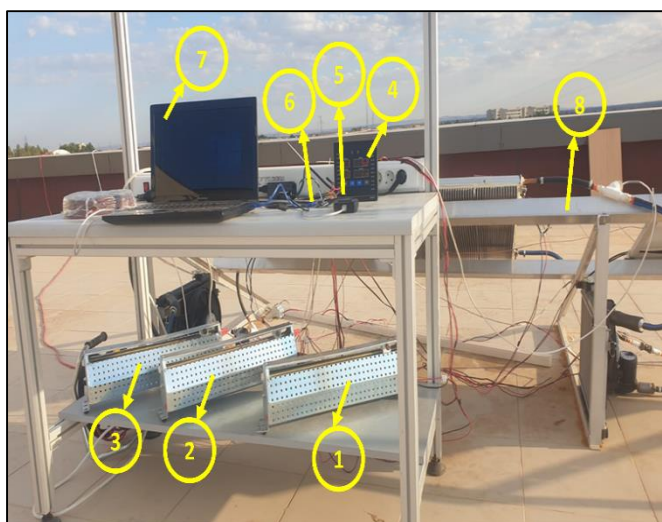


Figure 2. Back View of the Experimental Setup. 1-Refrans panel electrical load 2- HC Panel electrical load 3- AC Panel electrical load 4- SCN 100 data transfer device 5- USB-RS485 Converter 6- Arduino UNO R3 7-PC(laptop) 8- Mounting platform



Figure 3. Preparation Process of Panels with Cooling. 1-PV panel 2-Copper tube 3-Copper tube mounting behind the panel 4- Metal plate 5-AC panel 6- Aluminum led heatsink 7-HC panel

In the experimental setup, an electric pump commonly used in electric boilers was employed for the circulation of water. For the cooling process, an automotive radiator, radiator fan, adjustable electrical load (rheostat) for consuming electrical energy, hoses, a pump, converters to connect the radiator and copper pipes to hoses, and various sensors for measuring data such as current, voltage, and temperature were used. Sensor data was transferred to a PC via a USB-RS485 converter using an SCN 100 Scanner and Alarm Device. Data was processed using the OPIK 2016_scn 100 data transfer software on the PC. A liquid flow sensor and Arduino were used to measure the liquid flow rate. The block diagram of the cooling and measurement elements used for the HC panel in the experimental setup is shown in Figure 4. Data on radiation, ambient temperature, wind, and some meteorological data were

collected from a meteorological solar data station, as seen in Fig. 5.

In the conducted experiment, one liquid temperature sensor was used to measure the inlet and outlet temperatures of both the AC and HC methods. Surface temperature sensors were placed approximately in the middle of each panel's surface, taking care to avoid shading from the sensors. A liquid flow sensor was positioned between the pump and the inlet sensor to measure the flow rate of the water.

In this study, the energy required was sourced from a previously established 0.4 kW wind energy system, as per our previous research. During periods of insufficient wind, an adjacent 1 kW solar power plant was utilized.

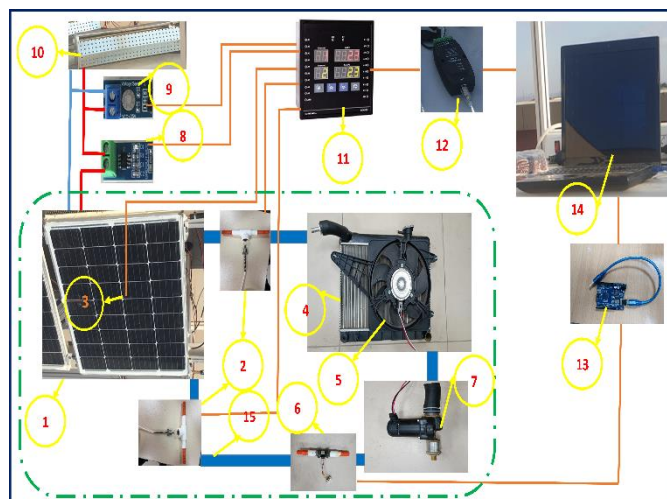


Figure 4. Experimental Setup Cooling and Measurement Block Diagram. 1- PV panel 2-Liquid temperature sensor 3- Surface temperature sensor 4- Radiator 5-Radiator fan 6-Liquid flow sensor 7-Pump 8-Current sensor 9- Voltage sensor 10-Adjustable electrical load (rheostat) 11- SCN 100 data transfer device 12- USB-RS485 Converter 13- Arduino UNO R3 14- PC(laptop)

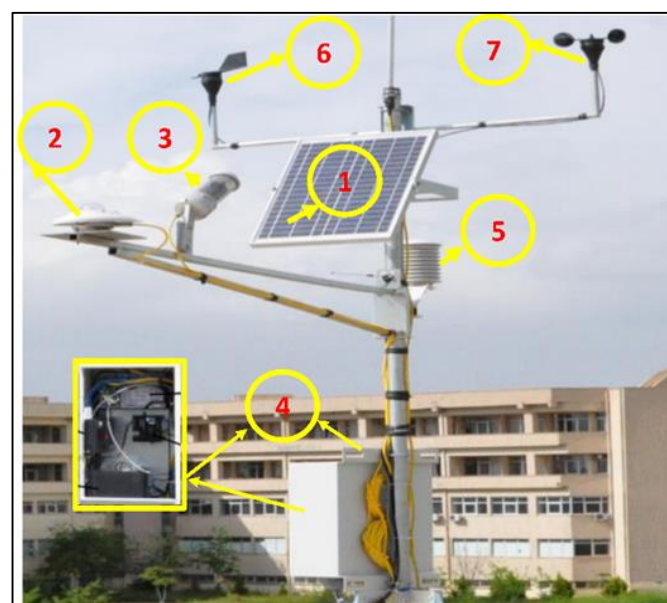


Figure 5. Image of the Meteorological Measurement Station. 1-Solar panel 2- Solar radiation sensör (Pyranometer) 3-Sunshine duration sensor 4-CR800(Datalogger), battery, Solar charge controller 5-Air temperature and relative humidity meter 6- Wind direction meter 7-Wind speed meter

2.2. Materials Used in the Experiment

In the study, three identical 100 W monocrystalline photovoltaic panels were used, one of which served as a reference while the other two had a 1.5 cm high liquid reservoir created on the back surface to accommodate transformer oil, and copper pipes were placed inside these reservoirs. The first panel was taken as the reference panel, the second one was subjected to active cooling (AC), and the third one was subjected to hybrid cooling (HC) methods. In the AC method, a liquid reservoir was created on the back of the panel to fill transformer oil, and the reservoir was sealed with a 2 mm thick flat metal plate. Copper pipes with a diameter of 0.5 inches were placed inside the reservoir and connected to an automotive radiator using suitable converters. Approximately 1.5 liters of water was circulated through the copper pipes using an electric combi pump (27W) connected to the back of the panel. With the help of the pump, the circulating water in the oil reservoir continuously absorbed the heat and transferred it to the radiator connected to the system, where it was cooled. A portion of the heat was dissipated through the large surface radiator fins in contact with the air. Thus, the heat in the oil reservoir was removed from the system. Active cooling was achieved by cooling the water inside the reservoir. In the HC method, the liquid reservoir was covered with an aluminum cooling plate with a rectangular fin geometry instead of a metal plate. The active cooling part was the same in both panels. Therefore, while active cooling was achieved through the radiator using a fan, passive cooling was achieved through the aluminum cooling plate. For this reason, this method was named the hybrid system.

In both methods, transformer oil was used to ensure both electrical insulation and heat conduction between the panel and the copper pipes on the back. Transformer oil is commonly used for cooling purposes in transformers due to its excellent electrical insulation properties. Additionally, transformer oil has reasonable thermal conductivity properties, with thermal conductivity coefficients ranging from approximately 0.13-0.17 (W/m K) at 20°C.

In this study, a circulation pump commonly used in electric combi boilers (capable of continuous operation and resistant to high temperatures) was used for the circulation of water in the cooling system. The experiment also utilized an adjustable DC power supply capable of supplying 0-50 Ohm resistance and a power of 1000W for the electric load, copper pipes with a length of approximately 7 meters and a diameter of 1.5 inches for each panel, a liquid flow sensor for measuring liquid flow, an Arduino for processing the measured liquid flow data and transferring it to a PC, and a triangular-type adjustable panel mounting platform with an adjustable angle for mounting the panels (the panel angle was set to 36 degrees for the conditions in Diyarbakır). Approximately 8 liters of Hyvolt Power Oil 60 UX (inhibited transformer oil) were used for transformer oil. Additionally, a meteorological measurement station was set up to measure parameters such as radiation, relative humidity, air temperature, wind speed, wind direction, and sunshine duration.

All measurements were automatically recorded using appropriate sensors in the experimental setup.

TABLE I
CHARACTERISTICS OF THE SOLAR PANELS USED

Specifications	Value
Tipi	Monokristal
Power	100W
Number of Cells	36
Open-Circuit Voltage (Voc)	23,8V
Maximum Voltage (Vmp)	20,70V
Short-Circuit Current (Isc)	5,07A
Maximum Current (Imp)	4,83A
Maximum System Voltage	1000V
Module Dimensions (mm)	791*679*25

(Standard Test Conditions: Am=1.5 E=1000W/m² Tc=25°C)

2.3. Photovoltaic Panel Electrical Circuit

The electrical equivalent circuit of the PV cell is modeled as shown in Fig. 6. This PV equivalent circuit consists of a current source, a diode in series, and parallel resistors.

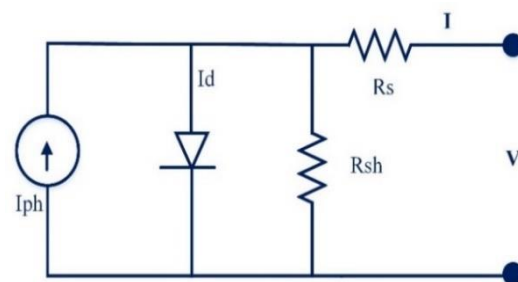


Figure 6. Equivalent Circuit of the Photovoltaic Cell

The output current of a PV cell;

$$I = I_{ph} - I_0 \left(e^{\frac{q(V+IR_s)}{nkT_c}} - 1 \right) - \left(\frac{V+IR_s}{R_{sh}} \right) \quad (1)$$

It is found with the formula. In PV systems, PV cells are connected in parallel to increase current, and in series to increase voltage. If the PV panel current is rearranged based on N_s , the number of series cells on the PV panel, and N_p , the number of parallel cells used on the panel

$$I = N_p I_{ph} - N_p I_0 \left(e^{\frac{q \left(\frac{V}{N_s} + \frac{IR_s}{N_p} \right)}{nkT_c}} - 1 \right) - \frac{1}{N_p} \left(\frac{V+IR_s}{R_{sh}} \right) \quad (2)$$

The R_{sh} parallel resistance, which represents the effect of leakage currents in the equivalent circuit, is much larger than the R_s series resistance that represents the voltage drop at the output. In the equivalent circuit of the PV cell, when $R_{sh} = \infty$ is taken (open circuit), the PV cell current and voltage;

$$I = N_p I_{ph} - N_p I_0 \left(e^{\frac{q(V - IR_s)}{nkT_c}} - 1 \right) \tag{3}$$

$$V = \frac{nkT_c}{q} \ln \left(\frac{I_{ph} + I_0 - I + N_p}{I_0} \right) - R_s I \tag{4}$$

Here; I is the cell output current, I_{ph} is the current generated by photons, R_s is the series resistance, the voltage drop at the output, R_{sh} is the parallel resistance, n is the ideality factor, V is the cell output voltage, k is the Boltzmann constant ($1.380622 \times 10^{-23} \text{ J}^0\text{K}$), I_0 is the reverse saturation current of the diode, q is the charge of an electron ($1.6021917 \times 10^{-19} \text{ C}$), T_c is the cell temperature (Ambient temperature: $25 \text{ }^\circ\text{C}$), Irradiance value: $1000 \text{ (W/m}^2\text{)}$, Wind speed: 1 (m/s) .

2.4. Energy analysis

The calculated current and voltage-dependent electrical power output of the PV panel;

$$Pe = V * I \tag{5}$$

Here, V corresponds to voltage, I to current, and Pe to electrical power.

The power generated by the PV panel varies depending on the angle of incidence of incoming sunlight, the degree of pollution on the panel surfaces, and whether the weather is clear or cloudy. The calculation of how much of the sunlight falling on the solar panel is converted into electricity is expressed as efficiency.

Efficiency;

$$\eta e = \frac{P_{max}}{G * S} * 100 = \frac{I_{max} * U_{max}}{G * S} * 100 \tag{6}$$

ηe electrical efficiency (%) can be expressed as follows, where I_{max} is the maximum panel current (A), U_{max} is the maximum panel voltage (V), P_{max} is the maximum power generated by the panel (W), G is the irradiance (W/m^2), S is the panel surface area (m^2);

$$FF = \frac{I_{max} * U_{max}}{I_{oc} * U_{oc}} \tag{7}$$

When expressed as V_{oc} (open-circuit voltage) and I_{sc} (short-circuit current), FF (fill factor) is defined as the fill factor.

In the study, the electrical power increase (P_{inc}) was calculated as follows by comparing the cooled panel power (P_{col}) with the reference panel.

$$P_{inc} = \frac{P_{col} - P_{ref}}{P_{ref}} * 100 \tag{8}$$

Similarly, electrical efficiency increase (ηe_{inc}) can be expressed as the difference between the efficiency of the cooled panel (ηe_{col}) and the efficiency of the reference panel ηe_{ref} .

$$\eta e_{inc} = \eta e_{col} - \eta e_{ref} \tag{9}$$

2.5. Effect of Temperature and Irradiance on PV Panel Power, Current, and Voltage

The mathematical model of the PV panel, as described earlier, was simulated in MATLAB Simulink to calculate the maximum current, voltage, and power. The intended model is presented in Figure 7.

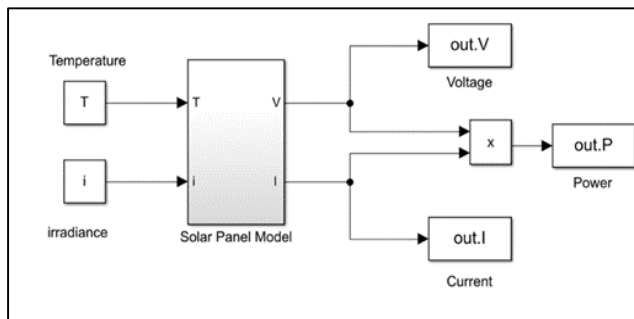


Figure 7. Solar panel MATLAB Simulink model

The impact of temperature is shown in the obtained I-V and P-V characteristics in Figures 8 and 9. When examining Figures 8 and 9, it can be observed that an increase in temperature, with constant irradiance, slightly increases the current while decreasing the voltage. Therefore, an increase in temperature reduces the power output.

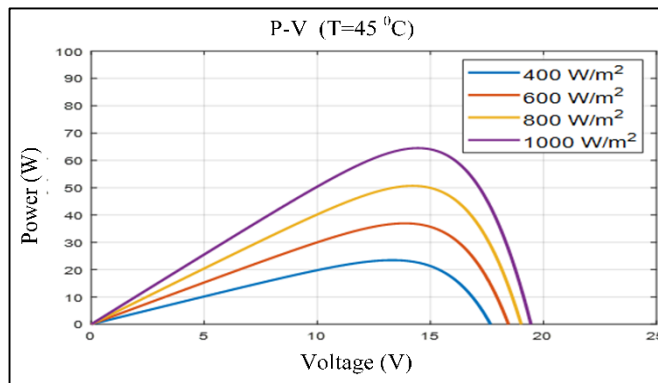


Figure 8. I-V characteristic of the panel under constant irradiance conditions (Irradiance = 1000 W/m^2 at temperatures of $20, 40, 60,$ and $80 \text{ }^\circ\text{C}$)

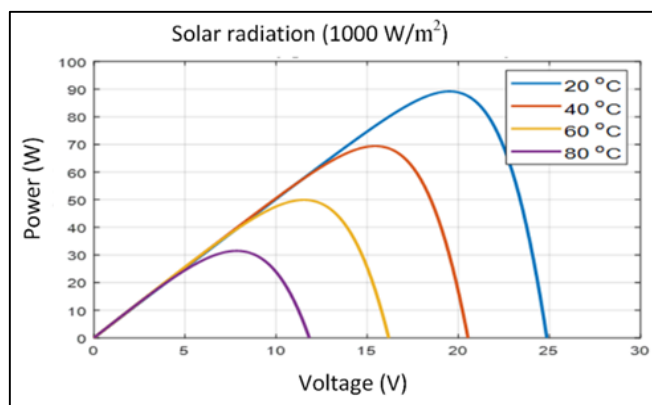


Figure 9. P-V characteristic of the panel under constant irradiance conditions (Irradiance = 1000 W/m² at temperatures of 20, 40, 60, and 80 °C)

When observing the effect of irradiance, the temperature was kept constant at 45°C, and changes in current, voltage, and power due to irradiance were investigated. While keeping the temperature constant, current, voltage, and power values were calculated for different irradiance levels (i = 400, 600, 800, and 1000 W/m²). The I-V and P-V characteristics obtained to observe the effect of irradiance are presented in Fig.10 and Fig.11. When examining the figures, it can be observed that, under constant temperature conditions, an increase in irradiance slightly increases voltage and significantly increases current, thereby increasing power.

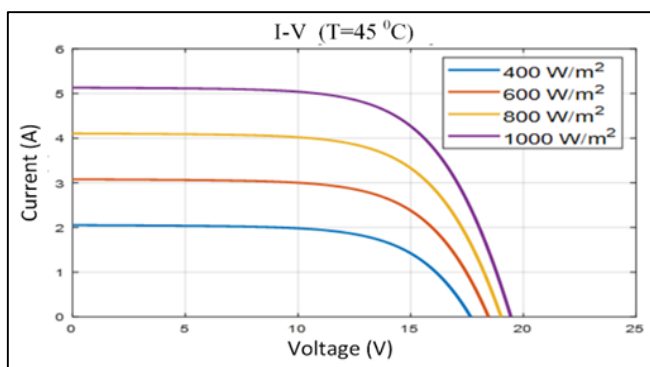


Figure 10. The panel I-V characteristic under constant temperature conditions (T=45°C) for irradiance levels of 400, 600, 800, and 1000 W/m²

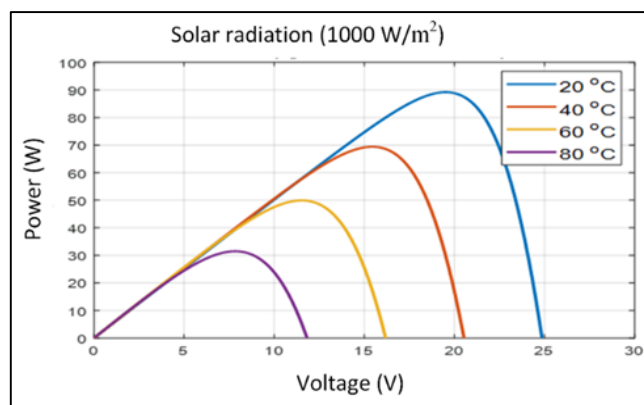


Figure 11 presents the panel P-V characteristic under constant temperature conditions (T=45°C) for irradiance levels of 400, 600, 800, and 1000 W/m².

3. DISCUSSION AND RESULTS

In this experimental study, instant measurements were taken for two days from 11:00 AM to 4:00 PM. Since the results for both days were very close to each other, data from a single day were used. During the experiment, temperature sensors were used to measure the inlet and outlet temperatures of the water passing through the copper pipes behind the panels, as well as the temperature of the transformer oil. Surface temperature sensors were used to measure the panel surface temperatures. Current and voltage sensors were used to measure the maximum current and voltage values of each panel. Sensor data were recorded on a computer using the SCN 100 scanner and alarm device.

Measurements were taken for aluminum AC panels and HC panels, including water inlet and outlet temperatures, transformer oil temperature, surface temperatures, and electrical parameters (current and voltage). For the reference panel, only surface temperatures and electrical parameters (maximum current and voltage) were measured. The measurements are presented in Figures 12-22.

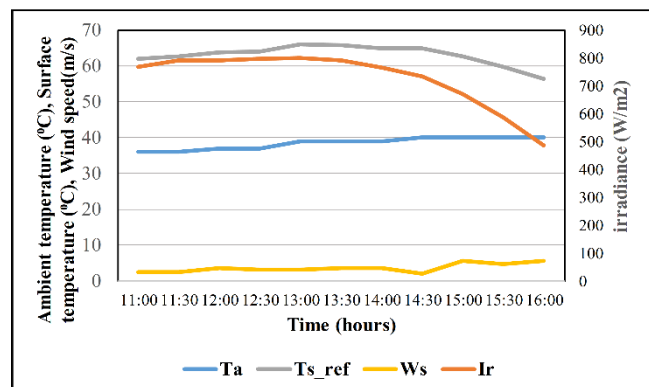


Figure 12. Variation of Ambient Temperature, Wind Speed, Irradiance, and Reference Panel Surface Temperature

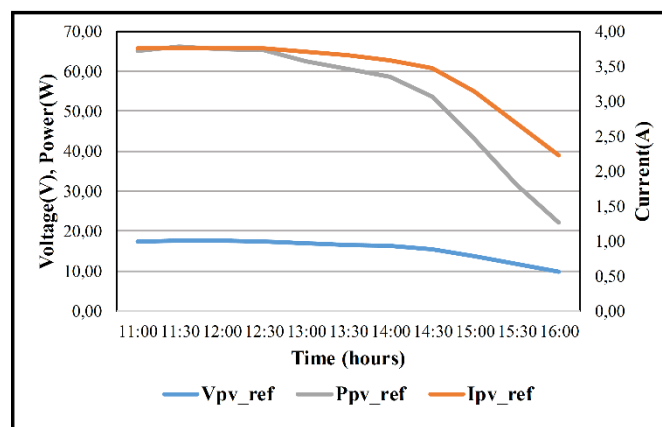


Figure 13. Maximum Current, Voltage, and Power of the Reference Panel

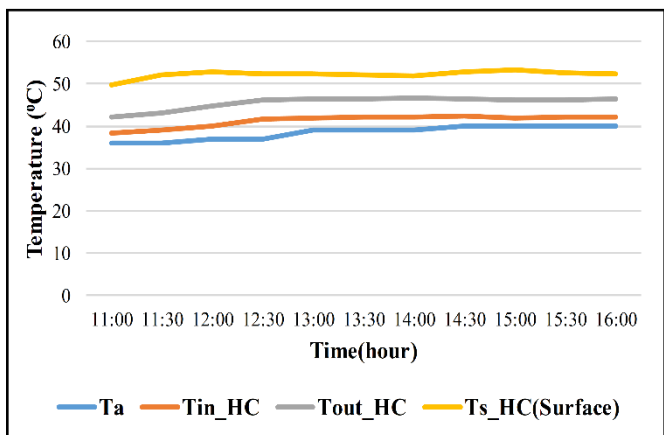


Figure 14. Changes in Inlet-Outlet Water Temperature and Panel Surface Temperature of the HC Panel

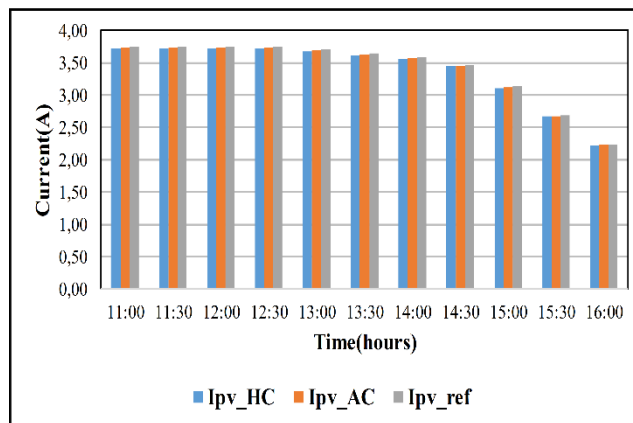


Figure 17. Measured Maximum Currents for HC, AC, and Reference Panels

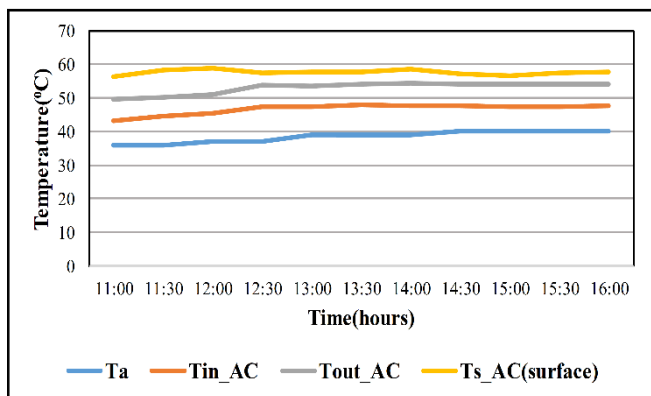


Figure 15. Changes in Inlet-Outlet Water Temperature and Panel Surface Temperature of the AC Panel

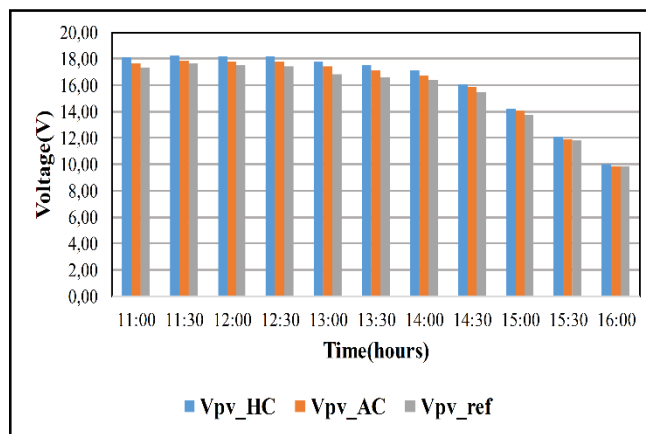


Figure 18. Measured Maximum Voltages for HC, AC, and Reference Panels

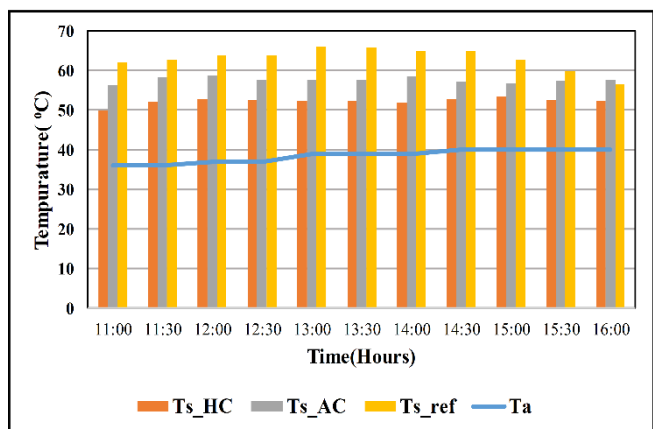


Figure 16: Changes in Surface Temperatures of HC, AC, and Reference Panels and Ambient Temperature

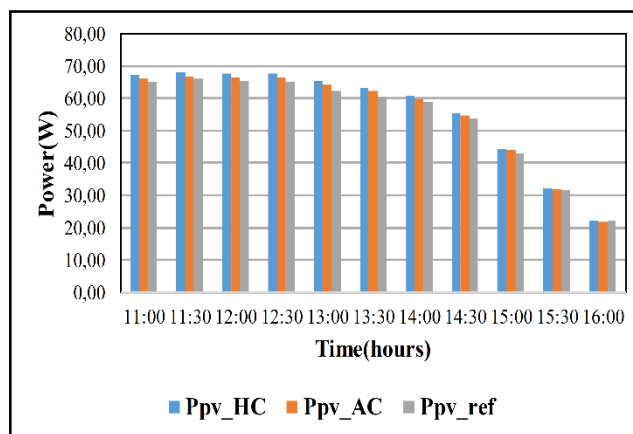


Figure 19. Measured Maximum Powers for HC, AC, and Reference Panels

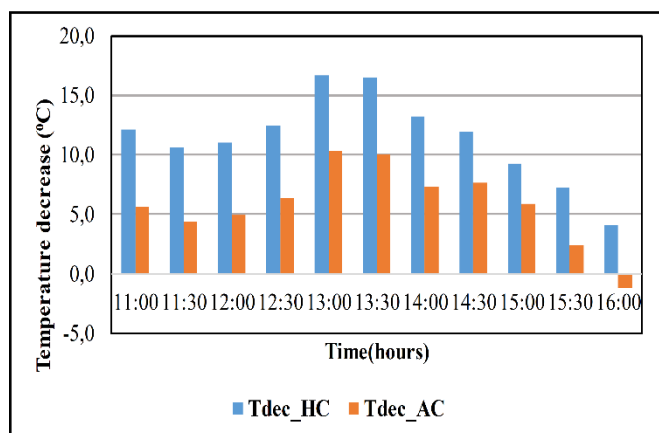


Figure 20: Decrease in Temperature for HC and AC Panels Compared to the Reference Panel

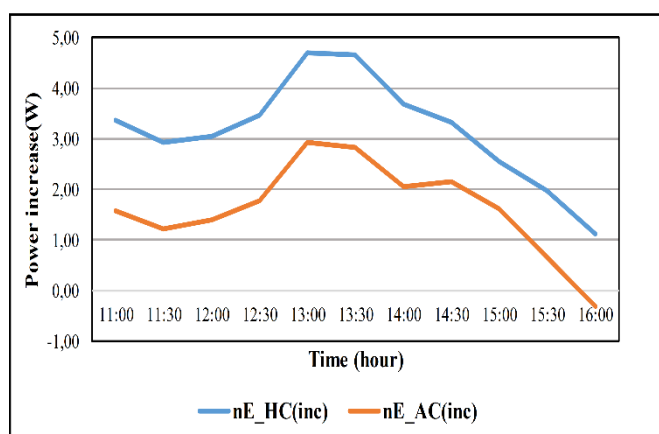


Figure 21: Increase in Electrical Power for HC and AC Panels Compared to the Reference Panel

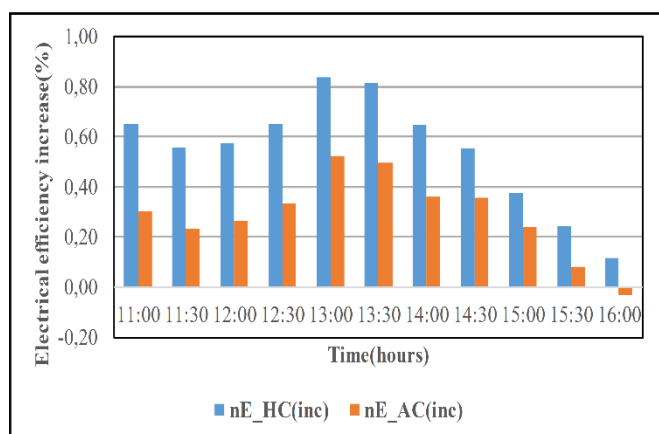


Figure 22: Increase in Electrical Efficiency in HC and AC Panel Temperatures Compared to the Reference Panel

In this experimental study, instant measurements were taken for two days from 11:00 AM to 4:00 PM. Since the results for both days were very close to each other, data from a single day were used. During the experiment, temperature sensors were used to measure the inlet and outlet temperatures of the water passing through the copper pipes behind the

panels, as well as the temperature of the transformer oil. Surface temperature sensors were used to measure the panel surface temperatures. Current and voltage sensors were used to measure the maximum current and voltage values of each panel. Sensor data were recorded on a computer using the SCN 100 scanner and alarm device.

Fig.12 and 13 provide the electrical parameters measured for the reference panel, including maximum current, voltage, and power, as well as irradiance, ambient temperature, wind speed, and surface temperature values.

Fig. 14 and 15 present the results of the copper pipe inlet and outlet measurements and surface temperatures for the HC panel and AC panel subjected to cooling. When examining the results, it can be observed that the HC panel, with its cooling system, had lower inlet and outlet water temperatures compared to the AC panel. Additionally, the surface temperature of the HC panel was lower than that of the AC panel. While water was actively circulated through the aluminum AC panel using a pump in conjunction with car radiator and fan cooling, passive cooling occurred simultaneously through the aluminum cooler on the HC panel. As a result, the HC panel was effectively cooled more than the AC panel.

Fig.16 displays the surface temperatures and ambient temperature for all three panels. As seen in the figure, the surface temperature of the reference panel, which was not subjected to any treatment, was higher than the two cooled panels. This temperature, which varies depending on irradiance and ambient temperature, reaches significantly high values during the noon hours when irradiance is high.

Fig. 17-19 compare the electrical parameters, including maximum current, voltage, and power, measured for all three panels. When analyzing the graphs, it can be observed that the HC panel and AC panel had higher voltage and power values compared to the reference panel, while the current value was lower for both HC and AC panels. The change in voltage due to temperature variation is more pronounced among the three panels, whereas the change in current is less significant. This is theoretically expected since, under constant irradiance, an increase in temperature leads to a decrease in voltage and power while causing an increase in current. However, the change in current is limited.

Figure 20 provides information about the temperature decrease in the HC and AC panels compared to the reference panel. The temperature decrease in the HC panel was greater than that in the AC panel. These temperature decreases were most significant around noon, between 13:00 and 13:30, where the temperature drop in the HC panel was approximately 16.6°C, while it was around 10.3°C for the AC panel. Around 11:00, the temperature decrease in the HC panel was about 12°C, whereas it was approximately 5.2°C for the AC panel. At 16:00, the HC panel showed a temperature decrease of about 4.1°C, while the AC panel displayed a negative value, indicating that the temperature was lower than that of the reference panel. This can be attributed to the closed heating of the transformer oil located behind the panel and the effect of wind.

Figures 21-22 analyze the increase in electrical power and efficiency compared to the reference panel. When examining these figures, it can be seen that the power increase in the HC panel was higher at noon but decreased around 16:00. The highest recorded power increase was 4.7 % for the HC panel

and 2.94 % for the AC panel at 13:00. The lowest recorded power increase was 1.11% for the HC panel and -0.32 % for the AC panel at 16:00, indicating a decrease in power for the AC panel. The electrical efficiency increase was also at its highest, with 0.84% for the HC panel and 0.52 % for the AC panel at 13:00. The lowest increase in electrical efficiency was 0.11 % for the HC panel and -0.03 % for the AC panel at 16:00. These results indicate that cooling is more effective during the noon hours when irradiance and ambient temperature are high, resulting in an increase in electrical power and efficiency.

Furthermore, the HC panel was equipped with a rectangular finned aluminum cooler and LED lighting. When comparing the results in Figure 12-22, it is evident that the aluminum cooler had a significantly positive effect

4. CONCLUSION

In this study, measurements of temperature, maximum current, maximum voltage, and maximum power generation were conducted at various points of the reference panel, HC, and AC panels. Additionally, meteorological data such as irradiation, ambient temperature, humidity, and wind intensity were measured. The measurements were carried out in Diyarbakır, over a one-day period in August, from 11:00 AM to 4:00 PM under the same conditions. Comparisons have been made based on these obtained data. The results have been written in bullet points:

- The HC system was observed to provide more cooling compared to the others and was measured to have higher power generation and higher electrical efficiency. In the hybrid method, the highest increase in power and electrical efficiency was measured as 4.7% and 0.84%, respectively, while in the AC system, it was found to be 2.94% and 0.52%, respectively.
- The effectiveness of using the aluminum cooler in cooling is evident from the difference in power increase and efficiency gain obtained in both methods.
- Although the thermal conductivity of transformer oil is not as high as water, it was used considering its insulation advantages, but no significant efficiency gain was recorded.
- All necessary parameters for the study were recorded using sensors, thereby minimizing measurement errors due to human factors in the results.

ACKNOWLEDGEMENT

This project was carried out with the support of Dicle University Scientific Research Projects (DÜBAP) unit within the scope of the project No. FBE.21.018 and named "Experimental analysis of efficiency increase with cooling in photovoltaic panels". We thank DÜBAP for their support.

REFERENCES

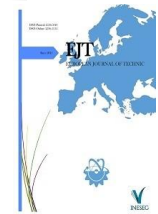
- [1] S. Fakouriyan, Y. Saboohi, and A. Fathi, "Experimental analysis of a cooling system effect on photovoltaic panels' efficiency and its preheating water production," *Renew. Energy*, 2019, doi: 10.1016/j.renene.2018.09.054.
- [2] J. Siecker, K. Kusakana, and B. P. Numbi, "A review of solar photovoltaic systems cooling technologies," *Renew. Sustain. Energy Rev.*, vol. 79, pp. 192–203, Nov. 2017, doi: 10.1016/J.RSER.2017.05.053.
- [3] A. Al Miaari and H. M. Ali, "Technical method in passive cooling for photovoltaic panels using phase change material," *Case Stud. Therm. Eng.*, vol. 49, 2023, doi: 10.1016/j.csite.2023.103283.
- [4] A. A. B. Baloch, H. M. S. Bahaidarah, P. Gandhidasan, and F. A. Al-Sulaiman, "Experimental and numerical performance analysis of a converging channel heat exchanger for PV cooling," *Energy Convers. Manag.*, vol. 103, 2015, doi: 10.1016/j.enconman.2015.06.018.
- [5] P. Dwivedi, K. Sudhakar, A. Soni, E. Solomin, and I. Kirpichnikova, "Advanced cooling techniques of P.V. modules: A state of art," *Case Stud. Therm. Eng.*, vol. 21, 2020, doi: 10.1016/j.csite.2020.100674.
- [6] M. H. Shojaeefard, N. B. Sakran, M. M. Sharfabad, O. A. Hussein, and H. A. Mohammed, "Experimental and Numerical Investigation of the Effect of Water Cooling on the Temperature Distribution of Photovoltaic Modules Using Copper Pipes," *Energies*, vol. 16, no. 10, 2023, doi: 10.3390/en16104102.
- [7] W. Gu, T. Ma, A. Song, M. Li, and L. Shen, "Mathematical modelling and performance evaluation of a hybrid photovoltaic-thermoelectric system," *Energy Convers. Manag.*, vol. 198, 2019, doi: 10.1016/j.enconman.2019.111800.
- [8] A. K. Suresh, S. Khurana, G. Nandan, G. Dwivedi, and S. Kumar, "Role on nanofluids in cooling solar photovoltaic cell to enhance overall efficiency," in *Materials Today: Proceedings*, 2018, doi: 10.1016/j.matpr.2018.06.442.
- [9] R. M., L. S., R. S., A. H., and D. A., "Experimental investigation on the abasement of operating temperature in solar photovoltaic panel using PCM and aluminium," *Sol. Energy*, vol. 188, 2019, doi: 10.1016/j.solener.2019.05.067.
- [10] F. Bayrak, H. F. Oztop, and F. Selimefendigil, "Experimental study for the application of different cooling techniques in photovoltaic (PV) panels," *Energy Convers. Manag.*, vol. 212, 2020, doi: 10.1016/j.enconman.2020.112789.
- [11] N. A. Pambudi, A. Sarifudin, R. A. Firdaus, D. K. Ulfa, I. M. Gandidi, and R. Romadhon, "The immersion cooling technology: Current and future development in energy saving," *Alexandria Engineering Journal*, vol. 61, no. 12, 2022, doi: 10.1016/j.aej.2022.02.059.
- [12] X. Yuan et al., "Phase change cooling in data centers: A review," *Energy and Buildings*, vol. 236, 2021, doi: 10.1016/j.enbuild.2021.110764.
- [13] C. Ventura, G. M. Tina, A. Gagliano, and S. Aneli, "Enhanced models for the evaluation of electrical efficiency of PV/T modules," *Sol. Energy*, vol. 224, 2021, doi: 10.1016/j.solener.2021.06.018.
- [14] F. Bayrak, H. F. Oztop, and F. Selimefendigil, "Effects of different fin parameters on temperature and efficiency for cooling of photovoltaic panels under natural convection," *Sol. Energy*, vol. 188, 2019, doi: 10.1016/j.solener.2019.06.036.
- [15] A. Aydın, İ. Kayri, and H. Aydın, "Determination of the performance improvement of a PV/T hybrid system with a novel inner plate-finned collective cooling with Al2O3 nanofluid," *Energy Sources, Part A Recover. Util. Environ. Eff.*, vol. 44, no. 4, 2022, doi: 10.1080/15567036.2022.2136801.
- [16] A. Aydın, İ. Kayri, and H. Aydın, "Electrical and thermal performance enhancement of a photovoltaic thermal hybrid system with a novel inner plate-finned collective cooling with different nanofluids," *Int. J. Green Energy*, 2023, doi: 10.1080/15435075.2023.2201345.
- [17] F. Rajaei, M. A. V. Rad, A. Kasaeian, O. Mahian, and W. M. Yan, "Experimental analysis of a photovoltaic/thermoelectric generator using cobalt oxide nanofluid and phase change material heat sink," *Energy Convers. Manag.*, vol. 212, 2020, doi: 10.1016/j.enconman.2020.112780.
- [18] S. Nižetić, E. Giama, and A. M. Papadopoulos, "Comprehensive analysis and general economic-environmental evaluation of cooling techniques for photovoltaic panels, Part II: Active cooling techniques," *Energy Convers. Manag.*, vol. 155, 2018, doi: 10.1016/j.enconman.2017.10.071.
- [19] M. King et al., "Mathematical modelling of a system for solar pv efficiency improvement using compressed air for panel cleaning and cooling," *Energies*, vol. 14, no. 14, 2021, doi: 10.3390/en14144072.
- [20] S. Navakrishnan, E. Vengadesan, R. Senthil, and S. Dhanalakshmi, "An experimental study on simultaneous electricity and heat production from solar PV with thermal energy storage," *Energy Convers. Manag.*, vol. 245, 2021, doi: 10.1016/j.enconman.2021.114614.
- [21] H. G. Teo, P. S. Lee, and M. N. A. Hawlader, "An active cooling system for photovoltaic modules," *Appl. Energy*, vol. 90, no. 1, 2012, doi: 10.1016/j.apenergy.2011.01.017.
- [22] J. Siecker, K. Kusakana, and B. P. Numbi, "A review of solar photovoltaic systems cooling technologies," *Renewable and Sustainable Energy Reviews*, vol. 79, 2017, doi: 10.1016/j.rser.2017.05.053.

- [23] Q. K. Jasim, "Studying the Effect of Cooling Methods on the Performance of Solar Cells," *Int. J. Heat Technol.*, vol. 41, no. 1, pp. 265–270, Feb. 2023, doi: 10.18280/ijht.410130.
- [24] I. Fernández, A. Ortiz, F. Delgado, C. Renedo, and S. Pérez, "Electric Power Systems Research Comparative evaluation of alternative fluids for power transformers," *Electr. Power Syst. Res.*, vol. 98, pp. 58–69, 2013, doi: 10.1016/j.epsr.2013.01.007.
- [25] S. Nižetić, D. Čoko, A. Yadav, and F. Grubišić-Čabo, "Water spray cooling technique applied on a photovoltaic panel: The performance response," *Energy Convers. Manag.*, vol. 108, 2016, doi: 10.1016/j.enconman.2015.10.079.

BIOGRAPHIES

Ömer Karaozan received an associate degree in the Industrial Electronics program at Artuklu University in Mardin. Later, he received the title of Electrical and Electronics Engineering at the Faculty of Engineering at Near East University. He completed his master's degree in Electrical and Electronics Engineering at Dicle University, Faculty of Engineering in 2022. He has been working as a business manager at Karaozan Engineering company since 2020.

Mehmet Emin ASKER received the B.S. degree in electrical electronics engineering, from Firat University, Elazig, Turkey in 1997, the M.S. degree and the Ph.D. degree in electrical machines, power electronics from Firat University, Elazig, Turkey, in 2009 and 2016, respectively. He is an Assistant Professor with Dicle University, Department of electrical power and energy. Where he teaches courses on power system, power electronics, circuit theory and electrical machines since 2007. His research interests include electrical machines, power electronics, chaos and power systems.



Research Article

Determining the Advantages of a Linear Driven 3-Axis Industrial Robot by Structural and Force Analysis

Savaş KOÇ^{1*} , İdris ŞANI² 

^{1*}Batman University, Mechanical Engineering Department, Batman, Turkey. (e-mail: savas.koc@batman.edu.tr).

²Disaster and Emergency Management Presidency (AFAD), Mardin, Turkey.

ARTICLE INFO

Received: Jan., 06. 2023
Revised: May., 13. 2023
Accepted: Agu., 18. 2023

Keywords:

Linear actuator
Measuring force and torque
Acceleration
Modal Analysis

Corresponding author: *Savas Koc*

ISSN: 2536-5010 / e-ISSN: 2536-5134

DOI: <https://doi.org/10.36222/ejt.1230193>

ABSTRACT

The most important factors affecting the operation of industrial robots are carrying capacity, the weight of the parts of robots, the vibrations in the arms and the manufacturing cost. The manufacturing cost of the robot increases as the weight of the parts and the size of the motors are increased. The forces on the motors and the accelerations at the top axes of the robot, which is driven by the linear movement or rotational moment were measured and compared in this study. In addition, modal analysis, forced vibration analysis and harmonic analysis of the robot were performed in two different drive systems. The structural condition of robot was examined. According to the calculations, smaller motors were used because the torque required for driving the axes using the ball screw system is very small. With the use of the smaller motors, the weights of the arms have been reduced due to the change in size of the motors. Similarly, the manufacturing costs of the robot have also been reduced. Hence, the robot designed in this study has advantages in terms of both structural and manufacturing cost compared to other robot arms. Likewise, it is seen that the robot can be operated using this design according to the accelerations measured at the top axes of the robot arm and the structural analysis.

1. INTRODUCTION

With rapid technological progress, innovations have a decisive impact on our lives [1]. Production quality and availability of cheap products have come as an inevitable need in the global industry [2]. Automation automatically controls the system by taking into account observation, decision-making and changes, rather than human interaction using mechanical or electronic devices [3]. Automation technologies are used both in order to accelerate serial production of parts and reduce production costs [4]. In order that a system to be fully automated, machine power must be superior than human power [5]. Manufacturers, who use modern techniques and applications, are provided by industrial automation in their production, have a strategy that will create competition among rival companies [6,7].

As we progress in the era of globalization, developments such as shortened product life cycles, reduced manufacturing cost, increasing innovations, shortage of skilled workers and continuous diversification of product range are observed in the manufacturing sector. Automation systems using industrial robots offer good solutions for productivity and flexibility [8,9]. With the developing technology, industrial robots also have high intelligence and sensitivity [10]. With the developments in robotics and mechatronics, they bring new

advantages such as providing convenience for human life, working in risky places instead of human, obtaining autonomy in manufacturing, and using limbs that can serve as prostheses [11]. Robotics is one of the most important technologies that will affect life both in the twenty-first century and in the future [12].

Industrial robots, which are among the most critical elements of industrial automation systems, are widely used in a series of industrial production activities such as spraying, welding and handling and increasing their importance day by day [13,14]. They are also used to protect human life in dangerous conditions such as mechanical vibrations, high temperatures, chemicals and nuclear energy. They perform operations made manually for long periods of time by operators in production sectors in a faster and error-free way [15,16]. By using robots, production is ensured in a way to obtain more products to meet customer expectations in shorter times and does not compromise on quality. The most important features that an industrial robot should have are the repeatability of the process, accuracy and the load capacity it can carry [17]. The load capacity it can carry varies depending on the movement speed of the mechanism used in the robot. As the load carrying capacity increases, the speed of the mechanism decreases. In order to increase the load capacity, different designs have to be obtained for the motors to be used

at lower torques. Accuracy is affected by the size and type of load as opposed to repeatability [18].

Industrial manipulators must have six degrees of freedom to reach points in their working environment or space. While the first three axes of the robot that provide the body movement are seen as separate kinematics, the wrist forming the last three axes is defined separately [19]. While the use of actuators has become increasingly important in the field of robotics, their use in industry and scientific research has become popular with the successful advances in actuator technology in recent years. Actuators are often used in robot applications such as mobile humanoid robots, walking mechanisms, and biomedical devices. It is also used in robotic applications with high specific power such as push-pull, rotation, lift-release and positioning [20-22].

As in every system in which movement occurs, vibrations occur in robot arms [23]. Natural vibrations consist of robot manipulators being moved from one point to another and suddenly stop [24]. From an industrial point of view, the residual vibration of robot manipulators is one of the undesirable situations [25]. These vibrations are generally desired for minimizing as much as possible by vibration control methods [26]. In robotic manipulators, good position accuracy is achieved by minimizing vibration of the end-effector. In conducted studies, it is generally preferred to use flexible links [27]. In addition, among the efforts to reduce the unwanted vibrations in the robot arms to low levels, it is preferred to perform the assembly process using bearings suitable for the joint parts [28]. Vibration analysis of a robotic arm with a single flexible link [29] and modal analysis of a robotic arm with a flexible link using the finite element method are examined up to the most dominant vibration modes [30]. A rigid two-degree-of-freedom robot arm forms modal analyzes using the finite element method in the Ansys workbench application [31].

When precision gear systems are used as a drive mechanism in industrial robots, high torque motors should be used to carry the load on the motors. The use of these motors causes weight on the system as well as increases the cost [32]. In order to enable the movement of a robot arm with a lower power motor, actuators that move linearly and can be controlled by stepper motors are used instead of precision gear systems. The use of this drive system, which consists of a ball screw system that delivers the same movement as linear moving systems, provides important advantages [33]. This system is designed at very small powers; and it is calculated to be able to lift more load when operated.

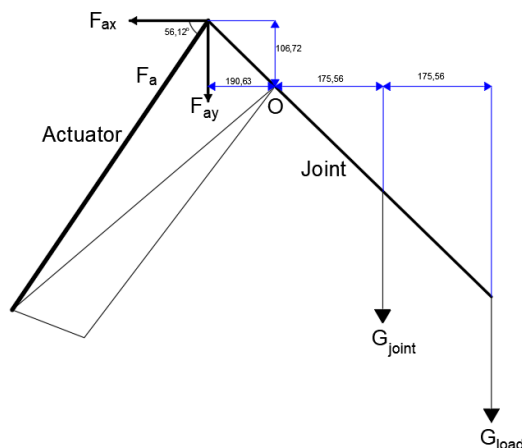


Figure 1. Torque calculation on the robot axis [33]

As shown in Fig. 1, at the O point on the 3rd axis, the motor performs movement by rotating the direct arm or by push-pull force of the actuator connected to the end of the arm. In order to calculate the torque on the motor directly connected to the O point, the weight of the bar is to be 4 kg, and the weight of the load and gripper connected to the end of the arm is accepted as 20 kg. To find the torque of the motor, the moment at point O is taken as;

$$T_{\text{motor}} = 4 \cdot 9.81 \cdot 0.17556 + 20 \cdot 9.81 \cdot 0.35111 = 75.78 \text{ Nm} \quad (1)$$

Similarly, the moment is taken at O point to calculate the force drawn by the actuator and how much torque this force creates on the motor over the ball screw (see Equation 2-4):

$$F_{\text{ax}} \cdot 0.10672 + F_{\text{ay}} \cdot 0.10963 = T_{\text{motor}} \quad (2)$$

$$F_{\text{a}} \cdot (\cos 56.12) \cdot 0.10672 + F_{\text{a}} \cdot (\sin 56.12) \cdot 0.10963 = 75.78 \quad (3)$$

$$F_{\text{a}} = 503.5 \text{ N} \quad (4)$$

When the shaft has a pitch of 5 mm and a diameter of 16 mm, the torque to the motor (Equation 5-6):

$$F_t = 0.005 \cdot 503.5 / (\pi \cdot 0.016) = 50.08 \text{ N} \quad (5)$$

$$T_{\text{motor}} = 50.08 \cdot 0.016 / 2 = 0.4 \text{ Nm} \quad (6)$$

According to these calculations, the use of smaller motors in the actuator is provided a great advantage in terms of both weight and cost.

In this study, the results are obtained by making a simulation that applies both rotation torque and linear movement in the analysis program to the rotation point that provides the movement of each arm in the robot arm that moves with the ball screw system. The aim of this study is to reveal the advantages provided by the reduction of the size of the motors used in the ball screw actuators, which produce force equivalent to the torque occurring in the arms in the propulsion system used in serial robots. In addition, when the robot is driven by a ball screw and torque, the forces applied to the system and the deformations that occur in the body of the robot are examined with the analyzes made under load. By making a modal analysis, the modes that give the behavior of the system under vibration and the natural frequencies of the system will be determined and the resonance situations will be examined. As a result of these analyses, the displacements caused by the weights on the robot arm while carrying the load and the vibrations that occur at the end of the robot are measured.

2. MATERIAL AND METHOD

In order to be efficient and reliable for the robots in the manufacturing industry, the best model is created by analyzing different designs. To optimize and improve the design, design processes such as structural analysis and dynamic simulation are utilized by using the model creation and simulation tools [34]. Modeling and simulation of robot systems using different software programs provide great advantages in design, construction and control processes. With the use of simulation, programmers take the right steps in analyzing behavior, predicting, optimizing and planning.

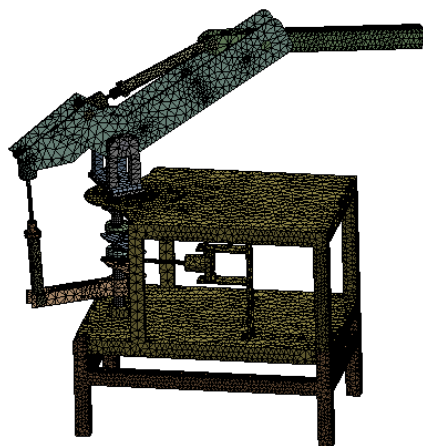


Figure 2. Meshing of the robot arm

The 3-axis robot arm is modeled in the Solidworks program as shown in Fig. 2 and moved to the Ansys program to perform the analysis. The mesh operation of the robot manipulator is applied by selecting the default setting in the mesh menu in the workbench interface.

As a result of the size meshing, it is seen that a total of 193754 points are formed on the body and all joints of the robot manipulator are divided into 85831 parts and the distance between the parts is also determined as 15 mm.

2.1. Applying Rotational Torque and Linear Force to the Robot

One of the aims of this study is to compare the torque on the motors by using the rotational torque and linear force. In order to provide three axes rotation, the robot arm is rotated by applying the linear force to the C, G and H points as shown in Fig. 3a. On the same body, torque is defined by applying rotational torque to C, G and A points as shown in Fig. 3b and as in Table 1 for moving the robot arm. When the analysis is performed, the rotation angle for the rotational movement and the progressing distance for the linear movement are defined for the driving parts. The torque applied to the axes of rotation is calculated by applying both linear force and torque to the robot.

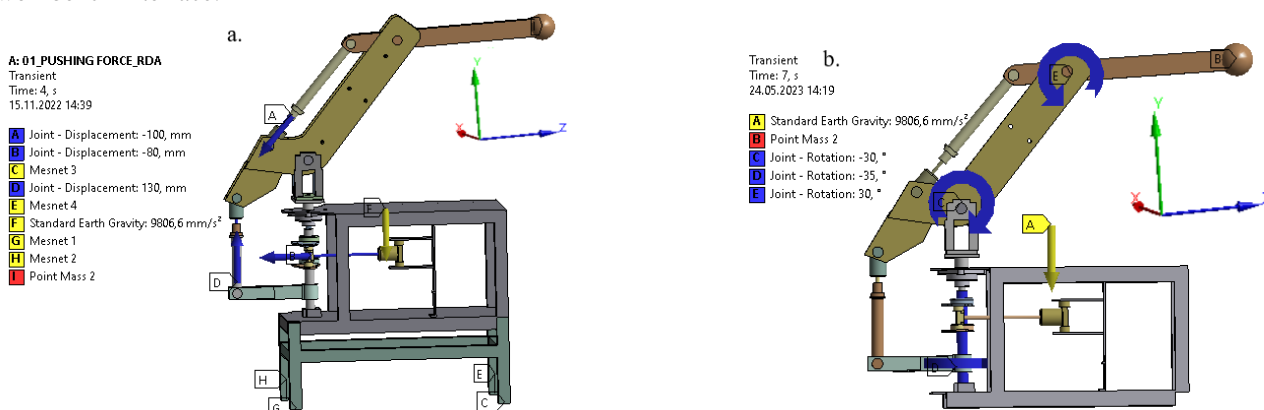


Figure 3. Applying linear force and rotational torque to the robot arm

Table 1. Angle and progression data for the movement of the robot arm

Rotational Movement Analysis Data								
Motor 1			Motor 2			Motor 3		
Steps	Time (s)	Rotation (°)	Steps	Time (s)	Rotation (°)	Steps	Time (s)	Rotation (°)
0	0	0	0	0	0	0	0	0
1	1	-10	1	1	-10	1	1	10
2	2	-20	2	2	-20	2	2	20
3	3	-30	3	3	-30	3	3	30
4	4	-35	4	4	-35	4	4	35
5	5	-30	5	5	-30	5	5	30
6	6	-20	6	6	-20	6	6	20
7	7	-10	7	7	-10	7	7	10

Linear Movement Analysis Data								
Motor 1			Motor 2			Motor 3		
Steps	Time (s)	Displacement (mm)	Steps	Time (s)	Displacement (mm)	Steps	Time (s)	Displacement (mm)
0	0	0	0	0	0	0	0	0
1	1	-25	1	1	40	1	1	-30
2	2	-50	2	2	80	2	2	-60
3	3	-75	3	3	120	3	3	-90
4	4	-80	4	4	130	4	4	-100
5	5	-75	5	5	120	5	5	-90
6	6	-50	6	6	80	6	6	-60
7	7	-25	7	7	40	7	7	-30

2.2. Modal analysis

Free vibration analysis of the system, as shown in Fig. 4, is the analysis without any external force on it. Every structure has a tendency to vibrate at certain natural frequencies. In

modal analysis, an input vibration is applied to the structure and the response of the structure to this input is measured in the form of modes. The mode shape is the shape the structure takes as it vibrates at its natural frequency. At the same time, mode shapes are the view of deformation shapes as a result of

analysis. In these Modes, natural frequency, damping and mode shapes are determined.

Modal analysis is examined in 6 modes in terms of the deformation of the structure. Thus, the vibration characteristics of the system are obtained. The linear contact group is selected for the analysis. The robot arm is fixed with four legs so that it is contacted to the ground from the bottom. Three stepper motors are placed in the robot arm. The rotational speed of each of these motors is assumed to be 500 rpm and their frequencies are calculated as 8.33 Hz.

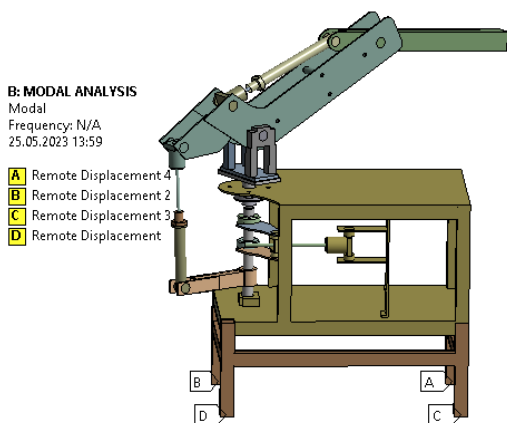


Figure 4. Modal analysis of the robot arm

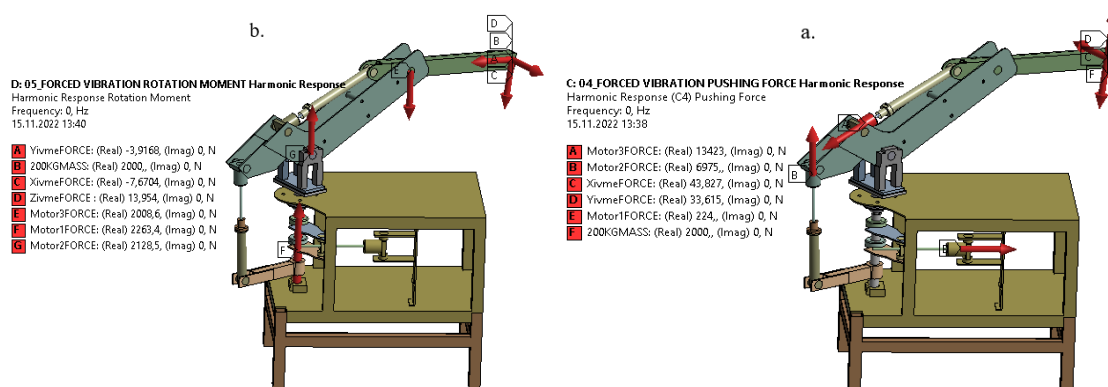


Figure 5. Modelling of harmonic analysis and frequency response a) linear b) rotational

3. RESULTS AND DISCUSSION

3.1. Torque and Force falling on the motor and the actuator

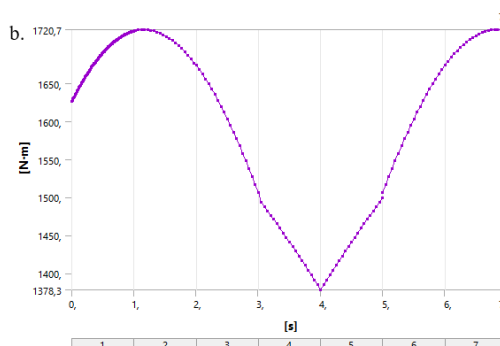
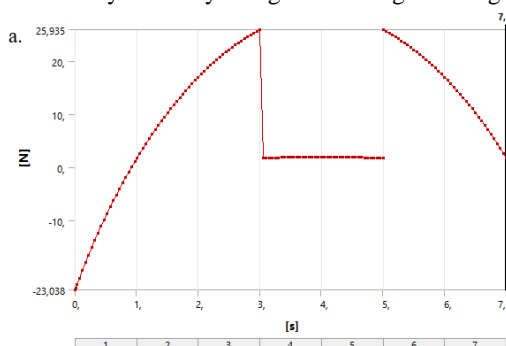
In the rigid dynamic analysis, the linear force and rotational torque graphs on each motor by moving linearly with the help of the linear force of the motors and by moving the arms with the torque applied to the rotation axes are shown in Fig. 6. When the graphics are examined, it is ensured moving the arms with less force in motor 1. In addition, the forces on the motors are measured to be very small by using the bearings moving

2.3. Harmonic response for rotational torque and pushing force

In the rigid dynamic analysis, the robot arm is moved with a free movement to a coordinate point. In order to compare the harmonic angular motion analysis and harmonic linear motion analysis results, the rigid dynamic analysis is calculated by taking values from both the rotational movement model as shown in Fig. 5a and the linear movement model as shown in Fig. 5b. Thus, results are obtained under the same conditions in the harmonic vibration analysis for both models.

In the harmonic analysis, a force of 200 kg is applied to the top axes of the robot arm as an external force in the direction of gravity, and a force of 4 kg in the direction of gravity is applied as the gripper weight in the same way. A total force of 204 kg at the top axes of the arm, multiplied by the maximum acceleration values obtained in X, Y and Z coordinates of the rigid dynamic analysis, is defined as the outer boundary condition for the harmonic analysis. These external forces are applied respectively in the direction of X, Y and Z coordinates and at the top axes of the arm. These forces are defined as the rotational torque in the rotational movement analysis and the linear force in the linear movement analysis to the shafts to which the motors are connected.

the first axis with the linear force. According to these values obtained in motor 1, motor selected very small provides great advantages in both weight of the robot and manufacturing cost. Likewise, when the force graphs on the motor 2 and motor 3 are examined, it is seen that smaller motors can be used to rotate the axes in movements generated with linear force. According to the results of the analysis, larger loads can be carried with smaller linear motors by reducing the manufacturing costs consisting of the torques on the motors and the motor weights.



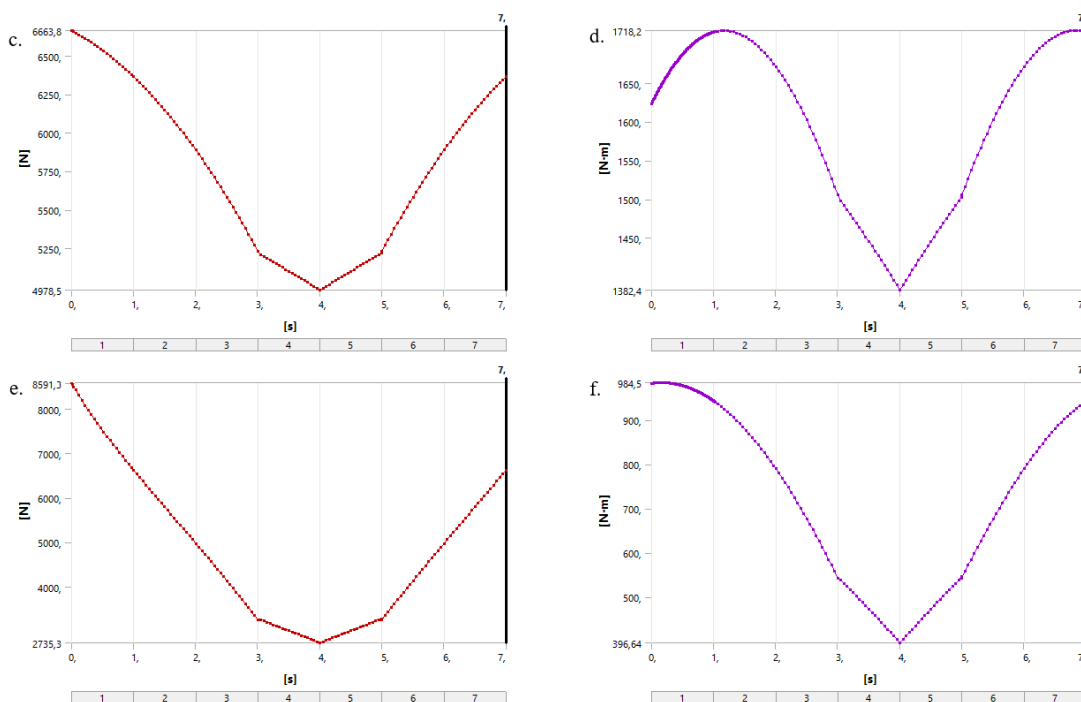
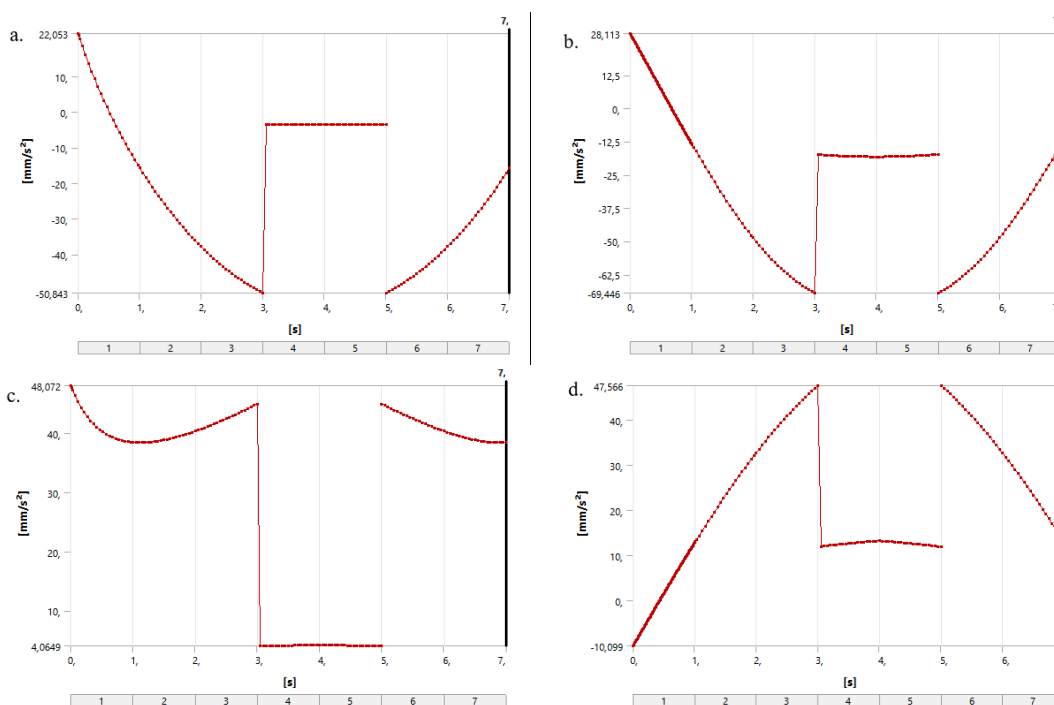


Figure 6. Forces falling on motors a) Motor 1, linear force b) Motor 1, rotational torque c) Motor 2, linear force d) Motor 2, rotational torque e) Motor 3, linear force f) Motor 3, rotational torque

3.2. Accelerations at the end-point of robot arm

According to the analysis results, the accelerations in the three-axis directions at the top axes of the robot arm are shown in Fig. 7. By using these accelerations, vibrations at the top axes are determined. The acceleration intervals in the X direction have changed between (22)-(-50) mm/s² in the linear force and between (28)-(-70) mm/s² in the rotational torque. The acceleration intervals in the Y direction have changed between (48)-(-4) mm/s² in the linear force and between (48)-(-

10) mm/s² in the rotational torque. The acceleration intervals in the Z direction also have changed between (-2) -(-126) mm/s² in the linear force and (-5) -(-98) mm/s² in the rotational torque. The acceleration graphs in X and Z directions are similar to each other, but it is seen that the value range of the linear movement is low in the accelerations in the Y direction. When the accelerations occurring in the axes defined in X, Y and Z directions at the top axes are examined, it is seen that the use of actuators moving with linear force provides an advantage.



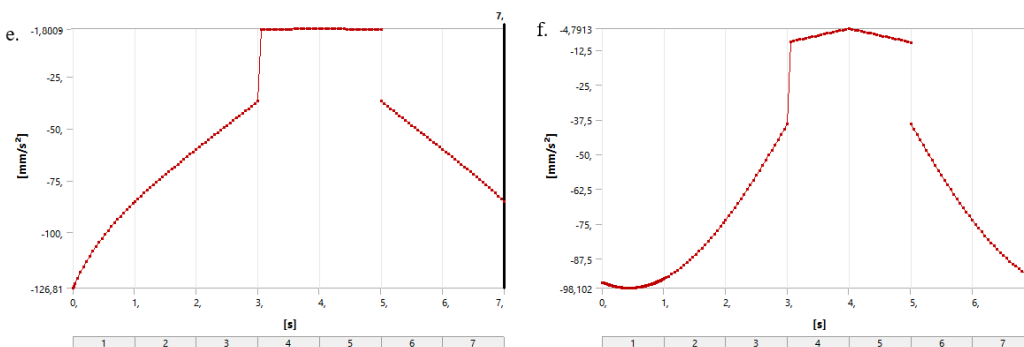


Figure 7. Accelerations at the robot end-point a) linear, in the X direction b) rotational, in X direction c) linear, in Y direction d) rotational, in Y direction e) linear, in Z direction f) rotational, in Z direction

3.3. Results of modal analysis

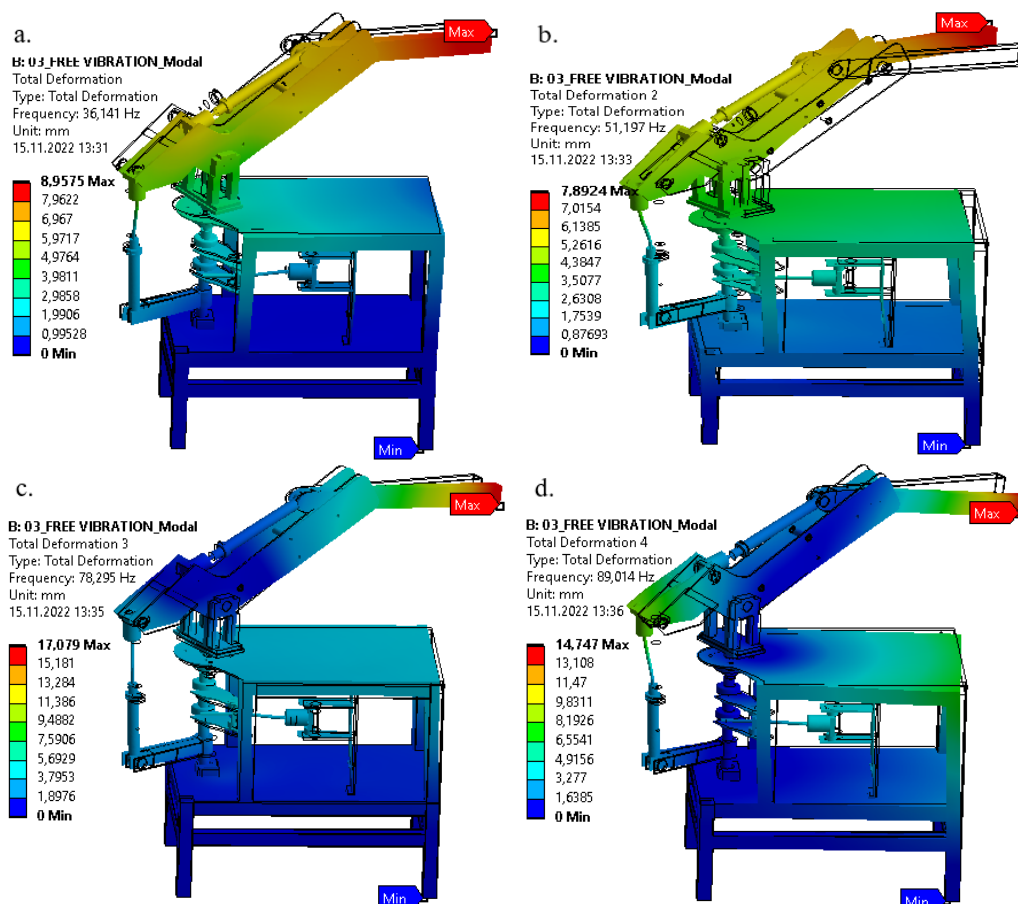
Modal analyzes of the three-axis robot arm are measured in 6 modes as shown in Table 2. The 1st mode is the vibration caused by the robot's movement to the right and left. The 2nd mode is the vibration caused by the robot pulling backwards in the Y direction. The 3rd and 5th mode is the vibration caused by the movement of the 2nd and 3rd axis to the right and left. The 4th and 6th modes are vibrations caused by the robot's rotation around itself.

In the analyzes made considering the operating frequency of the motors, as shown in Fig. 8, a total deformation of 8.95 mm has occurred at the 1st mode 36.141 Hz frequency. Similarly, respectively, the 2nd Mode is 7.89 mm at 51.197 Hz, the 3rd Mode is 17.079 mm at 78.295 Hz, the 4th Mode is 14.747 mm at 89.014 Hz, the 5th mode is 17.85mm at 100.86 Hz, and the 6th mode is 15.372 mm at 115.56 Hz.

By comparing the natural frequencies of the motors and the frequencies measured as a result of the modal analysis, the state of the system in resonance is examined. The purpose of the modal analysis of moving systems is to measure whether the system has come to its resonance value. While the natural frequency of the motors used in the three-axis robot is calculated as 8.33 Hz, the frequency values measured as the result of the modal analysis have changed between 36.141-115.56 Hz.

Table 2. Modes and frequencies formed as a result of analyzes.

Mod	Frekans (Hz)
1. Mod	36,141
2. Mod	51,197
3. Mod	78,295
4. Mod	89,014
5. Mod	100,86
6. Mod	115,56



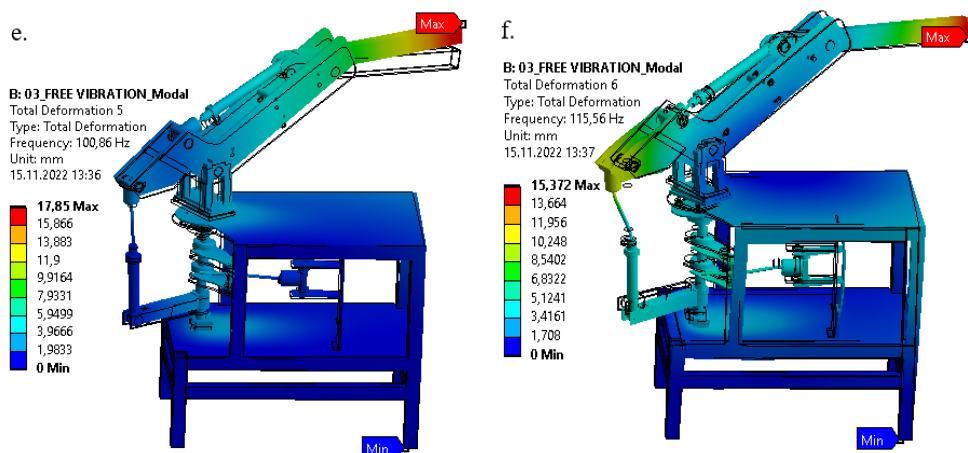


Figure 8. Total deformation in 6 modes a) mod 1 b) mod 2 c) mod 3 d) mod 4 e) mod 5 f) mod 6

3.3. Results of forced vibration analysis

In the harmonic analysis of the middle arm, which forms the 2nd axis of the robot, the maximum and minimum points, at which the total deformation and von-Mises stress have occurred in the arm, are shown in Fig. 9. When the harmonic analysis results of this arm are examined, it is observed that the maximum total deformation in linear movement in the middle arm is measured as 3.55 mm and von-Mises stress

as maximum 64.825 MPa. Likewise, the maximum total deformation in rotational movement is measured at 1.5 mm and von-Mises stress as 50.63 MPa maximum. According to these results, it is determined that the values of deformation and von-Mises stress are greater in linear movement. It is seen that it is more advantageous to drive this arm with the rotational movement since the small deformation and von-Mises stress of the structure is considered to be a better design.

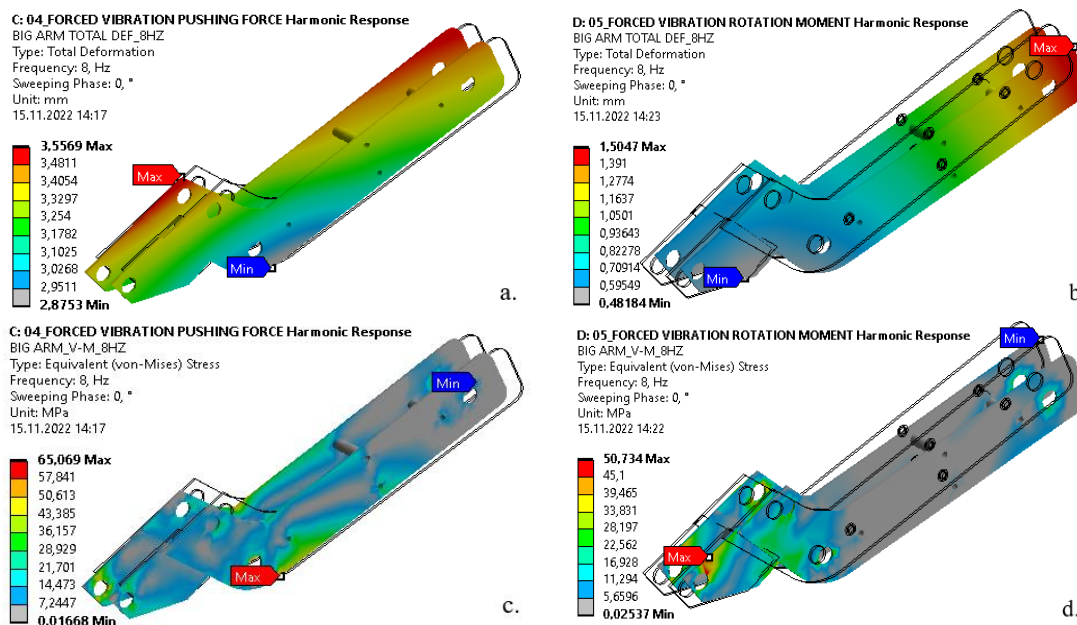


Figure 9. Results of 2nd arm harmonic analysis a) linear, total deformation (mm) b) rotational, total deformation (mm) c) linear, von-Mises stress (Mpa) d) rotational, von-Mises stress (Mpa)

In the harmonic analysis of the arm, which forms the 3rd axis of the robot, the maximum and minimum points where the total deformation and von-Mises stress have occurred in the arm are shown in Fig. 10. When the results of the harmonic analysis of this arm are examined, it is seen that the linear movement is measured the maximum total deformation as 3.52 mm and von-Mises stress as maximum 50.42 MPa. Likewise, the rotational movement is measured

the maximum total deformations as 2.8 mm and von-Mises stress as a maximum of 76.48 MPa. According to these results, it is determined that the deformation is greater in linear movement, and von Mises stress is greater in rotational movement. Since von-Mises stress is small in linear movement, moving the arm with the linear force is seen as a better design.

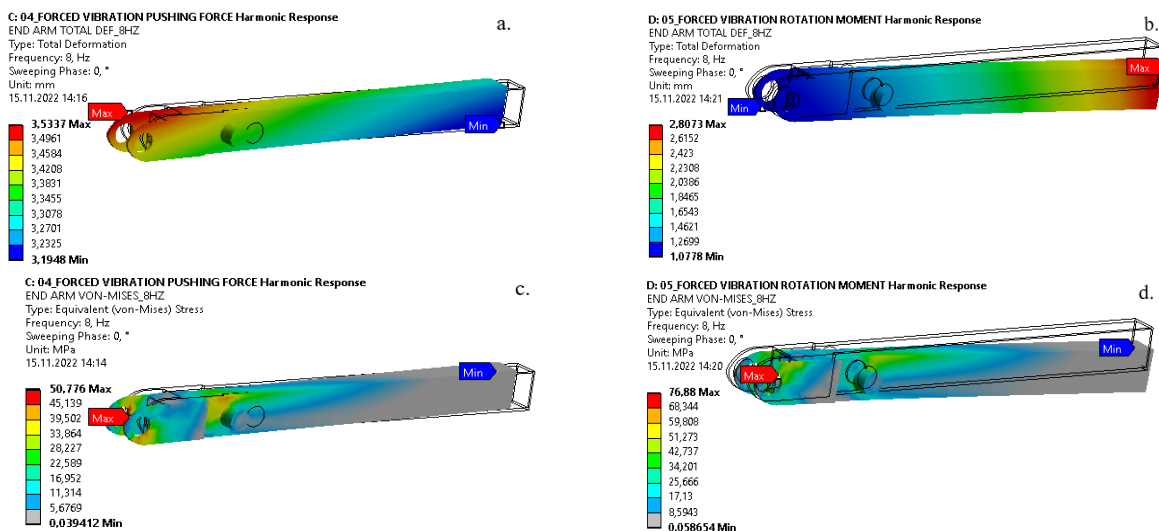


Figure 10. Harmonic analysis results of the 3rd arm a) linear, total deformation (mm) b) rotational, total deformation (mm) c) linear, von-misses (Mpa) d) rotational, von-misses (Mpa)

The maximum and minimum points of the total von-Mises stress on the body in the harmonic analysis for the robot's body are shown in Fig. 11. According to the results of the harmonic analysis, the maximum von-Mises is measured in linear movement as 460.89 MPa and in rotational movement as 474.38 MPa. Although von-Mises stress has

not changed much in the two different movements, it is more advantageous in linear movement as it is measured less. Thus, according to the results of all harmonic analyses, it is accepted that the robot driven by linear movement can be chosen as a better design model.

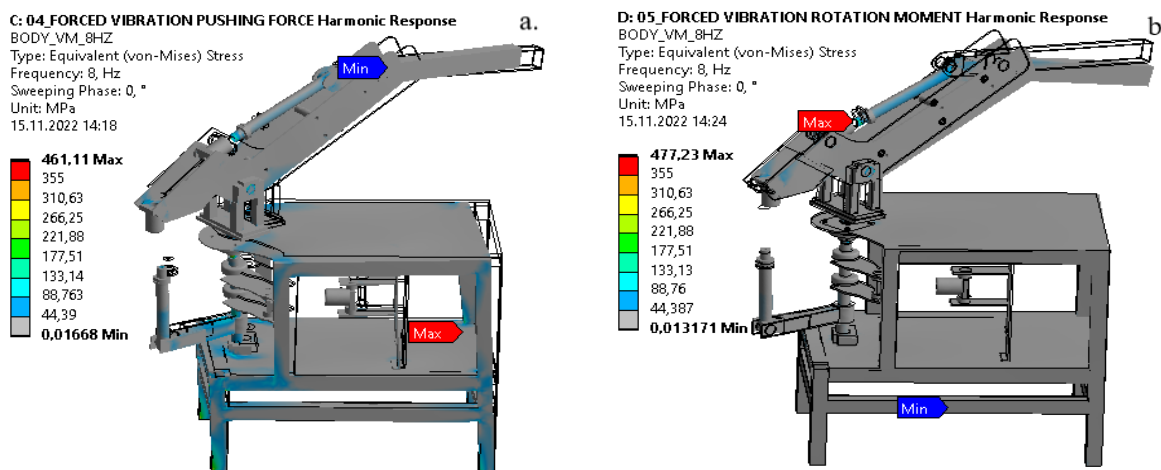


Figure 11. Body results of harmonic analysis a) linear, von-Mises stress (Mpa) b) rotational, von-Mises stress (Mpa)

In the forced vibration analysis of the system, the normal stress graph in linear movement and the normal stress graph in rotational movement are shown in Fig. 12. When the graphs are examined, in linear motion the maximum stress occurred at 100 Hz and the minimum stress at 35 Hz. In the

rotational movement, the maximum stress occurred at 100 Hz and the minimum stress at 112.5 Hz. In addition, the normal stress amplitude has increased up to 6 MPa in linear movement and up to 6.3 MPa in rotational movement.

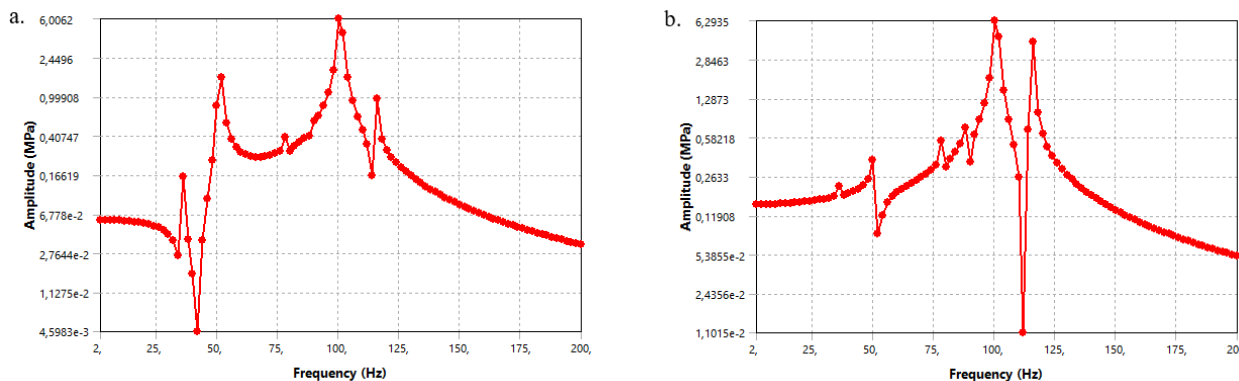


Figure 12. Graph of normal stress in a) linear movement and b) rotational movement

4. CONCLUSIONS

From past to present, the use of robots in developed industrial areas has gained importance day by day. The most important features of working robots in the industrial field have possessed the weight and the vibrations that have occurred at the endpoint. In robot arms used in industry, the parts used in drive and control should be chosen from quite light materials, since the weights of the parts are added to the weight on the previous arm. Since the size of the motors is increased in parallel with the magnitude of the force on the motor, the weight on each arm is also increased. In this study, the forces on the motors in the movements of the three axes industrial robot in two different drives and the torques created by these forces on the motor are examined. The robot is operated by applying torque to the rotation point of the arms with the linear force in the ball screw system. In the other system, it is also operated by applying a direct torque to the rotation point of the arms. The aim of this study is to determine which drive system is advantageous by comparing the torque created on the motor shaft by the forces falling on each motor in the linear drive system and the torque values applied to the rotation axis. In addition, the accelerations occurring at the endpoint of the robot during the operation of the motors in two different drive systems are measured, and the vibrations occurring at the endpoint of the system from these accelerations are compared.

As a result of the calculations, the torque value calculated for the 3rd motor in the drive system made with linear actuator was 0.4 Nm, while it was 75.78 Nm in the drive system made by applying rotation torque. The weight and cost of stepper motors increase in parallel with the torque they produce. The costs of the motors can be calculated by looking at the dimensions of the motors that must be used to meet these torques. In addition, as the dimensions of the engines increase, their weight will also increase, so the mass of the system and, accordingly, inertia will increase. As a result, it causes more weight on the system and increases its manufacturing cost.

As a result of the analyses, considering the torque on the motors and the vibrations at the endpoint, it is seen that the design created by applying linear force is more advantageous. In the modal analysis of the system, the natural frequencies and deformations occurring in 6 different modes and the resonance state of the stepper motors used in the robot arm at certain revolutions were examined. In addition, forced vibration and harmonic analysis of the system are made and total deformation, von Mises stress and normal stress graphs are obtained in each part and in all system. It has been calculated that this drive system can carry the same weight by applying approximately 1/20 of the torque value required to be applied according to the drive system used to move conventional robots. Thus, since the weights and costs of the motors will decrease at the same rate, the total weight of the robot arm, the weights of the arms forming each axis and the total cost will decrease.

REFERENCES

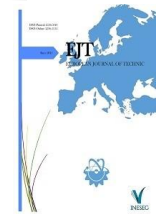
- [1] Ertuğrul Ş, Kaya O, Eraslan H, et al. Humanoid robot arm design, simulation, kinesthetic learning, impedance control and suggestions. *Journal of the Faculty of Engineering and Architecture of Gazi University*. Vol. 37, No. 2, pp. 1139-1154, 2022.
- [2] Mehrpouya M, Dehghanghadikolaei A, Fotovvati B, et al. The potential of additive manufacturing in the smart factory industrial 4.0: A review. *Applied Sciences*. Vol. 9, No. 18, pp. 3865, 2019.
- [3] Lu Y, Xu X and Wang L. Smart manufacturing process and system automation—a critical review of the standards and envisioned scenarios. *Journal of Manufacturing Systems*. Vol. 56, pp. 312-325, 2020.
- [4] Almurib HA, Al-Qrimli HF and Kumar N. A review of application industrial robotic design. In: 2011 Ninth International Conference on ICT and Knowledge Engineering. Bangkok, Thailand, 12-13 January 2012; pp. 105-112. IEEE.
- [5] Evjemo LD, Gjerstad T, Grøtli EI, et al. Trends in smart manufacturing: Role of humans and industrial robots in smart factories. *Current Robotics Reports*. Vol. 1, No. 2, pp. 35-41, 2020.
- [6] Hedelind M. and Jackson M. "How to improve the use of industrial robots in lean manufacturing systems", *Journal of Manufacturing Technology Management*. Vol. 22, No. 7, pp. 891-905, 2011.
- [7] Acharya V, Sharma SK and Gupta SK. Analyzing the factors in industrial automation using analytic hierarchy process. *Computers & Electrical Engineering*. Vol. 71, pp. 877-886, 2018.
- [8] Pan Z, Polden J, Larkin N, et al. Recent progress on programming methods for industrial robots. *Robotics and Computer-Integrated Manufacturing*. Vol. 28, No. 2, pp. 87-94, 2012.
- [9] Bal HÇ and Erkan Ç. Industry 4.0 and competitiveness. *Procedia computer science*. Vol. 158, pp. 625-631, 2019.
- [10] Li Z, Li S and Luo X. An overview of calibration technology of industrial robots. *IEEE/CAA Journal of Automatica Sinica*. Vol. 8, No. 1, pp. 23-36, 2021.
- [11] Tezel C, Günay O and Kayisli K. Implementation of a Robot Hand Controlled with Android Software. *International Journal of Engineering Science and Application*. Vol. 1, No. 4, pp. 137-141, 2017.
- [12] Luo X, Liu S, Xu M, et al. On research progress and development trend for motion control problems of industrial robots. In: 2018 8th International Conference on Manufacturing Science and Engineering (ICMSE 2018). Shenzhen, China, 30-31 March 2018, pp. 241-246. Atlantis Press.
- [13] Garcia E, Jimenez MA, De Santos PG, et al. The evolution of robotics research. *IEEE Robotics & Automation Magazine*. Vol. 14, No. 1, pp. 90-103, 2017.
- [14] Swevers J, Verdonck W and De Schutter J. Dynamic model identification for industrial robots. *IEEE control systems magazine*. Vol. 27, No. 5, pp. 58-71, 2007.
- [15] Tsitsimpelis I, Taylor CJ, Lennox B, et al. A review of ground-based robotic systems for the characterization of nuclear environments. *Progress in nuclear energy*. Vol. 111, pp. 109-124, 2019.
- [16] Pogliani M, Quarta D, Polino M, et al. Security of controlled manufacturing systems in the connected factory: the case of industrial robots. *J Comput Virol Hack Tech*. Vol. 15, pp. 161-175, 2019.
- [17] Lu Z, Chauhan A, Silva F, et al. A brief survey of commercial robotic arms for research on manipulation. In: 2012 IEEE Symposium on Robotics and Applications (ISRA). Kuala Lumpur, Malaysia, 3-5 June 2012. pp. 986-991. IEEE.
- [18] Ayyıldız M and Aşkar Ayyıldız E. Accuracy and Repeatability Performance of Prototype Linear Delta Robot. *Duzce University Journal of Science and Technology*. Vol. 8, No. 1, pp. 869-879, 2020.
- [19] Almurib HA, Al-Qrimli HF and Kumar N. A review of application industrial robotic design. In: 2011 Ninth International Conference on ICT and Knowledge Engineering. Bangkok, Thailand, 12-13 January 2012. pp. 105-112. IEEE.
- [20] Ehsani M, Gao Y and Gay S. Characterization of electric motor drives for traction applications. In: Proceedings of the IECON'03: 29th annual conference of the IEEE industrial electronics society (IEEE Cat. No. 03CH37468). Roanoke, VA, 2-6 November 2003, pp.891-896. New York: IEEE.
- [21] Madden JDW. Mobile robots: motor challenges and materials solutions. *Science*. Vol. 318, pp. 1094-1097, 2007.
- [22] Liang W, Liu H, Wang K, et al. Comparative study of robotic artificial actuators and biological muscle. *Advances in Mechanical Engineering*. Vol. 12, No. 6, pp. 1-25, 2020.

- [23] Kapsalas CN, Sakellariou JS, Koustoumpardis PN, et al. An ARX-based method for the vibration control of flexible beams manipulated by industrial robots. *Robotics and Computer-Integrated Manufacturing*. Vol. 52, pp. 76-91, 2018.
- [24] Thomsen DK, Sørensen R, Balling O, et al. Vibration control of industrial robot arms by multi-mode time-varying input shaping. *Mechanism and Machine Theory*. Vol. 155, pp. 1-32, 2021.
- [25] Chang PH and Park HS. Time-varying input shaping technique applied to vibration reduction of an industrial robot. *Control Engineering Practice*. Vol. 13, No. 1, pp. 121-130, 2005.
- [26] Mohamed Z, Chee AK, Hashim AM, et al. Techniques for vibration control of a flexible robot manipulator. *Robotica*. Vol. 24, No. 4, pp. 499-511, 2006.
- [27] Dwivedy SK and Eberhard P. Dynamic analysis of flexible manipulators, a literature review. *Mechanism and machine theory*. Vol. 41, No. 7, pp. 749-777, 2006.
- [28] Telli S and Kopmaz O. Two Different Methods to Investigate Dynamic Motion of Flexible Link That Rotates About Fixed Axes. *Turkish Journal of Engineering and Environmental Sciences*. Vol. 24, No. 3, pp. 127-134, 2000.
- [29] Tso SK, Yang TW, Xu WL, et al. Vibration control for a flexible-link robot arm with deflection feedback. *International journal of non-linear mechanics*. Vol. 38, No.1, pp. 51-62, 2003.
- [30] Garcia-Perez OA, Silva-Navarro G and Peza-Solis JF. Flexible-link robots with combined trajectory tracking and vibration control. *Applied Mathematical Modelling*. Vol. 70, pp. 285-298, 2019.
- [31] Sahu S, Choudhury BB and Biswal BB. A vibration analysis of a 6 axis industrial robot using FEA. *Materials Today: Proceedings*. Vol. 4, No. 2, pp. 2403-2410, 2017.
- [32] Pham AD and Ahn HJ. High precision reducers for industrial robots driving 4th industrial revolution: state of arts, analysis, design, performance evaluation and perspective. *International journal of precision engineering and manufacturing-green technology*. Vol. 5, No. 4, pp. 519-533, 2018.
- [33] Koç S and Doğan C. Manufacturing and controlling 5-axis ball screw driven industrial robot moving through G codes, Gümüşhane University Journal of Science and Technology. Vol. 12, No. 2, pp. 454-465, 2022.
- [34] Raza K, Khan T and Abbas N. Kinematic analysis and geometrical improvement of an industrial robotic arm. *Journal of King Saud University-Engineering Sciences*. Vol. 30, No. 3, pp. 218-223, 2018.

BIOGRAPHIES

Savaş KOÇ obtained his M.Sc degree in electrical Teaching from Firat University, Institute of Science and Technology and Ph.D degree in Mechanical Engineering from Harran University, Institute of Science and Technology. He is working as Assistant Professor at Department of Mechanical Engineering, Batman University. His main research fields are industrial robot and artificial intelligence..

İdris ŞANI obtained his M.Sc. degree in Mechanical Engineering from Batman University, Institute of Science and Technology. He is working as Technician at Mardin Disaster and Emergency Management Presidency (AFAD).



Research Article

MATLAB/Simulink Modeling of Regenerative Recovery Circuit with Bidirectional DC-DC Converter for Scooter

Ali Sinan Çabuk^{1*}

^{1*}Istanbul Technical University, Electrical Engineering Department, 34469, Maslak, Istanbul, Turkey. (e-mail: ascabuk@itu.edu.tr).

ARTICLE INFO

Received: Jun., 17. 2023

Revised: Jul., 06. 2023

Accepted: Jul., 06. 2023

Keywords:

DC-DC converter

Regenerative recovery

BLDCM

MATLAB/Simulink

Bidirectional

Corresponding author: *Ali Sinan Cabuk*

ISSN: 2536-5010 / e-ISSN: 2536-5134

DOI: <https://doi.org/10.36222/ejt.1316098>

ABSTRACT

Scooter, which is in the class of light electric vehicles, is a very common transportation vehicle, especially in big cities. Brushless direct current motor (BLDCM) is preferred in scooters. These motors are a type of electric motor used in light electric vehicles (LEV) due to their features such as high efficiency, long operating life, high speed and silence operation. Although the BLDCMs used in the propulsion system of the scooter have high efficiency, they do not have a long range due to their limited battery capacity. The biggest problem with scooters is their short range. In order to solve this negativity, manufacturers are working on different solutions.

In this study, MATLAB/Simulink modelling of bidirectional DC-DC converter regenerative recovery circuit for scooter was carried out. It is aimed to increase the range with regenerative recovery. The system in the proposed study is implemented for a 300W BLDCM with a rated voltage of 24V. The effect of bidirectional DC-DC converter regenerative recovery is proven by MATLAB/Simulink results.

1. INTRODUCTION

Today, electric vehicles are used to reduce the increasing environmental pollution problems. Small and light electric vehicles (LEV) are preferred in large cities with dense population. Scooters are widely used in today's big cities as LEV. The range of electric vehicles is limited by their battery capacity. An electric vehicle with widely used batteries today has a shorter range. However, the battery charge time required for the electric vehicle to start again is quite high. In order to eliminate these disadvantages mentioned in electric vehicles, the energy in the battery should be used efficiently [1-3]. There are many methods used in the literature to increase the range of electric vehicles. Among these methods are increasing the efficiency of the electric motor, using different mechanical designs and using the regenerative braking method. These methods are used in all electric vehicles. In recent years, scooters have been widely used due to their practical use and the absence of traffic problems [4, 5]. Methods of optimizing electric motors and using different mechanical designs are the methods used to increase the range of scooters. However, the use of regenerative braking, which is one of these methods, is not preferred by the manufacturers in scooters that have a lot of use in urban transportation.

The purpose of the regenerative braking method is to transfer the energy produced in the electric motor during

braking of the vehicle to the battery group. Thus, the vehicle has the opportunity to store a certain amount of an energy in the battery while driving. The energy is used again for the movement of the vehicle. Thus, the range value of the vehicle is increased.

The electric motors used in scooters are direct drive motors. The movement taken from the motor is designed without using any powertrain. Hereby, external rotor electric motors are preferred in scooters. The Brushless Direct Current Motor (BLDCM) is the most widely used in scooters. BLDCM controls are made with two methods, with and without sensors. In both methods, power electronic elements and microprocessor are used. The regenerative braking method used in BLDCM is unique to every electric vehicle. It is unique because of the power circuit components and software used [6].

Microprocessors suitable for Digital Signal Controller (dsPIC), Peripheral Interface Controller (PIC), Digital Signal Processing (DSP) and Sliding Mode Control (SMC) structure are used in sensor control algorithms. dsPICs are capable of stable, fast and high-resolution detection. In addition, it is preferred for regenerative control of electric motors used in electric vehicles, as it has special Pulse Width Modulation (PWM) channels for motor control [7, 8]. However, it is seen that the output of the microprocessor cannot provide sufficient current in the use of dsPIC. Therefore, motor driver

integration is used between the processor and semiconductor power electronics elements [9]. dsPIC needs the speed information obtained from the hall sensor and the data it receives from the current sensor in sensor control methods for system control [10]. It is important to use SMC as a control algorithm in regenerative systems using PIC. The SMC algorithm assists in detecting the time variation of BLDCM resistance and inductance values with temperature or other factors [11]. DSP is a special microprocessor that converts input signals from analog to digital and performs calculations on the signals more efficiently. One of the biggest advantages of DSP is that it allows system parameters to be easily changed to adapt to the application. Regenerative recovery circuits created with DSP are more complex than others. It has a more advanced architecture as software [12].

Sensorless algorithms are based on the back-EMF principle. The zero crossing points of the back-EMF are obtained by comparing the phase at the section with the star point. In some regenerative recovery systems, the back-EMF method is not preferred due to the noise and error rate in the signal. The noise and error rate in the signal create high torque vibrations. Therefore, vector control is preferred in system control. DSP is generally preferred in applications performed with Field Oriented Control (FOC). When the control is performed with FOC, the control algorithm is complex and the processor load is high. In such applications, DSP is used even if the software is complex [13, 14].

In this study, MATLAB/Simulink modeling of regenerative recovery circuit with bidirectional DC-DC converter for scooter is implemented. In the literature and applications, regenerative recovery system design has been found on the scooter, which is in the category of light electric vehicles. The outer rotor BLDCM used in electric scooters has been the focus of this study to fill this gap in the literature. In order for the BLDCM to work in the regenerative braking zone, the necessary control algorithm has been developed and the power electronics circuit has been modeled. The BLDCM used in the study has a rated power of 300 W, 24-36 V and a speed of 2120 rpm. Electronic circuit simulation was carried out with the LTspice software to determine the switching elements and other electronic elements that can be used in the driver circuit. The necessary algorithm for the control of the driver circuit and the test of this algorithm have been made. The model of the system required for the regenerative recovery circuit and the transfer of the recovered energy to the battery was created with the MATLAB/Simulink software. Recovery in scooters, which are frequently used in daily life, is an incomplete issue in the literature. In this study, the design of the bidirectional DC-DC converter regenerative recovery circuit, which is not included in the literature, has been realized.

2. PROPOSED SYSTEM MODEL

The outer rotor BLDCM works in 4 zones. BLDCM needs to operate in the regenerative braking zone for regenerative state. These regions are shown in Figure 1. The first quarter is the forward acceleration zone. This is the quarter positive speed-positive torque situation. The second quarter is the reverse braking zone. This is the quarter negative speed-positive torque situation. The third quarter is the region of reverse acceleration. This is the quarter negative speed-negative torque situation. The fourth quarter is the forward braking zone. This quarter is the positive speed-negative torque situation [15]. By changing the direction of the phase current in the regenerative braking region, a negative force is applied to the BLDCM. In this case, since the direction of the

current is towards the battery, the mechanical energy of the motor can be stored as electrical energy.

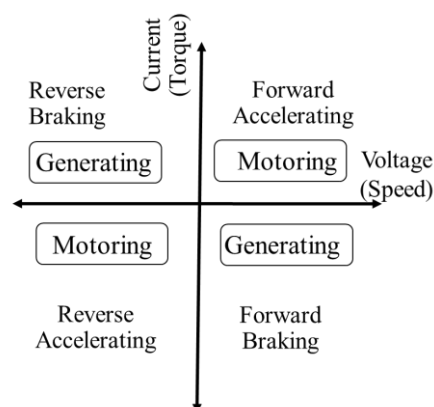


Figure 1. Quadrants of Operation Using a BLDCM [15]

If the switching sequence is set to reverse the direction of the current, the BLDCM will operate in the braking zone. The force to be applied to the motor can be adjusted in the opposite direction by adjusting the PWM. The operating zone of the BLDCM is determined by controlling the switching signals. This control is provided by the microprocessor. The signals received from the processor are transmitted to a driver circuit and transferred to the trigger terminals of the switching elements. The structure of the system is as in Figure 2.

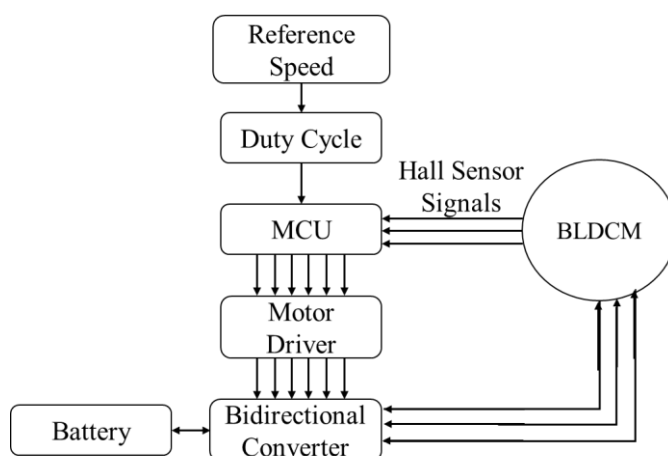


Figure 2. System Flow Diagram

The BLDCM is powered by the DC bus voltage, but the current is controlled by commutation stage semiconductor switching elements. The commutation time is determined by the rotor position. Rotor position is detected differently in sensorless and sensed motors. In this study, since sensor control is preferred, rotor position is obtained with hall sensors. When permanent magnets on the rotor surface pass by the hall sensors, the position of the rotor is known by giving a 0-1 digital signal. The digital signal string is transmitted to the microcontroller. This data is compared with the reference speed with the control algorithm. According to the comparison result, the PWM signal is generated. The digital code sequence coming from the hall sensor changes according to the rotation direction of the motor. The microcontroller controls the bidirectional converter according to which quarter mode the BLDCM operates.

The truth tables for the operation of the motor operating zone and the regenerative braking zone are as in Tables 1 and 2 [9, 16].

TABLE I
MOTOR OPERATING ZONE

Step	Hall Signals			Switching Signals					
	H1	H2	H3	S1	S3	S5	S2	S4	S6
I	1	0	1	0	0	1	0	1	0
II	1	0	0	1	0	0	0	1	0
III	1	1	0	1	0	0	0	0	1
IV	0	1	0	0	1	0	0	0	1
V	0	1	1	0	1	0	1	0	0
VI	0	0	1	0	0	1	1	0	0

TABLE II
REGENERATIVE BRAKING ZONE

Step	Hall Signals			Switching Signals					
	H1	H2	H3	S1	S3	S5	S2	S4	S6
I	1	0	1	0	0	1	0	1	0
II	1	0	0	1	0	0	0	1	0
III	1	1	0	1	0	0	0	0	1
IV	0	1	0	0	1	0	0	0	1
V	0	1	1	0	1	0	1	0	0
VI	0	0	1	0	0	1	1	0	0

2.1. Simulation of LTspice Circuit

The LTspice program was used to determine the current and voltage values and waveforms of the BLDCM driver of the proposed system. It is necessary to know the electrical characteristic Equation (1) of the motor for BLDCM driver design [17-19].

$$\begin{bmatrix} V_a & -e_a \\ V_b & -e_b \\ V_c & -e_c \end{bmatrix} = \begin{bmatrix} R & 0 & 0 \\ 0 & R & 0 \\ 0 & 0 & R \end{bmatrix} \begin{bmatrix} i_a \\ i_b \\ i_c \end{bmatrix} + \begin{bmatrix} L & M & M \\ M & L & M \\ M & M & L \end{bmatrix} \frac{d}{dt} \begin{bmatrix} i_a \\ i_b \\ i_c \end{bmatrix} \quad (1)$$

where V is the voltage applied to the stator windings, e is the EMF formed in the stator windings, R is the phase winding resistance of a phase, i is the current passing through the winding, L is the stator winding inductance, M is mutual inductance and a, b, c phase windings.

The driver circuit designed with the LTspice program is shown in Figure 3. There are six IRF540N type MOSFETs in the inverter circuit. The drain-source voltage of this MOSFET is 100V and the continuous drain current is 33A. This MOSFET is suitable for fast switching as its input parasitic capacitance is low.

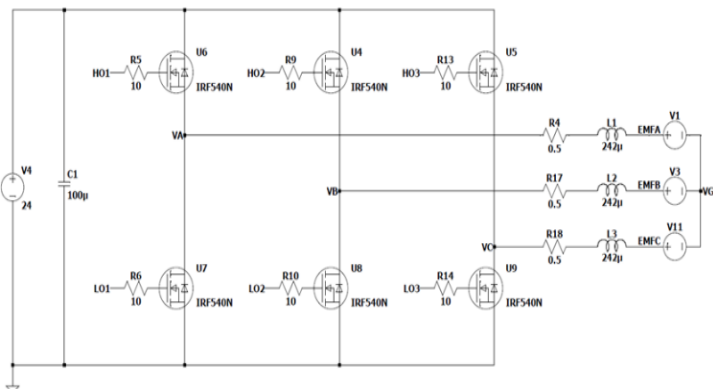


Figure 3. LTspice Model of Driver Circuit

BLDCM's back EMF waveform is designed as trapezoidal. There is a 60° phase difference between the trapezoidal waves seen in Figure 4.

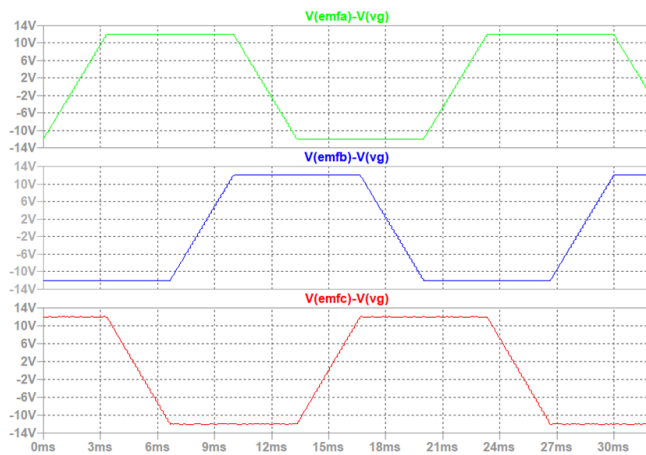


Figure 4. Back EMF voltages of phases A, B and C

The maximum and minimum values of the voltage depend on the speed of the motor and the voltage coefficient. Commutation is performed electronically in BLDCM. In the proposed circuit, 120° square wave commutation is implemented. Phase currents are shown in Figure 5. While the BLDCM phases are energized, the current passes through one phase and returns from another phase. In this case, there is no energy in the third phase. This process is carried out in accordance with a certain phase sequence and the movement of the motor is provided.

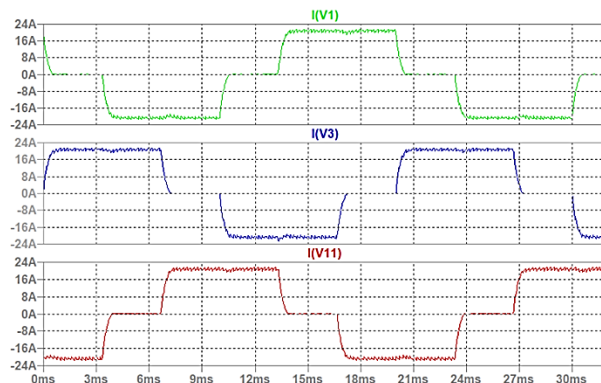


Figure 5. Phase currents A, B, C for 90% pulse width

It was observed that the phase current increased when the percentage of pulse width increased. This means more braking torque. Equation 2 is used to calculate the braking torque and compare the torque produced at two different pulse widths [17-19].

$$T = (e_a \cdot i_a + e_b \cdot i_b + e_c \cdot i_c) / 2\pi f \quad (2)$$

where f is the frequency. e is the back EMF voltage of the phase, i is the phase current. a, b and c represent phases A, B and C. The electromagnetic torque produced by the BLDCM is as in Equation 3 [17-19].

$$T_e = K_t / 2 (e(\theta_r) i_a + e(\theta_r - 2\pi/3) i_b + e(\theta_r + 2\pi/3) i_c) \quad (3)$$

where K_t is torque constant and θ_r is the rotor angle. Braking torque is given by Equation 4 [20].

$$T_{break} = K_t \cdot i \quad (4)$$

The output torques at 50% and 90% pulse width are compared for the increase of the braking torque specified in Equation 2. Figure 6 shows the electromagnetic torque.

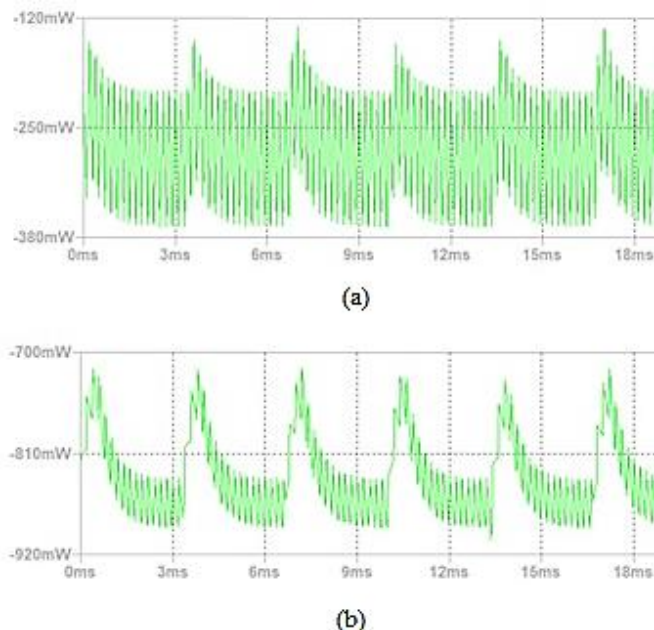


Figure 6. Electromagnetic Torque of BLDCM a) 50% pulse width b) 90% pulse width

It is seen that an average braking torque of 0.275 Nm is obtained in the case of 50% pulse width. An average braking torque of 0.834 Nm is produced at 90% pulse width. The braking torque produced increased when the percentage of pulse width was increased.

3. MATLAB/SIMULINK MODEL

In the study, outer rotor BLDCM, which is preferred by many scooter manufacturers, was used. The subject of the study is the BLDCM hall sensor. The parameters of the motor are given in Table 3.

TABLE III
PARAMETERS OF BLDCM

Parameter	Value
Power [W]	300
Voltage [V]	24
Speed [rpm]	2120

3.1. Bidirectional DC-to-DC converter

A bidirectional DC-to-DC converter is circuit that enables the conversion of DC power in both directions. It is commonly used in applications where power needs to be efficiently transferred and shared between two systems or energy storage devices. The bidirectional converter frequently consists of control circuits and power semiconductor switches. The control circuitry puts in order the switching of the semiconductor switches to acquire the target power flow direction and efficiency. It ensures that the power is warrantably interchanged between the input and output. Moreover, the converter contains feedback loops, control algorithms and protective features. The bidirectional DC-DC converter has many advantages. These are voltage regulation, energy efficiency and power flow control. It enables efficient energy transfer between different voltage levels or energy storage devices, enabling functions such as battery charging, discharging and power sharing between multiple sources or loads.

In the proposed system, there is a bidirectional DC-DC converter between the inverter and the battery as in Figure 7.

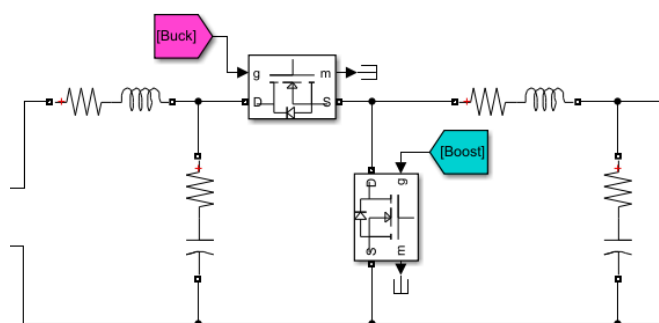


Figure 7. Bidirectional DC-to-DC Converter

When the motor is running in the forward direction (forward acceleration zone), the bidirectional converter works as a Buck DC-DC converter. In the regenerative braking state, the bidirectional converter works as a Boost DC-DC converter. Thus, bidirectional energy flow is provided both from the battery to the BLDCM and from the BLDCM to the battery. Another advantage of the bidirectional DC-DC converter is that the DC input voltage of the inverter can be adjusted. Thus, the speed control of the motor can be realized and the pulse width setting of the switch used in the step-down converter operating state is changed.

3.2. Inverting Block

The inverter block used for electronic commutation is given in Figure 8. This block consists of six power switching elements. Each switch has a control input. The data received from the Hall sensors are processed in the controller block and the order and duration of the power switches are set.

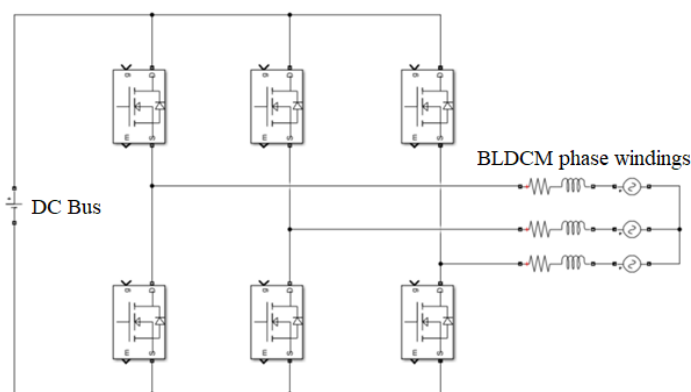


Figure 8. The Inverter Block and Motor Phase Windings

3.3. Controller

The internal structure of the controller block is shown in Figure 9. There are three basic structures in the controller block. These are inverter control, step-down converter control and step-up converter control. In the inverter control, the model in Table 1, which is used in the motor running condition, has been created.

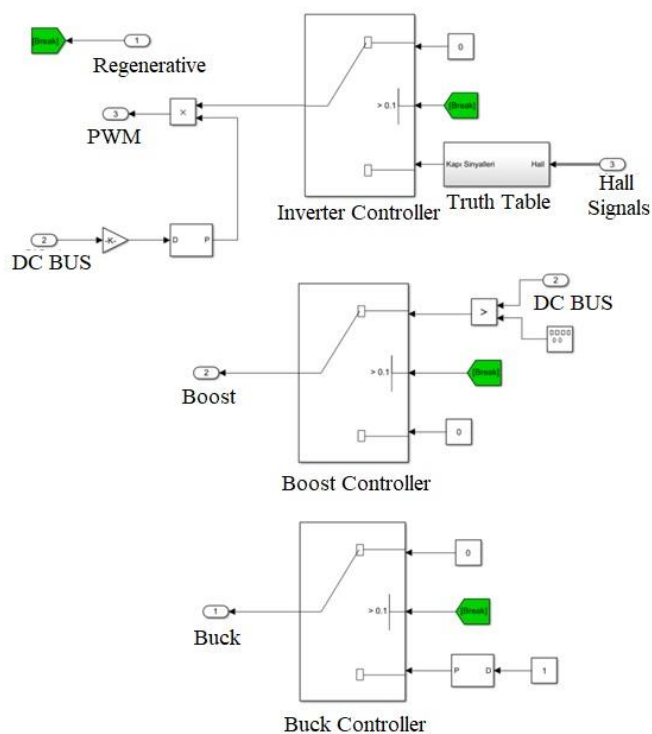


Figure 9. Controller Blocks of The System

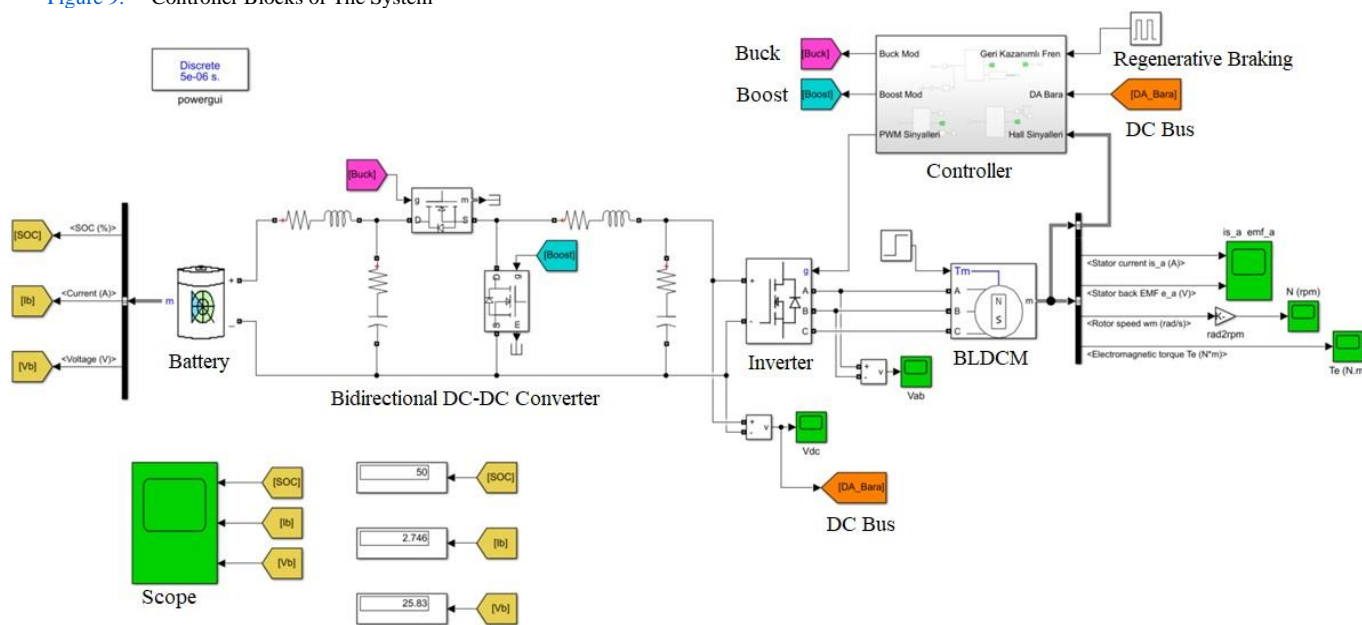


Figure 10. MATLAB/Simulink Model of The System

4. RESULTS OF SIMULATION

The external rotor BLDCM used in the proposed system can operate in the 24-36V range. A battery with a nominal voltage of 24 V is preferred as the supply of the scooter motor. The voltage induced in the rotor decreases as the motor slows down during regenerative braking. The decreasing voltage is increased above the battery voltage by the bidirectional converter working as an amplifier. However, the converter can increase this voltage up to a certain rate. The energy flow to the battery stops when this value is lower than the battery voltage. The DC voltage at the input of the inverter during braking is shown in Figure 11. The current flowing towards the battery is shown in Figure 12 with the increase of this voltage and the State of Charge (SOC) of the battery is shown in Figure 13.

The switching elements of the inverter go to turn-off with the signal to switch to the braking state to the controller. In the case of regenerative braking, reverse parallel connected diodes in the structure of the switching elements act as uncontrolled rectifiers and rectify the voltage induced in the motor and transfer it to the DC bus.

In the buck converter controller, the voltage of the DC bus can be adjusted by lowering the voltage in the battery. In the boost converter control, the DC bus voltage is compared with a saw-toothed signal and the control signal of the boost converter is produced. The battery is charged by increasing the voltage in the DC bus.

3.4. MATLAB/Simulink model of the system

A MATLAB/Simulink model of the system was created to find the energy transferred to the battery while the outer rotor BLDCM was operating in the regenerative braking zone. In this model, a bidirectional DC-DC converter is used to transfer the recovered energy to the battery and feed the vehicle in motor mode. The MATLAB/Simulink model of the proposed system is as in Figure 10.

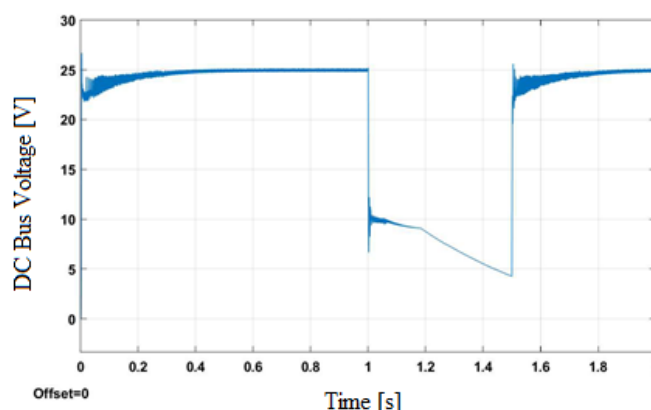


Figure 11. DC Bus Voltage of The Proposed System

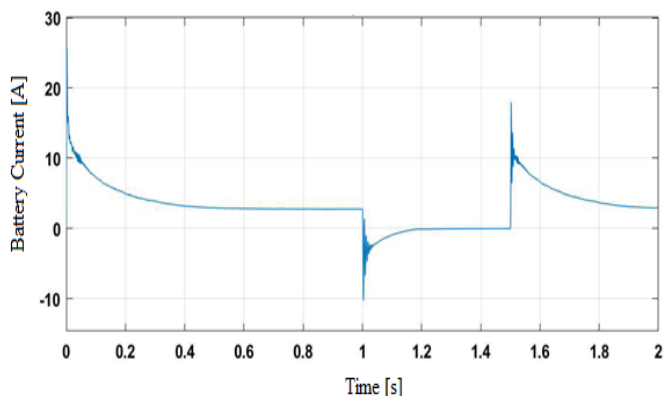


Figure 12. Battery Current of The Proposed System

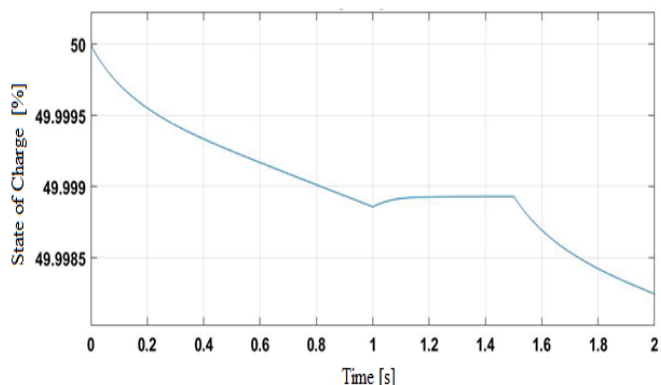


Figure 13. State of Charge of The Proposed System

Braking was applied between 1 and 1.5s as shown on the MATLAB/Simulink model. This is done to test bidirectional recovery. The generated brake signal is as in Figure 14.

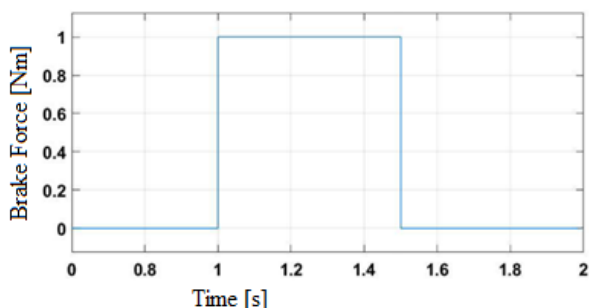


Figure 14. Brake Signal of The Proposed System

The change in BLDCM acceleration and braking is as in Figure 15.

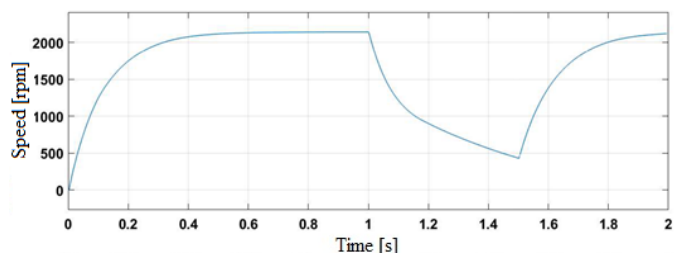


Figure 15. BLDCM Speed of The Proposed System

Figure 16 shows the electromagnetic torque of the BLDCM. It produces negative torque and the system tries to bring the torque production to zero as soon as the braking starts. When the stator current reaches zero, the electromagnetic

torque is zero. It is seen that it starts to produce torque positive torque again with the end of braking.

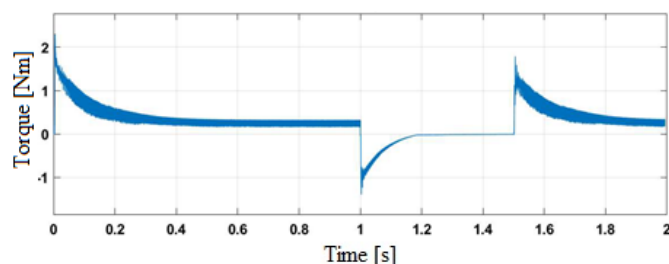


Figure 16. BLDCM Electromagnetic Torque

The BLDCM is decelerating with the brake signal. Accordingly, the back-EMF voltage induced in the motor windings will decrease. The transfer of the recovered energy to the battery is provided by increasing this voltage with a bidirectional DC-DC converter. Since the battery voltage cannot be reached after a certain voltage, the regenerative braking torque becomes zero. The back-EMF formed by the deceleration of the BLDCM is as in Figure 17.

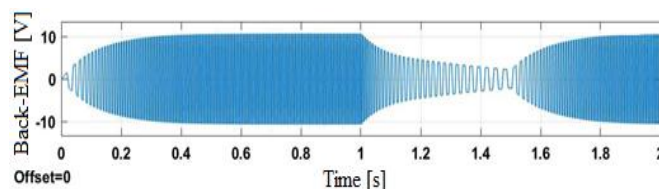


Figure 17. Back-EMF Curve of Phase A

Since the back-EMF is zero at the start of the BLDCM, the inrush current is high. The current curve of one of the phases of the BLDCM is as seen in Figure 18. Since the back-EMF voltage opposes the battery voltage, the stator current decreases with the increase of the back-EMF. During regenerative braking, since the phase-to-phase voltage is higher than the battery voltage, a higher amount of reverse current flows towards the battery. In this case, since the back-EMF will decrease with the deceleration of the BLDCM, the current flowing in the opposite direction will also decrease. The current becomes zero, when the DC bus voltage cannot be increased above the battery voltage.

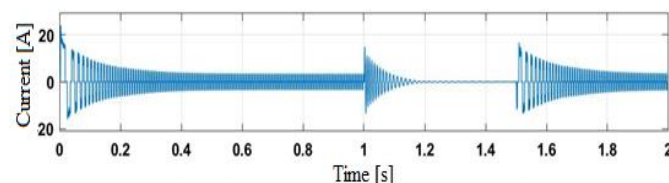


Figure 18. Current of Phase A

5. CONCLUSION

Scooters have become an integral part of life, especially in big cities. This transportation vehicle, which is in the class of light electric vehicles, has a very common use. The biggest problem with scooters is their short range. In this study, MATLAB/Simulink modeling of bidirectional DC-DC converter regenerative recovery circuit for scooter was carried out. The control algorithm required for BLDCM to operate in the regenerative braking region with regenerative recovery, which has not been given importance by scooter manufacturers and researchers, has been developed and the power electronic

circuit has been modeled. The biggest benefit of this modeled system is that the battery is charged with the regenerative recovery circuit during braking, thereby increasing the range. Although the proposed model is realistic, it is necessary to ensure the accuracy of the work with the real road test. In this study, a recovery was achieved within the first 0.2s with braking within a 0.5s time interval applied to the system as a regenerative brake. At the first moment, a pulse current of 10A was produced, and during the braking period, this current was damped and reached zero. It is predicted that the production of the prototype of the proposed system will be higher, since more braking time will be exposed with realistic road testing. In the near future, it is thought that this model will be produced and the gains obtained by the real road test will be modeled. It will be investigated how much the recovery will affect the battery for different operating situations with the work to be done.

REFERENCES

- [1] B. Saha and B. Singh, "Modified DSOGI-PLL Based Position Sensorless PMSM Drive for LEV Application," 2023 IEEE IAS Global Conference on Emerging Technologies (GlobConET), London, United Kingdom, 2023, pp. 1-6, doi: 10.1109/GlobConET56651.2023.10150087.
- [2] D. Maurya and R. Gupta, "Hybrid Converter for Roof-Top Mounted Solar PV and Battery Integrated Light Electric Vehicle," 2022 IEEE 10th Power India International Conference (PIICON), New Delhi, India, 2022, pp. 1-6, doi: 10.1109/PIICON56320.2022.10045144.
- [3] M Ergün, H. Kaymaz, Ü. Terzi, and I. Guney, "Development of a Cost-Effective Heavy-Duty Lead-Acid Battery Capacity Tester", European Journal of Technique (EJT), 10 (2), 378-385, 2020. doi: 10.36222/ejt.840329
- [4] M. N. Yuniarto, S. E. Wiratno, Y. U. Nugraha, I. Sidharta and A. Nasruddin, "Modeling, Simulation, and Validation of An Electric Scooter Energy Consumption Model: A Case Study of Indonesian Electric Scooter," in IEEE Access, vol. 10, pp. 48510-48522, 2022, doi: 10.1109/ACCESS.2022.3171860.
- [5] U.K. Terzi, H.E. Ilhan, H. Kaymaz, H. Erdal and H. Çalik, "A review of commercial electric vehicle charging methods". Promet-Traffic&Transportation, 32(2), pp.291-307, 2020. doi: 10.7307/ptt.v32i2.3252
- [6] A. Ramezankhani, D. Arab Khaburi, M. Bagheri Sadr, F. Bodaghi, M. Reza Arabshahi and J. Rodriguez, "Improved Commutation in Sensorless Control of Brushless DC Motors by Index Pulse Comparison," 2023 14th Power Electronics, Drive Systems, and Technologies Conference (PEDSTC), Babol, Iran, Islamic Republic of, 2023, pp. 1-5, doi: 10.1109/PEDSTC57673.2023.10087005.
- [7] N. Güler and E. Irmak, "Use of dsPIC in Microcontroller Based Systems and Sample Application Development Process", Gazi University Journal of Science Part C: Design and Technology, 4 (2), 71-82, 2016.
- [8] R. Gamoudi, D. Chariag and L. Sbita, "Conducted EMI Reduction in Boost Converter Using dsPIC Based Chaotic Pulse Position Modulation Technique," 2020 6th IEEE International Energy Conference (ENERGYCon), Gammarth, Tunisia, 2020, pp. 149-152, doi: 10.1109/ENERGYCon48941.2020.9236580.
- [9] M. S. Aspalli, F. M. Munshi and S. L. Medegar, "Speed control of BLDC motor with Four Switch Three Phase Inverter using Digital Signal Controller," 2015 International Conference on Power and Advanced Control Engineering (ICPACE), Bengaluru, India, 2015, pp. 371-376, doi: 10.1109/ICPACE.2015.7274975.
- [10] D. Mohanraj, R. Arulavid, R. Verma, K. Sathyasekar, A. B. Barnawi, B. Chokkalingam, L. Mihet-Popa, "A Review of BLDC Motor: State of Art, Advanced Control Techniques, and Applications", IEEE Access. Vol. 10, pp. 54833-54869, 2022. Doi:10.1109/ACCESS.2022.3175011.
- [11] B. Long, S. Lim, J. Ryu, and K. Chong, "Energy-Regenerative Braking Control of Electric Vehicles Using Three-Phase Brushless Direct-Current Motors," Energies, vol. 7, no. 1, pp. 99-114, Dec. 2013, doi: 10.3390/en7010099.
- [12] S. -M. Sue, Yi-Shuo Huang, J. -S. Syu and Chen-Yu Sun, "A bi-directional power flow IPM-BLDC motor drive for electrical scooters," 2010 5th IEEE Conference on Industrial Electronics and Applications, Taichung, Taiwan, 2010, pp. 1330-1334, doi: 10.1109/ICIEA.2010.5514921.
- [13] G. Boztaş, "Comparative Modelling and Experimental Verification of a PMSM Drive System", European Journal of Technique (EJT) , 12 (1) , 82-88, 2022 . doi: 10.36222/ejt.1101838
- [14] S. B. Shahapure and V. A. Kulkarni Deodhar, "Modeling and Field Oriented Control of Permanent Magnet Synchronous Motor Drive," 2023 IEEE 8th International Conference for Convergence in Technology (I2CT), Lonavla, India, 2023, pp. 1-5, doi: 10.1109/I2CT57861.2023.10126498.
- [15] C. S. Joice, S. R. Paranjothi and V. J. S. Kumar, "Digital Control Strategy for Four Quadrant Operation of Three Phase BLDC Motor with Load Variations," in IEEE Transactions on Industrial Informatics, vol. 9, no. 2, pp. 974-982, May 2013, doi: 10.1109/TII.2012.2221721.
- [16] C. -K. Lin, J. -t. Yu, L. -C. Fu, T. -H. Liu and C. -F. Hsiao, "Model-free predictive current controller for four-switch three-phase inverter-fed interior permanent magnet synchronous motor drive systems," 2012 IEEE/ASME International Conference on Advanced Intelligent Mechatronics (AIM), Kaohsiung, Taiwan, 2012, pp. 1048-1053, doi: 10.1109/AIM.2012.6265967.
- [17] B. K. Baby and S. George, "Torque ripple reduction in BLDC motor with 120-degree conduction inverter," 2012 Annual IEEE India Conference (INDICON), Kochi, India, 2012, pp. 1116-1121, doi: 10.1109/INDICON.2012.6420784.
- [18] A. H. Niasar, H. Moghbelli and A. Vahedi, "Modeling, simulation and implementation of four-switch, Brushless DC motor drive based on switching functions," IEEE EUROCON 2009, St. Petersburg, Russia, 2009, pp. 682-687, doi: 10.1109/EURCON.2009.5167707.
- [19] Rupam and S. Marwaha, "Mitigation of Cogging Torque for the Optimal Design of BLDC Motor," 2021 IEEE 2nd International Conference On Electrical Power and Energy Systems (ICEPES), Bhopal, India, 2021, pp. 1-5, doi: 10.1109/ICEPES52894.2021.9699544.
- [20] P. K. Abraham, J. Nambodiry and D. Mary, "Experimental Validation of a Constant Torque Variable Deceleration Regenerative Braking System for a Brushless DC Motor," 2022 2nd International Conference on Power Electronics & IoT Applications in Renewable Energy and its Control (PARC), Mathura, India, 2022, pp. 1-6, doi: 10.1109/PARC52418.2022.9726650

BIOGRAPHIES

Ali Sinan ÇABUK was born in Denizli, Turkey on September 11th, 1976. He received the B.S., M.S. and Ph.D. degrees from the Marmara University in Istanbul, Turkey. He is currently an Associate Professor in Electrical Engineering Department at Istanbul Technical University in Istanbul, Turkey. He had been studying on his doctorate thesis from 2012 to 2013 at the Department of Electrical Machines, Drives and Automation, Faculty of Electrical Engineering and Computing, University of Zagreb, Croatia. His research interests include electric machines and drives, electric vehicles, power electronic circuit design and simulation, mechatronic system design, automotive mechatronics, robotics, renewable energy and IoT systems.

Research Article

Investigating the Impact of Hydrogen Gas Moisture Content on Electricity Generation in PEM Fuel Cells

Berat Firat Dalğıç¹ , Selman Aydın² 

¹ Koluman Otomotiv Endüstri A.Ş., Mersin, Turkey. (e-mail: bfiratdalgic@gmail.com).

² Batman University, Vocational High School of Technical Sciences, Department of Mechanical and Metal Technology, Batman, Turkey. (e-mail: selman.aydin@batman.edu.tr).

ARTICLE INFO

Received: Nov., 20. 2023

Revised: Dec., 28. 2023

Accepted: Dec., 29. 2023

Keywords:

PEM Fuel Cell

Moisture

Hydrogen

Oxygen

Energy

Corresponding author: *Selman Aydın*

ISSN: 2536-5010 / e-ISSN: 2536-5134

DOI: <https://doi.org/10.36222/ejt.1393629>

ABSTRACT

In the realm of energy sources, non-renewable fossil fuels, such as petroleum derivatives, continue to pose a significant threat to our planet. Currently, hydrogen energy, derived from renewable sources, is under extensive research, primarily due to its high efficiency, versatile applications, and zero carbon emissions. Hydrogen gas has become an indispensable alternative energy source owing to its numerous advantages. The technology that enables efficient utilization of hydrogen gas as an energy source is fuel cells, with Polymer Electrolyte Membrane Fuel Cells (PEM Fuel Cells) being the most significant advancement in this field. In this study, anode and cathode moisture levels were investigated by experimental study on the obtained efficiency of PEM fuel cell performance. Pure hydrogen and oxygen gases were used in the anode and cathode sections of the experiment, respectively. The test stand and a 6 cell 35 watt fuel cell with 9 cm² active area were used for the test. Temperature and water accumulation, especially humidification in PEM fuel cells, can be achieved by keeping the hydrogen flow, oxygen flow and battery temperature under control. In the experimental study, the fuel cell humidification rate is gradually increased by keeping the flow and line temperature constant. 30% - 35% - 40% - 45% - 50% - 55% - 60% - 65% - 70% of the results obtained in the voltage, amperage and their effects on watts. As a result of the experimental study, humidification rate has a significant effect on the performance of PEM fuel cell. With the increased humidification temperature, the performance of the installed system increased significantly and nominal values were found. However, it is observed that the performance decreases after a certain period of time in the values higher than 60%.

1. INTRODUCTION

Fossil-derived non-renewable fuels, when used as an energy source, contribute significantly to environmental pollution by releasing high amounts of carbon into nature, leading to diseases such as cancer.

Moreover, considering the limited reserves of these resources, alternative ways for energy production have been explored, with renewable energy sources emerging as the most crucial solution. These sources, including solar, wind, geothermal, and bioenergy, are not only renewable but also environmentally friendly, causing minimal harm to the environment [1]. The amount of energy that humans require today is growing daily. PEM fuel cells create a substantial amount of energy. Thus, efforts to improve this fuel cell's efficiency are still ongoing.

Currently, one of the most extensively researched energy types worldwide, including our own studies, is hydrogen energy. Fuel cell technology enables the most efficient

utilization of hydrogen gas for energy production. Fuel cells operate with a simple and compact system compared to other energy systems. They generate direct electric current through a chemical reaction without the need for the combustion of hydrogen and oxygen gases, producing only pure water and low heat as byproducts. This heat is dissipated as the fuel cell's surface temperature, making it eco-friendly. The absence of moving parts and the presence of only gas inputs and outputs make fuel cells silent and, most importantly, safe. To generate more energy, multiple fuel cell units must be connected in series or parallel since the voltage of a single fuel cell unit ranges from approximately 0.9 to 1 volt. In the literature, this arrangement is referred to as a fuel cell stack [2].

Currently, Polymer Electrolyte Membrane Fuel Cells (PEM Fuel Cells) are considered the most important technology. Due to their portability, compact size, lightweight, high efficiency, lack of moving parts, and straightforward operation, almost all recent studies have been conducted on PEM Fuel Cells.

However, the use of a membrane with drying properties in the internal structure of PEM Fuel Cells leads to the formation of porous structures in the membrane, accelerating its degradation. It is reported that increasing the moisture content of hydrogen and oxygen gases supplied to the membrane enhances its durability and significantly impacts the fuel cell's performance.

This article presents experimental studies on the effects of gas moisture content on fuel cell performance. The results obtained are presented graphically.

2. LITERATURE SUMMARY

Choi (2017) developed the water and thermal management of Proton Exchange Membrane (PEM) fuel cell in this study. They established a bubble humidification system, one of the Balance of Plant (BOP) systems, to control the humidity, a critical factor of the fuel cell. The proposed fuzzy control system significantly increased the efficiency of the PEM fuel cell's output power [3].

In their study, Wang et al. (2003) experimentally investigated the effects of various operating parameters on the performance of PEM fuel cells using air on the cathode side and pure hydrogen on the anode side. The experiments demonstrated the impact of different fuel cell operating temperatures, cathode, and anode humidification temperatures, as well as different operating pressures on the PEM fuel cell performance through V-I curves [4].

İçingür (2011) conducted a study focusing on the temperature, pressure, and humidification parameters that enhance the efficiency of PEM fuel cells suitable for use in cars. Two fuel cells were designed, one made of aluminum and the other made of stainless steel, both utilizing a Nafion 115 membrane. The aluminum fuel cell achieved a maximum voltage of 2.98 volts, while the stainless steel one reached 3.12 volts in the experiments [5].

Eker (2012) utilized Fluent PEMFC module for simulation and experimental studies, comparing the results. The study compared the effects of humidification temperature, hydrogen, and oxygen flow rates on the system's efficiency. It was observed that increasing the humidification temperature significantly improved the system's efficiency. However, after a certain level, the efficiency remained constant and started decreasing as the temperature further increased [6].

In his experimental study, Yılmaz Ulu (2010) established a hybrid solar energy system. The equipment used in the system was analyzed in detail through energy production calculations. The electrolyzer's performance was 54.4%, and the energy efficiency ranged from 28.1% to 42.2% [7].

In a laboratory setting, Çelik (2006) generated energy by directly using sodium borohydride. Recommendations were made regarding the production of different plates and pipes made of durable materials with good conductivity, such as 304 stainless steel. [8].

Kaplan (2008) used Nafion 115 membrane, 304 stainless steel wire for the anode and cathode, and copper wire for the catalyst in his experimental study. The power obtained from the fuel cell was examined, and it was observed that the power value of the copper catalyst used was lower than that of platinum [9].

Ateş (2008) designed an algorithm using artificial neural networks, focusing on the control of a hybrid fuel cell/ultra-capacitor vehicle's energy system. The control algorithm aimed to optimize the regular state for the fuel cell content, enabling

the fuel cell system to meet the required load demand and respond to instantaneous load changes, as well as recover energy from the braking system [10].

Keskin (2014) integrated the energy control system into a PEMFC/Battery vehicle system. The application was designed to handle sudden load differences and recover excess energy during braking. The dual-sided DC-DC converter added extra cost to the system, but it significantly improved the system's efficiency and performance values [11].

In his study, Bilen (2015) developed a highly efficient electrolyzer by using pure water, aiming for a more economical hydrogen production method. The distance between the electrodes and increasing the electrode system's surface area were found to increase hydrogen production, as confirmed by theoretical calculations. However, it was observed in experiments that excessive electrode spacing led to decreased conductivity, resulting in reduced production [12].

Efendioğlu (2013) prepared a data system in line with the data obtained from his project for the "Response Surface Methodology of Central Compound Design," one of the five sections of his study. The study showed that the "Rate" factor significantly affected the "Power Density" at $\alpha=0.05$ significance level [13].

Türe (2006) compared the analysis of a hydrogen system operating with a photoelectrolysis cell, producing hydrogen from photovoltaic systems at 10% efficiency. Photoelectrolysis was considered the most efficient and economical production method among renewable energy sources. The high efficiency and economic viability of hydrogen production led him to combine the photovoltaic system, directly converting solar energy into electricity, with an electrolysis system using a semiconductor photoelectrode. Utilizing renewable and environmentally friendly hydrogen energy is essential for transitioning to hydrogen energy, and more studies should be conducted in this field [14].

In their study conducted abroad, Alniak, Karakaya, et al. (2008) examined the production of hydrogen gas storage tanks. However, such studies in our country have not gained commercial recognition, and many designed projects have remained in the experimental project phase. This study primarily investigated the production of a high-pressure hydrogen gas storage tank made of aluminum. Various methods of manufacturing these tanks and their usage areas were examined. The experiments resulted in obtaining three different aluminum tanks in various sizes, using three different Aluminum 6000 series. Despite numerous challenges faced during the production stage, the designed tanks were subjected to a hydrostatic pressure test. Ongoing research focuses on suitable materials, storage tank forms, and other related topics [15].

In his study, Muhtarlıoğlu (2012) designed an environmentally friendly system capable of charging portable and lightweight electronic devices such as smartphones, utilizing solar energy to convert it directly into electrical energy. This system consisted of solar panels, charge control parts, and batteries. The solar panel converted solar energy into electrical energy in DC form. To enable the system to be utilized when sunlight is insufficient or absent, a battery was used. Charge control units were added to prevent the battery from overcharging or discharging excessively and to maintain a constant voltage value. These control units allowed real-time monitoring and control of transmission parameters through a user-friendly interface [16].

Silver (2008) synthesized an effective and inexpensive catalyst for the electrocatalysis of the Oxygen Reduction

Reaction (ORR) in the cathode part of PEM fuel cells. The study introduced alternative catalysts, PtCuFe/C-611, and PtAgFe/C-611, for the cathode section of PEM fuel cells [17].

Oral (2005) designed a theoretical model to determine the effects of selected fundamental parameters on the Proton Exchange Membrane (PEM) fuel cell. The study aimed to determine the optimal value range by identifying the influences of certain basic parameters on a theoretically designed model. It was observed that air pressure was the most effective parameter in the designed model, significantly enhancing performance. However, a significant decrease in performance was observed when the compressor was disengaged at an approximate pressure of 1 bar. After 1 bar pressure, the performance levels ranged between 55% and 76%, indicating a substantial increase in performance. These achieved performance levels were the best in the model, demonstrating that air pressure was the most influential parameter [18].

3. MATERIALS AND METHODS

3.1. The Installation of Proton Exchange Membrane Fuel Cell System

Recent studies on PEM fuel cells have shown significant impacts on the efficiency and performance of the fuel cell system due to changes in parameters such as gas humidity, pressure, temperature, and flow rate. These changes affect the choice of membrane, catalyst, gas diffusion flow layer, flow channel variations, and other parameters. Additionally, excessive water in anode and cathode pipes can block pores and increase gas transfer resistance, leading to a decline in performance. Interestingly, in such fuel cells, it is necessary to both humidify the gases and remove accumulated water between the cells. Maintaining ideal humidity levels is a challenging task for all system conditions. Therefore, effective water management is crucial for PEM fuel cells to achieve high performance. Optimal parameters for the implemented systems need to be determined [20].

In this study, experimental research has been conducted on the effects of gas humidity on fuel cell performance. These experimental parameters were tested in a computer-assisted environment at TÜBİTAK-MAM Renewable Energy department, and the results were compared with differences observed in the system designed at the Batman University Technology Energy Systems Engineering Department Laboratory. The results obtained were compared, and the influence of humidity parameters on PEM Fuel Cell performance and efficiency was analyzed. Furthermore, to assess the performance and efficiency of these cells, simulations were conducted using the Fuel Cell 3 commercial software in a computer environment. The humidity levels of gases used in PEM fuel cells were measured using power, current, and voltage values recorded by measurement devices over time. The findings of these humidity-related investigations were presented in graphs and tables.

The experiment involved supplying hydrogen and oxygen gases to the system at appropriate levels after the setup of the PEM fuel cell. These gases were humidified, and the experiment was concluded. The experiment was conducted using the system established in the Batman University Technology Faculty Laboratories and tested in the TÜBİTAK Renewable Energy Laboratory. Additionally, the data were analyzed in a computer environment, and evaluations were made accordingly.

Study of Barbir, a PEM fuel cell produced with "Fuel Cell 3" technology was used. The fuel cell can generate a variable power demand with a maximum value of 35 W and consists of 24 MEA cells covering a total electrode area of 45 cm². The performance of the fuel cell was measured by changing the DC electronic load, and the generated data were recorded. Based on the evaluations, the optimal humidification temperature for achieving maximum power in the PEM fuel cell was determined [19].

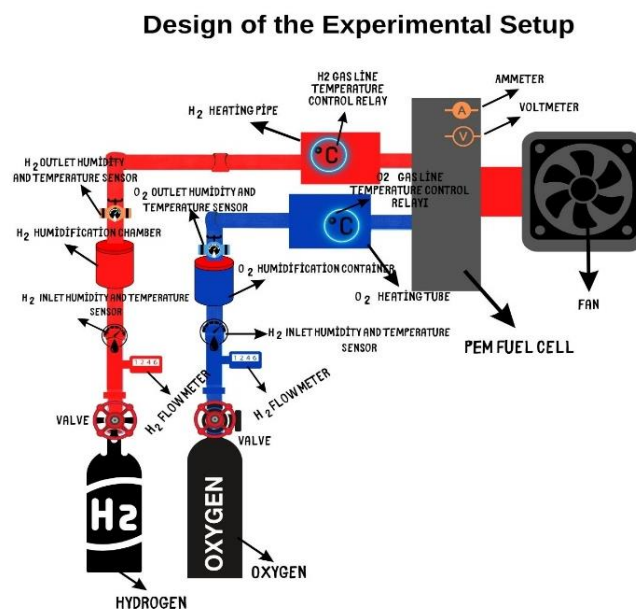


Figure 1. Schematic View of PEM Fuel Cell Experimental Setup

This project involved the successful installation of equipment and materials, provided by the project team, onto the experimental setup in the Renewable Energy Systems laboratory of Batman University Technology Faculty. Additionally, a portion of the experiment was conducted at Ankara TÜBİTAK Renewable Energy laboratory, where all stages of the test were completed successfully.



Figure 2. Data recording and testing device at TÜBİTAK MAM facility

3.2. Experimental Procedure Steps

1. The system design was initially drafted in a computer environment.
2. A list of required materials was compiled, and the materials were procured.
3. Pneumatic pipes were used to connect the Oxygen and Hydrogen cylinders to the flow meters.
4. Connections were established from the output points of Oxygen and Hydrogen flow meters to the humidification tubes via pipe connections.
5. Electronic humidity sensors were connected to the input and output points of oxygen and hydrogen humidification tubes.
6. Copper pipes, which would connect to the output pipes of Oxygen and Hydrogen humidification tubes, were procured and bent as necessary.
7. After bending the output pipes of Oxygen and Hydrogen humidification tubes, they were covered with heating bands and insulating material, and the necessary electrical connections were made.
8. Electronic thermometers were placed inside the copper pipes with heating bands for Oxygen and Hydrogen, and temperature control relays were installed to adjust and maintain the temperature.
9. These copper pipes' output points, i.e., the outlets for Oxygen and Hydrogen, were connected to the PEM Fuel Cell.
10. Voltmeter and ammeter, along with data logger and measurement devices, were attached to the PEM Fuel Cell transmission circuit for measurement purposes.
11. A fan was installed to regulate the temperature of the PEM Fuel Cell.
12. The system is up and running.

4. RESULTS AND DISCUSSIONS

In this section, the experimental setup we designed for the moisture-dependent variations of PEM fuel cell is described. The purpose was to observe the effects of moisture on efficiency using our PEM fuel cell system. The experimental method and the results obtained from the experiment are explained. We operated the P.E.M. fuel cell experimental setup, which we installed in the Batman University Technology Faculty laboratory, for a considerable period and stabilized it. Then, Hydrogen and Oxygen gases were gradually introduced into the system through the flow meters. The energy parameters of the system were observed. These observational data were recorded, graphed, and extensively analyzed using the Fuel Cell 3 commercial software. Parameters like moisture, flow rate, temperature, and line temperature were thoroughly examined, and optimal nominal values were determined.

Our P.E.M. fuel cell has a standard size consisting of 3×3 cells. However, due to membrane burning and piercing incidents in 5 of the cells during the experiment, the experiment continued with a single cell.

- P.E.M. Fuel Cell Temperature: 41°C

- Current: 1.8A, Hydrogen (H₂): 300 ml/min, Oxygen (O₂): 500 ml/min

After setting the values at their optimal positions, the moisture temperatures of hydrogen and oxygen channels were gradually increased while keeping them stable. The efficiency results of the fuel cell were graphically obtained.

In the experiments, the 6-cell fuel cell used in our P.E.M. experimental setup in the Batman University Technology Faculty laboratory was tested. Initially, as mentioned before, 5 cells were used due to the burning of one cell. For the purpose of verifying the accuracy of our values, the single-cell version of our fuel cell was taken to TÜBİTAK's Renewable Energy Laboratory in Ankara and tested only for this purpose. The values obtained in our self-designed system at Batman University were almost identical to the results obtained during the tests. The experiments were conducted at humidity levels of 30%, 35%, 40%, 45%, 50%, 55%, 60%, 65%, and 70%, respectively. According to the data in Table 1 and Figure 3, we see the volt, ampere and watt values per cm².

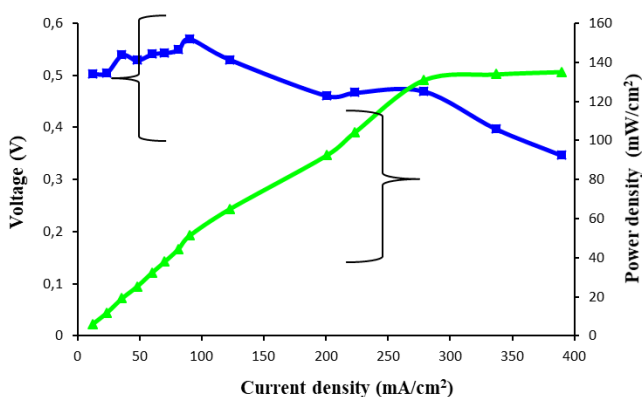


Figure 3. Voltage, current and power polarization curve on unit cm² area due to humidity change in PEM fuel cell

TABLE 1. VOLTAGE (VOLTS), CURRENT (AMPERES), AND POWER (WATTS) PER CM² DEPENDENT ON PEM FUEL CELL

Voltage	Current	Power	mA/cm ²	Voltage	W/ cm ²
0.503	0.11	0.05533	12.22222	0.503	6.147778
0.505	0.21	0.10605	23.33333	0.505	11.78333
0.539	0.32	0.17248	35.55556	0.539	19.16444
0.529	0.43	0.22747	47.77778	0.529	25.27444
0.541	0.54	0.29214	60	0.541	32.46
0.543	0.73	0.40077	81.11111	0.549	44.53
0.57	0.81	0.46176	90	0.57	51.3
0.53	1.105	0.58565	122.7778	0.53	65.07222
0.461	1.807	0.83302	200.7778	0.53	65.07222
0.467	2.01	0.93867	223.3333	0.467	104.2967
0.47	2.507	1.17829	278.5556	0.47	130.9211
0.398	3.03	1.20594	336.6667	0.398	133.9933
0.347	3.507	1.21692	389.6667	0.347	135.2143

The experiment was initially conducted with fixed values of hydrogen flow rate at 0.3, oxygen flow rate at 0.5, and cell temperature at 41°C. After operating in this stable condition for a day, gradual changes were made to other parameters, and data collection commenced. In the experiment, humidity levels were gradually increased to values of 30%, 35%, 40%, 45%, 50%, 55%, 60%, 65%, and 70%, respectively.

When observing the effect of moisture:

- Anode input gas flow rate (H₂): 0.300 l/min
- Cathode input gas flow rate (O₂): 0.580 l/min

- Current: 1.8 A were kept constant.

The obtained Watt-Volt and humidity values from the experiment are outlined below:

a) At 30%, we observe 0.432 V – 0.778 W.

b) At 35%, the values are 0.501 V – 0.901 W. Here, we witness a sudden increase in our fuel cell's stability and efficiency, which is a crucial observation. During our experiment, seeing our fuel cell, which we worked hard to stabilize over 24 hours, suddenly become efficient indicates that our efforts were successful.

c) Progress remains steady between 35% and 40%.

d) At 45%, the values are 0.922 V – 0.512 W, indicating another increase.

e) At 50%, we observe a slight decrease, marking a turning point for further increases. Our Watt value stabilizes within a specific range, and this observation is a significant finding. The Watt value and its corresponding Volt value rise up to a point, then exhibit fluctuations but overall remain stable.

f) The humidity level rises to 60%, and afterward, it shows a continuous decline trend. Voltage and power values rise initially, then begin to decrease, followed by another increase, and stabilize. In other words, at 60% humidity, we achieve the highest power and voltage values, recorded as 0.514 Volt, 1.8 Amperes, and 0.954 Watts.

g) Values obtained after 60% are at 65% and 70%. At 65%, the efficiency is 0.525 V – 0.945 W, and at 75%, the efficiency is 0.52 V – 0.936 W. However, what we observe from these values is that the cell stabilizes, operates steadily, and there won't be significant changes in temperature regardless of any subsequent additions.

5. CONCLUSION

As a result of our studies, the effects of the moisture parameter on the performance of PEM fuel cells have been investigated. In this study, consecutive tests were conducted at specific intervals to stabilize the fuel cell based on joint experiments conducted at Batman University and TÜBİTAK Renewable Energy laboratories. During these tests, the membrane of 5 fuel cells was pierced due to water accumulation inside the cells, caused by high humidity, rendering them unusable. Detailed images and diagrams related to this issue are attached. After this stage, experiments were continued with a single-cell PEM fuel cell at the TÜBİTAK Renewable Energy Laboratory.

During the experiments:

- Anode input gas flow rate (H₂): 0.300 l/min
- Cathode input gas flow rate (O₂): 0.580 l/min
- Current: 1.8 A

After being kept constant at these values, moisture levels were gradually increased to %30, %35, %40, %45, %50, %55, %60, %65, and %70, respectively. When evaluating the data obtained from the experiment:

In the power (watt) values, there was initially a good increase (0.123 W), followed by a period of stability, and then another increase of 0.021 W was observed. Upon further examination, a decrease occurred at a certain point. The highest efficiency obtained was 0.954 Watt at 60%, which was recorded as the highest electrical power value obtained from the experiment. However, we believe that this efficiency would

further increase if water formation within the plates (membrane) is prevented. Since all cells are interconnected, the formation of water affects the entire fuel cell, hindering the acquisition of watt and volt values. To achieve the desired efficiency, it is essential to work with robust membranes and prevent water formation. We believe that if our suggestions are taken into account, the energy efficiency of the fuel cell can be further improved, making significant contributions to other experiments.

Today, the energy needed by humanity is increasing day by day. The energy produced by pem fuel cells is at a significant level. Therefore, the search to increase the efficiency of this fuel cell continues. In this study, positive results were found as a result of the investigation of humidity in PEM fuel cells. In future studies, it is very important to continue studies to increase the efficiency of the PEM fuel cell.

ACKNOWLEDGEMENT

The data in this research are part of the results of the M.Sc. thesis project by Batman University Institute of Graduate Studies with Thesis Number of 573350. The research was performed at the Engine Research Laboratory, University of Batman, Batman, Turkey.

REFERENCES

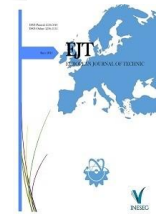
- [1] Aydın, A., Kayri, İ., & Aydın, H. Electrical and thermal performance enhancement of a photovoltaic thermal hybrid system with a novel inner plate-finned collective cooling with different nanofluids, *International Journal of Green Energy*, (2023) DOI: 10.1080/15435075.2023.2201345.
- [2] Şenaktaş, B., *Hydrogen Energy, Production, and Applications*, Master's Thesis, Pamukkale University Institute of Science, Denizli, 2005.
- [3] Ou, K., Yuan, WW., Choi, M., Yang, S., Kim, YB. Performance increase for an open-cathode PEM fuel cell with humidity and temperature control, *International Journal of Hydrogen Energy*, 42(50), 29852-29862, 2017.
- [4] Wang, L., Husar, A., Zhou, T., Liu, H., "A Parametric Study of PEM Fuel Cell Performances, *International Journal of Hydrogen Energy*, 28, 1263-1272, 2003.
- [5] İçingür, Y., Design and Testing of Gas Flow Plates for Use in a Polymer Electrolyte Membrane Fuel Cell, *Gazi University, Politeknik Dergisi*, 14, 31-34, 2011.
- [6] Eker, E., Modeling Heat and Water Management in PEM Fuel Cells, Master's Thesis, Sakarya University, Institute of Science, Sakarya, 2012.
- [7] Yılmaz Ulu, E., Experimental and Theoretical Energy, Exergy, and Electromagnetic Analysis of Solar-Hydrogen Hybrid Energy System, Ph.D. Thesis, Pamukkale University, Institute of Science, Denizli, 2010.
- [8] Çelik, C., Investigation of Process Parameters' Effects on Efficiency in Direct Sodium Borohydride Fuel Cell, Ph.D. Thesis, Kocaeli University, Institute of Science, Kocaeli, 2006.
- [9] Kaplan, R., "Comparison of Manufactured and Commercial PEM Fuel Cells' Performances," Master's Thesis, Dumlupınar University, Institute of Science, Kütahya, 2008.
- [10] Ateş, Y., Control of a Hybrid Fuel Cell/Ultra-Capacitor Vehicle Power System Using Artificial Neural Networks, Master's Thesis, Yıldız Technical University, Institute of Science, Istanbul, 2008.
- [11] Keskin, F., Energy Management in a Fuel Cell-Battery Hybrid Electric Vehicle, Master's Thesis, Yıldız Technical University, Istanbul, 2014.
- [12] Bilen, G., "Design of a 20 m³/h Capacity Hydrogen Generator Using Sharp Electrolysis Method and Investigation of Porous Electrode Materials' Effects on Parameters, *Journal of Engineering Research and Applied Science*, 3(1), 184-195, 2014.
- [13] Efendioğlu, D., Optimization of PEM Fuel Cell Performance Using Sharp Electrolysis Method, Master's Thesis, Istanbul University, Institute of Science, Istanbul, 2013.
- [14] İtüre, E., "Hydrogen Production via Photoelectrolysis," 10th Energy Congress of Turkey, pp. 417-421, 2006.

- [15] Alniak, O., OUR A., Karakaya, Ç., Ertürk, M., Güneş İ., Investigation of Manufacturing High-Pressure Resistant Composite Hydrogen Tank, 7th National Clean Energy Symposium, UTES'2008, Istanbul, December 17-19, 2008.
- [16] Muhtarlıoğlu, T. K., Design of an Environmentally Friendly System Converting Solar Energy to Electrical Energy," Master's Thesis, Gazi University, Institute of Science, Ankara, 2012.
- [17] Silver, G., Synthesis, Characterization, and Electrocatalytic Properties Investigation of Platinum-Based Ternary Catalysts for Use in PEM Fuel Cell Cathode, Master's Thesis, Gazi University Institute of Science and Technology, 2008.
- [18] Oral, E., Synthesis, Characterization, and Electrochemical Properties of Platinum-Based Ternary Catalysts for PEM Fuel Cell Cathode, Master's Thesis, Gazi University, Institute of Science, Ankara, 2005.
- [19] Barbir, F., PEM Fuel Cells: Theory and Practice, *Elsevier Academic Press*, USA, 2005. ISBN-13: 978-0-12-078142-3.
- [20] Yılmaz, A., Ünvar, S., Ekmen, M., & Aydın, S. Yakıt Pili Teknolojisi. *Technological Applied Sciences*, 12(4), 185-192, 2017.

BIOGRAPHIES

Berat Fırat DALĞIÇ was born in 1990 in Diyarbakır/Turkey. He graduated from Mersin University Mechanical Engineering Department in 2014, which he earned in 2010. During his university years, he participated in the Formula G and Electro-Mobile competitions organized by TÜBİTAK every year, by producing 4 efficient vehicles with the ANKA Alternative Energy Team. In 2016, he started his master's degree in Batman University, Institute of Science and Technology, Department of Renewable Energy Systems. In his working life, he worked at Onalsan Çatı, Essante, Stilteks Metal and Dal Mühendislik Group, respectively. Nowadays, Koluman Otomotiv Endüstri A.Ş. He works as a System Specialist in the Military Projects Directorate.

Selman Aydın was born in Batman, Turkey. He graduated from the Dicle University Technical Education Faculty Automotive Teaching B.Sc. degree between 2000-2004. In 2008, he started his M.Sc. degree at Firat University Institute of Science and Technology, Department of Mechanical Education/Automotive. In 2010, he graduated with an M.Sc. degree. In 2010, he started his Ph.D. at Marmara University Institute of Science and Technology, Department of Mechanical Education. In 2014, he graduated with a Ph.D. Between 2012-2015, he worked as a lecturer at Hakkari University, Department of Mechanical Engineering/Automotive. In 2015, he started to work as an assistant professor in the Batman University Faculty of Technology, Department of Automotive Engineering. In 2020, he received the title of associate professor in the field of automotive engineering. In 2021, he was appointed as an associate professor at Batman University Vocational High School of Technical Sciences. He is currently working as an associate professor in the same unit. Major research interests are internal combustion engines, engine dynamics, alternative fuels, fuel cells, and automotive engineering. He has published more than 50 papers in international and national journals and conferences.



Research Article

Leakage-Free Wood-Derived Activated Carbon/Methyl Palmitate Composite Phase Change Material for Thermal Management Applications

Gökhan Hekimoğlu

Karadeniz Technical University, Department of Metallurgical and Material Engineering, 61080 Trabzon, Turkey. (e-mail: ghekimoğlu@ktu.edu.tr).

ARTICLE INFO

Received: May., 06. 2023

Revised: Oct., 03. 2023

Accepted: Nov., 01. 2023

Keywords:

Phase change materials

Composites

Thermal energy storage

Latent heat

Activated Carbon

Corresponding author: Gökhan Hekimoğlu

ISSN: 2536-5010 / e-ISSN: 2536-5134

DOI: <https://doi.org/10.36222/ejt.1293404>

ABSTRACT

This study aimed to create a leakage-free composite phase change material (PCM) that has high potential for various thermal management applications. Activated carbon derived from wood (ACW) with a porous structure was used to address the leakage issue and improve the thermal conductivity of Methyl palmitate (MPt) used as the PCM. The optimum MPt impregnation ratio was found to be 53 wt% in the leakage-free ACW/MPt composite. The results of FTIR analysis showed that the integration of MPt and ACW was achieved through physical interaction. Scanning electron microscopy (SEM) analysis indicated that MPt was uniformly distributed within pores of the ACW scaffold. DSC analyses demonstrated that the fusion enthalpy and temperature of the ACW/MPt (53 wt%) were 129 J/g and 27.59 °C, respectively. Thermal gravimetric analysis (TGA) measurements confirmed that the ACW/MPt was thermally stable. By incorporating MPt with ACW, thermal conductivity of MPt was increased by 2.16 times. The fusion enthalpy of ACW/MPt did not change, and the melting temperature remained constant after 750 thermal cycles. The results of this study indicate that the fabricated leak-free ACW/MPt is cost-effective and environmentally friendly and has the potential to be utilized as a thermal energy storage (TES) material for temperature regulation in various applications.

1. INTRODUCTION

With the ever-increasing demand for thermal management systems due to increasing energy cost and decreasing the traditional energy sources, there is a need for more efficient and reliable methods for controlling temperature, particularly in buildings with the highest energy consumption rates [1]. One of the most favorable technologies for thermal management is the use of phase change materials (PCMs) that can store and release thermal energy during phase transition [2]. However, traditional PCMs have some drawbacks, such as low thermal conductivity and potential leakage while melting [3,4]. Therefore, there is a need for the development of new PCM-based composites with enhanced properties. Form-stable composite PCMs (FSC-PCMs) have emerged as a promising alternative to traditional PCMs. FSC-PCMs are materials that combine a PCM with a supporting material, such as clay-based materials, polymers, biochar or activated carbon [5,6]. The properties of FSC-PCMs can be tailored depending on the features of the selected supporting material and PCM. For example, the type of PCM and supporting material, the composition of components, the production route and the

particle size of the components can all affect the thermal properties of the FSC-PCMs. By optimizing these parameters, it is possible to develop FSC-PCMs with specific thermal properties to suit different applications [7,8]. Therefore, the resulting FSC-PCMs materials have improved shape-stability and thermal conductivity, making them suitable for various applications, including building insulation, electronics cooling, temperature management of batteries, transportation of food or medical products, textile products, etc [9-12].

Activated carbon (AC) is an ideal supporting material for creation FSC-PCMs due to its high surface area, porous structure, and thermal stability. The AC provides a large surface area and porous structure for the PCM to be adsorbed, thereby preventing leakage and improving shape-stability. Furthermore, relatively high thermal conductivity of AC allows for efficient heat transfer between PCMs and the surrounding environment. Therefore, recently many researches focused on the fabrication and application of FSC-PCMs comprising of AC and PCM for thermal management systems [13-15].

Gu et al [16] assessed the use of carbonized pepper straws as a carrier material to load palmitic acid and found that this composite had a fusion enthalpy of 95.50 J/g. Zhang et al. [17]

created a FSC-PCM of a fatty acid eutectic mix utilizing bio-carbon from waste corn. This composite, which contained about 78% PCMs, reached a fusion enthalpy of 148.30 J/g and an 87.5% improvement in thermal conductivity. Xu et al. [18] combined paraffin with carbonized orange peels, resulting in a leakage-free composite with high thermal stability. Wen et al. [19] proposed FSC-PCM using sunflower straw-based carbon loaded with melted stearic acid for TES applications.

In the current study, a novel FSC-PCM was developed by impregnating Methyl palmitate (MPt) selected as PCM into the pores of AC-derived from wood (ACW), which served as an effective framework. Wood is an important source of carbon due to its low cost and easy availability [20,21]. To date, there have been no investigations on the fabrication and extensive investigations of such a leak-resistant ACW/MPt composite in the literature. The composite's crystalline/chemical structures and surface morphology were analyzed using XRD, FTIR and SEM techniques. DSC and TGA analyses were conducted to evaluate the composite's TES potential, while its thermal reliability and conductivity were also measured. Overall, these analytical techniques provided comprehensive insights into the properties of the samples and facilitated a detailed assessment of their suitability for TES applications. The results indicated that the favorable energy storage capacity and thermal conductivity of this FSC-PCM make it a promising material for thermoregulation applications in different thermal management systems.

2. EXPERIMENTAL

2.1. Material

Methyl palmitate (MPt, assay 99%) was purchased from Sigma Aldrich Company, while ACW was provided from Rota Chemical Company (surface area: 1150 m²/g, density: 0.25-035 g/cm³, pore volume: 1.3 ml/g).

2.2. Preparation of leakage-free ACW/MPt composite

The leakage-free ACW/MPt composite was prepared using the sorption method with vacuum operation. Optimal impregnation conditions were achieved through a vacuum operation in a vacuum oven maintained at 80 kPa and 50 °C for a duration of 3 hours, facilitating the infiltration of liquid MPt into the ACW pores. To determine the maximum MPt loading capacity of ACW, various amounts (ranging from 30 to 70 wt%) of MPt was impregnated into its porous network. To avoid clumping of the ACW/MPt mixtures, the samples were periodically taken out of the oven and stirred every 30 minutes, ensuring an even infiltration of MPt throughout the ACW matrix. The form-stability of each fabricated composite was assessed through leakage tests. For this, each composite was heated on filter paper above the melting point of MPt. The sample that demonstrated the highest MPt rate without leaching out after heating for 2 h was identified as FSC-PCM. The leakage-free ACW/MPt was found to have a MPt ratio of 53 wt% and ACW ratio of 47 wt%, as depicted in the given test results in Fig. 1.

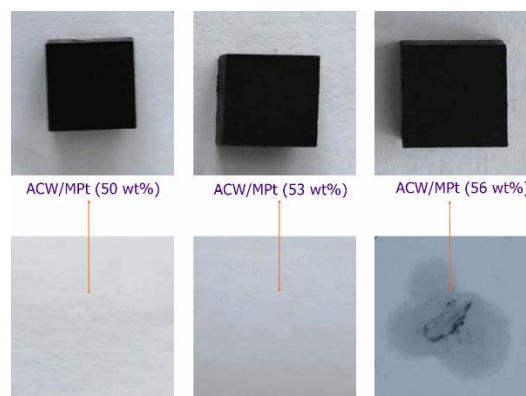


Figure 1. The leakage test result of ACW/MPt samples

2.2. Characterization

In this study, a range of experimental techniques were applied to reveal the micro-structure, chemical structure, TES properties, and thermal stability of ACW, MPt, and resulting ACW/MPt specimens. FTIR (Shimadzu, IRSpirit), DSC (Hitachi 7020), SEM (Zeiss LEO 440) and TGA (PerkinElmer) analyses were utilized to examine the samples. The thermal cyclers device (Prime3Techne) was conducted to assess the cycling stability of the ACW/MPt. The thermal conductivity of the specimens were measured using a thermal conductivity meter (Decagon KD2 Pro).

3. RESULTS

3.1. SEM Results

SEM images in Fig. 2 illustrate the morphology of pure ACW and the ACW/MPt samples prepared in the study. The SEM image of pure ACW reveals the presence of numerous pores, predominantly micro-sized, which is consistent with its high PCM loading capacity findings. These pores provide abundant space for loading MPt and were successfully occupied by the MPt, indicating good physical compatibility between the ACW and MPt. Additionally, ACW/MPt composite exhibited a uniform distribution of MPt embedded within the porous network structure of ACW. Consequently, the pores of ACW were compacted with the loadage of MPt, leading to a relatively smooth surface. Overall, the results suggest that the MPt was effectively integrated with ACW.

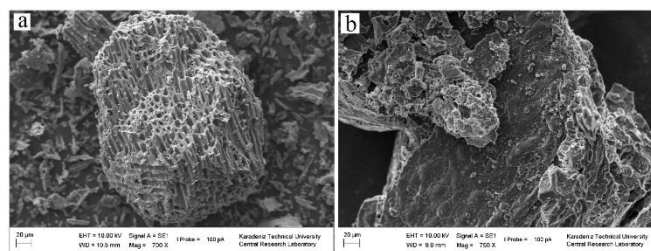


Figure 2. SEM images of ACW (a) and ACW/MPt (b)

3.2. FTIR Results

The FTIR spectra of MPt, ACW and ACW/MPt were demonstrated in Figure 3. The spectrum of MPt exhibited peaks at 2910 and 2857 cm⁻¹, which corresponded to CH₂ group stretching vibrations. Additionally, peaks at 1734 and 1169 cm⁻¹

¹ were observed, which were attributed to the carbonyl groups and the stretching vibrations of C-O-C, respectively. Peaks at 1460, 885, and 716 cm^{-1} were representative of the vibrations of the -OH functional group. The FTIR spectra of ACW was found to be similar with general carbon-based materials, with absorption bands between 1924 and 2285 cm^{-1} . Notably, the impregnation of MPt into ACW resulted in negligible changes in the position and intensity of the peaks, indicating that the MPt retained its phase change and chemical properties in the composite structure without the formation of new peaks.

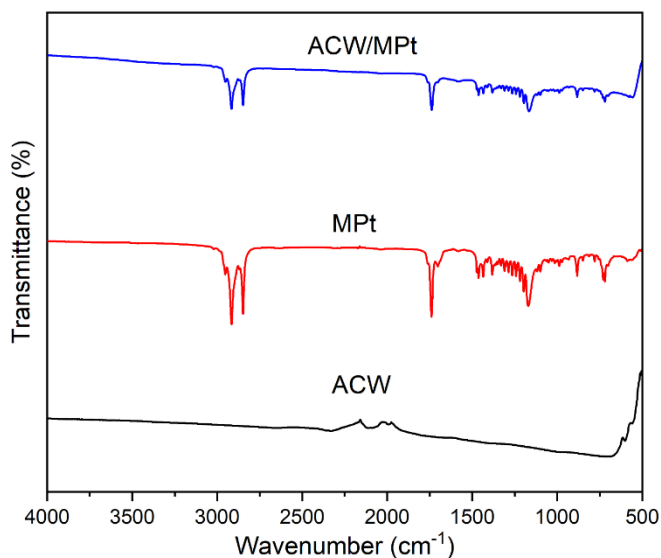


Figure 3. FTIR spectra of MPt, ACW and ACW/MPt

3.3. DSC Results

Figure 4 shows the DSC thermograms for MPt and ACW/MPt, while Table 1 presents the TES data for these materials. Three measurements were conducted for each sample to calculate the mean deviations. The results indicated that the mean deviations in phase transition temperatures and enthalpy values were ± 0.17 °C and $\pm 0.82\%$ J/g, respectively. The pure MPt has melting and freezing temperatures of 26.97 and 25.15°C, respectively, and its fusion and freezing latent heats are 245 and -242 J/g, respectively. The melting/freezing temperatures of ACW/MPt composite only changed slightly, with measurements of 27.59/26.27°C. The measured latent heats of ACW/MPt are 129/-127 J/g, respectively. The high surface area and porous structure of ACW led to higher latent heat capacity of ACW/MPt composite. The fusion and freezing enthalpy of ACW/MPt is about 52.65% and 52.47% of the pure MPt, respectively, which aligns with the impregnation ratios of MPt. Furthermore, the DSC thermogram for ACW/MPt is similar to that of MPt, indicating that MPt maintains its TES role throughout the phase changes.

It is worth noting that the fusion enthalpy of the leakage-free ACW/MPt composite is comparable to that of different bio-carbon-based FSC-PCM reported in the literature [14,16,22-24]. More specifically, the fusion enthalpy of the mentioned leakage-free AC-based composites was reported as 87.42, 95.5, 84.74, 108.0, and 90.2 J/g, respectively. When considering the measured fusion heat of 129 J/g for the suggested ACW/MPt composite, it is highly competitive.

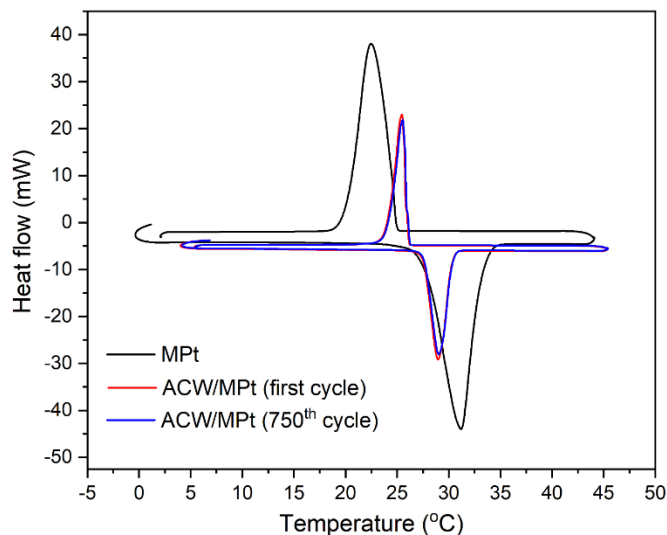


Figure 4. DSC thermograms of MPt and ACW/MPt

To assess the cycling thermal stability of the leakage-free ACW/MPt, a thermal cycle test was conducted by subjecting it to 750 melting/freezing cycles. The DSC curves for this composite before and after 750 thermal cycles are presented in Fig. 4. The DSC results revealed that its melting/freezing temperatures and enthalpy values hardly changed. These findings infer the cycling stability of ACW/MPt, which is critical for TES applications.

TABLE I

Sample	DSC DATA OF MPt AND ACW/MPt			
	Melting Temperature (°C)	Fusion Enthalpy (J/g)	Freezing Temperature (°C)	Freezing Enthalpy (J/g)
MPt	26.97	245	25.15	-242
ACW/MPt	27.59	129	26.27	-127
ACW/MPt (750 th cycle)	27.55	128	26.25	-127

3.4. TGA Results

The TGA curves in Figure 5 depict the thermal stability of ACW, MPt and ACW/MPt. The results demonstrate that MPt remained stable up to a temperature of 174 °C, after which it experienced substantial decomposition. ACW exhibited good thermal stability, with no signs of major decomposition, except for minor weight loss due to the evaporation of water and volatile organic substances. It experienced weight loss of 8.07% at 500 °C. Furthermore, the TGA curve of ACW/MPt not only determined its thermal stability, but also verified the amount of MPt present into ACW. It experienced similar rapid mass losses with pure MPt. Mass losses due to MPt in ACW/MPt occurred between 174 and 228 °C, and its corresponding mass losses were approximately 60%, which closely aligns with MPt impregnation rate and ACW-based mass losses. Overall, the decomposition temperature of ACW/MPt was significantly higher than its working temperature, indicating its high resistance to thermal degradation. In light of these findings, it can be concluded that ACW/MPt possess considerable strength against thermal degradation.

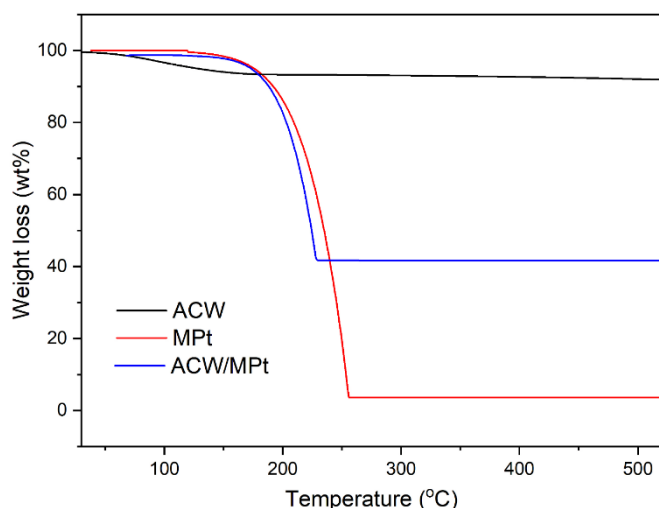


Figure 5. TGA curves of MPt, ACW and ACW/MPt

3.5. Thermal Conductivity Results

Thermal conductivity (TC) is a key factor that significantly affects the period of heat charging/discharging of PCM-based systems. The TC values of pure MPt, ACW, and the ACW/MPt were measured at 0.24, 0.33, and 0.52 W/m.K, respectively, at a temperature of 20 °C. Based on this finding, the TC of the ACW/MPt composite was 2.16 times higher than that of MPt, owing to the carbon skeleton of ACW that provides heat transfer channels and heat conduction framework. However, the TC of the ACW/MPt composite was found to be slightly higher than expected, compared to that of ACW and MPt. Although the TC of ACW is not high enough to theoretically supply this increase in the TC of MPt, it boosted significantly its TC. This is since the majority of the air molecules in the pores of ACW, which have much lower TC (0.025 W/m.K), were displaced by the MPt. As a result, the TC of ACW/MPt could be higher than that of either the MPt or ACW alone. Therefore, the used ACW not only provided form-stability for MPt as a supporter matrix, but also acted as a doping agent, significantly enhancing the low TC of MPt. These findings were also reported in previous studies [15,25,26].

4. CONCLUSION

This study utilized highly porous activated carbon derived from wood (ACW) to create novel leakage-free FSC-PCM for thermal energy storage (TES). Methyl palmitate (MPt) was successfully impregnated into the porous structure of ACW. The loading rate of MPt in the leakage-free ACW/MPt was 53 wt%. The fusion enthalpy of ACW/MPt was 129 J/g with a melting temperature of 27.59 °C. The composite had high thermal stability up to 174 °C, and admirable cycling stability even after 750 melting-freezing cycles. The thermal conductivity of ACW/MPt was 2.16 times higher than that of the pure MPt. Overall, the used ACW not only allowed for high loading of MPt, but also significantly enhanced the thermal conductivity of MPt without the need for additional fillers. As a result, the leak-free ACW/MPt composite has high potential for various TES applications including solar passive thermal management of buildings, cooling of electronic devices/batteries and textile products etc.

ACKNOWLEDGEMENT

Dr. G. Hekimoğlu thanks the KTU due to the instrumentation facilities.

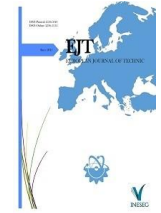
REFERENCES

- [1] F. Kuznik et al., "A review on phase change materials integrated in building walls", *Renewable and Sustainable Energy Reviews*, vol. 15, no. 1, pp. 379–391, 2011, doi: 10.1016/j.rser.2010.08.019i.
- [2] I. Sarbu and C. Sebarchievici, "A Comprehensive Review of Thermal Energy Storage," *Sustainability*, vol. 10, no. 1, p. 191, Jan. 2018, doi: 10.3390/SU10010191.
- [3] A. Sharma, V. V. Tyagi, C. R. Chen, and D. Buddhi, "Review on thermal energy storage with phase change materials and applications," *Renewable and Sustainable Energy Reviews*, vol. 13, no. 2, pp. 318–345, Feb. 2009, doi: 10.1016/J.RSER.2007.10.005.
- [4] S. Wu, T. Yan, Z. Kuai, and W. Pan, "Thermal conductivity enhancement on phase change materials for thermal energy storage: A review," *Energy Storage Mater.*, vol. 25, pp. 251–295, Mar. 2020, doi: 10.1016/j.enstm.2019.10.010.
- [5] Y. Zhang, Z. Jia, A. Moqet Hai, S. Zhang, and B. Tang, "Shape-stabilization micromechanisms of form-stable phase change materials-A review," *Compos Part A Appl Sci Manuf*, vol. 160, p. 107047, Sep. 2022, doi: 10.1016/j.compositesa.2022.107047.
- [6] P. Lv, C. Liu, and Z. Rao, "Review on clay mineral-based form-stable phase change materials: Preparation, characterization and applications," *Renewable and Sustainable Energy Reviews*, vol. 68, pp. 707–726, Feb. 2017, doi: 10.1016/j.rser.2016.10.014.
- [7] M. M. Kenisarin and K. M. Kenisarina, "Form-stable phase change materials for thermal energy storage," *Renewable and Sustainable Energy Reviews*, vol. 16, no. 4, pp. 1999–2040, May 2012, doi: 10.1016/j.rser.2012.01.015.
- [8] J. Paul et al., "Nano-enhanced organic form stable PCMs for medium temperature solar thermal energy harvesting: Recent progresses, challenges, and opportunities," *Renewable and Sustainable Energy Reviews*, vol. 161, p. 112321, Jun. 2022, doi: 10.1016/J.RSER.2022.112321.
- [9] S. Rostami et al., "A review of melting and freezing processes of PCM/nano-PCM and their application in energy storage," *Energy*, vol. 211, p. 118698, Nov. 2020, doi: 10.1016/J.ENERGY.2020.118698.
- [10] X. Huang, C. Zhu, Y. Lin, and G. Fang, "Thermal properties and applications of microencapsulated PCM for thermal energy storage: A review," *Appl Therm Eng.*, vol. 147, pp. 841–855, Jan. 2019, doi: 10.1016/J.APPLTHERMALENG.2018.11.007.
- [11] P. K. S. Rathore and S. kumar Shukla, "Improvement in thermal properties of PCM/Expanded vermiculite/expanded graphite shape stabilized composite PCM for building energy applications," *Renew Energy*, vol. 176, pp. 295–304, Oct. 2021, doi: 10.1016/j.renene.2021.05.068.
- [12] L. Yang, J. Huang, and F. Zhou, "Thermophysical properties and applications of nano-enhanced PCMs: An update review," *Energy Convers Manag.*, vol. 214, p. 112876, Jun. 2020, doi: 10.1016/j.enconman.2020.112876.
- [13] D. G. Atinafu, B. Y. Yun, S. Wi, Y. Kang, and S. Kim, "A comparative analysis of biochar, activated carbon, expanded graphite, and multi-walled carbon nanotubes with respect to PCM loading and energy-storage capacities," *Environ Res.*, vol. 195, no. February, p. 110853, 2021, doi: 10.1016/j.envres.2021.110853.
- [14] A. F. Nicholas, M. Z. Hussein, Z. Zainal, and T. Khadiran, "Palm kernel shell activated carbon as an inorganic framework for shape-stabilized phase change material," *Nanomaterials*, 2018, doi: 10.3390/nano8090689.
- [15] G. Hekimoğlu, A. Sari, Y. Önal, O. Gencel, V. V. Tyagi, and E. Aslan, "Utilization of waste apricot kernel shell derived-activated carbon as carrier framework for effective shape-stabilization and thermal conductivity enhancement of organic phase change materials used for thermal energy storage," *Powder Technol.*, vol. 401, p. 117291, Mar. 2022, doi: 10.1016/J.POWTEC.2022.117291.
- [16] X. Gu, P. Liu, C. Liu, L. Peng, and H. He, "A novel form-stable phase change material of palmitic acid-carbonized pepper straw for thermal energy storage," *Mater Lett*, 2019, doi: 10.1016/j.matlet.2019.03.130.

- [17] W. Zhang et al., "Lauric-stearic acid eutectic mixture/carbonized biomass waste corn cob composite phase change materials: Preparation and thermal characterization," *Thermochim Acta*, vol. 674, pp. 21–27, Apr. 2019, doi: 10.1016/J.TCA.2019.01.022.
- [18] Y. Xu et al., "Preparation and performance of shape-stable phase change materials based on carbonized-abandoned orange peel and paraffin," vol. 27, no. 4, pp. 289–298, Apr. 2019, doi: 10.1080/1536383X.2018.1543279.
- [19] R. Wen, W. Zhang, Z. Lv, Z. Huang, and W. Gao, "A novel composite Phase change material of Stearic Acid/Carbonized sunflower straw for thermal energy storage," *Mater Lett*, 2018, doi: 10.1016/j.matlet.2017.12.008.
- [20] H. Yang et al., "Low-cost, three-dimension, high thermal conductivity, carbonized wood-based composite phase change materials for thermal energy storage," *Energy*, vol. 159, pp. 929–936, Sep. 2018, doi: 10.1016/J.ENERGY.2018.06.207.
- [21] Z. Yang, Y. Deng, and J. Li, "Preparation of porous carbonized woods impregnated with lauric acid as shape-stable composite phase change materials," *Appl Therm Eng*, 2019, doi: 10.1016/j.applthermaleng.2019.01.063.
- [22] Y. Wan et al., "A promising form-stable phase change material prepared using cost effective pinecone biochar as the matrix of palmitic acid for thermal energy storage," *Sci Rep*, vol. 9, no. 1, p. 11535, Dec. 2019, doi: 10.1038/s41598-019-47877-z.
- [23] G. Hekimoğlu et al., "Walnut shell derived bio-carbon/methyl palmitate as novel composite phase change material with enhanced thermal energy storage properties," *J Energy Storage*, vol. 35, p. 102288, Mar. 2021, doi: 10.1016/j.est.2021.102288.
- [24] L. Feng, J. Zheng, H. Yang, Y. Guo, W. Li, and X. Li, "Preparation and characterization of polyethylene glycol/active carbon composites as shape-stabilized phase change materials," *Sol Energy Mater Sol Cells*, vol. 95, no. 2, pp. 644-650, Feb. 2011, doi: 10.1016/j.solmat.2010.09.033.
- [25] G. Hekimoğlu, A. Sarı, S. Arunachalam, H. Arslanoğlu, and O. Gencil, "Porous biochar/heptadecane composite phase change material with leak-proof, high thermal energy storage capacity and enhanced thermal conductivity," *Powder Technol*, vol. 394, pp. 1017–1025, Dec. 2021, doi: 10.1016/j.powtec.2021.09.030.
- [26] L. Feng, J. Zheng, H. Yang, Y. Guo, W. Li, and X. Li, "Cost-Effective Biochar Produced from Agricultural Residues and Its Application for Preparation of High Performance Form-Stable Phase Change Material via Simple Method," *Int J Mol Sci*, vol. 19, no. 10, p. 3055, Oct. 2018, doi: 10.3390/ijms19103055

BIOGRAPHIES

Gökhan Hekimoğlu obtained his BSc degree in Metallurgical and Material Engineering Department from Karadeniz Technical University (KTU) in 2012. He received his MSc. diploma in Material Science from the University of Manchester in England in 2016, and PhD degree in Graduate School of Science, Metallurgical and Material Engineering Department from Karadeniz Technical University in 2022. His research interests are heat storage materials, form stable composite phase change materials and thermal management systems. Since 2017 he has been working as a research assistant in Metallurgical and Material Engineering Department in KTU.



Research Article

Experimental Investigation of the Effect of Curing Pressure on Strength of Single Lap Adhesive Joints

İsmail Saraç^{1*} ^{1*}Aksaray University, Mechanical Engineering Department, 68100, Aksaray, Turkey. (e-mail: ismailsarac@aksaray.edu.tr).

ARTICLE INFO

Received: Jul., 17. 2023
 Revised: Sep., 12. 2023
 Accepted: Dec., 03. 2023

Keywords:
 Adhesive joints
 Curing pressure
 Epoksi adhesive
 Single lap joint

Corresponding author: *İsmail Saraç*

ISSN: 2536-5010 / e-ISSN: 2536-5134

DOI: <https://doi.org/10.36222/ejt.1328653>

ABSTRACT

It is a common method to apply a certain pressure to the bonded surfaces while bonding. In this way, it is ensured that the adhesive covers all surfaces and the air in the adhesive is evacuated. However, the effects of pressure changes on the curing process and mechanical properties, especially in adhesives that harden by chemical reaction, are an issue that should be handled with numerical data at a scientific level. When the literature is examined, there are limited studies on the effects of curing pressure on mechanical properties of adhesive joints.

In this study, the effect of curing pressure on bond strength in adhesive joints was investigated experimentally. Single lap adhesive joints were manufactured using steel plate and DP460 epoxy adhesive. At this stage, bonding joints with different curing pressure conditions were obtained by placing unit weights on the adhesive area. The samples fabricated five different curing pressure values were subjected to tensile tests. In consequence of the experiments, a reducing in the joint endurance was observed after a certain pressure value. When the test results are reviewed, by increasing the curing pressure from 0.22 N/cm² to 0.44 and 0.66 N/cm², the decrease in the failure loads was calculated as 0.8% and 6.8% respectively, while the decrease in the values of 0.88 and 1.1 N/cm² was computed as 20.9% and 49% respectively. Thus, it has been understood that the pressure applied to the adhesive area affects the curing process significantly, and must be taken within certain limits.

1. INTRODUCTION

Adhesive joints are widely used for joining due to their superior properties such as distributing the load over a wider area than the other connection types, not requiring holes, obtaining lightweight structures and having superior fatigue resistance [1]. Some of the factors affecting the performance of the bonded joints are; surface treatments applied to the bonded materials, the ambient temperature in which the adhesive joint is employed, the residual thermal stresses owing to the difference in the thermal expansion coefficient of the adhesive and the bonded materials, curing conditions, particles reinforcement to adhesive and joint geometry [2-3].

In bonding joints, the curing of the adhesive is a very significant issue that directly influences the strength of the joints. A poorly cured adhesive is a critical issue for the aerospace and automotive industries as it can jeopardize the integrity of adhesive joints [4]. Adhesion and cohesion forces are effective in bonding joints. Adhesion forces occur between the adhesive and adherent, the two surfaces are held together by interface forces. Cohesion occurs within the adhesive itself. In cohesion, the mass components that make up the adhesive are held together by chemical or physical forces. High-strength

adhesives used in engineering applications were harden by chemical reaction. This chemical process in which adhesives obtain their strength is called curing.

At the end of the curing process, chemical bonds are formed between the adhesive molecules and the necessary strength is gained. Since the adhesion properties of adhesives are very delicate to environmental circumstances, the load bearing capabilities of the adhesive joints are influenced by the pressure and temperature applied during curing operation. One of the adhesive types that cures by chemical reaction is epoxies. Epoxy adhesives can be in three different forms as one-component, two-component liquid and film. The two-component ones consist of an epoxy adhesive and a hardener, when both are mixed, covalent bonds are formed to become a thermoset polymer [6]. Covalent bonds are the primary bonds that hold atoms together. It is very strong in covalent bonds such as ionic and metallic bonds. Therefore, the strength values of adhesives cured by chemical reaction are considerably higher than adhesives cured by physical change [7].

Pure epoxy molecules at room temperature do not normally react with each other. Types of chemicals added to epoxy to provide network formation; it is divided into two parts as curing agents and catalysts. Curing agents, sometimes called

hardeners, are added to epoxies in considerable quantities and react with the epoxy to build a cross-linked network. Cured resins become insoluble, used to join almost all types of materials (metals, glass, ceramics, wood, composites). They are chemically resistant and have striking dielectric properties. Regarding the curing method, adhesives can be divided into three parts. These; curing at room temperature, curing at average temperature (up to 120 °C), curing at elevated temperatures (up to 250 °C). The mechanical properties of structural epoxy adhesives are strongly dependent on the curing temperature [8]. Curing times are directly related to the heat implemented to the adhesive. Curing time can be reduced at higher temperatures. For epoxy adhesives, curing times at room temperature are up to 24 hours, while curing times decrease with increasing temperature values. The curing times of DP460 Epoxy adhesive, which was also used in this experimental study, are recommended as 24 hours at 23 °C, while it can be reduced to 1.5 hours at 49 °C and 1 hour at 60 °C [9].

There are studies on the effect of curing temperature and curing times on the adhesion performance of structural and non-structural adhesives [10-17].

It is a common method to apply a certain pressure to the bonded surfaces while bonding. In this way, it is ensured that the adhesive covers all surfaces and the air in the adhesive is evacuated. However, the effects of pressure changes on the curing process and mechanical properties, especially in adhesives that harden by chemical reaction, are an issue that should be handled with numerical data at a scientific level. When the literature is examined, there are limited studies on the effects of curing pressure on mechanical properties of adhesive joints.

It has been stated that increasing the applied pressure during curing of cylindrical bonding joints produced using inflexible epoxy adhesive causes the residual stresses which reduces the joint performance. The curing process was done in an autoclave at different pressures [4]. The hydrostatic pressure applied to the adhesive injected between the shaft and the hub increased the performance of the joint in the shaft-hub connections [18]. In single-lap adhesive joints produced using flexible adhesive, the increase in curing pressure improved the joint performance [19].

In this experimental study, the effect of the curing pressure applied to the adhesion area on the tensile strength of the joints was examined in single-lap joints produced using inflexible epoxy adhesive. The purpose of the work is to show the effect of mechanically applied curing pressure on the strength of single-lap joints. The motivation of the study is that the data sheets prepared by the manufacturers of epoxy-type adhesives do not include detailed information on the effects of mechanically applied pressure on the adhesion performance.

2. MATERIAL METHOD

2.1. Adhesive and adherend materials

In the experimental study, AISI 304 steel sheet with a thickness of 2 mm was employed as adherend parts. DP460 epoxy manufactured by 3 M Company (St. Paul, MN, USA), was used as adhesive. DP 460 is a two-component and widely used structural adhesive. Mechanical properties of bonded and adhesive materials are presented in Table 1 [20-21].

Properties	AISI 304	DP460
Ultimate tensile strength, σ_t (MPa)	515-720	44.6 ± 1.2
Yield strength, σ (MPa)	210	38.4 ± 1.1
Modulus of elasticity, E (MPa)	190.000	1984 ± 43
Poisson's ratio, ν	0.29	0.37
Ultimate tensile strain, ϵ_t (%)	≥ 50	4.7

2.2. Fabrication of the tensile test samples

In order to produce single-lap adhesive joint samples, pieces of 130x25x2 mm were cut from AISI 304 plates by laser cutting method. The joint geometry and dimensions used in the study are shown in Figure 1.. Surface preparation process is necessary for adhesive joints to exhibit superior performance. Surfaces to be adhesive applied were eroded with P180 grade emery paper to take away pollutants and to roughen. Subsequent to this, abraded surfaces were washed with liquid detergent under tap water. Following this, the washed parts were dried with a cloth towel. The bonded surfaces were purified via acetone and washed by tap water again. Bonding surface conditioning procedures were completed by drying the adherends with paper towel and finally heated air.

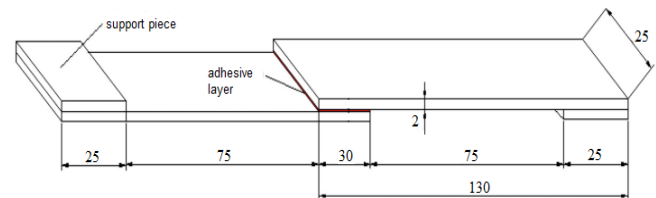


Figure 1. Test specimen geometry

Two-component epoxy adhesives consisting of hardener and epoxy resin were supplied in 50 ml tubes. The applicator was used to discharge equal amounts of hardener and epoxy resin. After the adhesive is poured into a clean container, the hardener and epoxy resin were blended using a wooden pin, in this way, the adhesive material was prepared (Figure 2).



Figure 2. Adhesive pouring applicator and adhesive

To fabricate test samples of single-lap joints in reference to joint geometry, adhesive was implemented on the bonding area and the specimens were placed into the pattern (Figure 3, Figure 4). Three samples were produced at once in the mold.

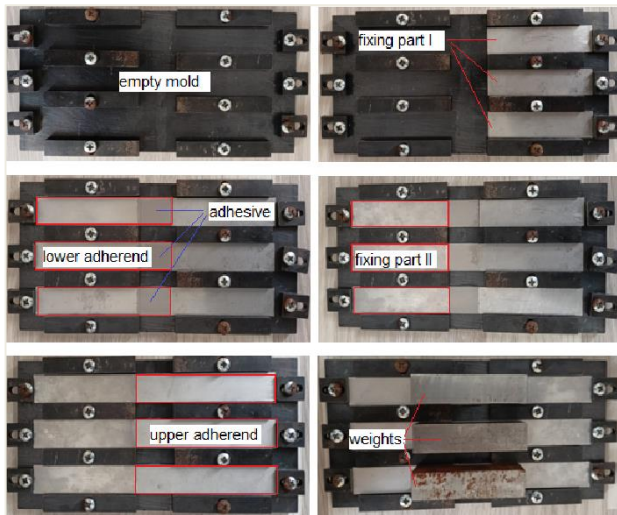


Figure 3. Manufacturing steps of specimens

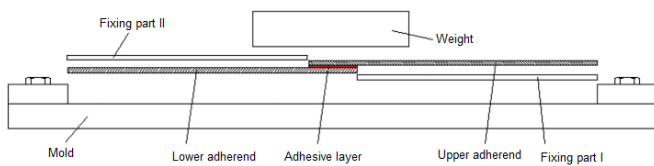


Figure 4. The schematic diagram of the mold

In this study, the effect of the pressure applied to the adhesive layer during the curing process on the tensile strength of the joints were examined. Pressure was applied to the adhesive layer using steel rectangular prism-shaped unit weights. Accordingly, in the bonding region; different pressure values were obtained by using one, two, three, four and five weights, respectively. The pressure values used in the study were calculated as 0.22 N/cm^2 , 0.44 N/cm^2 , 0.66 N/cm^2 , 0.88 N/cm^2 , 1.1 N/cm^2 according to the weights used. As an example, the molding step of samples produced at 0.88 N/cm^2 and 0.44 N/cm^2 curing pressure using four and two weights is shown in Figure 5. Other curing pressure values were obtained with the same method using different numbers of weights. The samples were kept at the desired curing pressure in the mold for 24 hours. Then, after the samples were carried away from the mold, they were coded and stored in a protective container until the experimental stage.



Figure 5. Applying pressure to the adhesive layer using weight

In the study, samples were produced without applying pressure to the adhesive coating. However, as a result of the experiments, it was understood that the adhesive did not spread well on the surface and the adhesive thickness was not stable in the samples, so the samples prepared without applying pressure were excluded from the test program. Therefore, it has been understood that a certain amount of pressure must be

applied to the adhesive area for fully spread the adhesive on the surface and to obtain an even adhesive thickness along the adhesive line.

2.3. Tensile testing of the joints

A series of tensile test were implemented to decide the effects of pressure variation in the adhesive layer during the curing phase.

Tensile tests were carried out under laboratory conditions at a tensile speed of 1 mm/min (Figure 6). Sample types were determined according to the curing pressure (Table 2). Experiments were made using five joint types. To raise the reliability of tests, four specimens were prepared for each specimen type, in all, 20 specimens ($5 \text{ joint type} \times 4$: 20).

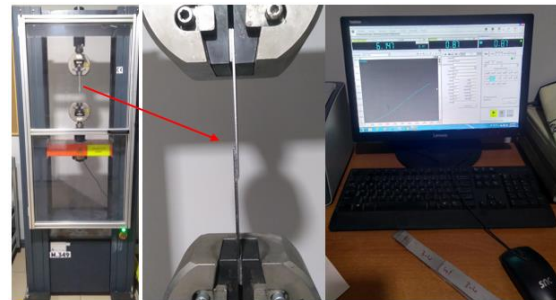


Figure 6. Tensile test application

Figure 7, shows 5 test samples produced for the P-1 sample type.

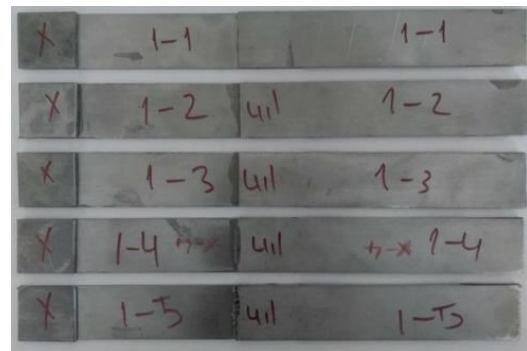


Figure 7. SLJs samples

The samples were carefully monitored while testing and the maximum damage loads and maximum tensile strains of single-lap joints were reported. The adhesive thickness of all samples removed from the mold was measured in the range of 0.05 mm - 0.1 mm . The curing process of the pressure applied samples was completed in 24 hours under room temperature conditions ($22 \text{ }^\circ\text{C}$). Boundary conditions for single-lap adhesive joints were determined in accordance with the tensile test conditions (Figure 8).

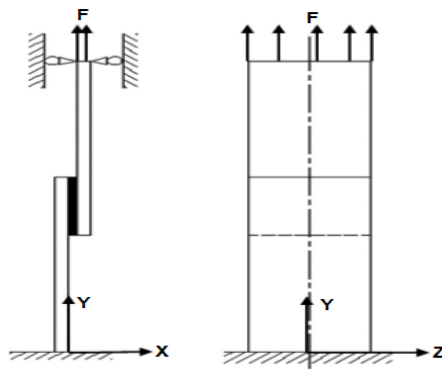


Figure 8. The boundary setup of the joints

TABLE 2
JOINT TYPES

Joint type	Curing pressure(N/cm ²)
P-1	0.22
P-2	0.44
P-3	0.66
P-4	0.88
P-5	1.1

3. RESULTS and DISCUSSION(Helvetica 10p Bold)

The experimental tensile failure loads of single-lap joints are obtained according to the curing pressure (Figure 9).

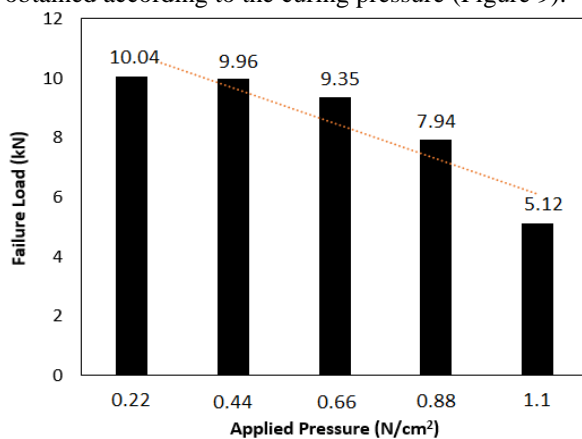


Figure 9. Failure load variation according to curing pressure

When the results are examined, the failure loads of the Single-lap joints, at the pressure values of 0.22 N/cm², 0.44 N/cm² and 0.66 N/cm² are close to each other as 10.04 kN, 9.96 kN and 9.35 kN, respectively. However, when the pressure values were increased to 0.88 N/cm² and 1.1 N/cm², a significant decrease was observed in the failure loads (At pressure values of 0.88 N/cm² and 1.1 N/cm², the failure loads were measured as 7.94 kN and 5.12 kN, respectively). When the adhesion theories in the literature are examined; the mechanical adhesion theory is based on the principle that the adhesive penetrates the pores on the surface of the material and is physically locked there [19]. Adsorption theory, developed by Sharpe and Schonhorn, suggests that adhesion occurs as a result of the formation of interatomic and intermolecular forces at the interface, provided that good contact between the base material and the adhesive is maintained [20]. Adsorption theory is still the most widely accepted and applicable theory in adhesive science. Therefore, it can be said that applying pressure to the adhesive layer increases the bond performance,

as it allows the adhesive to spread better on the surface and penetrate into the pores, according to these theories. However, it is seen in this study that this approach can be correct up to a certain pressure value and that increasing the pressure further reduces the joint strength. Accordingly, with an rise of 5 times the curing pressure, the average tensile failure load decreased by 50 %.

During the curing of the adhesive joints, residual thermal stresses occur because the adhesive and the bonded materials have different thermal properties. Especially in bonding processes at high temperatures, these stresses increase even more. At this stage, it can be thought that the pressure applied to the adhesive layer will affect the residual stresses that occur during curing. It is a research question, whether the pressure applied during curing will affect the joint strength positively or negatively. Another factor is the curing temperature. When the literature is examined, in a study using a flexible adhesive (SBT 9244), the curing was made using a hot press at 145 °C at two different pressures as 0.1 MPa and 0.5 MPa, and the effect of the curing pressure was experimentally measured [16]. Accordingly, it has been determined that the increase in pressure increases the joint strength. In another study, cylindrical bonding joints were formed by using steel as the bonded material and DP 460 (3M, USA) as the adhesive [1]. In the study, the effect of curing pressure on the joint strength was investigated experimentally by performing tensile tests. As a result of the experiments, it was determined that increasing the curing pressure decreases the joint strength. During the production of the test samples, the curing temperature was 80 °C. In a experimental study, while explaining the effect of curing pressure on the joint strength, they stated that the pressure increased the heat transfer coefficient of the air in the autoclave where the curing was carried out, and as a result, the curing operation accelerated and the adhesive temperature increased [1]. It was stated that as a result of the increase in the adhesive temperature, the thermal residual stresses increased and the joint was damaged earlier.

As stated in the literature, residual stresses negatively affect the joint performance. It is understood that the pressure applied to the adhesive layer during curing causes residual stresses and reduces the bond strength. It is known that the pressure applied to the adhesive causes the adhesive to completely wet the surface and establish a very good contact with the adhered material. However, after providing the required pressure value as seen in this study, the effect of further increasing the pressure on the strength was reduced.

Two-component epoxy adhesives start to react at ambient temperature after the two components are mixed. The reaction rate is greatly affected by the reaction temperature. For every 10 °C increase in temperature, the reaction time is doubled. Full cure times at ambient temperatures for two-component systems range from a few minutes to several days. The decrease in crosslinking levels results in low cohesion strength. Similarly, in this study, it is thought that the curing pressure change affects the bond strengths by changing the reaction rate.

At the end of the tensile tests, load displacement graphs were obtained (Figure 10). The load displacement graphs have been prepared by taking into account the data of the test sample with the largest failure load in the same test group. Accordingly, the displacement amount decreased with the increase of the curing pressure value.

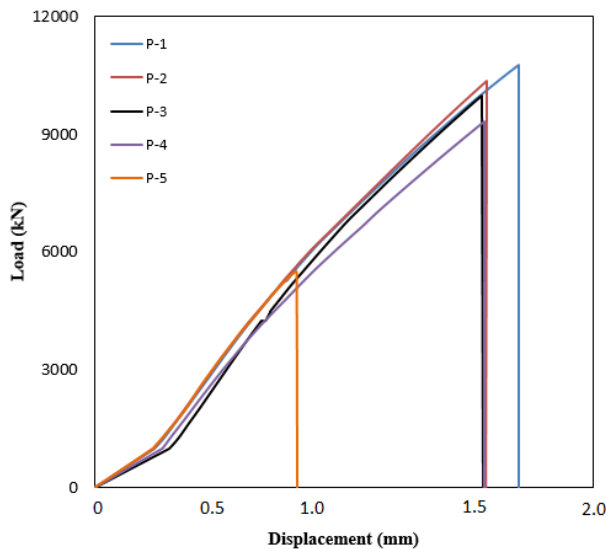


Figure 10. Load displacement graphs according to curing pressure

4. CONCLUSIONS and SUGGESTIONS

In this study, the effect of the curing pressure applied to the adhesive area on the strength was investigated by performing tensile tests. The general results obtained experimental study are given below:

In cases where two-component epoxy adhesives that can be cured at room temperature are used, pressure must be applied to the bonding area during curing in order to spread the adhesive over the entire surface and to obtain a homogeneous adhesive thickness. However, it should be noted that after a critical pressure value, there is a decrease in joint strength due to residual stresses.

In the experimental study, the highest average damage load was obtained with a value of 10.04 kN at 0.22 N/cm² curing pressure. Failure loads were close to each other at 0.22 N/cm², 0.44 N/cm² and 0.66 N/cm² curing pressure values. An important decrease in bond strength was seen at the curing pressure values of 0.88 N/cm² and 1.1 N/cm².

By increasing the curing pressure from 0.22 N/cm² to 0.44 and 0.66 N/cm², the decrease in the damage load value was calculated as 0.8% and 6.8%, respectively, while the decrease in the values of 0.88 and 1.1 N/cm² was computed as 20.9% and 49%, respectively. Therefore, the curing pressure affects the joint strength negatively after a certain pressure range. According to this study, the recommended curing pressure range is 0.11 N/cm² - 0.66 N/cm².

This study does not show how curing pressure affects the chemical mechanics/interaction in the adhesive. It would be beneficial to conduct studies on this subject in future.

REFERENCES

- [1] M.Ş. Adin, E. Kılıçkap, "Strength of double-reinforced adhesive joints," *Materials Testing*, vol. 63, no. 2, pp. 176-181, Feb. 2021.
- [2] H.B. Rachid, D. Noureddine, B. Benali, M.Ş. Adin, "Effect of nanocomposites rate on the crack propagation in the adhesive of single lap joint subjected to tension," *Mechanics of Advanced Materials and Structures*, pp. 1-9, Mar. 2023.
- [3] İ. Saraç, "Failure analysis of simple overlap bonding joints and numerical investigation of the adhered tip geometry effect on the joint strength," *Materials Testing*, vol. 63, no. 11, pp. 1007-1011, Nov. 2021.
- [4] J.K. Kim, D.G. Lee, "Effects of applied pressure and temperature during curing operation on the strength of tubular single-lap adhesive joints," *Journal of Adhesion Science and Technology*, vol. 18, no. 1, pp. 87-107, Apr. 2004.

- [5] D.N. Markatos, K.I. Tserpes, E. Rau, S. Markus, B. Ehrhart, S. Pantelakis, "The effects of manufacturing-induced and in-service related bonding quality reduction on the mode-I fracture toughness of composite bonded joints for aeronautical use," *Composites Part B: Engineering*, vol. 45, no. 1, pp. 556-564, Feb. 2013.
- [6] T. Şekerçioğlu, "Makine Elemanları Hesap Şekillendirme," Birsen Publisher İstanbul, 2018.
- [7] T. Şavaşkan, "Malzeme Bilimi ve Malzeme Muayenesi," Papatya Publisher, İstanbul, 2018.
- [8] A. Rudawska, "The influence of curing conditions on the strength of adhesive joints," *The Journal of Adhesion*, vol. 96, no. 1, pp. 402-422, Aug. 2019.
- [9] İ. Saraç, H. Adin, Ş. Temiz, "Experimental determination of the static and fatigue strength of the adhesive joints bonded by epoxy adhesive including different particles," *Composites Part B: Engineering*, vol. 155, pp. 92-103, Dec. 2018.
- [10] K. Matsui, "Effects of curing conditions and test temperatures on the strength of adhesive-bonded joints," *International Journal of Adhesion and Adhesives*, vol. 14, no. 4, pp. 277-284, Oct. 1990.
- [11] A. Agha, F. Abu-Farha, "Experimental methods to capture curing induced effects in adhesive bonded joints," *International Journal of Adhesion and Adhesives*, vol. 104, pp. 102735, Jan. 2021.
- [12] A. Tran, J. Konnerth, H.W. Van Herwijnen, W. Gindl-Altmutter, "Low temperature and moisture dependent curing behavior of selected wood adhesives," *International Journal of Adhesion and Adhesives*, vol. 117, pp. 103178, Sept. 2022.
- [13] M. Voss, J. Haupt, "Accelerated curing of adhesively bonded G-FRP tube connections—Part I: Experiments," *Composite Structures*, vol. 268, pp. 113999, Jul. 2021.
- [14] I. Morfini, L. Goglio, G. Belingardi, S.A. Nassar, "Effect of autoclave cure time and bonded surface roughness on the static and fatigue performance of polyurethane film Adhesive Single lap joints," *International Journal of Adhesion and Adhesives*, vol. 92, pp. 37-43, Jul. 2019.
- [15] F. Marchione, G. Chiappini, P. Munafò, "Effect of temperature and relative humidity on the shear performance of double-lap adhesive joints between steel and glass adherends," *Journal of Building Engineering*, vol. 45, pp. 103546, Jan. 2022.
- [16] Y. Jahani, M. Baena, C. Barris, R. Perera, L. Torres, "Influence of curing, post-curing and testing temperatures on mechanical properties of a structural adhesive," *Construction and Building Materials*, vol. 324, pp. 126698, March 2022.
- [17] A.I.M. Foletti, J.S. Cruz, A.P. Vassilopoulos, "Fabrication and curing conditions effects on the fatigue behavior of a structural adhesive," *International Journal of Fatigue*, vol. 139, pp. 105743, Oct. 2020.
- [18] R. Mengel, J. Häberle, M. Schlimmer, "Mechanical properties of hub/shaft joints adhesively bonded and cured under hydrostatic pressure," *International Journal of Adhesion and Adhesives*, vol. 27, no. 7, pp. 568-573, Oct. 2007.
- [19] M.D. Aydın, Ş. Temiz, A. Özel, "Effect of curing pressure on the strength of adhesively bonded joints," *Journal of Adhesion*, vol. 83, no. 6, pp. 553-571, Jul. 2007.
- [20] S. Akpınar, "The strength of the adhesively bonded step-lap joints for different step numbers," *Composites Part B: Engineering*, vol. 67, pp. 170-178, Dec. 2014.
- [21] M.S. Kim, H.T. Kim, Y.H. Choi, J.H. Kim, S.K. Kim, J.M.A. Lee, "A new computational method for predicting ductile failure of 304L stainless steel," *Metals*, vol. 12, no. 8, pp. 1309, Aug. 2022.
- [22] L.P. DeMejo, D.S. Rimai, L.H. Sharpe, "Fundamentals of Adhesion and Interfaces," Gordon and Breach Science Publishers, 1995.
- [23] J. Schultz, M. Nardin, "Theories and mechanisms of adhesion," *Materials engineering-New York*, vol. 14, pp. 1-26, 1999.

BIOGRAPHIES

İsmail Saraç obtained his BSc degree in mechanical engineering from Pamukkale University (PAU) in 2002. He received the MSc. diploma in Mechanical Engineering from the Fırat University in 2013, and received the PhD degrees in Mechanical Engineering from Batman University in 2018. His research interests are adhesive joints and topology optimization. In 2018 he joined the Faculty of Mechanical Engineering, Aksaray University as assistant prof. He is active in teaching and research in the general mechanical elements and FEM analysis.

Research Article

Cosistency Axioms of Choice for Ismail's Entropy Formalism(IEF) Combined with Information-Theoretic(IT) Applications to advance 6G Networks

I A Mageed Department of Computer Science, University of Bradford, United Kingdom (iammoham@bradford.ac.uk)

ARTICLE INFO

Received: May., 18, 2023

Revised: Agu., 06, 2023

Accepted: Agu., 30, 2023

Keywords:

IEF

Applications

6G Networks

Corresponding author: *Ismail A Mageed*

ISSN: 2536-5010 / e-ISSN: 2536-5134

DOI: <https://doi.org/10.36222/ejt.1299311>

ABSTRACT

An exposition is undertaken to analytically validate the credibility of IEF, by investigating the four axioms of consistency on IEF. More fundamentally, IE is by default the ultimate generalization to most entropy measures in the literature. The current paper also provides some applications of Information Theory to 6G Networks. Additionally, the latter review consolidates more foundational motivations and insights into further employment of information-theoretic advancements to 6G networks. Conclusions, open problems, and future directions are given.

1. INTRODUCTION

In principles, this current work supplies a complementary part of the research conducted (c.f., [1]). As the authors now feel that the task is completed and demonstrated with both analytic expressions as well as illustrative data to interpret the newly devised research results.

The non-extensive maximum entropy (NME) formalism was established in the aftermath of Rényi [2] and Tsallis [3] as a closed form expression tool for inductive reasoning mixed with "long-range" interactions-physical systems with non-extensive order. Having said that, their technique has generalized the well-known "short-range" interactions of Shannon's conventional "extensive" ME (EME) formalism [4].

Introducing Ismail's entropy, namely, $H_{(q,UG)}$ as the most generalized form ever to uniquely generalize all the available known generalized entropies in the literature, stable $M / G / 1$ queueing system probabilistic descriptors corresponding to states $\{p_{q,UG}(n), n = 0, 1, 2, \dots\}$ based on the previous two applications in EME format to stable $M / G / 1$ queues is devised.

Normalization, $\sum_n p(n) = 1$ and Pollaczec-Khinchin (P-K) mean queue length (MQL), $\langle n \rangle = \sum_n np(n)$ by Shore [5]. and Server utilization (SU), $1-p(0)$ by [6].

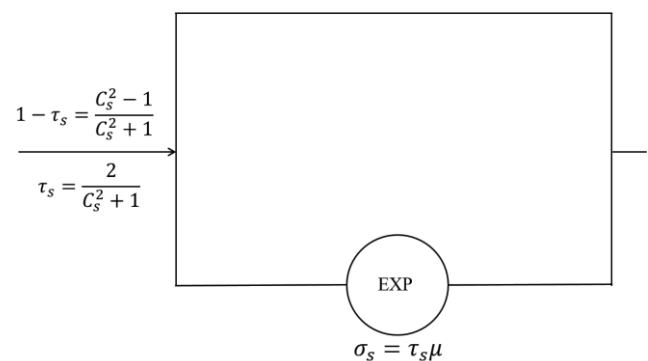


Figure 1. GE-type service time distribution with parameters $\{1/\mu, C_s^2 > 1\}$

Notably, the proposed closed form expression [6] was shown to be exact for a stable $M/G/1$ queueing system when the service (S) times followed GE distribution as described by Figure 1

$$F_s(t) = P(S \leq t) = 1 - \tau_s \exp(-\mu t \tau_s) \quad (1)$$

$$\tau_s = \frac{2}{1+C_s^2} \quad (2)$$

μ serves as service rate and C_s^2 serves as the service times' squared coefficient of variation (SCV). More intriguingly, the GE distribution has numerous real-life applications [3,6,7,8,9,12].

The Shannonian entropy functional $H_{1,S}(p)$ [4], is defined by:

$$H_{1,S}(p) = -c \sum_{S_n \in S} p_{1,S}(S_n) \log p_{1,S}(S_n), \quad n = 0, 1, 2, \dots \quad (3)$$

with a constant $c(c > 0)$ and $\{p_{1,S}(S_n), S_n \in S\}$ are the Extensive Maximum Entropy (EME) state probabilities, S_n serve as configurations or states. $H_{1,S}(p)$ is an information measure acted by $p_{1,S}(S_n)$ to a "short range" interactions-physical system [13].

If the above defined set S (c.f., equation (3)) is countably infinite or finite over the "long-range interaction"-physical system, then the proposed IE functional is defined by

$$H_{(q,UG)} = \sum_{n=0}^{\infty} \varphi((p(n)^q, a_1, a_2, \dots, a_k), k \leq n) \quad (4)$$

Here φ serves as any well – defined function, a_1, a_2, \dots, a_k serve as any universal parameters, $1 > q > 0.5$. The EME state steady probability of a stable $M/G/1$ queue that maximises Shannon's entropy function [4] has been demonstrated [6].

$$H(p_{1,S}) = -\sum_{n=0}^{\infty} p_{1,S}(n) \ln(p_{1,S}) \quad (5)$$

Under the constraints:

Normalization,

$$\sum_{n=0}^{\infty} p_{1,S}(n) = 1 \quad (6)1.$$

$$\text{SU, } p_{1,S}(0) = \sum_{n=0}^{\infty} h(n)p_{1,S}(n) = 1 - \rho = \lambda/\mu \quad (7)2.$$

where

$$h(n) = \begin{cases} 1, & n = 0 \\ 0, & \text{otherwise} \end{cases} \quad (8)$$

P-K MQL,

$$\langle n \rangle = \sum_{n=0}^{\infty} n p_{1,S}(n) = \frac{\rho}{2} \left(1 + \frac{1 + \rho C_{s,1,S}^2}{1 - \rho} \right) \quad (9)$$

is given by

$$p_{1,S}(n) = \begin{cases} p_{1,S}(0), & n = 0 \\ p_{1,S}(0) \tau_s x^n & n > 0 \end{cases} \quad (10)$$

where $p_{1,S}(0) = 1 - \rho$, $\tau_s = 2/(1 + C_{s,1,S}^2)$ and $x = \frac{\langle n \rangle - \rho}{\langle n \rangle}$.

Theorem 1(c.f., [1]) The $H_{(q,UG)}$ NME solutions $p_{q,UG}(n)$, for the stable $M/G/1$ queue subject to (6), (7) and (9) are given by

$$p_{q,UG}(n) = \begin{cases} p_{q,UG}(0), & n = 0 \\ p_{q,UG}(0) \tau_s^b x^n, b = G(q, a_1, a_2, \dots, a_k), & n \neq 0 \end{cases} \quad (11)$$

Such that $p_{q,UG}(0)$ satisfies (8), namely

$$1 - p_{q,UG}(0) = \rho_{GU} \quad (12)$$

Here τ_s and x serve as Lagrangian multipliers satisfying that:

$$\tau_s = \frac{2}{1 + C_{s,1,S}^2}, \quad x = \frac{\rho}{\left(\rho + (1 - \rho) \left(\frac{2}{1 + C_{s,1,S}^2} \right)^b \right)}, \frac{\rho(1-x)}{(1-\rho)x} = \tau_s^b \quad (13)$$

Theorem 2(c.f., [1])

$H_{(q,UG)}$'s NME steady-state probability, $p_{q,UG}(n)$ is exact $f_{s,q,UG}(t)$ is determined by

$$f_{s,q,UG}(t) = (1 - \tau_{s,UG}) u_0(t) + \mu \tau_{s,q,UG}^2 e^{-\mu t \tau_{s,UG}}$$

with $u_0(t)$ in the form

$$u_0(t) = \begin{cases} \infty, & t = 0 \\ 0, & \text{otherwise} \end{cases} \quad \text{with } \int_{-\infty}^{\infty} u_0(t) = 1 \quad (14)$$

and $\tau_{s,UG} = \tau_s^b$, $b = G(q, a_1, a_2, \dots, a_k)$, $\tau_s = \frac{2}{(1 + C_{s,1,S}^2)}$.

Corollary 2.1

The CDF, $F_{s,q,UG}(t)$ of the $GE_{q,UG}$ -types of service time with the pdf $f_{s,q,UG}(t)$ (c.f., (14)) is fully determined by cumulative

distribution function $F_{s,q,UG}(t)$, of $S_{q,UG}(t)$ and is determined by

$$F_{s,q,UG}(t) = 1 - \tau_s^b e^{-\mu \tau_s^b t}, \quad \tau_s = 2/(1 + C_{s,1,S}^2) \quad (15)$$

Corollary 2.2 Following CDF (c.f., equation (14)), the service time's SCV, S are given by:

$$E(S_{q,UG}) = \frac{1}{\mu} \quad (16)$$

$$E(S_{q,UG}^2) = \frac{2}{\mu^2 \tau_s^b} \quad (17)$$

$$C_{s,q,UG}^2 = \frac{E(S_{q,UG}^2)}{(E(S_{q,UG}))^2} - 1 = \frac{(2 - \tau_s^b)}{\tau_s^b} \quad (18)$$

where $\tau_s = 2/(1 + C_{s,1,S}^2)$.

[1] mainly contributes to:

- The Ismail's entropy (IE) measure is a generalization of all existing entropic measures in the literature.
- The provision of IE formalism of the stable $M/G/1$ queueing system, which is the ultimate generalization to all up to date formalisms.
- Highlighting possible ME applications to energy works, which will be critical in taking energy works to the next level.

2. UNIFIED GLOBAL NME FORMALISMS VS EME CONSISTENCY AXIOMS

2.1. Uniqueness

The uniqueness axiom reads as axiom, "If the same problem is solved twice in exactly the same way, the same answer is expected in both cases i.e., the solution should be unique" [14].

Let $f_{q,UG}, h_{q,UG}$ be defined on S such that:

$$H_{q,a_1,a_2,\dots,a_n,UG}^*(f_{q,a_1,a_2,\dots,a_n,UG}) = H_{q,a_1,a_2,\dots,a_n,UG}^*(h_{q,a_1,a_2,\dots,a_n,UG}) \quad (19)$$

Hence, for $k \leq n$,

$$\sum_{n=1}^N \varphi((f_{q,a_1,a_2,\dots,a_n,UG})^q, a_1, \dots, a_k) = \sum_{n=1}^N \varphi((h_{q,a_1,a_2,\dots,a_n,UG})^q, a_1, \dots, a_k) \quad (20)$$

This clearly implies

$$\varphi((f_{q,a_1,a_2,\dots,a_n,UG})^q, a_1, \dots, a_k) = \varphi((h_{q,a_1,a_2,\dots,a_n,UG})^q, a_1, \dots, a_k) \quad (21)$$

Assuming the contradictory statement, $f_{q,a_1,a_2,\dots,a_n,UG} \neq h_{q,a_1,a_2,\dots,a_n,UG}$, hence there is a constant $\gamma > 1$ satisfying:

$$f_{q,a_1,a_2,\dots,a_n,UG}^q = \gamma h_{q,a_1,a_2,\dots,a_n,UG}^q \quad (22)$$

Hence,

$$\begin{aligned} & \sum_{n=1}^N \varphi((\gamma (h_{q,a_1,a_2,\dots,a_n,UG})^q, a_1, a_2, \dots, a_k)) \\ &= \sum_{n=1}^N \varphi(((h_{q,a_1,a_2,\dots,a_n,UG})^q, a_1, a_2, \dots, a_k)), \\ & k \leq n \end{aligned} \quad (23)$$

By (23) and component-wise equality, clearly it follows that

$$h_{q,a_1,a_2,\dots,a_n,UG}^q = \gamma h_{q,a_1,a_2,\dots,a_n,UG}^q \quad (\text{Contradiction}) \quad (24)$$

(24) holds if and only if $\gamma = 1$, which is a contradiction. Since φ is uniquely represented by the definition of the UG formalism. Therefore, "there cannot be two distinct probability

distributions $f_{q,a_1,a_2,\dots,a_k,N}, h_{q,a_1,a_2,\dots,a_k,N} \in \Omega$ with equal Ω 'sNME. Thus, uniqueness holds [14].

2.2. Invariance

Invariance reads as "The same solution should be obtained if the same inference problem is solved twice in two different coordinate systems" [15]. Following analogous logic to [14], let W be transformed into a new variable V by a continuous one-to-one transformation. If the density functions of the variates are $f(w)$ and $g(v)$, then

$$g(v) = f(w) \left| \frac{dw}{dv} \right| = \left| \frac{dv}{dw} \right| \int_{-\infty}^{\infty} \varphi((f(w))^q, a_1, a_2, \dots, a_k) \left| \frac{dw}{dv} \right|^q dw \quad (27)$$

The entropy functional therefore changes. If however we consider a linear transformation

$$V = AW + B \quad (28)$$

We get after some manipulation,

$$H_{q,a_1,a_2,\dots,a_k,N,UG}(g(v)) = |A| \int_{-\infty}^{\infty} \varphi((f(w))^q, a_1, a_2, \dots, a_k) \frac{1}{|A|^q} dw \quad (29)$$

So, it is obvious from (28) and (29) that if the unique φ representation satisfies:

$$\varphi(\eta^q(f(w))^q, a_1, a_2, \dots, a_k) = \varphi((f(w))^q, a_1, a_2, \dots, a_k) \quad (30)$$

i.e., φ is invariant under scaling transformation it holds that in this case. For the case of multivariate distributions,

$$H_{q,a_1,a_2,\dots,a_k,N,UG}(g) = |A| \int_{-\infty}^{\infty} \varphi((f(x))^q, a_1, a_2, \dots, a_k) dx \quad (31)$$

Which show that $H_{q,a_1,a_2,\dots,a_k,N,UG}$ is invariant if and only if φ

is UG invariant under scale transformation.

By (26) and (27), the change is q -dependent and generally speaking, $H_{q,a_1,a_2,\dots,a_k,N,UG}$ is not invariant under transformation.

For the case of multivariate distributions,

$$H_{q,a_1,a_2,\dots,a_k,N,UG}(g) = |A| \int_{-\infty}^{\infty} \dots \dots \dots \int_{-\infty}^{\infty} \left(\varphi(w_1, w_2, \dots, w_N) \right)^q \left(\left| \frac{\partial(w_1, w_2, \dots, w_N)}{\partial(v_1, v_2, \dots, v_N)} \right| \right)^q dw_1 dw_2 \dots dw_N \quad (32)$$

where $f(w_1, w_2, \dots, w_N)$ and $g(v_1, v_2, \dots, v_N)$ are the density functions. Hence, Invariance is defied.

2.3. System Independence

System independence reads as "It should not matter whether one accounts for independent information about independent systems separately in terms of different probabilities or together in terms of the joint probability" [15]. In this context the joint probability is expressed by,

$$H_{q,a_1,a_2,\dots,a_k,N}(x_m, y_m) = \Pr(X = x_m, Y = y_m) = f_{q,a_1,a_2,\dots,a_k,N}(x_m) g_{q,a_1,a_2,\dots,a_k,N}(y_m) \quad (33)$$

For the joint probability $H_{q,a_1,a_2,\dots,a_k,N}(x_m, y_m)$, $H_{(q,UG)}$ of (4), reads:

$$H_{q,a_1,a_2,\dots,a_k,N,UG}^*(H_{q,a_1,a_2,\dots,a_k,N}) = \sum_l \sum_n \varphi(h_{q,a_1,a_2,\dots,a_k,N}^q) \quad (34)$$

Clearly, it follows from (4) that:

$$H_{q,a_1,a_2,\dots,a_k,N}^*(h_{q,N}) \neq H_{q,a_1,a_2,\dots,a_k,N}^*(f_{q,N}) + H_{q,a_1,a_2,\dots,a_k,N}^*(g(Y_{q,N})) \quad (35)$$

In information theory words, the un-equality (35) implies that "the joint EME state probability distribution of two independent non-extensive systems Q and V defies the axiom of system independence due to the presence of long-range interactions" [14].

$$\text{As } q \rightarrow 1, \varphi(p(n)) = -p(n) \ln(p(n)),$$

our defined UG Entropian functional reduces to the Shannon Boltzmannian entropy and the un-equality (35) becomes equality, namely

$$H_1^*(h_{1,N}) = H_1^*(f_{1,N}) + H_1^*(g(Y_{1,N})) \quad (36)$$

By (36), system independence is satisfied [14], which is "an appropriate property of EME formalism, as a method of inductive inference, for the study of extensive systems with short-range interactions" [16].

2.4. Subset Independence

Subset independence reads as "It does not matter whether one treats an independent subset of system states in terms of a separate conditional density or in terms of the full system density" [15].

Consider a general non-extensive system Q that has a finite number, L ($L > 0$) of disjoint sets of discrete states $\{S_i^*, i = 1, 2, \dots, L\}$, whose union is S . Let $\{x_{ij}, i, j = 1, 2, \dots, L\}$ be a conditional state in S_i^* . Let ξ_i be the probability that a state of the system Q is in the set $\{S_i^*, i = 1, 2, \dots, L\}$ such that $\sum_i \xi_i = 1$. Moreover, let probability $f_{q,a_1,a_2,\dots,a_k,N}(x_{ij}) \in \Omega_i$, where Ω_i , is the closed convex set of all probability distributions on S_i^* , i.e., $\{f_{q,a_1,a_2,\dots,a_k,N}(x_{ij}) = \Pr\{X_i = x_{ij}\}$, where X_i is the state conditional random variable of the system $S_i^*, i = 1, 2, \dots, L$. Moreover, let w be an aggregate state of system Q and probability $f_{q,a_1,a_2,\dots,a_k,N}(x) \in \Omega$, where Ω is the closed convex set of all probability distributions on S i.e., $f_{q,a_1,a_2,\dots,a_k,N}(x) = \Pr\{X = x\}$ where W is the random variable describing the aggregate state of the system S . Clearly, $\xi_i, i = 1, 2, \dots, L$ can be expressed by

$$\sum_{S_i^*} f_{q,a_1,a_2,\dots,a_k,N}(x_{ij}) = \xi_i \quad (37)$$

The overall non-extensive entropy function of system Q , $H_{q,a_1,a_2,\dots,a_k,N,UG}^*(f_q)$ is defined on the total number of states in the union S of states $\{S_i^*, i = 1, 2, \dots, L\}$. Hence, it can be shown that

$$H_{q,a_1,a_2,\dots,a_k,N}^*(f_q) = \sum_i \sum_{S_i^*} \xi_i \varphi(f_{q,a_1,a_2,\dots,a_k,N}^q(x_{ij})) \quad (38)$$

where $f_q(x) \in \Omega$. Equ. (38) rewrites to

$$H_{q,a_1,a_2,\dots,a_k,N}^*(f_q) = \sum_i \xi_i \left(\sum_{S_i^*} \varphi(f_{q,a_1,a_2,\dots,a_k,N}^q(x_{ij})) \right) \quad (39)$$

However, the conditional extensive entropy, $H_{q,a_1,a_2,\dots,a_k,N}^*(f_{q,i})$, defined on the set $\{S_i, i = 1, 2, \dots, L\}$ is expressed by the Poisson process as,

$$H_{q,i,a_1,a_2,\dots,a_k}^*(f_q) = \sum_{S_i^*} \varphi(f_{q,i,a_1,a_2,\dots,a_k}^q(x_{ij})) \quad (40)$$

This implies

$$H_{q,a_1,a_2,\dots,a_k}^*(f_q) = \sum_i \xi_i(H_{q,a_1,a_2,\dots,a_k}^*(f_{q,i})) \quad (41)$$

Therefore, “maximizing the generalized aggregate entropy function, $H_{q,a_1,a_2,\dots,a_k}^*(f_q)$, subject to an aggregate set of available constraints, it is equivalent to maximizing each generalized conditional entropy function, $H_{q,a_1,a_2,\dots,a_k}^*(f_{q,i})$ individually, subject to a conditional set of available constraints. Thus, the Unified Global ME formalism satisfies the axiom of subset independence [14].

3. THE INFLUENTIAL ROLE OF INFORMATION THEORY TO ADVANCE 6G NETWORKS

The traditional strategy of avoiding or ignoring interference in wireless networks is insufficient for the ambitious ultra dense cellular networks (CNs) have high quality-of-service (QoS) requirements. However, recent breakthroughs in information theory have shifted our perception of interference from a foe to a friend. [17] has shed light on how to reap the benefits of incorporating modern interference management (IM) techniques into future CNs. To that aim, a hybrid multiple-access (HMA) scheme that decomposes the network into sub topologies of alternative IM schemes for more efficient network resource utilization was developed [17], where preliminary findings indicate that an HMA method can improve nonorthogonal multiple-access (NOMA) performance, particularly in dense user deployments.

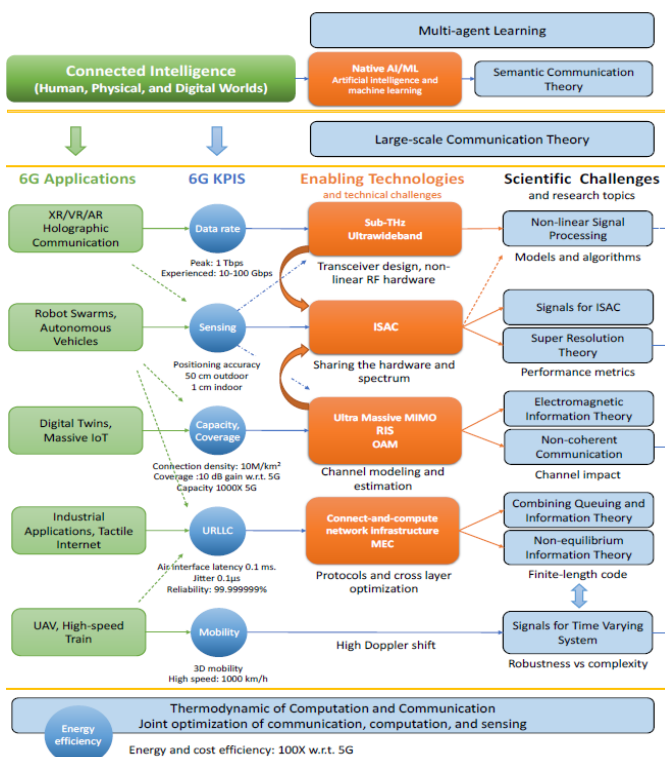


Figure 2. Collaboration amongst 6G Scientific Challenges [18].

The sixth generation [18] of wireless networks faces new challenges in meeting the requirements of emerging applications, such as high data rate, low latency, high reliability, and massive connectivity. To address these

challenges, the entire communication chain needs to be optimized, including the channel and surrounding environment. Investigating large intelligent surfaces, ultra-massive multiple-input-multiple-output, and smart constructive environments, as well as considering semantic and goal-oriented communications, emergent communication, and end-to-end communication system optimization, are among the scientific challenges identified for rebuilding the theoretical foundation of communications.

Figure 2 (c.f., [18]) shows how the scientific challenges discussed in [18] are key performance indicators (KPIs)-related. The goal of 6G is to provide connectivity and computation to interconnect the digital, physical, and human worlds through a high-performance network that connects different types of sensors, actuators, and computation platforms. This concept is referred to as "connected intelligence". Thus, we can observe some triggering questions on how to steer future 6G networks.

Electromagnetic information theory (EIT) is a field that explores the interplay between information theory and electromagnetism. It focuses on developing information theory principles and antenna engineering while considering the limitations imposed by the laws of electromagnetism. This field has emerged because of the interaction between wave physics and information theory and has been studied for decades.

The development of 6G networks [18] has led to the emergence of new communication technologies such as RIS, TR, OAM, surface wave communications, and ultra-massive MIMO. However, current information-theoretic tools are insufficient to fully understand the performance limits of these technologies due to assumptions made in network design and performance analysis. EIT is expected to play a key role in characterizing the fundamental limits of these technologies and building better communication system models that are physically consistent with real propagation environments.

To meet [18] the high data rate requirements of some 6G applications, exploiting ultra-wideband at the sub-THz band is a potential technology. However, this poses technical challenges in transceiver design due to the non-linear behavior of Radio Frequency (RF) components and hardware design constraints. To address these challenges, non-linear signal processing methods are necessary, which require proper modeling of transceiver components, developing low-complexity algorithms, and evaluating information theoretical limits.

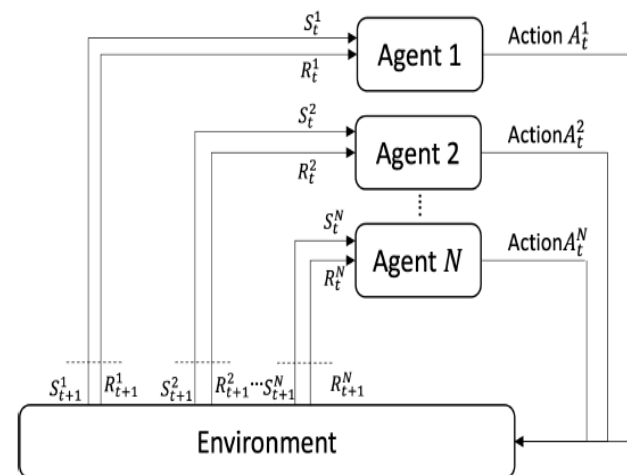


Figure 3. Multi-agent systems' architecture [21].

The development of 6G networks [19,20] is expected to support applications that require high data rates, low latency, and high quality of service. However, the feedback theory poses a challenge to realizing the full potential of 6G due to degraded spectral efficiency and increased delay.

Multi-agent theory is a promising approach to improving network throughput and eliminating feedback overhead, but efficient mechanisms for coordinating agent formation and stability in highly dynamic networks are yet to be explored. Emergent communication in multi-agent systems can potentially reduce communication costs and processing overhead by allowing agents to learn messages instead of coding/decoding them. This is illustrated by Figure 3(c.f., [21]).

Super-resolution [22] techniques can be used in 6G networks to extract information from radio signals, such as delay, Doppler, and angles, to achieve high position precision in various applications like robotics, healthcare, and augmented reality. However, the complexity of the problem increases with the number of signal sources and non-ideal effects like hardware impairments and interference can affect the performance of conventional approaches, as illustrated by both figures 4 and 5. Therefore, further research is needed to develop new methods and investigate the theoretical limits to optimize the performance and complexity trade-off.

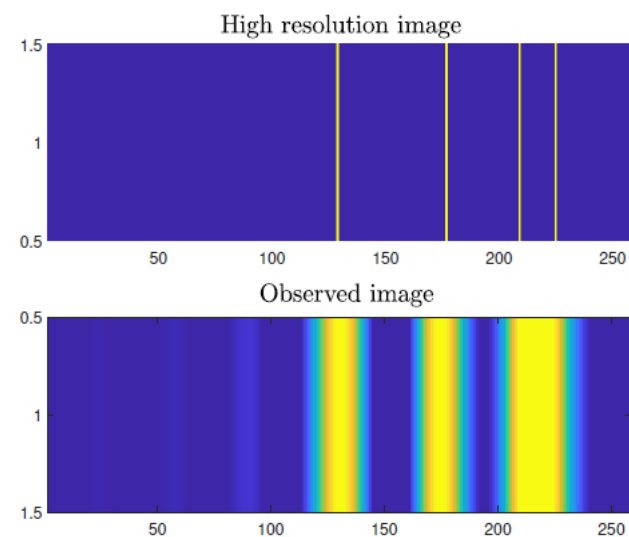


Figure 4. High-resolution picture and observed image comparison [18].

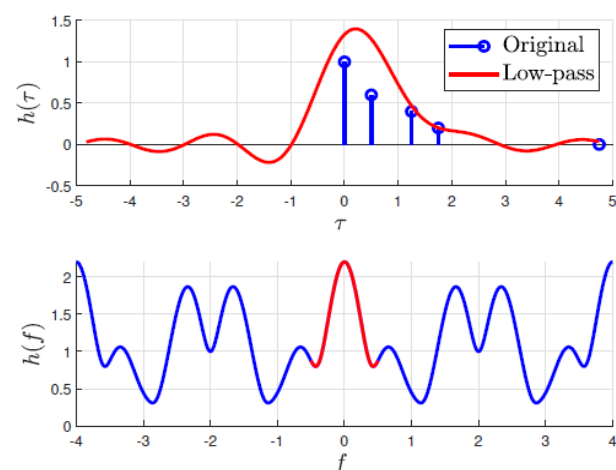


Figure 5. The observed baseband response and the multipath channel [18].

The upcoming 6G network [18] will enable new distributed applications that require extensive computation and high-speed communication with low latency. To ensure a sustainable system, new applications should consider joint optimization of communication and computation, with a focus on energy efficiency. While relying on the physical limits of communication and computation can provide insight into energy costs, practical constraints must also be considered when finding solutions to optimization problems.

6G networks [18] aim to support high mobility for various applications, which poses a challenge for estimating the communication channel due to its time-varying nature. Spreading waveforms, which distribute symbols over time and frequency, have been shown to be resilient to channel variations, but require complex iterative receivers to mitigate interference. Therefore, designing low-complexity receivers for spreading waveforms is a crucial research direction for communication signals in time-varying channels.

In [18], it is suggested that efforts should be made to integrate semantic communication in various use-cases of wireless networks, identify performance bottlenecks, and explore the potential of extending the semantic concept into communication protocol learning. Semantic communication protocols are expected to have task-specific control signaling messages, with acceptable communication, computing, energy consumption, and memory usage overhead, unlike classical medium access control (MAC) protocols.

Integrated sensing and communication [18] can be implemented using different radar architectures, such as monostatic and bistatic, but each presents its own challenges. One challenge with monostatic radar is signal leakage due to self-interference, which can be addressed by antenna separation or analog cancellation. A combination of these solutions can provide additional benefits, such as self-interference suppression by more than 70 dB, while various performance indicators can aid in designing integrated sensing and communication waveforms based on different channel models and application needs.

Large-scale communication networks [18] face challenges such as scalability, adaptivity, and automation, which can be addressed by incorporating AI. However, to better understand how AI operates and make informed decisions, it is important to develop solid mathematical foundations. Several tools, including RMT, decentralized stochastic optimization, and tensor algebra and low-rank tensor decomposition, offer potential approaches to achieve a flexible and reliable understanding of large-scale networks with AI.

The development of 6G networks [18] requires revisiting current coding schemes to ensure they can serve various use cases with different quality-of-service requirements. Joint designs for channel and source coding are being explored to replace conventional coding schemes, with the goal of achieving high data rates, shorter code lengths, and low-complexity decoding mechanisms.

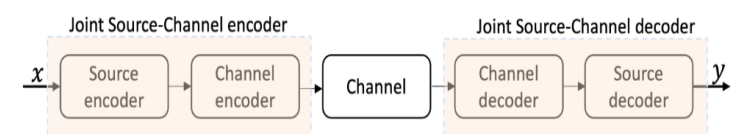


Figure 6. Source and channel coding are combined [18].

However, this approach comes with increased overhead in terms of compression complexity, minimum coding distance optimization, and sophisticated hardware design for supporting Tbps communication, this can be illustrated by figure 6(c.f., [18]).

Queuing theory and information theory [18] are often studied independently, which can lead to suboptimal solutions in scheduling algorithm design. Queuing theory focuses on delay analysis from a queuing perspective, while information theory ignores the bursty nature of data traffic and considers delay-insensitive sources. To address this issue, a cross-layer framework that combines both queuing theory and information theory is needed to jointly adapt to source and PHY layer dynamics.

Non-coherent schemes [18], such as Grassmannian signaling and non-coherent tensor modulation, are being explored as promising approaches to modulate waveforms in wireless networks. These approaches can relieve the pressure imposed by channel state information (CSI) acquisition and show superior performance in large-scale networks. However, before their adoption in 6G networks, concerns such as constellation design and symbols mapping/demapping need to be addressed.

4. CONCLUSION

The current paper emerges a considerable number of open problems.

IE Threshold

This open problem considers the feasibility of obtaining the sophisticated thresholds for IE parameters, to decide the regions of increasability(decreasability) for IE expression as a starting step to the visualization of IE's performance.

Matching Theory

Matching theory is a mathematical approach to solving problems of matching players in two groups. Depending on the players' quota, matching problems can be classified as one-to-one, many-to-one, and many-to-many matching, and can be further categorized as matching with single- or two-sided preferences. The deferred acceptance algorithm is a powerful matching procedure in which players iteratively make proposals that are either accepted or rejected by players of other groups respecting their preferences and quota [23].

Game Theory

Game theory is a mathematical framework used to analyze interactions between rational players, and it is classified as cooperative or noncooperative based on the nature of the interactions. In the context of network topology optimization, cooperative games are more suitable, and there are two main types: coalition formation games and network formation games. Coalition formation games seek optimal coalition size and members, while network formation games consider interdependencies among partitions. Auctioning games, on the other hand, involve bidders and an auctioneer who collects bids to decide who will buy which items at what cost, and they are well-suited for PST-based relaying schemes [24].

Auctioning games

Auctioning games are a type of game theory that involves bidders and an auctioneer who collects bids to determine who will buy which items at what cost. In the context of HMA schemes, auctioning can be used for PST-based relaying schemes where users with strong channels can bid for power or spectrum from users with weak channels. Combinatorial auctions are particularly useful for modeling complex clustering scenarios where users can join multiple clusters as both spectrum sellers and power buyers [17].

Machine Learning (ML)

ML techniques can adapt to the changing wireless environment and human behavior, enabling self-organizing, self-optimizing, and self-healing HMA schemes for beyond 5G. Deep neural networks (DNNs) are a type of ML that can deal with complex and nonlinear problems, such as channel estimation, coding, modulation, and equalization. DNNs can also be used to predict traffic load, mobility patterns, and content interest, making them a powerful tool for designing and evaluating fitness functions in HMA schemes [17].

This paper contributes to validating the credibility of IEF by investigating the four consistency axioms of choice on it. Some potential information-theoretic applications on 6G network were provided, combined with posing some intriguing research questions and open problems. Future road maps of research include the explorations of finding possible solutions to these research questions and the proposed challenging open problems.

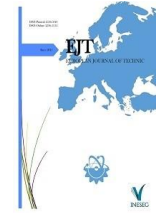
REFERENCES

- [1] I.A.Mageed, and Q. Zhang, "An Information Theoretic Unified Global Theory For a Stable M/G/1 Queue With Potential Maximum Entropy Applications to Energy Works", 2022 Global Energy Conference (GEC). IEEE, 2022.
- [2] S.Lahmiri, and S. Bekiros, "Renyi entropy and mutual information measurement of market expectations and investor fear during the COVID-19 pandemic", *Chaos, Solitons & Fractals* 139: 110084, 2020.
- [3] *Methods in Modern Physics*. 2016 May 31;13(05):1650063.
- [4] "Normal Distribution: Theory And Applications", *Infinite Study*, 2021.
- [5] M.Alkhalailah, et al. "Performance Analysis of Mobile, Edge and Cloud Computing Platforms for Distributed Applications" ,*Mobile Edge Computing*. Springer, Cham, 2021. 21-45.
- [6] J.M.Smith, "Properties and performance modelling of finite buffer M/G/1/K networks", *Computers & Operations Research*. 2011 Apr 1;38(4):740-54.
- [7] N. Kawasaki, "Parametric study of thermal and chemical nonequilibrium nozzle flow," M.S. thesis, Dept. Electron. Eng., OsakaUniv., Osaka, Japan, 1993
- [8] I.A. Mageed, and D.D. Kouvatso, "The Impact of Information Geometry on the Analysis of the Stable M/G/1 Queue Manifold", 2021, *Icores conference*.
- [9] D.D.Kouvatso and S.A.Assi, "On the Analysis of Queues with HeavyTails: A Non-Extensive Maximum Entropy Formalism and a Generalization of the Zipf-Mandelbrot Distribution", 2011,K.A. Hummel et al. (Eds.): *PERFORM 2010 (Haring Festschrift)*, LNCS 6821, IFIP, pp. 99-111.
- [10] W.Rödter , et al, " Power genesis in social networks: An entropy-driven decision support model with conditional data", *Decision Analytics Journal*. 2021 Nov 1;1:100003.
- [11] Q.Sibo, et al. "Online video popularity regression prediction model with multichannel dynamic scheduling based on user behavior" ,*Chinese Journal of Electronics* 30.5 (2021): 876-884.

- [12] M. Karsai, et al, "Bursty human dynamics", Berlin: Springer International Publishing, 2018.
- [13] G.Allon, et al, "Behavioral foundations of queueing systems", The handbook of behavioral operations , 2018,9325: 325-366.
- [14] R.L.Summers, "An Action Principle for Biological Systems", Journal of Physics: Conference Series. Vol. 2090. No. 1. IOP Publishing, 2021.
- [15] I.A.Mageed, and Q. Zhang, "The Rényiian-Tsallisian Formalisms of the Stable M/G/1 Queue with Heavy Tails Entropic Threshold Theorems for the Squared Coefficient of Variation", electronic Journal of Computer Science and Information Technology 9.1 (2023): 7-14.
- [16] D.D.Kouvatsos, I.A.Mageed, V.Anisimov, and N.Limnios, "Non-Extensive Maximum Entropy Formalisms and Inductive Inferences of Stable M/G/1 Queue with Heavy Tails", In"Advanced Trends in Queueing Theory" 2021 Mar (Vol. 2). Sciences by ISTE & J. Wiley.
- [17] C. Abdulkadir, et al, "Topology optimization for 6G networks: A network information-theoretic approach",IEEE vehicular technology magazine 15.4 (2020): 83-92.
- [18] M.Chafii, et al, "Twelve scientific challenges for 6G: Rethinking the foundations of communications theory",IEEE Communications Surveys & Tutorials (2023).
- [19] A. Lazaridou, and M. Baroni, "Emergent multi-agent communication in the deep learning era," arXiv preprint arXiv:2006.02419, 2020.
- [20] D. Simoes, et al, "Multi-agent deep reinforcement learning with emergent communication," in 2019 International Joint Conference on Neural Networks (IJCNN). IEEE, 2019, pp. 1–8.
- [21] A. Dorri, et al, "Multi-agent systems: A survey," IEEE Access, vol. 6, pp. 28 573–28 593, 2018.
- [22] M. Arnold, et al, "Maxray: A raytracing-based integrated sensing and communication framework," in 2022 2nd IEEE International Symposium on Joint Communications & Sensing (JC&S). IEEE, 2022, pp. 1–7.
- [23] D. Gale and L. S. Shapley, "College admissions and the stability of marriage," Amer. Math. Monthly, vol. 69, no. 1, pp. 9–15, 1962. doi:10.2307/2312726.
- [24] G. Iosifidis and I. Koutsopoulos, "Challenges in auction theory driven spectrum management," IEEE Commun. Mag., vol. 49, no. 8, pp.128-135, Aug. 2011. doi: 10.1109/MCOM.2011.5978426.

BIOGRAPHIES

Ismail A Mageed Dr. Ismail A Mageed completed his doctorate in Applied Probability at The University of Bradford, United Kingdom. His current research interests include the unification of queueing theory with information theory and information geometry. His leading research on the relativization of queueing theory and discovering the geodesic equation of motion for transient queues was greatly received by the world research community. Mageed's research on finding the analytic solutions of the longstanding simulative approach of The Pointwise Stationary Fluid Flow Approximation theory (PSFFA) was an exceptional discovery to advance PSFFA theory. Mageed has published numerous papers in many highly reputable journals and conferences. He is also a reviewer to several prestigious journals. Mageed's research has been internationally recognized as being revolutionary by providing several breakthroughs. Dr Mageed has published a chapter in a book of the best eight queueing theorists in the world by ISTE WILEY. He is currently leading several research teams in UK, India, Africa, and Saudi Arabia. He is also a fellow of the Royal Statistical Society (RSS), a member of INTISCC (Austria), IEANG (world council of engineering) and a life member of the Islamic Society of Statistical Sciences.



Research Article

The SMaRt: Design, implementation, and experiment

Ahmet TOP^{1*}, Gökhan GÜNGÖR², Muammer GÖKBULUT³

¹Firat University, Technology Faculty, Electrical Engineering Department, Elazığ, Turkey. (e-mail: atop@firat.edu.tr).

²Karabük University, Engineering Faculty, Mechatronics Engineering, Karabük, Turkey. (e-mail: gokhangungor@karabuk.edu.tr).

³Firat University, Technology Faculty, Electrical Engineering Department, Elazığ, Turkey. (e-mail: mgokbulut@firat.edu.tr).

ARTICLE INFO

Received: Aug., 10. 2023

Revised: Sep., 26. 2023

Accepted: Dec, 25. 2023

Keywords:

Mobile robot control

Motion planning

Image processing

Teaching

Education

Corresponding author: Ahmet TOP

ISSN: 2536-5010 / e-ISSN: 2536-5134

DOI: <https://doi.org/10.36222/ejt.1340895>

ABSTRACT

Mobile robots, for teaching and research activities, have an important place in all education levels, from higher to primary education. They provide a malleable platform to meet research and teaching needs in various engineering and science fields, such as mechanics, electronics, software, biology, and psychology. However, their high cost and the difficulty of learning the user interface and programming tools prevent the widespread use of mobile robots. In this study, we develop an affordable, symmetric, modular, interactive, human-aware, autonomous, and four-wheel-driven mobile robot to boost the quality of education and research. The proposed mobile system is fully customizable with open hardware, software, and data to meet the unique demands and specifications of teaching and research. The developed mobile robot has been successfully operated for education and research purposes.

1. INTRODUCTION

Today, robots are used extensively in industry and provide significant benefits, and their impact becomes more visible as their usage increases in daily life [1]. They have great potential in teaching and research activities [2]. Robotics systems provide learners and researchers with education and research environments allowing them to incorporate ideas within science, technology, engineering, and mathematics (STEM) [3]. The basic concept of robot usage in teaching and research fields is to improve one's soft skills and integrate technical knowledge with practical experience, enhancing interest, engagement, creativity, motivation, and accomplishments in various STEM fields [4]. Such systems have a wide range of usage from entry-level educational institutions [5] to universities [6]; they are also used for non-technical support, for instance, for those with learning disabilities [7].

Many teaching strategies have been studied, and the methods are mainly designed to be cost-effective and time-efficient [8]. The reader is addressed to [9] for more details regarding learning techniques and strategies. There is a growing interest in interactive learning methods, and emerging technologies have been prevalent and made learning easy to apprehend [10]. Although they are more costly than classical learning methods, such systems ensure that students are instructed using state-of-the-art technology, and researchers can have experience with advanced applications [11].

Several robot platforms, such as manipulators and mobile robots, have been developed for educational and research purposes [12,13]. However, price, functionality, compactness, and user-friendly interface are important to embark on the robot selection process before making the final decision. Ceccarelli [14] introduces some low-cost robots and discusses how the robots are appropriately adapted for research and teaching activities. Piepmeyer et al. [15] discuss robotics education principles and how they enhance teaching quality with robots.

The works related to the manipulators are given in [16–19]. Those works related to robot manipulators cover student experiences with kinematic analysis and computer vision. Humanoid robots such as the NAO [20] are used in numerous institutions, allowing one to gain multi-disciplinary skills and develop content with seamless cases. However, they are pricey for teaching and research institutions have a limited allocation. Although their usages are feasible for graduate studies, they are expensive for undergraduate studies considering a class size of more than 30 students. For instance, the NAO AI edition costs \$14990.

Mobile robots offer a cost-effective solution to explore these new learning and research methods [21–23]. There are several mobile robots presented for teaching and research activities. In order to integrate robotics research with undergraduate education, a university team developed a mobile robot called Rusty [24]. E-puck [25], designed at a low cost \$850, is a mobile robot platform operated as a swarm robot [26–28] due to its small size and modular structure. The E-puck

consists of four parts: the main body, the led ring, and two wheels.

The LEGO Mindstorms platforms allowing flexibility to construct various robot configurations are utilized in numerous educational institutions for basic and advanced classes [29–31]. Still, they have hardware and software limitations for research activities. The price of the LEGO Mindstorms Core robot kit is around \$850. Do [32] presents a mobile robot to apply image processing algorithms for multi-objective robot vision projects. For secondary education, the Scribbler robot, designed by Parallax [33], costs \$229. The Scribbler is sufficient for teaching activities for secondary education but has weak hardware equipment to fulfill the undergraduate and graduate-level course requirements.

The Quanser QBot 3 [34] is an autonomous two-wheel drop and cliff sensor, 3-axis gyroscope) and a Red-Green Blue-Depth (RGB-D) camera. This robotic platform is mainly designed for undergraduate teaching and advanced graduate-level research applications such as machine learning and computer vision. The Quanser QBot 3 deploys applications through Simulink, Python, and the Robot Operating System (ROS). Developed by Adept Mobile Robots, Pioneer 3-DX is also one of the mobile robots for research and teaching activities [35]. The microcontroller on the robot has firmware called ARCOS. There also exists its three-dimensional model in the Gazebo simulation environment. There are eight ultrasonic sensors, encoders, and microcontrollers on the robot, and sensors such as laser, microphone, and gyroscope are mounted when required. The robot's production currently has been discontinued.

Another mobile robot developed for educational and research purposes is Turtlebot 2, one of the most popular open-source commercial educational robots [36]. Application for any teaching and research activity is executed with ROS, OpenCV, and Point Cloud Library (PCL). Its list price is about \$1450. Studies by Gritti et al. [37], Wu et al. [38], and Barber et al. [39] are examples of works operated on this robot. The upgraded version of the Turtlebot 2 is named Turtlebot 3 [40]. It has two released versions: Burger and Waffle. The Waffle robot is larger and has extra sensors pushing it more expensive than the Burger. The Burger and the Waffle robot prices are approximately \$660 and \$1660, which are not high-cost robot platforms for higher education and research activities. The Turtlebot platform provides robust open-source software with the ROS environment. It has a modular plate so the user can modify the robot's shape. The hardware mounting kit consists of two dynamixel motors, a Light Detection and Ranging (LIDAR) sensor, a camera, and a single board computer with Intel Joule 570x. Amsters and Slaets [41] investigate how they successfully employ the Turtlebot 3 in graduate-level classes.

The latest version of the TurtleBot, called Turtlebot 4 [42] offers a Raspberry Pi 4 card running ROS 2, a spatial AI stereo camera, a LIDAR, an optical floor tracking sensor, and infrared and slip detection sensors. Turtlebot 4 costs \$1850 for the standard model. All the TurtleBots and the Quanser QBots are powerful open-source platforms for learning and research development, but they are not fully operational when they work in outdoor activities. Such robotic systems mainly employ indoor laboratories, limiting operating real-time outdoor scenarios.

The **Symmetric Modular Robot (SMaRt)** provides services in both structured and unstructured environments. Outdoor robot experiences are significant to the researchers working in the field of robotics to handle many challenges regarding different working environments. The developed robot allows

the implementation of advanced applications such as path-planning, mapping, and real-time image processing. For example, one can apply and test any algorithm to the SMaRt under different weather conditions. Moreover, the robot works in the military, service, and health research fields due to its durable, symmetric, and shock-reducing spring structure.

This paper presents the SMaRt design and its capabilities for both teaching and research activities. The developed robot is an affordable, modular, interactive, human-aware, autonomous, and four-wheel-driven system that is worked in structured and unstructured environments (see Figure 1), and it only costs \$ 1521\$. Thus, the students and researchers can operate many industrial and real-time scenarios with the developed robot; therefore, they can quickly adapt such experiences to real-time work and improve their debugging skills experimentally.

2. THE SMaRt MECHANICAL DESIGN

The mechanical design procedure of a mobile robot may not seem to be the central focus of the recent robotics work trend; however, it impacts the robot's reliability, durability, aesthetics, robustness, and safety. Adjusting the robot's weight-power ratio for energy efficiency with a low cost is one of the primary considerations of the mechanical design procedure; therefore, an ideal balance between robot dimensions and motor power is required to achieve a good design. Moreover, during the design procedure, it is important to consider how the robot will move, whether it will work around people, what kind of tasks it will perform, and how it will evaluate the environment.

In this study, the mechanical and electronic components of the mobile robot are positioned on the static platform as balanced as possible. There are two essential parameters to be considered in terms of weight properties during the robot design: the total mass/the weight per wheel and the center of the total mass. Each wheel is treated as the vertex of a polygon, and a support polygon is established with four wheels. Moreover, having a center of mass as far as away from the edges of the support polygon makes the system more stable in tipping over. Therefore, the components are placed where the center points further away from the edges, and the mass is concentrated near the center. This study uses the four-wheel-driven system to increase the support polygon's size, improving the robot's maneuverability and enacting its usage in indoor and outdoor applications. The SMaRt has wheels with wide, compliant tires suitable for traversal of mixed terrain with minor obstacles.

Four main components shape the backbone of the system: mechanical parts, a static platform, wheels, and motor holders. The robot's weight also plays a crucial role in the robot's mobility. It is a fact that the torque required to drive the robot will exponentially rise when an increase in the robot's weight is required. Lightweight metals are used to lighten the weight of the mechanical platform. Therefore, the design of the mobile robot with controllers and power supply is minimized for weight reduction to increase their moving abilities. The platform is constructed of 2-mm thick solid sheet metal, and holes are drilled to reduce the system's overall weight, allow ventilation, and include other optional add-ons. The material used for the chassis is determined to meet the structural needs of the potential robot operations. The total weight of the robot prototype is 9396 grams. The robot calculations during the design procedure are made with 10 kg weight under 10-degree road slope conditions. The actuator section gives details

regarding the required power to drive the robot. The mobile robot's mechanical design and its off-the-shelf component placements are shown in Figs. 1a and 1b, respectively.



Figure 1. (a) Views of the SMaRt from different angles and (b) the off-the-shelf 3D model rendered in SketchUp.

The wheels are inflatable and have a diameter of 21 cm and a width of 6 cm, providing the robot system with 5.5 cm ground clearance distancing from the platform to the wheel. The chassis length, height, and width are 40 cm, 10 cm, and 22.2 cm, respectively. The platform also has an offset of 3.5 cm from the robot chassis in both the up and down directions due to the wheel size being longer than the platform size in terms of height to protect against possible chassis crushing. Moreover, the robot ground clearance dimensions are kept similar to either side of the robot to construct the robot symmetric. So, the robot can sense the turning upside down with an Inertial Measurement Unit (IMU) and continue to work due to its symmetric dimensions even when the flipping over occurs.

The robot fix platform is easily attached and removed from the motor shafts with screws. Sensors and removable attachments are placed on the front. On the back side of the robot, there are connectors such as micro-universal serial bus (micro-USB), USB, and High-Definition Multimedia Interface (HDMI). Moreover, light-emitting diodes (LEDs), buttons, battery indicator, Light Dependent Resistor (LDR) module, and fan are mounted to the back panel with the robot's external electrical connections (see Fig. 1a). As seen in Fig. 2, the motor and motor holders are fixed to the body with nuts. The springs, located between the body and the engine holder in the lower and upper parts, act as shock absorbers and reduce external disturbances. Therefore, the suspension system allows the robot to work in challenging terrain operations. Since the

platform provides modularity, other add-ons are utilized for changing the driving system configuration if needed.

Moreover, mechanical power generated from the actuators is supervised according to a regulation defining robots having less than 80W mechanical power as safe since the developed robot is used for indoor and outdoor applications without being separated by a fence. The SMaRt, with a motor power of less than 80W, can be operated without installing a fence; therefore, it allows the robot to interact with humans, leading to the utilization of the SMaRt in many fields.



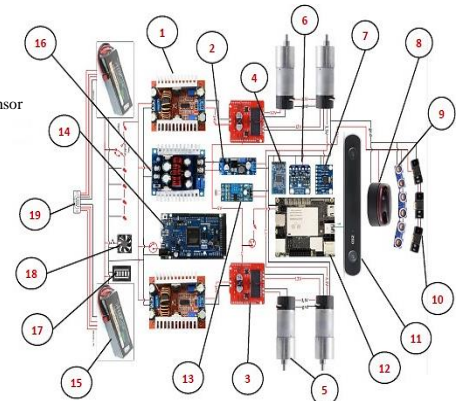
Figure 2. The drive system is used in the mobile platform.

3. THE SMaRt HARDWARE FEATURES

This paper considers a fully open hardware approach to improving the quality of education and research, which sustains innovation and enables the system to be used more efficiently. In addition, open-source hardware can significantly reduce research and education costs and contribute to collaborative science. The hardware architecture of SMaRt is shown in Fig. 3.

- 1: Boost converter
- 2: 3.3 V Buck converter
- 3: Motor driver
- 4: Bluetooth module
- 5: Actuator
- 6: Humidity and temperature sensor
- 7: IMU
- 8: Lidar
- 9: Ultrasonic sensor
- 10: Infrared sensor
- 11: Camera
- 12: LattePanda
- 13: LDR Module
- 14: Arduino Due
- 15: Battery
- 16: 5 V Buck converter
- 17: Battery display
- 18: Fan
- 19: Battery charger connector

Figure 3. Hardware architecture of the SMaRt.



Multiple sensor devices can be used separately or together depending on the robot's operations, allowing many different robot tasks. The robot is modular, so the sensors can be placed on the robot at any time and easily included on the circuit board (see Fig. 4). The hardware architecture will be described in three parts: control boards, motors and drivers, and sensors.

1) Control Boards: This study uses two development boards, Arduino Due and LattePanda. While the Arduino controls the motor and peripherals as a central controller, the LattePanda is used as an auxiliary controller for the front camera, LIDAR, and sensors.

The main reason for using the Arduino Due is that the Arduino architecture is compatible with the Arduino's opensource programming interface; therefore, we can build different scenarios and operate them at once. This low-cost Arduino board has an Atmel SAM3x8E Arm Cortex-M3 central processing unit built on easy-to-use open hardware [43]. It relies on a powerful 84 Mhz and 32-bit ARM-type core

microcontroller. It has more inputs and outputs than other usual Arduino boards, and it is faster and has more analog and communication pins. There are 54 digital input, and output pins, 12 of these pins provide pulse width modulation (PWM) output, 12 analog input pins, and 2 analog output pins. Moreover, the board can store enough data in the internal flash memory, around 512 KB providing more data allocation to operate complex tasks [44].

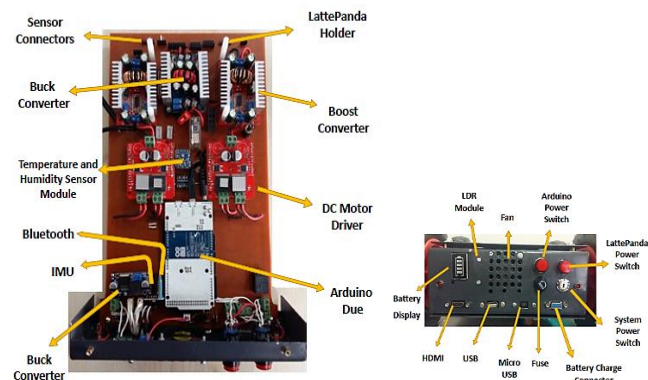


Figure 4. The SMaRt circuit board and its back view.

The developed robot has a wide range of sensor devices for interacting with the physical world. To process the sensors' data, the LattePanda development board [45] is utilized for the SMaRt. The LattePanda is a development board capable of running Windows 10 and Linux. We may connect USB supported devices, such as LIDAR, or a camera, to USB 3.0 and 2.0 ports. It is not only a low-cost regular Windows computer but also has a built-in Arduino that connects actuators and sensors if needed. The LattePanda has plug-and-play headers and general-purpose input/output (GPIO) pins that support standard 5V sensors and actuators, enabling the robot to interact with the working environment. Various information from the environment required is obtained instantly with the HDMI input or the display port, and the data is transferred to the secured digital (SD) card. As shown in Fig. 4, we also put a micro USB at the back side of the SMaRt to reprogram the Arduino card without removing it from the system. The LattePanda, connected to the system through HDMI or USB for motion vision, is an optional card exchanged with other cards such as Raspberry Pi 4 [46] and NVIDIA Nano [47]. The general circuit board and its back views are shown in Fig. 4.

2) Motors and Drivers: The SMaRt is constructed for various purposes, functions, and working environments, so there are several elements to contemplate when selecting a proper actuator. The SMaRt uses four 12V brushed direct current (DC) motors to provide its mobility. For details, refer to [48]. Determining the type of actuator required for convenient functionality is essential. Brushed DC motors have been operated in many fields. They are inexpensive and deliver continuous power and good torque for extended research and education purposes.

The physical size and weight of the actuator itself are also essential to see if it fits in the intended use and if the combined weight of the actuator and the static platform is appropriate. The actuators are chosen as much as lighter, and each weight is 210 grams, and they may not cause the system to fail under the actuator weight. The size of the actuator (37Dx72.5L mm) suits the mounting space on the system properly. It is also crucial that the selected actuator is strong enough to fulfill the robot's

working requirements. It provides enough power to move the robot and the robot's load in the operating environment. Its maximum output power and stall torque at 12V is 6W and 45 kg.cm, respectively. The worst-case scenarios are that the robot's load becomes overly heavy and the working condition is challenging to navigate, which are also considered during the actuator selection. The maximum weight of the system is presumed to be 10 kg. The criterion of climbing a 10-degree slope with an acceleration of 0.1 m/s is considered.

The DC motors have a 131.25:1 metal gearbox and an integrated incremental optic encoder that provides a resolution of 64 counts per revolution of the motor shaft. The motors are driven separately by the Sparkfun Monster motor driver modules with a dual output control ability [49]. The modules have 2 VN12SP30-E H-bridge integrated circuits and require a maximum of 16V, a continuous current draw of 14A, and a maximum PWM frequency 20kHz for each dual motor control performance. The drivers also have automatic shutdown in case of low voltage, over-voltage, overheating, and a current sensing feature.

3) Sensors: This section introduces the sensor selections and their placements. The SMaRt includes ultrasonic sensors (USs), infrared sensors (IRs), a stereo camera, a LIDAR, IMU, a humidity and temperature sensor, and a LDR. There are several factors in choosing convenient sensors for the SMaRt, such as application type, working environment, power consumption, and costs.

The SMaRt has three analog Sharp IRs [50] measuring distances from the obstacles and is used as an on-off switch to avoid obstacles. They are lower-cost sensors and offer faster response times than the US sensors, i.e., 38_10ms. However, infrared sensors have some limitations, like the inability to use them in sunlight, making it difficult for outdoor or dark indoor applications. Three affordable Hc-sr04 digital US sensors [51] installed on the robot are utilized to execute real-time obstacle avoidance. The robot can continually detect surroundings, avoid obstacles, and move toward the desired location. The US sensor, which works with 5V and draws a 15mA current, can measure distances up to 4 meters. However, US sensor measurement accuracy is sensitive to temperature and object shape changes. For example, US performance is ineffective on soft, curved, and thin object surfaces where there is low reflection. This study uses both US and IR sensors to decrease each sensor's sensitivity changing with the working environment.

The ambient temperature, humidity, and air pressure information are obtained from the pressure, temperature, and humidity sensor module connected to the Arduino. The robot's interior temperature is also measured with this sensor. So, the fan on the rear panel is activated based on the internal temperature where cooling is required. In addition, the ambient light intensity is measured through the LDR module on the rear panel. Thus, the environment is illuminated with the LEDs on the front and back of the robot if needed.

Moreover, the SMaRt requires an undersized, lightweight, compatible, and high-quality camera to identify objects, avoid obstacles safely, and find the path without human guidance through a large-scale 3D map of the working environment. The ZED camera [52] allows the SMaRt to provide an extended range of computer vision abilities for education and research purposes. The robot can sense the surroundings in 3D for indoor and outdoor usage up to 20m. It has a high field of view, i.e., 110°(H)x70°(V)x120°(D) at max, and is compatible with

Linux and Windows. However, environmental and lighting conditions can affect camera vision performance; therefore, accurate 3D measurement data is required over short to long ranges.

LIDAR technology can enable obstacle detection, avoidance, and safe navigation through various challenging terrain operations. This study uses a LIDAR designed by SLAMTEC [53]. It determines which obstacles are nearby and how far away they are. Not only do we detect and position objects, but we also identify what they are. We can even use it to predict how objects behave and adjust the SMaRt driving accordingly. However, the LIDAR system is an expensive sensor. It has moving parts, making it easier to break or malfunction and thus more costly to maintain. It also has difficulties in bad weather conditions such as heavy rain, snow, and fog.

For system localization and control purposes, such as inquiring about the current mobile platform position and orientation, an IMU module is also mounted on the system. This sensor adds cost-effective, practical, and ease-of-use solutions to the SMaRt. However, the accuracy of such sensors is affected due to the noise and drifts. It is noted that their performances are sensitive and unstable to changing working conditions.

The reason for installing the sensors mentioned above on the system is to overcome the individual sensor limitations through sensor fusion algorithms if required. Therefore, the students and researchers can build a variety of sensor fusion algorithms. Each sensor can be combined with other sensory data to provide more reliable required data in indoor and outdoor applications related to localization, mapping, path planning, and obstacle avoidance.

4. THE SMaRt SOFTWARE SPECIFICATION

As mentioned in the hardware section, the developed platform has two controllers: the Arduino Due and LattePanda. The main aim of this section is to present the software architectures used to program those control boards. This study uses the Arduino Integrated Development Environment (IDE) to manage the wheel control. The Arduino is used not only for the wheel but also for the IMU, LDR, pressure, temperature and humidity module, Bluetooth module, LEDs, and fan. Any control algorithm, either basic or advanced, can be written in the IDE and uploaded to the Arduino board quickly. The main reason for choosing the Arduino IDE is that it offers userfriendly and free-of-charge software; therefore, students and researchers can build, modify, and enhance their codes freely and operate many different operations ranging from building low-cost scientific instruments to advance robotics.

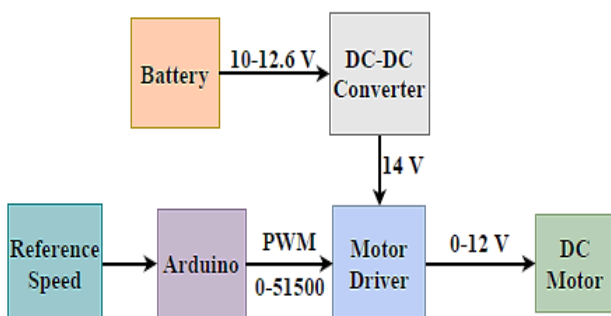


Figure 5. The power management scheme of the SMaRt.

For instance, teachers can quickly build a code to prove physics principles with various robotics applications for educational purposes. At the same time, because of its flexibility, researchers can apply advanced algorithms related to engineering and science fields and exhibit their projects on the SMaRt. One can also share ideas online with Arduino's open community and can improve their programming skills. If any problem occurs in the Arduino, one can easily communicate with the online forums and find answers freely. With advanced integrated sensors such as the camera and

LIDAR, the SMaRt can collect data in real-time to make informed decisions through the LattePanda. They can provide positional information that allows the SMaRt to self-localize and react to change. However, processing such data with any programming language and sending them from the LattePanda to the Arduino to control the wheels is not as easy as it looks. To handle this challenge, we make a serial connection with Arduino and LattePanda through the universal asynchronous receiver transmitter (UART) protocol.

The SMaRt allows the usage of many popular programming languages, such as Python and VB.Net, with its strong controller boards. For example, with its libraries, Python can detect obstacles with the ZED camera through the LattePanda. The instant robot information is transferred to the Arduino board to adjust the robot's positioning. Since LattePanda is compatible with Linux, the ROS environment can also be installed and allow to execution of many applications such as Simultaneous localization and mapping (SLAM) and path planning. Moreover, the developed robot supports MIT App Inventor's applications, allowing one to build fully functional applications for smartphones and tablets to control the robot.

5. THE SMaRt POWER SYSTEM

This section gives an overview of the robot's energy management. We first show how to generate motor power to operate the robot; then, we examine the hardware's energy consumption to uncover the system's required battery power.

5.1. Motor Power Management

This study uses a PWM signal to change the motors' speeds. The motor management scheme is shown in Fig. 5. PWM is an efficient and easy method to control the speed and manage motor power. It drives the motor with the desired speed through a series of ON-OFF pulses and the duty cycle alteration. The SMaRt has four 12V DC motors. Two Sparkfun Monster motor shields are used to manage the control signal of these motors, each with a double output. The PWM signals are sent to the motor drivers through the Arduino card to adjust the desired motor speed. Each of the motors' working ranges is between 0 and 12V, and the motor speed varies linearly with the voltage. The PWM signals typically work with a duty period ranging from 0 to 255 and are obtained from a microprocessor with 8-bit PWM resolution. To raise the motors' control precision, we adjust the PWM resolution to 16 bits, which pushes the maximum PWM value to 65535 from 255. So, the robot will not move with a 0 PWM value given to the driver fed with a 12V constant. When the PWM value of 65535 is assigned, the driver output becomes 12V, and the motor runs with the maximum motor speed.

The continuity of the robot's performance is also essential during the task. The robot needs to maintain its voltage

throughout the operation to obtain the same mechanical power while running. However, as the motors are powered by a 3S lipo battery, not a constant voltage source, and the battery powering the robot is depleted, the required motor voltage applied to the motors will drop over time, degrading the robot's motion performance. Therefore, the lower voltage provides less power and slower motor speeds. Moreover, the battery's voltage values, which have a nominal value of 11.1V, are 12.6V and 10V at full charge and critical level, respectively. So obtaining stable results with varying motor voltages is challenging.

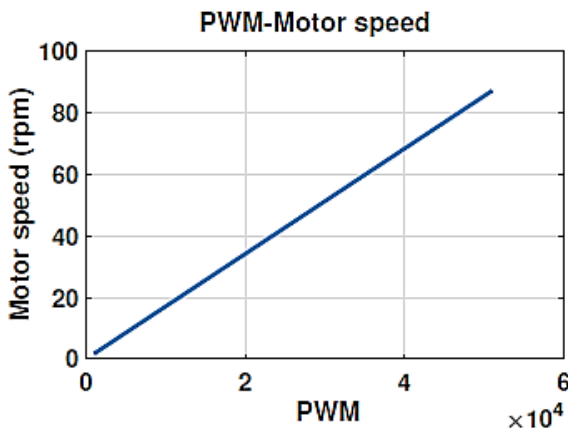


Figure 6. A relationship between the motor speed and PWM value.

DC-DC boost converters are used between the battery and the motor driver to stabilize the voltage applied to the motors, as seen in Fig. 5. The converter outputs are set to deliver a voltage of 14 V as they must be larger than the input. So the driver input remains constant at 14 V even if the battery voltage changes between 12.6 and 10 V. Thus, the maximum speed capability of the motors will not change over time. When the PWM value signaled from Arduino is limited between 0 and 65535, the corresponding applied voltage to the motors will be 0 and 14V, respectively. However, the motors run at a maximum of 12V. So we readjust the maximum PWM value to 51500 to decrease the maximum voltage to 12V. Since the PWM values are important to adjust the motor speed, we present a relationship between the motor speed and the motor PWM values, which is demonstrated in Fig. 6. The results show a straight line relationship between the motor speed and the PWM values, and the maximum speed of 88 rpm is achieved with the value of 51500 at 12V. The motor speed is calculated as follows:

$$w_i = \frac{T w_{max}}{T_{max}} \quad (1)$$

where w_i denotes the i -th instant motor speed, T is a given PWM value to adjust the speed, w_{max} means a maximum motor speed capacity, and T_{max} represents a maximum PWM value. From the experimental results presented in Fig. 7, it is observed that the measured motor speed matches the calculated motor speed. Moreover, it is seen that the relationship between the motor speed and period has an exponential decay characteristic, and the motor speed reaches its maximum speed at a period of 0.2 ms. As seen in Fig. 7, the motor speed falls exponentially over time before reaching a plateau at 1 ms.

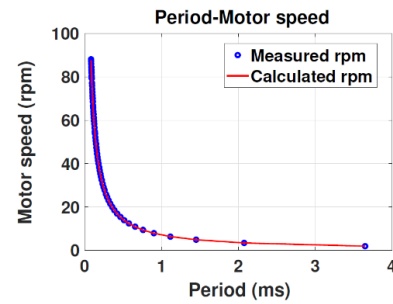


Figure 7. A relationship between the motor speed and motor period.

5.2. System Power Management

This section introduces the power management and power requirements of the SMArT. The robot power supply impacts the robot's performance, and any failure occurring in the power supply may prevent the completion of the task successfully. Therefore, it is necessary to calculate the required power to move the robot with a battery in unstructured and structured environments. The robot's power consumption has been calculated by considering the amount of each device's power consumption. When the system is activated without the motors, LattePanda, camera, IR, and US sensors, the electronic circuits draw a current of 0.23A. This provides the robot with approximately 26 hours of operation when the application is executed on the Arduino board with electronic circuits. When the robot is operated manually with the PWM value of 26000 in the absence of the LattePanda, camera, and object detection sensors in the laboratory environment where it is a flat floor without slope, it draws an instantaneous current of 1.05A. The robot's power consumption varies depending on the task's difficulty, changing the battery's service life. Moreover, we calculate the robot weight for two mounted batteries with 3S 6Ah during the design procedure, so one can install an extra battery to double the robot's operation time if required.

6. EXPERIMENTS AND RESULTS

This section presents the performances of the SMArT system and its components. The experimental results are introduced in three parts. The first part of the experiments is conducted to show the IR and US sensors' performances when they are operated in indoor and outdoor environments. Then, the second part of the experiments is realized to reveal the basic functionality of the motor control performances. The robot's suitability for computer vision is examined at the end of this section.

6.1. Performance results of the IR and US sensors

The performance of the IR and US proximity sensors are demonstrated in Figs. 8 and 9 for indoor working environments with bright and dark light conditions. Fig. 8 shows the performance results of the percentage measurement error for each surface color of the obstacle using the IR and US sensors. Fig. 8 demonstrates that the IR sensor has better overall accuracy than the US sensor despite changing surface colors. The results show that the US sensor outperforms the IR sensor when measuring the obstacle distance in close proximity. However, the measurement error increases when the distance between the obstacle and the robot is more than 300 mm. The minimum error for the IR sensor is achieved with the red color obstacle surface. However, it is noted that the percentage error

for the IR sensor is higher for the transparent surface obstacle, as shown in Fig. 8.

We also examine the impact of the changing environmental condition on the sensors' performances. Fig. 9 shows the sensors' performances in the dark indoor environment. The IR sensor outperforms the US sensor in case of measuring the obstacles in close proximity. The US sensor has a better performance when it is operated in a dark indoor working environment. Compared to long-distance measurement, the US sensor performs poorly when the obstacle is brought to a 300 mm distance. The IR sensor can detect an obstacle in the range of 300 to 1200 mm.

The sensors' performances are also examined in an outdoor environment, and the results are shown in Fig. 10. It is seen that the US sensor outperforms the IR sensor. The IR sensors can measure the obstacle distance at only 300 mm with almost 50 percent measurement error. However, the US sensor can measure distances ranging from 300 mm to 1500 mm except for the transparent surface at 300 mm.

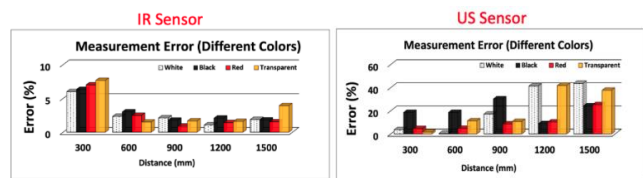


Figure 8. IR and US sensors' measurement errors in percentage with different surface colors in a bright indoor environment.

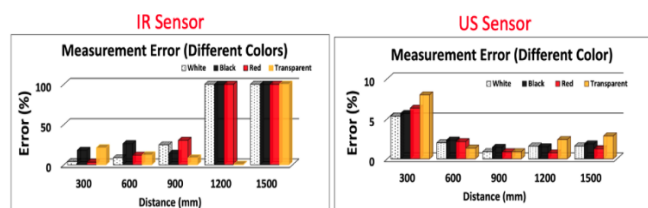


Figure 9. IR and US sensors measurement errors with different surface colors in a dark indoor environment.



Figure 10. IR and US sensors measurement errors with different surface colors in an outdoor working environment.

6.2. Performance results of the motor speed control

The experiments are performed at different motor speed levels for a closed loop case. The motor is assigned to the PWM generator, and the error is observed using the encoder. For the closed-loop case, we choose a PID controller to handle the motor speed error and show the closed-loop controller performance over the non-controller case. The motor control performances are demonstrated in Figs. 11-13. Fig. 11 shows the motor performance without a controller. From Fig. 11, it is seen that the motor speed does not converge to reference motor speed over time at different speeds. The motor control performance in tracking the reference is low at a slow pace. For the closed-loop scheme, we choose PID controller parameters after several trials to make the motor movement more smooth. Figs. 12 and 13 show the closed-loop motor performances with different controller parameters. The results shown in Fig. 12 is

obtained from choosing $k_p = 0:1$, $k_d = 0:1$, and $k_i = 0:01$. Keeping the derivative and integral control parameters the same and decreasing the proportional control parameter to 0.05, we have a reduced steady-state error, thus making the system performance more stable, as shown in Fig. 13. In addition, considering different environmental conditions, it may be necessary to change the parameters since dynamic equations are not used.

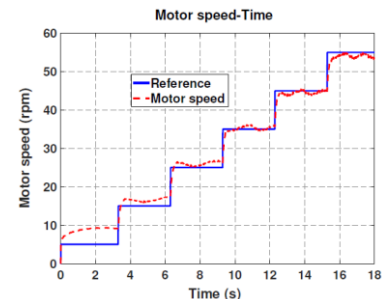


Figure 11. The motor control performances at different speed references without a controller.

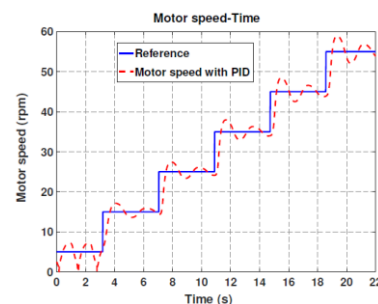


Figure 12. The motor control performances at different speed references with PID controller. The parameter coefficients are $k_p = 0:1$, $k_d = 0:1$, and $k_i = 0:01$.

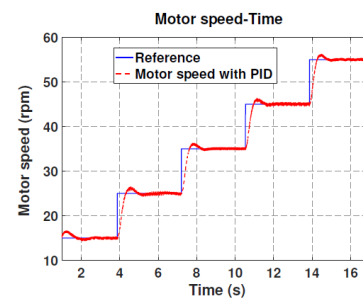


Figure 13. The motor control performances at different speed references. The parameter coefficients are $k_p = 0:05$, $k_d = 0:1$, and $k_i = 0:01$.

6.3. Performance results of the system motion

This section shows a simple motion describing how the robot approaches a traffic light with a PID controller. We show the motor speed control performance during the operation and the applicability of the SMARt's camera. We also designed an Android app through the MIT App Inventor to set the desired robot position, speed, and PID controller gains. We propose a camera-based algorithm for locating the traffic light and detecting the light colour during the performance.

The algorithm's first part explores the You only look once (YOLO) architecture [54] for real-time traffic light detection. The SMARt first need to locate the traffic light correctly and leave out the other objects around the working environment. So we can eliminate things lighting the green and red lights except for the traffic light. The YOLOv4 algorithm is used to predict

the traffic light probability and simultaneously bound it with a box.

After detecting the traffic light location, the instant camera images are loaded to identify green and red traffic lights through classic image processing to get the RGB image values as a second part of the algorithm. The images in RGB colour space are then converted to hue, saturation, and value (HSV) colour space, and a mask is applied to detect the candidate colours. The light candidates are determined based on colour intensity on the obtained HSV colour space image. The camera images during the performance and the results after applying the masks are shown in Fig. 14.

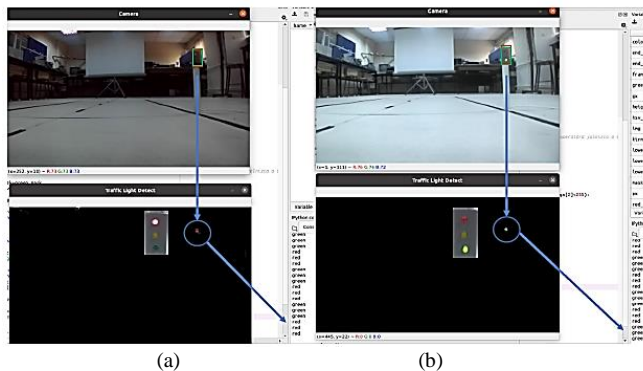


Figure 14. Traffic light detection and control (a) sensing the red traffic light and (b) sensing the green traffic light.

During the performance, we set the system parameters such as desired robot position, speed, and controller parameters through the Android application, designed for convenient usage. The proposed application with MIT App Inventor consists of three components: the main screen, the manual control screen, and the automatic control screen. The main screen is where the actions of the control preference selection, such as manual control and automatic control and the Bluetooth connection between the mobile robot and Android phone occur.

The manual control screen is employed to adjust the desired robot movement and speed by hand when the robot is operated manually for calibration or manual positioning purposes. In the case of the need for automatic motion control, the desired robot position, speed data, and control parameters are inserted into the mobile robot processor through the automatic control screen. The screen views of the mobile app are shown in Fig. 15. As shown in Fig. 15b, the user can easily insert the desired parameters and operate the robot through the app screen. For details regarding the interactive Android application, the reader is referred to [55].

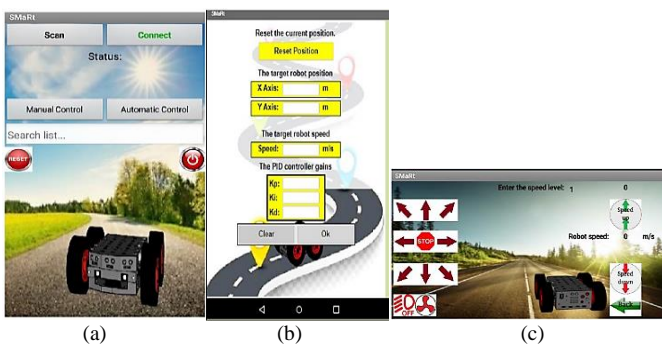


Figure 15. The SMaRt's mobile application screen views are designed with the MIT app inventor: (a) the main screen view, (b) the automatic control screen view, and (c) the manual screen view.

The predefined path is shown in Fig. 16. The motion planning scenario has three phases. The first is that the robot approaches the traffic light with a green light. Then, the robot continues to move toward the traffic light. The robot decreases speed and stops when the camera detects the red light. In the third phase, the robot starts to move forward when the red light turns green.

The motors' speed performances during the motion planning are given in Fig. 17. The robot moves through the path at 25 rpm for four seconds of motion. When it faces the traffic light at the red light, the motors stop for five seconds. When the traffic light turns green again, the motors start working at 25 rpm. After several trials, the control design parameters are chosen, and the results show that the reference speed tracking is achieved with the developed PID controller. The results reveal that each motor speed of the SMaRt converges to the desired speed during the motion performance. In addition, it may be difficult to detect the traffic light in dark weather conditions. Moreover, since the connection is provided via Bluetooth, the user must be closer than ten meters to the robot.

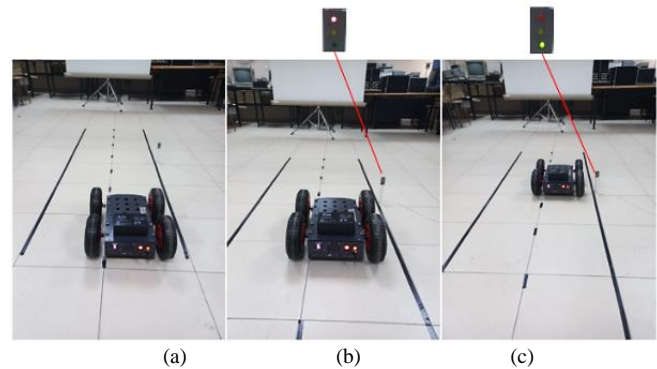


Figure 16. The SMaRt is on a pre-defined path: (a) moving through the path, (b) stopping at the red light, (c) moving at the green light and passing the traffic light.

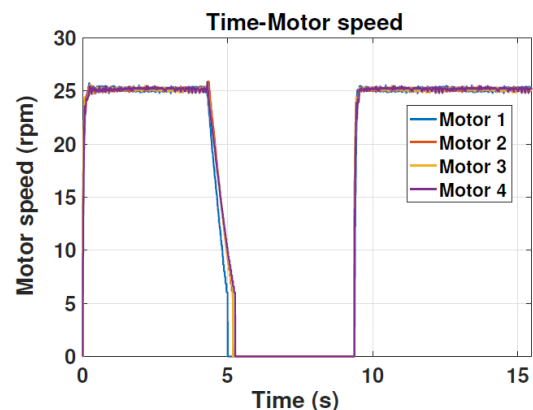


Figure 17. The SMaRt's motor speed performance with the PID controller during the motion planning.

7. CONCLUSION

This article presents SMaRt's features and capabilities. The SMaRt is operated in many educational fields, especially in engineering, with its advantages, such as reprogramming, remote control, and modular design. Due to its durable, symmetric, and shock-reducing spring structure, the robot works in the military, service, and health fields. Any required information about the working environment is obtained from the sensors so that the robot can complete the operation

smoothly. The developed robot allows the realization of advanced applications such as path-planning, mapping, and real-time image processing. We can easily reprogram the robot without disassembling any parts because the Arduino's programming port for the motor control and LattePanda's USB and HDMI ports for image processing or other related algorithms are conveniently placed on the robot. The battery charging slot is also located at the back, so it is charged without dismantling the platform. To increase the robot's mobility, the SMArT allows quickly exchanging the wheels type for the Mechanum and integrating the pallet system if required. The robot circuit allows an extra battery connection in parallel, which provides a longer robot performance. For future work, we will generate the robot's kinematic and dynamic models and apply advanced control algorithms for the system positioning. Moreover, path-planning algorithms will be performed so the robot can work autonomously in real time.

ACKNOWLEDGEMENT

This study is supported by Firat University Scientific Research Projects Unit (FUBAP) with the project number TEKF.19.07. So the authors would like to express their gratitude to the FUBAP for their financial support.

REFERENCES

- [1] Calo R. *The case for a federal robotics commission*. Available at SSRN 2529151, 2014.
- [2] Felicia A, Sharif S. A review on educational robotics as assistive tools for learning mathematics and science. *Int. J. Comput. Sci. Trends Technol*, vol. 2, no. 2, pp. 62–84, 2014.
- [3] Khine, M. S., Khine, M. S., & Ohmer. *Robotics in STEM Education*. Springer, 2017.
- [4] Merdan, M, Lepuschitz, W, Koppensteiner, G, & Balogh R. Balogh, *Robotics in education: Research and practices for robotics in STEM education*, vol. 457. Springer, 2016.
- [5] Eguchi, A. Robocup junior for promoting stem education, 21st-century skills, and technological advancement through robotics competition. *Robotics and Autonomous Systems*, vol. 75, pp. 692–699, 2016.
- [6] Curto B, Moreno V. Robotics in education. *Journal of Intelligent & Robotic Systems*, vol. 81, no. 1, p. 3, 2016.
- [7] Lindsay S, and Hounsell KG. Adapting a robotics program to enhance participation and interest in stem among children with disabilities: a pilot study. *Disability and Rehabilitation: Assistive Technology*, vol. 12, no. 7, pp. 694–704, 2017.
- [8] Rivera JH. Science-based laboratory comprehension: an examination of effective practices within traditional, online and blended learning environments. *Open Learning: The Journal of Open, Distance and e-Learning*, vol. 31, no. 3, pp. 209–218, 2016.
- [9] Felder RM, Soloman BA et al. *Learning styles and strategies*. 2000
- [10] Nguyen, K. A., DeMonbrun, R. M., Borrego, M. J., Prince, M. J., Husman, J., Finelli, C. J., ... & Waters, C. The variation of nontraditional teaching methods across 17 undergraduate engineering classrooms. in 2017 ASEE Annual Conference & Exposition, 2017.
- [11] Hernandez-de-Menendez, M., Escobar D'iaz, C., & Morales-Menendez, R. Technologies for the future of learning: state of the art. *International Journal on Interactive Design and Manufacturing (IJIDeM)*, vol. 14, no. 2, pp. 683–695, 2020.
- [12] Spolaor, N., & Benitti, F. B. V. Robotics applications grounded in learning theories on tertiary education: A systematic review. *Computers & Education*, vol. 112, pp. 97–107, 2017.
- [13] Giang, C., Piatti, A., & Mondada, F. Heuristics for the development and evaluation of educational robotics systems. *IEEE Transactions on Education*, vol. 62, no. 4, pp. 278–287, 2019.
- [14] Ceccarelli M. Robotic teachers' assistants. *IEEE Robotics & Automation Magazine*, vol. 10, no. 3, pp. 37–45, 2003.
- [15] Piepmeier, J. A., Bishop, B. E., & Knowles, K. A. Modern robotics engineering instruction. *IEEE Robotics & Automation Magazine*, vol. 10, no. 2, pp. 33–37, 2003.
- [16] Robinette M.F, Manseur R. Robot-draw, an internet-based visualization tool for robotics education. *IEEE Transactions on Education*, vol. 44, no. 1, pp. 29–34, 2001.
- [17] Nagai K. Learning while doing: practical robotics education. *IEEE Robotics & Automation Magazine*, vol. 8, no. 2, pp. 39–43, 2001.
- [18] Wu, M., She, J. H., Zeng, G. X., & Ohyama, Y. Internet-based teaching and experiment system for control engineering course. *IEEE Transactions on Industrial Electronics*, vol. 55, no. 6, pp. 2386–2396, 2008.
- [19] Gardun˜o-Aparicio, M., Rodr'iguez-Res'endiz, J., Macias-Bobadilla, G., & Thenozhi, S. A multidisciplinary industrial robot approach for teaching mechatronics-related courses. *IEEE Transactions on Education*, vol. 61, no. 1, pp. 55–62, 2017.
- [20] Nao the humanoid and programmable robot. [Online]. Website <https://www.softbankrobotics.com/emea/en/nao>
- [21] Giovannangeli C, and Gaussier P. Interactive teaching for visionbased mobile robots: A sensory-motor approach. *IEEE Transactions on Systems, Man, and Cybernetics-Part A: Systems and Humans*, vol. 40, no. 1, pp. 13–28, 2009.
- [22] Jojoa, E. M. J., Bravo, E. C., & Cortes, E.B.B. Tool for experimenting with concepts of mobile robotics as applied to children's education. *IEEE Transactions on Education*, vol. 53, DOI 10.1109/TE.2009.2024689, no. 1, pp. 88–95, 2010.
- [23] Arvin, F., Espinosa, J., Bird, B., West, A., Watson, S., & Lennox, B. Mona: an affordable open-source mobile robot for education and research. *Journal of Intelligent & Robotic Systems*, vol. 94, no. 3, pp. 761–775, 2019.
- [24] Maxwell B.A, and Meeden L.A. Integrating robotics research with undergraduate education. *IEEE Intelligent systems and their applications*, vol. 15, no. 6, pp. 22–27, 2000.
- [25] Mondada, F., Bonani, M., Raemy, X., Pugh, J., Cianci, C., Klapotcz, A., ... & Martinoli, A. The epuck, a robot designed for education in engineering. in Proc. of the 9th conference on autonomous robot systems and competitions, vol. 1, no. CONF, pp. 59–65. IPCB: Instituto Polit'ecnico de Castelo Branco, 2009.
- [26] Cianci, C. M., Raemy, X., Pugh, J., & Martinoli, A. Communication in a swarm of miniature robots: The e-puck as an educational tool for swarm robotics. in International Workshop on Swarm Robotics, pp. 103–115. Springer, 2006.
- [27] Francesca, G., Brambilla, M., Brutschy, A., Trianni, V., & Birattari, M. Automode: A novel approach to the automatic design of control software for robot swarms. *Swarm Intelligence*, vol. 8, no. 2, pp. 89–112, 2014.
- [28] Prieto, A., Becerra, J. A., Bellas, F., & Duro, R. J. Open-ended evolution as a means to self-organize heterogeneous multi-robot systems in real-time. *Robotics and Autonomous Systems*, vol. 58, no. 12, pp. 1282–1291, 2010.
- [29] Greenwald L, Kopena J. Mobile robot labs. *IEEE Robotics & Automation Magazine*, vol. 10, no. 2, pp. 25–32, 2003.
- [30] G'omez-de-Gabriel, J. M., Mandow, A., Fernandez-Lozano, J., & Garcia-Cerezo, A. Mobile robot lab project to introduce engineering.
- [31] Scribbler 3 (s3) robot. [Online]. Website <https://www.parallax.com/product/scribbler-3-s3-robot> students to fault diagnosis in mechatronic systems," *IEEE Transactions on Education*, vol. 58, no. 3, pp. 187–193, 2014. [accessed 7 May 2023].
- [32] Calvo, I., Cabanes, I., Quesada, J., & Barambones, O. A multidisciplinary pbl approach for teaching industrial informatics and robotics in engineering. *IEEE Transactions on Education*, vol. 61, no. 1, pp. 21–28, 2017.
- [33] Do Y. Self-selective multi-objective robot vision projects for students of different capabilities. *Mechatronics*, vol. 23, no. 8, pp. 974–986, 2013.
- [34] Quanser qbot 3. [Online]. Website <https://www.quanser.com/products/qbot-3/> [accessed 12 May 2023].
- [35] Pioneer 3-dx robot. [Online].Website <https://www.generationrobots.com/media/Pioneer3DX-P3DX-RevA.pdf> [accessed 12 May 2023].
- [36] Turtlebot 2 robot. [Online].Website <https://clearpathrobotics.com/turtlebot-2-open-source-robot> [accessed 12 May 2023].
- [37] Gritti, A. P., Tarabini, O., Guzzi, J., Di Caro, G. A., Caglioti, V., Gambardella, L. M., & Giusti, A. Kinect-based people detection and tracking from small-footprint ground robots. in International Conference on Intelligent Robots and Systems (IROS), pp. 4096–4103, 2014.
- [38] Wu, K., Ranasinghe, R., & Dissanayake, G. Active recognition and pose estimation of household objects in clutter. in International Conference on Robotics and Automation (ICRA), pp. 4230–4237. IEEE, 2015.
- [39] Barber, R., Rodriguez-Conejo, M. A., Melendez, J., & Garrido, S. Design of an infrared imaging system for robotic inspection of gas leaks in industrial environments. *International Journal of Advanced Robotic Systems*, vol. 12, no. 3, p. 23, 2015.

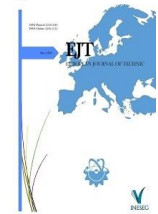
- [40] Turtlebot 3 robot. [Online]. Website <https://emanual.robotis.com/docs/en/platform/turtlebot3/overview> [accessed 15 May 2023].
- [41] Amsters R. and Slaets P. Turtlebot 3 as a robotics education platform. in International Conference on Robotics in Education (RiE), pp. 170–181. Springer, 2019.
- [42] Turtlebot 4 robot. [Online]. Website <https://clearpathrobotics.com/turtlebot-4> [accessed 15 May 2023].
- [43] Microcontroller. [Online]. Website <https://ww1.microchip.com/downloads/en/devicedoc/atmel-11057-32-bit-cortex-m3-micro-controller-sam3x-sam3a-datasheet.pdf> [accessed 15 May 2023].
- [44] Arduino due. [Online]. Website <https://store.arduino.cc/products/arduino-due> [accessed 15 May 2023].
- [45] Lattepanda. [Online]. Website <https://www.lattepanda.com> [accessed 17 May 2023].
- [46] Raspberry pi 4. [Online]. Website <https://www.raspberrypi.com/products/raspberry-pi-4-model-b> [accessed 17 May 2023].
- [47] Nvidia jetson nano developer kit. [Online]. Website <https://developer.nvidia.com/embedded/jetson-nano-developer-kit> [accessed 17 May 2023].
- [48] Dc motor. [Online]. Website <https://www.pololu.com/product/4756/specs> [accessed 17 May 2023].
- [49] Sparkfun monster moto shield. [Online]. Website <https://www.sparkfun.com/products/retired/10182> [accessed 17 May 2023].
- [50] Sharp infrared distance measuring sensor. [Online]. Website <https://www.sparkfun.com/datasheets/Sensors/Infrared/gp2y0a02yke.pdf> [accessed 17 May 2023].
- [51] Ultrasonic distance sensor - hc-sr04. [Online]. Website <https://www.sparkfun.com/products/15569> [accessed 17 May 2023].
- [52] Zed 1 stereo camera. [Online]. Website <https://www.stereolabs.com/zed-1> [accessed 17 May 2023].
- [53] Slamtec rplidar-a3 laser range scanner. [Online]. Website <https://www.slamtec.com/en/Lidar/A3> [accessed 17 May 2023].
- [54] Redmon, J., Divvala, S., Girshick, R., & Farhadi, A. You only look once: Unified, real-time object detection. In Proceedings of the IEEE conference on computer vision and pattern recognition, pp. 779–788, 2016.
- [55] Top, A., & Gökbulut, M. Android application design with mit app inventor for bluetooth based mobile robot control. *Wireless Personal Communications*, pp. 1–27, 2022.

BIOGRAPHIES

Ahmet Top received the B.Sc., M. Sc. and PhD degrees in electric and electronic engineering from the Firat University, Elazığ, Turkey, in 2011, 2016 and 2023, respectively. He is currently Research Assistant and working toward the Ph. D. degree at Department of Electrical and Electronics Engineering, Technology Faculty, Firat University. His current research interests include control systems and robotic.

Gökhan Güngör In 2011, graduating with a third degree of the department, received the M.Sc. and Ph.D. degrees in mechanical and mechatronics engineering from the University of Waterloo, Waterloo, ON, Canada, in 2014 and 2020, respectively. He is currently an Assistant Professor with the Department of Mechatronics Engineering, Karabük University, Karabük, Turkey. His current research interests include mechatronic systems, robotics, and control system design.

Muammer Gökbulut received the B.Sc. in electric education from Gazi University in 1980 and the M.Sc. degree in electric education from Gazi University, Ankara, Turkey, in 1989, and the PhD. degree in electronic engineering from Erciyes University, He is a full Professor at Department of Electrical and Electronics Engineering, Technology Faculty, Firat University, Elazığ, Turkey. His current research interests include Neural network and Adaptive control systems.



Research Article

A Deep Learning Approach for Motor Fault Detection using Mobile Accelerometer Data

Merve Ertarğın^{1*}, Turan Gürgeç², Özal Yıldırım^{3,4}, Ahmet Orhan⁵

¹Munzur University, Electrical and Electronics Engineering Department, Tunceli, Turkey (e-mail: merveboydak@munzur.edu.tr).

²Firat University, Automotive Engineering Department, Elazığ, Turkey. (e-mail: tgurgenc@firat.edu.tr).

³Firat University, Software Engineering Department, Elazığ, Turkey. (e-mail: ozal@firat.edu.tr).

⁴Firat University, Artificial Intelligence and Data Engineering Department, Elazığ, Turkey. (e-mail: ozal@firat.edu.tr).

⁵Firat University, Electrical and Electronics Engineering Department, Elazığ, Turkey. (e-mail: aorhan@firat.edu.tr).

ARTICLE INFO

Received: Aug., 01. 2023

Revised: Aug., 28. 2023

Accepted: Oct, 27. 2023

Keywords:

Motor Fault Diagnosis

Deep learning

1D-CNN

Corresponding author: *Merve Ertarğın*

ISSN: 2536-5010 / e-ISSN: 2536-5134

DOI: <https://doi.org/10.36222/ejt.1336342>

ABSTRACT

Electrical machines, which provide many conveniences in our daily life, may experience malfunctions that may adversely affect their performance and the general functioning of the industrial processes in which they are used. These failures often require maintenance or repair work, which can be expensive and time consuming. Therefore, minimizing the risk of malfunctions and failures and ensuring that these machines operate reliably and efficiently play a critical role for the industry. In this study, a one-dimensional convolutional neural network (1D-CNN) based fault diagnosis model is proposed for electric motor fault detection. Motor vibration data was chosen as the input data of the 1D-CNN model. Motor vibration data was obtained from a mobile application developed by using the three-axis accelerometer of the mobile phone. Three-axis data (X-axis, Y-axis and Z-axis) were fed to the model, both separately and together, to perform motor fault detection. The results showed that even a single axis data provides error-free diagnostics. With this fault detection method, which does not require any connection on or inside the motor, the fault condition in an electric motor has been detected with high accuracy.

1. INTRODUCTION

Electrical machines are indispensable for industry, especially in power generation, manufacturing and transportation. In these applications, they play a critical role in the conversion and control of energy and are essential to meeting the energy demands of modern society. Due to occasional malfunctions in electrical machines, they do not operate at high efficiency and may consume more energy than necessary. This leads to higher operating costs. Failures that occur can create safety hazards for workers, such as electric shock or fire. These hazards can cause injury, equipment damage, or even death. For these reasons, it is necessary to detect faults before they progress and to implement preventive maintenance and monitoring programs.

Electric motors have complex internal structures and mechanisms that make it difficult for humans to visually inspect and identify faults. Many faults occur in motor parts or electrical windings that are not easily accessible or visible without disassembling the motor. Many motor failures present as subtle changes in performance or behavior that are not immediately noticeable to humans [1]. Identifying motor failures often requires a deep understanding of motor operation, performance characteristics and failure patterns. Some faults in motor may occur intermittently or under certain operating

conditions. Detecting such errors in real time requires constant monitoring of various parameters and being able to analyze large volumes of data quickly. People can find it difficult to constantly monitor motors at such high frequencies and to analyze complex data patterns effectively. In contrast, machine-learning models can overcome these challenges by analyzing large amounts of data from engines, detecting fine patterns, and identifying error signatures more accurately and efficiently. These models process data in real time, providing continuous monitoring and timely fault detection, increasing overall motor reliability and minimizing downtime. Deep learning methods are based on the use of raw input data, unlike traditional approaches where it is necessary to manually extract the properties of the input data. Thus, the need for expert knowledge is minimized [2]. Due to these advantages, deep learning models have been applied in many different fields such as detecting brain abnormalities from magnetic resonance images (MRI) [3], diagnosing heart diseases from electrocardiography (ECG) signals [4, 5], face recognition [6], speech recognition [7], as well as motor fault detection [8-16], and successful results have been obtained.

The most preferred input data for detecting faults in motor bearings are current [8-10] and vibration [11-16] data. Vibration signals are very sensitive to the presence of bearing

defects or anomalies. Within the realm of deep learning models, convolutional neural networks (CNN) excel at learning features from mechanical vibration signals. As a result, many studies have utilized CNNs for intelligent fault diagnosis of machines [11-14].

Jia et al. [11] proposed an approach called deep normalized convolutional neural network (DNCNN) to solve the problem that CNNs do not take into account the unbalanced distribution of machine health conditions. In this approach, normalized layers based on weight normalization strategy and ReLU activation function are used to improve the training process. A weighted softmax loss has been developed to deal with the unbalanced distribution data problem. In addition, a neuron activation maximization (NAM) algorithm was developed to understand how DNCNN learns features from vibrational signals.

Machine learning models trained with data previously collected from another machine may not perform satisfactorily when the environment and operating conditions change on different machine instances. Asutkar et al. [12] presented a transfer-learning model to address this deficiency. With 1D-CNN and transfer learning, it has been determined that the accuracy rates are high even if datasets from different machines are used in training and testing. Shen et al. [14] developed an approach that embed the physical knowledge of bearing faults into the model training process. Fault detection has been successfully achieved with this deep learning approach, which consists of a simple threshold model and CNN model for error detection. In addition, generative adversarial networks (GAN) [15], long-short-term-memory (LSTM) [16] models were also used in motor fault diagnosis and motivating results were obtained.

Various sensor equipment and platforms installed around the motor are used to obtain vibration signals for motor fault diagnosis [10]. These platforms are both costly and impractical to use. In this study, motor vibration data were collected with a non-invasive mobile application in order to evaluate motor health with an easy method that does not require the use of expensive sensors and minimizes the need for expert knowledge. Today, the possibilities of smartphones, which are available to almost everyone, are used in motor fault diagnosis and the motor health status is evaluated without any cost. With the CNN model, which is one of the deep learning methods and has proven to be successful in diagnosis and classification in many areas, motor fault diagnosis has been carried out without error. Thus, a low-cost and practical method for the problem is presented.

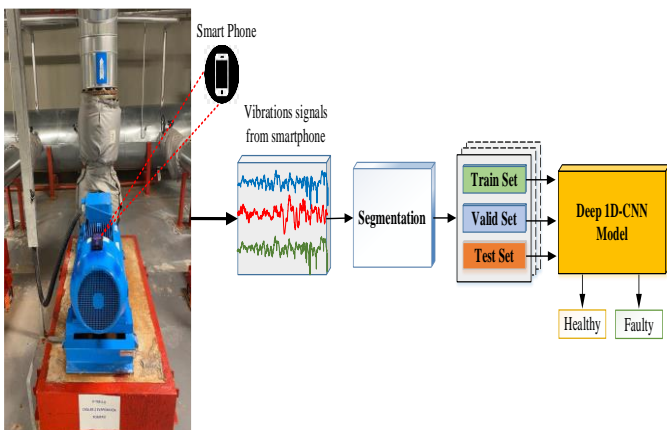


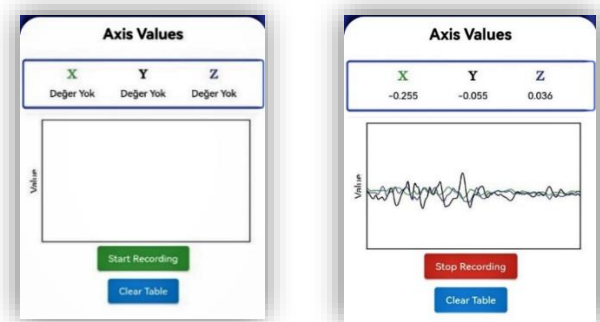
Figure 1. Illustration of the flowchart to build proposed approach.

2. MATERYAL VE METOD

In this study, a mobile application has been developed to detect motor failures from vibration data with 1D-CNN model. Illustration of the flowchart to build proposed approach is given in Figure 1. The phone, on which the mobile application was installed, was placed on the motor and data acquisition was performed in three axes (X, Y, Z). The data is segmented and divided into train set, validation set and test set. The 1D-CNN model was trained with the vibration data received, and then the performance of the model was evaluated with the test data.

2.1. Mobile Application

The mobile application used to get vibration data from the electric motor was realized with Flutter based on Dart language. Developed in 2011 by Google, Dart is defined as an object programming language. Flutter, developed by Google, makes it possible to develop applications for Android, iOS and web through a single toolkit. The reason why Flutter environment was preferred in this study is that Flutter enables the development of applications for different operating systems and devices through a single code base. The interface of the mobile application is as shown in Figure 2. Vibration data in the X-, Y- and Z-axes can be easily obtained by placing the phone with the application installed on it on an electric motor, opening the application screen and pressing the "Start Recording" button shown in Figure 2 (a). After starting the application, the application can show the vibrations in the X-, Y- and Z-axes both graphically and numerically as shown in Figure 2 (b). When the "Stop Recording" button is pressed, the application stops receiving vibration data and saves the received data in an excel spreadsheet. To delete the received data from the excel table, press the "Clear Table" button. Thus, the application becomes ready again to receive new data.



(a)

(b)

Figure 2. Visual interfaces of the mobile application (a) Application opening screen (b) When receiving real-time vibration data.

2.2. Proposed 1D-CNN Model

The CNN model proposed in this study is realized with an end-to-end learning structure. With this model, which does not require any feature extraction step, it is aimed to detect the motor health status. Since the vibration signals are one-dimensional, a 1D-CNN model is used.

The designed deep network model consists of 13 layers. The model has 1D Convolution (Conv1D), MaxPooling (MaxPool), flatten and dense layers. Figure 3 shows the structure of the proposed model for electric motor fault detection. Table I shows the parameters of the model in detail.

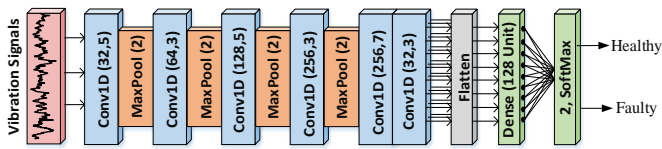


Figure 3. Architecture of proposed 1D-CNN model

TABLE I

DETAILED LAYERS AND PARAMETERS OF THE PROPOSED 1D-CNN MODEL

Layer	Layer Name	Kernel×Unit	Other Layer Parameters
1	Conv1D	5×32	Activation = ReLu, Strides = 1
2	MaxPooling1D	-	Strides = 2
3	Conv1D	3×64	Activation = ReLu, Strides = 1
4	MaxPooling1D	-	Strides = 2
5	Conv1D	5×128	Activation = ReLu, Strides = 1
6	MaxPooling1D	-	Strides = 2
7	Conv1D	3×256	Activation = ReLu, Strides = 1
8	MaxPooling1D	-	Strides = 2
9	Conv1D	7×256	Activation = ReLu, Strides = 1
10	Conv1D	3×32	Activation = ReLu, Strides = 1
11	Flatten	-	-
12	Dense	1×128	ReLu
13	Dense	1×2	Softmax

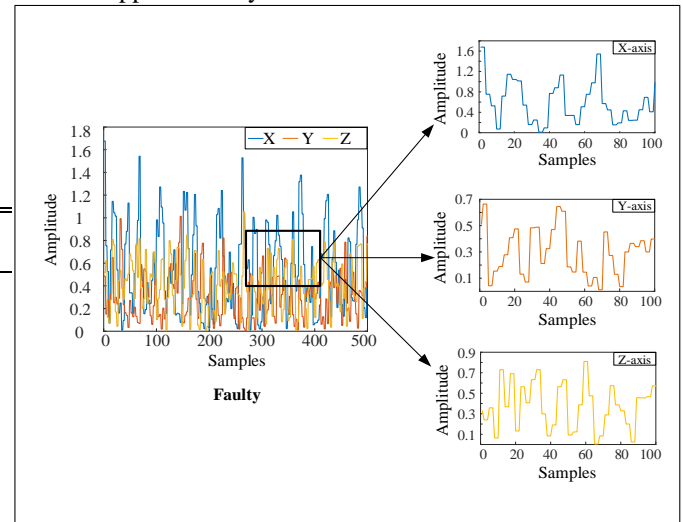
Convolutional layers are the fundamental building blocks of CNNs. Convolutional layers consist of filters that slide over the input image, scanning for relevant patterns and features. Pooling layers reduce the spatial dimensions of feature maps while preserving important information. Flatten layer flattens the feature maps into a 1D vector before transferring the data to the dense layers. The dense layer, also known as the fully connected layer, connects every neuron (or node) in the previous layer to every neuron in the current layer, creating a dense, fully connected network of neurons. In the last layer of the network, the softmax layer is used to predict the class to which the input signals belong. The optimizer selected was the Adam optimizer, and loss function was selected as the binary cross-entropy. After developing the model, the layer numbers, types and parameters of the deep algorithm are changed by brute force technique and the performance of the CNN model are observed.

2.3. Dataset

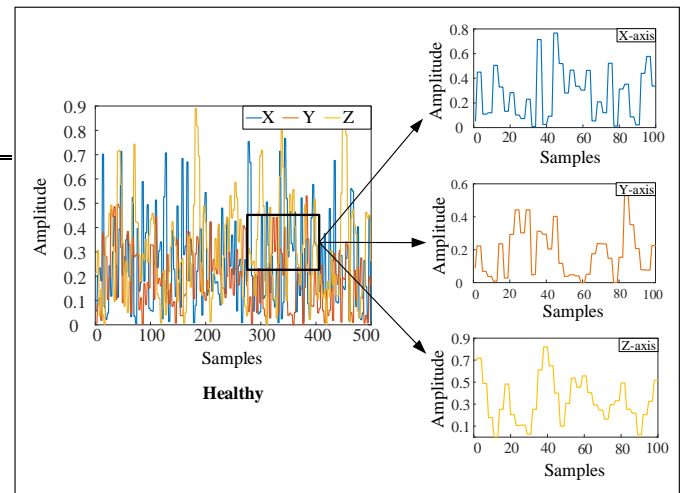
A three-phase, two-pole, 50 Hz, 5.5 kW asynchronous motor was selected for data acquisition. Firstly, data was obtained from the faulty motor and then the motor was repaired and data was obtained from the healthy motor in three axes (X, Y, Z). At 40 Hz operating frequency, vibration data of 64000×3 (1280 seconds) from the faulty motor (F) and 64000×3 (1280 seconds) from the healthy motor (H) were taken. These data were segmented in 500×3 dimension with 50 sample shifts. Thus, 1270 samples were obtained from each of the H and F classes, 2540 data samples in total. Then 80% of all data was used for training, 10% for validation and 10% for testing.

Figure 4 shows the X-, Y- and Z-axes vibration signal samples from the faulty and healthy motor. When the vibration samples are analyzed, it is seen that the peak value of the vibration amplitude of the defective motor is approximately 1.7

and the peak value of the vibration amplitude of the healthy motor is approximately 0.9.



(a)



(b)

Figure 4. Vibration samples a) Faulty motor b) Healthy motor

In this study, the performance of the proposed CNN model in motor fault detection is tested with four different cases:

- Case 1: Motor fault detection using X-axis data.
- Case 2: Motor fault detection using Y-axis data.
- Case 3: Motor fault detection using Z-axis data.
- Case 4: X-axis, Y-axis, Z-axis data were given to the deep learning model as three different features and motor fault detection was performed.

3. EXPERIMENTAL RESULTS

The 1D-CNN model was first trained on each axis data separately to obtain loss and accuracy values. Figure 5 shows the changes in the accuracy and loss values of the model over 10 epochs for the cases where X-axis, Y-axis and Z-axis data are used, respectively. Looking at the performance graphs, it is seen that the model does not have an overfitting problem.

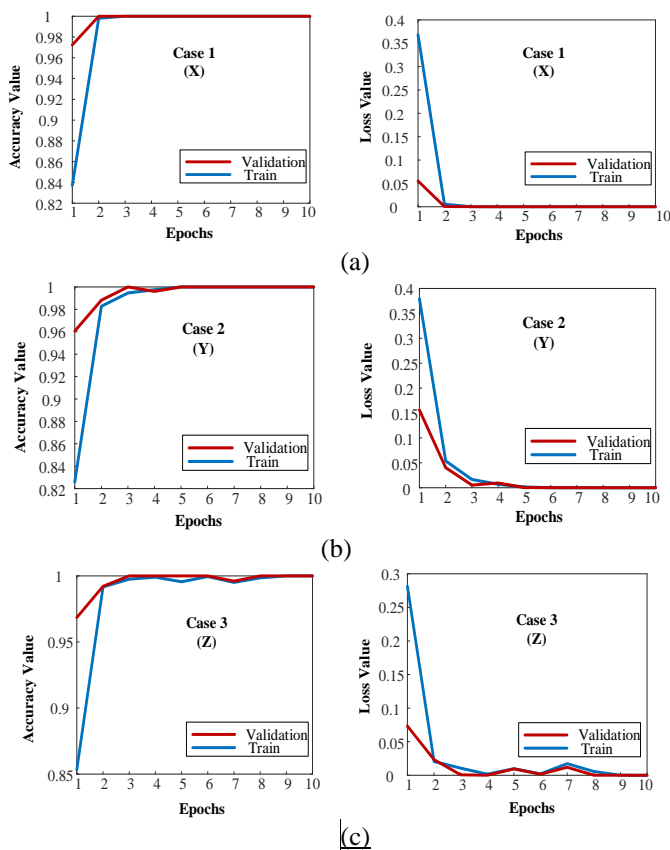


Figure 5. Accuracy and loss graphs for each case a) X-axis, b) Y-axis, c) Z-axis

The training performances of the model on each axis data were quite successful. However, considering the motor fault types, it was thought that providing all axis data to the model input would provide an even superior performance. In line with this idea, X-, Y- and Z-axes signals were combined and the training performance of the model was observed. Figure 6 shows the performance graphs obtained by combining X-axis, Y-axis and Z-axis signals and feeding them to the model input. As can be seen in the graphs, combining X-axis, Y-axis and Z-axis data provided similar performance in the performance measures of the model.

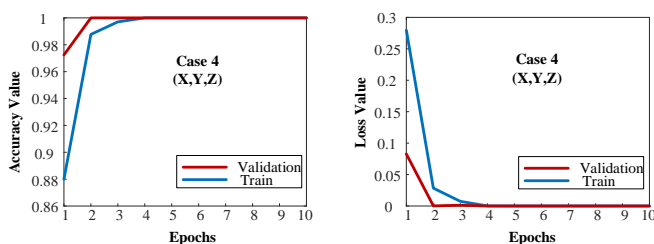


Figure 6. Accuracy and loss graphs for X-axis, Y-axis, Z-axis together

Accuracy, the most widely used performance evaluation metric, is used to evaluate the performance of the model. The accuracy value is calculated as in Equation 1:

$$Accuracy (\%) = \frac{TP + TN}{TP + TN + FP + FN} \times 100 \quad (1)$$

In the equation, TP represents true positives and TN represents true negatives. Similarly, FP represents false positives and FN represents false negatives. Table II shows the validation accuracy values of the model at each epoch for the

cases generated. When these values are analyzed, it is seen that the model quickly learns the motor fault condition.

TABLE II
VALIDATION ACCURACY VALUES OF THE 1D-CNN MODEL AT EACH EPOCH (%)

	X-axis	Y-axis	Z-axis	X,Y,Z-axis
Epoch 1	0.9724	0.9606	0.9685	0.9724
Epoch 2	1.0	0.9881	0.9921	1.0
Epoch 3	1.0	1.0	1.0	1.0
Epoch 4	1.0	0.9960	1.0	1.0
Epoch 5	1.0	1.0	1.0	1.0
Epoch 6	1.0	1.0	1.0	1.0
Epoch 7	1.0	1.0	0.9960	1.0
Epoch 8	1.0	1.0	1.0	1.0
Epoch 9	1.0	1.0	1.0	1.0
Epoch 10	1.0	1.0	1.0	1.0

The trained model was run on 254 test data. It was observed that the proposed model achieved 100% performance on the test data in all cases.

4. DISCUSSION

In this study, a deep learning model is trained using data obtained from a mobile platform to determine the motor fault status. The biggest advantage of the study is that it enables fault diagnosis only with the help of a smartphone without the need for any external sensor connection. Thus, fault conditions can be detected without the need for any platform installation inside or around the motor. The 1D-CNN model used in the study eliminates the need for any feature extraction step by providing end-to-end learning. The 1D-CNN model trained on the data obtained from the developed mobile application provided 100% accurate detection. In addition, fault recognition can be achieved by using any of the X-, Y- and Z-axes for the motor used.

In addition to its advantages, this study has several limitations. First of all, a single motor dataset was used for the study. Since the number of records in the dataset is limited, the number of data was increased with the 50-sample sliding window method. If more records are obtained, higher and more reliable accuracy values can be achieved. A single motor type was used in the study. The use of electric motors of different power and types will be useful in evaluating the generalizability of the proposed model.

In this study, only faulty and healthy motor diagnostics were performed. No classification of the type of failure was performed. The detection of different types of faults with the vibration information received from the mobile phone will be the subject of future studies.

5. CONCLUSION

In this study, motor vibration data is obtained from a mobile application and the health status of a motor is evaluated with a 1D-CNN model. The accuracy of the proposed 1D-CNN model is tested by first using the X-axis, Y-axis and Z-axis vibration data from the mobile application individually and then feeding these three axes data to the model simultaneously. In each case, the 1D-CNN model, which does not require any feature extraction and is easy to implement, performed an accurate classification with 100% accuracy rate. With this study, an experimental study is presented that the accelerometer sensors

in mobile phones are useful for evaluating the motor health status, and that healthy and faulty motor states can be detected without the need for any sensor or vibration meter.

REFERENCES

- [1] D. Neupane and J. Seok, "Bearing Fault Detection and Diagnosis Using Case Western Reserve University Dataset With Deep Learning Approaches: A Review," in *IEEE Access*, vol. 8, pp. 93155-93178, 2020, doi: 10.1109/ACCESS.2020.2990528.
- [2] S. Zhang, S. Zhang, B. Wang and T. G. Habetler, "Deep Learning Algorithms for Bearing Fault Diagnostics—A Comprehensive Review," in *IEEE Access*, vol. 8, pp. 29857-29881, 2020, doi: 10.1109/ACCESS.2020.2972859.
- [3] M. Talo, U. B. Baloglu, O. Yildirim, and U. R. Acharya, "Application of deep transfer learning for automated brain abnormality classification using MR images," in *Cognitive Systems Research*, vol. 54, pp. 176-188, 2019.
- [4] U. B. Baloglu, M. Talo, O. Yildirim, R. S. Tan, and U. R. Acharya, "Classification of myocardial infarction with multi-lead ECG signals and deep CNN," in *Pattern recognition letters*, vol. 122, pp. 23-30, 2019.
- [5] O. Yildirim, P. Plawiak, R. S. Tan, and U. R. Acharya, "Arrhythmia detection using deep convolutional neural network with long duration ECG signals," in *Computers in biology and medicine*, vol. 102, pp. 411-420, 2018.
- [6] M. Coşkun, A. Uçar, O. Yildirim and Y. Demir, "Face recognition based on convolutional neural network," *2017 International Conference on Modern Electrical and Energy Systems (MEES)*, Kremenchuk, Ukraine, 2017, pp. 376-379, doi: 10.1109/MEES.2017.8248937.
- [7] G. Hinton et al., "Deep Neural Networks for Acoustic Modeling in Speech Recognition: The Shared Views of Four Research Groups," in *IEEE Signal Processing Magazine*, vol. 29, no. 6, pp. 82-97, Nov. 2012, doi: 10.1109/MSP.2012.2205597.
- [8] T. Ince, S. Kiranyaz, L. Eren, M. Askar and M. Gabbouj, "Real-Time Motor Fault Detection by 1-D Convolutional Neural Networks," in *IEEE Transactions on Industrial Electronics*, vol. 63, no. 11, pp. 7067-7075, Nov. 2016, doi: 10.1109/TIE.2016.2582729.
- [9] Y. Li, Y. Wang, Y. Zhang, and J. Zhang, "Diagnosis of inter-turn short circuit of permanent magnet synchronous motor based on deep learning and small fault samples," in *Neurocomputing*, vol. 442, pp. 348-358, 2021.
- [10] R. N. Toma, A. E. Prosvirin, and J. M. Kim, "Bearing fault diagnosis of induction motors using a genetic algorithm and machine learning classifiers," in *Sensors*, vol. 20(7), 1884, 2020.
- [11] F. Jia, Y. Lei, N. Lu, and S. Xing, "Deep normalized convolutional neural network for imbalanced fault classification of machinery and its understanding via visualization," in *Mechanical Systems and Signal Processing*, vol. 110, pp. 349-367, 2018.
- [12] S. Asutkar, C. Chalke, K. Shivgan, and S. Tallur, "TinyML-enabled edge implementation of transfer learning framework for domain generalization in machine fault diagnosis," in *Expert Systems with Applications*, vol. 213, 119016, 2023.
- [13] M. Ertarğın, O. Yildirim and A. Orhan, "Motor Yataklarında Meydana Gelen Arızaları Tespit Etmek için Yeni Bir Tek Boyutlu Konvülsiyonel Sinir Ağı Modeli", *Firat Üniversitesi Mühendislik Bilimleri Dergisi*, vol. 35, no. 2, pp. 669-678, Sep. 2023, doi:10.35234/fumbd.1292390.
- [14] S. Shen, et al., "A physics-informed deep learning approach for bearing fault detection," in *Engineering Applications of Artificial Intelligence*, vol. 103, 104295, 2021.
- [15] K. Xu, X. Kong, Q. Wang, S. Yang, N. Huang, and J. Wang, "A bearing fault diagnosis method without fault data in new working condition combined dynamic model with deep learning," in *Advanced Engineering Informatics*, vol. 54, 101795, 2022.
- [16] D. K. Soother, S. M. Ujjan, K. Dev, S. A. Khowaja, N. A. Bhatti, and T. Hussain, "Towards soft real-time fault diagnosis for edge devices in industrial IoT using deep domain adaptation training strategy," in *Journal of Parallel and Distributed Computing*, vol. 160, pp. 90-99, 2022.

BIOGRAPHIES

Merve Ertarğın obtained her BSc degree in Electrical and Electronics Engineering from Firat University in 2016. In 2018 she joined the Electrical and Electronics Engineering Department, Munzur University as a research assistant. She received MSc. diploma in Electrical and Electronics Engineering

from Firat University in 2019. Currently, she continues her doctorate education in the Department of Electrical and Electronics Engineering at Firat University. Her research interests are electrical machines, power electronics, machine fault diagnosis and deep learning.

Turan Gürgeç received the MSc. diploma in Mechanical Engineering from Erciyes University in 2013. He obtained his PhD diploma from the Mechanical Engineering Department from Firat University in 2017. He is an Associate Professor in Automotive Engineering Department at Firat University. His research interests include surface coating, wear analysis, friction, manufacturing, and machine learning.

Özal Yildırım received the MSc. Diploma in Computer Engineering from Firat University in 2010. He obtained his PhD diploma in Electrical and Electronics Engineering from Firat University in 2015. He is currently working as an Associate Professor in the Software Engineering Department at Firat University. He has published over 60 articles in international peer-reviewed journals and conference proceedings. As a result of the research carried out on seven million researchers under the coordination of Stanford University, he was included in the "World's Most Influential Scientists" list. His main research interests include deep learning and medical signal and image processing.

Ahmet Orhan received the MSc. and PhD diploma in Electrical and Electronics Engineering from Firat University in 1987 and 1999 respectively. He is working as Associate Professor in Department of Electrical and Electronics Engineering at Firat University. His current research interests include synchronous motors, synchronous generators, induction motors, PM motors and generators, matrix converters.



Research Article

Artificial Intelligence-Based Tools in Software Development Processes: Application of ChatGPT

Zeynep Özpolat^{1*}, Özal Yıldırım¹ and Murat Karabatak¹

¹Firat University, Department of Software Engineering, 23200, Elazig, Turkey. (zypaltinterim@gmail.com).

ARTICLE INFO

Received: Jul., 20. 2023

Revised: Aug., 12. 2023

Accepted: Aug, 24. 2023

Keywords:

Artificial Intelligence
Software Development
ChatGPT-4
AI tools

Corresponding author: Zeynep Özpolat

ISSN: 2536-5010 / e-ISSN: 2536-5134

DOI: <https://doi.org/10.36222/ejt.1330631>

ABSTRACT

Software development processes are constantly evolving and transforming rapidly with rapid changes in technology. Recent innovations in Artificial Intelligence (AI) have led to significant changes in software development practices. AI tools can greatly improve traditional software development processes by giving developers the ability to build projects smarter, faster and more effectively. These tools can be used for a variety of tasks such as code generation, test automation, bug analysis, and performance improvements. ChatGPT, which is an artificial intelligence-based language model and has made a deep impact in almost every field, can help software developers write code faster and in a more natural language. In this study, the contributions of ChatGPT to a software development project were investigated. In the study, basic information about the use of ChatGPT in the software development process is presented. Implementations were carried out on a software project to evaluate some of ChatGPT's capabilities in the context of software development. For this purpose, a software development process was designed based on the answers given by ChatGPT. Various questions about software development processes were formulated and the answers produced by the GPT were evaluated. The results obtained showed that ChatGPT performed excellently in the software development process. Based on these findings, it has been observed that AI-based models such as ChatGPT can be effectively used as auxiliary tools in software development processes that accelerate traditional workflows. In addition, AI-based tools can save time and effort while improving software quality by automating testing processes.

1. INTRODUCTION

Software development processes are generally referred to as the steps followed during the design of a software project. These steps commence with identifying the necessary analyses for the desired software. Subsequently, the process continues with stages such as design, coding, testing, and deployment [1]. During project execution, collaborative efforts among stakeholders lead to the creation of requirements. Following the identification of requirements, the transition is made to the coding phase for the designated structures in the design stage. Finally, a testing phase is implemented to measure the efficiency of the resulting product [2]. Software projects must be completed within the defined timeframe, within the financial resources allocated to the project, and with the best possible quality that meets expectations. Throughout these steps, effective communication among the teams and stakeholders within the project stands as one of the most critical factors contributing to the success of projects. Human resources are prominent in each phase of traditional software development processes. These processes involve a wide array of integrated development environments (IDEs), test automation tools, project management tools (such as Jira,

Trello, Asana, etc.), and database management tools, which significantly support software developers [3]. Depending on project requirements and the team's preferences, appropriate tools are selected to manage the software development processes efficiently. Despite the facilitation provided by these software tools, there is a need for tools capable of making rapid and effective decisions and enabling automated process management in this domain. Therefore, Artificial Intelligence (AI)-based tools have gained significant usage in software development processes, just as they have in various other fields, as of late

In its simplest form, AI can be defined as computer software capable of imitating the human mind and a set of tools integrated into this software [4]. With AI systems used in software development processes, tasks such as decision-making, prediction, identification, and pattern recognition become more manageable. AI, which provides a different perspective to traditional software development coding, utilizes popular areas such as deep learning and machine learning in the process. Noteworthy applications of AI in social life include the generation of fake videos, creation of non-existent human faces, and manipulative voice applications. Recently, ChatGPT [5] has been released as a tool that has made a significant impact in this field. Generative Pre-trained

Transformer - 4, also known as ChatGPT-4, is an AI application. Designed as a multi-language processing platform, ChatGPT is an application that can be beneficial in various processes within the software field.

There are several research studies investigating how ChatGPT can assist in software development and engineering. Ahmad et al. [6] presented research on how architecture-centric software engineering (ACSE) professionals can benefit from ChatGPT. They focused on designing the software process with ChatGPT and the factors to consider in the ACSE & ChatGPT partnership. The authors discussed the advantages and disadvantages of ChatGPT-supported ACSE and provided solutions for implementing human-bot collaborative work. Nascimento et al. [4] compared the performance of software engineers and AI-based systems, including ChatGPT. Through various evaluation criteria, they analyzed the tasks assigned to ChatGPT and inferred that it outperformed engineers on certain software engineering tasks, especially those of easy to medium-level complexity. However, in some studies, human engineers were successful, while in others, AI prevailed. Katar et al. [7] employed ChatGPT in their research paper and presented results, highlighting both the positive and negative aspects of using ChatGPT as an auxiliary tool. The authors concluded that while ChatGPT is not yet efficient enough to write a research paper entirely on its own, it can be a valuable tool to assist researchers in the writing process. Akbar et al. [8] conducted a motivational, demotivational, and ethical evaluation of software engineers' usage of ChatGPT. They listed the ethical challenges posed by ChatGPT, such as risks of plagiarism, confidentiality breaches, data security issues, and the generation of malicious data. The authors conducted a comprehensive survey among software engineers and performed Cross-Impact Matrix Multiplication Applied to Classification (MICMAC) analysis to create a cluster-based decision model. Fraiwan and Khasawneh [9] provided an overview of emerging language models and chatbots. They emphasized that AI-based tools have the potential to offer different perspectives in areas such as education, software engineering, healthcare, and marketing. However, they also noted that these systems come with challenges, including issues of plagiarism and lack of transparency. The authors conducted a study investigating the positive and negative effects of language models actively used in fields like education, health, software engineering, and marketing, and discussed how to take precautions against potential negative consequences and misuse scenarios.

This study presents both traditional software development processes and the use of AI tools in these processes. Traditional software development processes are explained in general terms and the effects of contemporary AI tools on these processes are discussed. The contributions of this article to the literature can be listed as follows:

- As far as the authors know, the existing studies in the literature are generally completed with the support of a software development specialist. This study has been tried to be completed entirely with the support of AI.
- The answers to these questions are included in the article without making any changes to the questions asked to ChatGPT-4 for an ERP project.
- This article is of great importance as it sheds light on the effectiveness of using ChatGPT in software project development.

The remaining parts of the study are as follows: Section 2 gives general information about software development

processes. In Section 3, the material and method are mentioned. Questions directed to the AI system are given in this section. Section 4 includes the results of the experimental study created in line with the answers from ChatGPT-4. In Section 5, discussions about the study and the general results of working with Section 6 are mentioned.

2. SOFTWARE DEVELOPMENT PROCESSES

Software is a tool used by a software team to define the way devices behave. The sequence of cyclical stages used to describe a software process is defined as the software life cycle [1]. Each software follows a predefined sequence of steps according to the Software Development Life Cycle (SDLC) [10]. The Software Development Life Cycle is defined as a guideline and logical process used by system developers to develop systems [11]. A basic diagram of the software life cycle is given in Fig.1.

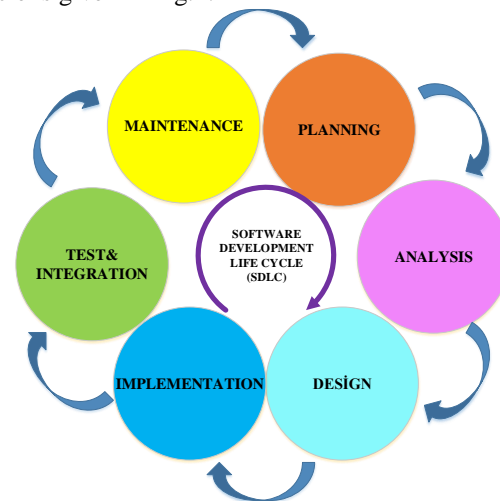


Figure 1. Software Development Life Cycle.

The steps of a basic software lifecycle and the operations performed in each of these steps can be listed as follows [7]:

- **Planning:** This is the first stage of the cycle where the requirements and needs of the users are taken into consideration. Here, the objectives are clarified by determining the systemic and technical needs required for the work to be created in parallel with the user requirements. The work given by the user for a purpose turns into a project at this stage.
- **Analysis:** It is a stage in which the estimated time for the desired outputs within the project and the risky situations that may be encountered in the project during this period are revealed. Possible situations are detailed using UML diagrams.
- **Design:** In line with the planning and analysis made in the previous stages, the drawing, i.e. the design of the project begins. The basic structure of the software to be used in the project, its algorithm, interface, software components and all kinds of technical details of the project are determined before proceeding to the next stage, implementation. All the theoretical and practical decisions regarding the project are made and the next phase begins.
- **Development:** Development is defined as the part where the decisions made in the design phase are now poured into a code environment. It is the stage where the project, which has all the theoretical infrastructure ready, is put into practice. Programming languages and software

development tools determined in accordance with the project are used.

- **Testing:** The start of the trial process of the codes, programs or software-based tools prepared for the project takes place in the testing phase. At this stage, the project's compatibility with real life is tested by applying techniques such as code correctness, detection of software errors, performance tests, usability evaluation. In addition to the control of software processes, providing software training to the people or units that will benefit from this project is also included in the testing phase.
- **Maintenance:** Where tasks such as eliminating errors and making improvements are carried out as long as the software or project is used the stage.

During the maintenance process, certain requirements that were not initially included in the software may arise in response to the users' needs. In this case, the cycle goes back to the beginning and is reconstructed from the planning stage. The reason why the software development process is presented as a life cycle can be summarized concisely. In this life cycle, which comprises fundamental stages, various traditional models are employed to organize and streamline the processes. Some of the traditional software development models include the 'Waterfall', 'V Model', 'Prototype', and 'Spiral'. The 'Waterfall' model is the first of the process development models and is the oldest SDLC approach. It follows a linear and sequential approach, often referred to as the linear-sequential life cycle model in some sources [12]. It includes 6 steps: planning, design, implementation, testing, deployment, and maintenance [13]. It is easy to comprehend and yields favorable results, particularly for small projects with well-defined requirements. The 'V Model' is often described as an extension of the waterfall model. This is because it has a similar sequential and linear flow. But differently, the process steps are bent upwards after the coding phase to form the V-shape [14]. The planning, design, implementation, and testing steps take place before coding, which saves time [13]. While early test preparation offers the advantage of detecting bugs at an early stage, excessive focus on the product itself rather than the testing phase can lead to potential issues [15]. The 'Prototype' model is an approach that facilitates the development of an initial prototype to comprehend customer requirements. Based on customer feedback, the prototype is continuously improved, and a process is followed to create the final product. The steps in this model encompass business modeling, data modeling, process modeling, implementation, and testing [14]. The 'Spiral' model was introduced in 1988 to solve the limitations of the waterfall model. It is an iterative software model, combining the features of prototyping and the waterfall model. The spiral model consists of four phases starting with planning, objectives, risk analysis, and development. The model organizes all activity inputs in a spiral, and all phases are repeated continuously. Spiral development commences on a smaller scale and expands based on the number of iterations. Since not all requirements are specified at once, additional studies may be needed [16].

2.1. Artificial Intelligence-Based Software Development Tools

Software development is the foundation of the information age society. It is one of the most important elements of the world of information processing, as well as being a complex structure that is constantly changing. In the modern digital age, the development of software solutions is a crucial issue to keep

pace with the rapidly evolving technology [17]. Software development processes play an active role in product quality and process efficiency. Issues such as requirements specification and error detection can be considered as basic initial activities. Supporting, changing, periodically evaluating, and increasing the potential of these activities requires continuous optimization. Software development processes are costly and time-consuming. At this point, AI-supported technologies work as a model that increases the effectiveness, speed, efficiency, and potential of software development processes [18].

AI has a long history in computer science, but more recently it has been making practical achievements, mostly in machine learning. It also develops software that can learn in an automated, human-free environment using sophisticated algorithms and large data sets. This environment of success not only provides a good understanding of decisions in critical decision-making processes but also increases the acceptance of AI-enabled developments [19]. The use of AI applications in development processes is usually aimed at automating software cycle phases. It can be applied to every phase of the software development cycle, including analysis, design, code, testing, and maintenance. When the most popular AI models in recent years are examined, it is seen that they are classified under the headings of natural language processing, computer vision, autonomous driving, and health [17]. In order to draw a framework for the integration of AI technologies into software development processes, models can be emphasized. Many AI models such as Automatic Programming, Artificial Neural Networks, Machine Learning, Knowledge-Based Systems, and Natural Language Processing can be applied in software engineering stages [20].

The phases where AI models contribute the most are requirements analysis and testing. Requirements analysis is the first stage of the software process. Researchers often incorporate AI into this first step of the cycle. The Natural Language Processing model, a semi-automated approach, provides useful results here, shortening the time needed for the requirements step and improving its quality [21]. Automated Programming is involved in the automated process of generating code, reusing code, and refactoring code and offers an intermediary association. The possibility of automated programming assistants to provide pre-made models for specific situations and to demonstrate best practices is very important here [22]. Machine Learning is used to link information from structural and fault-based testing to functional aspects of the program. This linked information links results to different test technique implementations and offers ease of testing [23].

In summary, it can be said that the goal of AI is to achieve intelligence. The software development cycle, on the other hand, aims to create a system that is valid, verified, cost-effective, and without any maintenance or user acceptance issues. Despite the dilemmas that these two fields have, it is also very difficult to achieve overlap. More studies are needed to increase the success and identify the needs correctly. At this point, some studies have raised questions such as "If the cycle succeeds in becoming fully intelligent, won't both domains become a single domain?", "if AI becomes the traditional software development life cycle itself, will this mean the end of the cycle?" [20]. There are some AI – support programs currently used by software developers such as TensorFlow, PyTorch, Keras, Scikit-learn, Apache MXNet, Microsoft

Cognitive Toolkit, IBM Watson Studio, H2O.ai, Google Cloud AutoML, Amazon CodeGuru, Bugspots [24]. Each of these and similar programs aims to automate tasks, reduce errors and maximize efficiency.

3. MATERIAL AND METHODS

In this study, software development processes were implemented step by step on a project using an AI-based tool.

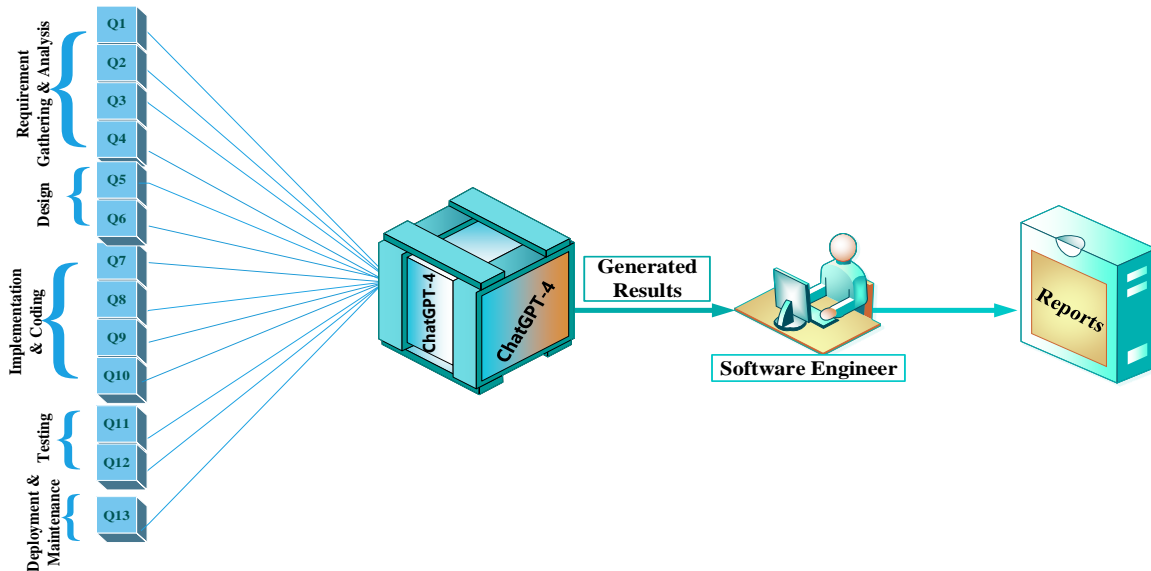


Figure 2. Block diagram of the material and method.

In this study, appropriate questions were formulated for each step of the software development process using the ChatGPT-4 tool, and the corresponding answers were obtained. During the question preparation phase, a suitable set of inquiries was carefully crafted, taking into account the software development processes. The intended software system to be constructed using ChatGPT was determined as an enterprise resource planning (ERP) project. The ERP system is a software solution designed to address both specific and general needs across all units within a company [25]. Traditionally employed by large companies, the demand for ERP systems has expanded in recent years to include medium and small-sized companies. Consequently, the software development field has experienced accelerated growth to meet the increasing market demands. To swiftly address these requirements, the development of AI-supported solutions has become imperative, complementing the efforts of human personnel.

TABLE I

Questions asked to ChatGPT-4 to create a software development process		
Categories	Q	Questions
Requirement Gathering & Analysis	Q1	Can you create a comprehensive flowchart for an ERP project?
	Q2	Can you create a flowchart for the new ERP system with these modules you suggest to add?
	Q3	Can you create a software lifecycle content in accordance with this flowchart?
	Q4	What can be done during the requirement gathering and analysis phase for the ERP project we plan to do?
Design	Q5	What can be done during the design phase for the ERP project we plan to do?
	Q6	Can you draw a UML diagram covering each stage for this ERP project you have designed?
Implementation/ Coding	Q7	What kind of process can be followed in implementation/coding? Can you inform me about the coding programs to be used, database system etc.?

Using the recently popular Chat-GPT model, software development processes were managed in line with the questions identified. The block diagram of the work carried out within the scope of this article is presented in Fig.2. As can be seen in Figure 2, the questions containing the parts of the software development processes are given as Q1, Q2,...,Q13. Prepared questions were directed to ChatGPT-4. Answers produced by ChatGPT have been evaluated by an expert.

This study seeks to address the question of "How can the software development process for an ERP project be realized?" utilizing ChatGPT, the most popular application of AI. Accordingly, various questions were posed to ChatGPT, and the ensuing answers are presented herein.

3.1. ChatGPT Input Data

In this article, which aims to demonstrate the use of an AI tool in a software development process, ChatGPT-4 was used in the process creation phase. For the ERP project that ChatGPT was asked to do, questions were asked at each step. In line with the answers given by ChatGPT, some suggestions given by ChatGPT were directed to ChatGPT as questions again. The question-and-answer process was carried out mutually in this way. The questions prepared within the scope of the article study and the categories that these questions correspond to in software development processes are given in Table 1.

Q8	It is planned to use Python programming language and Oracle as database for the designed ERP project. In this direction, can you first create the database?	
Q9	Can you create the ER diagram for the database you created?	
Q10	Can you give the Python codes for the ERP project based on the database created?	
Testing	Q11	What kind of process can be followed during the testing phase for the ERP project?
	Q12	Can you give an example ERP project where the performance test is applied from these tests?
Deployment & Maintenance	Q13	Can you talk about the steps required for deployment and maintenance in an ERP software development project?

4. EXPERIMENTAL RESULTS

Before designing an ERP project, ChatGPT-4 was asked to create a flowchart. The "Show Me Diagrams" plugin from the Plugin Store was used to generate the diagram. Figure 3

shows the question Q1 given as input for ChatGPT and the diagram created for this question. As can be seen in Figure 3, ChatGPT

presented a project scope consisting of 4 parts for an ERP system in response to the question asked. ChatGPT also referred to the compartments that may be needed in the subsections of each chapter.

Answer for (Q1):

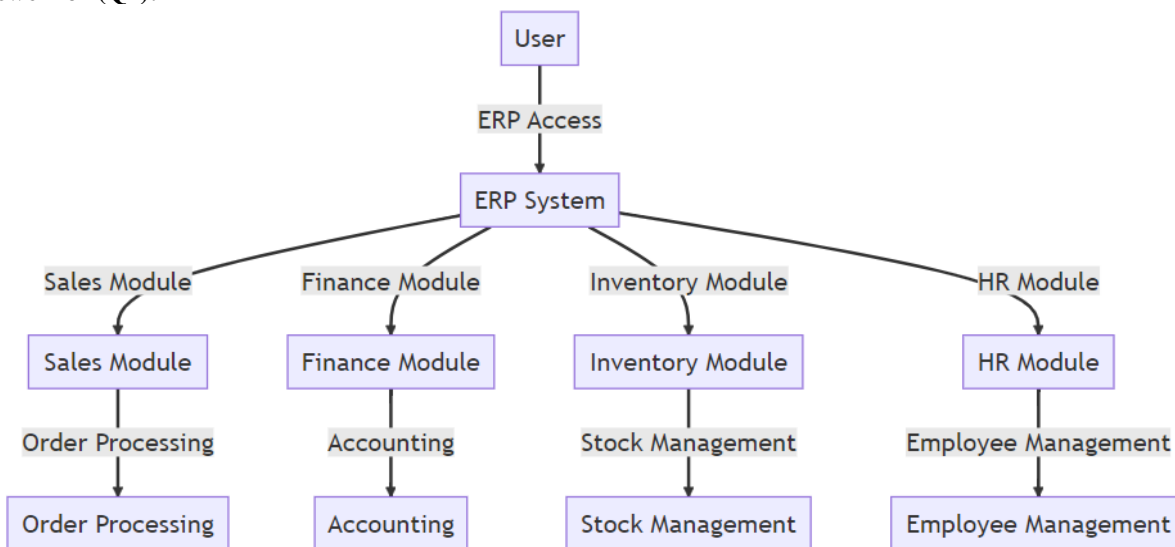


Figure 3. Flowchart for an ERP project

After this answer, ChatGPT-4 suggested "To view ideas for improving the diagram, use the key phrase "show ideas"." This question was asked again, taking into consideration the advice given by ChatGPT-4. Afterward, the flowchart was expanded a little more based on the suggestions given by ChatGPT-4.

Add More Detail: You could add more detail to each module. For example, the Sales Module could be broken down into "Lead Tracking", "Sales Forecasting", "Order Management", etc. Similarly, the Finance Module could be broken down into "Accounts Payable", "Accounts Receivable", "General Ledger", etc.

Answer for (Q2): Ideas to improve the diagram:

```

1 graph TD
2   U["User"] --> ERP_Access["ERP Access"]
3   ERP_Access --> ERP_System["ERP System"]
4   ERP_System --> SM["Sales Module"]
5   ERP_System --> FM["Finance Module"]
6   ERP_System --> IM["Inventory Module"]
7   ERP_System --> HM["HR Module"]
8   SM --> OP["Order Processing"]
9   SM --> LT["Lead Tracking"]
10  SM --> SF["Sales Forecasting"]
11  SM --> CM["Customer Management"]
12  FM --> AC["Accounting"]
13  FM --> FR["Financial Reporting"]
14  FM --> FA["Financial Analysis"]
15  IM --> SMG["Stock Management"]
16  IM --> IT["Inventory Tracking"]
17  IM --> AT["Asset Tracking"]
18  IM --> PI["Product Identification"]
19  IM --> IR["Inventory Reporting"]
20  HM --> EM["Employee Management"]
21  HM --> RO["Recruitment & Onboarding"]
22  HM --> PM["Payroll Management"]
  
```

Figure 4. Code page for editing flowchart on Mermaid program

There is a screen where the sections on the Code tab can be deleted and added and the given diagram can be edited as

desired. A part of the new diagram obtained after various modifications is shown in Fig.5 below

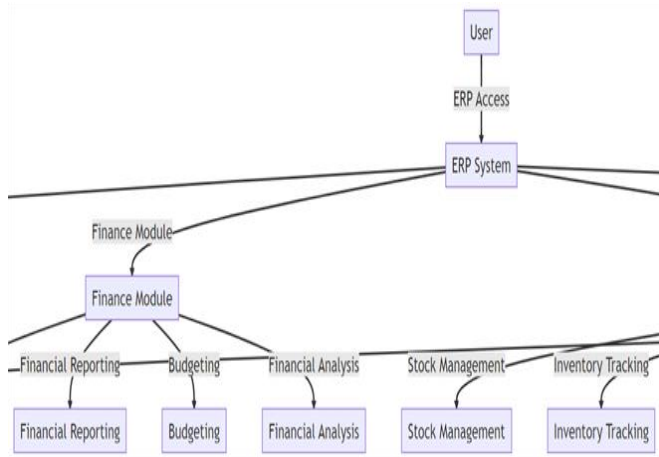


Figure 5. A part from the final version of the modified flowchart on Mermaid

After this diagram, ChatGPT-4 was asked to give the steps of the software lifecycle in accordance with the project (Q3). ChatGPT's mixed response to this request is presented in the following items.

Answer for (Q3):

- **Requirement Gathering and Analysis:** This is the initial stage where the project team (including business analysts, project managers, and key stakeholders) define the business requirements. They identify what modules are needed (Sales, Finance, Inventory, HR, etc.) and what features each module should have.

Answer for (Q4): During the Requirement Gathering and Analysis phase for the ERP project, several key activities should be undertaken:

Identify Stakeholders: Identify all the key stakeholders who will be using the ERP system. This could include employees from different departments such as Sales, Finance, Inventory, HR, etc. Their input is crucial in understanding the requirements of the system.

Conduct Interviews and Surveys: Conduct interviews and surveys with the identified stakeholders to understand their needs and expectations from the ERP system. This could include understanding their current challenges, processes, and what features they would like in the new system.

Document Requirements: All the requirements gathered from the stakeholders should be documented in a structured manner. This could be in the form of a Business Requirement Document (BRD) which outlines in detail the objectives of the project, the needs of the stakeholders, and the expected outcomes.

Prioritize Requirements: Not all requirements can be implemented at once. Hence, it's important to prioritize the requirements based on factors such as business value, cost, time, and resource availability.

Analyze and Validate Requirements: The project team should analyze the requirements to ensure they are clear, complete, feasible, and testable. Any ambiguities or conflicts in the requirements should be resolved at this stage.

Create Use Cases: For each requirement, create use cases that describe how the system should behave. This will help in understanding the system's functionality in a real-world scenario.

Approval of Requirements: Once the requirements are documented and analyzed, they should be approved by all the key stakeholders. This ensures everyone is on the same page before moving to the next phase of the project.

Answer for (Q5): During the design phase of the ERP project, several key activities should be undertaken:

- **Design:** Based on the requirements, the system architecture is designed. This includes how the different modules will interact with each other and the database schema. The user interface for each module is also designed in this phase.
- **Implementation/ Coding:** In this phase, the actual coding of the system begins. Developers start building the system module by module. For example, they might start with the Inventory Module, implementing features like Stock Management, Inventory Tracking, Reorder Point Setting, etc.
- **Testing:** After a module is developed, it's tested to ensure it works as expected. This includes unit testing, integration testing, system testing, and user acceptance testing. Any bugs or issues found are fixed.
- **Deployment:** Once all modules are developed and tested, the system is deployed. This could be on-premises or on the cloud, depending on the company's needs.
- **Maintenance:** After deployment, the system enters the maintenance phase. This includes fixing any issues, adding new features, and improving existing ones. For example, if the company decides they want to add a "Product Identification" feature to the Inventory Module, this would be done in the maintenance phase.

In line with these answers, the software development process will be started with ChatGPT-4. The questions and answers for each stage are given below.

System Architecture Design: This involves designing the overall structure of the ERP system. It includes defining how the different modules (Sales, Finance, Inventory, HR, etc.) will interact with each other, how data will flow between them, and how they will integrate with the database and other existing systems.

Database Design: This involves designing the database schema that will store all the data for the ERP system. It includes defining the tables, fields, relationships, indexes, and other database elements.

User Interface Design: This involves designing the user interfaces for each module. It includes defining the layout, colors, fonts, buttons, forms, and other visual elements. The goal is to make the interface intuitive and easy to use for the end-users.

Security Design: This involves designing the security measures for the ERP system. It includes defining the user roles and permissions, data encryption methods, authentication and authorization processes, and other security protocols.

Network Design: If the ERP system is to be deployed across multiple locations, this involves designing the network infrastructure that will support the system. It includes defining the servers, routers, firewalls, and other network elements.

Design Documentation: All the design elements should be documented in a Design Specification Document. This document serves as a blueprint for the developers in the next phase of the project.

Design Review and Approval: Once the design is complete, it should be reviewed and approved by the key stakeholders. This ensures that the design meets the requirements and is ready for implementation.

Answer for (Q6):

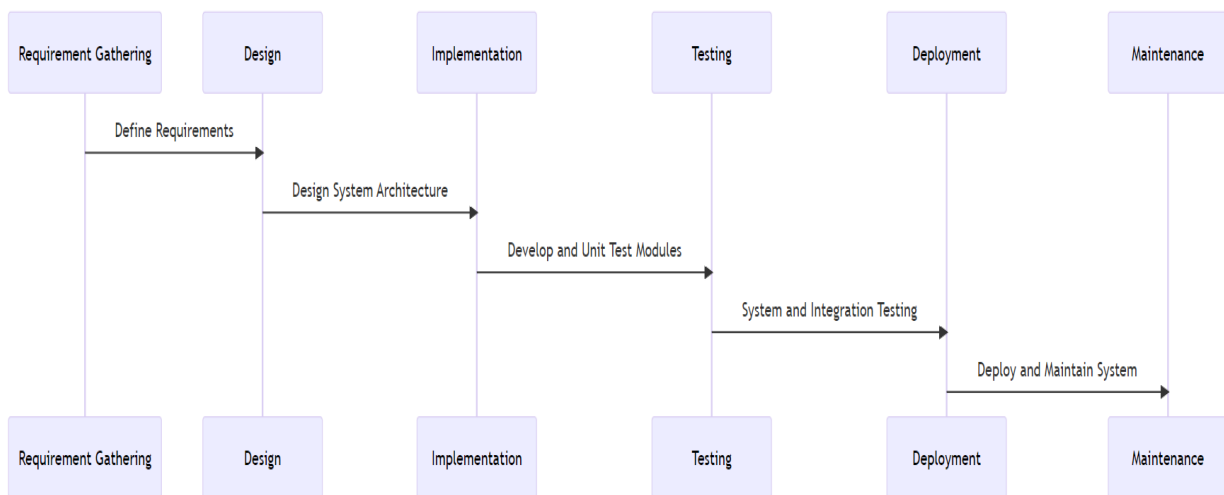


Figure 6. Drawing of the UML diagram for the project to be done.

Fig. 6 shows the UML diagram of the proposed scheme. In the previous questions, the "Show ideas" statement suggested by ChatGPT-4 has been used again to see the suggestions that it would give.

Ideas to improve the diagram:

Add More Details: You could add more details to each phase. For example, during the Requirement Gathering phase, you could include activities like "Identify Stakeholders", "Conduct Interviews", "Document Requirements", etc. Similarly, you could add more details to the other phases as well.

Add Interactions: You could add interactions between the phases. For example, after the Design phase, there could be a feedback loop back to the Requirement Gathering phase in case any changes are needed in the requirements.

Use Different Colors: You could use different colors for each phase to make the diagram more visually appealing and easier to understand. You can use the 'init' directive to

customize the theme of an individual diagram. For example, `%% {init: {'theme':'forest'}} %%`.

Explore the following themes:

default: This is the default theme for all diagrams.

neutral: This theme is great for black and white documents that will be printed.

dark: This theme goes well with dark-colored elements or dark-mode.

forest: This theme contains shades of green.

base: This is the only theme that can be modified. Use this theme as the base for customizations.

To customize the theme of an individual diagram, use the init directive. For example, `%% {init: {'theme':'forest'}} %%`

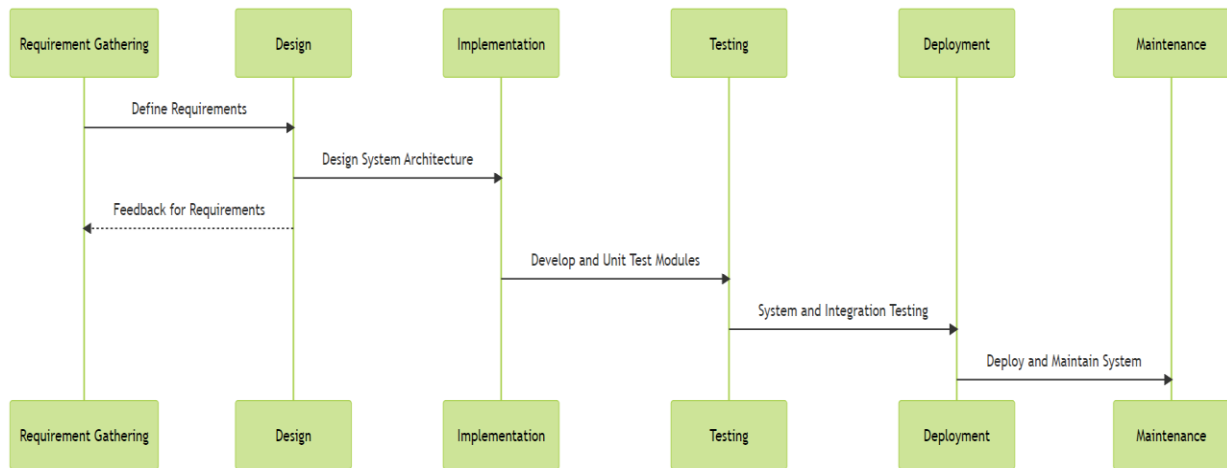


Figure 7. UML diagram edited using the "Forest" theme

The diagram given in Fig 7. was drawn using the "Forest" theme. After drawing the UML diagram, the responses of GTP-4 were taken again for the Implementation/Coding phase.

Answer for (Q7): During the Application/Coding phase of the ERP project, you would be translating the design documents into actual code. Here are some steps that could be followed:

Setup Development Environment: This involves setting up the development environment with the necessary software and tools. This could include the programming language, IDE, version control system, etc. For an ERP system, you might be using languages like Java, Python, or C#. The choice of language would depend on various factors like the expertise of the team, the requirements of the project, etc.

Database Design: Based on the requirements and the design, you would need to design the database for the ERP system. This could involve choosing a database system (like MySQL, PostgreSQL, Oracle, etc.), designing the schema, setting up the tables, etc.

Coding: This is where you actually start writing the code for the system. This would involve coding for the different modules like Inventory, HR, Sales, etc. The code should be written in a way that it is clean, efficient, and easy to understand.

Version Control: Use a version control system like Git to manage and track changes to your code. This would allow you to keep a history of changes, revert back to a previous version if needed, and manage multiple versions of the code.

Code Review: Regular code reviews should be conducted to ensure the code is clean, efficient, and adheres to coding standards. This helps to maintain the quality of the code and reduces the chances of bugs.

Unit Testing: As each module or part of a module is developed, it should be tested individually to ensure it works as expected. This is known as unit testing.

Integration Testing: Once individual modules are developed and tested, they should be combined and tested as a group. This is known as integration testing and it helps to identify any issues that occur when different parts of the system interact with each other.

Continuous Integration/Continuous Deployment (CI/CD): If possible, set up a CI/CD pipeline. This allows you to automate the testing and deployment of the code, ensuring that any changes to the code are immediately tested and deployed.

Answer for (Q8): Creating a database for an ERP system is a complex task that involves careful planning and design. Here's a simplified example of how you might create a few tables in an Oracle database for your ERP system using SQL.

```
-- Create a table for Employees
CREATE TABLE Employees (
  EmployeeID INT PRIMARY KEY,
  FirstName VARCHAR(50),
  LastName VARCHAR(50),
  Email VARCHAR(100),
  PhoneNumber VARCHAR(15),
  HireDate DATE,
  JobID INT,
  Salary FLOAT,
  ManagerID INT,
  DepartmentID INT
);
```

Please note that this is a very basic example and a real-world ERP system would be much more complex. In this example, we have four tables: Employees, Departments,

Inventory, and Sales. Each table has a primary key, which uniquely identifies each record in the table. There are also foreign keys which are used to link tables together. For example, the ManagerID in the Departments table would be a foreign key linking to the EmployeeID in the Employees table.

After the database was created, the request to draw the Entity-Relation (ER) diagram was directed as specified. ER diagram generated by ChatGPT after this request is shown in Fig.8.

Answer for (Q9):

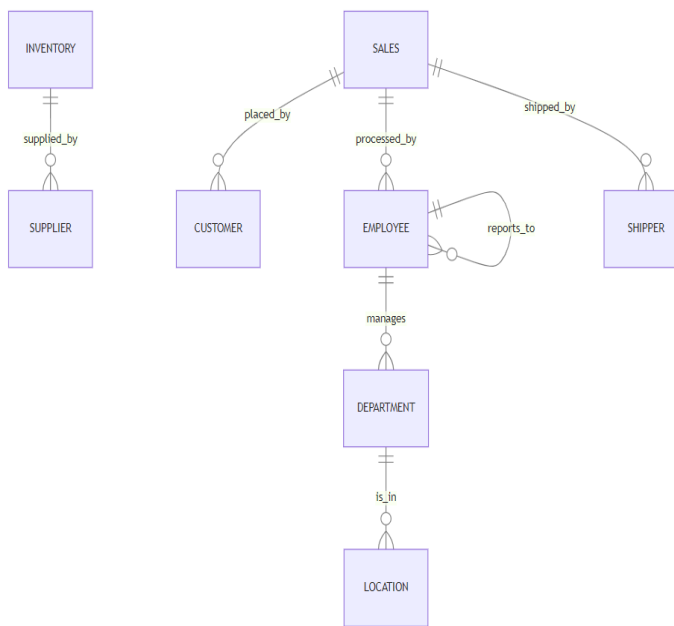


Figure 8. ER diagram of the database.

Answer for (Q10): Creating Python code for an entire ERP system is beyond the scope of this platform, as it would involve thousands of lines of code and a deep understanding of your specific business requirements. However, I can provide you with some basic examples of how you might use Python to interact with the SQL Server database we created earlier. Here's an example of how you might connect to the database:

```

import pyodbc
# Create a connection string
conn_str = (
    r'DRIVER={ODBC Driver 17 for SQL
Server};'
    r'SERVER=your_server;'
    r'DATABASE=your_database;'
    r'UID=your_username;'
    r'PWD=your_password;'
)
# Create a connection
conn = pyodbc.connect(conn_str)
    
```

Once you're connected, you can execute SQL queries. Here's an example of how you might insert a new employee into the Employees table:

```

# Create a cursor
cursor = conn.cursor()
# SQL query
sql = """
INSERT INTO Employees (EmployeeID,
FirstName, LastName, Email, PhoneNumber,
HireDate, JobID, Salary, ManagerID,
DepartmentID)
VALUES (?, ?, ?, ?, ?, ?, ?, ?, ?, ?)
"""
# Values
values = (1, 'John', 'Doe',
'john.doe@example.com', '555-555-5555',
'2023-01-01', 1, 50000, None, 1)
# Execute the query
cursor.execute(sql, values)
# Commit the transaction
conn.commit()
    
```

You can also retrieve data. Here's how you might get all employees:

```

# SQL query
sql = "SELECT * FROM Employees"
# Execute the query
cursor.execute(sql)
# Fetch all rows
rows = cursor.fetchall()
# Print rows
for row in rows:
    print(row)
    
```

These are very basic examples. A real-world ERP system would have much more complex interactions with the database, and would likely involve a web interface or other user interface, business logic, error handling, security measures, and more.

The code blocks given above contain some of the answers given by ChatGPT-4. It has the competence to realize the database connection of the ERP system with basic system codes. However, it needs an expert to do the necessary coding for the interface design. He was repeatedly asked in different ways to create a system in Python. But his answer to all of them was that he could not create such coding. Each time ChatGPT-4 provided Python code that provided a connection to the database.

After the answers were received in the Implementation/Coding phase, questions were asked to ChatGPT-4 for the next phase, the testing phase (Q11). The answers given by ChatGPT are presented below.

Answer for (Q11): The testing phase is a critical part of the software development lifecycle, especially for a complex system like an ERP. Here are the steps that can be followed during the testing phase of the ERP project:

- **Unit Testing:** This is the first level of testing where individual components of the software are tested. The purpose is to validate that each unit of the software performs as designed. In the context of an ERP system, this could mean testing individual functions or methods in the code.
- **Integration Testing:** After unit testing, integration testing is performed. This involves combining individual units and testing them as a group. The purpose of this level of testing is to detect any faults in the interaction between integrated units.
- **System Testing:** In this phase, the entire system is tested as a whole. The purpose of this testing is to evaluate the system's compliance with the specified requirements.
- **User Acceptance Testing (UAT):** This is the final phase of testing, where the software is tested in the "real world" by the intended audience. UAT can be done by the end-users of the software or subject matter experts in the business domain.
- **Performance Testing:** This is done to ensure that the system performs effectively under varying loads and volumes. It includes load testing (testing under expected load) and stress testing (testing under extreme loads).
- **Security Testing:** This is done to check how the ERP software protects against threats from external entities and maintains data integrity.
- **Regression Testing:** This is done after modifications such as enhancements or defect fixes to ensure that the changes haven't introduced new faults.

- **Compatibility Testing:** This is done to ensure the ERP system can effectively run in different environments – different operating systems, browser types, hardware configurations, etc.
- **Usability Testing:** This is done to ensure that the ERP system is user-friendly and easy to use.

Based on the test suggestions given by ChatGPT-4, one of the tests was selected and Q12 question was asked to conduct a sample study.

Answer for (Q12): Performance testing is a crucial part of ensuring that an ERP system can handle the expected load and perform optimally under different conditions. Here's a simplified example of how you might conduct performance testing on an ERP system using a tool like Apache JMeter, which is an open-source software designed to load test functional behavior and measure performance.

Please note that this is a simplified example and actual performance testing can be quite complex depending on the specific requirements and architecture of your ERP system.

Identify Key Scenarios to Test: Identify the most common and critical operations that users will perform on your ERP system. This could include operations like logging in, accessing and updating records, generating reports, etc.

Create Test Plan: In JMeter, you would create a new Test Plan and add Thread Groups to it. Each Thread Group represents a user scenario that you want to test. For example, you might have one Thread Group for logging in, another for accessing records, etc.

Deployment:

Environment Setup: The first step is to set up the production environment where the ERP system will be deployed. This includes setting up the servers, databases, networking equipment, and any other necessary hardware or software.

Installation: The ERP software is installed on the production servers. This may involve running installation scripts, setting up databases, configuring network settings, and other tasks.

Configuration: The ERP system is configured to meet the specific needs of the organization. This includes setting up user accounts, configuring security settings, setting up data feeds, and other tasks.

Data Migration: If the organization is moving from an old system to the new ERP, data from the old system will need to be migrated to the new one. This is a complex process that requires careful planning to ensure no data is lost or corrupted.

Testing: Before the system goes live, thorough testing is conducted in the production environment to ensure everything works as expected. This includes functional testing, performance testing, security testing, and user acceptance testing.

Training: End users are trained on how to use the new ERP system. This is a critical step to ensure user adoption and success of the project.

Go Live: Once everything has been tested and users have been trained, the system can go live. This is often done in stages, with a small group of users starting to use the system first, and more users added over time.

Configure Thread Properties: For each Thread Group, you would configure the number of threads (simulated users), the ramp-up period (how long to take to "ramp up" to the full number of users), and the number of iterations (how many times to execute the test).

Add and Configure Samplers: Samplers tell JMeter to send specific types of requests to a server. You would add HTTP Request samplers to your Thread Groups and configure them to send requests that simulate the user operations you're testing.

Add and Configure Listeners: Listeners provide access to the data gathered by JMeter about the test cases as a Sampler component is processed. For example, you might add a Summary Report listener to see a table of aggregated results for all samplers, or a Graph Results listener to see a visual graph of the performance results.

Run Tests and Analyze Results: Once everything is set up, you would run your tests and then analyze the results to identify any performance bottlenecks or issues.

As a result of the answers obtained from ChatGPT-4, it is foreseen that it can also provide ideas in the test phase. The answer to Q13 for the last two steps, distribution and maintenance, is as follows.

Answer for (Q13): Sure, deployment and maintenance are critical phases in the software development lifecycle, especially for complex systems like an ERP. Here's a general outline of the steps involved:

Maintenance:

Environment Setup: The first step is to set up the production environment where the ERP system will be deployed. This includes setting up the servers, databases, networking equipment, and any other necessary hardware or software.

Installation: The ERP software is installed on the production servers. This may involve running installation scripts, setting up databases, configuring network settings, and other tasks.

Configuration: The ERP system is configured to meet the specific needs of the organization. This includes setting up user accounts, configuring security settings, setting up data feeds, and other tasks.

Data Migration: If the organization is moving from an old system to the new ERP, data from the old system will need to be migrated to the new one. This is a complex process that requires careful planning to ensure no data is lost or corrupted.

Testing: Before the system goes live, thorough testing is conducted in the production environment to ensure everything works as expected. This includes functional testing, performance testing, security testing, and user acceptance testing.

Training: End users are trained on how to use the new ERP system. This is a critical step to ensure user adoption and success of the project.

Go Live: Once everything has been tested and users have been trained, the system can go live. This is often done in stages, with a small group of users starting to use the system first, and more users added over time.

4. DISCUSSION

Software development processes are one of the most fundamental elements that ensure the successful completion of the project given in the environment where engineers work. In order to accurately determine the inputs, outputs and requirements of the given project, each step of the software development life cycle must be worked carefully and diligently. By assigning employees to the necessary parts of the cycle according to their competencies, it ensures that the project emerges efficiently and quickly. The software development process can be a difficult process for engineers until they get to the coding part. AI multilingual chatbots have reached a level that can give ideas in the field of software development. These robots, which many researchers now include in their academic or non-academic studies, make the work of researchers easier. Despite various security vulnerabilities, many questions can be answered. Apart from the most popular ChatGPT, there are also robots such as YouChat, BingChat, JasperChat, Character.AI.

After the latest updates of ChatGPT, its use in academia has become more widespread. The fact that it can provide visual results such as graphics, tables, and pictures are important factors that attract the attention of users. Some studies in the literature reveal the positive and negative aspects of ChatGPT, ethical violations, and various plagiarism possibilities [4-6]. Since ChatGPT is also utilized while conducting these studies, it is actually an example of intelligence whose active learning process is constantly ongoing.

In this study, we investigated what role ChatGPT can play in a software development project. It was asked to realize an ERP project that constitutes the financial information systems of corporate companies by applying all stages of the software life cycle. All questions were planned step by step in accordance with the software life cycle and asked to ChatGPT-4 respectively. In addition to the planned questions, new questions were added to the question pool by taking into account the suggestions given by ChatGPT-4. As a result of the study, it is seen that ChatGPT-4 can be utilized

as a very good guide in all steps except Implementation&Coding and Test phases. The ideas obtained from the ChatGPT-4 in the requirements determination and Analysis, Design, Deployment and Maintenance phases are in a structure that will make the software developer's job much easier in this process. If the right questions are directed to ChatGPT-4 at the right points, the completion time and efficiency of the project will increase. The situation that can be stated as a disadvantage during the service received from ChatGPT-4 is that it is not fully efficient in coding. ChatGPT-4, who could provide assistance in coding up to a certain point, stated that the codes should be written under the supervision of a software engineer after a certain point. The codes given by ChatGPT-4 included the creation of the database system required in the software process and how the database connection can be made in Python in the codes to be used afterward. However, he stated that he could not help with the actual Python coding required to complete the project. Due to this shortcoming, the answers he gave in the Test phase could not go beyond suggestions. Although this may seem like a disadvantage for ChatGPT, it can be considered as an advantage from the point of view of the need for software engineers. When the limitations of working with ChatGPT are considered, it is seen that the most basic problems are plagiarism and security vulnerabilities. If questions about a project planned to be implemented are directed to ChatGPT by a third party, it may be possible for others to access the project details. In academic-based research, the literature sources given may be incorrect or non-existent. Although the plagiarism issue has been corrected a little more in ChatGPT-4, it still has deficiencies. The results obtained with the help of ChatGPT should always be checked by the user.

It is envisaged that a software development specialist can facilitate the processes in the initial stages by getting help from a multilingual robot such as ChatGPT while developing a project. Due to the lack of performance in the Implementation & Coding step, it is necessary to complete the software development process under the supervision of a

software developer. Due to ChatGPT's lack of performance in this area and its many disadvantages in terms of security, the need for software engineers continues.

In future studies, it is planned to create a software development project with the help of AI-supported robots other than ChatGPT. It is considered to design a working system by completing the missing points of AI systems by a software development specialist. For both ideas, the use of AI-supported software is inevitable.

5. CONCLUSION

The use of AI systems in software development processes has positive effects such as automating the process, reducing errors, and increasing productivity. For this purpose, there are many AI tools available online in the market. ChatGPT is making a difference among robots with the recent emergence of ChatGPT-4 version. In this paper, research questions on how to create a software development process using ChatGPT-4 and ChatGPT's answers to them are presented. As a result of the study, the answers obtained from ChatGPT-4 from the requirements determination, analysis, and design stages are logical and can be easily applied in such a process. Various deficiencies were encountered in the Implementation & Coding phase. One of the most important of these is that the coding part was not fully completed and it was suggested that a software engineer should help after a certain point. The software development process with ChatGPT-4 has progressed in a way to meet expectations despite the shortcomings in the coding and testing phase. The clearest conclusion that can be drawn from this study is that an expert software developer can complete the software development process with minimum errors and maximum efficiency with an AI robot.

REFERENCES

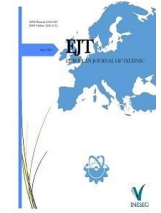
- [1] I. Sommerville, *Engineering Software Products: An Introduction to Modern Software Engineering*. Pearson, 2019.
- [2] B. W. Boehm, "A spiral model of software development and enhancement," *Computer*, vol. 21, no. 5, pp. 61–72, May 1988, doi: 10.1109/2.59.
- [3] M. U. Cheema and Q. Zearlish, "The Choice of Project Management Software by Project Managers; with the Moderating Impact of Top Management Support," vol. 2, no. 1.
- [4] E. Nascimento, A. Nguyen-Duc, I. Sundbø, and T. Conte, "Software engineering for artificial intelligence and machine learning software: A systematic literature review".
- [5] A. Radford, J. Wu, R. Child, D. Luan, D. Amodei, and I. Sutskever, "Language Models are Unsupervised Multitask Learners".
- [6] A. Ahmad, M. Waseem, P. Liang, M. Fahmideh, M. S. Aktar, and T. Mikkonen, "Towards Human-Bot Collaborative Software Architecting with ChatGPT," in *Proceedings of the 27th International Conference on Evaluation and Assessment in Software Engineering*, Oulu Finland: ACM, Jun. 2023, pp. 279–285. doi: 10.1145/3593434.3593468.
- [7] O. Katar, D. Özkan, G. -3, Ö. Yildirim, and U. R. Acharya, "Evaluation of GPT-3 AI Language Model in Research Paper Writing," *Turkish Journal of Science and Technology*, Jun. 2023, doi: 10.55525/tjst.1272369.
- [8] M. A. Akbar, A. A. Khan, and P. Liang, "Ethical Aspects of ChatGPT in Software Engineering Research." *arXiv*, Jun. 13, 2023. Accessed: Jul. 14, 2023. [Online]. Available: <http://arxiv.org/abs/2306.07557>
- [9] M. Fraiwan and N. Khasawneh, "A Review of ChatGPT Applications in Education, Marketing, Software Engineering, and Healthcare: Benefits, Drawbacks, and Research Directions".
- [10] R. A. Carter, A. I. Anton, A. Dagnino, and L. Williams, "Evolving beyond requirements creep: a risk-based evolutionary prototyping model," in *Proceedings Fifth IEEE International Symposium on Requirements Engineering*, Aug. 2001, pp. 94–101. doi: 10.1109/ISRE.2001.948548.
- [11] A. C. Nelson and J. T. C. Teng, "Do systems development methodologies and CASE tools decrease stress among systems analysts?," *Behaviour & Information Technology*, vol. 19, no. 4, pp. 307–313, Jan. 2000, doi: 10.1080/01449290050086417.
- [12] W. Model, "Waterfall model," *Luettavissa: http://www.waterfall-model.com/*. Luettu, vol. 3, 2015.
- [13] K. Rasheed, M. Imran, M. Noman, and M. Iqbal, "A Study On Traditional And Evolutionary Software Development Models," vol. 6, no. 07, 2017.
- [14] G. Kumar and P. K. Bhatia, "Comparative Analysis of Software Engineering Models from Traditional to Modern Methodologies," in *2014 Fourth International Conference on Advanced Computing & Communication Technologies*, Feb. 2014, pp. 189–196. doi: 10.1109/ACCT.2014.73.
- [15] G. Regulwar, P. Jawandhiya, V. Gulhane, and R. Tugnayat, "Variations in V Model for Software Development," Jan. 2021.
- [16] A. K. M. Z. Islam and Dr. A. Ferworn, "A Comparison between Agile and Traditional Software Development Methodologies," *GJCST*, pp. 7–42, Dec. 2020, doi: 10.34257/GJCSTCVOL20IS2PG7.
- [17] T. Clement, N. Kemmerzell, M. Abdelaal, and M. Amberg, "XAIR: A Systematic Metareview of Explainable AI (XAI) Aligned to the Software Development Process," *Machine Learning and Knowledge Extraction*, vol. 5, no. 1, Art. no. 1, Mar. 2023, doi: 10.3390/make5010006.
- [18] S. Russell, *Artificial Intelligence: A Modern Approach*, eBook, Global Edition. Pearson Education, Limited, 2016.
- [19] A. Holzinger, C. Biemann, C. S. Pattichis, and D. B. Kell, "What do we need to build explainable AI systems for the medical domain?" *arXiv*, Dec. 28, 2017. doi: 10.48550/arXiv.1712.09923.
- [20] F. A. Batarseh, R. Mohod, A. Kumar, and J. Bui, "10 - The application of artificial intelligence in software engineering: a review challenging conventional wisdom," in *Data Democracy*, F. A. Batarseh and R. Yang, Eds., Academic Press, 2020, pp. 179–232. doi: 10.1016/B978-0-12-818366-3.00010-1.
- [21] S. Vemuri, S. Chala, and M. Fathi, "Automated use case diagram generation from textual user requirement documents," in *2017 IEEE 30th Canadian Conference on Electrical and Computer Engineering (CCECE)*, Apr. 2017, pp. 1–4. doi: 10.1109/CCECE.2017.7946792.
- [22] M. Latinovic and V. Pammer-Schindler, "Automation and Artificial Intelligence in Software Engineering: Experiences, Challenges, and Opportunities: The 54th Hawaii International Conference on System Sciences," *Proceedings of the 54th Annual Hawaii International Conference on System Sciences*, HICSS 2021, pp. 146–155, 2021, doi: 10.24251/HICSS.2021.017.
- [23] A. Rafael Lenz, A. Pozo, and S. Regina Vergilio, "Linking software testing results with a machine learning approach," *Engineering Applications of Artificial Intelligence*, vol. 26, no. 5, pp. 1631–1640, May 2013, doi: 10.1016/j.engappai.2013.01.008.
- [24] <https://facebook.com/saiftheboss7>, "The Future of AI in Software Development in 2023 and Beyond - Appsero," Mar. 06, 2023. <https://appsero.com/user-guide/ai-in-software-development/> (accessed Jul. 13, 2023).
- [25] H. Klaus, M. Rosemann, and G. G. Gable, "What is ERP?," *Information Systems Frontiers*, vol. 2, no. 2, pp. 141–162, Aug. 2000, doi: 10.1023/A:1026543906354.

BIOGRAPHIES

Zeynep Özpolat obtained her BSc degree from Firat University, Department of Mathematics in 2012. She completed her master's degree at Firat University, Department of Mathematics. In 2018, she started her doctorate education at Firat University, Software Engineering. The doctoral process is still ongoing. Research areas; data science, quantum machine learning, artificial intelligence, software engineering.

Özal Yıldırım received his doctorate. I am a graduate of Firat University Electrical and Electronics Engineering. He is currently working as an Associate Professor in the Software Engineering Department at Firat University. He has published over 60 articles in international peer-reviewed journals and conference proceedings. As a result of the research carried out on seven million researchers under the coordination of Stanford University, he was included in the "World's Most Influential Scientists" list. His main research interests include deep learning and medical signal and image processing.

Murat Karabatak received his doctorate. He graduated from Firat University Electrical and Electronics Engineering. He works as a professor in the Department of Software Engineering at Firat University. His main research areas are data mining, software engineering, database systems and artificial intelligence.



Research Article

Leader-Follower Based Formation Control of Heterogeneous UAV-UGV Multi-Agent System

Kadir Aram^{1*}, Abdulmelik Bekmez²^{1*} Fatih Sultan Mehmet Vakıf University, Computer Engineering Department, 34445, Istanbul, Turkey. (e-mail: karam@fsm.edu.tr).² Fatih Sultan Mehmet Vakıf University, Computer Engineering Department, 34445, Istanbul, Turkey. (e-mail: abdulmelik.bekmez@gmail.com).

ARTICLE INFO

Received: Aug., 26. 2023
 Revised: Sep., 01. 2023
 Accepted: Sep, 05. 2023

Keywords:

Formation Control
 Leader-Follower
 Robotics
 Heterogeneous Swarm
 Mobile Robot

Corresponding author: *Kadir Aram*

ISSN: 2536-5010 / e-ISSN: 2536-5134

DOI: <https://doi.org/10.36222/ejt.1350641>

ABSTRACT

This paper deals with a leader-follower formation control of a heterogeneous robot swarm comprising unmanned ground vehicles (UGV) and unmanned aerial vehicles (UAV). The UGV is the leader robot, and the UAV's are the followers. A centralized system receives information about the robots, and the system makes decisions concerning the robots. Two different approaches were used to implement the leader-follower formation strategy. In the first approach, the formation points are calculated according to the position of the leader. In the second one, the position averages of the follower robots are also taken into account. The robots form a V-shape formation and are assigned to the formation points using the Hungarian algorithm. The robots move to the formation points with a proportional controller. The system was developed within the ROS2 framework and employed Turtlebot3 and Crazyflie robots for the robot swarm. The study was conducted in the Webots simulation environment, encompassing a variety of tests, with the subsequent observation and examination of the obtained results.

1. INTRODUCTION

An unmanned system encompasses a mechanical or apparatus outfitted with essential data processing components, sensors, automated control mechanisms, and communication systems, enabling it to independently carry out missions without human interference. Such systems encompass a variety of unmanned aerial vehicles (UAV), unmanned ground vehicles (UGV), underwater exploratory devices [1].

An unmanned aerial vehicle (UAV) is an aircraft capable of flight without the presence of a human pilot on board. In contemporary times, an increasing number of UAVs are being employed in civilian contexts due to their exceptional mobility and adaptability [2]. This attribute has enabled them to accomplish their objectives across numerous applications effectively. Nonetheless, incorporating multiple vehicles offers heightened versatility and efficacy in task execution. Moreover, utilizing multiple vehicles enhances resilience against failures compared to solitary units [3]. Studies on using multiple UAVs have been conducted in many areas, such as search and rescue [4], perimeter, surveillance [5] and loads carrying [6].

Agents exhibiting distinct dynamic attributes can surmount individual limitations, effectively accomplishing intricate and multifaceted missions. This elevation in capability expands the scope for tackling more challenging applications. Notably, the

synergistic integration of UAVs and UGVs amalgamates their strengths, encompassing proficient payload capacity, versatile task configuration, and robust localization capabilities, culminating in heightened overall performance [7].

In previous studies, various strategies have been applied for the formation control of multiple robots. Some key ones include leader-follower, behavior-based and virtual formation structure strategies [8].

In the leader-follower approach, one or more robots are considered as leaders while the other robots are considered as followers. The leader robot moves towards a specific goal. The follower robots move by maintaining a set distance and orientation from the leader. While providing this movement, it receives the position and orientation information of the leader robot [9,10]. In the virtual structure approach, robots move by creating a rigid structure. Geometrical shapes can be applied here. This formation has a center determined by shape, speed and orientation. The positions of the robots are defined relative to this reference point. Since the reference point is given relative to a trajectory, the position of each robot must be recalculated as time passes [11]. The behavioral control strategy is about each robot using certain behaviors. These behaviors can be trajectory following, obstacle avoidance and formation maintenance. After the relative weighting of these behaviors, the final control is performed [12]. Zhou et al. investigated the time-varying formation tracking problem for a heterogeneous

UAV-UGV swarm system. First, a collaborative control model is constructed with algebraic graph theory, and then a distributed observer-based formation tracking control protocol is designed [13]. In another study, an UAV lands on an UGV after delivering a package. A virtual structure approach is used here. Within this structure, there is a controller for the UGV to avoid obstacles as it moves forward [14]. Li and Zhu presented a UAV-UGV cooperative control mechanism. A leader-follower strategy is used for cooperative trajectory tracking. They used a fuzzy robust controller to control the UAV. The controller of the UGV uses a tracking algorithm and a PID controller [15]. Harik et al. designed a system for object transportation in unsafe locations. A UAV acts as a guide for obstacles. A group of UGVs performs the task using information from the UAV. The leader receives the information from the UAV and navigates while the follower robots follow the leader at a given distance using a vision-based target-tracking controller [16]. In their study, Akın and Şahin examined how UAVs and UGVs can efficiently collect data from IoT devices. They conducted these experiments in an obstacle environment. They used reinforcement learning principles to solve these problems [17].

This study presents a formation control of a heterogeneous multi-robot system consisting of one Turtlebot 3 as UGV and multiple Crazyflie robots as UAVs. The proposed work is a centralized system that utilizes a leader-follower strategy to implement the desired formation. PID controller is used for the control of the robots. The study was tested in a simulation environment. In Section 2, the methodology and materials used are described in detail. Section 3 presents the experiments done in the test phase and the simulation results. Finally, in Section 4, the results of the experiments are evaluated, and a conclusion to the study is made.

2. MATERIALS AND METHODS

The study consists of three stages. The first is for the leader robot to go to the target point, the second is to ensure that the follower robots follow the leader, and the third is to maintain the formation of the multi-robot group. V formation shape was chosen for multi-robots. The application was realized in the Webots Simulation environment using ROS.

2.1. Robot Operating System (ROS)

ROS is an open-source framework that enables the development of robotic applications with the help of libraries and packages. It is used in both commercial and research activities [18]. ROS allows application development using different programming languages. Also, an implemented program part can be used in other applications [19]. Processes in ROS communicate with each other, and these processes, called nodes, communicate using a publisher/subscriber structure. These nodes send data to each other using messages. The nodes that send data are called publisher nodes, and they send messages through topics to the receiver nodes, which are called subscribers. The ROS master is responsible for the nodes to locate each other, and it is initialized at startup to provide communication [20]. In ROS, different packages are offered to users to perform certain operations like mapping and navigation. For example, the move base package handles the operations to move a robot to a given destination point [21]. ROS includes a practical tool called Rviz (Ros Visualizer), which is a tool for visualizing robots, sensors, and algorithms in three dimensions. It can be used for all types of robots. Rviz

can plot data streaming on a ROS system, and its panel can be configured for various applications [22].

2.2. Webots

Webots is a simulation environment used both academic and industrial settings working on robots. Three-dimensional environments can be modeled using Webots, and robots defined in it can be used in these environments. It also has libraries containing sensors, actuators and other materials. Robot designs can be made using these libraries [23,24]. Figure 1 shows an example simulation environment.



Figure 1. Simulation environment

Figure 2 shows a Rviz visualization of the environment.

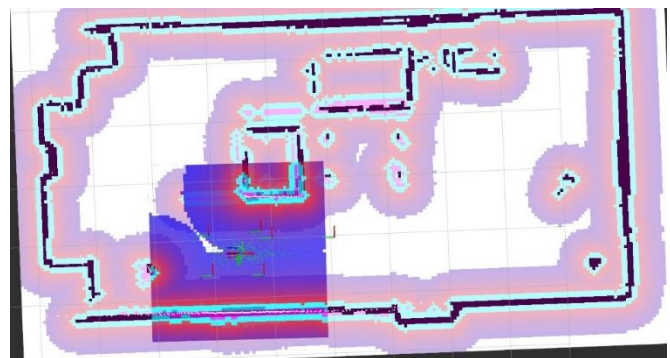


Figure 2. Rviz Visualization

2.3. Robots

In the study, simulation was performed with two different robots. One mobile robot and a multi-UAV group were used in the study.

The Turtlebot3 burger model was used as a mobile robot in the study. Turtlebot is a ROS based mobile robot used in both research and education. Many packages are provided with ROS to run simulations and control the robot [25]. Turtlebot is used as a ground robot and acts as the leader robot in the application.

In this study, the Crazyflie quadrotor robot was preferred as the follower robot group. Crazyflie is a robot platform used for educational and research purposes in robotics. With its small size and low weight, the robot is preferred in swarm robot applications [26,27]. It was preferred because it is compatible with ROS and because it has a ready-made model in the simulation.

2.4. Leader-Follower Strategy

The strategy aims for the leader robot to move to a given target location while other follower robots follow it. There must be continuous communication between the leader and the follower. The leader continuously broadcasts its position and orientation information with the data it receives from its

sensors. The follower robots receive this information from the leader robot. The follower robots use the leader's position to follow the leader and navigate a given formation. The target of the follower robots is the current position of the leader. Its orientation is the leader's orientation. The distance between the leader robot and the followers is continuously maintained during the tracking process [28–31]. Figure 3 shows the general structure of the leader-follower strategy.

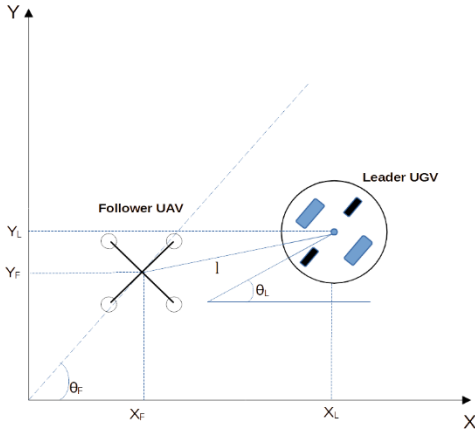


Figure 3. Leader-Follower Formation Scheme

In figure X_L, Y_L is the leader's position, θ_L is the leader's orientation, X_F, Y_F is the follower robot's position, and θ_F is the follower robot's orientation. l is the distance between the leader and the follower. The leader-follower strategy aims to maintain the desired distance and relative bearing between the robots.

The distance between the leader robot and the follower is calculated as in Equation 1.

$$\text{distance } (l) = \sqrt{(X_L - X_F)^2 + (Y_L - Y_F)^2} \quad (1)$$

In the ROS environment, the algorithm works as follows. The leader robot continuously broadcasts its instantaneous position as a publisher on the way to the specified target. The follower robots receive the leader's position as subscribers. For the follower robots, the target position is the leader's current position, and the target orientation is the current orientation of the leader. The distance between the follower and the leader is calculated by Equation 1. This process is repeated until the desired target point is reached.

2.5. Formation Process

The formation of the robots takes place in three steps. First, formation points should be calculated using the desired shape and the number of robots in the swarm. Then, which robot in the swarm should go to these points should be determined. In the last step, the robots should reach this point and maintain the formation. In this study, a V-formation shape was used.

The leader robot is located at the end of the V shape in the formation structure. Follower robots are lined up to the right and left of the leader robot. While forming formation points, the distance between the followers and the angle value they should be placed to the right and left are determined. The structure of the V formation is shown in Figure 4.

We used two different approaches to calculate the formation points. In the first approach, the rotation vector of the leader robot was taken and rotated 180 degrees. In order to find the direction vectors indicating the wings of the V

formation to be created, the leader's vector is expanded to the right and left by the theta angle. The desired distance value between these direction vectors and formation points is multiplied by the positions where the robots will be placed.

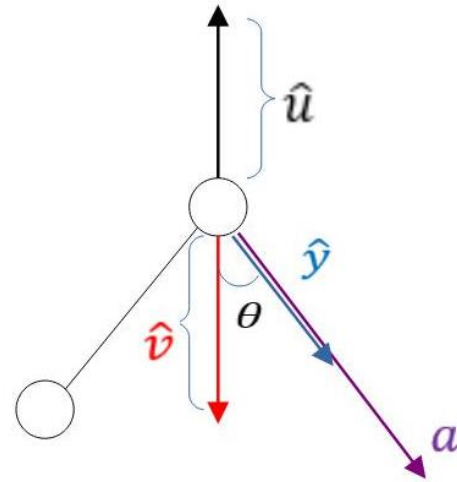


Figure 4. V-Formation Points

In the figure, θ is the angle of the triangle forming the V formation shape, \hat{u} is the leader's rotation vector, \hat{v} is the leader's rotation vector rotated 180 degrees, \hat{y} is the vector value extended by the angle θ , and a is the formation point. The formation point a is calculated according to Equation 2.

$$a = \hat{v} \times d \quad (2)$$

Where d is the distance between formation points.

In the second approach, the leader's rotation vector is not used. Instead, the average point of the positions of the follower robots was first determined. Then, the rotation between this and the leader's position is taken. Thus, the v value in equation 2 is calculated according to equations 3 and 4.

$$p_{avg} = \frac{p_1 + p_2 + \dots + p_n}{n} \quad (3)$$

$$\hat{v}_u = \frac{p_l - p_{avg}}{|p_l - p_{avg}|} \quad (4)$$

Where;

p_{avg} : Average position value of follower robots.

$p_1 \dots p_n$: Position of follower robots.

p_l : Position of leader robot.

\hat{v}_u : unit vector of the orientation of the formation

Once the formation positions are determined, the appropriate robot for each position needs to be identified. Hungarian algorithm was used for the assignment of positions. The first objective is to ensure that the robots take the shortest path to the positions. Another objective is to minimize collisions. Before starting the algorithm, the distance each robot needs to take for each position is calculated. The matrix containing these calculations is called the Cost matrix. The matrix is filled according to Equations 5-6.

$$\text{distance} = \sqrt{(X_{Ri} - X_{pj})^2 + (Y_{Ri} - Y_{pj})^2} \quad (5)$$

$$\text{Cost}_{ij} = \text{distance}^2 \quad (6)$$

Where (X_{Ri}, Y_{Ri}) is the position of the robot whose distance to the formation point will be calculated, and (X_{pj}, Y_{pj}) is the position of that formation point. After the cost matrix is filled, the algorithm process starts. These values are taken as input to the algorithm. As a result, the algorithm returns the row and column indices with the lowest cost. With these values, each formation point is assigned to the relevant robot in the robot group.

2.6. Controller Design

After determining the positions in the desired formation, which robots will go to these positions is determined. For the robot to go to this position, it must turn there and drive forward. For this process, a proportional controller was used due to the advantages of its applicability. The pseudo-code of the controller is given in Algorithm 1.

Algorithm 1 Controller Pseudo Code

- 1: Determine the reference point
- 2: Determine the K_p coefficient
- 3: **while** reference **do**
- 4: calculate distance to reference
- 5: calculate the angle difference from the reference point.
- 6: determine the angular and linear velocity by multiplying the error values by the coefficients
- 7: **end while**

The controller takes the position of the target point as the reference value. The distance to the reference position is calculated according to Equation 3, and the angle difference is calculated according to Equations 7 and 8.

$$\theta_{refi} = \arctan\left(\frac{y_T - y_R}{x_T - x_R}\right) \quad (7)$$

$$\theta_e = \theta_{refi} - \theta_R \quad (8)$$

θ_{refi} : The angle between the robot and the target point

x_R, y_R : Position of the robot

x_T, y_T : Target position

θ_R : Orientation of the robot

θ_e : Orientation error.

At the controller output, the linear and angular velocity of the robot is calculated, and it is ensured to go to the desired position.

An artificial potential field strategy was used to prevent the robots from bumping into each other as they move to their positions. According to this strategy, the robots are the repulsive force, and the target point is the attractive force [32].

The steps to create the formation are shown in the flow chart in Figure 5. First, the number of robots that will form the shape of the formation is determined, and the positions are calculated according to this number. Then, a cost matrix containing the distances of the robots to these points is created. According to this matrix, each robot is assigned a position to move. Finally, the robots are driven to these positions.

3. EXPERIMENTS

The study was conducted on Ubuntu 22.04 using the ROS 2 Humble version. In order to test the techniques used in the study, an environment with simulation was established. Webots was used as the simulation environment, and robots were

moved in this environment. Webots allows each robot to develop separate plugins that appear as a different process when running. CrazySwarm2, which was developed based on CrazySwarm[33], was used while performing the ROS 2 integration of the application. CrazySwarm2 was also used in the communication layer. Both ground and aerial robots were used in the application. Turtlebot 3 was used as a ground robot, and Crazyflie robots were used as aerial robots in the formation.

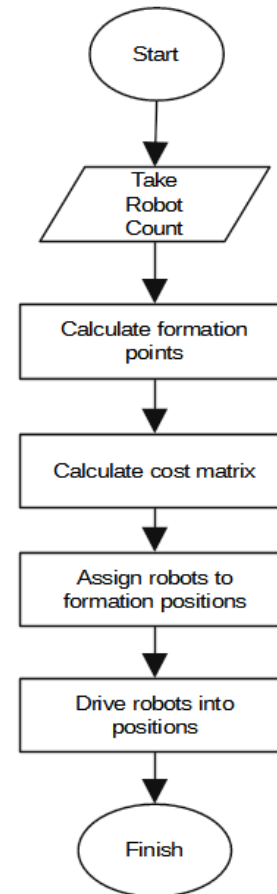


Figure 5. Formation Flow Chart

Two different scenarios were used in the developed environment. The formation process for each scenario was carried out using both approaches. At the beginning of the scenarios, the robots form a V-shape with the leader robot at the top of the formation. Here, the leader robot is tasked to reach a desired point. As the robot moves towards the target, the follower aerial robots follow it in the desired formation. These processes were confirmed by examining different graphs. In the first scenario, the starting position of the leader robot after the formation was (6.3, -4.3).

The leader robot moved to (8.7, -3.5), and the other robots followed it. The appearance of the robots in their initial positions is shown in Figure 6.

As seen in Figure 6, the robots wait at the starting point by forming the desired formation. The path graph of the robots is shown in Figure 7.

Figure 7 shows that the robots move from the starting point to the endpoint by maintaining the formation. The graph of the position errors of the follower robots as they move along the path is shown in Figure 8.

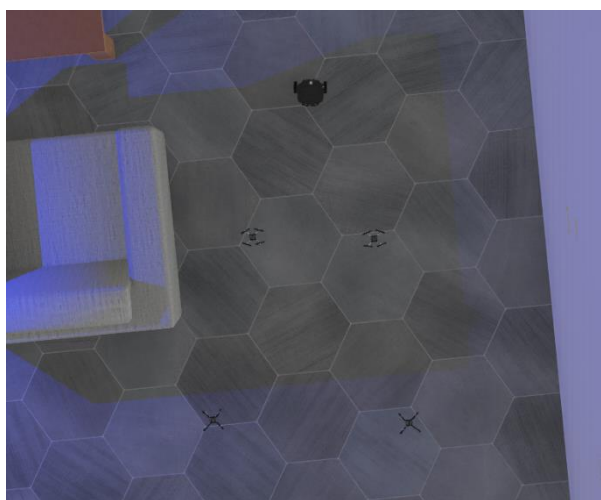


Figure 6. Initial Positions of Robots

the newly calculated formation points and the old ones. The final position of robots shown in Figure 9.



Figure 9. Final Positions of Robots

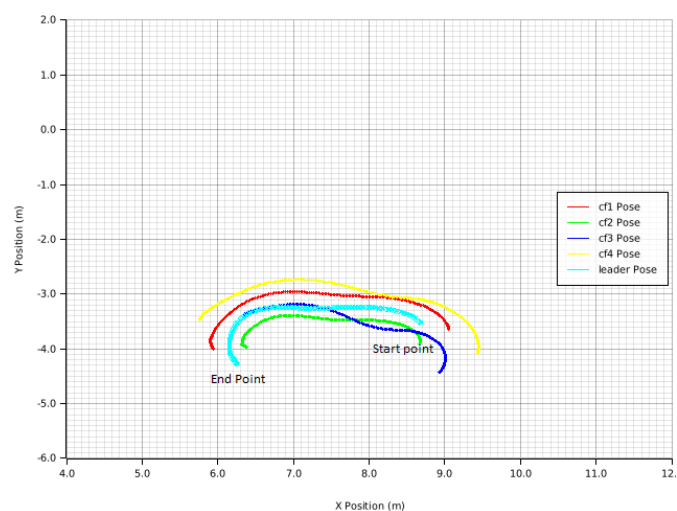


Figure 7. Scenario 1 the path Robots Follow for Approach 1

A similar experiment was performed for the second approach. The graph of the path followed by the robots is given in Figure 10.

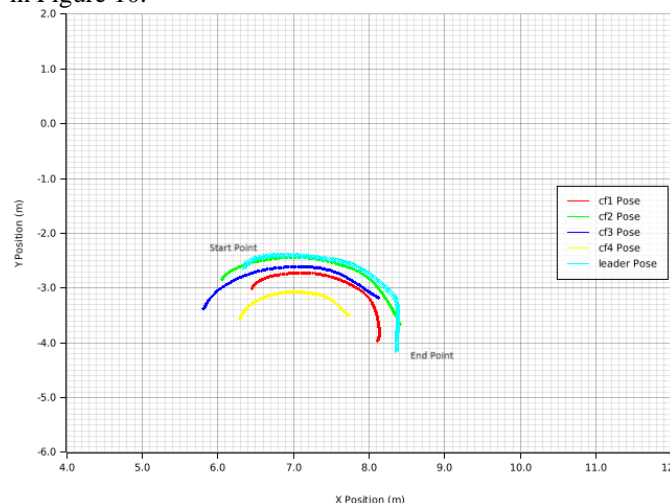


Figure 10. Scenario 1 The path robots follow for Approach 2

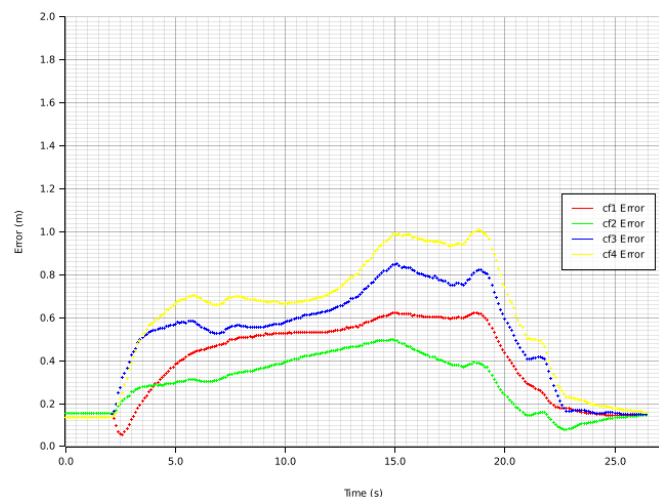


Figure 8. Scenario 1 Position Error of Followers for Approach 1

The position errors of the follower robots are shown in Figure 11.

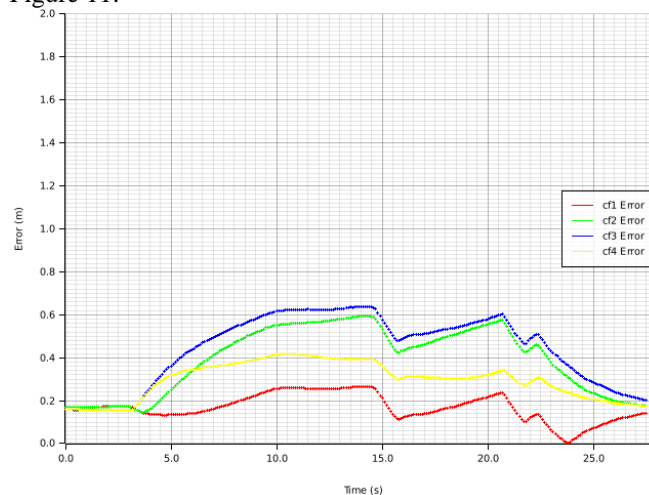


Figure 11. Scenario 1 Position Error of Followers for Approach 2

The error of about 0.17, consistently observed before and after the navigation starts and ends, is due to the robots' use of the artificial potential field algorithm. The error rate increases steadily in the navigation process because the Turtlebot 3 is more agile and faster. During the rotation, there are significant jumps in the error due to the increase in the difference between

Figure 11 shows that the position error decreased. In the second approach, the leader's changing orientation less affects the formation structure.

In the second scenario, robots were requested to follow different paths in the same environment. The starting and target points of the robots were changed, and their path and position errors were analyzed. Again, while moving along this path, the position errors increase, especially where the leader robot makes turns. In this scenario, unlike the first one, Rviz images of the start and end positions of the robots are also added. The path graph of the robots is shown in Figure 12.

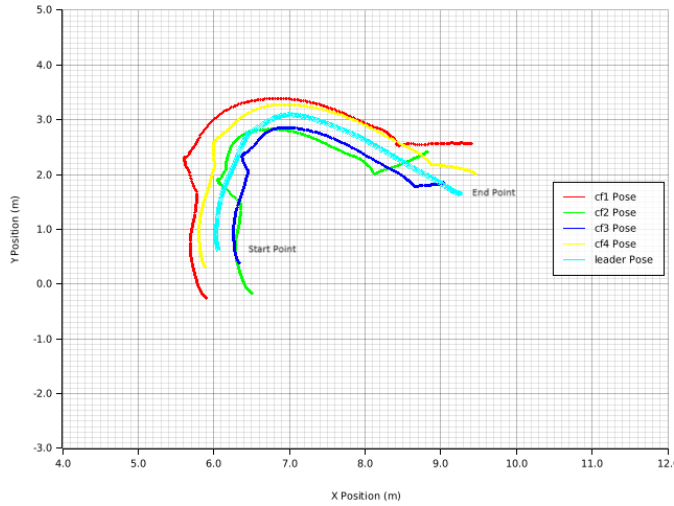


Figure 12. Scenario 2 The Path Robots Follow for Approach 1

For Scenario 2, the graph of the position errors of the follower robots as they move along the path is shown in Figure 12.

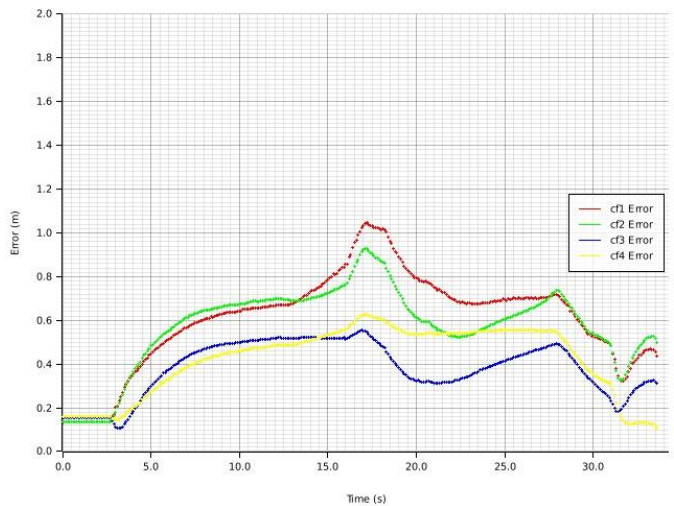


Figure 12. Scenario 2 Position Error of Followers for Approach 1

The Rviz image of the initial positions of the robots is shown in Figure 13. And the Rviz image of the final positions of the robots is shown in Figure 14.

For approach 2, the path graph of the robots is shown in Figure 15. The position errors along the path of the follower robots are shown in Figure 16. Examining the outcomes from this particular scenario, it becomes evident that the second approach yields significantly more favorable results.

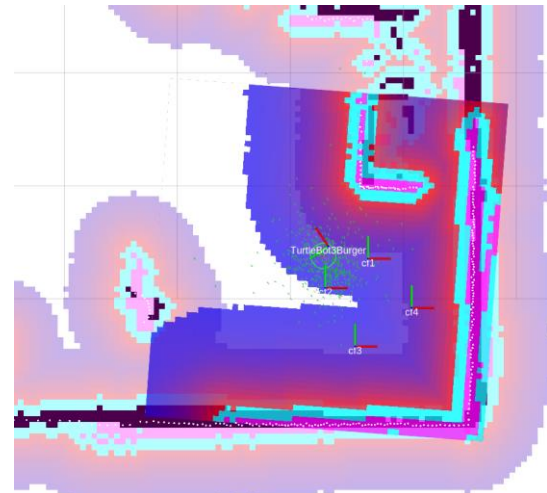


Figure 13. Rviz Image of Initial Positions of Robots

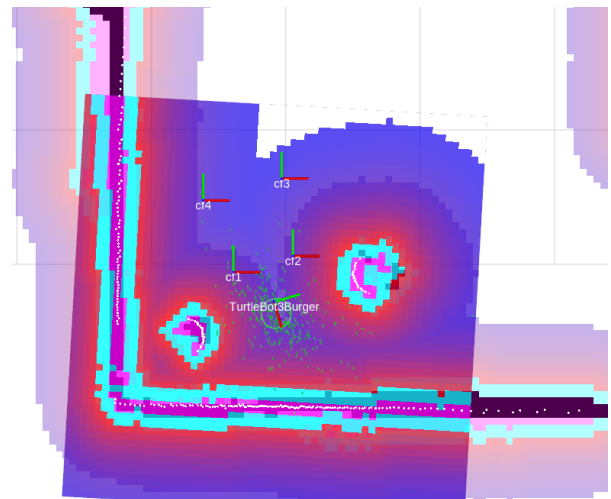


Figure 14. Rviz Image of Final Positions of Robots

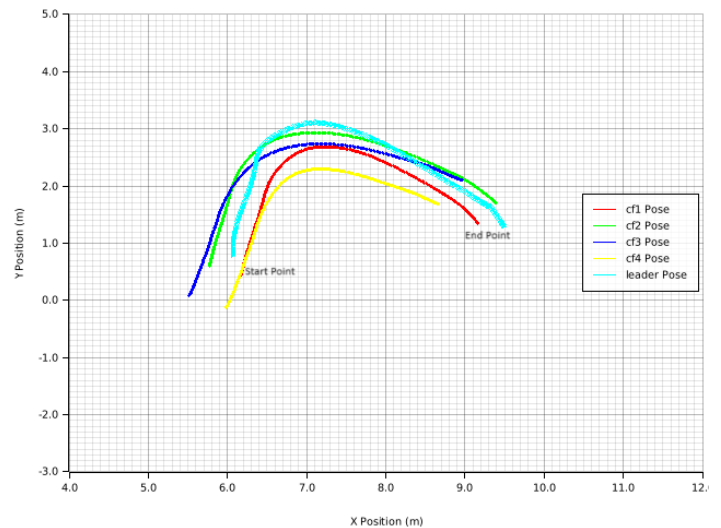


Figure 15. Scenario 2 The Path Robots Follow for Approach 2

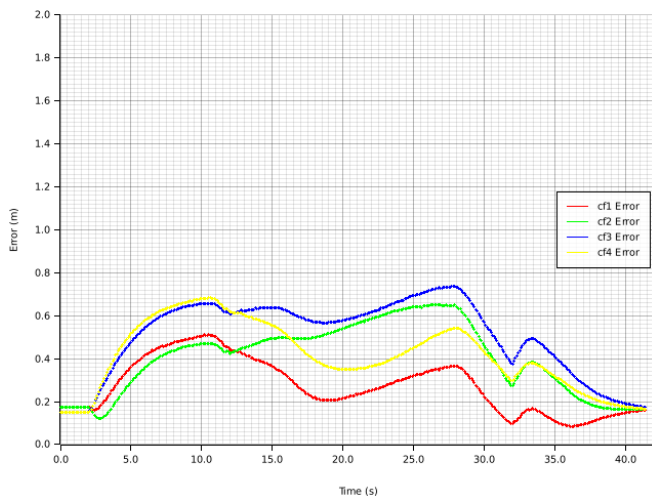


Figure 16. Scenario 2 Position Error of Followers for Approach 2

4. CONCLUSION

This study focused on implementing formation control for a heterogeneous multi-robot ensemble comprising ground and aerial robots. The strategy employed for formation was the leader-follower approach, wherein a ground robot assumed the role of the leader while the aerial robots operated as followers. A centralized control system was adopted to oversee the entirety of the study. Data received from the robot group were aggregated at a central point, where subsequent decisions were rendered. The formation configuration adopted for the robots was a V-shaped pattern. Following the determination of formation points based on the number of robots, the allocation of robots to their respective positions was achieved by applying the Hungarian algorithm. The experimental evaluation of this study was conducted within the Webots simulation environment, using Turtlebot3 and Crazyflie robots as the testbed.

During the experimental phase conducted within the test environment, an equal number of robots were deployed for each approach, with variations introduced into the traversed paths. Upon a comprehensive examination of the path trajectories and position errors associated with each approach, it becomes evident that both strategies effectively preserve the desired formation. However, distinctions emerge in their responses to specific factors. In the first approach, the formation tends to show more sensitivity when the leader robot makes a rotational movement. The second approach, characterized by a more centrally weighted reference point, displays a higher resilience in the face of such rotational deviations. Analyzing the position error data further reinforces the notion that the second approach surpasses the first in performance. Different formation strategies can be applied in future studies, and a distributed system can be preferred instead of a centralized one. Furthermore, different formation shapes can be applied in future research work beyond the V formation.

REFERENCES

- [1] S. Çaşka and A. Gayretli, "A survey of UAV/UGV collaborative systems," *CIE44 IMSS*, vol. 14, pp. 453–463, 2014.
- [2] Y. Lu, Z. Xue, G.-S. Xia, and L. Zhang, "A survey on vision-based UAV navigation," *Geo-spatial Inf. Sci.*, vol. 21, no. 1, pp. 21–32, 2018.
- [3] K. A. Ghamry and Y. Zhang, "Formation control of multiple quadrotors based on leader-follower method," in *2015 International Conference on Unmanned Aircraft Systems (ICUAS)*, 2015, pp. 1037–1042.
- [4] Y. Tian *et al.*, "Search and rescue under the forest canopy using multiple UAVs," *Int. J. Rob. Res.*, vol. 39, no. 10–11, pp. 1201–1221, 2020.
- [5] D. Kingston, R. W. Beard, and R. S. Holt, "Decentralized perimeter surveillance using a team of UAVs," *IEEE Trans. Robot.*, vol. 24, no. 6, pp. 1394–1404, 2008.
- [6] R. Ritz and R. D'Andrea, "Carrying a flexible payload with multiple flying vehicles," in *2013 IEEE/RSJ International Conference on Intelligent Robots and Systems*, 2013, pp. 3465–3471.
- [7] W. Cheng, B. Jiang, K. Zhang, and S. X. Ding, "Robust finite-time cooperative formation control of UGV-UAV with model uncertainties and actuator faults," *J. Franklin Inst.*, vol. 358, no. 17, pp. 8811–8837, 2021.
- [8] Z. A. Ali, A. Israr, E. H. Alkhamash, and M. Hadjouni, "A leader-follower formation control of multi-UAVs via an adaptive hybrid controller," *Complexity*, vol. 2021, pp. 1–16, 2021.
- [9] R. Rafifandi, D. L. Asri, E. Ekawati, and E. M. Budi, "Leader-follower formation control of two quadrotor UAVs," *SN Appl. Sci.*, vol. 1, pp. 1–12, 2019.
- [10] E. dos Santos Cardoso and V. Bacheti, "Package Delivery Based on the Leader-Follower Control Paradigm for Multirobot Systems."
- [11] N. H. M. Li and H. H. T. Liu, "Formation UAV flight control using virtual structure and motion synchronization," in *2008 American Control Conference*, 2008, pp. 1782–1787.
- [12] Y. Zhang and H. Mehrjerdi, "A survey on multiple unmanned vehicles formation control and coordination: Normal and fault situations," in *2013 International conference on unmanned aircraft systems (ICUAS)*, 2013, pp. 1087–1096.
- [13] S. Zhou, X. Dong, Q. Li, and Z. Ren, "Time-varying formation tracking control for UAV-UGV heterogeneous swarm systems with switching directed topologies," in *2020 IEEE 16th International Conference on Control & Automation (ICCA)*, 2020, pp. 1068–1073.
- [14] V. P. Bacheti, A. S. Brandao, and M. Sarcinelli-Filho, "A path-following controller for a uav-ugv formation performing the final step of last-mile-delivery," *IEEE Access*, vol. 9, pp. 142218–142231, 2021.
- [15] Y. Li and X. Zhu, "Design and testing of cooperative motion controller for UAV-UGV system," *Mechatronics Intell. Transp. Syst.*, 2022.
- [16] E. H. C. Harik, F. Guérin, F. Guinand, J.-F. Brethé, and H. Pelvillain, "UAV-UGV cooperation for objects transportation in an industrial area," in *2015 IEEE International Conference on Industrial Technology (ICIT)*, 2015, pp. 547–552. doi: 10.1109/ICIT.2015.7125156.
- [17] E. Arkin and Y. Şahin, "Q-Learning Based Obstacle Avoidance Data Harvesting Model Using UAV and UGV," *Eur. J. Tech.*, vol. 13, no. 1, pp. 54–60.
- [18] K. Aram, G. Erdemir, and B. Can, "Türkçe Dogal Dil Isleme Ile Ozerk Gezgin Robotun Yol Planlamasi, Path Planning of an Autonomous Mobile Robot by Turkish Natural Language Processing."
- [19] M. Quigley *et al.*, "ROS: an open-source Robot Operating System," in *ICRA workshop on open source software*, 2009, vol. 3, no. 3.2, p. 5.
- [20] L. Joseph and J. Cacace, *Mastering ROS for Robotics Programming: Design, build, and simulate complex robots using the Robot Operating System*. Packt Publishing Ltd, 2018.
- [21] Z. Tüfekçi and G. Erdemir, "Experimental Comparison of Global Planners for Trajectory Planning of Mobile Robots in an Unknown Environment with Dynamic Obstacles," in *2023 5th International Congress on Human-Computer Interaction, Optimization and Robotic Applications (HORA)*, 2023, pp. 1–6.
- [22] M. Quigley, B. Gerkey, and W. D. Smart, *Programming Robots with ROS: a practical introduction to the Robot Operating System*. "O'Reilly Media, Inc.," 2015.
- [23] O. Michel, "Cyberbotics Ltd. webots™: professional mobile robot simulation," *Int. J. Adv. Robot. Syst.*, vol. 1, no. 1, p. 5, 2004.
- [24] A. Farley, J. Wang, and J. A. Marshall, "How to pick a mobile robot simulator: A quantitative comparison of CoppeliaSim, Gazebo, MORSE and Webots with a focus on accuracy of motion," *Simul. Model. Pract. Theory*, vol. 120, p. 102629, 2022.
- [25] C. Williams and A. Schroeder, "Utilizing ROS 1 and the Turtlebot3 in a Multi-Robot System," 2020.
- [26] W. Hönig and N. Ayanian, "Flying multiple UAVs using ROS," *Robot Oper. Syst. Complet. Ref. (Volume 2)*, pp. 83–118, 2017.
- [27] W. Giernacki, M. Skwierczyński, W. Witwicki, and P. Wroński

- Pawel and Koziarski, "Crazyflie 2.0 quadrotor as a platform for research and education in robotics and control engineering," in *2017 22nd International Conference on Methods and Models in Automation and Robotics (MMAR)*, 2017, pp. 37–42.
- [28] Y. Liang, D. Qi, and Z. Yanjie, "Adaptive leader-follower formation control for swarms of unmanned aerial vehicles with motion constraints and unknown disturbances," *Chinese J. Aeronaut.*, vol. 33, no. 11, pp. 2972–2988, 2020.
- [29] J. Luo, C.-L. Liu, and F. Liu, "A leader-following formation control of multiple mobile robots with obstacle," in *2015 IEEE International Conference on Information and Automation*, 2015, pp. 2153–2158.
- [30] V. Walter, N. Staub, A. Franchi, and M. Saska, "Uvdar system for visual relative localization with application to leader-follower formations of multirotor uavs," *IEEE Robot. Autom. Lett.*, vol. 4, no. 3, pp. 2637–2644, 2019.
- [31] Y. Ziquan, Y. Zhang, B. Jiang, F. U. Jun, and J. I. N. Ying, "A review on fault-tolerant cooperative control of multiple unmanned aerial vehicles," *Chinese J. Aeronaut.*, vol. 35, no. 1, pp. 1–18, 2022.
- [32] M. J. Hong and M. R. Arshad, "A balance-artificial potential field method for autonomous surface vessel navigation in unstructured riverine environment," *Procedia Comput. Sci.*, vol. 76, pp. 198–202, 2015.
- [33] J. A. Preiss, W. Honig, G. S. Sukhatme, and N. Ayanian, "Crazyswarm: A large nano-quadcopter swarm," in *2017 IEEE International Conference on Robotics and Automation (ICRA)*, 2017, pp. 3299–3304.

BIOGRAPHIES

Kadir Aram obtained his BSc and MSc degree in computer and control education Marmara University. He completed his PH.D. in Computer Science and Engineering at Istanbul Sabahattin Zaim University in 2023. He is research assistant in Computer Engineering department at Fatih Sultan Mehmet Vakif University. His research interest are mobile robotics and natural language processing.

Abdulmelik Bekmez is currently studying in his bachelor's degree in the Department of Computer Engineering, Engineering Faculty, at the Fatih Sultan Mehmet Vakif University. His current research areas include robotics and formation control.



Research Article

Investigating the Relationship between Chuck and Tailstock Pressure in Turning by Using Full Factorial Design

Hüseyin GÜRBÜZ¹ , Şehmus BADAY² 

¹Batman University, Mechanical Engineering Department, Batman, Turkey. (e-mail: huseyin.gurbuz@batman.edu.tr).

²Batman University, Mechanical Engineering Department, Batman, Turkey (e-mail: sehmus.baday@batman.edu.tr).

ARTICLE INFO

Received: Sep., 13. 2023

Revised: Oct., 04. 2023

Accepted: Oct.,11. 2023

Keywords:

Full Factorial Design

ANOVA

Chuck pressure

Tailstock pressure

Surface roughness

Corresponding author: Hüseyin GÜRBÜZ

ISSN: 2536-5010 / e-ISSN: 2536-5134

DOI: <https://doi.org/10.36222/ejt.1359803>

ABSTRACT

The failure of the workpieces to be attached to the lathe at a suitable chuck and tailstock pressure values causes to the run-out rotation of the workpiece and surface irregularities, resulting in deterioration of the dimensional accuracy and surface roughness values. In order to eliminate such negativities, it is quite important to determine the ideal chuck and tailstock pressure values. The aim of this study is to obtain the lowest surface roughness value by determining the relations between the chuck and tailstock pressure and their optimum pressure via using a 2^k full factorial design. In order to see the effect of chuck and tailstock pressure, the experiments were repeated 3 times at the lowest and highest chuck and tailstock pressures determined in the constant cutting parameters of AISI 304 stainless steel. For the surface roughness values obtained as a result of 3 repetitions, the full factorial design, the optimum chuck and tailstock pressure and their relations with each other were determined with ANOVA table. According to the results of full factorial design and ANOVA, chuck and tailstock pressure and their relations with each other were found significant. The most effective parameters on surface roughness were obtained as chuck pressure, tailstock pressure and chuck- tailstock pressure, respectively. According to the full factorial design results, it was determined that the lowest surface roughness values were obtained at 17 chuck pressure and 5 tailstock pressure. The R² value obtained in the factorial regression was 98.24% and the corrected R² value was 96.77%. As a result, it is understood that the full factorial design is an efficient and effective method in determining the chuck and tailstock pressure.

1. INTRODUCTION

In machining, the requirements for correct machining of a workpiece include the correct attachment of the workpiece to the machine. Failure in attachment of a workpiece at ideal tailstock and chuck pressure will increase the vibrations, oscillations and stretching that will occur while the workpiece is being machined, resulting in undesirable high surface roughness values on the workpiece. The aim of the manufacturing process is to obtain parts with an ideal surface roughness according to a certain tolerance and accuracy level, both in terms of low cost and time, as well as geometry and dimensional. While the workpieces are being machined, the first step in eliminating the undesirable high surface roughness values is the attaching of the workpiece with a correct chuck and tailstock pressure. In order to evaluate the surface roughness results obtained while machining a workpiece, statistical tools should be used, which provides great convenience in terms of both time and cost, especially by

reducing the number of experiments. The first of these is the full factorial design (FFD). Experiment design methods are often preferred in the evaluation of the results obtained in turning experiments. These methods are used to determine the effect of control factors on the response and their relationships with each other. One of the experimental design methods used in the literature to evaluate the test results and to select the optimum parameters is FFD. In the literature, there are very few studies on the evaluation of surface roughness results with FFD, and the studies conducted are summarized below:

Kechagias et al. used FFD for the estimation of machinability in turning titanium alloys. According to the FFD results, they determined that the most important effect on the surface roughness is the feed rate, while the least effect is the depth of cut [1]. Athreya et al. investigated the effect of cutting parameters on surface roughness in turning medium carbon steel using FFD. In their FFD study, the authors obtained optimum surface roughness results using less number of experiments, when the cutting speed was 960 rpm,

the feed rate was 145 mm/rev and the depth of cut was 0.3 mm. In addition, they also performed a confirmation test for the validity of the experimental results in their study [2]. Das et al. used FFD to evaluate the surface roughness results in hard turning of AISI 4340 steel. According to FFD results, the authors determined that the most effective parameters on the surface roughness at the 95% confidence interval were the feed rate and the cutting speed, respectively. They also revealed that the two-level interactions of depth of cut-cutting speed, depth of cut-feed rate and feed rate-depth of cut have significant effects on surface roughness [3]. Leksycki and Feldshtein revealed the effect of machining parameters on the surface roughness values obtained in turning of AISI 316L steel using FFD. According to FFD results, the authors revealed that not only the feed rate and cutting speed but also the dual interaction, namely cutting speed-feed rate, is effective on the surface roughness [4]. Rafidah et al. carried out a study revealing the effect of surface roughness measurement parameters on surface roughness values using FFD. According to FFD results, the authors determined that the temperature, sampling length and cut of length parameters had no effect on the surface roughness values [5]. Vikram et al., using FFD, demonstrated the effect of cutting parameters on the surface roughness results obtained in turning brass material with HSS and carbide cutting tools. The authors found that cutting speed and feed rate had a significant effect on the surface roughness values, but the cutting speed-feed rate was less effective in their dual interaction [6].

When the literature is examined, very few experimental and statistical studies have been carried out with FFD, which is one of the experimental design methods, to determine the effects of cutting parameters on surface roughness [1-6]. At the same time, both experimental and statistical studies are available in the literature to reveal the effect of cutting conditions and cutting parameters on surface roughness [7-12]. However, no statistical study has been conducted with FFD to determine the effect of chuck and tailstock pressure on surface roughness values. Only a few studies on optimization have been carried out to determine the effect of chuck and tailstock pressure on surface roughness values [13-16]. With this experimental and statistical study, the optimum chuck and tailstock pressure will be determined, and it will contribute to those who will work on turning with the results obtained by reducing the machining costs in terms of both time and cost.

2. MATERIALS AND METHOD

2.1. Workpiece material, cutting tools and tool holder

In this research, AISI 304 stainless steel, which is the most widely used in the stainless steel group and has good corrosion resistance, was used as the workpiece material. The workpieces were supplied with a diameter of 36 mm, then they were first reduced to 35 mm in diameter on the CNC lathe in order to eliminate external negativities on the surface, and finally they were prepared with a length of 300 mm so that each workpiece could be processed under equal test conditions. The chemical composition in terms of weight percentage and hardness value of the workpiece are shown in Table 1.

TABLE I

Chemical composition and hardness value of the workpiece material

% Cr	% C	% Si	% Mn	% P
19.50-17.50	0.070-0.024	1.00-0.39	2.0-1.45	0.045-0.036
% N	% Ni	% Co	% S	Hardness
0.100-0.085	10.50-8.00	0.15(max)	0.030-0.029	215 HB

WNMG 080408-OMM PVD-coated inserts with positive rake angle were selected for the machining of AISI 304 austenitic stainless steel at different cutting parameters on a CNC lathe. PWLNR 2525M08 tool holder suitable for these inserts was used. The cutting tips and tool holder were obtained from the OKE cutting tool manufacturer Fidan Cutting Tool Company. Shapes of carbide inserts and tool holder are given in Figure 1.



Figure 1. a) WNMG cutting tool used in the experiments b) PWLNR 2525M08 tool holder

2.2. Cutting parameters and machine tool

Machining experiments were carried out on TAKISAWA EX-310 brand CNC lathe. In the selection of the cutting parameters used in the machining experiments, the experimental set was created by taking into account the cutting tool catalog values and ISO 3685 standards, which are the recommendations of the manufacturer cutting tool company. In the experiments, the constant feed rate, the cutting speed and the depth of cutting were determined as 0.2 mm/rev, 250 m/min and 2 mm, respectively. Machining experiments were carried out using five different chuck and tailstock pressures at constant cutting parameters. Chuck and tailstock pressure were determined as variable parameters and shown in Figure 2.

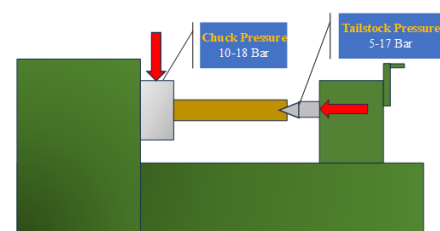


Figure 2. Parameters used in the experiments

The numerical values of the chuck and tailstock pressure and cutting parameters used in the turning experiments are given in Table 2.

TABLE II

Cutting parameters used in machining experiments

Chuck Pressure, P (bar)	10 - 18
Tailstock Pressure, P (bar)	5 - 17
Depth of cut, a (mm)	2
Feed rate (mm/rev)	0.2
Cutting Speed, V (m/min)	250

2.3. Surface Roughness Measurement

The surface roughness values on the workpiece surface resulting from the machining experiments were measured using a portable TR 200 measuring device. In determining surface roughness values, five different measurement zones were determined on the workpiece surface. Average surface roughness values were determined from each measurement

region with a measurement length of 5.6 mm. The average surface roughness values of the workpiece were calculated by taking the arithmetic average of the 5 detected surface roughness values. The experimental setup established to see the effect of chuck and tailstock pressure on surface roughness values in turning AISI 304 steel at constant cutting parameters is shown in Figure 3.

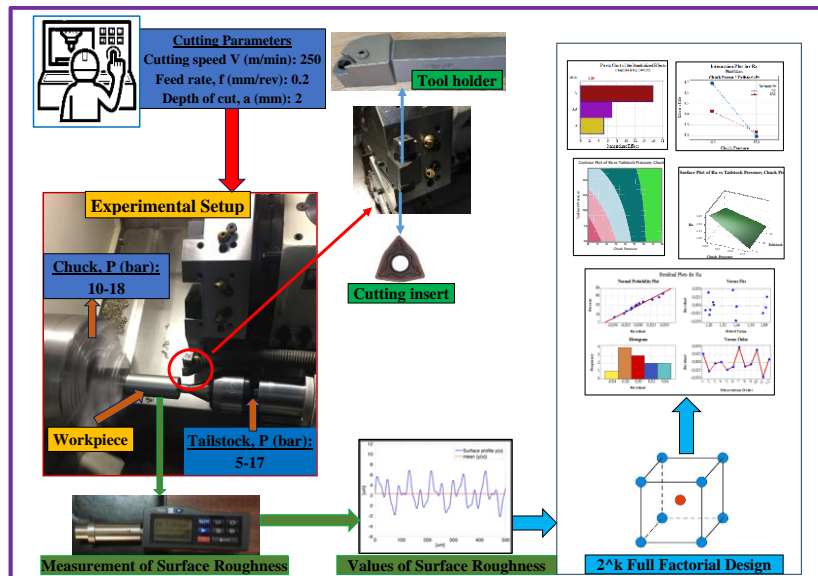


Figure 3. Schematic representation of the experimental setup.

2.4. Full Factorial Design (FFD)

FFD, a statistical methodology, was used in the experimental design, which was used to see the effect of chuck and tailstock pressure on the surface roughness of the experimental study. FFD is an experimental design method used to see the effects of 2 or more factors both separately and with each other. Full factorial regression is performed to show the effects of control factors on response [2, 4]. In this study, while the chuck and tailstock pressures were taken as control factors, the surface roughness values were taken as the response. FFD was performed to reveal the separate and dual relations on the surface roughness, which is the response of these control factors.

2.5. ANOVA

In ANOVA, which is a statistical method, there are two types of variables: control factors and response values. The purpose of ANOVA is to determine how effective the control factors are on the response value. The importance of control factors in ANOVA is determined according to the P values of each control factor in ANOVA table. If the P value is less than 0.05, it is significant, if the P value is greater than 0.05, it is meaningless. An ANOVA table generally includes: sum of squares (SS), degrees of freedom (DF), mean of squares (MS), significance level (P) and statistical (F) values [17-19].

3. RESULTS AND DISCUSSION

In this experimental study, the surface roughness values were optimized by using 2^2 FFD method with 3 repetitions by connecting the workpieces to the CNC lathe at the lowest and

highest chuck and tailstock pressures at constant cutting parameters. Surface roughness tests were carried out on a CNC lathe by taking two factors and the lowest and highest chuck and tailstock pressures in 3 repetitions. Considering the surface roughness values as the response, chuck and tailstock pressure as the control factors, and the lowest and highest levels of these factors, the relationships between these two factors on the response were revealed. The control factors used in the turning experiments and their minimum and maximum values are given in Table 3.

TABLE III
Minimum and maximum control factors

Factors	Low	High
Chuck Pressure	10	18
Tailstock Pressure	5	17

3.1. FFD Results

Surface roughness values obtained from the surfaces of the workpiece machined in constant machining parameters on the CNC lathe, control factors and the lowest and highest values of these control factors are given in Table 4. The experiment carried out and the 3 replications of these experiments and the order of the experiments for these blocks are also shown in Table 4. The Main Effects Plot graph showing the effects of the lowest and highest chuck and tailstock pressure on the surface roughness is given in Figure 4. When the Main Effect Plot in Figure 4 is examined, it is seen that the chuck and tailstock pressure have an effect on the surface roughness. It is seen in the graph in Figure 4 that as the chuck pressure value increases, the surface roughness values decrease, while the surface

roughness values decrease as the tailstock pressure values increase.

TABLE IV

2² (2^k) Full Factorial Design and 3 repetitive surface roughness values.

Run Order	Chuck Pressure, Bar	Tailstock Pressure, Bar	Surface Roughness, Ra (µm)	Prediction, Ra (µm)
1	1	10	5	1.735
2	1	18	5	1.179
3	1	10	17	1.441
4	1	18	17	1.247
5	2	10	5	1.651
6	2	18	5	1.159
7	2	10	17	1.458
8	2	18	17	1.199
9	3	10	5	1.695
10	3	18	5	1.240
11	3	10	17	1.391
12	3	18	17	1.248

In addition, it is clearly understood that the chuck pressure is more effective on the surface roughness than the tailstock pressure, due to the larger vertical distance between the mean lower and upper values.

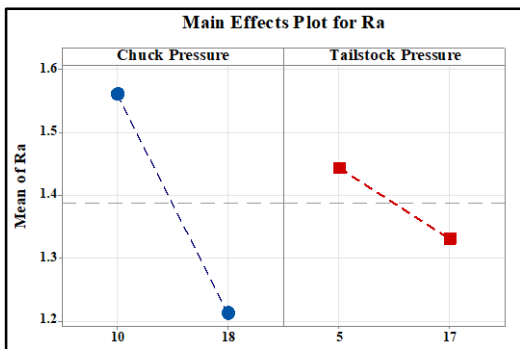


Figure 4. Main Effect Plots for Surface Roughness

The interaction plot graph showing the relationships between these factors is shown in Figure 5.

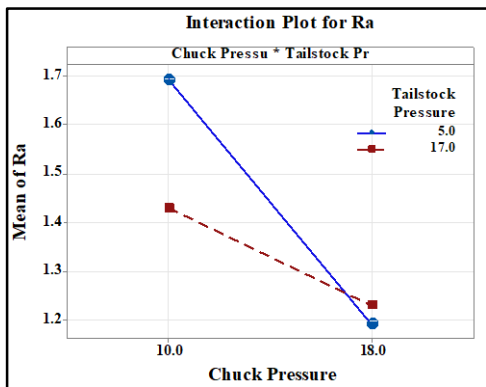


Figure 5. Interaction Plot for Surface Roughness

Interaction graph showing the effect between chuck and tailstock pressure is given in Figure 5. When the graph in the figure is examined, it is seen that there is a relationship between chuck and tailstock pressure. Since the blue line and the dashed maroon line intersect in this stage, it can be said that the chuck-tailstock pressure dual relationship is effective on the surface

roughness. As can be seen from the graph, it was determined that the chuck pressure intersects at 17 bar and the tailstock pressure at 5 bar and there is a high relationship between these values. The full factorial regression results performed according to the lowest and highest values of chuck and tailstock pressure are given in Table 5.

TABLE V

FFD regression results

Term	Effect	Coef	SE Coef	95% CI	T-Value	P-Value	VIF	
Constant		1.3869	0.0109	(1.3603; 1.4136)	127.29	0.000		
Blocks								
1		0.0136	0.0154	(-0.0241; 0.0513)	0.88	0.412	1.33	
2		-0.0202	0.0154	(-0.0579; 0.0175)	-1.31	0.239	1.33	
Chuck Pr. (A)		-0.3498	-0.1749	0.0109	(-0.2016; -0.1483)	-16.05	0.000	1.00
Tailstock Pr. (B)		-0.1125	-0.0563	0.0109	(-0.0829; -0.0296)	-5.16	0.002	1.00
A*B		0.1512	0.0756	0.0109	(0.0489; 0.1022)	6.94	0.000	1.00

The equation obtained as a result of factorial regression is given in Equation 1 below. This equation was formed as a result of the interaction of chuck pressure, tailstock pressure and chuck*tailstock pressure. R² value of the equation estimating the surface roughness values is 98.24% and the corrected R² value is 96.77%. According to R² results of the equation estimating the surface roughness values, factorial regression was found to be successful.

$$Ra = 2.5872 - 0.07837 \text{ Chuck Pressure} - 0.05347 \text{ Tailstock Pressure} + 0.003149 \text{ Chuck Pressure} \times \text{Tailstock Pressure} \quad (1)$$

3.2. ANOVA results

ANOVA (Analysis of Variance) is a statistical tool that reveals the effect of control factors on response. In this experimental study, chuck and tailstock pressures were taken as control factors, while surface roughness values were taken as a response. ANOVA results based on Full Factorial regression depending on the lowest and highest chuck and tailstock pressure are given in Table 6.

Table VI ANOVA results

Source	DF	Seq SS	Cont.	Adj SS	Adj MS	F-Value	P-Value
Model	5	0.476211	98.24%	0.476211	0.095242	66.85	0.000
Blocks	2	0.002538	0.52%	0.002538	0.001269	0.89	0.458
Linear	2	0.405119	83.57%	0.405119	0.202559	142.18	0.000
Chuck Pressure	1	0.367150	75.74%	0.367150	0.367150	257.71	0.000
Tailstock Pressure	1	0.037969	7.83%	0.037969	0.037969	26.65	0.002
2-Way Interac.	1	0.068554	14.14%	0.068554	0.068554	48.12	0.000
Chuck*Tai lstock	1	0.068554	14.14%	0.068554	0.068554	48.12	0.000
Error	6	0.008548	1.76%	0.008548	0.001425		
Total	11	0.484759	100.00%				

Whether the control factors in the ANOVA table and their relations with each other are statistically significant can be expressed by whether P-Value value is less than 0.05 [17-19]. When the "P-values" in Table 6 are examined, it can be concluded that only not the "Blocks" value is statistically significant but also the others are significant. In order to understand which control factor has the greatest effect on surface roughness, when the "contribution" values in Table 6 are examined, it will be seen that it is chuck pressure with 75.74%. This value is then followed by the chuck-tailstock pressure at the rate of 14.14%, while the tailstock pressure with the least effect is followed by 7.83%. "F-value" value in ANOVA table is a value that shows the effect of control factors on the response. A high F-value indicates that that value is very effective on the response. In this context, it can be said that the chuck pressure has the greatest effect on surface roughness. The Pareto chart showing the effect of chuck and tailstock pressure on the surface roughness is given in Figure 6.

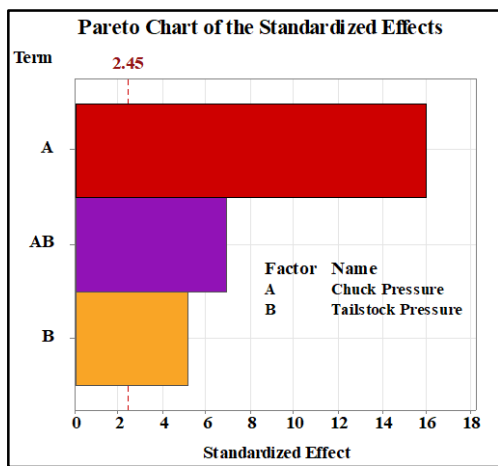


Figure 6. Pareto Chart for Ra values

When the Pareto chart of standardized effects in Figure 6 are examined, it is understood that the parameters that affect the surface roughness most are A (Chuck pressure) and AB (Chuck-tailstock pressure) and finally B (tailstock pressure) from top to bottom. In other words, it shows that the area that takes up the most space on the line is more effective on the surface roughness. The normal probability plot graph obtained as a result of the factorial regression is given in Figure 7.

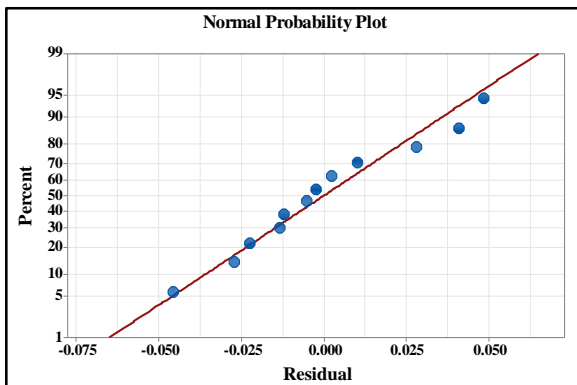


Figure 7. Normal probability plot for Ra values

When the graph in Figure 7 is examined, it is seen that the surface roughness values are estimated at very high rates since the values are collected around the normal probability plot linear line. The contour plot graph of the surface roughness created according to the FFD depending on the chuck and tailstock pressure is given in Figure 8.

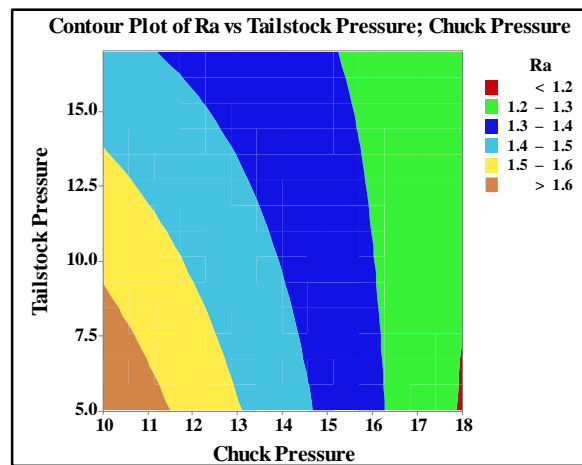


Figure 8. Contour plot

When the contour plot graph in Figure 8 is examined, each color range and area represent the surface roughness value. It is seen that the lowest surface roughness values occur when the chuck pressure is between 17 and 18 and the tailstock pressure is between 5 and 7. It can be seen from this graph that as the chuck pressure increases and the tailstock pressure decreases, the surface roughness values decrease. The surface plot graph showing the effect of chuck and tailstock pressure on the surface roughness is given in Figure 9.

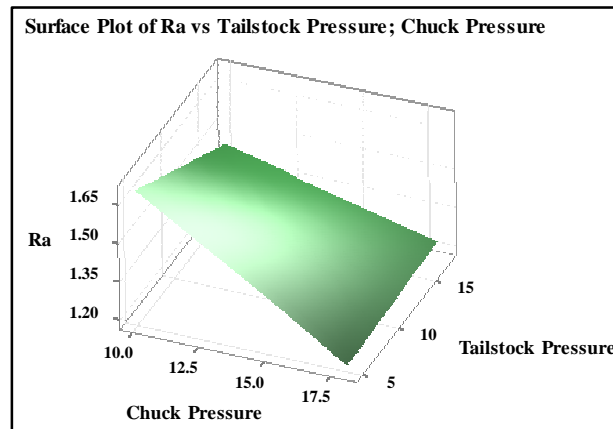


Figure 9. Surface plot for surface roughness values

When the surface response graph in Figure 9 is examined, it is understood that the lowest surface roughness value is 18 bars at chuck pressure and 5 bars at tailstock pressure. In addition, it is understood that the chuck pressure is more effective on the surface roughness than the tailstock pressure. As the chuck pressure decreases, the surface roughness values increase; on the other hand, the surface roughness values increase as the tailstock pressure values increase. In other words, chuck and tailstock pressure affect the surface roughness inversely proportionally. While it is recommended to use high chuck pressures for low surface roughness values,

the opposite should be preferred for tailstock pressure. The graphics and values obtained with the multiple response performed to obtain the optimum chuck and tailstock pressure in order to minimize the surface roughness are given in Figure 10.

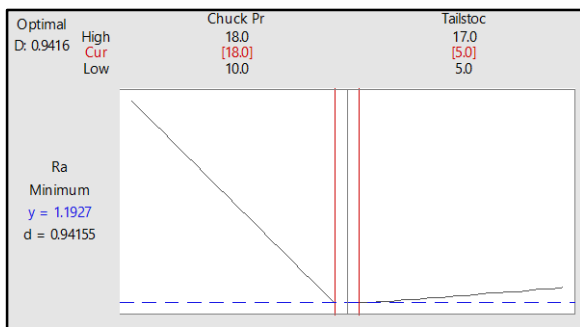


Figure 10. Optimization results for Ra values

When the graph obtained according to the surface response method in Figure 10 is examined, it is seen that the values that minimize the surface roughness value are 18 bar for the chuck pressure and 5 bar for the tailstock pressure. It is seen that the “y” value that minimizes the surface roughness value is 1.927, while the “d” value is 0.94155. It is understood that the values that minimize the surface roughness according to the chuck and tailstock pressure are high chuck pressure and low tailstock pressure. Figure 11 shows the comparison of the estimations and the actual values obtained according to the factorial regression results created to estimate the surface roughness values.

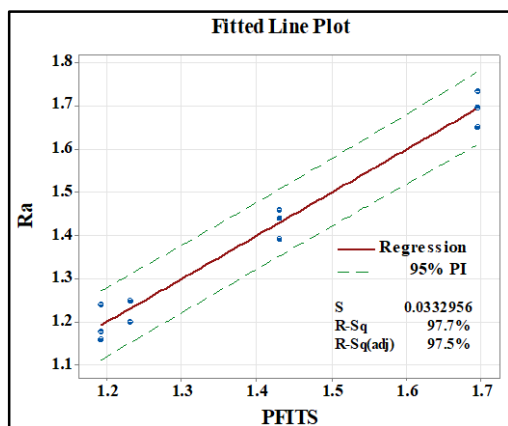


Figure 11. Fitted line plot chart

When the Fitted line plot graph in Figure 11 is examined, it is seen that the surface roughness and estimated values are at 95% confidence interval, while R^2 value is at 97.7%. It is clearly seen that the actual values and the predicted values are gathered around the fitted line and provide this confidence interval.

4. RESULTS

In this experimental and statistical study, FFD was used to reveal the effect of chuck and tailstock pressure on the surface roughness values formed as a result of turning AISI 304 austenitic stainless steel on a CNC lathe at constant cutting parameters. Obtained results are summarized below.

- According to the Main Effect Plot graph, it was determined that as the chuck pressure value increases, the surface roughness value decreases and as the tailstock pressure value increases, the surface roughness values decrease. In addition, it was observed that the chuck pressure is more effective than the tailstock pressure on the surface roughness.
- According to the Interaction graph showing the effect between the chuck and the tailstock pressure, it has been determined that there is a relationship between the chuck and tailstock pressure. At the same time, it can be said that the chuck and the tailstock pressure intersect at 17 and 5 bar, respectively; and there is a high correlation at these values.
- According to the ANOVA results, it was determined that the greatest effect on the surface roughness values was the chuck pressure with 75.74%, then the chuck-tailstock pressure with 14.14%; on the other hand, the least effect on surface roughness was the tailstock pressure with 7.83%. This situation is similarly obtained from the Pareto chart of standardized effects.
- Since the surface roughness values were collected around the linear line in the normal probability plot graph, it was observed that the surface roughness values are estimated at very high rates.
- When the fitted line plot graph was examined, it was determined that the surface roughness and estimated values are at the 95% confidence interval, and the R^2 value is 97.7%. In addition, it was determined that the actual and estimated values gathered around the fitted line and provided this confidence interval.
- When the multiple response graph was examined, it was determined that the chuck pressure was 18 bar and the tailstock pressure was 5 bar for the optimum surface roughness value.
- It was understood that the values that minimize the surface roughness according to the chuck and tailstock pressure are high chuck pressure and low tailstock pressure.
- According to the surface response graph, the lowest surface roughness value was determined to be at 18 bar chuck pressure and 5 bar tailstock pressure. In addition, it was understood that the effect of chuck pressure on surface roughness is more effective than tailstock pressure. While it was recommended to use high chuck pressures for low surface roughness values, the opposite should be preferred for tailstock pressure.
- When the contour plot graph was examined, it was seen that the lowest surface roughness values were in the range of chuck pressure, while the tailstock pressure was in the range of 5-7, and the surface roughness values decreased when the chuck pressure increased and the tailstock pressure decreased.

ACKNOWLEDGEMENT

The authors would like to thank TÜBİTAK (Support program: 2209/B industry-oriented undergraduate thesis support program), Yavuz Kardeşler Makine in Batman organized industry and Batman University Mechanical Engineering Department for providing all kinds of contributions and support in the realization of this study.

REFERENCES

- [1] Kechagias, J.D., Aslani, K.E., Fountas, N.A., Vaxevanidis, N.M., Manolakos, D.E., A comparative investigation of Taguchi and full factorial design for machinability prediction in turning of a titanium alloy, *Measurement*, (2020), 151, 107213.
- [2] Athreya, S., Venkatesh, Y.D., Application of Taguchi method for optimization of process parameters in improving the surface roughness of lathe facing operation, *International Refereed Journal of Engineering and Science*, (2012), 1(3), 13-19.
- [3] Das, S.R., Dhupal, D., Kumar, A., Experimental Study & Modeling of Surface Roughness in Turning of Hardened AISI 4340 Steel Using Coated Carbide Inserted, *International Journal of Automotive Engineering*, (2013), 3 (1), 284-292.
- [4] Leksycki, K., Feldshtein, E., Study of the finish turning process based on the Parameter Space Investigation method, *The International Journal of Advanced Manufacturing Technology*, (2023). 126:5487–5499.
- [5] Rafidah, A., Nurulhuda, A., Azrina, A., Suhaila, Y., Anwar, I. S., Syafiq, R.A., Comparison design of experiment (doe): Taguchi method and full factorial design in surface roughness. *Applied mechanics and materials*, (2014), 660, 275-279.
- [6] Vikram, K.A., Ratnam, C., Narayana, K.S., Ben, B.S., Assessment of surface roughness and MRR while machining brass with HSS tool and carbide inserts, *Indian Journal of Engineering and Materials Sciences*, (2015). 22, 321-330.
- [7] Liu, N., Liu, B., Jiang, H., Wu, S., Yang, C., Chen, Y., Study on vibration and surface roughness in MQCL turning of stainless steel. *Journal of Manufacturing Processes*, (2021), 65, 343-353.
- [8] Saliminia, A., Abootorabi, M.M., Experimental investigation of surface roughness and cutting ratio in a spraying cryogenic turning process, *Machining Science and Technology*, (2019), 23(5), 779-793.
- [9] Arbizu, I.P., Perez, C.L., Surface roughness prediction by factorial design of experiments in turning processes, *Journal of Materials Processing Technology*, (2003), 143, 390-396.
- [10] Singh, D., Rao, P.V., A surface roughness prediction model for hard turning process, *The International Journal of Advanced Manufacturing Technology*, (2007). 32, 1115-1124.
- [11] Çelik, Y.H., Kilickap, E., Güney, M., Investigation of cutting parameters affecting on tool wear and surface roughness in dry turning of Ti-6Al-4V using CVD and PVD coated tools, *Journal of the Brazilian Society of Mechanical Sciences and Engineering*, (2017), 39, 2085-2093.
- [12] Ferreira, R., Carou, D., Lauro, C.H., Davim, J.P., Surface roughness investigation in the hard turning of steel using ceramic tools, *Materials and Manufacturing Processes*, (2016), 31(5), 648-652.
- [13] Gürbüz, H., and Baday, Ş. Determination of the Effect of Tailstock and Chuck Pressure on Vibration and Surface Roughness in Turning Operations with Gray Relational Analysis Method, in: *Mechanical Engineering, Materials Science Research And Applications*, (Ed. ŞAHİN Y., et al.), Güven plus, İstanbul, 2022, 44-73.
- [14] Gürbüz, H., Baday, Ş., Sönmez, F., Evaluation of the Effect of Chuck and Tailstock Pressure on Machining Parameters in CNC Lathe by Response Surface Method, *Bitlis Eren University Journal of Science*, (2021), 10(1), 160-169.
- [15] Gürbüz, H., Baday, Ş., Optimization of Effect of Chuck and Tailstock Pressure on Surface Roughness and Vibration with Taguchi Method in CNC Lathes, *Bilecik Şeyh Edebali University Journal of Science*, (2019). 6(2), 119-134.
- [16] Gürbüz, H., Baday, Ş., Ertuğrul, İ., The Effect of Chuck and Tailstock Pressure on Surface Roughness and Vibration Values in CNC Turning Machine, *International Engineering and Science Symposium*, Siirt, Türkiye, 2019, 20-22.
- [17] Camposeco-Negrete, C., Optimization of cutting parameters for minimizing energy consumption in turning of AISI 6061 T6 using Taguchi methodology and ANOVA, *Journal of Cleaner Production*, (2013), 53, 195-203.

- [18] Kuntoğlu, M., Sağlam, H., Investigation of progressive tool wear for determining of optimized machining parameters in turning, *Measurement*, (2019), 140, 427-436.
- [19] Das, A., Patel, S.K., Hotta, T.K., Biswal, B.B., Statistical analysis of different machining characteristics of EN-24 alloy steel during dry hard turning with multilayer coated cermet inserts, *Measurement*, (2019), 134, 123-141.

BIOGRAPHIES

Hüseyin GÜRBÜZ completed completed a MSc degree in 2006 and a PhD degree in 2012, respectively, in the Department of Mechanical Education from Gazi University in Ankara, Turkey. He works as an associate professor in the Department of Mechanical Engineering of Faculty of Engineering and Architecture of Batman University, Batman, Turkey. Assoc. Prof. Gürbüz teaches the undergraduate and the postgraduate level courses at Batman university. His areas of interest are metal cutting, machinability, surface integrity, mechanics of metal cutting, cryogenic heat treatment and MQL on metal cutting and mathematical modeling of machining parameters. Gürbüz published many articles in national/international journals and proceedings presented and published in the international conferences. Also, he has served as researcher, project manager and advisor in various research projects.

Şehmus BADAY graduated from Department of Mechanical Education from Gazi University in Ankara in 2005. He gained his Ph.D. degree at the same university in 2015. He is working as Association Professor at Department of Machinery and Metal Technologies of Beşiri Organized Industrial Zone Vocational School of Batman University. His main research fields are machinability, cryogenically treatment, MQL in machining, mathematical modelling.

Research Article

Determination of Winding Deformations in Power Transformers by Sweep Frequency Response Analysis and a Sample Field Study

Cenk GEZEGİN¹ , Orhan Cengiz USTA² 

¹Ondokuz Mayıs University, Electrical and Electronic Engineering Department, 55200, Samsun, Istanbul, Türkiye. (e-mail: cenk.gezeGIN@omu.edu.tr).

²10th Regional Directorate, Turkish Electricity Transmission Inc., Samsun, Türkiye (e-mail: orhancengiz.usta@teias.gov.tr).

ARTICLE INFO

Received: Nov., 05. 2023

Revised: Nov., 25. 2023

Accepted: Dec, 22. 2023

Keywords:

Power transformers

Transformer windings

Sweep frequency response analysis

Fault diagnosis

Corresponding author: Cenk GEZEGİN

ISSN: 2536-5010 / e-ISSN: 2536-5134

DOI: <https://doi.org/10.36222/ejt.1386336>

ABSTRACT

Power transformers are expensive pieces of electrical equipment that are used to connect transmission and distribution networks. Power transformers are inspected and tested on a regular basis throughout production, shipment, installation, and operation. There are several ways for determining the mechanical integrity of power transformers. Power transformers are monitored using these diagnostic procedures, and any breakdowns and issues are avoided. Sweep Frequency Response Analysis (SFRA) is an efficient method for determining the condition of the transformer core and windings. To evaluate the state of the transformer winding, SFRA, winding direct current resistance, and winding capacitance tests were done in this study. In the case study, a comprehensive case analysis was done on the SFRA test findings for a 50/62.5 MVA power transformer, and the results were analyzed. The results reveal that the SFRA test finds structural winding problems in transformers with high accuracy.

1. INTRODUCTION

Power transformers are among the most critical and costly components of power transmission infrastructure. It is extremely difficult to repair or replace a transformer promptly following a breakdown. A new transformer is expensive, and it might take a long time to arrive on site. Power transformers operate in a variety of climatic, electrical, and mechanical settings and might be subjected to significant risks. The maintenance function includes monitoring their status and diagnosing faults [1]. As a result, energy transmission firms devote considerable financial resources to transformer failure detection and repair. Correctly executed diagnostics enable for the verification of transformer electrical and mechanical properties, as well as the estimation of approximate maintenance time [2]. Sweep frequency response analysis is a popular diagnostic approach for determining the mechanical system condition of a power transformer. This approach is extremely sensitive to changes in the transformer's mechanical structure. This SFRA test is effective in identifying a wide range of flaws and

malfunctions produced by short circuit currents in transformer windings [3-6].

Power transformers are subjected to various electrical and chemical tests from the time they are manufactured in the factory until they are commissioned in the field. Routine and type tests specified in the standards are applied in factory tests. After the transformers are commissioned, many additional electrical and chemical tests are carried out in order to maintain them for trouble-free operation, to determine the fault conditions in advance and to determine the fault location if it has occurred. These tests are: Capacitance, loss factor, DC insulation resistance, winding ratio, DC resistance, power factor (%PF) and puncture resistance on oil and oil dissolved gas analysis (DGA). Recently, tests such as partial discharge, sweep frequency response analysis and dielectric frequency response, which are called new generation test methods, have also started to be applied in the field. SFRA is a very sensitive method especially in the determination of problems such as short circuit and breakage in transformer windings, deformations and insulation faults in the core, axial displacement and shifts that may occur in windings and core [7].

The study by Hashemnia et al. provides valuable insights into the impact of mechanical faults on transformer frequency response analysis. Their simulation analysis demonstrates that axial and radial faults, in particular, have a noticeable influence on the SFRA signature.

Specifically, these faults manifest as shifts in the anti-resonance and resonance peaks, particularly within the medium to high frequency ranges. This information is crucial for accurately interpreting SFRA data and identifying potential mechanical faults in transformers. The comprehensive table summarizing the sensitivity of transformer SFRA to mechanical faults serves as a useful reference for engineers and technicians involved in transformer maintenance and condition monitoring [8]. Murawwi et al. stated that 2D time frequency distribution plots are superior in interpreting SFRA and are more successful in eliminating noise sources [9]. Devadiga et al., tests investigating the effect of SFRA voltage source size in a laboratory environment showed a significant effect on the SFRA test, which was evident both in the low frequency range and at high frequencies [10]. Almehdhar et al. showed that the SFRA method is more sensitive compared to measuring the short-circuit reactance of windings [11]. Secue et al. considered the optimal number of frequencies in SFRA to be 2000 spot frequencies, which they showed to be sufficient to represent the frequency response and to obtain a satisfactory approximation model [12]. Yang et al. compared two methods for diagnosing winding faults in transformers: pulse wave and sweep frequency response analysis. They designed a step-up transformer and built test platforms to record voltage responses on both the high and low voltage sides and calculate the corresponding transfer functions. They then compared the statistical indicators of the two methods and found that they were similar in their sensitivity to detect winding-ground and winding-interlayer short-circuit conditions [13]. Gahani et al. investigated the use of the SFRA method to diagnose the condition of transformer main mechanical parts such as the core and winding. They used a MV Dyn11 30 MVA transformer and found that symmetrical phase comparison of both high voltage (HV) and low voltage (LV) windings was the best way to find transformer historical SFRA measurement data and interpret SFRA measurement data. Both studies suggest that new methods are being developed to diagnose transformer faults more accurately. These methods could help to prevent transformer failures and improve the reliability of the power grid [14].

Kumar et al. showed that in the frequency region up to 2 kHz, a core magnetization effect will be observed and to get rid of the magnetization effect, it is necessary to demagnetize before starting the SFRA measurement [15]. Murawwi et al.'s research on the effect of terminal connections on SFRA test results for three-winding transformers found that different terminal connections can produce different SFRA responses, which could lead to a misdiagnosis of the transformer's condition. The authors recommend that the same terminal connections be used for a particular test type in order to ensure accurate results. This finding has important implications for the interpretation of SFRA results. SFRA is a diagnostic technique that is commonly used to assess the mechanical integrity of power transformers. By measuring the frequency response of the transformer's windings, SFRA can detect a variety of faults, such as loose connections, cracked windings, and core damage. However, as Murawwi et al. have shown, the interpretation of SFRA results can be complicated by the use of different terminal connections. Different terminal connections can produce different

frequency responses, even for a healthy transformer. This can make it difficult to determine if a particular feature in the SFRA spectrum is due to a fault or simply to the terminal connections. To avoid this problem, Murawwi et al. recommend that the same terminal connections be used for all SFRA tests on a particular transformer. This will ensure that any changes in the SFRA spectrum are due to changes in the transformer's condition, not to changes in the terminal connections. This recommendation is important for all users of SFRA, but it is especially important for utilities that use SFRA to monitor the condition of their transformers in-service. By using the same terminal connections for all SFRA tests, utilities can be confident that the results they are getting are accurate and that they are not missing any potential faults. In conclusion, Murawwi et al.'s research on the effect of terminal connections on SFRA test results is important for the interpretation of SFRA results and for the diagnosis of transformer faults. Their recommendation that the same terminal connections be used for all SFRA tests on a particular transformer is an important step in ensuring the accuracy of SFRA results [16].

This revised text emphasizes the distinct optimal combinations of terminal connections and system functions for SFRA in single-phase and three-phase transformers. It also highlights the positive impact of modifying the terminal configuration on the sensitivity of SFRA measurements for three-phase transformers. Specifically, the study determined that for single-phase transformers, the optimal terminal connection involves connecting the primary and secondary windings in series, while the system function is the transfer function between the voltage across the primary winding and the current in the secondary winding. These findings have significant implications for SFRA measurement practices and the interpretation of SFRA results. SFRA is a diagnostic technique widely used to evaluate the mechanical integrity of power transformers. By analyzing the frequency response of the transformer's windings, SFRA can detect various faults, including loose connections, cracked windings, and core damage. However, as Arumugam's research highlights, the interpretation of SFRA results can be influenced by the choice of terminal connections. Different terminal connections can produce distinct frequency responses, even for a healthy transformer. This can complicate the identification of whether a specific feature in the SFRA spectrum stems from a fault or simply from the terminal connections. To address this challenge, Arumugam's study recommends employing identical terminal connections for all SFRA tests on a particular transformer. This approach ensures that any alterations in the SFRA spectrum are attributable to changes in the transformer's condition, not variations in the terminal connections. This recommendation is crucial for all SFRA users, but it holds particular importance for utilities that utilize SFRA to monitor the condition of their in-service transformers. By adopting consistent terminal connections for all SFRA tests, utilities can gain confidence in the accuracy of their results and minimize the risk of overlooking potential faults. In summary, Arumugam's research on the impact of terminal connections on SFRA test outcomes provides valuable insights for interpreting SFRA results and diagnosing transformer faults. The recommendation to use identical terminal connections for all SFRA tests on a particular transformer represents a significant step towards ensuring the accuracy and reliability of SFRA results. For three-phase transformers, the best terminal connection is to connect the primary windings in wye and the secondary windings in delta, and the system function is the transfer function

between the voltage across one of the primary windings and the current in one of the secondary windings. The study also found that for three-phase transformers, using the neutral connection can improve sensitivity in some cases. However, the use of the neutral connection is not always necessary, and it can sometimes make the measurement more difficult. Overall, the study found that the best way to make SFRA measurements on transformers is to use the terminal connection and system function that is recommended for the specific type of transformer being tested [17].

Kumar et al. identified four fault levels by finding the amplitude differences in specified frequency regions and made predictions about winding and core condition [18]. In a study by Yoon et al., RLC circuit was designed in Matlab™, compared with real SFRA tests and found to be compatible [19]. Brandt et al. considered the condition assessment of a 40 MVA power transformer. This revised text provides a more concise and clear explanation of the diagnostic methods used to identify faults in the study. It also highlights the successful application of inter-winding SFRA measurements to detect axial distortion in the tertiary winding [20]. Statistical indices are preferred for the comparison of SFRA test results on transformers due to their simple and easy application [21, 22]. Recently, statistical indices have been used in the evaluation and interpretation of SFRA results and many studies have been carried out in this regard [23-26, 27, 28]. Comparative studies have been carried out to reveal the characteristics of statistical methods in fault diagnosis and accordingly their performance has been evaluated [22, 29, 30].

In this study, conventional tests and SFRA test, which are among the tests for diagnosing power transformer faults, are discussed and the relationship between the two methods is tried to be explained. The easy detection of winding deformation by SFRA test is evaluated. A case analysis is performed on a power transformer and the results are interpreted.

2. SFRA TEST

For many years, short-circuit impedance (SCI) measurement has been used as a simple technique to detect transformer winding deformation and core displacement. It is still applied in many countries for transformer diagnostics. As a more sensitive method, frequency response analysis for transformers was first introduced by Dick and Erven in 1978 [31]. Frequency domain measurement involves injecting a sinusoidal waveform that sweeps within a predetermined frequency band. The voltage measured at this input terminal is used as a reference signal, and a second voltage signal (response signal) is measured at a second terminal. The frequency response amplitude is the scalar ratio between the response signal (V_{out}) and the reference voltage (V_{input}) (presented in dB) as a function of frequency. The phase of the frequency response is the phase difference between V_{input} and V_{out} (presented in degrees). The response voltage measurement is made across a $50\ \Omega$ impedance. Any coaxial cable connected between the test object terminal and the voltage meter will have a matching impedance. Frequency domain measurement is also a relatively fast and inexpensive technique. As a result, it is becoming increasingly popular for transformer diagnosis.

SFRA has several advantages over traditional methods like SCI measurement, including:

- Higher sensitivity to defects
- Faster measurement times
- Lower cost

As a result, SFRA has become the preferred method for transformer diagnosis in many industries. The SFRA measurement scheme is shown in Figure 1. The reference voltage V_{input} is injected into the test object at terminal 1, and the response voltage V_{out} is measured at terminal 2. The voltage meter measures the amplitude and phase of V_{out} and calculates the frequency response amplitude and phase. The frequency response is then compared to a reference frequency response to identify any changes in the transformer.

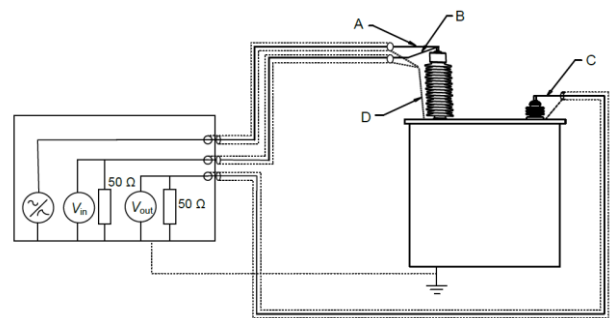


Figure 1. SFRA measurement scheme [32] (A: source, B: reference, C: response, D: earth connection)

The transfer function is the ratio of the measured output voltage V to the reference input voltage V . The amplitude response of the system is calculated from Equation 1 and the phase angle response of the signal is calculated from Equation 2.

$$A_{\text{amplituderresponse}}[\text{dB}] = 20 \log_{10} \left(\frac{V_{\text{out}}(j\omega)}{V_{\text{input}}(j\omega)} \right) \quad (1)$$

$$\varphi_{\text{phaserresponse}}[^\circ] = \tan^{-1} \left(\frac{V_{\text{out}}(j\omega)}{V_{\text{input}}(j\omega)} \right) \quad (2)$$

To ensure all resonance frequencies are detected in the SFRA spectrum, measurements can be taken in the 20 Hz-2 MHz range for all transformers, regardless of their voltage ratings. However, for exceptional transformers or reactors, the upper frequency limit may be increased further. In the case of air core reactors, this limit can be extended up to 20 MHz. SFRA measurements can be used to identify undesirable oscillations or supplementary fluctuations at frequencies above 2 MHz. SFRA measurements conducted during factory testing provide a winding fingerprint [33].

This allows for the analysis of diagnostic data on the physical structure of the transformer viewed as a complex RLC circuit. Changes to the transformer's internal structure impact the passive components in the RLC circuit, thus affecting the transfer function. Modifications to the winding configuration will result in changes to the frequency response analysis. Additionally, it would be beneficial to compare the initial readings of the distributed resistance and capacitance of a coil with the respective readings taken after carrying out

maintenance, repairs, or transportation of the transformer. Three types of comparison should be considered: (1) comparing the current SFRA spectrum with the previous baseline, (2) comparing the current SFRA spectrum with that of a sister (twin) transformer, and (3) comparing the SFRA spectrum between separate phases (utilising winding symmetry) [32, 32-36]. Technical term abbreviations will be defined when first used, and language will remain clear, objective, and value-neutral. Consistent use of technical terminology and simple sentence structures will ensure grammatical accuracy. Adherence to academic conventions and impartial language will also be prioritised.

2.1. SFRA connection types

Four different measurement methods are applied in SFRA measurements. The measurement connections to be made according to star, delta and winding number are specified in both standards [32, 37]. Circuit connections are open-circuit, short-circuit, capacitive inter-winding and inductive inter-winding which are described below and shown in Figure 2. The reference voltage (V_r) and response voltage (V_m) is just showing the point that the measurement should be done in each of the connections.

2.1.1. End to end

In Figure 2(a), the end-to-end measurement is conducted from one end of the transformer winding to the other. Simultaneously, all other transformer terminals remain open. The measuring signal is applied to one end of each winding, and the signal transmitted across the winding is measured at the opposite end. Due to its simplicity and ease of use, this test is more widely employed. Each winding can be tested individually.

2.1.2. End-to-end short circuit

Figure 2(b) illustrates end-to-end short-circuit measurements, which are performed from one end of the high-voltage winding to the other end while the low-voltage winding is short-circuited. However, the neutral connection should not be included in the measurement.

2.1.3. Between capacitive windings

Figure 2(c) demonstrates capacitive inter-winding measurements, which involve applying the voltage (signal/signal) to one end of the winding and measuring the response signal from one end of the other winding of the same phase. Meanwhile, the other terminals are disconnected. Measurements between windings are inherently capacitive.

2.1.4. Inductive inter-winding

Inductive inter-winding measurements are depicted in Figure 2(d). In an inter-winding inductive measurement, the signal is applied to the HV terminal. The response signal is measured at the LV terminal of the same phase. Meanwhile, the other ends of both windings are grounded.

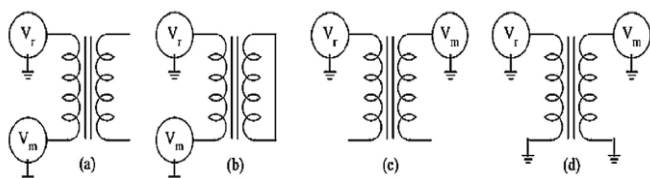


Figure 2. SFRA standard test setups

2.2. SFRA evaluation

2.2.1. Visual assessment

Visual assessment of the SFRA spectrum is a common practice, relying on physical principles and expert knowledge. To interpret SFRA signatures and evaluate transformer condition, the transformer's frequency response spectrum needs to be categorized. For easier classification, the frequency response data can be divided into frequency bands. The European and American standards [32, 33] divide it into four frequency bands, while the Chinese Standard divides it into three frequency bands (low, medium, and high frequency). Transformer characteristics differ across frequency bands, resulting in variations in the SFRA spectrum across each frequency region. Consequently, interpretation depends on the frequency band in which the winding will operate.

The frequency regions in Figure 3, the part indicated by A is up to 2 kHz. This region gives information about the core. The part indicated with B is the 2 kHz-20 kHz frequency region. This region shows the interaction states between the windings. The part indicated by C is the 20 kHz-1 MHz region. This region is mostly affected by inter-winding coupling. D is the frequency region above 1 MHz. This region gives information about winding end connections and earth connections.

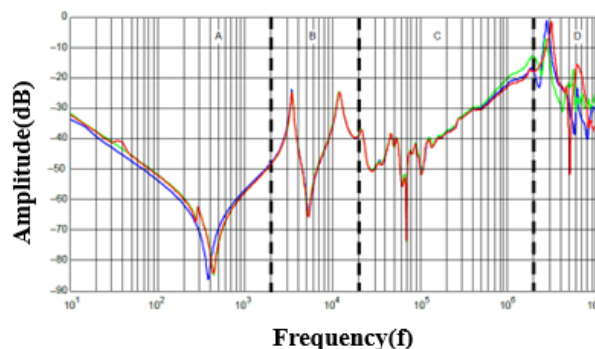


Figure 3. SFRA frequency regions [29]

The condition of the transformer is determined by the comparison between two SFRA measurements, before and after. If there is no deviation between these two results, it is understood that the transformer is sound. In order to detect a malfunction that may occur later in the transformer, it is important for a healthy evaluation that the previous measurement and the next measurement connections, step, measurement types are the same.

If there is no displacement or structural change in the windings inside the transformer, the previous and subsequent test curves overlap exactly. Shifting resonance points or deviations in SFRA magnitude indicate the presence of a fault.

Several factors influence the outcomes of SFRA measurements. The IEC standard recommends conducting the SFRA test solely at the tap position with the highest effective winding count and at the tap position with the tap winding disabled [32]. This ensures consistent and reliable results by minimizing the impact of tap changer positions and tap winding connections. The measurement direction affects the SFRA measurement, especially at high frequencies [32, 38]. SFRA measurement voltage is affected by temperature, connection group, core short circuits, screen between high

winding and low winding, oil, residual magnetization of the core, resistance of test cables [36, 39], humidity [40].

2.2.2. Statistical evaluation

An alternative method for interpreting SFRA data [41] involves employing statistical indicators, such as the correlation coefficient (CC), standard deviation (SD) [42, 21], and the relative factor [43]. These statistical measures provide a quantitative assessment of the similarity between two SFRA spectra, enabling the detection of anomalies and potential transformer faults. The mathematical statistical indicators frequently employed when performing SFRA spectrum analysis can be categorised into two distinct groups. The first group is directly calculated from the SFRA amplitude vector, while the second group is derived from resonance and anti-resonance points [44]. Jianqiang and colleagues assessed the SFRA findings by gauging the extent of transformer winding deformation errors through mathematical measures [44].

Bagheri et al. conducted offline short-circuit impedance and SFRA tests on a transformer that malfunctioned owing to the deformation of the B-phase of its HV winding. The short-circuit impedance values, according to IEEE Standard 62-1995, revealed no winding deformations; however, as per IEC Standard 60076-5, each of the three windings experienced deformations. The statistical indicators CC and SD, derived from comparing fingerprint and measured SFRA data, showed that the phase B winding was deformed, and a third index - the relative factor - indicated its slight deformation. Furthermore, visual inspection of the faulty transformer confirmed that the phase B winding suffered from deformation [41].

CC is defined in equation 3:

$$CC_{(X,Y)} = \frac{\sum_{i=1}^{N_s} X_i Y_i}{\sqrt{\sum_{i=1}^{N_s} [X_i]^2 \sum_{i=1}^{N_s} [Y_i]^2}} \tag{3}$$

The correlation coefficient (CC) is a numerical value ranging from 0 to 1 that quantifies the similarity between two SFRA spectra. It is a useful tool for identifying anomalies and potential transformer faults. A higher correlation coefficient indicates a greater similarity between the two spectra, while a lower correlation coefficient suggests significant differences. X_i and Y_i represent the i -th elements of the fingerprint and the measured SFRA traces, respectively. N_s denotes the number of elements (or samples) In the context of SFRA analysis, the CC is used to compare a measured SFRA spectrum to a reference spectrum. The reference spectrum is typically obtained from a healthy transformer or from a previous measurement of the same transformer. A low CC value indicates that the measured spectrum is significantly different from the reference spectrum, which could be a sign of a transformer fault. The CC is a relatively simple and easy-to-understand metric, but it is important to note that it is not a foolproof indicator of transformer health. Other factors, such as the specific type of transformer and the operating conditions, can also affect the CC value. Therefore, it is important to use the CC in conjunction with other diagnostic techniques, such as visual inspection and analysis of individual resonances, to make a definitive diagnosis of transformer health.

SD is defined by equation 4.

$$SD_{(X,Y)} = \sqrt{\frac{\sum_{i=1}^{N_s} [Y_i - X_i]^2}{N - 1}} \tag{4}$$

CC and SD values have been assessed across different sub-bands in the SFRA spectrum [4], although the frequency range used varies amongst authors. In Nirgude et al.'s investigation, transformer windings were intentionally deformed both radially and axially, achieving physical deformation up to 1%. Subsequently, CC and SD values were computed at each stage. It was established that in any frequency band between 10 Hz and 3 MHz, single CC and SD values are appropriate as indicators of winding deformation. In the context of winding deformation, $|CC| < 0.9998$ and $SD > 1$ are reliable indicators [45].

Winding deformation refers to R_{XY} , a relative factor that is defined in [39].

$$R_{XY} = \begin{cases} 10 & 1 - P_{XY} < 10^{-10} \\ -\log_{10}(1 - P_{XY}) & Other \end{cases} \tag{5}$$

Here, P_{xy} is given by

$$P_{XY} = \frac{\left(\frac{1}{N_s}\sum_{i=1}^{N_s} \left(X_i - \left(\frac{1}{N_s}\sum_{i=1}^{N_s} X_i\right)\right)^2 \left(Y_i - \left(\frac{1}{N_s}\sum_{i=1}^{N_s} Y_i\right)\right)^2\right)}{\sqrt{D_X D_Y}} \tag{6}$$

D_X and D_Y are obtained;

$$D_X = \frac{1}{N_s} \sum_{i=1}^{N_s} \left(X_i - \frac{1}{N_s} \sum_{i=1}^{N_s} X_i\right)^2 \tag{7}$$

$$D_Y = \frac{1}{N_s} \sum_{i=1}^{N_s} \left(Y_i - \frac{1}{N_s} \sum_{i=1}^{N_s} Y_i\right)^2 \tag{8}$$

D_X and D_Y are the standard variances of the fingerprint measured values (X_i) and the last measured (Y_i) data, respectively [37]. Frequency bands for R_{XY} and deformation levels related to R_{XY} values are defined in the Chinese standard [42] and by some other workers [35] (Table 1). These definitions are widely used for SFRA monitoring assessment using the R_{XY} method.

This revised text provides a more concise and clear explanation of the definitions and applications of D_X , D_Y , R_{XY} , and their associated frequency bands in SFRA monitoring assessment. It also highlights the widespread adoption of these definitions in the field.

TABLE I
DEFORMATION LEVELS AND THE CORRESPONDING R_{XY} VALUES [33]

Level	R_{XY} Values
Severe	RDF < 0.6
Lightweight	1.0 > RDF ≥ 0.6 or ROF < 0.6
Less	2.0 > RDF ≥ 1.0 or 0.6 ≤ ROF < 1.0
Normal winding	RDF ≥ 2.0, ROF ≥ 1.0 and RYF ≥ 0.6

DF:1-100 kHz, OF:100-600 kHz, YF: 600 kHz-1MHz.

3. SAMPLE FIELDWORK

This field study concerns a 154/31.5 kV, 62.5 MVA power transformer with connection group YNyn0. The transformer

was manufactured and commissioned in 1993. The power transformer was out of service in 2022 as a result of the operation of the buchholz and thermal protection relay. After the failure, it was determined that the pressure valve was working, the 154 kV bushings were damaged at the mounting flange and porcelain connection points due to the dynamic effect inside the boiler at the time of failure and oil leakage occurred from these points. Flammable gas accumulation occurred in the shutter valve. Since the fault from the medium voltage feeder was very close to the transformer, the fault current flowing on the 154 kV side of the transformer was 1.5 kA in A and C phase and 8.58 kA in B phase.

3.1. Traditional electrical tests

After the transformer was taken out of circuit after the fault, chemical tests of %PF and capacity, DC resistance, excitation current, SFRA and insulating oil were performed on the transformer. As shown in table 2, the %PF and capacity test values of the transformer after the fault, compared to the previous ones, CH capacity value increased by 1.2%, CHL capacity value increased by 16.7% and CL capacity value increased by 6.2%. %PF values CH, CL and CHL increased excessively. Due to the HV/Tank insulation fault, the DC insulation resistor device could not raise the voltage and no measurement could be taken.

TABLE II
TRANSFORMER %PF AND CAPACITY VALUES

Measured	Routine Test		After Failure	
	%PF (20 °C)	capacitance (pF)	%PF (20 °C)	capacitance (pF)
CH+CHL	0.07	10051	345.59	11120.6
CH	0.09	3506.3	0.65	3551.7
CHL	0.07	6544.7	316.62	7639.2
CL+CHL	0.08	19342.1	106.95	21456.3
CL	0.08	12797.2	0,39	13595

The magnetizing current values are shown in Table 3. Magnetizing current measurement could not be made at high voltage B phase.

TABLE III
TRANSFORMER INRUSH CURRENT

Measurement	Routine Test	After Failure
	Inrush (mA)	Inrush (mA)
A-N	35.78	66.53
B-N	26.56	No measurement could be made.
C-N	35.90	66.66

DC resistance measurement results of the transformer at tap 1 are shown in Table 4. After the fault, HV B-N winding DC resistances show a decrease of approximately 5% compared to phases A and C.

TABLE IV
TRANSFORMER DC RESISTANCE VALUES

Level	Measurement	Routine Test	After Fault
		DC (mΩ)	DC (mΩ)
1	A-N	596.05	617.694
1	B-N	596.77	584.742
1	C-N	595.55	616.918

Oil sample was taken from the transformer after the failure. The results of dissolved gas analysis in oil are shown in Table 5. Combustible gas change rates of combustible gases according to the sampling date were calculated according to the IEC-60599 standard and the result values were found to be above the flammable gas range specified in the standard. In addition, the combustible gas amounts exceeded the typical limit values for power transformers specified in the IEC-60599 standard.

TABLE V
DISSOLVED GASES IN TRANSFORMER OIL

GASES	Routine	After fault	Combustible
	Test (ppm) 28.04.2022	(ppm) 02.09.2022	Gas Change Rate (ppm/year)
H2 (Hydrogen)	2	334	522
CH ₄ (Metan)	2	225	351
C ₂ H ₆ (Etan)	0	31	49
C ₂ H ₄ (Ethylene)	0	287	452
C ₂ H ₂ (Acetylene)	0	232	365
CO (Carbon monoxide)	128	186	91
CO ₂ (Carbon dioxide)	876	820	-88

Different techniques, including the Doernenborg ratio method, Rogers ratio method, and Duval triangle method, are utilised for interpreting oil-dissolved gas data in faulty or suspected transformers [46]. It has been noted that any small deviations between the different methods' assessments do not yield highly conflicting findings. Duval triangle1 is applied as a fault interpretation method in power transformers [47]. Figure 4 depicts the flammable gases CH₄, C₂H₄ and C₂H₂ placed inside Duval triangle1. As stated by Duval Triangle 1, the D2 area indicates the presence of high-energy discharges within the transformer. D2 fault can arise from high local energy arcing, jumping, or magnetic flux around closed circuits between two adjacent conductors, metal rings holding the core legs and insulated bolts in the core, between windings, at the junction and tank, between windings and core or due to short circuits in oil [47].

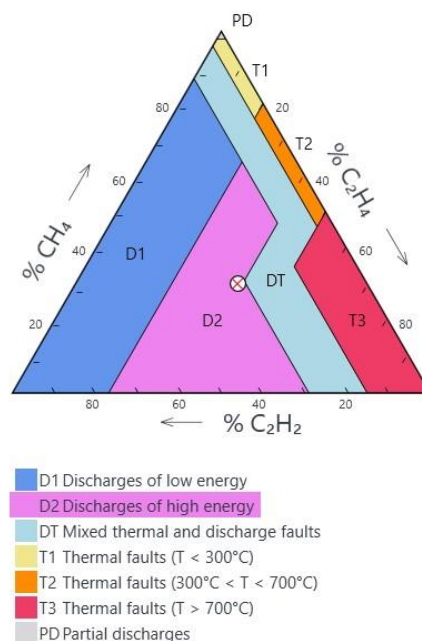


Figure 4. Representation of flammable gases in duval triangle 1

3.2. SFRA measurements

SFRA test was performed by applying 10 V to each winding and measuring the amplitude at 1000 different frequencies. The test was performed with Omicron brand Freneo 800 device. Figure 5 shows high voltage (HV) A-N winding end to end measurement, Figure 6 shows B-N winding HV end to end measurement and Figure 7 shows C-N winding HV end to end measurement.

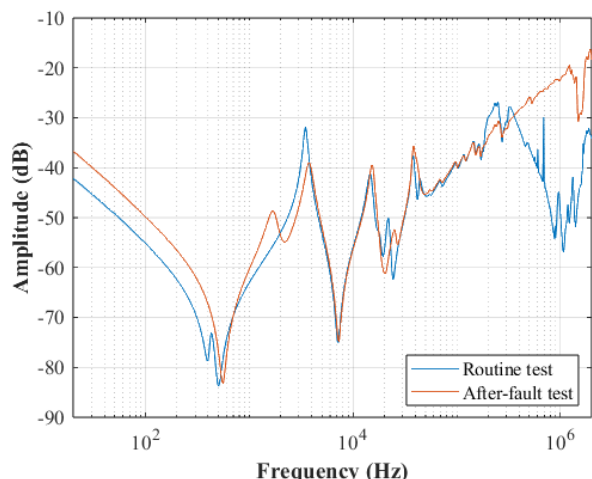


Figure 5. HV A-N SFRA plot

Figure 5 shows deviations at all frequencies in all frequency regions compared to the previous SFRA measurement. In the region up to 2 kHz, it is seen that the core may be damaged. In the region between 2 kHz-20 MHz, it is seen that the windings are deformed. The difference in the last frequency region indicates that the transformer's bushings are cracked and deformed and there is a problem in the conductor connections.

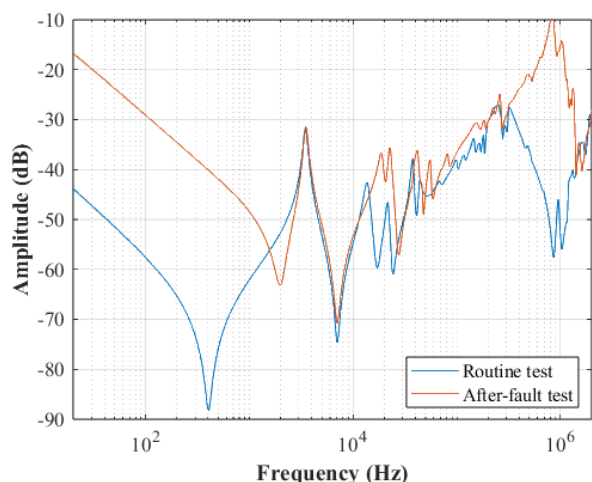


Figure 6. HV B-N SFRA plot

Figure 6 shows deviations at all frequencies in all frequency regions compared to the previous SFRA measurement. In the region up to 2 kHz, it is seen that the core may be damaged and the winding is short-circuited. The difference in the last frequency region indicates that the transformer's bushings are cracked and deformed and there is a problem in the conductor connections.

Figure 7 shows deviations at all frequencies in all frequency regions compared to the previous SFRA measurement. In the region up to 2 kHz, it is seen that the core may be damaged. In the region between 2 kHz-20 MHz, it is seen that the windings are deformed. The difference in the last frequency region indicates that the transformer's

bushings are cracked and deformed and there is a problem in the conductor connections.

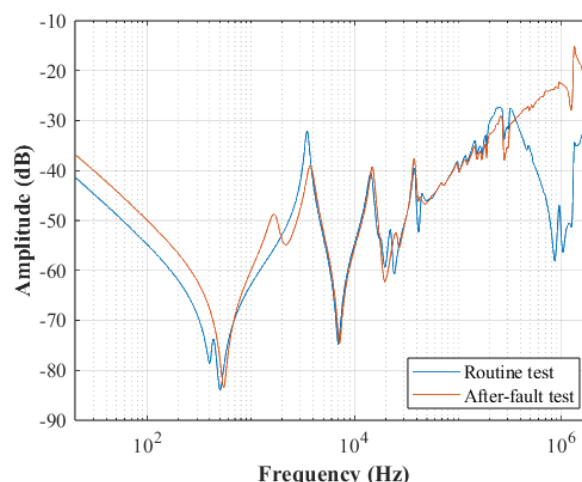


Figure 7. HV C-N SFRA plot

3.3. Statistical results

In this study, CC, SD and relative factor were used as the most common and effective methods for evaluating SFRA test results. The statistical factors calculated according to frequency regions are shown in Table 6.

TABLE VI
CC AND SD VALUES OF SFRA AFTER FAILURE

Frequency Region	CC			SD		
	A phase	B phase	C phase	A phase	B phase	C phase
f ₁	0.9986	0.9625	0.9988	5.5847	27.8710	5.1530
f ₂	0.9982	0.9924	0.9983	3.3418	6.6439	3.2865
f ₃	0.9768	0.9475	0.9733	9.2056	14.2053	9.9284
f ₄	0.9779	0.9093	0.9856	23.6437	18.8954	20.7449
f	0.9829	0.9480	0.9843	10.1749	19.2628	9.6348

TABLE VII
SFRA, R_{xy} VALUES AFTER FAILURE

Frequency Region	R _{xy}		
	A phase	B phase	C phase
Low	1.25	0.49	1.35
Medium	-0.04	-0.11	-0.05
High	-0.25	-0.26	-0.20

4. CONCLUSION

In order to evaluate the SFRA test results of the transformer in terms of fault condition, the measurement results were analyzed in the range of IEC four different frequency zones determined in relation to the possible fault type. For all frequency regions, a difference between the

SFRA measurement results was observed in all frequency regions, especially in the f1, f3 and f4 region in the B phase, also A and C phases showed similar SFRA measurement results. The calculation results of the statistical methods (CC and SD) obtained for the transformer are given in Table 6. The calculated values of the relative factor are shown in table 7. All values in Tables 6 and 7 show that the evaluation indices are above the threshold values. When the results are analyzed; for almost all frequency regions, all available methods (CC, SD and relative factor) indicate the presence of winding deformation.

REFERENCES

- [1] M. Bagheri, Mohammad S. Naderi, T. Blackburn, and B. T. Phung, "Dean-Stark vs FDS and KFT methods in moisture content recognition of transformer," presented at the IEEE International Conference on Power Energy (PECON'12), Kota Kinabalu, Malaysia, Dec 2-5, 2012.
- [2] H. William and P.E. Bartley, "Life cycle management of utility transformer assets," The Hartford Steam Boiler Inspection and Insurance Company, Breakthrough Asset Management for the Restructured Power Industry, Salt Lake City, Utah, 2002.
- [3] A. Paleri et al., "Frequency Response Analysis (SFRA) in power transformers: An approach to locate inter-disk SC fault," presented at 2017 IEEE PES Asia-Pacific Power and Energy Engineering Conference (APPEEC), IEEE, Bangalore, India, 2017.
- [4] J.R. Secue and E. Mombello, "Sweep frequency response Analysis (SSFRA) for the assessment of winding displacements and deformation in power transformers," *Electric Power Research*, vol. 78, no. 6, pp. 1119 – 1128, 2008.
- [5] A.A. Pandya and B.R. Parekh, "Interpretation of sweep frequency response analysis (SFRA) traces for the open circuit and short circuit winding fault damages of the power transformer," *Int. J. Electr. Power Energy Syst.*, vol. 62, pp. 890-896, 2014.
- [6] A.A. Pandya and B.R. Parekh, "Interpretation of sweep frequency response analysis (SSFRA) traces for the multiple winding faults which are practically simulated on the 10 kVA power transformer," *Journal of Electrical and Electronics Engineering*, vol. 9, no. 1, pp. 1-6, 2014.
- [7] M.H. Samimi et al., "Improving the numerical indices proposed for the SFRA interpretation by including the phase response," *Int.J. Electr. Power Energy Syst.*, vol. 83, pp. 585-593, 2016.
- [8] N. Hashemnia et al., "Characterization of transformer SFRA signature under various winding faults," presented at the International Conference on Condition Monitoring and Diagnosis (CMD), Bali-Indonesia, September 23-27, 2012.
- [9] E. Al Murawwi and B. Barkat, "A new technique for a better sweep frequency response analysis interpretation," presented at the 2012 IEEE International Symposium on Electrical Insulation, IEEE, San Juan, PR, USA, June 10-13, 2012.
- [10] A. A. Devadiga et al., "An alternative measurement approach to sweep frequency response analysis (ssfra) for power transformers fault diagnosis," presented at the 2019 54th International Universities Power Engineering Conference (UPEC), IEEE, Bucharest, Romania, Nov. 7, 2019.
- [11] A. Almehdhar et al., "Application of SSFRA method for evaluation of short-circuit tests of power transformers," 2022 International Conference on Diagnostics in Electrical Engineering (Diagnostika), IEEE, Pilsen, Czech Republic, September 6-8, 2022.
- [12] J. Secue et al., "Approach for determining a reliable set of spot frequencies to be used during a sweep frequency response analysis (SSFRA) for power transformer diagnosis," 2008 IEEE/PES Transmission and Distribution Conference and Exposition: Latin America, IEEE, Bogota, Colombia, October 10, 2008.
- [13] Q. Yang, S. Peiyu and C. Yong Chen, "Comparison of impulse wave and sweep frequency response analysis methods for diagnosis of transformer winding faults," *Energies* vol. 1, no. 4, pp. 431, 2017.
- [14] S. Ab Ghani et al., "Condition monitoring of distribution transformer's mechanical parts using sweep frequency response analysis (SSFRA)," *Procedia Engineering*, vol. 68, pp. 469-476, 2013.
- [15] A. Kumar et al., "Core magnetization effect in sweep frequency response analysis for transformer diagnosis," 2015 Second International Conference on Advances in Computing and Communication Engineering, IEEE, Dehradun, India, May 1-2, 2015.
- [16] E. Al Murawwi, R. Mardiana and C.Q Su, "Effects of terminal connections on sweep frequency response analysis of transformers," *IEEE Electrical Insulation Magazine*, vol. 28, no.3, pp. 8-13, 2012.
- [17] Saravanakumar Arumugam, "Experimental investigation on terminal connection and system function pair during SSFRA testing on three phase transformers," *International Journal of Electrical Power & Energy Systems*, vol. 58, pp. 101-110, 2014.
- [18] J. Kumar and U. Prasadr, "Expert system for sweep frequency response analysis of transformer using MATLAB," 2012.
- [19] Y. Yoon et al., "High-frequency modeling of a three-winding power transformer using sweep frequency response analysis," *Energies*, vol. 14, no. 13, pp. 4009, 2021.
- [20] M. Brandt and A. Peniak, "Identification of the power transformer 110/23 kV failure," 2014 ELEKTRO, IEEE, Rajecke Teplice, Slovakia, May 19-20, 2014.
- [21] V. Behjat and M. Mahvi, "Statistical approach for interpretation of power transformers frequency response analysis results," *IET Sci. Meas. Technol.*, vol. 9, no. 3, pp. 367-375, 2015.
- [22] N. Wesley et al., "Evaluation of statistical interpretation methods for frequency response analysis based winding fault detection of transformers," *IEEE International Conference on Sustainable Energy Technologies (ICSET)*, Hanoi-Vietnam, pp. 36-41, November 14-16, 2016.
- [23] M.F.M Yousof et al., "Using absolute average difference (DABS) in interpreting the frequency response of distribution transformer," *IOP Conf. Ser.: Mater. Sci. Eng.*, vol. 226, no. 1, pp. 1-9, 2017.
- [24] M.F.M Yousof, C. Ekanayake, T.K. Saha, "Frequency response analysis to investigate deformation of transformer winding," *IEEE Trans. Dielectr. Electr. Insul.*, vol. 22, pp. 2359-2367, 2015.
- [25] A.S. Murthy et al., "Investigation of the effect of winding clamping structure on frequency response signature of 11 kV distribution transformer," *Energies*, vol. 11, no. 9, pp. 1-13, 2018.
- [26] S.M. Saleh, S.H. El-Hoshy and O.E. Gouda, "Proposed diagnostic methodology using the cross-correlation coefficient factor technique for power transformer fault identification," *IET Electr. Power Appl.*, vol. 11, no. 3, pp. 412-422, 2017.
- [27] Bigdeli M., Azizian D., Gharehpetian G.B., Detection of probability of occurrence, type and severity of faults in transformer using frequency response analysis based numerical indices, *Measurement*, 168, 108322, 1-11, 2021.
- [28] Ni, Jianqiang & Zhao, Zhongyong & Tan, Shan & Chen, Yu & Yao, Chenguo & Tang, Chao. (2020). The actual measurement and analysis of transformer winding deformation fault degrees by FRA using mathematical indicators. *Electric Power Systems Research*. 184. 106324. 10.1016/j.epsr.2020.106324.
- [29] M. Tahir, S. Tenbohlen and M.H. Samimi, "Evaluation of numerical indices for objective interpretation of frequency response to detect mechanical faults in power transformers," presented at the 21st International Symposium on High Voltage Engineering, Budapest-Hungary, August 26- 30, 2019.
- [30] E. Rahimpour, M. Jabbari and S. Tenbohlen, "Mathematical comparison methods to assess transfer functions of transformers to detect different types of mechanical faults," *IEEE Trans. Power Delivery*, vol. 25, pp. 2544-2555, 2010.
- [31] E. P. Dick and C. C. Erven, "Transformer diagnostic testing by frequency response analysis," *IEEE Trans. Power App. Syst.*, vol. 97, no. 6, pp. 2144-2150, 1978.
- [32] IEC 60076-18 Ed.1: Power Transformers - Part 18, "Measurement of Frequency Response," International Electrotechnical Commission, Geneva, Switzerland, 2012.
- [33] A.A. Siada, 2018, "IET power transformer condition monitoring and diagnosis," *Energy Engineering*, ISBN-13: 978-1-78561-254-1.
- [34] Odođlu H, "Transformer and shunt reactor experiments", EMO Publications, 2012.
- [35] A. Kraetge, M. Kruger and P. Fong, "Frequency response analysis— Status of the worldwide standardization activities," presented at the 2008 International Conference on Condition Monitoring and Diagnosis. IEEE, Beijing, China, April 21-24, 2008.
- [36] CIGRE, "Mechanical-condition assessment of transformer windings using frequency response analysis (SFRA)", Technical Brochure, 2008.
- [37] IEEE Std C57.149™-2012, "IEEE guide for the application and interpretation of frequency response analysis for oil-immersed transformers," New York/USA: IEEE Power Engineering Society, March 8, 2013.
- [38] K. Selim et al., "The use of statistical methods in the evaluation of power transformer faults with frequency response analysis," *Journal of The Faculty of Engineering and Architecture of Gazi University*, 2022.

- [39] R.K. Senobari, J. Sadeh and H. Borsi, "Frequency response analysis (SFRA) of transformers as a tool for fault detection and location: a review," *Electr. Power Syst. Res.*, vol. 155, pp. 172-183, 2018.
- [40] A.A. Reykherdt and V. Davydov "Case studies of factors influencing frequency response analysis measurements and power transformer diagnostics," *IEEE Electr. Insul. Mag.*, vol. 27, no. 1, 22-30, 2011.
- [41] M. Bagheri et al., "Frequency response analysis and short-circuit impedance measurement in detection of winding deformation within power transformers," *IEEE Electrical Insulation Magazine*, vol. 29, no. 3, pp. 33-40, 2013.
- [42] The Electric Power Industry Standard of People's Republic of China, "Frequency response analysis on winding deformation of power transformers," *Std. DL/T911-2004, ICS 27.100, F24, Document No. 15182-2005*, June 2005.
- [43] M Yousof et al., "The influence of data size in statistical analysis of power transformer frequency response," presented at the 2016 IEEE International Conference on Power and Energy (PECon). IEEE, Melaka, Malaysia, November 28-29, 2016.
- [44] J. Ni et al., "The actual measurement and analysis of transformer winding deformation fault degrees by SFRA using mathematical indicators," *Electric Power Systems Research*, vol. 184, pp. 106324, 2020.
- [45] P.M. Nirgude, et al., "Application of numerical evaluation techniques for interpreting frequency response measurements in power transformers," *IET Science, Measurement & Technology*, vol. 2, no. 5 pp. 275-285, 2008.
- [46] H. C. Sun, Y. C. Huang and C. M. Huang, "A review of dissolved gas analysis in power transformers," *Energy Procedia*, vol. 14, pp. 1220-1225, 2012.
- [47] IEC, "Mineral oil-impregnated electrical equipment in service –guide to the interpretation of dissolved and free gases analysis," *IEC Standard 60599*, 2015.

BIOGRAPHIES

Cenk GEZEGİN was born in Amasya in 1982. He graduated from Kocaeli University Electrical Education Department in 2002. He received his M.Sc. and Ph.D. degrees from Ondokuz Mayıs University, Department of Electrical and Electronics Engineering in 2006 and 2018, respectively. From 2007 to 2020, he served as Head of the Electricity and Energy Department of Vocational School of Amasya University, Department of Technical Sciences. He has been working as an Assist. Prof. in the Department of Electrical and Electronics Engineering at Ondokuz Mayıs University since 2020. His main research interests include hotspots in transformers, technical and economic analysis of renewable energy systems, and power quality in electrical networks.

Orhan Cengiz USTA was born in Trabzon in 1981. He received his bachelor's and master's degrees in electrical and electronic engineering from Karadeniz Technical University in 2003 and 2010 respectively. He has been working as Chief Test Engineer at Turkish Electricity Transmission Corporation since 2007. His working areas are: power transmission lines, power transformers, reactors, autotransformers, high voltage switchgear testing.